Computational Analyses of the Molecular Behaviour of Membrane Proteins

Oakes, Victoria

Award date:
2019

Awarding institution:
University of Bath

Computational Analyses of the Molecular Behaviour of Membrane Proteins

Oakes, Victoria

Award date:
2019

Awarding institution:
University of Bath

Computational Analyses of the Molecular Behaviour of Membrane Proteins

Victoria Oakes

Under the supervision of Prof Carmen Domene

A thesis submitted for the degree of Doctor of Philosophy University of Bath

Department of Chemistry

15 February 2019

Contents

Acknowledgements

Firstly, I would like to thank my supervisor Professor Carmen Domene for her support during my time at King's College London and the University of Bath. I could not have achieved as much without her motivation and advice. She has also provided me with countless opportunities to travel abroad, for which I am grateful.

I would like to thank BBSRC and Pfizer Neusentis for providing me with a CASE studentship, and Dr David Pryde (from Pfizer Neusentis) for his guidance in the first year of my PhD. I would also like to thank Dr Simone Furini for providing me with additional supervision and technical support during my PhD and hosting me for a project at his institution, in the beautiful city of Siena. I would also like to thank previous members of the Domene group for their help, support over the course of my PhD. In particular, Leonardo Darré for his help in the first few months.

Next, I would like to thank my family for their support, especially my Uncle who provided me with an incredible place to live in London. I am also very thankful for amazing friends from Halesowen, Sheffield, London, and now my final year here in Bath, who have supported and encouraged me throughout. If I thanked everyone personally, I would end up writing another thesis! Finally, I would like to thank Mike for his continuous love and encouragement.

Abstract

Membrane proteins are proteins which are embedded in (integral membrane proteins) or interact with (peripheral membrane proteins) the plasma membrane. Membrane proteins are responsible for a wide-range of processes, including transport, signalling and enzymatic reactions. Ion channels are an important class of membrane protein which enable the passive diffusion of ions across the membrane. G-protein coupled receptors are another class of membrane protein which propagate chemical signals between the cell interior and exterior. There is substantial interest in understanding the molecular behaviour of such membrane proteins in a physiological and pharmaceutical context, in order to discern how they function and how they can be regulated when they function incorrectly. Simulation methods, such as classical molecular dynamics, are can be employed for this purpose. This thesis details the use of molecular dynamics simulations, and related simulation methods, to analyse phenomena related to membrane transport by ion channels and G-protein coupled receptors.

Principally, research presented in this thesis has unveiled several novel aspects concerning the molecular behaviour of K^+-channels. The size and dynamics of openings in the surface of ion channels, known as fenestrations, has been assessed in several K^+-channels to delineate their potential as drug access pathways. By analyses of the archetypal K^+-channel KcsA, a bacterial K^+ -channel, and an atypical K^+-channel, TWIK-1, from the two-pore domain K^+-channel family, specific residues in the domain of the selectivity filter have been shown to be important in maintaining the structural stability of the selectivity filter and/or facilitating quintessential conduction processes. Moreover, the molecular mechanism pairing the dynamics of the KcsA selectivity filter and phospholipid molecules bound on the channel surface has been outlined.

Simulation methods have also been applied to structures of other membrane proteins, which have been recently resolved at high-resolution, by either cryo-electron microscopy or X-ray crystallography. The interfacial regions between the transient receptor potential vanilloid channel 1 (TRPV1) and several protein assemblies have been predicted. Furthermore, cholesterol-phospholipid and cholesterol-protein complexes have been characterized, in order to assess the functional effect of membrane cholesterol on the activation state on the 5-HT_{1B} and 5-HT_{2B} G-protein coupled receptors.

List of Abbreviations

4-AP	4-aminopyridine
5-HT	5-hydroxytryptamine (Serotonin)
5-HT$_{1B}$	5-hydroxytryptamine Receptor Subtype 1B
5-HT$_{2B}$	5-hydroxytryptamine Receptor Subtype 2B
ABF	Adaptive Biasing Force
AMOEBA	Atomic Multipole Optimized Energetics for Biomolecular Simulation
ARD	Ankyrin Repeat Domain
ATP	Adeonisine Triphosphate
BPTI	Bovine Pancreatic Trypsin Inhibitor
BR	Bottleneck Radius
CARC	Inverted form of the CRAC Motif
CCM	Cholesterol Consensus Motif
CFA	Complete Freund's Adjuvant
CG	Coarse-Grain
CGenff	CHARMM General Force Field
CHARMM	Chemistry at HARvard Macromolecular Mechanics
CHEq	CHARMM Charge Equilibration
CMAP	Correction Map
CPMD	*Car–Parrinello* Molecular Dynamics
CRAC	Cholesterol Recognition Amino Acid Consensus
CV	Collective Variables
DDM	*n*-Dodecyl β-D-maltoside
DFT	Density Functional Theory
DkTx	Double Knot Toxin
DMPC	1,2-dimyristoyl-sn-glycero-3-phosphocholine
DNA	Deoxyribonucleic acid
DOPC	1,2-dioleoyl-sn-glycero-3-phosphocholine
DPPC	1,2-dipalmitoyl-sn-glycero-3-phosphocholine
DRG	Dorsal Root Ganglion
ECL1	Extracellular Loop 1
ECL2	Extracellular Loop 2
ECL3	Extracellular Loop 3
ECS	Extracellular Surface
eIF2α	Eukaryotic Initiation Factor 2
EOM	Equations of Motion
ERK1,2	Extracellular Signal–Regulated Kinase 1,2
FEP	Free Energy Perturbation
FF	Forcefield
gA	Gramicidin A
GABA	Gamma-aminobutyric acid
GIRK	GPCR-activated Kir
GlyR	Glycine Receptor
GpA	Glycophorin A
GPCRs	G-protein Coupled Receptors
GROMACS	Groningen Machine for Chemical Simulations
H-bond	Hydrogen bond
HEKA	Human Epidermal Keratinocytes, adult
HEPES	4-(2-hydroxyethyl)-1-piperazineethanesulfonic acid
HSQC	Heteronuclear Single Quantum Correlation spectroscopy
IF$_C$	Inward-Facing Closed
IFN-γ	Interferon-γ
IF$_O$	Inward-Facing Open
IKK	IκB Kinase
IL-1β	Interleukin 1β
JNK	C-Jun N-terminal Kinases
K$_{2P}$	Two-pore Domain Potassium Channel
K$_{IR}$	Inwardly Rectifying Potassium Channel

KO	Knock-out
K_V	Voltage-Gated Potassium Channel
LC-MS	Liquid Chromatography-Mass Spectrometry
LeuT	Leucine Transporter
LJ	Lennard-Jones
MAPKs	Mitogen Activated Protein Kinases
MD	Molecular Dynamics
MES	2-(N-morpholino)ethanesulfonic acid
MM	Molecular Mechanics
nAChR	Nicotinic Acetylcholine Receptor
NAMD	Nanoscale Molecular Dynamics
NF-κB	Nuclear Factor-κB
NMA	N-methylacetamide
NMR	Nuclear Magnetic Resonance
NSS	Neurotransmitter Sodium Symporter
OF_O	Outward-Facing Open
OF_O	Outward-Facing Closed
OPLS	Optimized Potential for Liquid Simulations
OXTR	Oxytocin Receptor
P1	Pore Domain 1
P1	Pore Domain 2
PA/POPA	1-palmitoyl-2-oleoyl phosphatidic acid
PBC	Periodic Boundary Conditions
PC/POPC	1-palmitoyl-2-oleoyl-sn-glycero-3-phosphocholine
PG/POPG	Phosphatidylglycerol
PKA	Protein Kinase A (cAMP-dependent)
PKC	Protein Kinase C
PKR	Protein Kinase R
PME	Particle Mesh Ewald
PMF	Potential of Mean Force
PS/POPS	1-palmitoyl-2-oleoylphosphatidylserine
PVN	hypothalamic paraventricular
QM	Quantum Mechanics
QM/MM	Quantum Mechanics/Molecular Mechanics
QA	Quaternary Ammonium
RMSD	Root-Mean-Square Deviation
RNA	Ribonucleic acid
SASA	Solvent-Accessible Surface Area
S_{CD}	Deuterium Order Parameter
SF	Selectivity Filter
siRNA	Small Interfering RNA
SMD	Steered Molecular Dynamics
SON	Supraoptic
TALK	Two-pore Domain Alkaline Activated Potassium Channel
TASK	Two-pore Domain, Acid-sensitive Potassium Channel
TBA	Tetrabutylammonium
TEA	Tetraethylammonium
THIK	Two-Pore Domain Halothane Inhibited Potassium Channel
TM	Transmembrane Helix
TM	Transmembrane Helix
TNF-α	Tumor Necrosis Factor-α
TREK	TWIK-related Potassium Channel
TRESK	TWIK-Related Spinal Cord Potassium Channel
TRP	Transient Receptor Potential
TRPA	Transient Receptor Potential Ankyrin
TRPC	Transient Receptor Potential Canonical
TRPM	Transient Receptor Potential Melastatin
TRPML	Transient Receptor Potential Mucolipin
TRPN	Transient Receptor Potential No Mechanoreceptor

TRPP	Transient Receptor Potential Polycystic
TRPV	Transient Receptor Potential Vanilloid
TRPV1	Transient Receptor Potential Vanilloid Channel 1
TWIK	Two pore Domain Weak Inward rectifying Potassium Channel
US	Umbrella Sampling
V1aR	Vasopressin 1a Receptors
VGIC	Voltage-Gated Ion Channel
VMD	Visual Molecular Dynamics
VR1	Vanilloid Receptor 1
vSGLT	Sodium/Galactose Transporter from Vibrio Parahaemolyticus
WHAM	Weighted Histogram Analysis Method
WT	Wild-type
β_1AR	β1 Adrenergic Receptor
β_2AR	β2 Adrenergic Receptor

Part I: Introduction

1 Structural Biology of Membrane Proteins

1.1 Introduction

Biological membranes are fundamental components of life, which compartmentalise cells and regulate transport to and from the inside of cells. The plasma membrane is essentially a phospholipid bilayer, also containing proteins, cholesterol, and other lipid molecules. Proteins associated with the membrane, known as integral membrane proteins, perform a diverse range of biological functions. Channels and transporters, for example, enable the transport of solutes which cannot pass through the hydrophobic core. Membrane proteins also act as receptors (involved in cell signalling), enzymes (catalysing chemical process), and are critical structural constituents of the membrane. The dynamic interrelationship between membrane proteins and their environment has retarded experimental efforts to determine the three-dimensional structure of membrane proteins by X-ray crystallography.[1] High-resolution crystal structures of membrane proteins first materialised in 1985.[2] However, significant advancements in X-ray crystallography and nuclear magnetic resonance (NMR) spectroscopic techniques, as well as the emergence of novel protocols for structure determination, such as cryo-electron microscopy, has resulted in almost exponential increases in the number of membrane protein structures available in the years since.[3,4]

1.2 Ion channels

One class of membrane proteins are ion channels. Ion channels are responsible for the passive diffusion of ions across the plasma membrane and are therefore critical to regulation of the membrane potential. In general, ion channels open and close in response to a wide-range of stimuli, such as membrane potential in voltage-gated ion channels or ligand-binding in ligand-gated ion channels. K^+-channels are arguably the most widely studied family of ion channels, which permit the influx and efflux of K^+ ions into or out of the cell. The ability of K^+-channels to conduct K^+ ions at a rate close to diffusion with tremendous selectivity has been studied experimentally for more than half a century; early insights include Hodgkin and Keynes' suggested 'knock-on' mechanism of conduction, associated with concerted transitions of individual ions through a narrow pore,[5] several proposed theories of ion selectivity, concerning the size and hydration free energy of ions,[6-8] and the identification of a conserved sequence (TVGYG) responsible for ionic selectivity, now known as the selectivity filter.[9,10]

Taking into account structural and functional attributes, three main classes of K^+ channel have currently been characterised: voltage-gated (K_V), inwardly rectifying (K_{IR}) and two-pore domain

(K_{2P}) K^+ channels.[11] The pore domain is the most highly conserved region of K^+ channel in these major K^+ channel families. Channels in K_{IR} family, from subfamilies K_{IR}1-7, permit inward currents in favour of outward currents, against the electrochemical gradient, which supports the maintenance of the resting potential.[12] The K_V channel family, which currently span subfamilies Kv1-9, display outward rectification and are responsible for restoring the resting potential following depolarization during the action potential.[13] K_{2P} channels generate leak potassium currents, by weak inward currents.[14,15] Six subfamilies of K2P channels have been identified to date (TWIK, TREK, TALK, TASK, THIK, and TRESK). Impairment of K^+-channels are the cause of several cardiac, kidney and neurological disorders, such as Bartters syndrome, long QT syndrome and episodic ataxia.[16]

The first X-ray crystal structure of a bacterial K^+-channel (KcsA from *Streptomyces lividans*) revealed the structure of the conserved pore domain (Figure 1A).[17] The tetrameric pore domain is composed of four identical subunits, each containing two transmembrane α-helices connected by a pore loop. The pore loop contains an additional α-helix and the selectivity filter, which exhibits a cage-like structure of adjacent binding sites that can hold dehydrated K^+ ions in single file. Directly underneath the selectivity filter, a water-filled cavity enables hydrated K^+ ions to traverse the membrane hydrated. Considering the lack of structures from eukaryotic channels and the high homology between the pore domain of KcsA and its eukaryotic counterparts, the KcsA channel has emerged as the conventional model to investigate various phenomena in K^+-channels. Well-known ideologies concerning ion permeation, selectivity (the process in which the channel discriminates between ionic species) and gating at both the intracellular (where the transmembrane helices occlude ion permeation) and the extracellular (where the selectivity filter occlude ion permeation) sides of the membrane, have been derived from KcsA.

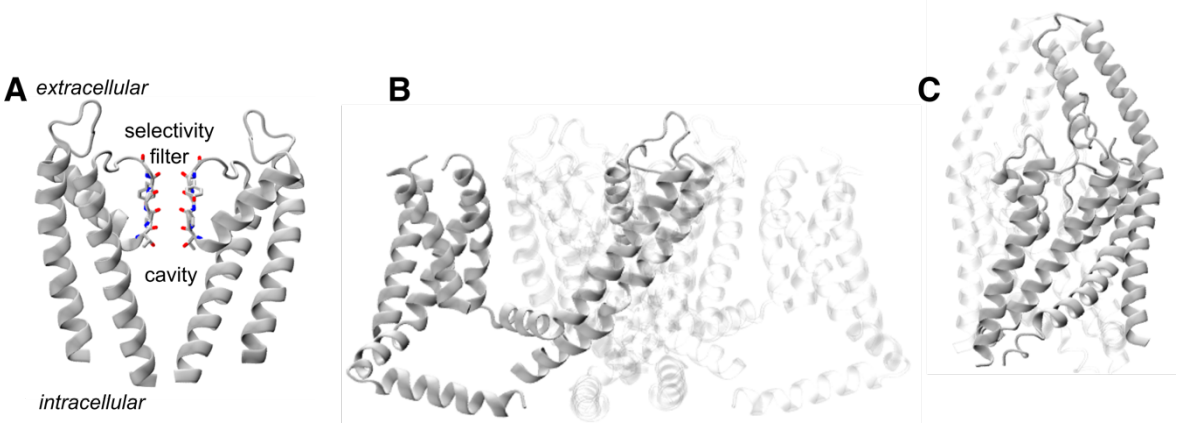

Figure 1. Transmembrane domain structures of (A) KcsA,[17] (B) Kv1.2[18] and (D) TWIK-1.[19] In (A), two subunits are shown for clarity; oxygen, nitrogen and carbon atoms in the selectivity filter are coloured red, blue and grey, respectively. In (B), a single subunit is shown in grey, and the remaining three are transparent.

Nowadays, representative structures from all K^+-channel families are available. K_{IR} channels contain a conserved pore-domain, with two transmembrane α-helices, and a substantial intracellular domain, first demonstrated by the structure of KirBac1.1 in 2003 (Fig. 1A).[20] The framework of channels in the K_V family, was delineated by the crystal structures of prokaryotic K_VAP[21] and eukaryotic $K_V1.2$ channels, in 2003 and 2005 respectively.[18,22] Here, the transmembrane domain of each subunit contains six transmembrane α-helices; two helices constitute the canonical pore domain, with the remaining four helices forming the regulatory voltage-sensor domain, connected to the by an α-helical linker (Fig. 1B). A 'domain swap' assembly is observed whereby the voltage-sensor domain of one subunit interacts with the transmembrane domain of an adjacent subunit. Structural determination of K_{2P} channels lagged behind both K_{IR} and K_V channels, finally accomplished in 2012 with the structures of TWIK-1[19] and TRAAK.[23] In this case, the pore domain is assembled as a 'dimer of dimers', with each subunit containing the equivalent of two monomers typical of the K^+ channel pore domain (Fig. 1C). The exact arrangement of this dimer has several consequences for the permeation pathway of K_{2P} channels: 1) the cytoplasmic gate is permanently open, 2) a broad extracellular cap restricts ion diffusion at the extracellular side and 3) the selectivity filter is constituted of two non-identical sequences. These divergent structural features have been linked to distinct functional properties of the K_{2P} channel family.

The field of membrane protein structure determination has also been thriving in other families of ion channels. Structures have been reported for Na^+-selective channels and transient receptor potential (TRP) channels, to name a few. Recent developments concerning Na^+-channels are reviewed in Appendix A. TRP channels are non-selective ion channels which have received notable interest in recent years, from both structural and functional perspectives. Seven distinct mammalian TRP channel families are known at present: transient receptor potential ankyrin (TRPA), canonical (TRPC), melastatin (TRPM), mucolipin (TRPML), no mechanoreceptor (TRPN), polycystic (TRPP) and vanilloid (TRPV) families.[24] TRP channels generate ionic currents in response to a broad-range of chemical and physical stimuli,[25] such as temperature, membrane potential, membrane composition, extracellular pH, intracellular Ca^{2+} concentration and several vanilloid agonists (capsaicin, for example) and animal toxins.[26] In line with this, TRP channels participate on a molecular level in a plethora of physiological mechanisms, including our response to pain, sight, hearing, touch, smell and taste. A multitude of channelopathies can also arise from faulty TRP channels;[27] in fact, several hereditary diseases have been attributed to defects in TRP genes. Accordingly, understanding the molecular behaviour of these channels are important to understand human physiology, and aid relevant pharmaceutical efforts.

Crystallographic attempts to reveal the architecture of a TRP channel to near-atomic resolution did not achieve success until 2016, posterior to a landmark 2013 study,[28] where single particle cryo-electron microscopy was utilized to resolve the structure of TRPV1, the prototypical member of the vanilloid subfamily.[29] The TRPV1 structure revealed a transmembrane

architecture analogous to those observed in voltage-gated ion channels, with each subunit containing six transmembrane helices. The pore loop exists between the pore-domain helices, containing the selectivity filter which is specific to TRP channels (GMGD in TRPV1). Ankyrin repeat domains (ARDs) and a number of transmembrane connector domains (membrane-proximal domain, pre-S1 helix, a TRP domain and a C-terminal domain) form the intracellular domain. The resolution of several TRPV1 structures in distinct activation states, has provided information regarding gating in the TRP channel family.[30] Similar to K^+-channels, conduction in TRPV1 can be obstructed at either the selectivity filter or the C-terminal end of the transmembrane helices. Structures of TRPA[31] and TRPP channels,[32] in addition to TRPV channels,[33] have since been resolved using the same technique. TRP channels are homotetramers, consisting of a transmembrane domain and a cytosolic domain formed from the N- and C- termini.

1.3 G-Protein Coupled Receptors

Another class of membrane protein that has been studied from a structural viewpoint and will be examined in this thesis are G-protein coupled receptors (GPCRs). GPCRs are membrane proteins which initiate intracellular signalling mechanisms, following recognition of extracellular signalling molecules. This is done via coupling to intracellular heterotrimeric G-proteins following conformational changes in the transmembrane domain of the receptor. GPCRs respond to hormones, neurotransmitters, and sensory stimuli, in a subtype-dependent manner. Signal transduction in GPCRs underlies most processes required for basic physiological function in eukaryotic organisms, from sensory processes to mechanisms critical for most organ systems.[34] Incorrect functioning of GPCRs can therefore contribute to numerous ailments, including neurological disorders, cardiac failure, cancer and diabetes. Appropriately, GPCRs represent a major pharmaceutical target.[35,36]

Figure 2. Transmembrane domain structures of the 5-HT_{1B} receptor structure, which is representative of the architecture of the GPCR superfamily.[37,38]

The structure of the conserved seven α-helical arrangement of the transmembrane domain in class A GPCRs was first revealed by the crystal structure of light sensitive pigment, rhodopsin.[2] Structures are now available for various types of 'rhodopsin-like' class A receptors, including but not limited to adenosine, adrenergic, chemokine, cannabinoid, dopamine, muscarinic acetylcholine, neurotensin and opioid receptors. The multifarious structures of GPCRs have disclosed details of the molecular interactions determining binding of ligands, membrane components and G-protein coupling, in addition to the activation process which connects all these features. Recently, the structures of several members of the serotonin (5-HT) receptor family, the largest family of GPCR's (5-HT_{1-7} subfamilies, with the exception of 5-HT_3, a ligand-gated ion channel), have been resolved (Figure 2). 5-HT receptors have specifically been associated with neurological conditions, such as Alzheimer's disease[39] and schizophrenia,[40] and therefore represent a putative drug target.

1.4 Research Overview

The availability of high-resolution structures has motivated the investigation of membrane protein structural dynamics via simulation methods. In the broadest terms, the work presented in this thesis pertains to this. In section 2, an outline of the theory and practicalities of computational analyses of membrane proteins is provided (section 2.2), alongside relevant applications to illustrate the scope of contemporary research in the field of membrane protein simulations (section 2.3). The research presented in this thesis poses the following questions, in line with this:

- How does the selectivity filter of ion channels regulate ion conduction?
- How do certain entities (i.e. drug-like compounds, constituents of the plasma membrane, peptides/proteins) interact with membrane proteins, inciting a functional response?

The first question is addressed in the context of K^+-channels, by examining the selectivity filter of several channels. The second question is approached from several directions. In the first instance, the presence of drug-binding cavities in K^+-channels are hypothesized and assessed entirely by molecular dynamics simulations. Thereafter, a combined computational-experimental approach is utilized. Accordingly, several types of ion channels and membrane receptors are investigated, considering the availability of structural information and experimental data from our collaborators. In Part II, published and draft manuscripts are presented, organized by protein type: TWIK-1 channel (section 3), KcsA channel (section 4), TRPV1 channel (section 5) and 5-HT_{1B}/5HT_{2B} receptors (section 6).

1.5 References

(1) Carpenter, E. P.; Beis, K.; Cameron, A. D.; Iwata, S. Overcoming the challenges of membrane protein crystallography. *Current Opinion in Structural Biology* **2008,** *18* (5), 581.

(2) Deisenhofer, J.; Epp, O.; Miki, K.; Huber, R.; Michel, H. structure of the protein subunits in the photosynthetic reaction center of rhodopseudomonas-viridis at 3a resolution. *Nature* **1985,** *318* (6047), 618.

(3) Ishchenko, A.; Wacker, D.; Kapoor, M.; Zhang, A.; Han, G. W.; Basu, S.; Patel, N.; Messerschmidt, M.; Weierstall, U.; Liu, W.et al. Structural insights into the extracellular recognition of the human serotonin 2B receptor by an antibody. *P. Natl. Acad. Sci. USA* **2017,** *114* (31), 8223.

(4) Rawson, S.; Davies, S.; Lippiat, J. D.; Muench, S. P. The changing landscape of membrane protein structural biology through developments in electron microscopy. *Mol. Memb. Biol.* **2016,** *33* (1-2), 12.

(5) Hodgkin, A. L.; Keynes, R. D. The potassium permeability of a giant nerve fibre. *The J. Physiol.* **1955,** *128* (1), 61.

(6) Eisenman, G. Cation Selective Glass Electrodes and their Mode of Operation. *Biophys. J.***1962,** *2* (2 Pt 2), 259.

(7) Eisenman, G.; Horn, R. Ionic selectivity revisited: The role of kinetic and equilibrium processes in ion permeation through channels. *J. Memb. Biol.* **1983,** *76* (3), 197.

(8) Bezanilla, F.; Armstrong, C. M. Negative conductance caused by entry of sodium and cesium ions into the potassium channels of squid axons. *J. Gen. Physiol.* **1972,** *60* (5), 588.

(9) Smart, O. S.; Goodfellow, J. M.; Wallace, B. A. The pore dimensions of gramicidin A. *Biophys. J.***1993,** *65* (6), 2455.

(10) Heginbotham, L.; Lu, Z.; Abramson, T.; MacKinnon, R. Mutations in the K+ channel signature sequence. *Biophys. J.***1994,** *66* (4), 1061.

(11) Buckingham, S. D.; Kidd, J. F.; Law, R. J.; Franks, C. J.; Sattelle, D. B. Structure and function of two-pore-domain K^+ channels: contributions from genetic model organisms. *Trends Pharmacol. Sci.* **2005,** *26* (7), 361.

(12) Bhave, G.; Lonergan, D.; Chauder, B. A.; Denton, J. S. Small-molecule modulators of inward rectifier K^+ channels: recent advances and future possibilities. *Future Med. Chem.* **2010,** *2* (5), 757.

(13) MacKinnon, R. Potassium channels. *FEBS Letters* **2003,** *555* (1), 62.

(14) Chen, H.; Zuo, D.; Zhang, J.; Zhou, M.; Ma, L. Classification of 2-pore domain potassium channels based on rectification under quasi-physiological ionic conditions. *Channels* **2015,** *8* (6), 503.

(15) Rajan, S.; Plant, L. D.; Rabin, M. L.; Butler, M. H.; Goldstein, S. A. N. Sumoylation Silences the Plasma Membrane Leak K+ Channel K2P1. *Cell* **2005,** *121* (1), 37.

(16) Bagal, S.; Brown, A. D.; Cox, P. J.; Omoto, K.; Owen, R. M.; Pryde, D. C.; Sidders, B.; Skerratt, S. E.; Stevens, E. B.; Storer, R. I.et al. Ion Channels as Therapeutic Targets: A Drug Discovery Perspective. *J. Med. Chem.* **2013,** *56* (3), 593.

(17) Doyle, D. A.; Cabral, J. M.; Pfuetzner, R. A.; Kuo, A. L.; Gulbis, J. M.; Cohen, S. L.; Chait, B. T.; MacKinnon, R. The structure of the potassium channel: Molecular basis of K+ conduction and selectivity. *Science* **1998,** *280* (5360), 69.

(18) Long, S. B.; Campbell, E. B.; MacKinnon, R. Crystal structure of a mammalian voltage-dependent Shaker family K+ channel. *Science* **2005,** *309* (5736), 897.

(19) Miller, A. N.; Long, S. B. Crystal Structure of the Human Two-Pore Domain Potassium Channel K2P1. *Science* **2012,** *335* (6067), 432.

(20) Kuo, A. L.; Gulbis, J. M.; Antcliff, J. F.; Rahman, T.; Lowe, E. D.; Zimmer, J.; Cuthbertson, J.; Ashcroft, F. M.; Ezaki, T.; Doyle, D. A. Crystal structure of the potassium channel KirBac1.1 in the closed state. *Science* **2003,** *300* (5627), 1922.

(21) Jiang, Y. X.; Lee, A.; Chen, J. Y.; Ruta, V.; Cadene, M.; Chait, B. T.; MacKinnon, R. X-ray structure of a voltage-dependent K+ channel. *Nature* **2003,** *423* (6935), 33.

(22) Long, S. B.; Campbell, E. B.; MacKinnon, R. Voltage sensor of kv1.2: Structural basis of electromechanical coupling. *Science* **2005,** *309* (5736), 903.

(23) Brohawn, S. G.; del Marmol, J.; MacKinnon, R. Crystal Structure of the Human K2P TRAAK, a Lipid- and Mechano-Sensitive K+ Ion Channel. *Science* **2012,** *335* (6067), 436.
(24) Saotome, K.; Singh, A. K.; Yelshanskaya, M. V.; Sobolevsky, A. I. Crystal structure of the epithelial calcium channel TRPV6. *Nature* **2016,** *534* (7608), 506.
(25) Venkatachalam, K.; Montell, C. TRP Channels. *Annu. Rev. Biochem.* **2007,** *76*, 387.
(26) Zheng, J. Molecular Mechanism of TRP Channels. *Compr. Physiol.* **2013,** *3* (1), 221.
(27) Nilius, B.; Owsianik, G. Transient receptor potential channelopathies. *Pflug. Arch. Eur. J. Phy.* **2010,** *460* (2), 437.
(28) Hoenderop, J. G. J.; Voets, T.; Hoefs, S.; Weidema, F.; Prenen, J.; Nilius, B.; Bindels, R. J. M. Homo- and heterotetrameric architecture of the epithelial Ca(2+) channels TRPV5 and TRPV6. *EMBO J.* **2003,** *22* (4), 776.
(29) Liao, M.; Cao, E.; Julius, D.; Cheng, Y. Structure of the TRPV1 ion channel determined by electron cryo-microscopy. *Nature* **2013,** *504* (7478), 107.
(30) Cao, E.; Liao, M.; Cheng, Y.; Julius, D. TRPV1 structures in distinct conformations reveal mechanisms of activation. *Nature* **2013,** *504* (7478), 113.
(31) Paulsen, C. E.; Armache, J.-P.; Gao, Y.; Cheng, Y.; Julius, D. Structure of the TRPA1 ion channel suggests regulatory mechanisms. *Nature* **2015,** *520* (7548), 511.
(32) Grieben, M.; Pike, A. C. Structure of the polycystic kidney disease TRP channel Polycystin-2 (PC2). **2017,** *24* (2), 114.
(33) Zubcevic, L.; Herzik, M. A.; Chung, B. C.; Liu, Z.; Lander, G. C.; Lee, S.-Y. Cryo-electron microscopy structure of the TRPV2 ion channel. *Nat. Struct. Mol. Biol.* **2016,** *23* (2), 180.
(34) King, N.; Hittinger, C. T.; Carroll, S. B. Evolution of Key Cell Signaling and Adhesion Protein Families Predates Animal Origins. *Science* **2003,** *301* (5631), 361.
(35) Jacobson, K. A. New paradigms in GPCR drug discovery. *Biochem. Pharmacol.* **2015,** *98* (4), 541.
(36) Lappano, R.; Maggiolini, M. G protein-coupled receptors: novel targets for drug discovery in cancer. *Nat. Rev. Drug Disc.* **2011,** *10* (1), 47.
(37) Wang, C.; Jiang, Y.; Ma, J. M.; Wu, H. X.; Wacker, D.; Katritch, V.; Han, G. W.; Liu, W.; Huang, X. P.; Vardy, E.et al. Structural Basis for Molecular Recognition at Serotonin Receptors. *Science* **2013,** *340* (6132), 610.
(38) Wacker, D.; Wang, C.; Katritch, V.; Han, G. W.; Huang, X. P.; Vardy, E.; McCorvy, J. D.; Jiang, Y.; Chu, M. H.; Siu, F. Y.et al. Structural Features for Functional Selectivity at Serotonin Receptors. *Science* **2013,** *340* (6132), 615.
(39) Ramírez, M. J. 5-HT(6) receptors and Alzheimer's disease. *Alzheimers Res. Ther.* **2013,** *5* (2), 15.
(40) Akhondzadeh, S. The 5-HT hypothesis of schizophrenia. *IDrugs* **2001,** *4* (3), 295.

2. Simulation Techniques for Structural Analyses of Membrane Proteins

2.1 Commentary

In this chapter, an overview of the theoretical background of molecular dynamics (MD) simulations, and related methods, is provided in the context of studying membrane proteins. This is intended to be done via sections of two published book chapters, which are reproduced in full in section 2.2.1 and section 2.2.3. The first manuscript enclosed was produced for "Computational Biophysics of Membrane Proteins", part of the RSC Theoretical and Computational Chemistry series. Attention should be drawn to methods described in the manuscript sections 2.2 ("Classical Molecular Dynamics") and 2.5 ("Enhanced Sampling Techniques and Free Energy Methods") which have been used in this thesis. The second manuscript included in this section, was produced for "Computational Tools for Chemical Biology", part of the RSC Chemical Biology series. The aim of this chapter was to illustrate the application of computational methods to research membrane transport phenomenon. Sections 10.4 ("Passive Transport by Ion Channels") and 10.6 ("Signalling via Receptors") in the manuscript are the most pertinent to the research presented. The suggested sections provide relevant examples where simulation methods have been applied to ion channels, in the context of ion permeation, selectivity filter behaviour and drug binding, and GPCRs, in terms of activation and the involvement of the membrane environment. For further applications of MD simulations to membrane proteins, several other review articles can be found in the Appendices A-B.

2.2 Molecular Dynamics Simulations: Principles and Applications for the Study of Membrane Proteins, *Computational Biophysics of Membrane Proteins,* 2016

2.2.1 Authorship and Permissions

<table>
<tr><th colspan="10">This declaration concerns the article entitled</th></tr>
<tr><td colspan="10">Molecular Dynamics Simulations: Principles and Applications for the Study of Membrane Proteins.</td></tr>
<tr><td colspan="10">Publication status (tick one)</td></tr>
<tr><td>Draft manuscript</td><td></td><td>Submitted</td><td></td><td>In review</td><td></td><td>Accepted</td><td></td><td>Published</td><td>✓</td></tr>
<tr><td>Publication details</td><td colspan="9">*Computational Biophysics of Membrane Proteins,* 2016, 19-58, Royal Society of Chemistry
DOI: 10.1039/9781782626695-00019
Print publication date: 05 Dec 2016

Reproduced by permission of The Royal Society of Chemistry:
https://pubs.rsc.org/en/content/chapter/bk9781782624905-00019/978-1-78262-490-5</td></tr>
<tr><td>Candidates contribution to the paper (detailed and also given as a percentage)</td><td colspan="9">The candidate contributed to/considerably contributed/predominantly executed the…
Formulation of ideas (90%):
V. Oakes and C. Domene contributed to the content.

Design of methodology:
NA

Experimental work:
NA

Presentation of data in journal format (90%):
V. Oakes: Main author of manuscript
C. Domene: Critically assessed and appended manuscript</td></tr>
<tr><td>Statement from Candidate</td><td colspan="9">This paper reports on original research I conducted during the period of my Higher Degree by Research candidature.</td></tr>
<tr><td>Signed</td><td colspan="5"></td><td>Date</td><td colspan="3"></td></tr>
</table>

CHAPTER 2

Molecular Dynamics Simulations: Principles and Applications for the Study of Membrane Proteins

VICTORIA OAKES[a] AND CARMEN DOMENE*[a,b]

[a] Department of Chemistry, Britannia House, 7 Trinity Street, King's College London, London SE1 1DB, UK; [b] Chemistry Research Laboratory, Mansfield Road, University of Oxford, Oxford OX1 3TA, UK
*Email: carmen.domene@kcl.ac.uk

2.1 Introduction

Research into novel chemical problems is now commonly facilitated by computational methods in order to supplement experimental data, instruct future work and, in many cases, provide details for which no experimental methods are applicable. This is of particular importance in the context of membrane proteins, where the complexity of the membrane prevents established techniques to be utilised in order to understand structure–function relationships for soluble proteins.[1] Three-dimensional structures of membrane proteins have only began to emerge in the last two decades, due to the difficulty in their expression and purification, and their instability when removed from their native environment.[2] Progress in this field[3] and the emergence of new techniques for structure determination, such as cryo-electron microscopy,[4] have led to a wealth of available structures from many

RSC Theoretical and Computational Chemistry Series No. 10
Computational Biophysics of Membrane Proteins
Edited by Carmen Domene

Published by the Royal Society of Chemistry, www.rsc.org

membrane protein families.[4–13] Molecular dynamics (MD) simulations have become a powerful technique to describe the structure and dynamics of these systems in atomistic detail, resulting in appreciable contributions to the molecular understanding of membrane protein function.

Ion channels (Chapter 4 and 6), transporters (Chapter 7) and membrane receptors (Chapter 8) facilitate the communication and transport between the cell interior and exterior; the elucidation of such mechanisms and how they are influenced by their environment (Chapter 5) is key to understanding fundamental sensations related to light, taste, smell, sound, heat, pain and hormones, for which computational approaches have presented considerable insights. It is also imperative to understand when the behaviour of membrane proteins veers from normal physiological function. Incorrect modulation of membrane proteins has been linked to a wide range of diseases that include cardiac disorders, neurological indications, muscle afflictions and kidney failure; hence, they are arguably the most important pharmaceutical drug targets.[14–17] Computational algorithms are becoming increasingly more popular in the drug discovery context; the identification of putative binding sites provides an optimal starting-point for targeted design, resulting in the discovery of novel effector molecules to be used as lead compounds.[18] MD simulations have proven particularly fruitful in this respect, with numerous studies emerging in recent years.[19–22] With the increasing speed and availability of supercomputers, and the development of new algorithms, the scope for novel discoveries is continuously expanding.

In this chapter, we provide an overview of the theoretical background of MD simulations on biological macromolecules, some practical considerations when performing such calculations, and their application to membrane proteins. This review is intended as a precursor to the following chapters, which provide an extensive survey of dynamical insights obtained from computational simulations, related to the structure and function of membrane proteins, and additional techniques to study these features.

2.2 Classical Molecular Dynamics

In MD simulations, the motion of interacting particles is calculated by the integration of Newton's equations of motion (EOM). The potential energy of the system and the force, derived from the negative gradient of potential with respect to the displacement in a specified direction, can be used to calculate the acceleration, and hence forecast the time evolution of the system, in the form of a trajectory. The potential energy can be obtained by classical or quantum mechanical methods, with the former predominant due to its reduced computational expense by utilising empirical force fields and associated parameters (Section 2.2.1).

In systems with a couple of atoms, the solutions to the EOM can be gained analytically, resulting in a continuous trajectory over time. However, in larger systems, the subsistence of a continuous potential instigates a many body problem for force evaluations, rendering analytic solutions unattainable.

In these circumstances, finite difference methods can be used; forces are assessed at discrete intervals, and considered constant in the hiatus. Positions and velocities at the next timestep, as these intervals are known, are computed using force evaluations for each atom combined with current positions and velocities. Forces are then recalculated and this procedure is repeated, propagating a trajectory describing the flux of the atomic coordinates over time in a given equilibrium state, which can then be analysed for the properties of interest. An overview of this procedure is given in Figure 2.1. The timestep suitable for stable dynamics is dictated by the

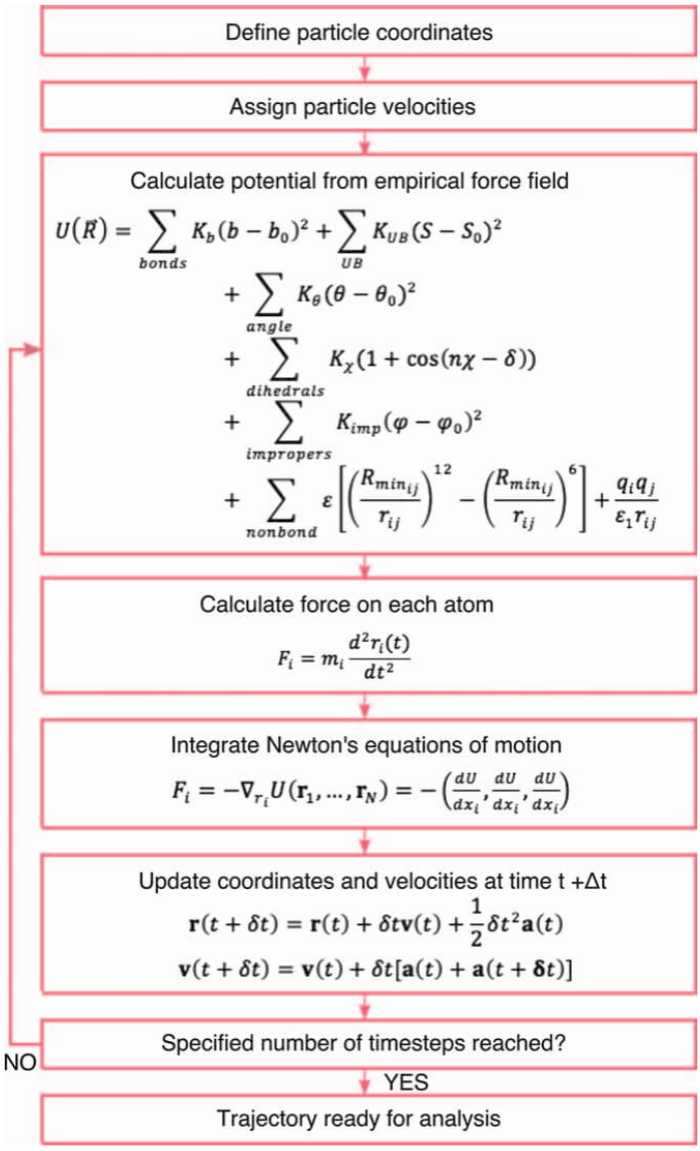

Figure 2.1 An overview of the molecular dynamics procedure, using the CHARMM force field and the Velocity-Verlet integration algorithm.

highest vibrational frequency of the molecule, typically 1 fs corresponding to a fraction of the vibrational motion of a C–H bond (10 fs), and the integration algorithm used. Details on this can be found in Section 2.2.3.

2.2.1 Additive Force Fields

Molecular mechanics (MM) is a mathematical model utilising the approximation that atoms can be considered as balls and, subsequently, nuclear motion can be evaluated using the EOM from classical physics. The consideration of only nuclear coordinates is based on the Born–Oppenheimer approximation; this states that electronic and nuclear wave functions can be treated separately due to the vast difference in mass, and hence velocity, of electrons and nuclei. Electrons are said to adjust 'instantaneously' to changes in nuclear position, thus they can be ignored when calculating motion. For this reason, the analytic expression for the energy of a system described by MM, known as the force field, is composed solely of inter- and intramolecular energetic contributions, including bond stretching, angle bending, bond rotations and non-bonded terms. This architecture neglects the electronic properties, such as dipole moments and vibrational frequencies, but allows for the evaluation of molecular motion in (biological) systems with a large number of degrees of freedom. A wide variety of force fields for biological molecules are available, including, but not limited to, CHARMM (Chemistry at Harvard Molecular Mechanics),[23] AMBER (Assisted Model Building with Energy Requirement)[24] and OPLS (Optimized Potentials for Liquid Simulations).[25] Each one varies in their functional form and the parameters therein, which are generally obtained to provide a suitable reproduction of experimental and/or quantum mechanical data. The CHARMM force field will be used as a representative example to demonstrate these aspects, with a recent comparison of the aforementioned force field available in ref. 26.

In the CHARMM force field, the individual terms for bond lengths and angles are based on simple harmonic potentials on the basis of an energetic penalty associated with a deviation from the equilibrium value.[23] A torsional angle potential function is also used to model the steric barriers (between 1, 4 pairs) associated with the rotation of atoms. The inclusion of a Urey–Bradley term, defined by the distance separated by two bonds, has provided notable improvements for the representation of in-plane deformations and the separation of symmetric and asymmetric bond stretching modes. Furthermore, improper terms assist the replication of out-of-plane bending modes. For the reproduction of non-bonding interactions, Coulomb and Lennard-Jones (LJ) potentials are used to express electrostatic and van der Waals forces, respectively. Cross terms are also included to account for the interdependence of internal coordinates, which are ordinarily a function of two internal coordinates, such as stretch-stretch or stretch-bend.

The functional form of the potential energy function in the current CHARMM force field is as follows:

$$\begin{aligned} \mathrm{U}(\vec{R}) = & \sum_{\text{bonds}} K_{\mathrm{b}}(b-b_0)^2 + \sum_{\text{UB}} K_{\mathrm{UB}}(S-S_0)^2 \\ & + \sum_{\text{angle}} K_\theta(\theta-\theta_0)^2 + \sum_{\text{dihedrals}} K_\chi(1+\cos(n\chi-\delta)) \\ & + \sum_{\text{impropers}} K_{\mathrm{imp}}(\varphi-\varphi_0)^2 + \sum_{\text{nonbond}} \varepsilon\left[\left(\frac{R_{\min_{ij}}}{r_{ij}}\right)^{12} - \left(\frac{R_{\min_{ij}}}{r_{ij}}\right)^{6}\right] + \frac{q_i q_j}{\varepsilon_1 r_{ij}} \end{aligned}$$

where K is representative of the force constant of the respective terms, b is the bond length, S is the Urey–Bradley 1,3 distance, θ is the bond angle, n is the multiplicity, χ is the dihedral angle, δ is the phase factor, φ is the improper angle, ε is the LJ well depth, $R_{\min}$ is the distance at the LJ minimum, q is the partial atomic charge, ε_1 is the effective dielectric constant and r_{ij} is the interatomic distance between atoms i and j. Symbols throughout associated with the subscript zero denote the equilibrium values. The generation of such parameters is generally based on the reproduction of vibrational and crystallographic data supplemented by *ab initio* calculations.

The CHARMM force field encompasses parameters for proteins,[27–29] lipids,[30–32] sterols,[32,33] nucleic acids[34–36] and carbohydrates.[37–40] The accurate parameterisation of protein and lipid molecules is crucial for the investigation of membrane proteins *via* computational methods. CHARMM22 provided the first all-atom parameter set for proteins developed to accurately produce condensed-phase properties.[27] Optimisation of the ϕ, ψ dihedral parameters lead to the inclusion of grid-based energy correction maps (CMAP).[28] The current release includes additional refinements to overcome issues with force field bias for α-helices.[29] The development of lipid parameters has been hindered due to the complex phase behaviour of lipid bilayers and the difficulties in gaining detailed structural information of this phenomenon. The publication of the CHARMM36 lipid parameters showed a significant improvement in the reproduction of bilayer surface areas, density profiles and deuterium order parameters over previous releases.[32] Further sets of parameters are required for ionic species. Ions are ordinarily used in solution to neutralise the simulation system in molecular simulations. However, the situation is complicated by the presence of additional interaction sites localised on the proteins. Traditionally, LJ parameters for ionic interactions are optimised to emulate the free energies of ions in bulk water.[41] Nonetheless, specific pairwise interactions can be substituted corresponding to the free energy of solvation of an ion in liquid *N*-methylacetamide (NMA), indistinguishable to those in bulk water to emulate cation–protein interactions.[42,43] Finally, the CHARMM General FF (CGenFF)[44] was developed to account for the diverse range of compounds of

pharmacological interest, particularly in drug design, where MD simulations are growing in popularity.

2.2.2 Polarisable Force Fields

The veracity of insights gained from MD simulations is inherently reliant on the quality of the underlying force fields. Force fields are generally parameterised under certain conditions, such as temperature, pressure and pH, which are specific to each individual force field; when the simulation conditions diverge from those in the parameterisation process, the accuracy of the data can suffer. A significant limitation inherent to all additive force fields is the absence of polarisation, leading to much deprecation of the treatment of electrostatic interactions. The term polarisation appertains to the fluctuation of the charge distribution in response to an external electric field, induced by the presence of additional atoms or molecules.[45] The use of fixed-point charges assigned at the nuclei and the evaluation of the Coulomb formula to appertain the magnitude of the electrostatic forces ignore this phenomenon, which can account for up to 30% of the interaction energy.[46]

Despite initial efforts to include polarisation effects,[47] significant efforts to develop polarisable force fields for biological molecules were not realised until the turn of the century, and are now considered particularly beneficial where ion channels are concerned. All-atom MD simulations of lipid bilayers significantly underestimate the dielectric constant of lipid hydrocarbons, and accordingly overestimate the energetic barriers facing permeating species.[48] In addition, the behaviour of ions interacting with protein atoms may considerably deviate from that in a solvated environment. The selectivity filter of K^+ channels is a prime example where dehydrated ions accommodate a narrow channel lined with carbonyl oxygens, for which specialised parameters have been derived. Furthermore, substantial inaccuracies of simulations with multivalent cations, such as Mg^{2+} and Ca^{2+} have been noted as a consequence of their high charge density and the polarisation of surrounding molecules that is not captured in typical simulations.[49] Polarisable force fields, therefore, potentially provide a uniform solution to such issues.

Three schemes have been proposed, namely the fluctuating charge model, the induced dipole model and the Drude oscillator approach.[50] In the fluctuating charge model, molecular charges remain constant throughout the simulation with individual point charges readjusted in consonance with the electronegativity.[51] Deficiencies concerning out-of-plane polarisation in conjugated systems limit its applicability to some extent, despite some successes within the CHeq force field[52,53] in recent biomolecular studies.[54] AMOEBA is the most noteworthy force field utilising an induced dipole model, where atomic multipoles are used explicitly to represent electrostatics, calculated *via* a self-consistent field procedure, heightening the computational expense of this procedure.[55]

Finally, in the Drude oscillator approach, a subsidiary charged particle is attached to the nucleus by a harmonic spring, and treated as an extra degree

of freedom.[56] This protocol is easily executable in established MD platforms with the computational expense, relative to a non-polarizable FF, increasing by a maximum factor of two. Studies concerning protein secondary structure formation[57] and structural perturbations of DNA–ion interactions,[58] for example, have emerged since the release of the Drude-2013 force field.[59,60] Recent parameterisation efforts have shown significant improvements for the accurate representation of ion–protein interactions in comparison to additive force fields, reproducing energetics obtained from QM calculations of 30 unique ion-bound enzymatic proteins.[61] The ability of such force fields to replicate such quantum mechanical methods at a fraction of the computational expense will have significant implications for the modelling and understanding of metalloproteins, including membrane transport proteins such as ion channels. The reader is directed to ref. 62 for an extensive review of the field, with details on the mathematical background, accompanying parameterisation protocols and recent applications.

2.2.3 Practical and Technical Considerations

Simulations of membrane protein systems are now extremely accessible to any researcher in an academic or industrial institution; force fields are widely available for all the components required,[27–32] with many MD algorithms available on open-source platforms such as NAMD,[63] AMBER,[64] or GROMACS,[65] for example. In recent years, web-servers have also been developed that set up the initial system and provide the necessary input to use such software, with the CHARMM-GUI service leading this field.[66,67] A conscientious practitioner, however, will understand the inner workings that allow a successful simulation to be performed. On these grounds, the basic principles will be outlined in the following section.

Since the first simulation of a biological macromolecule, bovine pancreatic trypsin inhibitor (BPTI), was published, the complexity and accuracy has significantly increased.[68] For example, the initial simulations of BPTI were performed *in vacuo*[68] with subsequent simulations incorporating an implicit water model by the inclusion of a dielectric constant in the electrostatic energy term.[69] Advanced implicit[70] and explicit[71] water models are currently available for MD simulations; the latter are arguably more accurate[72–74] and are therefore predominant in contemporary membrane protein studies, despite the heightened expense.[75–77] The present-day availability of computational resources and efficient models to calculate interaction potentials renders such computations feasible.[78] TIP3P,[79] for example, is a 'simple' pairwise model where water molecules are assigned partial atomic charges at three sites. In this model, electrostatic interactions are calculated between balanced anionic oxygen and cationic hydrogen atoms, and van der Waals interactions are determined by a single oxygen centred point charge, providing a popular model for MD due to its level of accuracy and affordability. Concurrently, octane slabs originally served as lipid bilayers for embedded proteins,[80] with a full atomistic description of

lipid molecules now standard. Implicit membrane models are still utilised for protein-folding investigations, where higher-order timescales are required.[81] Overall, simulation systems are continuously transitioning to more realistic descriptions of biological systems, with membrane protein simulations generally constituting explicit protein atoms, lipid bilayers, water molecules and ions.[82]

In any respect, simulation systems must be of finite size and peripheral regions encounter an anomalous environment, introducing practical difficulties for performing MD simulations. Periodic boundary conditions (PBC) are generally used to mimic an infinite environment, with a finite number of atoms, to account for the system size and deleterious boundary effects.[83] Any particles that leave the simulation box throughout the simulation are simultaneously replaced by an identical particle on the opposite side. Furthermore, each particle is liable to interactions with particles in adjacent boxes removing unphysical interactions with the system boundary (Figure 2.2). Any geometry that can fill an infinite space by translational operations alone is a suitable choice.[84] However, the utmost efficiency can be achieved when the simulation box reflects the geometry of the system in question. The use of the cube/parallelepiped is the most widely recorded, and suitable for proteins embedded in a lipid bilayer.[82] When simulating proteins that require a concentration gradient akin to that experienced in ion channels, for example, PBC can be troublesome as the ion concentration is inherently equal.[85] The most straightforward method to overcome this is to simulate the ion channel in the presence of an electrochemical driving force, by the application of a constant electric field in the direction

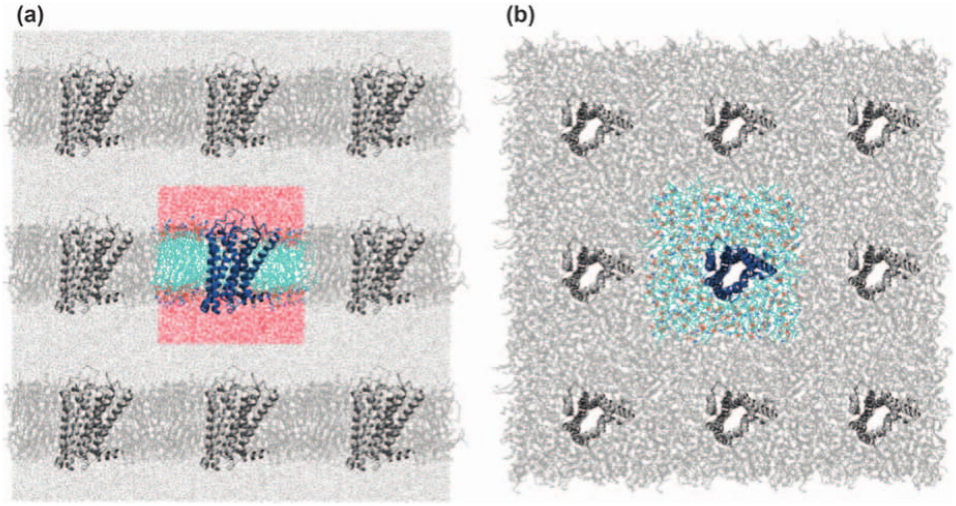

Figure 2.2 (a) Side and (b) top view of a membrane protein (the 5-HT_{1B} G-protein coupled receptor)[88] simulation system, with the atoms explicitly present coloured, and the atoms replicated as a consequence of cubic periodic boundary conditions in grey. Water molecules are excluded in the latter for clarity.

orthogonal to the membrane.[86] Alternatively, PBC can be exploited. The simulation system can be separated into two chambers by parallel model bilayers, with the ionic concentration controlled in such a manner to induce an electrochemical gradient to observe permeation.[87]

Further approximations are, however, generally required to realise feasible computational costs when utilising PBC. Theoretically, non-bonded interactions (van der Waals and electrostatic interactions) should be calculated for all atoms present in the system, including those in neighbouring boxes. Therefore, a minimum image convention is employed in which each atom interacts with only one image of the recurrent atoms.[89] Furthermore, on the basis of the underlying LJ potential, which decays proportionally to r^{-6}, short-range non-bonded (van der Waals) interactions are truncated above a specified interatomic distance.[90] A non-bonded neighbour list is generated at regular intervals to indicate which atom pairs should be considered in this calculation, avoiding the calculation of all interatomic distances at each timestep.[91] The Verlet neighbour list stores such information, using a distance criterion slightly larger than the cut-off to extend the applicability of the list in future timesteps in which atoms may enter the calculation threshold.[92] Switching functions are also required to diminish discontinuities in force and energy calculations. These can be applied throughout the whole potential range or between lower and upper cut-off distances to moderately abate the potential in this range. The latter is recommended to avoid perturbing the equilibrium structures.[93]

Electrostatic interactions must also be considered to ensure efficient molecular simulations. Interactions of single-point charges decay proportionally to r^{-1}; hence, switching functions are arguably unsuitable in this case.[94–96] A numerical solution to the Ewald summation, an infinite sum of electrostatic interactions for a charge neutral system, can be derived using the Particle Mesh Ewald (PME) method as an alternative. This procedure reduces the calculation expense from the order of N^2 to $N \log N$, where N is the total number of atoms in the system.[97–100]

By utilising all of the above, calculations can feasibly be performed; thereafter, it is important to consider the relationship between the resulting trajectory and the experimental data. Microscopic properties, identified within the simulations, are connected to macroscopic properties of the system *via* statistical mechanics.[101] An ensemble can be defined as a collection of independent microstates that displays indistinguishable macroscopic conditions. This provides a key concept in this field and is fundamental in the accurate reproduction of experimental data throughout simulations. Isothermal-isobaric conditions are most widely used experimentally; therefore, simulations require regulation, by thermostats and barostats, to sample the appropriate ensemble.[102,103]

Firstly, to achieve a given temperature, the velocities can be scaled by a constant.[104] Furthermore, the temperature can be coupled to an external heat bath, which can supply or remove heat where required. There are a variety of schemes designed to generate a statistical ensemble at a constant

temperature using these means. In the Berendson thermostat, for example, velocities are scaled at each step according to the rate of change at each step.[105] This is often used to achieve the initial temperature, but influences the fluctuations in the kinetic energy throughout simulations, failing to sample the correct canonical ensemble.[106] Extensions have been proposed where a properly constructed random force is added, controlling the kinetic energy and removing such shortcomings.[104] The Langevin thermostat is an alternative stochastic method to achieve temperature control *via* heat bath coupling.[107] All particles simultaneously obtain random and frictional forces, the balance of which generates the correct canonical ensemble. In extended system methods, such as the Nosé–Hoover, a thermal reservoir is considered as an extra degree of freedom in the equations of motions.[108] Both Langevin and Nosé–Hoover thermostats are widely used in MD simulations.[102]

Methods for pressure control are generally analogous to those of temperature, replacing the velocity term with volume. The hybrid Nosé–Hoover[103] Langevin piston[109] barostat is an extended system method, using a compressing piston as an additional degree of freedom described by a Langevin equation. The combination with Langevin dynamics overcomes the earlier bias caused by the fictitious mass of the piston. This approach also allows isotropic, anisotropic or semi-isotropic coupling of volume fluctuations; the latter is recommended in membrane simulations to allow proportional scaling of the x and y dimensions of the lipid bilayer.[82]

Finally, the time evolution of the energy of the system should be of paramount importance within MD simulations.[110] To truly abide by classical Newtonian dynamics, the trajectory must be time-reversible with the total energy of the closed system conserved. Discretisation of variables, introduced by the use of a finite timestep in MD simulations, can cause an energy drift, an unphysical phenomenon where the energy of the system gradually changes over time.

Integration algorithms are generally optimised to accommodate discrete timesteps and maintain the conservation of energy, alongside considerations for computational efficiency.[111] Taylor expansions are used to approximate the key terms (positions, velocities and acceleration) in all algorithms, differing in their interpretation. The Verlet algorithm provides an inexpensive method, in terms of both computational time and storage, using positions at previous timesteps (t, and $(t - \mathrm{d}t)$) to calculate those at future $(t + \mathrm{d}t)$ timesteps.[112] Nonetheless, the inclusion of an explicit velocity term in both the Leap-Frog[113] and Velocity-Verlet[114] algorithms demonstrated paramount accuracy; the latter is somewhat preferred as all terms are evaluated at the same timestep, whereas velocities and positions sequentially 'leap' over each other in the so-called Leap-Frog method. The complexity of the velocity expression is increased in Beeman's algorithm providing a more accurate, yet intensive, method.[115] Higher-order methods, such as the Runge–Kutta family,[116] are generally unsuitable for biomolecular simulations, as a consequence of their inefficiency and inability to

maintain the fundamental properties of a simulation system, such as energy conservation.[117] Overall, the Velocity-Verlet algorithm provides a symplectic, time reversible method that conserves momentum and energy, with an excellent compromise between accuracy and expense, therefore finding a place in most MD software of common usage. It is worth noting that supplementary algorithms in these packages are included to increase the timestep; the SETTLE[118] algorithm, an analytical version of the SHAKE function,[119] is used, for example, to restrain bonds involving hydrogen atoms, and increase the timestep from 1 to 2 fs.

2.2.4 Applications

Despite the universal availability of MD algorithms and force fields applicable to biological macromolecules, simulations of intrinsic membrane proteins, whose system size regularly exceeds 100 000 atoms, are inherently limited by computing resources. However, expansions in computer hardware and high-performance computing facilities and improved software means that MD simulations on the nanosecond timescale are now routine, with microsecond simulations attained in recent years.[120] Equilibrium MD simulations are therefore relevant to study a wide range of biological phenomena; substrate binding, for example, is a fundamental process for which a nanosecond timescale is appropriate. Ligand binding is integral for activation, and hence basic function, of many integral membrane proteins. MD simulations have provided considerable insight into such mechanisms. In membrane transporters, ATP or ions are required as a driving force for large-scale conformational changes between the inward facing and outward facing edges that are functional to transport species against the electrochemical gradient. In Na^+ coupled secondary transporters, for example, the location of ion binding sites, the progression of binding events and the following structural perturbations have been unearthed to some extent by MD simulations.[121–124]

In a pharmaceutical environment, classical MD has become an established tool to identify putative binding sites and consequentially establish how drugs function on a molecular level. The microscopic mechanisms of anaesthesia, for example, remain elusive despite its ubiquity in modern medicine. Isoflurane, a common general anaesthetic, is a known inhibitor of proton-gated ion channels[125] and mammalian nicotinic acetylcholine receptors,[126] for which MD simulations have enabled the identification of multiple pore and subunit interface binding sites[127,128] before crystallographic data was available,[129,130] and advocating a multi-site model for anaesthetic action in the Cys-loop receptor family. Modulation of voltage-gated sodium channels by anaesthesia has also been pensively studied by computational methodologies,[131–133] with particular focus on the role of lateral fenestrations between the central pore and the surrounding bilayer as hydrophobic drug access pathways.[134] In-depth understanding of drug entry and binding mechanisms is, in general, essential to guide future drug

discovery advances, in a continued effort to develop subtype-selective blockers with optimal response properties in an affordable manner.

Unfortunately, the high computational expense of atomistic MD simulations for membrane proteins remains a significant weakness for the investigation of other aspects of protein structure and function. Many biological phenomena that occur on extended timescales, such as protein folding, complex association and conformational changes associated with gating, are generally unattainable by atomistic equilibrium MD without the use of tailor-made software. The Shaw group has pioneered the production of millisecond long unbiased simulations by the development of the Supercomputer Anton, optimised for use with in-house MD software.[135] However, such technology is not widely available, leading to the development of alternative approaches to accelerate sampling.

2.3 Coarse-grained Molecular Dynamics Simulations

Using a reduced representation is one such approach, utilising classical MD simulations, to increase the speed and hence the timescales obtainable. Coarse-grained (CG) molecular dynamics, as this is known, reduces the number of degrees of freedom in a simulation system by treating a group of atoms as a single entity, significantly curtailing the computational expense of each iteration. To convert an all-atom structure to a coarse-grained model, hydrogen atoms are not considered, with a number of heavy atoms (typically three or four) grouped into a single interaction site, known as a "bead". Interaction potentials are then characterised dependent on the CG model, with required parameters generally developed to reproduce microscopic properties recorded in atomistic simulations and thermodynamic data derived by experimental means.

Klein and co-workers developed an initial CG model for phospholipids, using a distance dependent model for pairwise potentials and utilising an LJ style potential to calculate non-bonded interactions and reproduce the biophysical properties of the membrane.[136,137] Parameterisation efforts subsequently focused towards lipid and surfactant molecules.[138,139] With regards to the Klein model for amino acids, backbone and side chain atoms are generally classified as a single site, with exceptions for bulky constituents.[140] Interaction potentials are optimised to reproduce the surface tension and density of a representative side-chain analogue in bulk solution, leading to unique parameters for most amino acids with high accuracy and excluding the use of protein structural data during parameterisation.

Marrink and colleagues undertook similar work to construct CG representations of lipid and surfactant molecules.[141,142] The MARTINI force field, as this is known, was quickly expanded to include proteins,[143–146] sterols,[143,147] carbohydrates,[148,149] polymers,[150–152] dendrimers,[153,154] nanoparticles[155,156] and DNA[157] providing a versatile, ever-expanding toolkit for bio-molecular simulations, the most popular CG model to date. In this method, individual sites are classified to maintain the chemical nature of

the region: polar, non-polar, apolar (a mixture of polar and non-polar groups) and charged, with further sub-groups representing the hydrogen bonding capabilities, polarity, and alternative grouping schemes for specific cases, such as rings, where the overall symmetry defines the number of sites required (Figure 2.3).

Short-range non-bonded interaction energies are calculated according to the standard LJ 12-6 and Coulomb potentials, with parameters developed to reproduce the free energy of hydration, free energy of vaporisation and oil/water partitioning coefficients through extensive validation against experimental data concerning the physical properties of the bilayer.[141,143,158] The deficiencies of the LJ potential have been noted in this case, demonstrating the diminished stability of liquid phases[159] and the inaccurate representation of the surface tension at the air–water interface[160] and water–oil interfaces,[161] leading to possible corrections in a future release.[162]

Overall, the implementation of both the Klein and Marrink models, alongside other CG schemes,[163] reduces the number of degrees of freedom in the system, curtailing the number of required calculations in each iteration, as well as increasing the timesteps (20–40 fs) whilst maintaining a level of chemical specificity without fine chemical details, thereby providing a powerful tool to generate molecular simulations on an extended timescale.

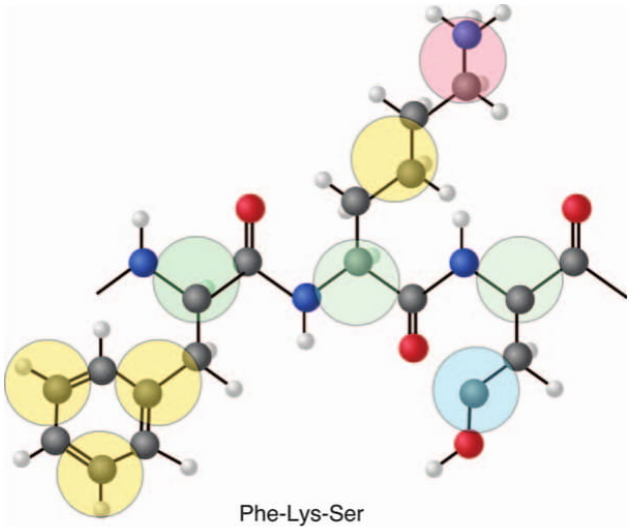

Figure 2.3 Representation of a coarse-grain map of a short polypeptide sequence (Phe-Lys-Ser), with coloured circles representing the interaction sites, known as beads. The yellow, blue and red circles correspond to N-type (non-polar), P-type (polar) and Q-type (charged) beads, respectively. The polypeptide backbone atoms (green circles) are a unique case, where their classification is dependent on the secondary structure; a P-type bead defines a helix or a bend, with polarity considerably reduced in α-helices or β-strands due to inter-helical hydrogen bonding.

The limitations of CGMD must also be evaluated when considering such approaches.[162] CG models generally have difficulties reproducing physical properties for which they are not parameterised, arising from the reduced representations.[164] The chemical resolution is restricted; the subtle differences between lipid molecules, for example, cannot be captured accurately in this manner.[162] Specific bonded parameters or an elastic network are often required to constrain the protein in the appropriate secondary structure, which is inherently maintained in atomistic simulations by the explicit representation of hydrogen bonds. In addition, long-range non-bonded interactions are generally neglected throughout. Finally, the speed-up of CGMD is not universal across all molecule types;[162] therefore, it is often difficult to assess the acceleration *versus* the loss of detail and hence the utility of CGMD in some cases.

However, CGMD methodologies are in common usage today, tackling a wide range of biophysical scenarios. The MARTINI force field has been at the forefront of developments in numerous areas of biochemical research, with an exhaustive review of such applications provided by Marrink and Tieleman in ref. 162. Investigations concerning membrane proteins, in particular, have had notable success in elucidating lipid–protein and protein–protein association mechanisms, as well as the conformational changes in proteins in biological membranes due to the extended timescales the techniques have enabled.[165]

Identification of specific lipid[166–168] and cholesterol[165,168] binding sites in G-protein coupled receptor (GPCR) proteins is an area of research where both atomistic and CGMD simulations are employed; the advancements by both experimental and computational means are reviewed in Chapter 5. Furthermore, the available timescales are appropriate to observe protein self-assembly. Therefore, CGMD is an integral tool to observe GPCR oligomerisation. In the case of rhodopsin, transmembrane helices 1, 2 and amphipathic helix 8 were identified to be the primary dimer interface.[169] Oligomerisation properties of β2-adrenergic receptor were also elucidated by this method, with transmembrane helices 1, 4 and 7 being the preferable interfacial region for energetic reasons concerning the hydrophobic mismatch of the monomer in the membrane.[170]

Lipid self-assembly is also within the bounds of CGMD, which can be used to optimise the setup of atomistic membrane simulations. Enveloping proteins by self-assembled lipid bilayers ensures the most energetically favourable orientation of the proteins within the membrane, demonstrating notable benefits to manual insertion. CG models can then be transformed into atomistic representations to perform MD simulations.

It is also worth noting that dual-resolution approaches (denoted MM/CG) have been developed, where atoms in regions of chemical interest are treated explicitly and the remaining system coarse-grained, to exploit the chemical detail and extended timescales of the respective methods.[171–176] The method was applied to the β2-adrenergic receptor as a means of predicting ligand poses at a high-throughput, with key attributes of ligand–receptor

interactions conserved between atomistic and multi-scale simulations.[177] Subsequently, this method was applied to bitter taste receptors TAS2R38 and TAS2R46, with the binding predictions consistent with site-directed mutagenesis and functional assays.[178–180] These initial results suggest that CGMD can provide an accurate yet economical method to obtain GPCR/ligand complexes and aid drug design.[181]

2.4 *Ab initio* Molecular Dynamics

Advanced techniques are also required at the other end of the spectrum; where complex chemical phenomena occur on a sub-nanosecond timescale yet require the knowledge of molecular electronic properties. Bond making and breaking in chemical reactions and excited state dynamics are two such examples that cannot be described by empirical force fields alone. A full electronic description of a system can be derived from first principles *via* quantum mechanical (QM) methods; the theoretical and mathematical background of the QM treatment can be found, for example, in ref. 182. Density functional theory (DFT) is a popular QM method, providing an attractive compromise between the accuracy of the exchange-correlation functionals and the scaling properties with respect to the number of atoms in the system.[183,184]

Car and Parrinello spearheaded the integration of DFT within an MD framework, leading to the emergence of the *ab initio* method, CPMD.[185] In this scheme, electronic degrees of freedom are included explicitly and coupled to the motion of the nuclei by dynamic variables. Protocols based on Born–Oppenheimer MD,[186] which employs the time-independent Schrödinger equation to evaluate the electronic structure, and combinatory approaches have since been proposed.[187] These approaches have been applied to investigate the mechanism of proton transport in aqueous solution,[188–191] at hydrophobic interfaces,[192] in enzymes and in the cation-selective membrane channel gramicidin A (gA).[193,194] In a study using *ab initio* metadynamics, Dreyer *et al.* identified a free energy barrier at the mouth of the gA channel,[194] implicating a membrane dipole potential in the relationship between the proton transfer rate and the transmembrane voltage observed experimentally.[195] The authors note that these conclusions are somewhat speculative, as a result of limited timescales and hence partially converged trajectories, as well as the potential boundary effects induced by the relatively small system size (~2000 atoms). Such limitations arise from the substantial computational requirements of performing *ab initio* MD, meaning it is generally unsuited to large-scale biological assemblies.

As a means to reduce such expense and broaden the range of biological processes that can be studied, hybrid quantum mechanics/molecular mechanics (QM/MM) methods have been developed.[47] In QM/MM simulations, the bulk of the system is treated using classical mechanics, with the specific region of biochemical interest evaluated by quantum mechanical methods and a coupling scheme to account for the boundary region.[196,197]

As with both classical and quantum MD simulations, the timescales and phenomena that can be sampled by unbiased QM/MM simulations are limited by the computational resources, and enhanced sampling techniques as described in the following section are regularly used. These approaches have provided extensive insight into the mechanism of enzymatic reactions,[198,199] as well as phenomena in several classes of membrane proteins.[200–206]

QM/MM simulations have found obvious applications in the investigation of proton migration in membrane proteins. For example, a mechanism for proton transport across aquaporin GlpF has been proposed.[200] In the light-sensitive GPCR bacteriorhodopsin, QM/MM has been used to determine the structure and IR spectra of protonated local water networks to provide information on the photosynthetic cycle.[201,202]

QM/MM simulations have also been applied to study the structure and energetics of binding sites in ion channels. Analysis of the prototypical K^+ channel, KcsA, suggested that ion-binding energetics are manipulated by polarisation and charge transfer effects between the carbonyls and cations, potentially screening the ion-ion repulsion integral, but maintaining the canonical structure throughout.[203] Proton transfer was also observed between two residues constituting part of the selectivity filter, imposing additional energetic consequences on the permeation profile.[204] Furthermore, the coordination numbers of K^+ and Na^+ were found to be similar in the filter and water, but overestimated in atomistic simulations.[205] The conduction of anionic Cl^- ions through the NanC porin has also been re-investigated by QM/MM methods; this study supported extensive solvation in the binding sites proposed from atomistic simulations, yet highlighted distinct differences concerning the average water–Cl distance and polarisation effects resulting from proximal protein residues.[206] The observed differences in the binding of charged species indicate that conduction and selectivity mechanisms cannot be truly quantified without the inclusion of polarisation effects.[207]

2.5 Enhanced Sampling Techniques and Free Energy Methods

Additional techniques are often required to sample phenomena where standard atomistic, coarse-grain and QM methodologies are not appropriate. In order to obtain statistically significant estimates of conductance in ion channels, for example, a copious amount of conduction events should be observed and, therefore, atomistic MD simulations must be performed at length, *i.e.* trajectories of tens of microseconds, which are generally at odds with current computational capabilities. Furthermore, large-scale conformational changes, integral to the function of membrane channels, receptors and transporters, can occur on the second time-scale, and involve high-energy barriers between stable structures which cannot be overcome by

thermal fluctuations in equilibrium simulations. Accordingly, advanced techniques are required to calculate the underlying free energy of what is called a 'rare event', as well as accelerate sampling.

In the archetypal method, known as free energy perturbation (FEP), the relative free energy differences of multiple processes can be calculated by using alchemical transformations *via* a thermodynamic cycle.[208,209] Figure 2.4(a) demonstrates a generalised cycle to calculate the relative free binding energies and assess the affinity of related molecules to a known binding site.

Instead of attempting to overcome energetic barriers and extended time-scales directly to observe binding events, the ligands can be artificially transformed in the bound and unbound states to calculate the relative free energy by an alternative route:

$$\Delta(\Delta G) = \Delta G_2 - \Delta G_2 = \Delta G_4 - \Delta G_3$$

Practically, intermediate (non-physical) steps are required to perform this conversion in a stepwise manner, for which a coupling parameter (λ), scaled between 0 and 1, is used to dictate the contributions of the initial (U_1) and final (U_2) states to the potential energy of the whole system (U).[210]

$$U = \lambda U_2 + (1 - \lambda)U_1$$

FEP simulations provided the earliest insight into the conduction mechanism in K^+ channels.[211] The primary permeation axis, known as the selectivity filter, is constituted of a conserved amino acid sequence arranged to form rings of oxygen atoms, which are able to bind dehydrated ions in a cage-like structure, in four adjoining sites (S1–S4), with intermediary binding sites in the central cavity (SC), and at the extracellular mouth (S0 and S_{EXT}) of the protein, displayed in Figure 2.4(b).[5] These initial simulations

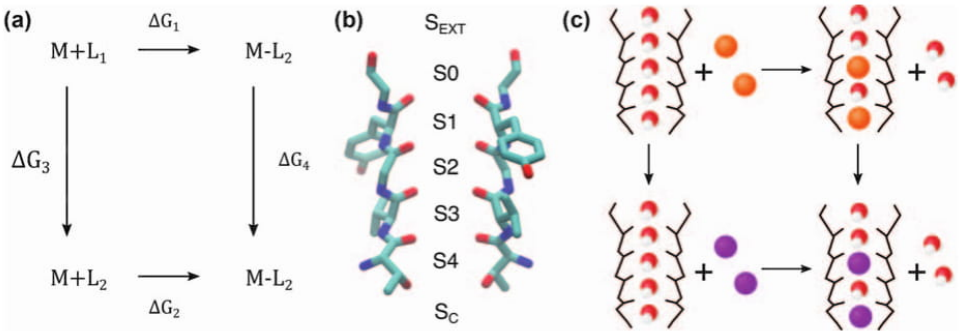

Figure 2.4 (a) General thermodynamic cycle to calculate the relative free binding energies of two molecules (L_1 and L_2) to an identical binding site. (b) Structure of the selectivity filter in K^+ channels.[5] (c) An example thermodynamic cycle to assess the relative affinity of K^+ and Na^+ ions (orange and purple spheres, respectively) towards the S2 and S4 sites of a K^+ channel selectivity filter (black trace).

provided evidence that S1/S3 and S2/S4 ion configurations play a crucial role in conduction, with the latter being the most thermodynamically favourable loading state.[211] FEP computations have also been utilised to understand the molecular origins of selectivity in the K^+ channel filter. An exemplar thermodynamic cycle to elucidate the relative free energies of K^+ binding *vs.* Na^+ binding in the S2–S4 configuration is shown in Figure 2.4(c). Initial calculations proposed an energetic penalty of 4.5 ± 0.5 kcal mol^{-1} for this transformation;[211] a general consensus has since emerged that Na^+ occupancy of K^+ binding sites is less favourable, with the selectivity of the S2 site being the most pronounced.[43,211–213] Alternative binding sites for Na^+ have also been proposed in the plane of the four carbonyl atoms, which displayed paramount stability.[214]

FEP calculations are also becoming increasingly useful in modern day drug discovery for the characterisation of the ligand affinity ratios of drug–protein complexes.[215] By obtaining the relative binding energies of different ligands to an identical binding site[216] or, conversely, of one ligand to wild type and mutated sites,[217–219] FEP provides computational analogues to competition assays[220] and site-directed mutagenesis studies,[221] respectively, which play a major role in industry to elucidate the key determinants of ligand binding and identify and optimise lead compounds.

Several algorithms also exist to enhance sampling along a pre-defined set of reaction coordinates and estimate the potential of mean force (PMF), such as umbrella sampling,[222] metadynamics,[223] steered MD[224] or adaptive biasing force.[225] These reaction coordinates, known as collective variables (CVs), are chosen to investigate a specific transition. An estimate of the free energy profile as a function of such CVs can be recovered, in addition to the equilibrium properties of the system, to provide a wealth of information about the simulation system at a fraction of the expense of unbiased simulations. An overview of how simulation algorithms explore the potential energy surface is given in Figure 2.5, with the theoretical background and relevant applications of each method described from this point forward. To the best of our knowledge, few studies using QM approaches with rare-event techniques to investigate the behaviour of membrane proteins have been published to date.[195,226] Therefore, it is noted that the selected applications described have been performed by entirely classical means.

Umbrella sampling (US)[222] is perhaps one of the most popular enhanced sampling methods in this field, where a bias potential along user-defined CVs provokes the conversion between stable thermodynamic states. Independent MD simulations are performed at intermediary steps (Figure 2.5(b)), known as windows, which can be combined using the weight histogram analysis method (WHAM)[227,228] or umbrella integration.[229] Each window represents equilibrium sampling of energetically distinct locales; accordingly, such evaluation estimates the consolidated equilibrium free-energy surface.

US simulations have also proven popular when deciphering the conduction mechanism in K^+ channels.[42,214,230–233] In order to obtain a free energy profile of this pathway, the windows are defined by different ionic

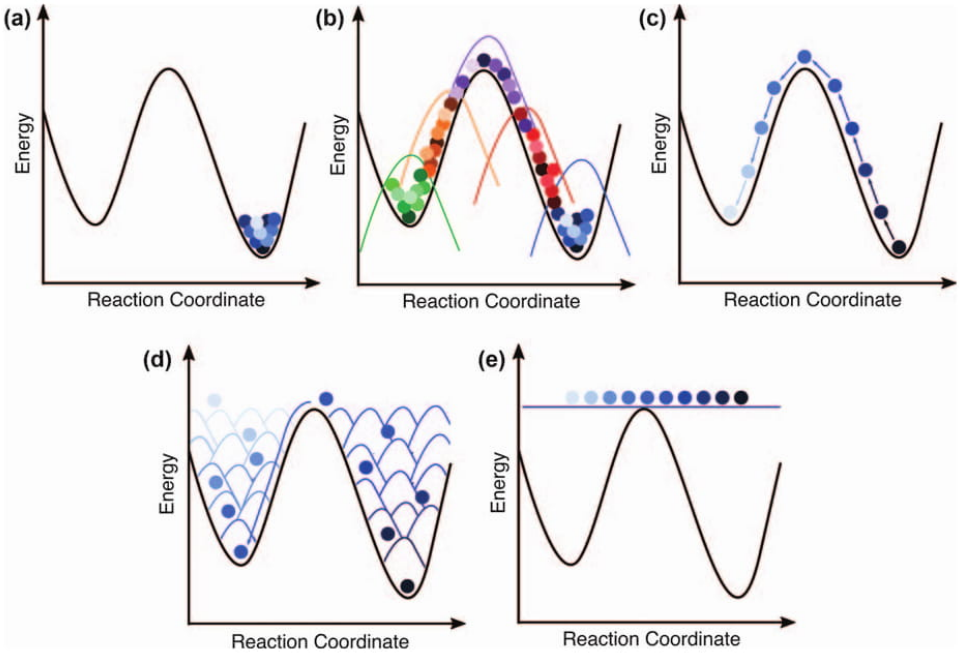

Figure 2.5 Simplified representation of how enhanced sampling methods explore the potential energy surface in comparison to unbiased MD simulations. Different colours denote independent simulations, with the progression from dark to light representing the evolution of the trajectory. (a) In classical molecular dynamics, the trajectory represents an ensemble of microstates that generally remain well within an energy level unless thermal fluctuations can overcome the surrounding barriers, something usually unlikely. (b) In umbrella sampling, a biased potential is used to perform independent simulations in different but overlapping regions on the potential energy surface, which can be combined to obtain the potential of mean force. (c) In steered molecular dynamics, an external force is applied to an atom, or group of atoms, to enforce an alternative stable thermodynamic state, regardless of the barrier. (d) In metadynamics, biasing potentials (Gaussians) are added to promote sampling of less probable regions of the energy surface. (e) In adaptive biasing force, the instantaneous force along the reaction coordinate is evaluated directly and counteracted by an external biasing force of equal and opposite magnitude, effectively flattening the surface.

configurations in the selectivity filter. Initial umbrella sampling calculations suggested a conduction mechanism whereby ions cycle between occupying the S1/S3 and S2/S4 positions, with the remaining sites containing a single water molecule throughout, prompted by approaching ions in the central cavity (Figure 2.6(a)),[42] in line with FEP computations.[211] Subsequent umbrella sampling calculations demonstrated a mechanism in which direct ion–ion contacts and vacant sites could feasibly compete with those previously calculated by the inclusion of additional ionic configurations (Figure 2.6(b)).[230] The expanse of the estimated energy landscape is inherently limited by the input of such configurations, highlighted further by a

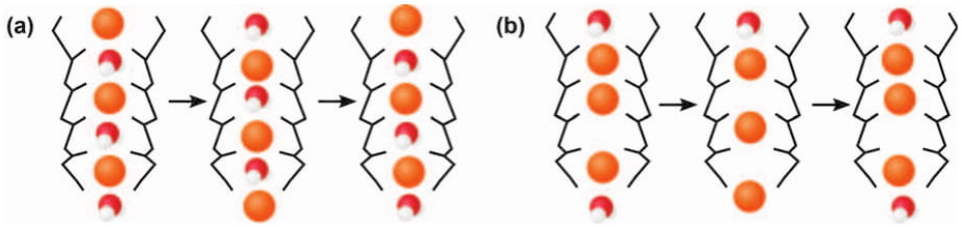

Figure 2.6 Proposed mechanisms of ion conduction in K^+ channels: (a) chains of alternating K^+ ions and water molecules cross the selectivity filter,[42] or (b) cation pairs move through the selectivity filter without intervening water molecules.[230] Coloured spheres represent individual K^+ ions. The approach of an ion from the central cavity prompts a simultaneous ion movement throughout the selectivity filter, resulting in the exit of one ion that rapidly diffuses into the extracellular solution.

systematic comparison with metadynamics simulations that identified further possible iterations.[234]

Steered molecular dynamics (SMD) is a further enhanced sampling method, with applications for a wide range of membrane proteins (Figure 2.5(c)).[224] SMD are akin to well-established experimental techniques, such as atomic force microscopy or optical tweezers, where an external force is applied to an atom or group of atoms to overcome the barriers and sample a specific process.[224] Relative free energies can then be obtained by Jarzynki's equality.[235] This method can be used to quantify protein–ligand binding energies, for example, with understanding of the transport, binding and unbinding mechanisms observed on-the-fly, gaining notable insights relevant to the drug discovery process.[236] Potential inhibitors of the M2 channel protein have been discovered in this manner.[237] SMD simulations of the $5HT_{2A}$ have also elucidated specific driving forces for GPCR activation,[238] in addition to key translocation properties in substrate-specific channel proteins[239] and ATP binding cassette transporters.[240]

Metadynamics is another enhanced sampling technique employed in this field to sample rare events and obtain the free energy underlying the events.[223] In this case, a biased potential is utilised to advance the sampling along suitable CVs, diverting from the configurational space previously inhabited. The biasing potential is adjusted by the addition of a Gaussian function, augmenting the energy of the system and departing from the local free energy minima, allowing the exploration of alternative thermodynamic states separated by energetic barriers. Once convergence has been achieved, effectively when the entire free energy profile has been flattened, it can be easily reconstructed to provide an unbiased estimate of the landscape as a function of the CVs, hence elucidating the underlying properties of the system. The CV definition, therefore, is of paramount importance in the accuracy of such profiles, which should include all the degrees of freedom relevant to the process in question. In practice, however, only a minimal set is used to alleviate the computational cost, which increases exponentially with each CV. This can be problematic when considering systems with

complex conformational transitions, such as ion channels,[241] and thus specialised methods are often preferred.

Extensive CV selection can be avoided by replica-exchange methods. In parallel tempering metadynamics, metadynamics runs are performed at different temperatures and configurations are exchanged at regular intervals.[242] Runs at elevated temperatures are more likely to overcome barriers, and consequentially introduce uncharted transitions *via* exchange. In bias-exchange metadynamics, multiple replicas are undertaken with different CVs, instead of temperatures.[243] Configurations from random runs are exchanged, so numerous CVs and high dimensional transitions can be explored in a more efficient manner than traditional metadynamics.

The latter has recently been proposed as an efficient method to study conduction in bacterial voltage-gated sodium (NaV) channels.[244] In Na_VAb, for example, an arrangement of four glutamates, the so-called 'EEEE ring', forms a highly charged region at the extracellular mouth of the selectivity filter known as binding site S_{HFS}.[6] Deeper sites formed of rings of carbonyl atoms, denoted S_{CEN} and S_{IN}, are proposed to form the remainder of the permeation pathway, demonstrating a notably wider and shorter selectivity filter than in K^+ channels, able to accommodate hydrated ions throughout. In order to investigate permeation in Na_VAb by US, the number and species of ions involved must be defined at the outset, yet this is unknown. Therefore, multiple independent simulations are required to assess the feasibility of single and multi-ion conduction events, none of which are representative of the entire energy landscape.[245,246] When considering traditional metadynamics, a single CV along the channel axis is insufficient to characterise the conduction pathway in Na^+ channels, as in K^+ channels; an additional CV describing radial displacement from the axis is required to properly accommodate on- and off-axis sites, requiring a 4-dimensional energy profile (when two ions are involved).[247] Metadynamics is more efficient than classical US simulations at sampling this 4-dimensional space. Furthermore, when coupled with replica-exchange methods, like in bias-exchange metadynamics, this technique can be used to investigate permeation events that involve a variable number of ions or different ion species.[244] Consequently, this method is likely to gain traction in non-selective channels such as TRPV, for which crystal structures are now available but equivalent properties are unknown. Further examination of the role of metadynamics in the analysis of ion channels can be found in ref. 248.

Metadynamics simulations can also be likened to the adaptive biasing force method (ABF),[225] an additional rare-event technique which aims to provide homogenous sampling of the potential energy surface. This approach is largely based on thermodynamic integration,[249] whereby the instantaneous force along the reaction coordinate is evaluated directly and counteracted by an external biasing force of equal and opposite magnitude. This effectively provides a smooth energy landscape and uniform sampling irrespective of the energetic barriers allowing for accelerated dynamics.

The application of ABF to the study of membrane protein structural organisation was established in its infancy, examining the reversible folding processes of alanine-rich α-helical peptides[250–252] to probe the secondary structure formation prior to membrane insertion, in line with the 'two-stage' model proposed by Popot and Engelman.[253] Subsequently, the transmembrane region of Glycophorin A (GpA) embedded in a membrane mimetic environment was used to chronicle the *in situ* α-helical recognition and association mechanisms.[254] Independent GpA α-helices were found to exhibit stable dynamics oriented perpendicular to the membrane interface, prior to the formation of native contacts and tilting to generate the canonical structure, lending further evidence to the 'two-stage' scheme.

ABF has also been applied to understand selective transport phenomena in membrane proteins, in a similar vein to other enhanced sampling methods. Ivanov *et al.* investigated members of the Cys-loop receptor family, the nicotinic acetylcholine (nAChR) and glycine (GlyR) receptors, in order to explore the origin of cation and anion selectivity in the respective channels.[255] Rings of oppositely charged residues at the extracellular mouth of the channels were found to stabilise the translocating ions, notably contributing to their selectivity. A barrier in the central region of the nAChR pore also supported evidence of a hydrophobic gating mechanism and the proposed closed state of the crystal structure.[256] ABF has since been used in multiple studies concerning ammonium,[257] glycerol,[258] CLC,[259] and urea[260] transporters.

2.6 Conclusions

The accessibility of three-dimensional crystal structures, advanced empirical force fields and efficient setup/simulation protocols has enabled MD to become an established tool to probe structure–function relationships of membrane proteins. With the continual expansion of enhanced sampling algorithms and high-performance computing resources, as well as the development of dual-resolution techniques, MD simulations are now able to illustrate an immense range of biological phenomena. Computational investigations of this nature have provided considerable insights in the area of biophysics, contributing to our fundamental understanding of transport and communication across the cell membrane on a molecular level. The applicability of such techniques to membrane proteins of pharmaceutical interest can also aid the affordable, rational design of drug molecules, setting a precedent for the next generation of drug discovery. The continuous increase of high-resolution structures from a diverse range of protein families and organisms will significantly advance this field in the future.

References

1. E. P. Carpenter, K. Beis, A. D. Cameron and S. Iwata, Overcoming the challenges of membrane protein crystallography, *Curr. Opin. Struct. Biol.*, 2008, **18**(5), 581–586.

2. M. C. Deller, L. Kong and B. Rupp, Protein stability: a crystallographer's perspective, *Acta Crystallogr., Sect. F: Struct. Biol. Commun.*, 2016, **72**(Pt. 2), 72–95.
3. I. Moraes, G. Evans, J. Sanchez-Weatherby, S. Newstead and P. D. S. Stewart, Membrane protein structure determination — The next generation, *Biochim. Biophys. Acta, Biomembr.*, 2014, **1838**(1, Part A), 78–87.
4. M. Liao, E. Cao, D. Julius and Y. Cheng, Structure of the TRPV1 ion channel determined by electron cryo-microscopy, *Nature*, 2013, **504**(7478), 107–112.
5. D. A. Doyle, J. Morais Cabral, R. A. Pfuetzner, A. Kuo, J. M. Gulbis, S. L. Cohen, B. T. Chait and R. MacKinnon, The structure of the potassium channel: molecular basis of K^+ conduction and selectivity, *Science*, 1998, **280**(5360), 69–77.
6. J. Payandeh, T. Scheuer, N. Zheng and W. A. Catterall, The crystal structure of a voltage-gated sodium channel, *Nature*, 2011, **475**(7356), 353–358.
7. N. Shi, S. Ye, A. Alam, L. Chen and Y. Jiang, Atomic structure of a Na^+- and K^+-conducting channel, *Nature*, 2006, **440**(7083), 570–574.
8. K. Palczewski, T. Kumasaka, T. Hori, C. A. Behnke, H. Motoshima, B. A. Fox, I. Le Trong, D. C. Teller, T. Okada, R. E. Stenkamp, M. Yamamoto and M. Miyano, Crystal structure of rhodopsin: A G-protein-coupled receptor, *Science*, 2000, **289**(5480), 739–745.
9. S. G. F. Rasmussen, H.-J. Choi, D. M. Rosenbaum, T. S. Kobilka, F. S. Thian, P. C. Edwards, M. Burghammer, V. R. P. Ratnala, R. Sanishvili, R. F. Fischetti, G. F. X. Schertler, W. I. Weis and B. K. Kobilka, Crystal structure of the human β2 adrenergic G-protein-coupled receptor, *Nature*, 2007, **450**(7168), 383–387.
10. L. Qin, I. Kufareva, L. G. Holden, C. Wang, Y. Zheng, C. Zhao, G. Fenalti, H. Wu, G. W. Han, V. Cherezov, R. Abagyan, R. C. Stevens and T. M. Handel, Structural biology. Crystal structure of the chemokine receptor CXCR4 in complex with a viral chemokine, *Science*, 2015, **347**(6226), 1117–1122.
11. M. Hohl, C. Briand, M. G. Grütter and M. A. Seeger, Crystal structure of a heterodimeric ABC transporter in its inward-facing conformation, *Nat. Struct. Mol. Biol.*, 2012, **19**(4), 395–402.
12. D. Deng, C. Xu, P. Sun, J. Wu, C. Yan, M. Hu and N. Yan, Crystal structure of the human glucose transporter GLUT1, *Nature*, 2014, **510**(7503), 121–125.
13. B. P. Pedersen, H. Kumar, A. B. Waight, A. J. Risenmay, Z. Roe-Zurz, B. H. Chau, A. Schlessinger, M. Bonomi, W. Harries, A. Sali, A. K. Johri and R. M. Stroud, Crystal structure of a eukaryotic phosphate transporter, *Nature*, 2013, **496**(7446), 533–536.
14. S. K. Bagal, A. D. Brown, P. J. Cox, K. Omoto, R. M. Owen, D. C. Pryde, B. Sidders, S. E. Skerratt, E. B. Stevens, R. I. Storer and N. A. Swain, Ion Channels as Therapeutic Targets: A Drug Discovery Perspective, *J. Med. Chem.*, 2013, **56**(3), 593–624.

15. R. J. Harvey and B. K. Yee, Glycine transporters as novel therapeutic targets in schizophrenia, alcohol dependence and pain, *Nat. Rev. Drug Discovery*, 2013, **12**(11), 866–885.
16. L. Lin, S. W. Yee, R. B. Kim and K. M. Giacomini, SLC transporters as therapeutic targets: emerging opportunities, *Nat. Rev. Drug Discovery*, 2015, **14**(8), 543–560.
17. K. A. Jacobson and Z. G. Gao, Adenosine receptors as therapeutic targets, *Nat. Rev. Drug Discovery*, 2006, **5**(3), 247–264.
18. M. De Vivo, M. Masetti, G. Bottegoni and A. Cavalli, Role of Molecular Dynamics and Related Methods in Drug Discovery, *J. Med. Chem.*, 2016, **59**(9), 4035–4061.
19. C. Jorgensen, L. Darre, K. Vanommeslaeghe, K. Omoto, D. Pryde and C. Domene, In silico identification of PAP-1 binding sites in the Kv1.2 potassium channel, *Mol. Pharmaceutics*, 2015, **12**(4), 1299–1307.
20. H. Van Nguyen, H. T. Nguyen and L. T. Le, Investigation of the free energy profiles of amantadine and rimantadine in the AM2 binding pocket, *Eur. Biophys. J.*, 2016, **45**(1), 63–70.
21. C. G. Gadhe, A. Balupuri and S. J. Cho, In silico characterization of binding mode of CCR8 inhibitor: homology modeling, docking and membrane based MD simulation study, *J. Biomol. Struct. Dyn.*, 2015, **33**(11), 2491–2510.
22. F. K. Brewer, C. A. Follit, P. D. Vogel and J. G. Wise, In silico screening for inhibitors of p-glycoprotein that target the nucleotide binding domains, *Mol. Pharmacol.*, 2014, **86**(6), 716–726.
23. B. R. Brooks, R. E. Bruccoleri, B. D. Olafson, D. J. States, S. Swaminathan and M. Karplus, CHARMM: A program for macromolecular energy, minimization, and dynamics calculations, *J. Comput. Chem.*, 1983, **4**(2), 187–217.
24. W. D. Cornell, P. Cieplak, C. I. Bayly, I. R. Gould, K. M. Merz, D. M. Ferguson, D. C. Spellmeyer, T. Fox, J. W. Caldwell and P. A. Kollman, A Second Generation Force Field for the Simulation of Proteins, Nucleic Acids, and Organic Molecules, *J. Am. Chem. Soc.*, 1995, **117**(19), 5179–5197.
25. W. L. Jorgensen and J. Tirado-Rives, The OPLS [optimized potentials for liquid simulations] potential functions for proteins, energy minimizations for crystals of cyclic peptides and crambin, *J. Am. Chem. Soc.*, 1988, **110**(6), 1657–1666.
26. F. MartÌn-GarcÌa, E. Papaleo, P. Gomez-Puertas, W. Boomsma and K. Lindorff-Larsen, Comparing Molecular Dynamics Force Fields in the Essential Subspace, *PLoS One*, 2015, **10**(3), e0121114.
27. A. D. MacKerell, D. Bashford, M. Bellott, R. L. Dunbrack, J. D. Evanseck, M. J. Field, S. Fischer, J. Gao, H. Guo, S. Ha, D. Joseph-McCarthy, L. Kuchnir, K. Kuczera, F. T. K. Lau, C. Mattos, S. Michnick, T. Ngo, D. T. Nguyen, B. Prodhom, W. E. Reiher, B. Roux, M. Schlenkrich, J. C. Smith, R. Stote, J. Straub, M. Watanabe, J. Wiórkiewicz-Kuczera, D. Yin and M. Karplus, All-Atom Empirical Potential for Molecular

Modeling and Dynamics Studies of Proteins, *J. Phys. Chem. B*, 1998, **102**(18), 3586–3616.

28. A. D. Mackerell Jr., M. Feig and C. L. Brooks 3rd, Extending the treatment of backbone energetics in protein force fields: limitations of gas-phase quantum mechanics in reproducing protein conformational distributions in molecular dynamics simulations, *J. Comput. Chem.*, 2004, **25**(11), 1400–1415.
29. R. B. Best, X. Zhu, J. Shim, P. E. M. Lopes, J. Mittal, M. Feig and A. D. MacKerell, Optimization of the Additive CHARMM All-Atom Protein Force Field Targeting Improved Sampling of the Backbone ϕ, ψ and Side-Chain $\chi 1$ and $\chi 2$ Dihedral Angles, *J. Chem. Theory Comput.*, 2012, **8**(9), 3257–3273.
30. S. E. Feller and A. D. MacKerell, An Improved Empirical Potential Energy Function for Molecular Simulations of Phospholipids, *J. Phys. Chem. B*, 2000, **104**(31), 7510–7515.
31. S. E. Feller, K. Gawrisch and A. D. MacKerell Jr., Polyunsaturated fatty acids in lipid bilayers: intrinsic and environmental contributions to their unique physical properties, *J. Am. Chem. Soc.*, 2002, **124**(2), 318–326.
32. J. B. Klauda, R. M. Venable, J. A. Freites, J. W. O'Connor, D. J. Tobias, C. Mondragon-Ramirez, I. Vorobyov, A. D. MacKerell Jr. and R. W. Pastor, Update of the CHARMM all-atom additive force field for lipids: validation on six lipid types, *J. Phys. Chem. B*, 2010, **114**(23), 7830–7843.
33. J. B. Lim, B. Rogaski and J. B. Klauda, Update of the cholesterol force field parameters in CHARMM, *J. Phys. Chem. B*, 2012, **116**(1), 203–210.
34. A. D. MacKerell, J. Wiorkiewicz-Kuczera and M. Karplus, An all-atom empirical energy function for the simulation of nucleic acids, *J. Am. Chem. Soc.*, 1995, **117**(48), 11946–11975.
35. N. Foloppe and J. A. D. MacKerell, All-atom empirical force field for nucleic acids: I. Parameter optimization based on small molecule and condensed phase macromolecular target data, *J. Comput. Chem.*, 2000, **21**(2), 86–104.
36. A. D. MacKerell and N. K. Banavali, All-atom empirical force field for nucleic acids: II. Application to molecular dynamics simulations of DNA and RNA in solution, *J. Comput. Chem.*, 2000, **21**(2), 105–120.
37. M. Kuttel, J. W. Brady and K. J. Naidoo, Carbohydrate solution simulations: producing a force field with experimentally consistent primary alcohol rotational frequencies and populations, *J. Comput. Chem.*, 2002, **23**(13), 1236–1243.
38. O. Guvench, S. N. Greene, G. Kamath, J. W. Brady, R. M. Venable, R. W. Pastor and A. D. Mackerell Jr., Additive empirical force field for hexopyranose monosaccharides, *J. Comput. Chem.*, 2008, **29**(15), 2543–2564.
39. E. R. Hatcher, O. Guvench and A. D. MacKerell, CHARMM Additive All-Atom Force Field for Acyclic Polyalcohols, Acyclic Carbohydrates, and Inositol, *J. Chem. Theory Comput.*, 2009, **5**(5), 1315–1327.

40. O. Guvench, E. Hatcher, R. M. Venable, R. W. Pastor and A. D. MacKerell, CHARMM Additive All-Atom Force Field for Glycosidic Linkages between Hexopyranoses, *J. Chem. Theory Comput.*, 2009, **5**(9), 2353–2370.
41. D. B. A. B. Roux, Finite representation of an infinite bulk system: Solvent boundary potential for computer simulations, *J. Chem. Phys.*, 1994, **100**(12), 14.
42. S. Berneche and B. Roux, Energetics of ion conduction through the K^+ channel, *Nature*, 2001, **414**(6859), 73–77.
43. S. Y. Noskov, S. Berneche and B. Roux, Control of ion selectivity in potassium channels by electrostatic and dynamic properties of carbonyl ligands, *Nature*, 2004, **431**(7010), 830–834.
44. K. Vanommeslaeghe, E. Hatcher, C. Acharya, S. Kundu, S. Zhong, J. Shim, E. Darian, O. Guvench, P. Lopes, I. Vorobyov and A. D. Mackerell Jr., CHARMM general force field: A force field for drug-like molecules compatible with the CHARMM all-atom additive biological force fields, *J. Comput. Chem.*, 2010, **31**(4), 671–690.
45. S. W. Rick and S. J. Stuart, Potentials and Algorithms for Incorporating Polarizability in Computer Simulations, *Reviews in Computational Chemistry*, John Wiley & Sons, Inc., 2003, pp. 89–146.
46. A. Milet, R. Moszynski, P. E. S. Wormer and A. van der Avoird, Hydrogen Bonding in Water Clusters: Pair and Many-Body Interactions from Symmetry-Adapted Perturbation Theory, *J. Phys. Chem. A*, 1999, **103**(34), 6811–6819.
47. A. Warshel and M. Levitt, Theoretical studies of enzymic reactions: Dielectric, electrostatic and steric stabilization of the carbonium ion in the reaction of lysozyme, *J. Mol. Biol.*, 1976, **103**(2), 227–249.
48. I. V. Vorobyov, V. M. Anisimov and A. D. MacKerell, Polarizable Empirical Force Field for Alkanes Based on the Classical Drude Oscillator Model, *J. Phys. Chem. B*, 2005, **109**(40), 18988–18999.
49. D. Jiao, C. King, A. Grossfield, T. A. Darden and P. Ren, Simulation of Ca^{2+} and Mg^{2+} Solvation Using Polarizable Atomic Multipole Potential, *J. Phys. Chem. B*, 2006, **110**(37), 18553–18559.
50. H. S. Antila and E. Salonen, Polarizable Force Fields, in *Biomolecular Simulations: Methods and Protocols*, ed. L. Monticelli and E. Salonen, Humana Press, Totowa, NJ, 2013, pp. 215–241.
51. S. W. Rick, S. J. Stuart and B. J. Berne, Dynamical fluctuating charge force fields: Application to liquid water, *J. Chem. Phys.*, 1994, **101**(7), 6141–6156.
52. S. Patel and C. L. Brooks, CHARMM fluctuating charge force field for proteins: I parameterization and application to bulk organic liquid simulations, *J. Comput. Chem.*, 2004, **25**(1), 1–16.
53. S. Patel, A. D. Mackerell Jr. and C. L. Brooks 3rd, CHARMM fluctuating charge force field for proteins: II protein/solvent properties from molecular dynamics simulations using a nonadditive electrostatic model, *J. Comput. Chem.*, 2004, **25**(12), 1504–1514.

54. Y. Hu, S. Ou and S. Patel, Free Energetics of Arginine Permeation into Model DMPC Lipid Bilayers: Coupling of Effective Counterion Concentration and Lateral Bilayer Dimensions, *J. Phys. Chem. B*, 2013, **117**(39), 11641–11653.
55. Y. Shi, Z. Xia, J. Zhang, R. Best, C. Wu, J. W. Ponder and P. Ren, Polarizable Atomic Multipole-Based AMOEBA Force Field for Proteins, *J. Chem. Theory Comput.*, 2013, **9**(9), 4046–4063.
56. G. Lamoureux, A. D. MacKerell and B. T. Roux, A simple polarizable model of water based on classical Drude oscillators, *J. Chem. Phys.*, 2003, **119**(10), 5185–5197.
57. J. Huang and A. D. MacKerell Jr., Induction of peptide bond dipoles drives cooperative helix formation in the (AAQAA)3 peptide, *Biophys. J.*, 2014, **107**(4), 991–997.
58. A. Savelyev and A. D. MacKerell, Differential Impact of the Monovalent Ions Li^+, Na^+, K^+, and Rb^+ on DNA Conformational Properties, *J. Phys. Chem. Lett.*, 2015, **6**(1), 212–216.
59. P. E. M. Lopes, J. Huang, J. Shim, Y. Luo, H. Li, B. Roux and A. D. MacKerell, Polarizable Force Field for Peptides and Proteins Based on the Classical Drude Oscillator, *J. Chem. Theory Comput.*, 2013, **9**(12), 5430–5449.
60. A. Savelyev and A. D. MacKerell Jr., All-atom polarizable force field for DNA based on the classical Drude oscillator model, *J. Comput. Chem.*, 2014, **35**(16), 1219–1239.
61. H. Li, V. Ngo, M. C. Da Silva, D. R. Salahub, K. Callahan, B. Roux and S. Y. Noskov, Representation of Ion–Protein Interactions Using the Drude Polarizable Force-Field, *J. Phys. Chem. B*, 2015, **119**(29), 9401–9416.
62. J. A. Lemkul, J. Huang, B. Roux and A. D. MacKerell, An Empirical Polarizable Force Field Based on the Classical Drude Oscillator Model: Development History and Recent Applications, *Chem. Rev.*, 2016, **116**(9), 4983–5013.
63. J. C. Phillips, R. Braun, W. Wang, J. Gumbart, E. Tajkhorshid, E. Villa, C. Chipot, R. D. Skeel, L. Kale and K. Schulten, Scalable molecular dynamics with NAMD, *J. Comput. Chem.*, 2005, **26**(16), 1781–1802.
64. D. A. Case, T. E. Cheatham 3rd, T. Darden, H. Gohlke, R. Luo, K. M. Merz Jr., A. Onufriev, C. Simmerling, B. Wang and R. J. Woods, The Amber biomolecular simulation programs, *J. Comput. Chem.*, 2005, **26**(16), 1668–1688.
65. D. Van Der Spoel, E. Lindahl, B. Hess, G. Groenhof, A. E. Mark and H. J. Berendsen, GROMACS: fast, flexible, and free, *J. Comput. Chem.*, 2005, **26**(16), 1701–1718.
66. S. Jo, T. Kim, V. G. Iyer and W. Im, CHARMM-GUI: a web-based graphical user interface for CHARMM, *J. Comput. Chem.*, 2008, **29**(11), 1859–1865.
67. J. C. Mathai, A. Missner, P. Kügler, S. M. Saparov, M. L. Zeidel, J. K. Lee and P. Pohl, No facilitator required for membrane transport of hydrogen sulfide, *Proc. Natl. Acad. Sci.*, 2009, **106**(39), 16633–16638.

68. J. A. McCammon, B. R. Gelin and M. Karplus, Dynamics of folded proteins, *Nature*, 1977, **267**(5612), 585–590.
69. M. Levitt and R. Sharon, Accurate simulation of protein dynamics in solution, *Proc. Natl. Acad. Sci. U. S. A.*, 1988, **85**(20), 7557–7561.
70. J. Kleinjung and F. Fraternali, Design and application of implicit solvent models in biomolecular simulations, *Curr. Opin. Struct. Biol.*, 2014, **25**(100), 126–134.
71. P. Florová, P. Sklenovský, P. Banáš and M. Otyepka, Explicit Water Models Affect the Specific Solvation and Dynamics of Unfolded Peptides While the Conformational Behavior and Flexibility of Folded Peptides Remain Intact, *J. Chem. Theory Comput.*, 2010, **6**(11), 3569–3579.
72. H. Nymeyer and A. E. García, Simulation of the folding equilibrium of α-helical peptides: A comparison of the generalized Born approximation with explicit solvent, *Proc. Natl. Acad. Sci.*, 2003, **100**(24), 13934–13939.
73. R. Zhou, Free energy landscape of protein folding in water: explicit vs. implicit solvent, *Proteins*, 2003, **53**(2), 148–161.
74. C. Tan, L. Yang and R. Luo, How Well Does Poisson – Boltzmann Implicit Solvent Agree with Explicit Solvent? A Quantitative Analysis, *J. Phys. Chem. B*, 2006, **110**(37), 18680–18687.
75. V. Tsui and D. A. Case, Molecular Dynamics Simulations of Nucleic Acids with a Generalized Born Solvation Model, *J. Am. Chem. Soc.*, 2000, **122**(11), 2489–2498.
76. M. Feig, Kinetics from Implicit Solvent Simulations of Biomolecules as a Function of Viscosity, *J. Chem. Theory Comput.*, 2007, **3**(5), 1734–1748.
77. R. E. Amaro, X. Cheng, I. Ivanov, D. Xu and J. A. McCammon, Characterizing loop dynamics and ligand recognition in human- and avian-type influenza neuraminidases via generalized born molecular dynamics and end-point free energy calculations, *J. Am. Chem. Soc.*, 2009, **131**(13), 4702–4709.
78. R. Anandakrishnan, A. Drozdetski, Walker, C. Ross, Onufriev and V. Alexey, Speed of Conformational Change: Comparing Explicit and Implicit Solvent Molecular Dynamics Simulations, *Biophys. J.*, 2015, **108**(5), 1153–1164.
79. W. L. Jorgensen, J. Chandrasekhar, J. D. Madura, R. W. Impey and M. L. Klein, Comparison of simple potential functions for simulating liquid water, *J. Chem. Phys.*, 1983, **79**(2), 926–935.
80. C. Domene, A. Grottesi and M. S. P. Sansom, Filter Flexibility and Distortion in a Bacterial Inward Rectifier K^+ Channel: Simulation Studies of KirBac1.1, *Biophys. J.*, 2004, **87**(1), 256–267.
81. B. L. Kim, N. P. Schafer and P. G. Wolynes, Predictive energy landscapes for folding α-helical transmembrane proteins, *Proc. Natl. Acad. Sci.*, 2014, **111**(30), 11031–11036.
82. C. Kandt, W. L. Ash and D. Peter Tieleman, Setting up and running molecular dynamics simulations of membrane proteins, *Methods*, 2007, **41**(4), 475–488.

83. B. J. Alder and T. E. Wainwright, Studies in Molecular Dynamics. I. General Method, *J. Chem. Phys.*, 1959, **31**(2), 459–466.
84. T. A. Wassenaar and A. E. Mark, The effect of box shape on the dynamic properties of proteins simulated under periodic boundary conditions, *J. Comput. Chem.*, 2006, **27**(3), 316–325.
85. F. Khalili-Araghi, B. Ziervogel, J. C. Gumbart and B. Roux, Molecular dynamics simulations of membrane proteins under asymmetric ionic concentrations, *J. Gen. Physiol.*, 2013, **142**(4), 465–475.
86. J. Gumbart, F. Khalili-Araghi, M. Sotomayor and B. Roux, Constant electric field simulations of the membrane potential illustrated with simple systems, *Biochim. Biophys. Acta*, 2012, **1818**(2), 294–302.
87. C. Kutzner, H. Grubmüller, de Groot, L. Bert and U. Zachariae, Computational Electrophysiology: The Molecular Dynamics of Ion Channel Permeation and Selectivity in Atomistic Detail, *Biophys. J.*, 2011, **101**(4), 809–817.
88. C. Wang, Y. Jiang, J. Ma, H. Wu, D. Wacker, V. Katritch, G. W. Han, W. Liu, X.-P. Huang, E. Vardy, J. D. McCorvy, X. Gao, E. X. Zhou, K. Melcher, C. Zhang, F. Bai, H. Yang, L. Yang, H. Jiang, B. L. Roth, V. Cherezov, R. C. Stevens and H. E. Xu, Structural Basis for Molecular Recognition at Serotonin Receptors, *Science*, 2013, **340**(6132), 610–614.
89. H. C. Andersen, Molecular dynamics simulations at constant pressure and/or temperature, *J. Chem. Phys.*, 1980, **72**(4), 2384–2393.
90. J. E. Jones, On the Determination of Molecular Fields. II. From the Equation of State of a Gas, *Proc. R. Soc. London, A*, 1924, **106**(738), 463–477.
91. V. Yip and R. Elber, Calculations of a list of neighbors in molecular dynamics simulations, *J. Comput. Chem.*, 1989, **10**(7), 921–927.
92. L. Verlet, Computer ''experiments'' on classical fluids. I. Thermodynamical properties of Lennard-Jones molecules, *Phys. Rev.*, 1967, **159**(1), 98.
93. M. Levitt, M. Hirshberg, R. Sharon and V. Daggett, Potential energy function and parameters for simulations of the molecular dynamics of proteins and nucleic acids in solution, *Comput. Phys. Commun.*, 1995, **91**(1–3), 215–231.
94. P. E. Smith and B. M. Pettitt, Peptides in ionic solutions: A comparison of the Ewald and switching function techniques, *J. Chem. Phys.*, 1991, **95**(11), 8430–8441.
95. S. Piana, K. Lindorff-Larsen, R. M. Dirks, J. K. Salmon, R. O. Dror and D. E. Shaw, Evaluating the Effects of Cutoffs and Treatment of Long-range Electrostatics in Protein Folding Simulations, *PLoS One*, 2012, **7**(6), e39918.
96. J. Norberg and L. Nilsson, On the Truncation of Long-Range Electrostatic Interactions in DNA, *Biophys. J.*, 2000, **79**(3), 1537–1553.
97. T. Darden, D. York and L. Pedersen, Particle mesh Ewald: An N·log(N) method for Ewald sums in large systems, *J. Chem. Phys.*, 1993, **98**(12), 10089–10092.

98. U. Essmann, L. Perera, M. L. Berkowitz, T. Darden, H. Lee and L. G. Pedersen, A smooth particle mesh Ewald method, *J. Chem. Phys.*, 1995, **103**(19), 8577–8593.
99. D. York and W. Yang, The fast Fourier Poisson method for calculating Ewald sums, *J. Chem. Phys.*, 1994, **101**(4), 3298–3300.
100. A. Y. Toukmaji and J. A. Board Jr., Ewald summation techniques in perspective: a survey, *Comput. Phys. Commun.*, 1996, **95**(2–3), 73–92.
101. D. Chandler, *Introduction to Modern Statistical Mechanics*, Oxford University Press, 1987, p. 228.
102. P. H. Hünenberger, Thermostat Algorithms for Molecular Dynamics Simulations. in *Advanced Computer Simulation: Approaches for Soft Matter Sciences* ed. C. Holm and K. Kremer, Springer Berlin Heidelberg, Berlin, Heidelberg, 2005, pp. 105–149.
103. G. J. Martyna, D. J. Tobias and M. L. Klein, Constant pressure molecular dynamics algorithms, *J. Chem. Phys.*, 1994, **101**(5), 4177–4189.
104. G. Bussi, D. Donadio and M. Parrinello, Canonical sampling through velocity rescaling, *J. Chem. Phys.*, 2007, **126**(1), 014101.
105. H. J. C. Berendsen, J. P. M. Postma, W. F. van Gunsteren, A. DiNola and J. R. Haak, Molecular dynamics with coupling to an external bath, *J. Chem. Phys.*, 1984, **81**(8), 3684–3690.
106. T. Morishita, Fluctuation formulas in molecular-dynamics simulations with the weak coupling heat bath, *J. Chem. Phys.*, 2000, **113**(8), 2976–2982.
107. R. Zwanzig, Nonlinear generalized Langevin equations. *J. Stat. Phys.*, 1973, **9**(3), 215–220.
108. D. J. Evans and B. L. Holian, The Nose–Hoover thermostat, *J. Chem. Phys.*, 1985, **83**(8), 4069–4074.
109. S. E. Feller, Y. Zhang, R. W. Pastor and B. R. Brooks, Constant pressure molecular dynamics simulation: the Langevin piston method, *J. Chem. Phys.*, 1995, **103**(11), 4613–4621.
110. S. Toxvaerd, O. J. Heilmann and J. C. Dyre, Energy conservation in molecular dynamics simulations of classical systems, *J. Chem. Phys.*, 2012, **136**(22), 224106.
111. S. K. Gray, D. W. Noid and B. G. Sumpter, Symplectic integrators for large scale molecular dynamics simulations: A comparison of several explicit methods, *J. Chem. Phys.*, 1994, **101**(5), 4062–4072.
112. H. Grubmüller, H. Heller, A. Windemuth and K. Schulten, Generalized Verlet algorithm for efficient molecular dynamics simulations with long-range interactions, *Mol. Simul.*, 1991, **6**(1–3), 121–142.
113. W. Van Gunsteren and H. Berendsen, A leap-frog algorithm for stochastic dynamics, *Mol. Simul.*, 1988, **1**(3), 173–185.
114. M. G. Paterlini and D. M. Ferguson, Constant temperature simulations using the Langevin equation with velocity Verlet integration, *Chem. Phys.*, 1998, **236**(1), 243–252.
115. D. Beeman, Some multistep methods for use in molecular dynamics calculations, *J. Comput. Phys.*, 1976, **20**(2), 130–139.

116. D. Janezic and B. Orel, Implicit Runge-Kutta method for molecular dynamics integration, *J. Chem. Inf. Comput. Sci.*, 1993, **33**(2), 252–257.
117. H. Qian and T. Schlick, Molecular Modeling and Simulation: An Interdisciplinary Guide, JSTOR, 2005.
118. S. Miyamoto and P. A. Kollman, SETTLE: an analytical version of the SHAKE and RATTLE algorithm for rigid water models, *J. Comput. Chem.*, 1992, **13**(8), 952–962.
119. J.-P. Ryckaert, G. Ciccotti and H. J. Berendsen, Numerical integration of the cartesian equations of motion of a system with constraints: molecular dynamics of n-alkanes, *J. Comput. Phys.*, 1977, **23**(3), 327–341.
120. R. O. Dror, M. O. Jensen, D. W. Borhani and D. E. Shaw, Exploring atomic resolution physiology on a femtosecond to millisecond time-scale using molecular dynamics simulations, *J. Gen. Physiol.*, 2010, **135**(6), 555–562.
121. K. Khafizov, C. Perez, C. Koshy, M. Quick, K. Fendler, C. Ziegler and L. R. Forrest, Investigation of the sodium-binding sites in the sodium-coupled betaine transporter BetP, *Proc. Natl. Acad. Sci.*, 2012, **109**(44), E3035–E3044.
122. C. Perez, B. Faust, A. R. Mehdipour, K. A. Francesconi, L. R. Forrest and C. Ziegler, Substrate-bound outward-open state of the betaine transporter BetP provides insights into Na^+ coupling, *Nat. Commun.*, 2014, **5**, 4231.
123. E. Zomot, M. Gur and I. Bahar, Microseconds simulations reveal a new sodium-binding site and the mechanism of sodium-coupled substrate uptake by LeuT, *J. Biol. Chem.*, 2015, **290**(1), 544–555.
124. C. Zhao, S. Stolzenberg, L. Gracia, H. Weinstein, S. Noskov and L. Shi, Ion-controlled conformational dynamics in the outward-open transition from an occluded state of LeuT, *Biophys. J.*, 2012, **103**(5), 878–888.
125. Y. Weng, L. Yang, P. J. Corringer and J. M. Sonner, Anesthetic sensitivity of the Gloeobacter violaceus proton-gated ion channel, *Anesth. Analg.*, 2010, **110**(1), 59–63.
126. J. M. Violet, D. L. Downie, R. C. Nakisa, W. R. Lieb and N. P. Franks, Differential sensitivities of mammalian neuronal and muscle nicotinic acetylcholine receptors to general anesthetics, *Anesthesiology*, 1997, **86**(4), 866–874.
127. G. Brannigan, D. N. LeBard, J. Henin, R. G. Eckenhoff and M. L. Klein, Multiple binding sites for the general anesthetic isoflurane identified in the nicotinic acetylcholine receptor transmembrane domain, *Proc. Natl. Acad. Sci. U. S. A.*, 2010, **107**(32), 14122–14127.
128. D. Willenbring, L. T. Liu, D. Mowrey, Y. Xu and P. Tang, Isoflurane alters the structure and dynamics of GLIC, *Biophys. J.*, 2011, **101**(8), 1905–1912.
129. R. Spurny, B. Billen, R. J. Howard, M. Brams, S. Debaveye, K. L. Price, D. A. Weston, S. V. Strelkov, J. Tytgat, S. Bertrand, D. Bertrand, S. C. Lummis and C. Ulens, Multisite binding of a general anesthetic to

the prokaryotic pentameric Erwinia chrysanthemi ligand-gated ion channel (ELIC), *J. Biol. Chem.*, 2013, **288**(12), 8355–8364.
130. Q. Chen, M. N. Kinde, P. Arjunan, M. M. Wells, A. E. Cohen, Y. Xu and P. Tang, Direct Pore Binding as a Mechanism for Isoflurane Inhibition of the Pentameric Ligand-gated Ion Channel ELIC, *Sci. Rep.*, 2015, **5**, 13833.
131. S. G. Raju, A. F. Barber, D. N. LeBard, M. L. Klein and V. Carnevale, Exploring Volatile General Anesthetic Binding to a Closed Membrane-Bound Bacterial Voltage-Gated Sodium Channel via Computation, *PLoS Comput. Biol.*, 2013, **9**(6), e1003090.
132. A. F. Barber, V. Carnevale, M. L. Klein, R. G. Eckenhoff and M. Covarrubias, Modulation of a voltage-gated Na^+ channel by sevoflurane involves multiple sites and distinct mechanisms, *Proc. Natl. Acad. Sci. U. S. A.*, 2014, **111**(18), 6726–6731.
133. C. Boiteux, I. Vorobyov, R. J. French, C. French, V. Yarov-Yarovoy and T. W. Allen, Local anesthetic and antiepileptic drug access and binding to a bacterial voltage-gated sodium channel, *Proc. Natl. Acad. Sci. U. S. A.*, 2014, **111**(36), 13057–13062.
134. J. A. Kaczmarski and B. Corry, Investigating the size and dynamics of voltage-gated sodium channel fenestrations, *Channels*, 2014, **8**(3), 264–277.
135. D. E. Shaw, P. Maragakis, K. Lindorff-Larsen, S. Piana, R. O. Dror, M. P. Eastwood, J. A. Bank, J. M. Jumper, J. K. Salmon, Y. Shan and W. Wriggers, Atomic-Level Characterization of the Structural Dynamics of Proteins, *Science*, 2010, **330**(6002), 341–346.
136. J. C. Shelley, M. Y. Shelley, R. C. Reeder, S. Bandyopadhyay and M. L. Klein, A Coarse Grain Model for Phospholipid Simulations, *J. Phys. Chem. B*, 2001, **105**(19), 4464–4470.
137. J. C. Shelley, M. Y. Shelley, R. C. Reeder, S. Bandyopadhyay, P. B. Moore and M. L. Klein, Simulations of Phospholipids Using a Coarse Grain Model, *J. Phys. Chem. B*, 2001, **105**(40), 9785–9792.
138. X. He, W. Shinoda, R. DeVane, K. L. Anderson and M. L. Klein, Paramaterization of a coarse-grained model for linear alkylbenzene sulfonate surfactants and molecular dynamics studies of their self-assembly in aqueous solution, *Chem. Phys. Lett.*, 2010, **487**(1–3), 71–76.
139. W. Shinoda, R. DeVane and M. L. Klein, Coarse-grained molecular modeling of non-ionic surfactant self-assembly, *Soft Matter*, 2008, **4**(12), 2454–2462.
140. R. DeVane, W. Shinoda, P. B. Moore and M. L. Klein, Transferable Coarse Grain Nonbonded Interaction Model for Amino Acids, *J. Chem. Theory Comput.*, 2009, **5**(8), 2115–2124.
141. S. J. Marrink, A. H. de Vries and A. E. Mark, Coarse Grained Model for Semiquantitative Lipid Simulations, *J. Phys. Chem. B*, 2004, **108**(2), 750–760.
142. C. A. Lopez, Z. Sovova, F. J. van Eerden, A. H. de Vries and S. J. Marrink, Martini Force Field Parameters for Glycolipids, *J. Chem. Theory Comput.*, 2013, **9**(3), 1694–1708.

143. S. J. Marrink, H. J. Risselada, S. Yefimov, D. P. Tieleman and A. H. de Vries, The MARTINI Force Field: Coarse Grained Model for Biomolecular Simulations, *J. Phys. Chem. B*, 2007, **111**(27), 7812–7824.
144. L. Monticelli, S. K. Kandasamy, X. Periole, R. G. Larson, D. P. Tieleman and S.-J. Marrink, The MARTINI Coarse-Grained Force Field: Extension to Proteins, *J. Chem. Theory Comput.*, 2008, **4**(5), 819–834.
145. D. H. de Jong, G. Singh, W. F. D. Bennett, C. Arnarez, T. A. Wassenaar, L. V. Schäfer, X. Periole, D. P. Tieleman and S. J. Marrink, Improved Parameters for the Martini Coarse-Grained Protein Force Field, *J. Chem. Theory Comput.*, 2013, **9**(1), 687–697.
146. A. Gautieri, A. Russo, S. Vesentini, A. Redaelli and M. J. Buehler, Coarse-Grained Model of Collagen Molecules Using an Extended MARTINI Force Field, *J. Chem. Theory Comput.*, 2010, **6**(4), 1210–1218.
147. J. D. Perlmutter and J. N. Sachs, Inhibiting lateral domain formation in lipid bilayers: simulations of alternative steroid headgroup chemistries, *J. Am. Chem. Soc.*, 2009, **131**(45), 16362–16363.
148. C. A. López, A. J. Rzepiela, A. H. de Vries, L. Dijkhuizen, P. H. Hünenberger and S. J. Marrink, Martini Coarse-Grained Force Field: Extension to Carbohydrates, *J. Chem. Theory Comput.*, 2009, **5**(12), 3195–3210.
149. J. Wohlert, L. A. Berglund and A. Coarse-Grained, Model for Molecular Dynamics Simulations of Native Cellulose, *J. Chem. Theory Comput.*, 2011, **7**(3), 753–760.
150. G. Rossi, P. F. J. Fuchs, J. Barnoud and L. Monticelli, A Coarse-Grained MARTINI Model of Polyethylene Glycol and of Polyoxyethylene Alkyl Ether Surfactants, *J. Phys. Chem. B*, 2012, **116**(49), 14353–14362.
151. G. Rossi, L. Monticelli, S. R. Puisto, I. Vattulainen and T. Ala-Nissila, Coarse-graining polymers with the MARTINI force-field: polystyrene as a benchmark case, *Soft Matter*, 2011, **7**(2), 698–708.
152. A. Milani, M. Casalegno, C. Castiglioni and G. Raos, Coarse-Grained Simulations of Model Polymer Nanofibres, *Macromol. Theory Simul.*, 2011, **20**(5), 305–319.
153. H. Lee and R. G. Larson, Molecular Dynamics Simulations of PAMAM Dendrimer-Induced Pore Formation in DPPC Bilayers with a Coarse-Grained Model, *J. Phys. Chem. B*, 2006, **110**(37), 18204–18211.
154. H. Lee and R. G. Larson, Coarse-grained molecular dynamics studies of the concentration and size dependence of fifth- and seventh-generation PAMAM dendrimers on pore formation in DMPC bilayer, *J. Phys. Chem. B*, 2008, **112**(26), 7778–7784.
155. J. Wong-Ekkabut, S. Baoukina, W. Triampo, I. M. Tang, D. P. Tieleman and L. Monticelli, Computer simulation study of fullerene translocation through lipid membranes, *Nat Nanotechnol.*, 2008, **3**(6), 363–368.
156. L. Monticelli, On Atomistic and Coarse-Grained Models for C60 Fullerene, *J. Chem. Theory Comput.*, 2012, **8**(4), 1370–1378.
157. J. J. Uusitalo, H. I. Ingólfsson, P. Akhshi, D. P. Tieleman and S. J. Marrink, Martini Coarse-Grained Force Field: Extension to DNA, *J. Chem. Theory Comput.*, 2015, **11**(8), 3932–3945.

158. H. J. Risselada and S. J. Marrink, The molecular face of lipid rafts in model membranes, *Proc. Natl. Acad. Sci.*, 2008, **105**(45), 17367–17372.
159. R. Baron, D. Trzesniak, A. H. de Vries, A. Elsener, S. J. Marrink and W. F. van Gunsteren, Comparison of thermodynamic properties of coarse-grained and atomic-level simulation models, *ChemPhysChem*, 2007, **8**(3), 452–461.
160. S. Baoukina, L. Monticelli, S. J. Marrink and D. P. Tieleman, Pressure – Area Isotherm of a Lipid Monolayer from Molecular Dynamics Simulations, *Langmuir*, 2007, **23**(25), 12617–12623.
161. S. Baoukina, S. J. Marrink and D. P. Tieleman, Lateral pressure profiles in lipid monolayers, *Faraday Discuss.*, 2010, **144**, 393–409, discussion 445–81.
162. S. J. Marrink and D. P. Tieleman, Perspective on the Martini model, *Chem. Soc. Rev.*, 2013, **42**(16), 6801–6822.
163. M. G. Saunders and G. A. Voth, Coarse-graining methods for computational biology, *Annu. Rev. Biophys.*, 2013, **42**, 73–93.
164. P. Carbone, H. A. Varzaneh, X. Chen and F. Muller-Plathe, Transferability of coarse-grained force fields: the polymer case, *J. Chem. Phys.*, 2008, **128**(6), 064904.
165. D. Sengupta and A. Chattopadhyay, Molecular dynamics simulations of GPCR-cholesterol interaction: An emerging paradigm, *Biochim. Biophys. Acta*, 2015, **1848**(9), 1775–1782.
166. C. Neale, H. D. Herce, R. Pomès and A. E. García, Can Specific Protein-Lipid Interactions Stabilize an Active State of the Beta 2 Adrenergic Receptor? *Biophys. J.*, 2015, **109**(8), 1652–1662.
167. A. C. Kalli, M. S. P. Sansom and R. A. F. Reithmeier, Molecular Dynamics Simulations of the Bacterial UraA H^+-Uracil Symporter in Lipid Bilayers Reveal a Closed State and a Selective Interaction with Cardiolipin, *PLoS Comput. Biol.*, 2015, **11**(3), e1004123.
168. J. N. Horn, T.-C. Kao and A. Grossfield, Coarse-grained Molecular Dynamics Provides Insight into the Interactions of Lipids and Cholesterol with Rhodopsin, *Adv. Exp. Med. Biol.*, 2014, **796**, 75–94.
169. X. Periole, A. M. Knepp, T. P. Sakmar, S. J. Marrink and T. Huber, Structural Determinants of the Supramolecular Organization of G Protein-Coupled Receptors in Bilayers, *J. Am. Chem. Soc.*, 2012, **134**(26), 10959–10965.
170. S. Mondal, J. M. Johnston, H. Wang, G. Khelashvili, M. Filizola and H. Weinstein, Membrane Driven Spatial Organization of GPCRs, *Sci. Rep.*, 2013, **3**, 2909.
171. S. Izvekov and G. A. Voth, A Multiscale Coarse-Graining Method for Biomolecular Systems, *J. Phys. Chem. B*, 2005, **109**(7), 2469–2473.
172. Q. Shi, S. Izvekov and G. A. Voth, Mixed Atomistic and Coarse-Grained Molecular Dynamics: Simulation of a Membrane-Bound Ion Channel, *J. Phys. Chem. B*, 2006, **110**(31), 15045–15048.
173. E. Villa, A. Balaeff and K. Schulten, Structural dynamics of the lac repressor–DNA complex revealed by a multiscale simulation, *Proc. Natl. Acad. Sci. U. S. A.*, 2005, **102**(19), 6783–6788.

174. M. Neri, C. Anselmi, M. Cascella, A. Maritan and P. Carloni, Coarse-grained model of proteins incorporating atomistic detail of the active site, *Phys. Rev. Lett.*, 2005, **95**(21), 218102.
175. M. Neri, M. Baaden, V. Carnevale, C. Anselmi, A. Maritan and P. Carloni, Microseconds dynamics simulations of the outer-membrane protease T, *Biophys. J.*, 2008, **94**(1), 71–78.
176. A. J. Rzepiela, M. Louhivuori, C. Peter and S. J. Marrink, Hybrid simulations: combining atomistic and coarse-grained force fields using virtual sites, *Phys. Chem. Chem. Phys.*, 2011, **13**(22), 10437–10448.
177. M. Leguèbe, C. Nguyen, L. Capece, Z. Hoang, A. Giorgetti and P. Carloni, Hybrid Molecular Mechanics/Coarse-Grained Simulations for Structural Prediction of G-Protein Coupled Receptor/Ligand Complexes, *PLoS One*, 2012, **7**(10), e47332.
178. A. Marchiori, L. Capece, A. Giorgetti, P. Gasparini, M. Behrens, P. Carloni and W. Meyerhof, Coarse-Grained/Molecular Mechanics of the TAS2R38 Bitter Taste Receptor: Experimentally-Validated Detailed Structural Prediction of Agonist Binding, *PLoS One*, 2013, **8**(5), e64675.
179. M. Sandal, M. Behrens, A. Brockhoff, F. Musiani, A. Giorgetti, P. Carloni and W. Meyerhof, Evidence for a Transient Additional Ligand Binding Site in the TAS2R46 Bitter Taste Receptor, *J. Chem. Theory Comput.*, 2015, **11**(9), 4439–4449.
180. A. Brockhoff, M. Behrens, M. Y. Niv and W. Meyerhof, Structural requirements of bitter taste receptor activation, *Proc. Natl. Acad. Sci.*, 2010, **107**(24), 11110–11115.
181. G. Rossetti, D. Dibenedetto, V. Calandrini, A. Giorgetti and P. Carloni, Structural predictions of neurobiologically relevant G-protein coupled receptors and intrinsically disordered proteins, *Arch. Biochem. Biophys.*, 2015, **582**, 91–100.
182. J. J. Sakurai and J. Napolitano, *Modern Quantum Mechanics*, Addison-Wesley, 2011.
183. R. G. Parr, *Density Functional Theory of Atoms and Molecules*, Springer, 1980.
184. F. A. Hamprecht, A. J. Cohen, D. J. Tozer and N. C. Handy, Development and assessment of new exchange-correlation functionals, *J. Chem. Phys.*, 1998, **109**(15), 6264–6271.
185. R. Car and M. Parrinello, Unified Approach for Molecular Dynamics and Density-Functional Theory, *Phys. Rev. Lett.*, 1985, **55**(22), 2471–2474.
186. J. VandeVondele, M. Krack, F. Mohamed, M. Parrinello, T. Chassaing and J. Hutter, Quickstep: Fast and accurate density functional calculations using a mixed Gaussian and plane waves approach, *Comput. Phys. Commun.*, 2005, **167**(2), 103–128.
187. T. D. Kühne, M. Krack, F. R. Mohamed and M. Parrinello, Efficient and Accurate Car-Parrinello-like Approach to Born-Oppenheimer Molecular Dynamics, *Phys. Rev. Lett.*, 2007, **98**(6), 066401.

188. L. Vilčiauskas, M. E. Tuckerman, G. Bester, S. J. Paddison and K.-D. Kreuer, The mechanism of proton conduction in phosphoric acid, *Nat. Chem.*, 2012, **4**(6), 461–466.
189. M. E. Tuckerman, D. Marx and M. Parrinello, The nature and transport mechanism of hydrated hydroxide ions in aqueous solution, *Nature*, 2002, **417**(6892), 925–929.
190. T. C. Berkelbach, H. S. Lee and M. E. Tuckerman, Concerted hydrogen-bond dynamics in the transport mechanism of the hydrated proton: a first-principles molecular dynamics study, *Phys. Rev. Lett.*, 2009, **103**(23), 238302.
191. S. Izvekov and G. A. Voth, Ab initio molecular-dynamics simulation of aqueous proton solvation and transport revisited, *J. Chem. Phys.*, 2005, **123**(4), 044505.
192. C. Zhang, D. G. Knyazev, Y. A. Vereshaga, E. Ippoliti, T. H. Nguyen, P. Carloni and P. Pohl, Water at hydrophobic interfaces delays proton surface-to-bulk transfer and provides a pathway for lateral proton diffusion, *Proc. Natl. Acad. Sci.*, 2012, **109**(25), 9744–9749.
193. D. E. Sagnella, K. Laasonen and M. L. Klein, Ab initio molecular dynamics study of proton transfer in a polyglycine analog of the ion channel gramicidin A, *Biophys. J.*, 1996, **71**(3), 1172–1178.
194. J. Dreyer, C. Zhang, E. Ippoliti and P. Carloni, Role of the Membrane Dipole Potential for Proton Transport in Gramicidin A Embedded in a DMPC Bilayer, *J. Chem. Theory Comput.*, 2013, **9**(8), 3826–3831.
195. S. Cukierman, Proton Mobilities in Water and in Different Stereoisomers of Covalently Linked Gramicidin A Channels, *Biophys. J.*, 2000, **78**(4), 1825–1834.
196. A. Laio, J. VandeVondele and U. Rothlisberger, A Hamiltonian electrostatic coupling scheme for hybrid Car–Parrinello molecular dynamics simulations, *J. Chem. Phys.*, 2002, **116**(16), 6941–6947.
197. M. Eichinger, P. Tavan, J. Hutter and M. Parrinello, A hybrid method for solutes in complex solvents: Density functional theory combined with empirical force fields, *J. Chem. Phys.*, 1999, **110**(21), 10452–10467.
198. M. W. van der Kamp and A. J. Mulholland, Combined Quantum Mechanics/Molecular Mechanics (QM/MM) Methods in Computational Enzymology, *Biochemistry*, 2013, **52**(16), 2708–2728.
199. R. Lonsdale, K. E. Ranaghan and A. J. Mulholland, Computational enzymology, *Chem. Commun.*, 2010, **46**(14), 2354–2372.
200. M. Ø. Jensen, U. Röthlisberger and C. Rovira, Hydroxide and Proton Migration in Aquaporins, *Biophys. J.*, 2005, **89**(3), 1744–1759.
201. R. Rousseau, V. Kleinschmidt, U. W. Schmitt and D. Marx, Assigning protonation patterns in water networks in bacteriorhodopsin based on computed IR spectra, *Angew. Chem., Int. Ed.*, 2004, **43**(36), 4804–4807.
202. G. Mathias and D. Marx, Structures and spectral signatures of protonated water networks in bacteriorhodopsin, *Proc. Natl. Acad. Sci.*, 2007, **104**(17), 6980–6985.

203. D. Bucher, S. Raugei, L. Guidoni, M. Dal Peraro, U. Rothlisberger, P. Carloni and M. L. Klein, Polarization effects and charge transfer in the KcsA potassium channel, *Biophys. Chem.*, 2006, **124**(3), 292–301.
204. D. Bucher, L. Guidoni and U. Rothlisberger, The Protonation State of the Glu-71/Asp-80 Residues in the KcsA Potassium Channel: A First-Principles QM/MM Molecular Dynamics Study, *Biophys. J.*, 2007, **93**(7), 2315–2324.
205. D. Bucher, L. Guidoni, P. Carloni and U. Rothlisberger, Coordination Numbers of K^+ and Na^+ Ions Inside the Selectivity Filter of the KcsA Potassium Channel: Insights from First Principles Molecular Dynamics, *Biophys. J.*, 2010, **98**(10), L47–L49.
206. V. Calandrini, J. Dreyer, E. Ippoliti and P. Carloni, Hydration of chloride anions in the NanC Porin from Escherichia coli: A comparative study by QM/MM and MD simulations, *J. Chem. Phys.*, 2014, **141**(22), 22D521.
207. D. Bucher and U. Rothlisberger, Molecular simulations of ion channels: a quantum chemist's perspective, *J. Gen. Physiol.*, 2010, **135**(6), 549–554.
208. R. W. Zwanzig, High-Temperature Equation of State by a Perturbation Method. I. Nonpolar Gases, *J. Chem. Phys.*, 1954, **22**, 1420–1426.
209. D. L. Beveridge and F. M. DiCapua, Free Energy Via Molecular Simulation: Applications to Chemical and Biomolecular Systems, *Annu. Rev. Biophys. Biophys. Chem.*, 1989, **18**(1), 431–492.
210. D. A. Pearlman, Free energy derivatives: A new method for probing the convergence problem in free energy calculations, *J. Comput. Chem.*, 1994, **15**(1), 105–123.
211. J. Aqvist and V. Luzhkov, Ion permeation mechanism of the potassium channel, *Nature*, 2000, **404**(6780), 881–884.
212. T. W. Allen, A. Bliznyuk, A. P. Rendell, S. Kuyucak and S.-H. Chung, The potassium channel: Structure, selectivity and diffusion, *J. Chem. Phys.*, 2000, **112**(18), 8191–8204.
213. V. B. Luzhkov and J. Aqvist, K^+/Na^+ selectivity of the KcsA potassium channel from microscopic free energy perturbation calculations, *Biochim. Biophys. Acta*, 2001, **1548**(2), 194–202.
214. I. Kim and T. W. Allen, On the selective ion binding hypothesis for potassium channels, *Proc. Nat.l. Acad. Sci.*, 2011, **108**(44), 17963–17968.
215. D. A. Goldfeld, R. Murphy, B. Kim, L. Wang, T. Beuming, R. Abel and R. A. Friesner, Docking and free energy perturbation studies of ligand binding in the kappa opioid receptor, *J. Phys. Chem. B*, 2015, **119**(3), 824–835.
216. L. Wang, Y. Wu, Y. Deng, B. Kim, L. Pierce, G. Krilov, D. Lupyan, S. Robinson, M. K. Dahlgren, J. Greenwood, D. L. Romero, C. Masse, J. L. Knight, T. Steinbrecher, T. Beuming, W. Damm, E. Harder, W. Sherman, M. Brewer, R. Wester, M. Murcko, L. Frye, R. Farid, T. Lin, D. L. Mobley, W. L. Jorgensen, B. J. Berne, R. A. Friesner and R. Abel, Accurate and Reliable Prediction of Relative Ligand Binding Potency in

Prospective Drug Discovery by Way of a Modern Free-Energy Calculation Protocol and Force Field, *J. Am. Chem. Soc.*, 2015, **137**(7), 2695–2703.
217. L. Boukharta, H. Gutierrez-de-Tern and J. Åqvist, , Computational Prediction of Alanine Scanning and Ligand Binding Energetics in G-Protein Coupled Receptors, *PLoS Comput. Biol.*, 2014, **10**(4), e1003585.
218. H. Keränen, H. Gutierrez-de-Tern and J. Åqvist, Structural and Energetic Effects of A2A Adenosine Receptor Mutations on Agonist and Antagonist Binding, *PLoS One*, 2014, **9**(10), e108492.
219. H. Keranen, J. Aqvist and H. Gutierrez-de-Teran, Free energy calculations of A2A adenosine receptor mutation effects on agonist binding, *Chem. Commun.*, 2015, **51**(17), 3522–3525.
220. R. Zhang and X. Xie, Tools for GPCR drug discovery, *Acta Pharmacol. Sin.*, 2012, **33**(3), 372–384.
221. K. Kristiansen, Molecular mechanisms of ligand binding, signaling, and regulation within the superfamily of G-protein-coupled receptors: molecular modeling and mutagenesis approaches to receptor structure and function, *Pharmacol. Ther.*, 2004, **103**(1), 21–80.
222. G. M. Torrie and J. P. Valleau, Monte Carlo free energy estimates using non-Boltzmann sampling: Application to the sub-critical Lennard-Jones fluid, *Chem. Phys. Lett.*, 1974, **28**(4), 578–581.
223. A. Laio and M. Parrinello, Escaping free-energy minima, *Proc. Natl. Acad. Sci.*, 2002, **99**(20), 12562–12566.
224. S. Park and K. Schulten, Calculating potentials of mean force from steered molecular dynamics simulations, *J. Chem. Phys.*, 2004, **120**(13), 5946–5961.
225. E. Darve and A. Pohorille, Calculating free energies using average force, *J. Chem. Phys.*, 2001, **115**(20), 9169–9183.
226. W. Huang and J.-L. Liao, Catalytic Mechanism of the Maltose Transporter Hydrolyzing ATP, *Biochemistry*, 2016, **55**(1), 224–231.
227. S. Kumar, J. M. Rosenberg, D. Bouzida, R. H. Swendsen and P. A. Kollman, THE weighted histogram analysis method for free-energy calculations on biomolecules. I. The method, *J. Comput. Chem.*, 1992, **13**(8), 1011–1021.
228. M. Souaille and B. T. Roux, Extension to the weighted histogram analysis method: combining umbrella sampling with free energy calculations, *Comput. Phys. Commun.*, 2001, **135**(1), 40–57.
229. J. Kästner and W. Thiel, Bridging the gap between thermodynamic integration and umbrella sampling provides a novel analysis method: ''Umbrella integration'', *J. Chem. Phys.*, 2005, **123**(14), 144104.
230. S. Furini and C. Domene, Atypical mechanism of conduction in potassium channels, *Proc. Natl. Acad. Sci. U. S. A.*, 2009, **106**(38), 16074–16077.
231. B. Egwolf and B. Roux, Ion Selectivity of the KcsA Channel: A Perspective from Multi-Ion Free Energy Landscapes, *J. Mol. Biol.*, 2010, **401**(5), 831–842.

232. S. Furini and C. Domene, Selectivity and permeation of alkali metal ions in K^+ channels, *J. Mol. Biol.*, 2011, **409**(5), 867–878.
233. P. W. Fowler, O. Beckstein, E. Abad and M. S. P. Sansom, Detailed Examination of a Single Conduction Event in a Potassium Channel, *J. Phys. Chem. Lett.*, 2013, **4**(18), 3104–3109.
234. E. Piccinini, F. Affinito, R. Brunetti, C. Jacoboni and M. Ceccarelli, Exploring free-energy profiles through ion channels: Comparison on a test case, *J. Comput. Electron.*, 2007, **6**(1), 373–376.
235. S. Park, F. Khalili-Araghi, E. Tajkhorshid and K. Schulten, Free energy calculation from steered molecular dynamics simulations using Jarzynski's equality, *J. Chem. Phys.*, 2003, **119**(6), 3559–3566.
236. J. S. Patel, A. Berteotti, S. Ronsisvalle, W. Rocchia and A. Cavalli, Steered Molecular Dynamics Simulations for Studying Protein–Ligand Interaction in Cyclin-Dependent Kinase 5, *J. Chem. Inf. Model.*, 2014, **54**(2), 470–480.
237. H. Nguyen and L. Le, Steered molecular dynamics approach for promising drugs for influenza A virus targeting M2 channel proteins, *Eur. Biophys. J.*, 2015, **44**(6), 447–455.
238. V. Isberg, T. Balle, T. Sander, F. S. Jorgensen and D. E. Gloriam, G protein- and agonist-bound serotonin 5-HT2A receptor model activated by steered molecular dynamics simulations, *J. Chem. Inf. Model.*, 2011, **51**(2), 315–325.
239. J. Parkin and S. Khalid, Atomistic Molecular-Dynamics Simulations Enable Prediction of the Arginine Permeation Pathway through OccD1/OprD from Pseudomonas aeruginosa, *Biophys. J.*, 2014, **107**(8), 1853–1861.
240. R. X. Gu, V. Corradi, G. Singh, H. G. Choudhury, K. Beis and D. P. Tieleman, Conformational Changes of the Antibacterial Peptide ATP Binding Cassette Transporter McjD Revealed by Molecular Dynamics Simulations, *Biochemistry*, 2015, **54**(38), 5989–5998.
241. C. Domene, M. L. Klein, D. Branduardi, F. L. Gervasio and M. Parrinello, Conformational changes and gating at the selectivity filter of potassium channels, *J. Am. Chem. Soc.*, 2008, **130**(29), 9474–9480.
242. G. Bussi, F. L. Gervasio, A. Laio and M. Parrinello, Free-Energy Landscape for β Hairpin Folding from Combined Parallel Tempering and Metadynamics, *J. Am. Chem. Soc.*, 2006, **128**(41), 13435–13441.
243. S. Piana, A. Laio and A. Bias-Exchange, Approach to Protein Folding, *J. Phys. Chem. B*, 2007, **111**(17), 4553–4559.
244. C. Domene, P. Barbini and S. Furini, Bias-Exchange Metadynamics Simulations: An Efficient Strategy for the Analysis of Conduction and Selectivity in Ion Channels, *J. Chem. Theory Comput.*, 2015, **11**(4), 1896–1906.
245. B. Corry and M. Thomas, Mechanism of Ion Permeation and Selectivity in a Voltage Gated Sodium Channel, *J. Am. Chem. Soc.*, 2012, **134**(3), 1840–1846.

246. S. Furini and C. Domene, On Conduction in a Bacterial Sodium Channel, *PLoS Comput. Biol.*, 2012, **8**(4), e1002476.
247. L. Stock, L. Delemotte, V. Carnevale, W. Treptow and M. L. Klein, Conduction in a Biological Sodium Selective Channel, *J. Phys. Chem. B*, 2013, **117**(14), 3782–3789.
248. S. Furini and C. Domene, Computational studies of transport in ion channels using metadynamics, *Biochim. Biophys. Acta*, 2016, **1858**(7 Pt B), 1733–1740.
249. T. P. Straatsma and H. J. C. Berendsen, Free energy of ionic hydration: Analysis of a thermodynamic integration technique to evaluate free energy differences by molecular dynamics simulations, *J. Chem. Phys.*, 1988, **89**(9), 5876–5886.
250. J. Henin and C. Chipot, Overcoming free energy barriers using unconstrained molecular dynamics simulations, *J. Chem. Phys.*, 2004, **121**(7), 2904–2914.
251. C. Chipot and J. Hénin, Exploring the free-energy landscape of a short peptide using an average force, *J. Chem. Phys.*, 2005, **123**(24), 244906.
252. J. Hénin, K. Schulten and C. Chipot, Conformational Equilibrium in Alanine-Rich Peptides Probed by Reversible Stretching Simulations, *J. Phys. Chem. B*, 2006, **110**(33), 16718–16723.
253. J. L. Popot and D. M. Engelman, Membrane protein folding and oligomerization: the two-stage model, *Biochemistry*, 1990, **29**(17), 4031–4037.
254. J. Hénin, A. Pohorille and C. Chipot, Insights into the Recognition and Association of Transmembrane α-Helices. The Free Energy of α-Helix Dimerization in Glycophorin A, *J. Am. Chem. Soc.*, 2005, **127**(23), 8478–8484.
255. I. Ivanov, X. Cheng, S. M. Sine and J. A. McCammon, Barriers to Ion Translocation in Cationic and Anionic Receptors from the Cys-Loop Family, *J. Am. Chem. Soc.*, 2007, **129**(26), 8217–8224.
256. P. Aryal, M. S. P. Sansom and S. J. Tucker, Hydrophobic Gating in Ion Channels, *J. Mol. Biol.*, 2015, **427**(1), 121–130.
257. G. Lamoureux, M. L. Klein and S. Bernèche, A Stable Water Chain in the Hydrophobic Pore of the AmtB Ammonium Transporter, *Biophys. J.*, 2007, **92**(9), L82–L84.
258. J. Hénin, E. Tajkhorshid, K. Schulten and C. Chipot, Diffusion of Glycerol through Escherichia coli Aquaglyceroporin GlpF, *Biophys. J.*, 2008, **94**(3), 832–839.
259. M. H. Cheng and R. D. Coalson, Molecular Dynamics Investigation of Cl^- and Water Transport through a Eukaryotic CLC Transporter, *Biophys. J.*, 2012, **102**(6), 1363–1371.
260. Z. Wang, T. Yu, J.-P. Sang, X.-W. Zou, C. Yan and X. Zou, Computation and Simulation of the Structural Characteristics of the Kidney Urea Transporter and Behaviors of Urea Transport, *J. Phys. Chem. B*, 2015, **119**(16), 5124–5131.

2.3 Novel Insights into Membrane Transport from Computational Methodologies, *Computational Tools for Chemical Biology*, 2017

2.3.1 Authorship and Permissions

<table>
<tr><th colspan="10">This declaration concerns the article entitled</th></tr>
<tr><td colspan="10">Novel Insights into Membrane Transport from Computational Methodologies</td></tr>
<tr><td colspan="10">Publication status (tick one)</td></tr>
<tr><td>Draft manuscript</td><td></td><td>Submitted</td><td></td><td>In review</td><td></td><td>Accepted</td><td></td><td>Published</td><td>✓</td></tr>
<tr><td>Publication details</td><td colspan="9">Computational Tools for Chemical Biology, 2017, 247-280, Royal Society of Chemistry

Print publication date: 02 Nov 2017
Reproduced by permission of The Royal Society of Chemistry:
http://pubs.rsc.org/en/content/chapter/bk9781782627005-00247/978-1-78262-700-5</td></tr>
<tr><td>Candidates contribution to the paper (detailed and also given as a percentage)</td><td colspan="9">The candidate contributed to/considerably contributed/predominantly executed the…
Formulation of ideas (90%):
V. Oakes and C. Domene contributed to the content.

Design of methodology:
NA

Experimental work:
NA

Presentation of data in journal format (90%):
V. Oakes: Main author of manuscript
C. Domene: Critically assessed and appended manuscript</td></tr>
<tr><td>Statement from Candidate</td><td colspan="9">This paper reports on original research I conducted during the period of my Higher Degree by Research candidature.</td></tr>
<tr><td>Signed</td><td colspan="5"></td><td>Date</td><td colspan="3"></td></tr>
</table>

CHAPTER 10

Novel Insights into Membrane Transport from Computational Methodologies

VICTORIA OAKES[a] AND CARMEN DOMENE*[a,b]

[a] Department of Chemistry, Britannia House, 7 Trinity Street, King's College London, London SE1 1DB, UK; [b] Chemistry Research Laboratory, Mansfield Road, University of Oxford, Oxford OX1 3TA, UK
*Email: mcdn20@bath.ac.uk

10.1 Introduction

The plasma membrane is an integral constituent of both prokaryotic and eukaryotic cells, enclosing the cytoplasm and other cell components. In the latter, the biological membrane is the primary instrument governing the passage of solutes to the cell interior. A phospholipid bilayer forms the basic structural unit establishing a hydrophobic barrier in the membrane core, thus whilst hydrophobic molecules may be admitted passage, additional biological assemblies are required for the transmission of many molecules. Membrane proteins, as these assemblies are known, also play a role in cell signalling, invoking internal processes on recognition of external stimuli. A schematic of membrane transport phenomenon can be found in Figure 10.1.

The availability of atomic resolution structural information is pivotal to discern the underlying principles of membrane transport and communication phenomenon. Vast developments in X-ray crystallographic techniques, NMR and innovative structural determination methods, such as

Chemical Biology No. 3
Computational Tools for Chemical Biology
Edited by Sonsoles Martín-Santamaría

Published by the Royal Society of Chemistry, www.rsc.org

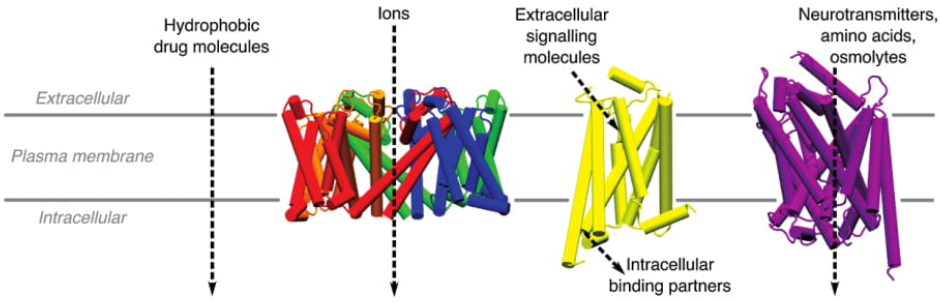

Figure 10.1 Schematic of transport phenomenon across the plasma membrane: hydrophobic drug molecules transit directly through the lipid membrane; ions passively diffuse down the electrochemical gradient of the membrane *via* ion channels, represented as the Na_VAb sodium voltage-gated channel (individual subunits coloured blue, red, yellow and green); binding of extracellular molecules to G-protein coupled receptors initiates coupling with intracellular partners and subsequent signalling, represented as the β2-adrenergic receptor (yellow); molecules can also be actively transported across the membrane, such as amino acids through Na^+-coupled secondary symporters, represented as the leucine transporter (purple).

electron cryo-microscopy, have revolutionised our understanding of the three-dimensional structure of membrane proteins.[1] In combination with the current availability of state-of-the-art computational algorithms and high-performance computing facilities, molecular dynamics (MD) simulations of membrane proteins in a model environment can now be performed routinely to explore a wide range of biological phenomena providing insight for which no experimental methods are applicable. Exploration of the dynamic behaviour of such entities in atomic detail has become particularly important in the realm of medicinal chemistry, where familiarity of ligand transport and binding processes, and subsequent activation or deactivation mechanisms, can lead to the rational design of drugs with improved potency and efficacy, reduced toxicity and subtype specificity. In the following text, we aim to review the considerable insights gained from computational methodologies in recent years.

10.2 Computational Methods

A wide variety of computational methods are currently applied in the field of computational chemistry. MD is a common method used to obtain time-dependent behaviour of a chemical system. In this method, the motion of interacting particles is calculated by the integration of Newton's equations of motion (EOM). The potential energy of the system and the forces, derived from the negative gradient of the potential with respect to displacement in a specified direction, can be used to calculate the acceleration, and hence forecast the time evolution of the system, in the form of a trajectory.

In systems with a couple of atoms, solutions of the EOM can be gained analytically, resulting in a continuous trajectory over time. However, in larger systems, the subsistence of a continuous potential instigates a many body problem for force evaluations, rendering analytic solutions unattainable. In these circumstances, finite difference methods can be used; forces are assessed at discrete intervals, and considered constant in the hiatus. Positions and velocities at the next time step, as these intervals are known, are computed using force evaluations for each atom combined with current positions and velocities. Forces are then recalculated and this procedure is repeated, propagating a trajectory describing the flux of the atomic coordinates over time in a given equilibrium state, which can then be analysed for the properties of interest.

The potential energy can be obtained by quantum or molecular mechanical methods. In the former, only the nuclear motion is evaluated using classical physics; atoms and bonds are considered as balls and springs, respectively, and an analytical expression for the energy of a system, known as a force field, can be derived. This is composed entirely of inter- and intramolecular energetic contributions, including bond stretching, angle bending, bond rotations and non-bonded terms. This architecture neglects electronic properties, such as dipole moments, polarisabilities and vibrational frequencies, but allows for the evaluation of molecular motion for (biological) systems with a large number of degrees of freedom due to reduced computational expense. A wide variety of force fields for biological molecules are available including, but not limited to CHARMM (Chemistry at Harvard Molecular Mechanics),[2] AMBER (Assisted Model Building with Energy Requirement),[3] and OPLS (Optimised Potentials for Liquid Simulations).[4] Each varies in their functional form, parameterisation protocol and parameters therein, which are generally obtained to provide a suitable reproduction of experimental and/or quantum mechanical data.

Most commonly, individual terms for bond lengths and angles utilise simple harmonic potentials on the basis of an energetic penalty associated with a deviation from the equilibrium value.[2] A torsional angle potential function is also typical to model steric barriers associated with the rotation of atoms. With respect to non-bonded interactions, Coulomb and Lennard–Jones potentials are used to express electrostatic and van der Waals forces respectively. In order to appertain electrostatic forces *via* the Coulomb formula, fixed-point charges are assigned at the nuclei. However, in reality, molecules are subject to polarisation effects, *i.e.* the charge fluctuates response to an external electric field, induced by the presence of additional molecules, thus highlighting a limitation of additive force fields.[5]

Significant efforts to develop polarisable FF have been undertaken in recent years. Several schemes have been proposed, among which are the fluctuating charge model, the induced dipole model and the Drude oscillator approach. In the fluctuating charge model, adopted in in the CHeq force field[6,7] for example, molecular charges remain constant throughout the simulation with individual point charges readjusted in consonance with

the electronegativity. AMOEBA is the most noteworthy force field utilising an induced dipole model, where atomic multipoles are used explicitly to represent electrostatics; multipoles are calculated *via* a self-consistent field procedure, heightening the computational expense of this protocol.[8] Finally, in the Drude oscillator approach, a subsidiary charged particle is attached to the nucleus by a harmonic spring, and treated as an extra degree of freedom.[9] A comprehensive review of the field can be found in ref. 10.

Despite the universal availability of MD algorithms and force fields applicable to biological macromolecules, the size of model systems of intrinsic membrane proteins, and the computing resources this requires, poses inherent limitations. The time step suitable for stable dynamics is dictated by the highest vibrational frequency of the molecule, usually the C–H bond; 1 fs is commonplace, with 2 fs permitted when supplementary algorithms such as SETTLE,[11] an analytical version of the SHAKE function, are employed to the movement of these bonds. In combination with system size up to 1 000 000 atoms, dynamics can be extremely intensive.[12] Recent expansions in computer hardware and high-performance computing facilities, means MD simulations on a nanosecond timescale are now routine, with microsecond simulations attainable in recent years. Such methodologies are therefore relevant to study a wide range of biological phenomena. Many biological phenomena that occur on extended timescales, such as protein folding, complex association and conformational changes associated with gating, are generally unattainable by atomistic equilibrium MD without the use of tailor-made software. The Shaw Group has pioneered the production of millisecond long unbiased simulations by the development of the Supercomputer Anton, optimised for use with MD software.[13] However, this technology is not widely available, leading to the development of alternative approaches to accelerate sampling.

Using a reduced representation is one such approach, utilising classical MD simulations, to increase the speed and hence timescales obtainable, as well as simulate larger systems with increased complexity. Coarse-grained (CG) molecular dynamics, as this is known, reduces the number of degrees of freedom in a simulation system by treating a group of atoms as a single entity, significantly curtailing the computational expense of each step. To convert an all-atom structure to a coarse-grained model, hydrogen atoms are not considered, with a number of heavy atoms (typically three or four) grouped into a single interaction site, known as a 'bead'. Interaction potentials are then characterised dependent on the CG model, with required parameters generally developed to reproduce microscopic properties recorded in atomistic simulations and thermodynamic data derived by experimental means. Originally developed to capture the extended time and large-scale behaviour of membranes, a number of CG force fields have emerged from the research groups of Klein,[14,15] Marrink[16,17] and others.[18] The implementation of these schemes reduces the number of required calculations, as well as increasing the time step of each iteration (20–40 fs) providing a powerful tool to accelerate molecular simulations. Methods to

maintain a level of chemical specificity are also embedded in each scheme; in the Martini force field, from Marrink *et al.*, sites are classified by the chemical nature of the region, *i.e.* polar, non-polar, apolar (a mixture of polar and non-polar groups) and charged, for example. Additional techniques are often required to sample phenomena where both atomistic and coarse-grain methodologies are not appropriate, such as those that occur on an extended timescale or involve an energetic barrier.

From MD trajectories of the system in time structural and dynamical quantities as well as kinetic and thermodynamic properties can be calculated using the principles of statistical mechanics. Among the thermodynamic quantities, it is the free energy that provides a direct link between statistical mechanics and thermodynamics, and through which other thermodynamic quantities can be obtained. A long-standing method to calculate the underlying free energy of a system is known as free energy perturbation (FEP). In this method, alchemical transformations are performed to overcome energetic barriers, and the relative free energy differences are calculated by a thermodynamic cycle.[19,20] Several algorithms also exist to accelerate sampling along a pre-defined set of reaction coordinates and estimate the potential of mean force (PMF), such as umbrella sampling, metadynamics, adaptive biasing force or steered MD. Such reaction coordinates, known as collective variables (CV), are chosen to elucidate a specific conformational transition. A free energy estimate as a function of the collective variables, as well as the equilibrium properties, can be obtained providing a wealth of information about the simulation system at a fraction of the expense of traditional all-atom MD.

Umbrella sampling (US)[21] is perhaps one of the most popular enhanced sampling method in this field, where a bias potential along user-defined CVs provokes conversion between stable thermodynamic states. Independent MD simulations are performed at intermediary steps, known as windows, which can be combined using the weight histogram analysis method (WHAM)[22,23] or umbrella integration.[24] Each window represents equilibrium sampling of energetically distinct locales; accordingly such evaluation estimates the consolidated equilibrium free-energy surface.

Another method in this group is steered molecular dynamics (SMD) simulations.[25] SMD are akin to well-established experimental techniques, such as atomic force microscopy or optical tweezers, where an atom is external force is applied to an atom, or group of atoms, to overcome barriers and sample a specific process.[25] Relative free energies can then be obtained by the Jarzynki equality.[26]

In metadynamics, a superficial bias potential is utilised to advance sampling along suitable CVs, diverting from configurational space previously inhabited. The biasing potential is adjusted by the addition of a Gaussian function, augmenting the energy of the system and departing from local free energy minima, allowing the exploration of alternative thermodynamic states separated by energetic barriers. Once convergence has been achieved, effectively when the entire free energy profile has been flattened, it can be

easily reconstructed to provide an unbiased estimate of the landscape as a function of the CVs.

The adaptive biasing force method (ABF)[27] is largely based on thermodynamic integration, whereby the instantaneous force along the reaction coordinate is evaluated directly and counteracted by an external biasing force of equal and opposite magnitude. This effectively provides a smooth energy landscape, and uniform sampling irrespective of energetic barriers allowing accelerated dynamics.

In the following sections, a wide range of literature will be discussed to illustrate how conventional and accelerated MD methods have been used to provide crucial insights into the functioning of the plasma membrane and its constituents on an atomistic level.

10.3 Unassisted Diffusion Across Lipid Bilayers

In the first instance, MD simulations have become an established tool to characterise unassisted transport across lipid bilayers, as a model for the biological membrane. The properties of lipid bilayers are generally characterised by a hydrophilic exterior and hydrophobic interior, favourably interacting with aqueous intra- and extracellular compartments (Figure 10.2(a)). In reality, of course, the situation is significantly more complex; membranes are highly heterologous systems that are capable of transporting small solutes and impermeable to many others. Even though overall permeability coefficients can be obtained by experimental and computational means, the latter is required to explicitly represent structural and dynamical fluctuations across lipid bilayers and, hence, gain atomistic mechanistic details of transport phenomenon. Although embedded proteins are instrumental in a manifold of transport events as described in later sections, unassisted diffusion is the prevailing manner by which small molecules, including drugs, gain access to the cell. In the following section, we aim to review a selection of recent publications to illustrate the use of computational simulations to

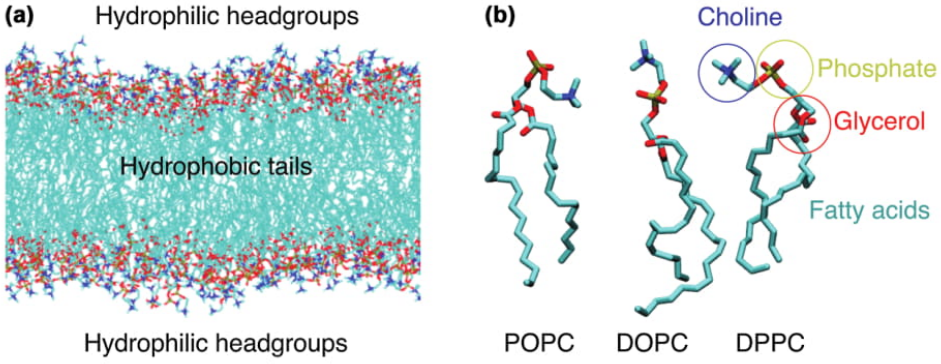

Figure 10.2 (a) Representation of a single-component lipid bilayer typically used as a model plasma membrane. (b) Structures of common phospholipid molecules used in MD simulations.

explore membrane permeability properties. Model membranes comprised of a single species of phospholipid, such as 1-palmitoyl-2-oleoyl-sn-glycero-3-phosphocholine (POPC), 1,2-dioleoyl-sn-glycero-3-phosphocholine (DOPC) and 1,2-dipalmitoyl-sn-glycero-3-phosphocholine (DPPC) are typically used in this context (Figure 10.2(b)).

Passive diffusion across lipid bilayers is historically characterised by a solubility–diffusion mechanism; the solute diffuses from the extracellular solution and negotiates the membrane prior to accessing the cytoplasm. If partitioning at the membrane–water interfaces is assumed to be at equilibrium, and the membrane is considered as a homogenous oil slab in line with Overton's correlation between membrane permeability and oil/water partitioning coefficient of a solute[28] a simple relationship between the oil/water-partitioning coefficient (K), the diffusion coefficient of the solute in solvent (D) and the membrane thickness can be used to yield the membrane permeability coefficient (P):[29]

$$P = \frac{KD}{h} \tag{10.1}$$

The inhomogeneous solubility–diffusion model provides notable improvements by taking into account the heterogeneous behaviour of lipid bilayers, procuring permeability coefficients as a function of membrane depth.[30] Comprehensive sampling of the entire diffusion process is currently unattainable by all-atom MD simulations, due to the computational expense and the stochastic nature of the technique. Therefore, the applicability of this model to MD simulations[31] is dependent on enhanced sampling techniques; the original implementation utilised the z-constraint method[31] whereby the centre of mass of the molecule in question is constrained at defined positions along the z-axis, obtaining free-energies and depth-dependent diffusion coefficients as a function of the constraining force required at each position. Methods outlined in computational methods such as umbrella sampling[21] can also be applied. Such practices remain commonplace today, with alternative techniques to calculate such parameters emerging in recent years.[32–34]

The earliest studies utilising MD simulations to probe passive diffusion primarily focused on small molecules, such as water, oxygen and carbon dioxide.[31] The predictions obtained qualitatively agreed with known transport phenomenon of such molecules: oxygen and carbon dioxide are able to permeate relatively unhindered, whereas water diffusion is impeded and therefore, requires aquaporins for fast and efficient transport. This analysis was extended to the most common functional groups. However, the inaccuracy of observed permeability coefficients was notable in comparison to experimental determinations. Fortunately, advancements in computer hardware and empirical force fields have enabled the characterisation of transport properties to be undertaken at increasing timescales and levels of accuracy.

In a recent study by Riahi and Rowley,[35] the permeability of water and hydrogen sulphide was evaluated using the Drude polarisable model, where experimental diffusion coefficients have been used to optimise parameters for both substances[36–38] and the lipid DPPC.[39] Incorporation of induced polarisation effects enabled agreement between calculated and experimental diffusion coefficients at a value of $(2.6 \pm 0.5) \times 10^{-5}$ cm s^{-1} for water,[40] previously calculated as two orders of magnitude greater by additive force fields.[41] In comparison, a coefficient of 11.9 ± 0.7 was obtained, suggesting hydrogen sulphide permeates approximately 400 000 times faster, and reinforcing experimental suggestions that hydrogen sulfide permeability is at least four orders of magnitude greater than water[35] rendering facilitated transport unnecessary.[42] This is attributed to distinct energetic barriers arising from electrostatic contributions (27 kJ mol^{-1} for water *vs.* 2.6 kJ mol^{-1} for hydrogen sulfide); the dominant hydrogen bonding character of water cannot be obtained in the hydrophobic tail region disfavouring the permeation of individual molecules; in contrast, hydrogen sulfide is relatively hydrophobic, thus hydrogen bonding capabilities with water are limited, and occupation of the inner membrane is encouraged. Therefore, hydrogen sulfide demonstrates permeability on a similar scale to non-polar solutes,[43] undeterred by its innate polarity. This phenomenon likely contributes to the remarkable potency of hydrogen sulfide in biological systems.[44]

The inherent relationship between membrane permeability and biological activity is also important in a drug discovery context. Penetration of cell membranes is imperative to gain access to target sites; the evaluation of permeability coefficients and free-energy profiles of drug molecules evaluation, in a similar manner to small molecules, can be used to assess the likelihood of reaching such sites and hence elicit a functional response. Experimental determination of drug permeabilities requires intensive experimental techniques, thus a plethora of computational studies to characterise the behaviour of clinically relevant molecules in model membranes have emerged to complement experimental work. A chemically diverse range of molecules has been investigated, establishing the partitioning properties of a broad spectrum of drug classes. Orsi and Essex, for example, demonstrated steroid hormones are centralized in the glycerol region, whereas, β-blockers tended towards the headgroup region, due to favourable interactions between the central oxygen's and polar moieties in the membrane.[45] Overall, a general consensus has emerged that large drug molecules primarily accumulate at the extended polar–apolar interface to accommodate their amphiphilic nature.[46] Such molecules are found to have a lower energy than in bulk water, with small barriers to overcome, providing an energetically permissible route for drug transit. The calculated ΔG values can sometimes diverge from those determined experimentally, which could be attributed to the use of bilayers containing a single species of lipid and/or consideration of a single drug molecule in the majority of models, even though simultaneous diffusion of a number of molecules may actually occur.[47]

The interrelationship between solute concentration and membrane permeabilities has been examined *via* MD simulations. Comparison of ABF-generated free energy profiles of the anti-cancer drug, paclitaxel permeation through a pure POPC bilayer and POPC bilayers containing 12 mol% paclitaxel suggested incorporation of paclitaxel endorsed the transportability of the drug by increasing the partitioning from water to the bilayer ($\sim$9 *vs.* $\sim$21 kcal mol^{-1}) and decreasing the barrier to transfer between leaflets in the bilayer ($\sim$7 *vs.* $\sim$4 kcal mol^{-1}).[48] In the paclitaxel-rich bilayers, aggregates are formed from both random and lattice-based starting configurations, which decrease the lipid tail order parameter and promote translocation of water into the membrane, confirming earlier experimental predictions of pore formation in a concentration-dependent manner.[49]

The ability of small membrane bound molecules to cause significant perturbations in membrane structure and accelerate drug permeation has been exploited particularly where transdermal drug delivery is concerned.[50] Molecules such as dimethyl sulfoxide,[51] ethanol,[52] acetone[53] and oleic acid[54] have been proposed as chemical penetration enhancers, to breach the skin barrier by improving permeability of the lipid bilayers of the stratum corneum. The molecular mechanisms by which such molecules act have been investigated in a number of computational studies to date.[55–61]

Dimethyl sulfoxide molecules, for example, were found to freely partition into bilayer and accumulate beneath the lipid headgroups, swelling the distance between adjacent headgroups and dispersing the tails, increasing membrane flexibility and decreasing thickness.[55] Above a certain concentration threshold structural defects generate transient water pores, in a similar manner to paclitaxel, with a further increase expelling individual lipids from the membrane and destroying the bilayer structure.[56] The concentration dependence of dimethyl sulfoxide permeability enhancement experimentally[52] and for pore formation computationally suggests the two phenomena could be related, providing a feasible explanation for the amplified permeabilities of both hydrophobic and hydrophilic compounds through the skin.[52] Comparison of DPPC and DOPC showed that the latter is less susceptible to these effects, demonstrating enhanced stability and diminished dimethyl sulfoxide diffusion.[57]

These examples demonstrate how computational methodologies have provided a mechanistic understanding of experimentally established phenomenon, such as the exclusion of charged and hydrophilic molecules, the partitioning properties of hydrophobic drug molecules and membrane perturbations as a result of molecule entry. The alternative entry routes to membrane passage, *via* embedded proteins, will be explored in the following sections.

10.4 Passive Transport by Ion Channels

Ion channels facilitate the passive diffusion of ionic species down their electrochemical gradient from the extracellular medium into the cell

cytoplasm. Permeation is controlled by the onset of various external stimuli, such as transmembrane voltage, heat, ligand binding, and mechanical stretch, and is responsible for regulating electrical signals across the cellular membrane.

The voltage-gated ion channel (VGIC) family that specifically conduct Na^+ (Na_V channels) and K^+ ions (K_V) channels, for example, are responsible for the generation of action potentials in excitable cells in various tissues in the heart, brain and nervous system, and thus play a crucial physiological role. VGIC's are a common target for antiarrhythmic agents, local anaesthetics, anticonvulsants and pain therapeutics.[62,63] Understanding how such proteins assemble and function is therefore of great pharmacological importance.

Elucidation of the crystal structure of the KcsA channel from *Streptomyces lividans* in 1998, provided the first atomistic description of the pore structure of an ion channel, a tetrameric arrangement with each monomer containing two transmembrane α-helices and an intermittent pore loop (Figure 10.3).[64]

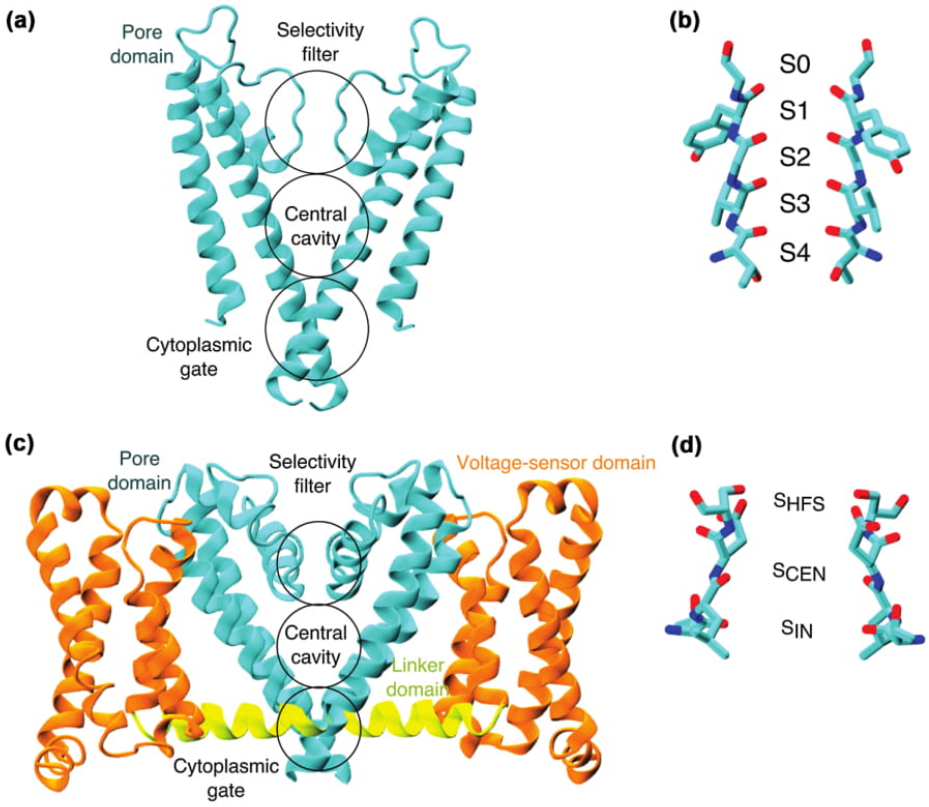

Figure 10.3 (a) Structure of KcsA potassium channel. (b) Proposed ion binding sites in the KcsA K^+-channel selectivity filter. (c) Structure of voltage-gated sodium channel Na_VAb. (d) Proposed ion binding sites in Na_VAb Na^+-channel selectivity filter. Only two domains are shown for clarity throughout.

The latter was found to contain a pore helix and the signature selectivity sequence and thus has become known as the selectivity filter.[65,66] Between the selectivity filter and the cytoplasm, a water-filled cavity is present to provide an ideal environment for ion transfer.[67] MD simulations, using KcsA, have extensively analysed the mechanism by which K^+ channels selectively and efficiently conduct K^+ ions.[68–72] The abundance of K^+ channel structures now available has enabled various aspects of K^+ channel function, such as voltage-sensing, cytoplasmic gating and drug blockage to be examined by computational analyses.[73–75] Several comprehensive reviews are available on this subject.[76,77] Similarly, since the publication of the first crystal structure of the Na_VAb from *Arcobacter butzleri*,[78] and subsequent structures from bacterial sources,[79–82] significant efforts have been focused towards elucidating analogous functional properties in NaV channels. The pore structure of NaVAb showed similar characteristics to K^+ channels, displaying a voltage-domain attached *via* a linker domain, as shown in Figure 10.3. In this section, recent insights gained from the Na_VAb channel will be used to illustrate the application of computational methodologies to complex questions regarding ion channels.

The resolved selectivity filter structure identified three possible ion-binding sites which were apparently capable of coordinating partially hydrated ions; at the extracellular entrance, the S_{HFS} site formed of a ring of anionic glutamate residues Glu177, was proposed to attract extracellular cations; deeper sites proposed (S_{IN} and S_{CEN}) were composed of carbonyl backbones Leu76 and Thr175, respectively, (Figure 10.3(d)). The observed ion dynamics in early MD simulations was consistent with predictions from structural data.[83] The binding sites were also confirmed as energy minima in single and multi-ion PMF conduction profiles[84,85] and later MD simulations on a microsecond timescale. The conformation of the residues forming the binding sites was largely unchanged irrespective of the presence of ions,[86] in contrast with K^+ channels whose sites depend on the presence of K^+ ions for stability.[87–89]

The precise sequence of events inducing Na^+ conduction was examined *via* umbrella sampling calculations, sampling conduction along the permeation axis. As expected, a deep energy well between -5 kcal mol^{-1} [90] and -8 kcal mol^{-1} [85] was observed at S^{HFS}. Entrance to further sites, however, was subject to a barrier of 4 kcal mol^{-1},[85,90] suggesting movement of isolated ions was not the primary mechanism of conduction, as proposed from flux measurements.[91] Accompanying multi-ion profiles displayed a reduced energy barrier below 3 kcal mol^{-1} for penetration of the selectivity filter, advocating translocation of Na^+ ions likely occurs *via* sequential movement through doubly occupied extracellular/S_{HFS}, S_{HFS}/S_{HFS}, S_{HFS}/S_{CEN}, S_{HFS}/S_{IN}, S_{HFS}/intracellular conformations, in a so-called loosely coupled 'knock-on' mechanism. Additional efforts to characterise the minimum energy pathway utilising metadynamics, taking into account binding as a function of the radial distribution around the pore axis, identified an additional 'drive-by' mechanism of conduction.[92] Extensive MD simulations of $\sim$22 μs in the

absence of a transmembrane voltage, provided direct observations of knock-on/off transitions, multi-ion configurations constituted over 90% of the simulation trajectory.[93] Interestingly, more than 20% were triply occupied states of the selectivity filter, which have also been observed in bias-exchange metadynamics simulations.[94]

The presence of such states has been associated with conformational states of the selectivity filter, divergent from the crystal structure. Multi-microsecond simulations revealed Glu177 could occupy an additional conformational state directed towards the selectivity filter, as opposed to the extracellular medium, which is thought to catalyse Na^+ permeation.[93] Boiteux *et al.* disclosed PMF profiles with a double energy well at this site, resulting in reduced energy barriers, supporting this proposal.[95] An increased occupancy of the selectivity filter is observed in this case, providing further evidence of a conduction mechanism involving three ions. Studies have since proposed distinct multi-ion conduction mechanisms may be in operation during inward and outward conduction.[96]

The protonation state of Glu177 has also been under intense scrutiny throughout MD simulations. Multiple studies utilizing both equilibrium[95] and free-energy MD.[84,97] methodologies conclude conduction is favoured in the wholly deprotonated state, and is unfeasible when multiple residues are protonated.

The mechanism by which Na^+ channels exclude other monovalent and divalent ions has been explored by comparison of single and multi-ion PMF profiles.[84,85] These profiles demonstrated that even though K^+ ions were capable of penetrating the channel with a favourable network of coordinating ligands, a heightened barrier was identified in the plane of the Glu177 side-chains.[84] This observation was rationalised using geometric arguments, as K^+ is unable to permeate this region unperturbed in an optimum geometry, and supported by a systematic comparison between selectivity and pore radius in the same study. The overall free-energy difference for K^+ relative to Na^+ was calculated as 3 kcal mol^{-1} in line with experimental permeability ratios. PMF profiles of Ca^{2+} conduction displayed distinct energy landscapes from both Na^+ and K^+, suggesting further mechanisms of selectivity in the Na_V filter. Corry *et al.* proposed the desolvation energies of Ca^{2+} likely results in hindered permeation;[90] in addition, Ke *et al.* advocated that transfer from S_{CEN} to the central pore was energetically unfavourable, thus sustained inhabitancy of this site blocks inward conduction of Ca^{2+}.[98]

As well as exploring mechanistic aspects of Na_V channel conduction and selectivity, aspects of channel modulation have also been explored computationally. Na_V channels represent a putative target for local and general anaesthetics, yet the functional binding sites of such molecules, and the pathway by which they can access them are not widely understood. A multitude of experimental studies have proposed the existence of a 'hydrophobic pathway' enabling the entrance of hydrophobic molecules, when entrance is obstructed from both extracellular and intracellular vestibules.[99] The Na_VAb structure revealed the presence of hydrophobic

side-portals, termed fenestrations, thought to represent such a route. Thus, the dynamics of these sites and their accessibility to drug molecules have been the focus of several studies in recent years.

Using a structural model of NaChBac, Raju *et al.* identified three binding sites of the general anaesthetic isoflurane, in the extracellular, linker and pore domains using flooding simulations, with subsequent FEP calculations to estimate the free energy of binding of each site.[100] Entry/exit routes were observed on the fly, including traversal of the fenestrations to the central pore site, confirming the feasibility of the portals as access pathways. The evolution of the size and dynamics of the fenestrations and hence, the size restrictions imposed on incoming drug molecules were subsequently explored by Kaczmarski and Corry.[101] A range of bacterial NaV channels displayed an average bottleneck radii between $\sim$1.6 and 2.2 Å, reaching a maximum bottleneck radii between $\sim$2.6 and 2.8 Å. Thus, in the maximally extended state, the portals are capable of accommodating phenyl rings, a key constituent of most sodium-channel blocking drugs.[102] Entrance of larger drugs would, therefore, require considerable perturbations of the fenestration or drug conformation. In Na_VAb, F203 acted as the central gate to fenestration size, illustrating that fluctuations in bottleneck radii are primarily determined by rapid side-chain rotations. The entrance of lipid molecules was also found to modulate fenestration size and dynamics. Further studies investigated access of the local anaesthetic benzocaine and the anti-epileptic drug phenytoin to the central pore; in agreement with the predicted physical constrictions, free energy maps constructed from umbrella sampling simulations,[103] and extensive unbiased MD simulations indicated a larger barrier for the entrance for the larger phenytoin, although both exhibited a minimum energy pathway through the lateral fenestrations.[104] The possible existence of lateral fenestrations in K^+ channels has subsequently been investigated using MD simulations, identifying tuneable openings in the two-pore domain K^+ channel family.[105]

In conclusion, MD simulations have revealed key principles of ion conduction in bacterial Na_V channels. It is now understood that permeation at high-throughput requires two ions at a minimum, which are loosely coupled with each other and water molecules in the selectivity filter, in stark contrast to K^+ channels. Furthermore, lateral fenestrations have been confirmed as viable entry routes for small hydrophobic molecules to reach high-affinity binding sites in the central pore. The molecular determinants of conduction and selectivity of Ca^{2+} channels are yet to be distinguished, and will likely be the subject of computational studies when high-resolution structural information is available.

10.5 Facilitated Diffusion by Transporters

Membrane transporters are a highly specialised class of membrane proteins, which couple substrate translocation to a variety of cellular energy sources. A wide range of chemical species are admitted passage *via* transporters,

often against the electrochemical gradient of the plasma membrane. This process is thought to occur by means of an *alternating access* mechanism, whereby the transporter interior is sequentially exposed to the intracellular and extracellular frontiers of the membrane. Primary transporters utilise energy input directly from chemical reactions, whilst secondary transporters are driven by an electrochemical gradient. MD simulations have provided considerable insights into the interrelationship between transporters and chemical driving forces, and how this is coupled to the large-scale conformational changes underlying the alternating access model. In this section, we have limited our discussion to the Leucine transporter (LeuT), which has become a prototype for structural and dynamical analyses of neurotransmitter sodium symporter (NSS) family, to illustrate the progression of our understanding in this field.

NSS's are responsible for the selective re-uptake of substrates to terminate neurotransmission at synapses.[106] These transporters function in a Na^+ dependent manner, coupling the passive diffusion of Na^+ down the electrochemical gradient, to the active transport of substrate molecules, including monoamine neurotransmitters (serotonin, dopamine, norepinephrine), amino acids and osmolytes (betaine, taorine, creatine). Eukaryotic NSS are pharmacological targets for important drugs, such as anti-depressants,[107] as well as psychoactive substances, such as cocaine.[108] Determination of the structure of the bacterial amino acid transporter LeuT elucidated the basic transmembrane architecture of NSS's,[109] denoted the 'LeuT fold', comprised of two five-helical bundles in an anti-parallel arrangement (Figure 10.4(a)).[110] A wealth of atomic resolution structural information of LeuT from *Aquifex aeolicus* has since emerged,[111–114] revealing various novel aspects of NSS assembly. The available structural information advocates a mechanism of alternating access in which Na^+ ions and the substrate bind to an outward-facing open (OF_O) state, and released by a series of concerted transitions between outward-facing closed (OF_C), inward-facing closed (IF_C) and inward-facing open (IC-O) states, where the transporter can loop back to the initial conformation. The availability of LeuT structures has allowed in-depth investigation of its behaviour by MD simulations, as a paradigm for the NSS transporter function.

Crystallographic information of LeuT has elucidated the presence of two Na^+ binding sites (Na1, Na2), in close proximity to the substrate-binding site (S1) in the membrane core (Figure 10.4(b)).[110] Na1 explicitly coordinates the substrate, alongside residues Ala22, Asn27, Thr254 and Asn286 in an octahedral arrangement. In contrast, Na2 is entirely composed by LeuT residues Gly20, Val23, Ala351, Thr354 and Ser355 coordinating ions in a trigonal bipyramidal manner. In the initial computational studies, the dynamics of such sites was investigated.

In the first MD study, Celik *et al.* performed a series of unbiased MD simulations on the initial crystal structure of an OF_C, which contained the bound substrate and two Na^+ ions, to explore dynamics of this LeuT complex.[115] The most notable interactions in the observed substrate binding

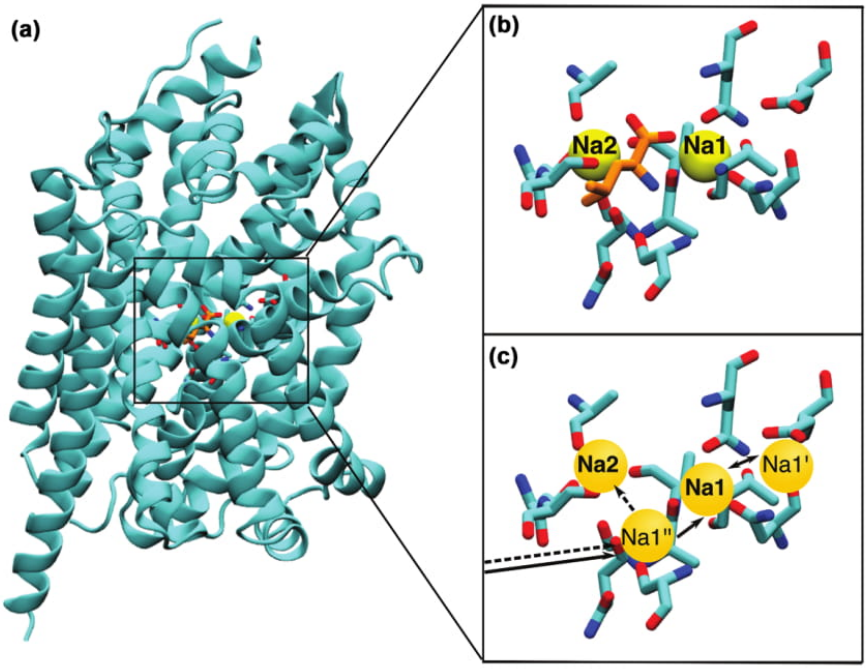

Figure 10.4 (a) Crystal structure of LeuT receptor in OF_C conformation with two Na^+ ions and leucine bound. (b) Close-up of substrate and ion binding sites. (c) Proposed sequence of ion binding; straight and dashed lines represent the movement of the first and second ions respectively. Throughout, protein residues are shown in liquorice representation, with blue, red, cyan and orange parts representing nitrogen, oxygen, carbon in LeuT and carbon in leucine. Sodium ions are shown as yellow spheres.

process of the zwitterionic leucine involved a salt bridge in the extracellular vestibule (Arg30 and Asp404) and an ion occupying Na1 on occupation of the canonical binding site. FEP/MD simulations were undertaken by Noskov and Roux to discern the mechanism by which other cations are excluded from Na^+ binding sites, and hence the specificity of LeuT to Na^+ ions.[116] Interestingly, distinct mechanisms of selectivity were observed; in Na1, coordination to a negatively charged residue results in preferred binding of Na^+, whereas geometric constraints were proposed to operate in Na2. The influence of ion occupation on substrate binding was also assessed using FEP simulations, revealing optimum substrate coupling to Na^+ when both sites are occupied, and enhanced structural stability of the substrate and Na^+ site selectivity when Na2 is inhabited.[117]

Celik *et al.* also undertook a series of steered MD experiments to probe the formation of IF_C complex. Entrance to the site required an open state of the aromatic lid (Phe353), which closed upon stable binding, thus illustrating as a key transition between OF_O and OF_C states.[115] Later unbiased simulations of the OF_C state, with the substrate removed, displayed spontaneous opening to a conformation poised for substrate binding, similar to the OF_O crystal

structure, demonstrating Na^+ binding in isolation to biases the transporter towards this state and further elucidating the conformational changes involved in this transition.[118] The authors noted that the affinity for Na1 is inversely proportional with the progression of the transition of the IF_O state, thus it is likely occupation of Na2 contributes to the stability of this conformation. This has recently been confirmed by mutagenesis of the Na2 site (Thr354 and Ser355), which was found to stabilize the IF_O state by direct interactions with helices 1 and 8.[119]

Computational analyses have also been able to predict additional Na^+ sites, not identified during crystallographic data, in order to delineate the precise series of events constituting Na^+ and substrate entrance (Figure 10.4(c)). Zhao *et al.* identified an additional binding site in close proximity to Na1 located on Glu290, referred to as Na1' from this point forward.[118] The evolution of the protonation state of Glu290 is known to be an integral part of the transport cycle, corroborating this prediction.[120] Using extensive all-atom MD simulations (~20 μs), Zomot *et al.* identified an additional binding site, namely Na1″, constituted of Ser256 and Ser355 side-chains and the backbone carbonyl of Asn21, and have provided an exhaustive account of Na^+ translocation events, and associated conformational changes.[121] Site Na1″ constitutes the first point of contact for Na^+ ions, attracting anions from the extracellular medium throughout; within hundreds of nanoseconds, this ion shifts to Na1 where it maintains residence, or transiently occupies Na1′. The Na1″ site may remain vacant whilst Na1 is occupied, or hold a further incoming ion, which can subsequently enter Na2. Simultaneous population of both sites is consistently correlated with expansion of the extracellular entrance, permitting access of the substrate to S1. Following binding, the entrance is concealed by local rearrangements, notably the side-chain isomerization of Phe253. Subsequently, the surrounding helices undergo global rearrangements to evolve conformations capable of releasing the bound species.

In the OF_O state, Zhao and Noskov observed the formation of water wires from the cytoplasm to the S1 and Na2 sites in the IFO state, which may facilitate ion release and prompt inter-helical arrangement and flooding of the intracellular opening.[122] Using free energy calculations, Thr345 was shown to occupy single rotameric state when Na2 is occupied, as opposed to two degenerate states when it is vacant, and thus may act as a switch to vacate Na2 and advance the transport cycle.

Significant efforts were directed towards prediction of further intermediates in the transport cycle, such as the IF_O structure.[123–125] Tajkhorshid *et al.* produced an IF_O model by homology modelling of the inward-facing state,[126] based on the structures of outward-facing LeuT[110] and inward facing vSGLT.[127] Simulations of this state consistently displayed intracellular release of Na2. Quick *et al.* proposed a similar structure, in addition to other unknown states, by varying the presence of leucine in the binding site and Na^+ ions in known crystal structures and performing accelerated MD simulations in combination with principal component analysis.[123] All

inward-facing conformations were found to contain a vacant Na2 site. The eventual crystallization of a LeuT inward-facing state[111] further corroborated earlier predictions that Na2 initiates intracellular release; Na^+ ions were weakly coupled with the Na2 site, persistently exiting to the intracellular medium and initiating release of the bound substrate and ion in Na1 in the same direction.[128] The protonated/neutral state of Glu290 (Na1′ site) in the inward-open state is proposed to enhance dissociation of ions to the intracellular solution.[129] These observations provide a mechanistic understanding of how negative charges in close proximity to the characteristic Na^+ binding sites, such as Glu290 in the LeuT transporter or chloride ions in eukaryotic NSS, may regulate ion binding and release.[120]

The overall mechanism of release has been a source of controversy throughout the literature. Early SMD simulations by Shi *et al.* revealed a second substrate-binding site (S2), leading to proposals of an allosteric mechanism of transport whereby occupation of the secondary binding site, triggers release of the inhabitants of S1 and Na1.[130] Furthermore, the observed overlap of the S2 site with the binding site of tricyclic antidepressants has led to suggestions that the S2 site could exert an activator or inhibitory effect dependent on the manner of binding.[112,113]

Championed by Javitch and Weinstein,[130–132] the presence of the S2 binding site has been widely disputed throughout the literature, with Gauaux *et al.*, for example, endorsing the functional significance of the S1 site only.[110,133–136] Differing reports have also emerged in computational studies. Extensive unbiased simulations by Zomot *et al.*, do not observe alanine binding, and only partial leucine binding in the S2 site.[121] However, using a complex protocol combining of accelerated, targeted and conventional MD, Cheng *et al.* have identified an increase in the substrate-binding affinity of the S2 site whilst progressing towards an inward-facing state and subsequent displacements in the putative S1 site.[137] Furthermore, unbiased simulations with Ala and Leu and inhibitors known inhibitors bound at the S2 site revealed key structural alterations in the extracellular portion of TM6 which may be propagated throughout the transporter and influence its functional state.[138] FEP/MD simulations yielded favourable absolute binding free energies for tricyclic antidepressants in the range of -12 to -14 kcal mol^{-1}.[139] These energies were dissimilar on removal of the substrate, supporting a thermodynamic coupling mechanism between the two sites.[112]

The final question remaining of LeuT transport involves the inward-to-outward transition to restart the translocation mechanism. The recent crystallisation of WT LeuT in a Na^+ and substrate-free state by Malinauskaite *et al.* provided the first insights into the structure of an intermediate involved in this transformation.[114] MD simulations confirmed both Na^+ sites are inaccessible to extracellular ions in the structure, with a distinct Na1 conformation observed stable throughout. Highly conserved residue, Leu25, is found to consistently occupy the S1 site, and occlude Glu290 from the extracellular environment, reportedly acting as gatekeeper for Na^+ binding

and playing an intimate role in H^+-counter-transport during the return transition. The authors propose release of the counter-ion stimulates re-orientation of Leu25, allowing entry to the sites and initiation of the forward transport cycle.

Remarkably, using the available crystal structures of LeuT, MD simulations have provided a full atomistic description of the entire transport cycle. Key questions concerning the locality and behaviour of Na^+ binding sites, the interrelationship between such sites and substrate binding at different stages of the transport cycle, as well as a possible allosteric mechanism involving a second substrate-binding site have been addressed.

In a wider context, these studies have examined the key principles of membrane active transport: molecular determinants of substrate binding, coupling to external energy sources and conformational changes constituting the alternative access mechanism. These fundamental principles of active transport have been examined in a number of transporter families, and it is likely that a detailed description of active transport in these assemblies will emerge in the future.

10.6 Signalling *via* Receptors

Cell surface receptors are intrinsic membrane proteins forming the primary communication mechanism between the cell exterior and interior. The functionality of receptors is dependent on the transformation of the protein transmembrane between conformational states, in response to the binding of extracellular molecules. Ligand-gated ion channels are a family of membrane receptors that allow ion influx/efflux in response to bound neurotransmitters. G-protein coupled receptors (GPCR's) constitute a significant class of membrane receptors, which couple to heterotrimeric G-proteins on activation to initiate intracellular signalling cascades. GPCR's are susceptible to hormones, neurotransmitters, and sensory stimuli, thus they are critical for basic physiological function of eukaryotic organisms.[140] As a consequence, GPCR's have been implicated in neurological disorders, cardiac failure, cancer and diabetes, and are the target of a significant proportion of pharmaceuticals available on the market today.[141,142]

As GPCR activation is a profoundly dynamic process reliant on large-scale conformational changes, elucidation of high-resolution three-dimensional structures has proven difficult.[143] The ground breaking crystal structure of light sensitive pigment, rhodopsin, revealed the conserved transmembrane arrangement of seven α-helices of class A GPCR's and provided high-resolution data appropriate for MD simulations. In recent years, computational analyses of GPCR's has been significantly aided by the increase in X-ray crystallographic information and state-of-art homology modelling tools, exploring numerous facets of GPCR behaviour, such as ligand binding, G-protein coupling, lipid modulation the highly concerted conformational changes associated with activation/inactivation processes. The β2-adrenergic receptor has been the focus of seminal studies exploring the

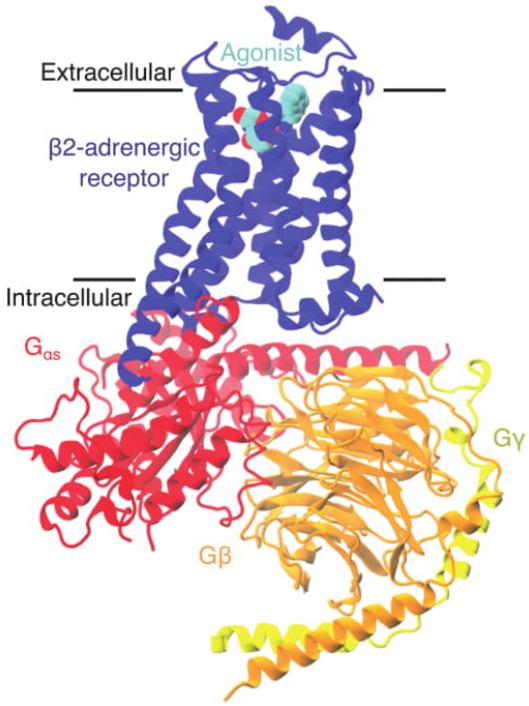

Figure 10.5 Crystal structure of β2-adrenergic receptor (PDB ID 3SN6) in fully activated state with bound agonist and heterotrimeric G-protein. The position of the plasma membrane is indicated by a solid black line.

latter, due to the availability of structural information in multiple functional states, including a fully activated state in complex with extracellular agonist and intracellular G-protein complex (Figure 10.5). Thus, it will be used as an archetypal example of how computational methodologies have advanced our understanding of the relationship between GPCR structure and function.

Multiple studies have advocated that an ensemble of conformational states exist for individual GPCR functional states.[144,145] The initial β2AR structures, in complex with inverse agonist carazolol and timolol,[146–149] allowed theoreticians to characterise the ensemble of conformational states representing the inactive state of the receptor.[150] Unexpectedly, a salt bridge between the intracellular ends of helices III and VI, dubbed the 'ionic lock', was broken in the inactive state structures, in defiance of biochemical evidence arguing this event represents a crucial activation step.[151] Microsecond simulations of these structures were able to demonstrate that inactive β2AR actually exists in conformational equilibrium between states with a broken and intact ionic lock.[150] These observations suggest the receptor is likely biased towards the broken state upon receptor activation, reconciling with the previous experimental work mentioned.[151]

The elucidation of the agonist bound β2A receptor lead to further investigation of GPCR conformational states and the transitions between them. Rosenbaum *et al.* explored the dynamics of this complex on an

extended timescale using the Anton Supercomputer.[152] This seminal study demonstrated the feasibility of simulations up to 30 μs in length for the study of integral proteins, and provided unprecedented insights into the behaviour of this complex. After approximately 11 μs, the active state receptor spontaneously transitioned to the inactive structure that remained stable for the duration of the simulations, advocating that binding to an intracellular partner was absolutely required for stabilisation of a fully activated conformation. Later experimental and computational works supported this hypothesis.[153]

Dror *et al.* proposed an atomically detailed activation mechanism based on the transition between functionally active and inactive states, *via* a number of previously unreported intermediates, observed reproducibly in over 30 independent simulations.[154] Three functionally important regions were identified, the intracellular G-protein-binding site, the extracellular ligand-binding site and the junction in between, the so-called 'connector' region. The regions are loosely coupled, although the connector region is largely responsible for communicating small-scale ligand related movements and large-scale helical movements surrounding the intracellular binding pocket. Interestingly, the simulations suggest the activation process originates from the latter; outward movements of helix VI initiate conversion to an intermediate state, which incorporates an expanded G-protein site, and an equilibrium between active and inactive states in the ligand binding site and connector region. Subsequent agonist binding biases this equilibrium towards active conformations. Finally, an intracellular binding partner may interact and trigger the final stage of the activation process. Detailed understanding of specific receptor conformations, as described here, may contribute to the design of drugs targeting specific functional states of GPCR's. Knowledge of the interrelationship between cellular entities, such as G-proteins and arrestins, and the multitude of conformational states of the β2AR will refine this scheme further.

A key question that has not been addressed throughout these mechanistic studies is the assembly of GPCR dimers and higher-order oligomers, and their functional role of in the intracellular signalling pathway. Hydrophobic mismatch, where the length of the membrane spanning segments conflicts with the length of the hydrophobic core of the membrane, has been proposed to stimulate GPCR dimerisation, and has consequently been explored using MD simulations.[155] Using a novel multi-scale approach known as continuum-molecular dynamics, Mondal *et al.* quantified energetic penalties emerging from this phenomenon in individual transmembrane helices of GPCR's, enabling the prediction of energetically favourable contact interfaces by comparison of such energetic costs in monomeric and oligomeric states.[156] In the β2A receptor, the hydrophobic mismatch was considerably reduced in the transmembrane helices I, IV and V consistent with the typical interfacial regions elucidated from unbiased CGMD (helices I–I, V–V and IV–V),[157] with similar results obtained using a bilayer containing 10% cholesterol. Duplicate analysis of the β1A receptor displayed distinct

oligomerisation patterns, with a single predicted contact interface localized on helix I. Overall, these results were akin to experimental evidence showing the β1A preferentially forms dimers,[158] whereas the β2A receptor can form more extensive dimers as well as higher-order oligomers.[159]

Prasanna *et al.* performed extensive CGMD of the β2A receptor in bilayers containing increasing concentrations of cholesterol to examine the effect of cholesterol on the dimerisation process.[160] In 0% cholesterol, the receptors form a homo-interface involving helices IV and V; in 50% cholesterol, a homo-interface between helices II and I is formed; whilst in the concentrations between (9 and 30%) a hetero-interface is observed comprising a combination of the two. Increased cholesterol occupancy at helix V is observed throughout, advocating specific cholesterol interactions bias the oligomer towards distinct oligomeric states.

It is well established throughout the literature that functionality of integral membrane proteins is dependent on the composition of the plasma membrane, thus it is possible the influence of membrane organisation extends further than GPCR dimerisation. Many GPCR's have demonstrated a functional dependence on membrane cholesterol in particular, which is considered to act either by direct interactions or indirect effects involving the biophysical properties of the membrane.

Unbiased MD simulations, either CG or atomistic, of GPCR's embedded in lipid bilayers enriched with cholesterol molecules have become a popular tool to identify cholesterol binding sites.[161–164] Utilising this protocol, Cang *et al.* revealed the presence of three extracellular and four intracellular high occupancy sites. The accuracy of such predictions was supported by the likeness between three sites and those observed in crystal structures of GPCR's with bound cholesterol molecules. Of note, two cholesterol molecules occupy the surface of helix I and VIII, consistent with that observed in the dimeric structure of the β2AR (PDB 2RH1), contrasting with claims that the observed organization was an artefact caused by crystal packing.[147] Furthermore, a cleft between the extracellular ends of helices I, II and VII, accommodated a cholesterol molecule in a stable manner for the duration of the trajectories. The authors suggest habitation of this site, and the resulting stabilisation of residue Trp313, may facilitate ligand-receptor binding.

Prasanna *et al.* identified a specific POPC binding site between helices I and VII, in a similar position in the extracellular leaflet.[165] This site had been previously suggested to accommodate lipids from X-ray crystallographic information of the α2-adenosine receptor. Neale *et al.* explored the relationship between specific phospholipid interactions and receptor activation state.[161] Using MD simulations with a cumulative time of 0.25 ms, the authors observed individual phospholipid molecules entering the receptor by an opening in the cytoplasmic leaflet between helices VI and VII and forming a salt-bridge that directly impedes ionic lock formation, thus stabilising the active state. This phenomenon was enhanced by the presence of anionic lipids, elucidating a possible mechanism by which such lipids perpetuate receptor activation.

In conclusion, MD has provided crucial insights into how GPCR's convert between functional states to convey signals, as a result of highly synchronised structural transitions emanating from atomic fluctuations. The driving forces of receptor dimerisation have been studied, and the functional significance of higher order oligomers considered. The close association between membrane lipids and receptor state has been explored, with the identification of multiple functional binding sites of both cholesterol and phospholipid molecules.

10.7 Conclusions

Molecular dynamics simulations have become an essential tool to study the dynamics of biological systems in atomic resolution, and elucidate the molecular mechanisms of numerous phenomena that cannot be gained by experimental means. A detailed understanding of how many small molecules interact with lipid bilayers, and consequential diffusion or exclusion processes has been gained, which can be applied in a medicinal chemistry context to assess the likelihood of drug molecules reaching intracellular targets. Furthermore, computational methodologies in combination with high-resolution structural information of integral membrane proteins have provided crucial insights into how such assemblies function as highly efficient transport machinery. For ion channels, multiple conduction mechanisms for selective transport through K^+ and Na^+ channels have emerged, as well as characterisation of a novel pore access pathway through lateral fenestrations in the latter. In the case of GPCR's, conformational ensembles of active and inactive functional states have been described, and the interconversion transitions delineated, providing a general mechanism of GPCR activation. The influence of the membrane environment on GPCR dynamics by direct and indirect effects has been explored intensively. Finally, significant advances have been made in understanding the alternating access mechanism underlying transporter function, and how such changes are driven by cellular energy sources. Overall, such insights have considerably contributed to our understanding of membrane transport, and will significantly advance the rational design of drugs in the future. The increasing availability of high-resolution structural information, growth in computer capabilities and development of state-of-the art MD algorithms and accompanying force fields will markedly amplify the use of computational simulations for the study of intrinsic membrane proteins in the coming years.

Acknowledgements

V.O. acknowledges a BBSRC-CASE studentship, in association with Pfizer Neusentis. C.D. acknowledges use of ARCHER, the UK National Supercomputing Service, the National Service for Computational Chemistry Software (NSCCS), the 'Red Española de Supercomputación' (RES), and the

Hartree Center. Research in the Domene group is supported by the Engineer and Physical Sciences Research Council (EPSRC) and the Biotechnology and Biological Sciences Research Council (BBSRC).

References

1. M. Luckey, *Membrane Structural Biology: With Biochemical and Biophysical Foundations*, Cambridge University Press, 2014.
2. B. R. Brooks, R. E. Bruccoleri, B. D. Olafson, D. J. States, S. Swaminathan and M. Karplus, CHARMM: A program for macromolecular energy, minimization, and dynamics calculations, *J. Comput. Chem.*, 1983, **4**(2), 187–217.
3. W. D. Cornell, P. Cieplak, C. I. Bayly, I. R. Gould, K. M. Merz, D. M. Ferguson, D. C. Spellmeyer, T. Fox, J. W. Caldwell and P. A. Kollman, A Second Generation Force Field for the Simulation of Proteins, Nucleic Acids, and Organic Molecules, *J. Am. Chem. Soc.*, 1995, **117**(19), 5179–5197.
4. W. L. Jorgensen and J. Tirado-Rives, The OPLS [optimized potentials for liquid simulations] potential functions for proteins, energy minimizations for crystals of cyclic peptides and crambin, *J. Am. Chem. Soc.*, 1988, **110**(6), 1657–1666.
5. I. V. Vorobyov, V. M. Anisimov and A. D. MacKerell, Polarizable Empirical Force Field for Alkanes Based on the Classical Drude Oscillator Model, *J. Phys. Chem. B*, 2005, **109**(40), 18988–18999.
6. S. Patel and C. L. Brooks, CHARMM fluctuating charge force field for proteins: I parameterization and application to bulk organic liquid simulations, *J. Comput. Chem.*, 2004, **25**(1), 1–16.
7. S. Patel, A. D. Mackerell Jr. and C. L. Brooks, 3rd, CHARMM fluctuating charge force field for proteins: II protein/solvent properties from molecular dynamics simulations using a nonadditive electrostatic model, *J. Comput. Chem.*, 2004, **25**(12), 1504–1514.
8. Y. Shi, Z. Xia, J. Zhang, R. Best, C. Wu, J. W. Ponder and P. Ren, Polarizable Atomic Multipole-Based AMOEBA Force Field for Proteins, *J. Chem. Theory Comput.*, 2013, **9**(9), 4046–4063.
9. G. Lamoureux, A. D. MacKerell and B. Roux, A simple polarizable model of water based on classical Drude oscillators, *J. Chem. Phys.*, 2003, **119**(10), 5185–5197.
10. J. A. Lemkul, J. Huang, B. Roux and A. D. MacKerell, An Empirical Polarizable Force Field Based on the Classical Drude Oscillator Model: Development History and Recent Applications, *Chem. Rev.*, 2016, **116**(9), 4983–5013.
11. S. Miyamoto and P. A. Kollman, SETTLE: an analytical version of the SHAKE and RATTLE algorithm for rigid water models, *J. Comput. Chem.*, 1992, **13**(8), 952–962.
12. J. R. Perilla, B. C. Goh, C. K. Cassidy, B. Liu, R. C. Bernardi, T. Rudack, H. Yu, Z. Wu and K. Schulten, Molecular dynamics simulations of large macromolecular complexes, *Curr. Opin. Struct. Biol.*, 2015, **31**, 64–74.

13. D. E. Shaw, P. Maragakis, K. Lindorff-Larsen, S. Piana, R. O. Dror, M. P. Eastwood, J. A. Bank, J. M. Jumper, J. K. Salmon, Y. Shan and W. Wriggers, Atomic-Level Characterization of the Structural Dynamics of Proteins, *Science*, 2010, **330**(6002), 341–346.
14. J. C. Shelley, M. Y. Shelley, R. C. Reeder, S. Bandyopadhyay and M. L. Klein, A Coarse Grain Model for Phospholipid Simulations, *J. Phys. Chem. B*, 2001, **105**(19), 4464–4470.
15. J. C. Shelley, M. Y. Shelley, R. C. Reeder, S. Bandyopadhyay, P. B. Moore and M. L. Klein, Simulations of Phospholipids Using a Coarse Grain Model, *J. Phys. Chem. B*, 2001, **105**(40), 9785–9792.
16. S. J. Marrink, A. H. de Vries and A. E. Mark, Coarse Grained Model for Semiquantitative Lipid Simulations, *J. Phys. Chem. B*, 2004, **108**(2), 750–760.
17. C. A. Lopez, Z. Sovova, F. J. van Eerden, A. H. de Vries and S. J. Marrink, Martini Force Field Parameters for Glycolipids, *J. Chem. Theory Comput.*, 2013, **9**(3), 1694–1708.
18. M. G. Saunders and G. A. Voth, Coarse-graining methods for computational biology, *Annu. Rev. Biophys.*, 2013, **42**, 73–93.
19. R. W. Zwanzig, High-Temperature Equation of State by a Perturbation Method. I. Nonpolar Gases, *J. Chem. Phys.*, 1954, **22**, 1420.
20. D. L. Beveridge and F. M. DiCapua, Free Energy Via Molecular Simulation: Applications to Chemical and Biomolecular Systems, *Annu. Rev. Biophys. Biophys. Chem.*, 1989, **18**(1), 431–492.
21. G. M. Torrie and J. P. Valleau, Monte Carlo free energy estimates using non-Boltzmann sampling: Application to the sub-critical Lennard–Jones fluid, *Chem. Phys. Lett.*, 1974, **28**(4), 578–581.
22. S. Kumar, J. M. Rosenberg, D. Bouzida, R. H. Swendsen and P. A. Kollman, The weighted histogram analysis method for free-energy calculations on biomolecules. I. The method, *J. Comput. Chem.*, 1992, **13**(8), 1011–1021.
23. M. Souaille and B. T. Roux, Extension to the weighted histogram analysis method: combining umbrella sampling with free energy calculations, *Comput. Phys. Commun.*, 2001, **135**(1), 40–57.
24. J. Kästner and W. Thiel, Bridging the gap between thermodynamic integration and umbrella sampling provides a novel analysis method: ''Umbrella integration'', *J. Chem. Phys.*, 2005, **123**(14), 144104.
25. S. Park and K. Schulten, Calculating potentials of mean force from steered molecular dynamics simulations, *J. Chem. Phys.*, 2004, **120**(13), 5946–5961.
26. S. Park, F. Khalili-Araghi, E. Tajkhorshid and K. Schulten, Free energy calculation from steered molecular dynamics simulations using Jarzynski's equality, *J. Chem. Phys.*, 2003, **119**(6), 3559–3566.
27. E. Darve and A. Pohorille, Calculating free energies using average force, *J. Chem. Phys.*, 2001, **115**(20), 9169–9183.
28. E. Overton, *Vierteljahrsschr. Naturforsch. Ges. Zurich*, 1896, **41**, 383.

29. A. Finkelstein, Water and nonelectrolyte permeability of lipid bilayer membranes, *J. Gen. Physiol.*, 1976, **68**(2), 127–135.
30. J. M. Diamond; Y. Katz, Interpretation of nonelectrolyte partition coefficients between dimyristoyl lecithin and water, *J. Membr. Biol.*, 1974, **17**(1), 121–154.
31. S. J. Marrink and H. J. C. Berendsen, Simulation of water transport through a lipid membrane, *J. Phys. Chem.*, 1994, **98**(15), 4155–4168.
32. G. Parisio, M. Stocchero and A. Ferrarini, Passive Membrane Permeability: Beyond the Standard Solubility-Diffusion Model, *J. Chem. Theory Comput.*, 2013, **9**(12), 5236–5246.
33. J. Comer, K. Schulten and C. Chipot, Calculation of Lipid-Bilayer Permeabilities Using an Average Force, *J. Chem. Theory Comput.*, 2014, **10**(2), 554–564.
34. J. Comer, K. Schulten and C. Chipot, Diffusive Models of Membrane Permeation with Explicit Orientational Freedom, *J. Chem. Theory Comput.*, 2014, **10**(7), 2710–2718.
35. S. Riahi and C. N. Rowley, Why Can Hydrogen Sulfide Permeate Cell Membranes?, *J. Am. Chem. Soc.*, 2014, **136**(43), 15111–15113.
36. G. Lamoureux, E. Harder, I. V. Vorobyov, B. Roux, MacKerell Jr. and A. D. , A polarizable model of water for molecular dynamics simulations of biomolecules, *Chem. Phys. Lett.*, 2006, **418**(1–3), 245–249.
37. S. Riahi, C. N. Rowley and A. Drude, Polarizable Model for Liquid Hydrogen Sulfide, *J. Phys. Chem. B*, 2013, **117**(17), 5222–5229.
38. S. Riahi and C. N. Rowley, Solvation of Hydrogen Sulfide in Liquid Water and at the Water–Vapor Interface Using a Polarizable Force Field, *J. Phys. Chem.*, 2014, **118**(5), 1373–1380.
39. J. Chowdhary, E. Harder, P. E. M. Lopes, L. Huang, A. D. MacKerell and B. Roux, A Polarizable Force Field of Dipalmitoylphosphatidylcholine Based on the Classical Drude Model for Molecular Dynamics Simulations of Lipids, *J. Phys. Chem. B*, 2013, **117**(31), 9142–9160.
40. E. Terreno, A. Sanino, C. Carrera, D. D. Castelli, G. B. Giovenzana, A. Lombardi, R. Mazzon, L. Milone, M. Visigalli and S. Aime, Determination of water permeability of paramagnetic liposomes of interest in MRI field, *J. Inorg. Biochem.*, 2008, **102**(5–6), 1112–1119.
41. D. Bemporad, J. W. Essex and C. Luttmann, Permeation of Small Molecules through a Lipid Bilayer: A Computer Simulation Study, *J. Phys. Chem. B*, 2004, **108**(15), 4875–4884.
42. J. C. Mathai, A. Missner, P. Kügler, S. M. Saparov, M. L. Zeidel, J. K. Lee and P. Pohl, No facilitator required for membrane transport of hydrogen sulfide, *Proc. Natl. Acad. Sci.*, 2009, **106**(39), 16633–16638.
43. W. K. Subczynski, J. S. Hyde and A. Kusumi, Oxygen permeability of phosphatidylcholine–cholesterol membranes, *Proc. Natl. Acad. Sci. U. S. A.*, 1989, **86**(12), 4474–4478.
44. R. O. Beauchamp Jr., J. S. Bus, J. A. Popp, C. J. Boreiko and D. A. Andjelkovich, A critical review of the literature on hydrogen sulfide toxicity, *Crit. Rev. Toxicol.*, 1984, **13**(1), 25–97.

45. M. Orsi and J. W. Essex, Permeability of drugs and hormones through a lipid bilayer: insights from dual-resolution molecular dynamics, *Soft Matter*, 2010, **6**(16), 3797–3808.
46. M. Paloncýová, R. DeVane, B. Murch, K. Berka and M. Otyepka, Amphiphilic Drug-Like Molecules Accumulate in a Membrane below the Head Group Region, *J. Phys. Chem. B*, 2014, **118**(4), 1030–1039.
47. H. Wang, X. Ren and F. Meng, Molecular dynamics simulation of six β-blocker drugs passing across POPC bilayer, *Mol. Simul.*, 2016, **42**(1), 56–63.
48. M. Kang and S. M. Loverde, Molecular Simulation of the Concentration-Dependent Interaction of Hydrophobic Drugs with Model Cellular Membranes, *J. Phys. Chem. B*, 2014, **118**(41), 11965–11972.
49. M. Ashrafuzzaman, C. Y. Tseng, M. Duszyk and J. A. Tuszynski, Chemotherapy drugs form ion pores in membranes due to physical interactions with lipids, *Chem. Biol. Drug Des.*, 2012, **80**(6), 992–1002.
50. R. Notman and J. Anwar, Breaching the skin barrier — Insights from molecular simulation of model membranes, *Adv. Drug Delivery Rev.*, 2013, **65**(2), 237–250.
51. A. N. C. Anigbogu, A. C. Williams, B. W. Barry and H. G. M. Edwards, Fourier transform raman spectroscopy of interactions between the penetration enhancer dimethyl sulfoxide and human stratum corneum, *Int. J. Pharm.*, 1995, **125**(2), 265–282.
52. A. C. Williams and B. W. Barry, Penetration enhancers, *Adv. Drug Delivery Rev.*, 2004, **56**(5), 603–618.
53. P. Kumar, S. K. Singh, D. N. Mishra and P. Girotra, Enhancement of ketorolac tromethamine permeability through rat skin using penetration enhancers: An ex-vivo study, *Int. J. Pharm. Invest.*, 2015, **5**(3), 142–146.
54. B. W. Barry, Mode of action of penetration enhancers in human skin, *J. Controlled Release*, 1987, **6**(1), 85–97.
55. R. Notman, M. Noro, B. O'Malley and J. Anwar, Molecular Basis for Dimethylsulfoxide (DMSO) Action on Lipid Membranes, *J. Am. Chem. Soc.*, 2006, **128**(43), 13982–13983.
56. A. A. Gurtovenko and J. Anwar, Modulating the structure and properties of cell membranes: the molecular mechanism of action of dimethyl sulfoxide, *J. Phys. Chem. B*, 2007, **111**(35), 10453–10460.
57. Z. E. Hughes, A. E. Mark and R. L. Mancera, Molecular Dynamics Simulations of the Interactions of DMSO with DPPC and DOPC Phospholipid Membranes, *J. Phys. Chem. B*, 2012, **116**(39), 11911–11923.
58. A. P. Dabkowska, F. Foglia, M. J. Lawrence, C. D. Lorenz and S. E. McLain, On the solvation structure of dimethylsulfoxide/water around the phosphatidylcholine head group in solution, *J. Chem. Phys.*, 2011, **135**(22), 225105.
59. A. A. Gurtovenko and J. Anwar, Interaction of Ethanol with Biological Membranes: The Formation of Non-bilayer Structures within the

Membrane Interior and their Significance, *J. Phys. Chem. B*, 2009, **113**(7), 1983–1992.
60. Y. O. Posokhov and A. Kyrychenko, Effect of acetone accumulation on structure and dynamics of lipid membranes studied by molecular dynamics simulations, *Comput. Biol. Chem.*, 2013, **46**, 23–31.
61. R. Notman, M. G. Noro and J. Anwar, Interaction of Oleic Acid with Dipalmitoylphosphatidylcholine (DPPC) Bilayers Simulated by Molecular Dynamics, *J. Phys. Chem. B*, 2007, **111**(44), 12748–12755.
62. N. W. John and B. James, Voltage-Gated Sodium Channel Blockers; Target Validation and Therapeutic Potential, *Curr. Top. Med. Chem.*, 2005, **5**(6), 529–537.
63. S. K. Bagal, M. L. Chapman, B. E. Marron, R. Prime, R. I. Storer and N. A. Swain, Recent progress in sodium channel modulators for pain, *Bioorg. Med. Chem. Lett.*, 2014, **24**(16), 3690–3699.
64. D. A. Doyle, J. Morais Cabral, R. A. Pfuetzner, A. Kuo, J. M. Gulbis, S. L. Cohen, B. T. Chait and R. MacKinnon, The structure of the potassium channel: molecular basis of K^+ conduction and selectivity, *Science*, 1998, **280**(5360), 69–77.
65. O. S. Smart, J. M. Goodfellow and B. A. Wallace, The pore dimensions of gramicidin A, *Biophys. J.*, 1993, **65**(6), 2455–2460.
66. L. Heginbotham, Z. Lu, T. Abramson and R. MacKinnon, Mutations in the K^+ channel signature sequence, *Biophys. J.*, 1994, **66**(4), 1061–1067.
67. A. Parsegian, Energy of an Ion crossing a Low Dielectric Membrane: Solutions to Four Relevant Electrostatic Problems, *Nature*, 1969, **221**(5183), 844–846.
68. S. Berneche and B. Roux, Energetics of ion conduction through the K + channel, *Nature*, 2001, **414**(6859), 73–77.
69. S. Y. Noskov, S. Berneche and B. Roux, Control of ion selectivity in potassium channels by electrostatic and dynamic properties of carbonyl ligands, *Nature*, 2004, **431**(7010), 830–834.
70. J. Aqvist and V. Luzhkov, Ion permeation mechanism of the potassium channel, *Nature*, 2000, **404**(6780), 881–884.
71. S. Furini and C. Domene, Atypical mechanism of conduction in potassium channels, *Proc. Natl. Acad. Sci. U. S. A.*, 2009, **106**(38), 16074–16077.
72. D. A. Köpfer, C. Song, T. Gruene, G. M. Sheldrick, U. Zachariae and B. L. de Groot, Ion permeation in K^+ channels occurs by direct Coulomb knock-on, *Science*, 2014, **346**(6207), 352–355.
73. C. Jorgensen, L. Darré, K. Vanommeslaeghe, K. Omoto, D. Pryde and C. Domene, In Silico Identification of PAP-1 Binding Sites in the Kv1.2 Potassium Channel, *Mol. Pharm.*, 2015, **12**(4), 1299–1307.
74. Y. Li, F. Barbault, M. Delamar, R. Zhang and R. Hu, Targeted molecular dynamics (TMD) of the full-length KcsA potassium channel: on the role of the cytoplasmic domain in the opening process, *J. Mol. Model.*, 2013, **19**(4), 1651–1666.

75. L. Monticelli, K. M. Robertson, J. L. MacCallum and D. P. Tieleman, Computer simulation of the KvAP voltage-gated potassium channel: steered molecular dynamics of the voltage sensor, *FEBS Lett.*, 2004, **564**(3), 325–332.
76. B. Roux, Ion Conduction and Selectivity in K^+ Channels, *Annu. Rev. Biophys. Biomol. Struct.*, 2005, **34**(1), 153–171.
77. S. Furini and C. Domene, K^+ and Na^+ Conduction in Selective and Nonselective Ion Channels Via Molecular Dynamics Simulations, *Biophys. J.*, 2013, **105**(8), 1737–1745.
78. J. Payandeh, T. Scheuer, N. Zheng and W. A. Catterall, The crystal structure of a voltage-gated sodium channel, *Nature*, 2011, **475**(7356), 353–358.
79. J. Payandeh, T. M. Gamal El-Din, T. Scheuer, N. Zheng and W. A. Catterall, Crystal structure of a voltage-gated sodium channel in two potentially inactivated states, *Nature*, 2012, **486**(7401), 135–139.
80. E. C. McCusker, C. Bagneris, C. E. Naylor, A. R. Cole, N. D'Avanzo, C. G. Nichols and B. A. Wallace, Structure of a bacterial voltage-gated sodium channel pore reveals mechanisms of opening and closing, *Nat. Commun.*, 2012, **3**, 1102.
81. C. Bagnéris, P. G. DeCaen, B. A. Hall, C. E. Naylor, D. E. Clapham, C. W. M. Kay and B. A. Wallace, Role of the C-terminal domain in the structure and function of tetrameric sodium channels, *Nat. Commun.*, 2013, **4**, 2465.
82. D. Shaya, F. Findeisen, F. Abderemane-Ali, C. Arrigoni, S. Wong, S. R. Nurva, G. Loussouarn, Minor Jr. and D. L. , Structure of a Prokaryotic Sodium Channel Pore Reveals Essential Gating Elements and an Outer Ion Binding Site Common to Eukaryotic Channels, *J. Mol. Biol.*, 2014, **426**(2), 467–483.
83. V. Carnevale, W. Treptow and M. L. Klein, Sodium Ion Binding Sites and Hydration in the Lumen of a Bacterial Ion Channel from Molecular Dynamics Simulations, *J. Phys. Chem. Lett.*, 2011, **2**(19), 2504–2508.
84. B. Corry and M. Thomas, Mechanism of Ion Permeation and Selectivity in a Voltage Gated Sodium Channel, *J. Am. Chem. Soc.*, 2012, **134**(3), 1840–1846.
85. S. Furini and C. Domene, On conduction in a bacterial sodium channel, *PLoS Comput. Biol.*, 2012, **8**(4), e1002476.
86. H. Qiu, R. Shen and W. Guo, Ion solvation and structural stability in a sodium channel investigated by molecular dynamics calculations, *Biochim. Biophys. Acta*, 2012, **1818**(11), 2529–2535.
87. C. Domene, M. L. Klein, D. Branduardi, F. L. Gervasio and M. Parrinello, Conformational changes and gating at the selectivity filter of potassium channels, *J. Am. Chem. Soc.*, 2008, **130**(29), 9474–9480.
88. Y. Zhou, J. H. Morais-Cabral, A. Kaufman and R. MacKinnon, Chemistry of ion coordination and hydration revealed by a K^+ channel-Fab complex at 2.0 Å resolution, *Nature*, 2001, **414**, 43–48.
89. C. Domene and S. Furini, Dynamics, energetics, and selectivity of the low-K^+ KcsA channel structure, *J. Mol. Biol.*, 2009, **389**(3), 637–645.

90. B. Corry, Na^+/Ca^{2+} selectivity in the bacterial voltage-gated sodium channel NavAb, *PeerJ*, 2013, **1**, e16.
91. D. J. Benos, B. A. Hyde and R. Latorre, Sodium flux ratio through the amiloride-sensitive entry pathway in frog skin, *J. Gen. Physiol.*, 1983, **81**(5), 667–685.
92. L. Stock, L. Delemotte, V. Carnevale, W. Treptow and M. L. Klein, Conduction in a Biological Sodium Selective Channel, *J. Phys. Chem. B*, 2013, **117**(14), 3782–3789.
93. N. Chakrabarti, C. Ing, J. Payandeh, N. Zheng, W. A. Catterall and R. Pomès, Catalysis of Na^+ permeation in the bacterial sodium channel NaVAb, *Proc. Natl. Acad. Sci.*, 2013, **110**(28), 11331–11336.
94. C. Domene, P. Barbini and S. Furini, Bias-Exchange Metadynamics Simulations: An Efficient Strategy for the Analysis of Conduction and Selectivity in Ion Channels, *J. Chem. Theory Comput.*, 2015, **11**(4), 1896–1906.
95. C. Boiteux, I. Vorobyov and T. W. Allen, Ion conduction and conformational flexibility of a bacterial voltage-gated sodium channel, *Proc. Natl. Acad. Sci.*, 2014, **111**(9), 3454–3459.
96. S. Ke, E. N. Timin and A. Stary-Weinzinger, Different inward and outward conduction mechanisms in NaVMs suggested by molecular dynamics simulations, *PLoS Comput. Biol.*, 2014, **10**(7), e1003746.
97. S. Furini, P. Barbini and C. Domene, Effects of the Protonation State of the EEEE Motif of a Bacterial Na^+-channel on Conduction and Pore Structure, *Biophys. J.*, 2014, **106**(10), 2175–2183.
98. S. Ke, E.-M. Zangerl and A. Stary-Weinzinger, Distinct interactions of Na^+ and Ca^{2+} ions with the selectivity filter of the bacterial sodium channel NaVAb, *Biochem. Biophys. Res. Commun.*, 2013, **430**(4), 1272–1276.
99. B. Hille, Local anesthetics: hydrophilic and hydrophobic pathways for the drug-receptor reaction, *J. Gen. Physiol.*, 1977, **69**(4), 497–515.
100. S. G. Raju, A. F. Barber, D. N. LeBard, M. L. Klein and V. Carnevale, Exploring Volatile General Anesthetic Binding to a Closed Membrane-Bound Bacterial Voltage-Gated Sodium Channel via Computation, *PLoS Comput. Biol.*, 2013, **9**(6), e1003090.
101. J. A. Kaczmarski and B. Corry, Investigating the size and dynamics of voltage-gated sodium channel fenestrations: A molecular dynamics study, *Channels*, 2014, **8**(3), 264–277.
102. A. Nardi, N. Damann, T. Hertrampf and A. Kless, Advances in targeting voltage-gated sodium channels with small molecules, *ChemMedChem*, 2012, **7**(10), 1712–1740.
103. L. J. Martin and B. Corry, Locating the Route of Entry and Binding Sites of Benzocaine and Phenytoin in a Bacterial Voltage Gated Sodium Channel, *PLoS Comput. Biol.*, 2014, **10**(7), e1003688.
104. C. Boiteux, I. Vorobyov, R. J. French, C. French, V. Yarov-Yarovoy and T. W. Allen, Local anesthetic and antiepileptic drug access and binding to a bacterial voltage-gated sodium channel, *Proc. Natl. Acad. Sci.*, 2014, **111**(36), 13057–13062.

105. C. Jorgensen, L. Darré, V. Oakes, R. Torella, D. Pryde and C. Domene, Lateral Fenestrations in K^+-Channels Explored Using Molecular Dynamics Simulations, *Mol. Pharm.*, 2016, **13**(7), 2263–2273.
106. G. Rudnick, Mechanisms of Biogenic Amine Neurotransmitter Transporters, in *Neurotransmitter Transporters: Structure, Function, and Regulation*, ed. M. E. A. Reith, Humana Press, Totowa, NJ, 1997, pp. 73–100.
107. L. Iversen, Neurotransmitter transporters and their impact on the development of psychopharmacology, *Br. J. Pharmacol.*, 2006, **147**(Suppl 1), S82–S88.
108. S. G. Amara and M. S. Sonders, Neurotransmitter transporters as molecular targets for addictive drugs, *Drug Alcohol Depend.*, 1998, **51**(1–2), 87–96.
109. I. Bisha and A. Magistrato, The molecular mechanism of secondary sodium symporters elucidated through the lens of the computational microscope, *RSC Adv.*, 2016, **6**(12), 9522–9540.
110. A. Yamashita, S. K. Singh, T. Kawate, Y. Jin and E. Gouaux, Crystal structure of a bacterial homologue of Na^+/Cl^- dependent neurotransmitter transporters, *Nature*, 2005, **437**(7056), 215–223.
111. H. Krishnamurthy and E. Gouaux, X-ray structures of LeuT in substrate-free outward-open and apo inward-open states, *Nature*, 2012, **481**(7382), 469–474.
112. S. K. Singh, A. Yamashita and E. Gouaux, Antidepressant binding site in a bacterial homologue of neurotransmitter transporters, *Nature*, 2007, **448**(7156), 952–956.
113. Z. Zhou, J. Zhen, N. K. Karpowich, R. M. Goetz, C. J. Law, M. E. Reith and D. N. Wang, LeuT-desipramine structure reveals how antidepressants block neurotransmitter reuptake, *Science*, 2007, **317**(5843), 1390–1393.
114. L. Malinauskaite, S. Said, C. Sahin, J. Grouleff, A. Shahsavar, H. Bjerregaard, P. Noer, K. Severinsen, T. Boesen, B. Schiott, S. Sinning and P. Nissen, A conserved leucine occupies the empty substrate site of LeuT in the Na^+-free return state, *Nat. Commun.*, 2016, **7**, 11673.
115. L. Celik, B. Schiøtt and E. Tajkhorshid, Substrate Binding and Formation of an Occluded State in the Leucine Transporter, *Biophys. J.*, 2008, **94**(5), 1600–1612.
116. S. Y. Noskov and B. Roux, Control of ion selectivity in LeuT: two Na^+ binding sites with two different mechanisms, *J. Mol. Biol.*, 2008, **377**(3), 804–818.
117. D. A. Caplan, J. O. Subbotina and S. Y. Noskov, Molecular mechanism of ion-ion and ion-substrate coupling in the Na^+-dependent leucine transporter LeuT, *Biophys. J.*, 2008, **95**(10), 4613–4621.
118. C. Zhao, S. Stolzenberg, L. Gracia, H. Weinstein, S. Noskov and L. Shi, Ion-controlled conformational dynamics in the outward-open transition from an occluded state of LeuT, *Biophys. J.*, 2012, **103**(5), 878–888.
119. S. Tavoulari, E. Margheritis, A. Nagarajan, D. C. DeWitt, Y.-W. Zhang, E. Rosado, S. Ravera, E. Rhoades, L. R. Forrest and G. Rudnick, Two

Na^+ Sites Control Conformational Change in a Neurotransmitter Transporter Homolog, *J. Biol. Chem.*, 2015.
120. E. Zomot, A. Bendahan, M. Quick, Y. Zhao, J. A. Javitch and B. I. Kanner, Mechanism of chloride interaction with neurotransmitter:sodium symporters, *Nature*, 2007, **449**(7163), 726–730.
121. E. Zomot, M. Gur and I. Bahar, Microseconds simulations reveal a new sodium-binding site and the mechanism of sodium-coupled substrate uptake by LeuT, *J. Biol. Chem.*, 2015, **290**(1), 544–555.
122. C. Zhao and S. Y. Noskov, The role of local hydration and hydrogen-bonding dynamics in ion and solute release from ion-coupled secondary transporters, *Biochemistry*, 2011, **50**(11), 1848–1856.
123. J. R. Thomas, P. C. Gedeon, B. J. Grant and J. D. Madura, LeuT conformational sampling utilizing accelerated molecular dynamics and principal component analysis, *Biophys. J.*, 2012, **103**(1), L1–L3.
124. M. H. Cheng and I. Bahar, Complete mapping of substrate translocation highlights the role of LeuT N-terminal segment in regulating transport cycle, *PLoS Comput. Biol.*, 2014, **10**(10), e1003879.
125. M. Gur, E. Zomot, M. H. Cheng and I. Bahar, Energy landscape of LeuT from molecular simulations, *J. Chem. Phys.*, 2015, **143**(24), 243134.
126. S. A. Shaikh and E. Tajkhorshid, Modeling and dynamics of the inward-facing state of a Na^+/Cl^- dependent neurotransmitter transporter homologue, *PLoS Comput. Biol.*, 2010, **6**(8), e1000905.
127. S. Faham, A. Watanabe, G. M. Besserer, D. Cascio, A. Specht, B. A. Hirayama, E. M. Wright and J. Abramson, The crystal structure of a sodium galactose transporter reveals mechanistic insights into Na^+/sugar symport, *Science*, 2008, **321**(5890), 810–814.
128. J. Grouleff, S. Sondergaard, H. Koldso and B. Schiott, Properties of an inward-facing state of LeuT: conformational stability and substrate release, *Biophys. J.*, 2015, **108**(6), 1390–1399.
129. R. Chen and S.-H. Chung, Molecular dynamics simulations of Na^+ and leucine transport by LeuT, *Biochem. Biophys. Res. Commun.*, 2015, **464**(1), 281–285.
130. L. Shi, M. Quick, Y. Zhao, H. Weinstein and J. A. Javitch, The mechanism of a neurotransmitter:sodium symporter–inward release of Na^+ and substrate is triggered by substrate in a second binding site, *Mol. Cell*, 2008, **30**(6), 667–677.
131. M. Quick, L. Shi, B. Zehnpfennig, H. Weinstein and J. A. Javitch, Experimental conditions can obscure the second high-affinity site in LeuT, *Nat. Struct. Mol. Biol.*, 2012, **19**(2), 207–211.
132. Y. Zhao, D. S. Terry, L. Shi, M. Quick, H. Weinstein, S. C. Blanchard and J. A. Javitch, Substrate-modulated gating dynamics in a Na^+-coupled neurotransmitter transporter homologue, *Nature*, 2011, **474**(7349), 109–113.
133. S. K. Singh, C. L. Piscitelli, A. Yamashita and E. Gouaux, A competitive inhibitor traps LeuT in an open-to-out conformation, *Science*, 2008, **322**(5908), 1655–1661.

134. C. L. Piscitelli, H. Krishnamurthy and E. Gouaux, Neurotransmitter/sodium symporter orthologue LeuT has a single high-affinity substrate site, *Nature*, 2010, **468**(7327), 1129–1132.
135. H. Wang and E. Gouaux, Substrate binds in the S1 site of the F253A mutant of LeuT, a neurotransmitter sodium symporter homologue, *EMBO Rep.*, 2012, **13**(9), 861–866.
136. H. Wang, J. Elferich and E. Gouaux, Structures of LeuT in bicelles define conformation and substrate binding in a membrane-like context, *Nat. Struct. Mol. Biol.*, 2012, **19**(2), 212–219.
137. M. H. Cheng and I. Bahar, Coupled global and local changes direct substrate translocation by neurotransmitter-sodium symporter ortholog LeuT, *Biophys. J.*, 2013, **105**(3), 630–639.
138. M. Quick, A. M. Winther, L. Shi, P. Nissen, H. Weinstein and J. A. Javitch, Binding of an octylglucoside detergent molecule in the second substrate (S2) site of LeuT establishes an inhibitor-bound conformation, *Proc. Natl. Acad. Sci. U. S. A.*, 2009, **106**(14), 5563–5568.
139. C. Zhao, D. A. Caplan and S. Y. Noskov, Evaluations of the Absolute and Relative Free Energies for Antidepressant Binding to the Amino Acid Membrane Transporter LeuT with Free Energy Simulations, *J. Chem. Theory Comput.*, 2010, **6**(6), 1900–1914.
140. N. King, C. T. Hittinger and S. B. Carroll, Evolution of Key Cell Signaling and Adhesion Protein Families Predates Animal Origins, *Science*, 2003, **301**(5631), 361–363.
141. K. A. Jacobson, New paradigms in GPCR drug discovery, *Biochem. Pharmacol.*, 2015, **98**(4), 541–555.
142. R. Lappano and M. Maggiolini, G protein-coupled receptors: novel targets for drug discovery in cancer, *Nat. Rev. Drug Discovery*, 2011, **10**(1), 47–60.
143. R. C. Stevens, V. Cherezov, V. Katritch, R. Abagyan, P. Kuhn, H. Rosen and K. Wuthrich, The GPCR Network: a large-scale collaboration to determine human GPCR structure and function, *Nat. Rev. Drug Discovery*, 2013, **12**(1), 25–34.
144. S. Galandrin and M. Bouvier, Distinct signaling profiles of beta1 and beta2 adrenergic receptor ligands toward adenylyl cyclase and mitogen-activated protein kinase reveals the pluridimensionality of efficacy, *Mol. Pharmacol.*, 2006, **70**(5), 1575–1584.
145. B. K. Kobilka and X. Deupi, Conformational complexity of G-protein-coupled receptors, *Trends Pharmacol. Sci.*, 2007, **28**(8), 397–406.
146. S. G. F. Rasmussen, H.-J. Choi, D. M. Rosenbaum, T. S. Kobilka, F. S. Thian, P. C. Edwards, M. Burghammer, V. R. P. Ratnala, R. Sanishvili, R. F. Fischetti, G. F. X. Schertler, W. I. Weis and B. K. Kobilka, Crystal structure of the human [bgr]2 adrenergic G-protein-coupled receptor, *Nature*, 2007, **450**(7168), 383–387.
147. V. Cherezov, D. M. Rosenbaum, M. A. Hanson, S. G. F. Rasmussen, F. S. Thian, T. S. Kobilka, H.-J. Choi, P. Kuhn, W. I. Weis, B. K. Kobilka and R. C. Stevens, High Resolution Crystal Structure of an Engineered

Human β(2)-Adrenergic G protein-Coupled Receptor, *Science*, 2007, **318**(5854), 1258–1265.
148. D. M. Rosenbaum, V. Cherezov, M. A. Hanson, S. G. F. Rasmussen, F. S. Thian, T. S. Kobilka, H.-J. Choi, X.-J. Yao, W. I. Weis, R. C. Stevens and B. K. Kobilka, GPCR Engineering Yields High-Resolution Structural Insights into β2-Adrenergic Receptor Function, *Science*, 2007, **318**(5854), 1266–1273.
149. M. A. Hanson, V. Cherezov, M. T. Griffith, C. B. Roth, V.-P. Jaakola, E. Y. T. Chien, J. Velasquez, P. Kuhn and R. C. Stevens, A Specific Cholesterol Binding Site Is Established by the 2.8 Å; Structure of the Human β2-Adrenergic Receptor, *Structure*, 2008, **16**(6), 897–905.
150. R. O. Dror, D. H. Arlow, D. W. Borhani, M. Ø. Jensen, S. Piana and D. E. Shaw, Identification of two distinct inactive conformations of the β2-adrenergic receptor reconciles structural and biochemical observations, *Proc. Natl. Acad. Sci.*, 2009, **106**(12), 4689–4694.
151. J. A. Ballesteros, A. D. Jensen, G. Liapakis, S. G. Rasmussen, L. Shi, U. Gether and J. A. Javitch, Activation of the beta 2-adrenergic receptor involves disruption of an ionic lock between the cytoplasmic ends of transmembrane segments 3 and 6, *J. Biol. Chem.*, 2001, **276**(31), 29171–29177.
152. D. M. Rosenbaum, C. Zhang, J. A. Lyons, R. Holl, D. Aragao, D. H. Arlow, S. G. F. Rasmussen, H.-J. Choi, B. T. DeVree, R. K. Sunahara, P. S. Chae, S. H. Gellman, R. O. Dror, D. E. Shaw, W. I. Weis, M. Caffrey, P. Gmeiner and B. K. Kobilka, Structure and function of an irreversible agonist-[bgr]2 adrenoceptor complex, *Nature*, 2011, **469**(7329), 236–240.
153. R. Nygaard, Y. Zou, R. O. Dror, T. J. Mildorf, D. H. Arlow, A. Manglik, A. C. Pan, C. W. Liu, J. J. Fung, M. P. Bokoch, F. S. Thian, T. S. Kobilka, D. E. Shaw, L. Mueller, R. S. Prosser and B. K. Kobilka, The dynamic process of beta(2)-adrenergic receptor activation, *Cell*, 2013, **152**(3), 532–542.
154. R. O. Dror, D. H. Arlow, P. Maragakis, T. J. Mildorf, A. C. Pan, H. Xu, D. W. Borhani and D. E. Shaw, Activation mechanism of the beta2-adrenergic receptor, *Proc. Natl. Acad. Sci. U. S. A.*, 2011, **108**(46), 18684–18689.
155. A. V. Botelho, T. Huber, T. P. Sakmar and M. F. Brown, Curvature and hydrophobic forces drive oligomerization and modulate activity of rhodopsin in membranes, *Biophys. J.*, 2006, **91**(12), 4464–4477.
156. S. Mondal, G. Khelashvili, J. Shan, O. S. Andersen and H. Weinstein, Quantitative modeling of membrane deformations by multihelical membrane proteins: application to G-protein coupled receptors, *Biophys. J.*, 2011, **101**(9), 2092–2101.
157. S. Mondal, J. M. Johnston, H. Wang, G. Khelashvili, M. Filizola and H. Weinstein, Membrane Driven Spatial Organization of GPCRs, *Sci. Rep.*, 2013, **3**, 2909.

158. D. Calebiro, F. Rieken, J. Wagner, T. Sungkaworn, U. Zabel, A. Borzi, E. Cocucci, A. Zürn and M. J. Lohse, Single-molecule analysis of fluorescently labeled G-protein–coupled receptors reveals complexes with distinct dynamics and organization, *Proc. Natl. Acad. Sci.*, 2013, **110**(2), 743–748.
159. J. J. Fung, X. Deupi, L. Pardo, X. J. Yao, G. A. Velez-Ruiz, B. T. DeVree, R. K. Sunahara and B. K. Kobilka, Ligand-regulated oligomerization of β(2)-adrenoceptors in a model lipid bilayer, *EMBO J.*, 2009, **28**(21), 3315–3328.
160. X. Prasanna, A. Chattopadhyay and D. Sengupta, Cholesterol Modulates the Dimer Interface of the β_2-Adrenergic Receptor via Cholesterol Occupancy Sites, *Biophys. J.*, 2014, **106** (6), 1290–1300.
161. C. Neale, H. D. Herce, R. Pomès and A. E. García, Can Specific Protein-Lipid Interactions Stabilize an Active State of the Beta 2 Adrenergic Receptor? *Biophys. J.*, 2015, **109** (8), 1652-1662.
162. A. C. Kalli, M. S. P. Sansom and R. A. F. Reithmeier, Molecular Dynamics Simulations of the Bacterial UraA H^+-Uracil Symporter in Lipid Bilayers Reveal a Closed State and a Selective Interaction with Cardiolipin, *PLoS Comput. Biol.*, 2015, **11**(3), e1004123.
163. J. N. Horn, T.-C. Kao and A. Grossfield, Coarse-grained Molecular Dynamics Provides Insight into the Interactions of Lipids and Cholesterol with Rhodopsin, *Adv. Exp. Med. Biol.*, 2014, **796**, 75–94.
164. D. Sengupta and A. Chattopadhyay, Molecular dynamics simulations of GPCR-cholesterol interaction: An emerging paradigm, *Biochim. Biophys. Acta,*, 2015, **1848**(9), 1775–1782.
165. X. Prasanna, A. Chattopadhyay and D. Sengupta, Role of Lipid-Mediated Effects in β2-Adrenergic Receptor Dimerization, in *Biochemical Roles of Eukaryotic Cell Surface Macromolecules*, ed. Chakrabarti, A., Surolia, A., Springer International Publishing, Cham, 2015, pp. 247–261.

Part II: Research Projects

3. Atypical Behaviour of the TWIK-1 Channel

3.1 Commentary

3.1.1 Introduction

The newly resolved high-resolution crystal structures of K_{2P} channels (TWIK-1,[1] TRAAK,[2-4] TREK-2[5] and TREK-1[6] in order of publication), have exposed unveiled structural attributes in the pore domain divergent to other K^+-channels. The pore domain is assembled as a dimer, containing 1) an open cytoplasmic gate, 2) a non-conserved selectivity filter sequence, 3) an extracellular domain and 4) lateral openings, known as fenestrations, between the protein interior and exterior.

Lateral openings in ion channels were first exposed in the inaugural structure of a Na^+-selective channel in 2011;[7] subsequently, analogous regions have been determined in a number of Na^+-channels from prokaryotic sources, advocating fenestrations are a conserved feature of this channel type.[8] In K^+ channels, fenestrations have since been identified in K_{2P} channels, and structures of KcsA in complex with quaternary ammonium blockers.[9] The structures of TREK-2, a member of the K_{2P} channel family, revealed state-dependent binding of norfluoxetine, the active metabolite of Prozac, within the intramembrane fenestrations.[5] Simulation methods have been employed to characterise the size and dynamics of the fenestration region in the context of Na^+-channels, in order to supplement static structural data and provide further insight into the function of this region.[10-12] With this in mind, our research group, in collaboration with Pfizer Neusentis, sought to evaluate the behaviour of the equivalent region in distinct mammalian K^+-channel subfamilies, by means of unbiased MD dynamics simulations. In the publication entitled "Lateral Fenestrations in K^+-Channels Explored Using Molecular Dynamics Simulations", results from representative members of the K_V (K_V1.2), K_{IR} (K_{IR}3.2) and K_{2P} (K2P1, also known as TWIK-1) channel families are presented (section 3.2). Christian Jorgensen, Leonardo Darré and I performed the MD simulations and analysis for individual channels (K_V1.2, K_{IR}3.2 and TWIK-1, respectively), and Ruben Torella provided the Pfido analysis. Overall, the size and dynamics of the fenestrations are calculated, and sequence identity of the fenestration region is mapped and evidence, providing that fenestrations only exist in the K_{2P} subfamily.

Further to this, the behaviour of the TWIK-1 channel was examined in the context of ion permeation. The distinct selectivity filter sequence and extracellular domain structure are

relevant considering experimental data, documenting conduction properties in TWIK-1 divergent to other K_{2P} channels. Negligible K^+ currents in physiological K^+ concentrations,[13] as well as robust inward Na^+ currents in sub physiological K^+ concentrations are amongst the most striking traits of the TWIK-1 channel.[14] In the publication presented in section 3.3, the molecular behaviour of the TWIK-1 selectivity filter and extracellular cap is analysed and interpreted considering the available experimental data. It should be noted that the MD simulation data from section 3.2 is utilised, as well as separate MD simulation trajectories I performed and analysed, where the protonation state of several residues is modified. Overall, the atypical conduction properties of TWIK-1 are rationalised by the presence of anomalous residues in the selectivity filter, and instability in the surrounding environment.

3.1.2 References

(1) Miller, A. N.; Long, S. B. Crystal Structure of the Human Two-Pore Domain Potassium Channel K2P1. *Science* **2012,** *335* (6067), 432.

(2) Brohawn, S. G.; del Marmol, J.; MacKinnon, R. Crystal Structure of the Human K2P TRAAK, a Lipid- and Mechano-Sensitive K^+ Ion Channel. *Science* **2012,** *335* (6067), 436.

(3) Brohawn, S. G.; Campbell, E. B.; MacKinnon, R. Physical mechanism for gating and mechano sensitivity of the human TRAAK K^+ channel. *Nature* **2014,** *516* (7529), 126.

(4) Brohawn, S. G.; Campbell, E. B.; MacKinnon, R. Domain-swapped chain connectivity and gated membrane access in a Fab-mediated crystal of the human TRAAK K^+ channel. *P. Natl. Acad. Sci. USA* **2013,** *110* (6), 2129.

(5) Dong, Y. Y.; Pike, A. C. W.; Mackenzie, A.; McClenaghan, C.; Aryal, P.; Dong, L.; Quigley, A.; Grieben, M.; Goubin, S.; Mukhopadhyay, S.et al. K2P channel gating mechanisms revealed by structures of TREK-2 and a complex with Prozac. *Science* **2015,** *347* (6227), 1256.

(6) Lolicato, M.; Arrigoni, C.; Mori, T.; Sekioka, Y.; Bryant, C.; Clark, K. A.; Minor, D. L. K(2P)2.1 (TREK-1)-activator complexes reveal a cryptic selectivity filter binding site. *Nature* **2017,** *547* (7663), 364.

(7) Payandeh, J.; Scheuer, T.; Zheng, N.; Catterall, W. A. The crystal structure of a voltage-gated sodium channel. *Nature* **2011,** *475* (7356), 353.

(8) Ruiz, M. D.; Kraus, R. L. Voltage-Gated Sodium Channels: Structure, Function, Pharmacology, and Clinical Indications. *J. Med. Chem.* **2015,** *58* (18), 7093.

(9) Lenaeus, M. J.; Burdette, D.; Wagner, T.; Focia, P. J.; Gross, A. Structures of KcsA in Complex with Symmetrical Quaternary Ammonium Compounds Reveal a Hydrophobic Binding Site. *Biochemistry* **2014,** *53* (32), 5365.

(10) Kaczmarski, J. A.; Corry, B. Investigating the size and dynamics of voltage-gated sodium channel fenestrations A molecular dynamics study. *Channels* **2014,** *8* (3), 14.

(11) Martin, L.; Corry, B. Finding the Route of Entry and Binding Site of Local Anaesthetics in Bacterial Voltage Gated Sodium Channels Using Molecular Dynamics Simulation. *Biophys. J.* **2014,** *106* (2), 130A.

(12) Martin, L. J.; Corry, B. Locating the Route of Entry and Binding Sites of Benzocaine and Phenytoin in a Bacterial Voltage Gated Sodium Channel. *Plos Comput. Biol.* **2014,** *10* (7), 12.

(13) Lesage, F.; Guillemare, E.; Fink, M.; Duprat, F.; Lazdunski, M.; Romey, G.; Barhanin, J. TWIK-1, a ubiquitous human weakly inward rectifying K^+ channel with a novel structure. *EMBO J.* **1996,** *15* (5), 1004.

(14) Ma, L. Q.; Zhang, X. X.; Chen, H. J. TWIK-1 Two-Pore Domain Potassium Channels Change Ion Selectivity and Conduct Inward Leak Sodium Currents in Hypokalemia. *Sci. Signal.* **2011,** *4* (176), 10.

3.3 Lateral Fenestrations in K+-Channels Explored Using Molecular Dynamics Simulations, *Mol. Pharmaceutics*, 2016

3.3.1 Authorship and Permissions

<table>
<tr><td colspan="10">This declaration concerns the article entitled</td></tr>
<tr><td colspan="10">Lateral Fenestrations in K+-Channels Explored Using Molecular Dynamics Simulations</td></tr>
<tr><td colspan="10">Publication status (tick one)</td></tr>
<tr><td>Draft manuscript</td><td></td><td>Submitted</td><td></td><td>In review</td><td></td><td>Accepted</td><td></td><td>Published</td><td>✓</td></tr>
<tr><td>Publication details</td><td colspan="9">*Mol. Pharmaceutics*, 2016, 13 (7), 2263-2273
DOI: 10.1021/acs.molpharmaceut.5b00942
Received: 15 December 2015
Accepted: 12 May 2016
Published online: 12 May 2016
Published in print: 5 July 2016

Reprinted with permission from C. Jorgensen, L. Darre, V. Oakes, R Torella, D. Pryde and C. Domene, *Mol. Pharmaceutics*, 2016, 13 (7), 2263-2273. Copyright 2016 American Chemical Society.</td></tr>
<tr><td>Candidates contribution to the paper (detailed and also given as a percentage)</td><td colspan="9">The candidate contributed to/considerably contributed/predominantly executed the…
Formulation of ideas (20%):
C. Jorgensen, L. Darre, V. Oakes, D. Pryde and C. Domene

Design of methodology (25%):
Methodology was agreed between C. Jorgensen, L. Darre, V. Oakes and C. Domene

Experimental work (30%):
C. Jorgensen: K_V1.2 simulation and analysis
L. Darre: K_{IR}3.2 simulation and analysis
V.Oakes: TWIK-1 simulation and analysis
R. Torella: Pfido druggability analysis

Presentation of data in journal format (25%):
Manuscript preparation was distributed between C. Jorgensen, L. Darre, V. Oakes and C. Domene
R. Torella: Critically assessed and revised the manuscript.
D. Pryde: Critically assessed and revised the manuscript.</td></tr>
<tr><td>Statement from Candidate</td><td colspan="9">This paper reports on original research I conducted during the period of my Higher Degree by Research candidature.</td></tr>
<tr><td>Signed</td><td colspan="5"></td><td>Date</td><td colspan="3"></td></tr>
</table>

molecular pharmaceutics

Article

pubs.acs.org/molecularpharmaceutics

Lateral Fenestrations in K^+-Channels Explored Using Molecular Dynamics Simulations

Christian Jorgensen,[†] Leonardo Darré,[†] Victoria Oakes,[†] Rubben Torella,[‡] David Pryde,[‡] and Carmen Domene*[,†,§]

[†]Department of Chemistry, King's College London, Britannia House, 7 Trinity Street, London SE1 1DB, U.K.

[‡]Pfizer Neuroscience and Pain Research Unit, Worldwide Medicinal Chemistry, Portway Building, Granta Park, Great Abington, Cambridge CB21 6GS, U.K.

[§]Chemistry Research Laboratory, University of Oxford, Mansfield Road, Oxford OX1 3TA, U.K.

Supporting Information

ABSTRACT: Potassium channels are of paramount physiological and pathological importance and therefore constitute significant drug targets. One of the keys to rationalize the way drugs modulate ion channels is to understand the ability of such small molecules to access their respective binding sites, from which they can exert an activating or inhibitory effect. Many computational studies have probed the energetics of ion permeation, and the mechanisms of voltage gating, but little is known about the role of fenestrations as possible mediators of drug entry in potassium channels. To explore the existence, structure, and conformational dynamics of transmembrane fenestrations accessible by drugs in potassium channels, molecular dynamics simulation trajectories were analyzed from three potassium channels: the open state voltage-gated channel Kv1.2, the G protein-gated inward rectifying channel GIRK2 (Kir3.2), and the human two-pore domain TWIK-1 (K2P1.1). The main results of this work were the identification of the sequence identity of four main lateral fenestrations of similar length and with bottleneck radius in the range of 0.9−2.4 Å for this set of potassium channels. It was found that the fenestrations in Kv1.2 and Kir3.2 remain closed to the passage of molecules larger than water. In contrast, in the TWIK-1 channel, both open and closed fenestrations are sampled throughout the simulation, with bottleneck radius shown to correlate with the random entry of lipid membrane molecules into the aperture of the fenestrations. Druggability scoring function analysis of the fenestration regions suggests that Kv and Kir channels studied are not druggable in practice due to steric constraining of the fenestration bottleneck. A high (>50%) fenestration sequence identity was found in each potassium channel subfamily studied, Kv1, Kir3, and K2P1. Finally, the reported fenestration sequence of TWIK-1 compared favorably with another channel, K2P channel TREK-2, reported to possess open fenestrations, suggesting that K2P channels could be druggable via fenestrations, for which we reported atomistic detail of the fenestration region, including the flexible residues M260 and L264 that interact with POPC membrane in a concerted fashion with the aperture and closure of the fenestrations.

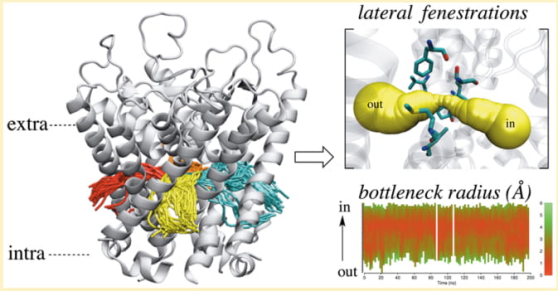

KEYWORDS: *cavities, tunnels, druggability, ion channels*

INTRODUCTION

The term "druggability" refers to the ability of a small molecule to modulate the function of a target receptor protein. It is estimated that 10−15% of the genes identified by the Human Genome Sequencing Consortium constitute useful druggable targets, of which only half may constitute real protein targets.[1] Because of their vast range of physiological roles, ion channels are of paramount pharmacological importance and are targets for over 20% of drugs on the market.[2] Potassium channel druggability mechanisms remain an active area of research, for which no single unified mechanism is known.[3] Potassium channels form selective pores that span cell membranes, enabling the selective and rapid conduction of potassium ions down the electrochemical gradient.[4] Their structure comprises two or four subunits forming dimers of dimers or tetramers. A pore−loop structure lines the top of the pore, known as the selectivity filter that modulates the selective ion permeability. Currently, at least 60 unique potassium channel X-ray crystal structures are available,[3] of which representatives of three families of potassium channels were considered here.

The first channel employed in this study belongs to the voltage-gated (Kv) channel family, which spans at least nine known subfamilies, Kv1−9.[5] Small-molecule druggability of the

Received: December 15, 2015
Revised: May 6, 2016
Accepted: May 12, 2016
Published: May 12, 2016

DOI: 10.1021/acs.molpharmaceut.5b00942
Mol. Pharmaceutics 2016, 13, 2263−2273

Kv1 subfamily has been proposed to occur via a cooperative mechanism involving two main blocking sites: the inner-pore site, located below the selectivity filter, and a side-pocket cavity located between the pore and the voltage-sensor, for which it is thought fenestrations could play an active role in modulating the blockage mechanism.[6−8] Current well-established inner-pore Kv1 blockers include 4-aminopyridine (4-AP), tetraethylammonium (TEA),[9] tetrabutylammonium (TBA),[10] and correolide.[11] Because of the highly conserved inner-pore sequence, these drugs do not show specificity among Kv1 subtypes, which has hindered further therapeutic applications. A new generation of phenoxyalkoxypsoralen derivatives has shown increased Kv1 subtype specificity and holds therapeutic promise.[12,13] Kv1.2 is an active druggable target for neurological and autoimmune disorders such as multiple sclerosis, type-1 diabetes mellitus, and rheumatoid arthritis.[12,13]

The second channel employed belongs to the inward-rectifying (Kir) channels, which preferentially conduct current in the inward direction into the cell. Kir channels constitute therapeutic target for many common disorders including hypertension, cardiac arrhythmia, and pain.[14] Kir channels span at least seven subfamilies, Kir1−7, with the Kir3 subfamily having their activity critically regulated by G protein-coupled receptors (GPCRs).[15] Thus, they are referred to as GPCR-activated Kir (GIRK) channels. The broad range of Kir-regulatory functions means that some Kir channels occupy a unique physiological "niche".[15] Kir3.2 small-molecule druggability is currently limited to nonselective cardiovascular and neurological drugs with off-target activity toward Kir channels. This means that the real therapeutic potential and druggability of most Kir channels has not yet been determined experimentally.[15] Current work on neuronal Kir3 (GIRK) pharmacology has focused on well-studied neurological drugs, all of which exhibit low affinity toward GIRK, including the serotonin-reuptake inhibitor fluoxetine,[15,16] as well as pore-blocking opiates, small-molecule analgesics for pain management. Crucially, a clear understanding of the potential of neutral GIRK channels in pain requires the development of selective Kir3.1/Kir3.2 small-molecule drugs.[15] A mechanistic understanding of drug binding pathways and knowledge of specific chemical sequence of fenestrations may prove useful for this purpose. An example of a common small-molecule pore blocker, Vernakalant, reached clinical trials and showed efficacy in terminating the onset of atrial fibrillation. However, Vernakalant also inhibits the cardiac Kv1.5 and Kv4 channels by blocking the highly conserved Kv family pore, thus precluding further therapeutic assays.[17]

The third and final channel studied belongs to the two pore domain potassium (K2P) channels, which generate leak potassium currents, and thus plays an essential role in cell excitability. K2P channels have been proposed to show weak inward rectification,[18,19] suggesting resemblance with inward-rectifying (Kir) potassium channels.[19] Six subfamilies, TWIK, TREK, TALK, TASK, THIK, and TRESK, have been identified, primarily implicated in a range of cardiovascular and neurological disorders. A unique structural attribute of K2P channels is the absence of the classical cytoplasmic bundle crossing that leads to structural changes at the selectivity filter, the primary mode of gating.[20−22] The crystal structure of TWIK-1 helped elucidate the topology of the plasmatic membrane. A vast range of regulatory stimuli are proposed to modulate this gate,[23] such as hydrophobic compounds and various lipids that readily enter the membrane bilayer through lateral fenestrations.[24] Small molecule block of K2P channels is currently limited to the targeting of TREK-1. K2P channels are poorly inhibited by classical K^+ channel blockers such as TEA, Cs^+, and 4-aminopyridine when applied from the extracellular site, but it has recently been shown that a known family of Kv1 blockers, the quaternary ammonium (QA) ions, potently block TREK-1 when applied from the intracellular side.[25] In Kv and Kir channels, QA ions are known to bind from the intracellular side by binding to a site deep within the pore just below the selectivity filter (the pore site). K2P block has been studied with spadin, a sortillin-derived peptide, which has been identified as a novel antidepressant treatment,[26] but with no reported binding site. Sortillin binding has been reported to be akin to fluoxetine inhibition of TREK-1, which does not target the pore but instead a C-terminal site.[27] In addition, a series of substituted caffeate esters have been shown to relieve pain by targeting TREK-1 and therefore might contribute to the next generation of analgesic drugs.[28]

To understand the mechanism of drug modulation of ion channels, it is necessary to understand the location of small-molecule binding sites and how they can be accessed. Drug binding depends both on the target conformational state (open, closed, or inactivated) as well as the real-time dynamics of the residues lining the fenestrations and entry tunnels of the target. Many studies have probed the energetics of potassium ion permeation,[29−32] and the mechanisms of gating,[33−35] but little is known about the role and presence of fenestrations in potassium channels. Work on fenestrations in Kir1.1 channels found a specific cholesterol binding pocket accessible from the membrane via lateral fenestrations by docking studies.[36] Such a cavity was proposed to be absent in Kir2.2 and all Kir3 members from sequence alignment. Additionally, bound molecules were identified in the fenestration regions of the X-ray crystal structures of the TWIK-1[20] and TREK-2 (K2P10.1),[37] specifically lipid density in TWIK-1 fenestrations, and norfluoxetine (the active metabolite of Prozac) bound to TREK-2 fenestrations. Comparison of TREK-2 structures in multiple activation states revealed distinct structural differences in the spatial attributes of fenestration regions, implicating "open" fenestrations, and key residues within them, in the state-dependent block of TREK-2 by Prozac.

In this work, we are utilizing the predictive power of computational modeling to characterize the fenestration regions in other potassium channels where crystal structures in several activation states are unknown, or the presence of fenestrations has not been examined in detail, to assess the accessibility and hence potential druggability of such regions. The availability, topology, and conformational dynamics of lateral fenestrations in the transmembrane domain of three potassium channels are studied using molecular dynamics (MD) simulation trajectories comprising around one microsecond of accumulated sampling. The channels selected are the voltage-gated potassium ion channel Kv1.2, the inward-rectifying GPCR-activated Kir3.2 (GIRK2) channel, and the two-pore domain channel TWIK-1 (K2P1.1). The results are compared to the reported X-ray structure of TREK-2 in complex with norfluoxetine.[37] The information reported may potentially aid in the design of next generation potassium channel blocking drugs.

METHODS

Systems Set-up. MD simulations were carried out on the structure of open-state Kv1.2 (PDB id 3LUT, resolution 2.9

DOI: 10.1021/acs.molpharmaceut.5b00942
Mol. Pharmaceutics 2016, 13, 2263−2273

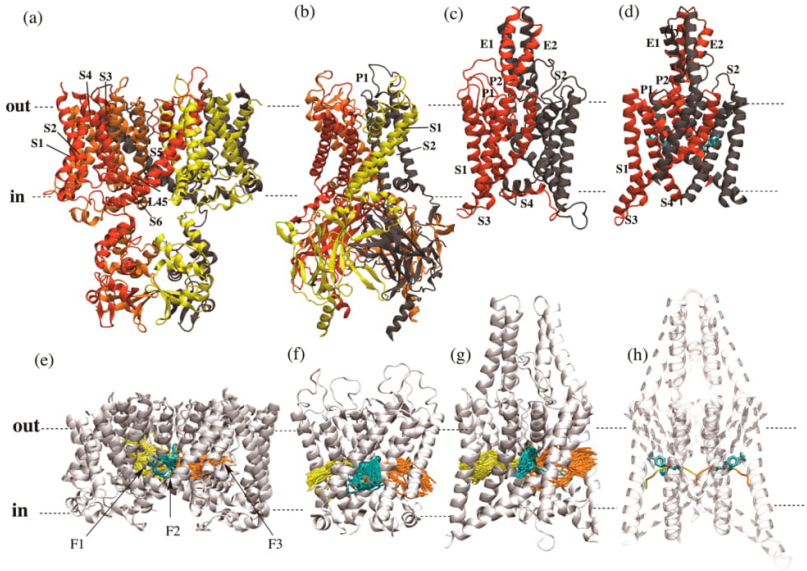

Figure 1. Structures of the ion channels involved in this study. (a) Kv1.2, (b) Kir3.2, (c) TWIK-1, and (d) TREK-2 channel structures. Illustrations of the fenestrations found in the transmembrane domains of structures (d, e, f) obtained from MD trajectories and (h) those observed in the crystal structure of TREK-2. Chains A, B, C, and D are in red, yellow, orange, and black, respectively. Fenestration clusters 1, 2, and 3 are in yellow, cyan, and orange, respectively. Fenestration cluster 4 is in the rear view of each channel.

Å),[38] the closed and open states of the murine G protein-gated inward rectifying K^+ channel GIRK2 (Kir3.2) (Kir3.2/C, PDB id 3SYA, resolution 2.98 Å;[39] and Kir3.2/O, PDB id 3SYQ, resolution of 3.44 Å,[39] respectively) and of the open-state human two-pore domain potassium channel TWIK-1 (PDB id 3UKM, resolution 3.4 Å)[20] (Figure 1). The initial structure of Kir3.2/O was generated using MODELER 9.11,[40] using the crystal structure of the murine Kir3.2 solved in complex with the beta-gamma G protein subunits (PDB id: 4KFM)[41] as a template to model the missing loops (residues 70−80 or 67−81 in chains A or B respectively, and 118−133 in both chains). For TWIK1, residues 18−281 were used for the structure of TWIK-1, and missing residues (95−99 and 169−174) were modeled using Modloop[42] in MODELER.

The pore of each channel was initially hydrated by employing the SOLVATE software,[43] which facilitates the hydration of irregularly shaped solutes, particularly relevant in filling the central pore of the channels. The resulting system was then embedded in a pre-equilibrated lipid bilayer of 1-palmitoy-l,2-oleoyl-*sn*-glycero-3-phosphocholine (POPC) molecules, with the central pore axis aligned to the bilayer normal. Lipid molecules overlapping with protein atoms were removed. A rectangular box of dimensions specific to each system was used to center the system, and the void space was filled with water molecules using the Solvate plugin of VMD, which removed those overlapping with protein or lipid atoms. Potassium and chloride ions were added to the system to achieve neutralization up to a final concentration of 150 mM to mimic a biological environment. Three potassium ions in the selectivity filter of the crystal structures were kept. In addition, in the case of Kir3.2/C, four sodium ions (one per subunit) present in the crystal structure were also included. PIO ([(2R)-2-octanoyloxy-3-[oxidanyl-[(1R,2R,3S,4R,5R,6S)-2,3,6-tris-(oxidanyl)-4,5-diphosphonooxy-cyclohexyl]oxy-phosphoryl]-oxy-propyl] octanoate) molecules present in both crystal structures of Kir3.2 were used to reconstruct the PIP2 molecules proposed to bind in each state of the channel. The same stoichiometry as observed in the crystal structures was kept in the simulated systems, that is, four and two PIP2 molecules for the closed and open states, respectively. Recently developed CHARMM parameters for PIP2 were used.[44] The CHARMM 36 force field[45] was used for the lipids, CHARMM 27[46] was used for the protein, the TIP3P model[47] was used for water, and the standard CHARMM parameters and NBFIXES were used for the ions.[48]

MD Simulations. The NAMD2.9[49] software was used to perform the computations. Each system was subjected to 5000 steps of energy minimization followed by a set of MD equilibration steps in the NpT ensemble including using a 1 kcal/mol/Å^2 force constant throughout: (i) 500 ps applying restraints on the protein, the water in the pore cavity, and the crystallographic potassium ions. The NAMD Tcl Forces module was used to avoid hydrating the void space in the hydrophobic interface between the channel transmembrane domain and the membrane by applying an inverse force on water molecules crossing the hydrophobic interface, thereby excluding them, while the lipids pack around the protein; (ii) 500 ps applying restraints on the protein atoms, relaxing the solvent in the cavity; (iii) 500 ps applying restraints on the protein backbone atoms, relaxing the amino-acid side chains; (iv) 500 ps applying restraints on the selectivity filter alone. Semi-isotropic pressure coupling at 1 atm was accomplished using the Nosé-Hoover Langevin piston using a damping time constant of 50 fs and a period of 200 fs, while temperature was maintained at 310 K by means of the Langevin thermostat with a damping coefficient of 1 ps^{-1}. Long-range electrostatic interactions were treated using the particle mesh Ewald algorithm with a grid spacing of 1 Å, and van der Waals forces were smoothly switched off between 10 and 12 Å, with NAMD defaults for spline and κ values.[50] A Verlet neighbor list with

DOI: 10.1021/acs.molpharmaceut.5b00942
Mol. Pharmaceutics 2016, 13, 2263−2273

pairlist distance of 13 Å was used. The lengths of covalent bonds involving hydrogen atoms were constrained by the SETTLE algorithm to use a 2 fs time-step. The multi time step algorithm Verlet-I/r-RESPA was used to integrate the equations of motion. Nonbonded short-range forces were computed every time step, while long-range electrostatic forces were updated every two time steps. The total available MD production runs amount to 0.8 μs. The Kir3.2/O trajectory was of 100 ns, the TWIK-1 trajectory of 200 ns, and the Kv1.2 trajectory of 400 ns. An additional 100 ns trajectory of Kir3.2 closed state (Kir3.2/C) was used to compare the Kir3.2/O result.

Fenestration Search. The output of the MD simulation trajectories of each channel was scanned for fenestrations using the CAVER 3.0 software,[51] in which the outer surface of the protein is calculated by rolling a large spherical probe around its surface, and then internal fenestrations are identified using a probe comprising 12 spheres of radius 0.8 Å. All identified fenestrations are then grouped into clusters based on relative proximities and with an 8 Å cutoff for each cluster node. In this way, fenestrations differing from the node by more than 8 Å are excluded.

Residues lining the fenestrations were compared using a multiple sequence alignment considering Kv1.2 (Uniprot P16389), Kv1.3 (Uniprot P22001), Kv1.5 (Uniprot P22460), Kv7.1 (Uniprot P51787), mammalian Kir3.2 (Uniprot P48542), Kir3.1 (Uniprot P48549), Kir2.2 (Uniprot Q14500), human TWIK-1 (Uniprot O00180), K2P10 (Uniprot P57789), and K2P6.1 (Uniprot Q9Y257) employing the ClustalO[52] algorithm. Electrostatic potential iso-surface calculations were performed using APBS v1.4,[53] with results presented in Figures S3 and S4.

Pfido Druggability Scoring Function Analysis. The cavity analysis is a useful tool for obtaining specific residues and physical parameters about the dimensions of fenestrations; however, it does not provide a quantitative indication of the likelihood or druggability of fenestration sites, as quantified by, for example, the binding free-energy at the site. Pfido[54] is a relevant alternative method, which can yield a druggability score (kcal/mol) for each channel. Pfido is a druggability prediction method developed by Pfizer that aims to predict the druggability of pharmaceutical targets based solely on the binding-site structure. A Pfido calculation requires the definition of a binding site and a ligand probe. Norfluoxetine was chosen as the probe for these systems. The binding site was represented using computational geometry methods[55,56] and defined as the cavity spanned by fenestrations residues in a 5 Å radial distance from the molecule probe origin. Three parameters were used to quantify the druggability of the binding: fraction lipophilic (nonpolar) surface area (SA), fenestration surface curvature, and calculated druggability score. The calculated druggability score (kcal/mol) is the maximal affinity predicted (MAP) binding energy ΔG_{MAP}, eq 1, which is an estimate of the maximal achievable affinity for a binding pocket from a hit-to-lead optimization effort:

$$\Delta G_{MAP} \simeq -\gamma(r)\mathrm{SA}_{np}^{target}\left(\frac{\mathrm{SA}_{druglike}^{target}}{\mathrm{SA}_{total}^{target}}\right) + C \quad (1)$$

Here, $\gamma(r)$ describes the solvent surface tension and depends on the surface curvature. The curvature was estimated from a least-squares fit (LSF) of a sphere to a surface patch. The total surface area of the pocket, $\mathrm{SA}_{total}^{target}$ is a normalization factor to the drug-like surface area $\mathrm{SA}_{druglike}^{target}$ size set to 300 Å^2 (Table 2). The constant C accounts for the ligand desolvation free energy and assumes that the lipophilic surface area is constant. The fraction lipophilic surface area is a direct measure of the ratio between the lipophilic surface area and the polar surface area ($\mathrm{SA}_{np}^{target}$) of the binding site, while the curvature gives a three-dimensional representation of the binding-site shape. The output druggability score ΔG_{MAP} (kcal/mol) was converted to a nM affinity K_d value through eq 2, where R is the gas constant in units kcal/mol/K, and T is 298 K:

$$K_d = \exp(\Delta G_{MAP}/RT) \quad (2)$$

The Pfido analysis was obtained for each potassium channel using five representative structures from the MD simulations chosen at intervals of 10 ns from the last 50 ns of simulation for each potassium channels, with the error estimates reported as one standard deviation ($\pm\sigma$).

RESULTS AND DISCUSSION

To establish the stability of the proteins during the simulations, changes in the backbone root−mean−square deviation (RMSD) of each structure with respect to the crystal with time were calculated and shown in Figure S1. In all cases, the RMSD remains stable (<2 Å). In all three systems simulated, four clusters of lateral fenestrations were found, and are illustrated in Figure 1, panels a and c and Figure 2, panels a−c, with over 70% of analyzed snapshots having fenestrations with bottleneck radius (BR) greater than the threshold 0.8 Å (Table 1). For each system, the analysis was repeated at subsets of the whole trajectory length to show reproduction of the results obtained here were consistent over the time scales analyzed. For Kv1.2, fenestration analysis was repeated for the first 100, 200, and 400 ns of simulation, yielding fenestration parameters within the same standard deviation of statistical error (Table S3). For TWIK-1, the available 200 ns trajectory was analyzed for the first 100 and 200 ns, obtaining the same results (Table S4).

In Kv1.2, the lateral fenestrations are formed at the interface of adjacent subunits and can therefore be referred to as interchain tunnels. TWIK-1 is a structural homodimer possessing a pseudotetrameric architecture, with two tunnels on the dimer interface (lateral-A/B) and an additional set at the interface between individual domains (intrasubunit) within each subunit (lateral A and lateral B), in analogous positions to those in Kv1.2 yet displaying asymmetry between each subset. In Kir3.2, the lateral fenestrations correspond to pathways across individual subunits, denoted intrachain tunnels. Interchain fenestrations, similar to Kv1.2 and TWIK-1, are also found in Kir3.2 but with low populations (<40%), suggesting that they are less favorable in Kir3.2. Such lateral fenestrations are similar to what is observed for Nav channels.[57] Results indicate that, within each analyzed channel, no significant differences between lateral fenestration lengths exist (Table 1).

Fenestrations can be classified in two functional states depending on their BR: open and closed. In this work, an arbitrary cutoff of 1.6 Å was employed to discriminate between closed (BR < 1.6 Å) and open (BR > 1.6 Å) fenestrations. In all three systems simulated, the identified fenestrations proved stable with time. In the case of the simulations of Kv1.2 and Kir3.2, closed fenestration states with an average BR of ∼1 Å are sampled, with maximum values up to 1.6 Å (Figure 2d,e). In the closed fenestration state, only transient (∼1−2 ns) pore access is available for water-sized molecules.

DOI: 10.1021/acs.molpharmaceut.5b00942
Mol. Pharmaceutics 2016, 13, 2263−2273

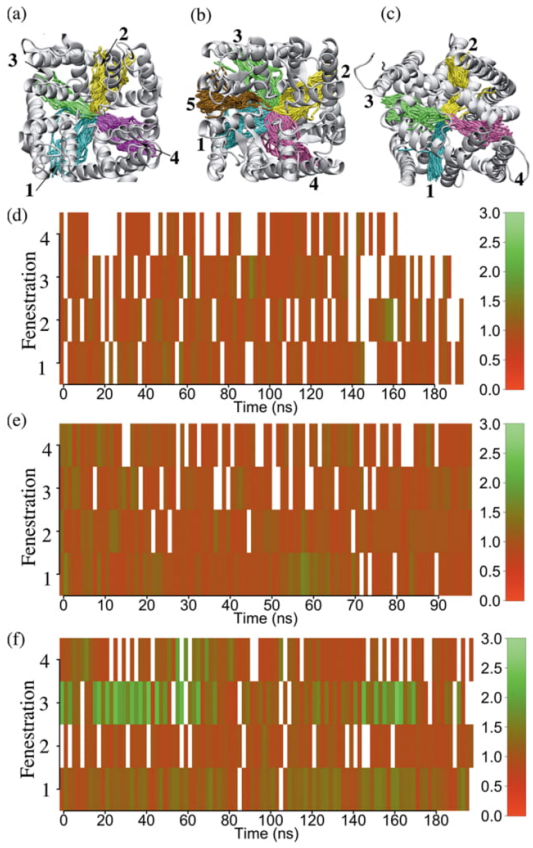

Figure 2. Lateral fenestrations and dynamics of the BR. Main lateral fenestrations oriented related to membrane plane, labeled and colored by cluster ID, (a) Kv1.2 fenestrations 1−4, (b) Kir3.2/O fenestrations 1−5, and (c) TWIK-1 fenestrations 1−4. Temporal evolution of the BR for each fenestration cluster is presented as a color-map with radii values ranging from 0.0 Å (red) to 3.0 Å (green) is shown for (d) Kv1.2, (e) Kir3.2/O, and (f) TWIK-1.

In the TWIK-1 X-ray crystal structure, the interchain fenestrations show bottleneck radii of 2.5 Å. Upon simulation with this density removed, the fenestrations display average BR of 1.4 ± 0.5 and 1.0 ± 0.2 Å, respectively (Figure 2f). The former fenestration is able to sample the open fenestration state (maximum opening of 2.5 Å), with the latter consistently in the closed state (BR of ∼1 Å) resembling that in Kv1.2 and Kir3.2 (Figure 2d,e). The values indicate that TWIK-1 fenestrations are mainly closed, as in Kv1.2 and Kir3.2, but they can spontaneously sample open states by adopting a BR close to that in the TWIK-1 X-ray structure.

To study the characteristics of the bottlenecks in detail, the fenestration radius along the progression from the outside of the membrane to the inside toward the central pore was measured, and it is shown in Figure 4 for each analyzed fenestration of Kv1.2, Kir3.2 and TWIK-1. One main constriction site is observed in all four lateral fenestrations. The reduction of the radius at that position is due to the presence of residues V399, I402, and A403 in Kv1.2, T105, E152, G180; V183 in Kir3.2; and V139, I142, P143, F220, S224, M260, and L264 in TWIK-1 (Table S2 and Figure 4).

The amino acid composition and sequence alignment of the main fenestration lining residues for Kv1.2, Kir3.2, and TWIK-1 are reported in Table S2, the consensus set of contacts is illustrated in Figure 3, panels b−d, and the bottleneck-lining residues are illustrated in Figure 4, panels a−c. For Kv1.2, the lining residues are L328, I332, A397, V399, L400, T401, I402, A403, V406, P407, and V410 in each monomer (Figure 3b). This path appears to be flanked with a higher content of hydrophobic (82%) than polar residues (18%). For Kir3.2, the main lining residues in each lateral fenestration are V188, N184, V183, G180, L179, T154, T153, E152, W106, T105, V104, Y102, and V101 (Figure 3c). The path in Kir3.2 appears more hydrophilic with 46% of hydrophobic residues, 46% of polar residues, and 8% of negatively charged residues. For TWIK-1, the main lining residues for intrasubunit fenestrations (fenestrations 1 and 2) are S116, T117, T145, L146, L149, T225, L254, and L257, constituting 50% polar residues, while for interchain fenestrations (fenestrations 3 and 4) they are T117, V139, I142, L146, S224, T225, M260, L261, and L264, constituting 45% polar residues (Figure 3d), with the remaining residues of both sets hydrophobic. The residues responsible for the equilibrium between open and closed fenestration states in TWIK-1 were identified as M260 and L264 (Figure 5a−d), with a transition time on the order of 10^1 ns (Figure 5f) meaning that MD simulations can adequately capture this side-chain movement on a 200 ns simulation scale. Fenestration accessibility for lipids was considered by occupancy density iso-surfaces (Figure S5), which reveal lipid density only around Kv1.2 and Kir3.2 fenestrations on the iso-0.2 surface without any lipid entry observed.

It was considered whether a correlation exists between the channel activation state and fenestration opening. The open, activated Kv1.2 channel has only closed fenestrations, while the open, activated Kir3.2 channel state and the closed Kir3.2 channel states both possessed closed fenestrations. For TWIK-1, lipid penetration at the periphery of the intersubunit (A/B) fenestrations (3,4) was observed (Figure 5a,b), and the lipid entry correlates with a BR >1.5 Å (Figure 5e compared to f). The BR fluctuation correlates with the M260-L264 distance and the fenestration-lipid distance, as was shown in Figure 5, panel e compared to f. Channel conformational changes, in particular those responsible for the opening or closing processes, can affect the structure of the lateral fenestration and, consequently, drug accessibility. This has been reported to depend on the channel type. In TREK-2, changes in functional state impact the availability of the fenestrations.[37] Comparison of TREK-2 structures in multiple activation states revealed distinct structural differences in the spatial attributes of fenestration regions, implicating "open" fenestrations, and key residues within them, in the state-dependent block of TREK-2 by Prozac. Analysis of the fenestrations from MD simulations in both the open and closed states of Kir3.2 (Table 1) showed that both states possessed the four reported fenestrations with similar average and maximum bottleneck radii as well as similar fenestration length, suggesting that fenestrations are not state-dependent in this case.

To supplement these results, a Pfido druggability analysis was performed on MD snapshots of the fenestration regions of Kv1.2, Kir3.2, and TWIK-1 (Table 2) and compared to the crystal structure of TREK-2. This analysis revealed Kir3.2 fenestrations to be outliers, possessing half the magnitude of hydrophobic surface area (165 ± 21 $Å^2$) compared to the other channels (Kv1.2:399 ± 28 $Å^2$; TWIK-1:387 ± 25 $Å^2$; TREK-

DOI: 10.1021/acs.molpharmaceut.5b00942
Mol. Pharmaceutics 2016, 13, 2263−2273

Table 1. Fenestration Bottleneck Features[a]

channel	cluster ID	% snapshots BR > 0.8 Å	fenestration type	av. BR (Å)	max. BR (Å)	length (Å)
Kv1.2	1	82	lateral-A/D	1.0 ± 0.1	1.3	21 ± 4
	2	70	lateral-B/C	1.0 ± 0.1	1.5	23 ± 4
	3	74	lateral-A/C	1.0 ± 0.1	1.5	24 ± 3
	4	49	lateral-B/D	0.9 ± 0.1	1.2	23 ± 4
	5	42	lateral-A	1.3 ± 0.2	1.7	29 ± 6
Kir3.2/O	1	95	lateral-B	1.0 ± 0.2	1.6	30 ± 3
	2	95	lateral-D	1.0 ± 0.1	1.3	29 ± 3
	3	84	lateral-A	1.0 ± 0.1	1.3	31 ± 3
	4	79	lateral-C	1.0 ± 0.1	1.4	30 ± 3
	5	75	lateral-C/D	0.9 ± 0.1	1.2	32 ± 3
Kir3.2/C	1	98	lateral-D	1.0 ± 0.1	1.4	28 ± 2
	2	87	lateral-C	1.0 ± 0.1	1.4	29 ± 3
	3	87	lateral-B	0.9 ± 0.1	1.3	29 ± 3
	4	58	lateral-A	0.9 ± 0.1	1.3	30 ± 3
	5	53	lateral-B/C	0.9 ± 0.1	1.2	31 ± 5
TWIK-1	1	97	lateral-A	1.2 ± 0.2	1.6	22 ± 2
	2	83	lateral-B	0.9 ± 0.1	1.3	26 ± 2
	3	90	lateral-A/B	1.4 ± 0.5	2.5	24 ± 2
	4	80	lateral-A/B	1.0 ± 0.2	1.9	26 ± 4

[a]Fenestration cluster ID (clustering threshold of 8 Å), percentage of PDB snapshots analyzed with a BR > 0.8 Å, fenestration type (intra or inter-chain), average (Av.) BR (Å), maximum (max.) BR (Å), and length of the fenestration (Å) are reported. Protein monomers are referred as A, B, C, and D. Open and closed ion channel states are indicated by O and C.

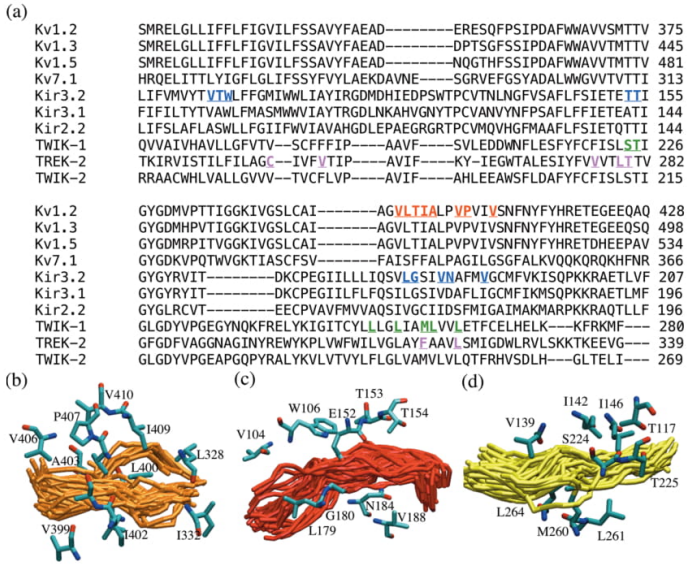

Figure 3. Sequence and structural alignment. (a) Multiple sequence alignment of the human Kv1.2 (Uniprot P16389), Kv1.3 (Uniprot P22001), Kv1.5 (Uniprot P22460), Kv7.1 (Uniprot P51787), mammalian Kir3.2 (Uniprot P48542), Kir3.1 (Uniprot P48549), Kir2.2 (Uniprot Q14500), human TWIK-1 (Uniprot O00180), TREK-2 (Uniprot P57789), and TWIK-2 (Uniprot Q9Y257) highlighting the regions where the bottleneck lining residues are located. Color code: Kv1.2 (red), Kir3.2 (blue), TWIK-1 (green), TREK-2[37] (purple). Representative lining residues (>90% of each fenestration): (b) Kv1.2, (c) Kir3.2/O, and (d) TWIK-1 A/B lateral fenestration.

2:401 Å^2), with double the magnitude of polar surface area (122 ± 15 Å^2) compared to the other channels (Kv1.2:42 ± 6 Å^2; TWIK-1:30 ± 5 Å^2; TREK-2:85 Å^2). This surface-area analysis was then complemented by an electrostatic potential (EP) iso-surface analysis of Kv1.2, Kir3.2, and TWIK-1 (Figures S3 and S4). The analysis revealed that Kv1.2 fenestrations containing 82% hydrophobic residues displayed their EP iso-surface uniformly around zero, while the Kir3.2 iso-surface showed the presence of polar lining residues in the fenestrations (N184 and Y102 in each fenestration). The Pfido analysis outputs a druggability score of magnitude < −10 kcal/mol for all channel fenestrations studied herein, with more negative score indicating greater druggable potential. By calculating K_d values and comparing to reference data sets of targets,[54] it is possible to class the channels as potentially druggable because their nM affinity druggability scores K_d

DOI: 10.1021/acs.molpharmaceut.5b00942
Mol. Pharmaceutics 2016, 13, 2263−2273

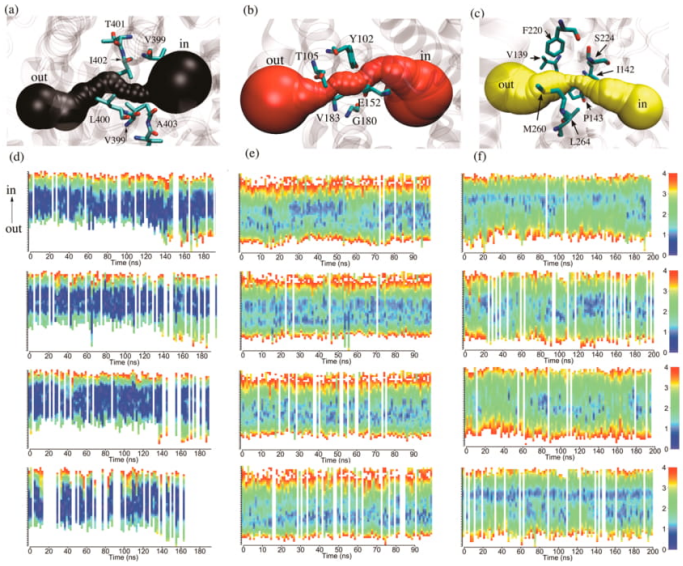

Figure 4. Fenestration dynamics as a function of time. (a, b, c) Radii spherical representation for fenestrations in Kv1.2, Kir3.2, and TWIK-1. Residues constituting the bottleneck are highlighted in licorice representation. (d, e, f) Evolution of fenestration bottleneck radii in Å, using a color gradient ranging from 0 (blue) to 4 Å (red), during MD simulation of Kv1.2, Kir3.2/O, and TWIK-1, respectively. The white gaps represent snapshots in which fenestrations with a probe radius > 0.8 Å threshold were not identified in the specific cluster.

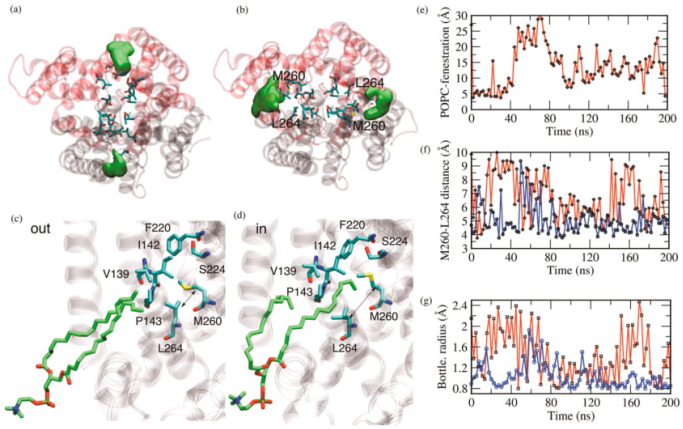

Figure 5. TWIK-1 fenestrations. Lipid−protein interaction iso-0.2 surfaces for fenestrations measured as the density of lipid within a 4 Å cutoff criteria of the fenestration-lining residues of TWIK-1 for (a) fenestrations 3,4 (interchain) and (b) fenestrations 1,2 (intrasubunit). (c) TWIK-1 lipid−protein interaction contacts to residues M260 and L264. (e) Distance between POPC tail (C atom) and C atom of side-chain of M260 (color red) as a function of simulation time in the TWIK-1 system. (f) Distance between the C atoms of side-chains of M260 and L264 in the A/B interchain lateral fenestrations 3 and 4 as a function of simulation time in the TWIK-1 system. Fenestration values for 3 vary from open (distance >7 Å) to closed (distance 4−5 Å). (g) BR for interchain fenestrations 3 (red) and 4 (blue) over the course of the trajectory. Changes in the bottleneck size are correlated with the side-chain motion of M260 and L264.

(Table 2) all range between 10^{-3} and 38 nM, which according to data set comparisons ranks as druggable targets with K_d < 100 nM.[54]

To understand the role of chemical sequence in fenestrations, a multiple sequence alignment was generated for mammalian Kv1.2, Kv1.3, Kv1.5, Kv7.1, Kir3.2, Kir3.1, Kir2.2, human TWIK-1, TREK-2, and TWIK-2(Figure 3a). This reveals that the lining residues of the fenestrations in Kv1.2, Kir3.2, and TWIK-1 share a common region in the sequence, where residues T154 and T153 in Kir3.2 correspond to S224 and T225 in TWIK-1, or T280 and T281 in TREK-2; L179 in Kir3.2 is conserved as L400 in Kv1.2; G180 in Kir3.2 corresponds to T401 in Kv1.2; V183 in Kir3.2 is conserved as V262 in TWIK-1, while the latter is not a lining residue. Finally, N184 in Kir3.2 was not conserved and corresponded to V263 in TWIK-1 and P405 in Kv1.2. In addition, the TWIK-1 fenestration bottleneck shares a common region with the sequence of TREK-2 (K2P10.1). The TREK-2 fenestration

DOI: 10.1021/acs.molpharmaceut.5b00942
Mol. Pharmaceutics 2016, 13, 2263−2273

Table 2. Pfido Druggability Analysis of Fenestrations from MD Snapshots of Kv1.2, Kir3.2, and TWIK-1 Compared to TREK-2 Crystal Structure[a]

protein	SA (lipo) Å^2	SA (polar) Å^2	SA (total) Å^2	fraction SA (lipo)	curvature (Å)	druggability ΔG_{MAP} (kcal/mol)	K_d (nM)
Kv1.2	399 ± 28	42 ± 6	441 ± 28	0.9 ± 0.0	6.2 ± 0.2	−15.8 ± 0.4	2.5×10^{-3}
Kir3.2	165 ± 21	122 ± 15	287 ± 15	0.6 ± 0.1	6.1 ± 0.2	−10.1 ± 0.9	38.4
TWIK-1	387 ± 25	30 ± 5	417 ± 29	0.9 ± 0.0	6.1 ± 0.1	−16.3 ± 0.1	1.1×10^{-3}
TREK-2	401	85	486	0.8	6.1	−14.5	2.3×10^{-2}

[a]Individual Pfido components are (a) lipophilic surface area (SA; Å^2) showing the total hydrophobic surface area of fenestration cavities, (b) polar surface area (SA; Å^2), (c) total surface area (SA; Å^2), which is the sum of hydrophobic and polar SAs, (d) fraction of lipophilic SA, (e) protein surface curvature, (f) druggability score as a maximum affinity predicted (MAP) ΔG_{MAP} (kcal/mol), and (g) druggability score as a dissociation constant (K_d). The results indicate that the channels are characterized by high lipophilic surface area (except Kir3.2, which has charged polar fenestration residues), low fenestration curvature, and high druggability score for fenestrations.

residues when binding norfluoxetine were reported to be I194, P198, C249, V253, V276, L279, T280, F316, and L320.[37] Crucially, fenestration residues M260 and L264 in TWIK-1 correspond to fenestration residues F316 and L320 in TREK-2 as shown in Figure 3. This high similarity in fenestration bottleneck sequence could suggest that drugs targeting TREK-2 could also target TWIK-1 and that agonist/antagonist mechanisms of K2P channels could be similar.

Previous MD simulation studies reported the sequence conservation of fenestration-lining residues in sodium channels to be generally high[57,59] and claimed this to be higher than the reported low conservation in other ion channel families, including potassium channels, but did not distinguish between sequence identities among different sodium subfamilies. In this work, potassium channel sequence alignment found low global sequence conservation, with only ∼4% of the transmembrane domains of mammalian Kv1.2, Kir3.2, and TWIK-1 conserved and a ∼2% of local transmembrane fenestration sequence identity. However, potassium channel subfamilies display very high fenestration identities, 86% for Kv1 subtype members, 63% for Kir3 subfamily members, and 47% for the K2P1 subfamily members. While previous studies have claimed to find higher conservation in sodium channels, they reported only Nav channel subfamily identities to be above 50%,[57] which is not different from our reported sequence conservations. These higher identities thus suggest that a common role for fenestrations in individual potassium channel subfamilies may be possible. This work has complemented earlier work on TREK-2[37] by identifying open fenestrations in a second K2P channel, TWIK-1, and has concluded that the size of fenestrations renders this unlikely in Kv1.2 and Kir3.2. In this case, if the role of fenestrations in drug access is of secondary importance, it has been proposed that fenestrations bestow conformational flexibility on the pore domain and thus play a role in gating.[58]

Links between Fenestrations and Druggability. The blocking mechanism in Kv1.2 and Kv1.5 channels has been described as involving two primary binding sites: an inner pore site with sequence T···VIAV, and a nonpore site with sequence LLL···FIL···T,[6,8] with locations conserved across Kv1 and non-Kv1 members. In Kv1.2, the nonpore site is located in a voluminous side-pocket cavity delineated by residues L317 and L321 from the S4−S5 linker, F334, I337, and L341 from the S5 helix, and T401 from S6 helix.[8] In Kv1.5, the nonpore site is located in a cleft delineated by contacts L420, L423, L427, F440, I443, L447, and T507.[6] In open-state Kv7.1, the nonpore site is located in a side-pocket of contacts L250, L251, and V254 in the S4−S5 linker, together with the phenyl ring of F351 from the S6 helix.[60] The pore site alone is most likely unable to confer the acute selectivity of a given drug for different Kv channels mainly because the sequence of the inner pore is conserved among Kv channels as well as due to the vast chemical range of Kv inner-pore blockers, namely 4-AP, TEA,[9] TBA,[10] and correolide.[11] It has been argued that selectivity for a given drug arises from a putatively allosteric or cooperative interplay between the pore site and a side-pocket in Kv1.2[8] and Kv1.5.[6] Psora-4 and PAP-1 of the 5-phenylalkoxypsoralen family of drugs, designed to target autoimmune disorders,[12,13] were found to show Kv1 subtype specificity by cooperatively interacting with both the inner pore and the nonpore site.[6,8] The fenestration lining residues identified herein for Kv1.2 is partially in agreement with the residues constituting the Kv1 side-pocket, suggesting that the potential for cooperative interactions is a possibility. As suggested for the blocking mechanism in Kv1.3 and Kv1.5 (Psora-4 block),[6,13] and Kv2.1 (Flecainide and Propafenone block), the existence of lateral fenestrations connecting the pore and side-pocket sites might allow for allosteric interactions were the BR larger.[6,8] The BR sampled in the MD simulations revealed it to be too small to allow the aromatic ring of PAP-1 to percolate from the side pocket to the inner pore. This suggests that the cooperative effect between the side-pocket and the inner pore pocket in Kv1.2 is more probable to be mediated by the protein residues lining the fenestrations than a result of direct contacts between drugs located in such pockets. Alternatively, conformational changes taking place in a time-scale not accessed by the MD simulations presented here could be responsible for widening the bottleneck of the lateral fenestrations. Similarly, for the Kir3.2 channel in both open and closed conformations, the BR sampled during the simulations corresponds only to closed fenestration states. On average, the size of the fenestration is too small to allow the entrance of even water molecules, except for very short time periods (1−2 ns) where maximum BR of ∼1.5 Å are observed.

For TWIK-1, the intersubunit fenestrations can sample an open fenestration state during the MD trajectory (Table 1), and additionally, the X-ray crystal structure of the "open state" TWIK-1 is argued here to compare to the "down state" of TREK-2[37] (Table S1 and Figure 1c,d) owing to its helical arrangement and the presence of such open intersubunit fenestrations. Both structures contained lipid density in the fenestrations, with TREK-2 having the bound drug norfluoxetine in the fenestrations. However, TREK-2 fenestrations are only observed in the "down state" (the putative closed or inactivated channel state).[37] In the absence of norfluoxetine, the up-state conformation is adopted, and two hydrophobic residues, F316 and L320, occlude the fenestration as a consequence of the conformational transition. Thus, fenestra-

DOI: 10.1021/acs.molpharmaceut.5b00942
Mol. Pharmaceutics 2016, 13, 2263−2273

tion dynamics explains the state selective binding and action of norfluoxetine in TREK-2. In line with these observations, intersubunit fenestrations in TWIK-1 predominantly adopt a closed conformation throughout the simulations, likely due to the removal of crystallized lipids during simulation setup. However, an interconversion between closed (BR ~ 1.0 Å) and open (BR > 2.0 Å) fenestration states occurs throughout, which provides ample opportunities for the entrance of lipid molecules and small drug compounds. This process appears to correlate with the extent of constriction between M260 and L264 residues (Figure 5c,d). The position of these residues is conserved with respect to TREK-2 (F316 and L320), suggesting potential implications across the K2P family.

The result found for the open state of TWIK-1 suggests that it behaves qualitatively like the up-state of TREK-2 with closed fenestration states but that it is able to also sample the open fenestration states reported in the "down-state" of TREK-2.[37] Our results support the existence of a wide enough hydrophobic fenestration bottleneck in TWIK-1, which is mostly closed but can spontaneously open to allow for hydrophobic compounds to enter and either bind or access the pore via the lateral fenestrations.[24] This could contribute to the understanding of how the TWIK-1 pore gate is modulated by a large range of regulatory stimuli and molecules, as suggested experimentally.[23]

■ CONCLUSIONS

In this study, MD simulation trajectories of three representative potassium channels have been used to investigate the presence and chemical characteristics and structural dynamics of lateral fenestrations, for which four fenestrations are identified in each channel. Additionally, over the time course of the simulations, no statistically significant fluctuations in fenestration length were recorded suggesting that transient fast protein side-chain motions and rotations do not appear to exert significant effects upon fenestration lengths. From BR analyses, results indicate that the fenestrations in Kv1.2 and Kir3.2 could not modulate drug access (BR ≈ 1.0 Å), while in the case of TWIK-1 (maximum BR of 2.5 Å), the fenestrations can potentially work as drug access pathways. It was shown that the rise in BR correlates with the entry of lipid molecules into TWIK-1 fenestrations, which is then argued to be responsible for allowing TWIK-1 to sample both open and closed fenestrations. While our analysis shows Kv1.2 and Kir3.2 fenestrations to be closed, experiments have found Kv channel fenestrations to have the possibility of undergoing conformational rearrangements of lining residues to turn on the ability of binding drugs, with a recent X-ray crystal of KcsA containing the known Kv blocker QA ion bound in the fenestration region in the intersubunit space, akin to the fenestrations 1−4 of Kv1.2 reported here; thus, the potential for druggable Kv1 and Kir3 targets can not be ruled out.[61] The existence of slow transitions at time scales above 100 ns, which cannot be sampled with ns MD time scales, suggests the next step in fully mapping the significance of the Kv1 and Kir3 fenestration regions in perturbing protein structure and function.

TWIK-1 exhibited asymmetry in its fenestrations, with the side-chains of M260 and L264 responsible for the channel sampling an equilibrium state between closed and open fenestration, with state lifetimes on the order of 10^1−10^2 ns. In the open state of TWIK-1, the fenestrations are mainly closed but can also sample the open fenestration state. Because the reported fenestration sequence of TWIK-1 had overlap with that of TREK-2, including the identification of bottleneck residues M260 and L264 that are in correspondence with TREK-2 fenestration residues F316 and L320, with the latter channel reported to possess open fenestrations, it is concluded that K2P channels could be druggable via fenestrations. We reported atomistic detail of the fenestration region including the flexible residues M260 and L264 that interact with POPC membrane in a concerted fashion with the aperture and closure of the fenestrations.

In conclusion, the study identified four lateral fenestrations across the range of potassium channels studied. Using structural and sequence alignment, a detailed analysis was given of how these identified fenestrations differ among the K^+-channel subtypes analyzed. This information provides a framework for rationalizing the differential response of potassium channels to drugs targeting the transmembrane domain.

■ ASSOCIATED CONTENT

Supporting Information

The Supporting Information is available free of charge on the ACS Publications website at DOI: 10.1021/acs.molpharmaceut.5b00942.

Supplementary figures of protein stability, BR distributions, EP iso-surface of lateral fenestrations using APBS v1.4, EP iso-surface, and lipid−protein interaction iso-surfaces;, cavity analysis of the crystal structures TWIK-1 and TREK-2 channels;, LR consensus and BRs for each lateral fenestration; cavity analysis as a function of time for Kv1.2; and cavity analysis for the TWIK-1 channel as a function of time (PDF)

■ AUTHOR INFORMATION

Corresponding Author

*E-mail: carmen.domene@kcl.ac.uk. Phone: +44 - (0) 2078483868.

Notes

The authors declare no competing financial interest.

■ ACKNOWLEDGMENTS

We would like to acknowledge the use of computational resources from the EPSRC UK National Service for Computational Chemistry Software (NSCCS), the Hartree Center, and Archer. This work was supported by the Engineering and Physical Sciences Research Council (EPSRC) and the Biotechnology and Biological Sciences Research Council (BBSRC). C.J. thanks King's College London for a Graduate Teaching Assistance studentship. V.O. is supported by a CASE studentship funded by BBSRC and Pfizer Neusentis.

■ REFERENCES

(1) Grigoriadis, D. E.; Hoare, S. R. J.; Lechner, S. M.; Slee, D. H.; Williams, J. A. Drugability of Extracellular Targets: Discovery of Small Molecule Drugs Targeting Allosteric, Functional, and Subunit-Selective Sites on GPCRs and Ion Channels. *Neuropsychopharmacology* **2009**, *34* (1), 106−125.

(2) Huang, X.; He, Y.; Dubuc, A. M.; Hashizume, R.; Zhang, W.; Reimand, J.; Yang, H.; Wang, T. A.; Stehbens, S. J.; Younger, S.; Barshow, S.; Zhu, S.; Cooper, M. K.; Peacock, J.; Ramaswamy, V.; Garzia, L.; Wu, X.; Remke, M.; Forester, C. M.; Kim, C. C.; Weiss, W. A.; James, C. D.; Shuman, M. A.; Bader, G. D.; Mueller, S.; Taylor, M. D.; Jan, Y. N.; Jan, L. Y. EAG2 potassium channel with evolutionarily conserved function as a brain tumor target. *Nat. Neurosci.* **2015**, *18* (9), 1236−1246.

(3) Fernández-Ballester, G.; Fernández-Carvajal, A.; González-Ros, J. M.; Ferrer-Montiel, A. Ionic Channels as Targets for Drug Design: A Review on Computational Methods. *Pharmaceutics* **2011**, *3* (4), 932−953.
(4) Choe, S. Ion Channel Structurepotassium Channel Structures. *Nat. Rev. Neurosci.* **2002**, *3* (2), 115−121.
(5) MacKinnon, R. Potassium channels. *FEBS Lett.* **2003**, *555* (1), 62−65.
(6) Marzian, S.; Stansfeld, P. J.; Rapedius, M.; Rinné, S.; Nematian-Ardestani, E.; Abbruzzese, J. L.; Steinmeyer, K.; Sansom, M. S. P.; Sanguinetti, M. C.; Baukrowitz, T.; Decher, N. Side pockets provide the basis for a new mechanism of Kv channel−specific inhibition. *Nat. Chem. Biol.* **2013**, *9* (8), 507−513.
(7) Seebohm, G. Molecular Determinants of KCNQ1 Channel Block by a Benzodiazepine. *Mol. Pharmacol.* **2003**, *64* (1), 70−77.
(8) Jorgensen, C.; Darré, L.; Vanommeslaeghe, K.; Omoto, K.; Pryde, D.; Domene, C. In Silico Identification of PAP-1 Binding Sites in the Kv1. 2 Potassium Channel. *Mol. Pharmaceutics* **2015**, *12* (4), 1299−1307.
(9) Grissmer, S.; Nguyen, A. N.; Aiyar, J.; Hanson, D. C.; Mather, R. J.; Gutman, G. A.; Karmilowicz, M. J.; Auperin, D. D.; Chandy, K. G. Pharmacological characterization of five cloned voltage-gated K+ channels, types Kv1. 1, 1.2, 1.3, 1.5, and 3.1, stably expressed in mammalian cell lines. *Mol. Pharmacol.* **1994**, *45* (6), 1227−1234.
(10) Zhou, M.; Morais-Cabral, J. H.; Mann, S.; MacKinnon, R. Potassium channel receptor site for the inactivation gate and quaternary amine inhibitors. *Nature* **2001**, *411* (6838), 657−661.
(11) Koo, G. C.; Blake, J. T.; Shah, K.; Staruch, M. J.; Dumont, F.; Wunderler, D.; Sanchez, M.; McManus, O. B.; Sirotina-Meisher, A.; Fischer, P.; Boltz, R. C.; Goetz, M. A.; Baker, R.; Bao, J.; Kayser, F.; Rupprecht, K. M.; Parsons, W. H.; Tong, X.-C.; Ita, I. E.; Pivnichny, J.; Vincent, S.; Cunningham, P.; Hora, D.; Feeney, W.; Kaczorowski, G.; Springer, M. S. Correolide and Derivatives Are Novel Immunosuppressants Blocking the Lymphocyte Kv1.3 Potassium Channels. *Cell. Immunol.* **1999**, *197* (2), 99−107.
(12) Schmitz, A. Design of PAP-1, a Selective Small Molecule Kv1.3 Blocker, for the Suppression of Effector Memory T Cells in Autoimmune Diseases. *Mol. Pharmacol.* **2005**, *68* (5), 1254−1270.
(13) Vennekamp, J. Kv1.3-Blocking 5-Phenylalkoxypsoralens: A New Class of Immunomodulators. *Mol. Pharmacol.* **2004**, *65* (6), 1364−1374.
(14) Hibino, H.; Inanobe, A.; Furutani, K.; Murakami, S.; Findlay, I.; Kurachi, Y. Inwardly Rectifying Potassium Channels: Their Structure, Function, and Physiological Roles. *Physiol. Rev.* **2010**, *90* (1), 291−366.
(15) Bhave, G.; Lonergan, D.; Chauder, B. A.; Denton, J. S. Small-molecule modulators of inward rectifier K+channels: recent advances and future possibilities. *Future Med. Chem.* **2010**, *2* (5), 757−774.
(16) Kobayashi, T.; Washiyama, K.; Ikeda, K. Inhibition of G protein-activated inwardly rectifying K+channels by fluoxetine (Prozac). *Br. J. Pharmacol.* **2003**, *138* (6), 1119−1128.
(17) Dobrev, D.; Carlsson, L.; Nattel, S. Novel molecular targets for atrial fibrillation therapy. *Nat. Rev. Drug Discovery* **2012**, *11* (4), 275−291.
(18) Chen, H.; Zuo, D.; Zhang, J.; Zhou, M.; Ma, L. Classification of 2-pore domain potassium channels based on rectification under quasi-physiological ionic conditions. *Channels* **2014**, *8* (6), 503−508.
(19) Rajan, S.; Plant, L. D.; Rabin, M. L.; Butler, M. H.; Goldstein, S. A. N. Sumoylation Silences the Plasma Membrane Leak K+ Channel K2P1. *Cell* **2005**, *121* (1), 37−47.
(20) Miller, A. N.; Long, S. B. Crystal structure of the human two-pore domain potassium channel K2P1. *Science* **2012**, *335* (6067), 432−6.
(21) Bagriantsev, S. N.; Peyronnet, R.; Clark, K. A.; Honoré, E.; Minor, D. L. Multiple modalities converge on a common gate to control K2P channel function. *EMBO J.* **2011**, *30* (17), 3594−3606.
(22) Brohawn, S. G.; del Marmol, J.; MacKinnon, R. Crystal Structure of the Human K2P TRAAK, a Lipid- and Mechano-Sensitive K+ Ion Channel. *Science* **2012**, *335* (6067), 436−441.
(23) Feliciangeli, S.; Chatelain, F. C.; Bichet, D.; Lesage, F. The family of K2P channels: salient structural and functional properties. *J. Physiol.* **2015**, *593* (12), 2587−2603.
(24) Braun, A. P. Two-pore domain potassium channels: variation on a structural theme. *Channels* **2012**, *6* (3), 139−140.
(25) Piechotta, P. L.; Rapedius, M.; Stansfeld, P. J.; Bollepalli, M. K.; Erhlich, G.; Andres-Enguix, I.; Fritzenschaft, H.; Decher, N.; Sansom, M. S. P.; Tucker, S. J.; Baukrowitz, T. The pore structure and gating mechanism of K2P channels. *EMBO J.* **2011**, *30* (17), 3607−3619.
(26) Mazella, J.; Pétrault, O.; Lucas, G.; Deval, E.; Béraud-Dufour, S.; Gandin, C.; El-Yacoubi, M.; Widmann, C.; Guyon, A.; Chevet, E.; Taouji, S.; Conductier, G.; Corinus, A.; Coppola, T.; Gobbi, G.; Nahon, J.-L.; Heurteaux, C.; Borsotto, M. Spadin, a Sortilin-Derived Peptide, Targeting Rodent TREK-1 Channels: A New Concept in the Antidepressant Drug Design. *PLoS Biol.* **2010**, *8* (4), e1000355.
(27) Sandoz, G.; Bell, S. C.; Isacoff, E. Y. Optical probing of a dynamic membrane interaction that regulates the TREK1 channel. *Proc. Natl. Acad. Sci. U. S. A.* **2011**, *108* (6), 2605−2610.
(28) Rodrigues, N.; Bennis, K.; Vivier, D.; Pereira, V.; Chatelain, F. C.; Chapuy, E.; Deokar, H.; Busserolles, J.; Lesage, F.; Eschalier, A.; Ducki, S. Synthesis and structure−activity relationship study of substituted caffeate esters as antinociceptive agents modulating the TREK-1 channel. *Eur. J. Med. Chem.* **2014**, *75*, 391−402.
(29) Åqvist, J.; Luzhkov, V. Ion permeation mechanism of the potassium channel. *Nature* **2000**, *404* (6780), 881−884.
(30) Furini, S.; Domene, C. K+ and Na+ Conduction in Selective and Nonselective Ion Channels Via Molecular Dynamics Simulations. *Biophys. J.* **2013**, *105* (8), 1737−1745.
(31) Egwolf, B.; Roux, B. Ion Selectivity of the KcsA Channel: A Perspective from Multi-Ion Free Energy Landscapes. *J. Mol. Biol.* **2010**, *401* (5), 831−842.
(32) Jensen, M. O.; Borhani, D. W.; Lindorff-Larsen, K.; Maragakis, P.; Jogini, V.; Eastwood, M. P.; Dror, R. O.; Shaw, D. E. Principles of conduction and hydrophobic gating in K+ channels. *Proc. Natl. Acad. Sci. U. S. A.* **2010**, *107* (13), 5833−5838.
(33) Chanda, B.; Kwame Asamoah, O.; Blunck, R.; Roux, B.; Bezanilla, F. Gating charge displacement in voltage-gated ion channels involves limited transmembrane movement. *Nature* **2005**, *436* (7052), 852−856.
(34) Treptow, W.; Tarek, M. Environment of the Gating Charges in the Kv1.2 Shaker Potassium Channel. *Biophys. J.* **2006**, *90* (9), L64−L66.
(35) Delemotte, L.; Tarek, M.; Klein, M. L.; Amaral, C.; Treptow, W. Intermediate states of the Kv1.2 voltage sensor from atomistic molecular dynamics simulations. *Proc. Natl. Acad. Sci. U. S. A.* **2011**, *108* (15), 6109−6114.
(36) Fürst, O.; Nichols; Colin, G.; Lamoureux, G.; D'Avanzo, N. Identification of a Cholesterol-Binding Pocket in Inward Rectifier K+ (Kir) Channels. *Biophys. J.* **2014**, *107* (12), 2786−2796.
(37) Dong, Y. Y.; Pike, A. C. W.; Mackenzie, A.; McClenaghan, C.; Aryal, P.; Dong, L.; Quigley, A.; Grieben, M.; Goubin, S.; Mukhopadhyay, S.; Ruda, G. F.; Clausen, M. V.; Cao, L.; Brennan, P. E.; Burgess-Brown, N. A.; Sansom, M. S. P.; Tucker, S. J.; Carpenter, E. P. K2P channel gating mechanisms revealed by structures of TREK-2 and a complex with Prozac. *Science* **2015**, *347* (6227), 1256−1259.
(38) Chen, X.; Wang, Q.; Ni, F.; Ma, J. Structure of the full-length Shaker potassium channel Kv1.2 by normal-mode-based X-ray crystallographic refinement. *Proc. Natl. Acad. Sci. U. S. A.* **2010**, *107* (25), 11352−11357.
(39) Whorton, M. R.; MacKinnon, R. Crystal Structure of the Mammalian GIRK2 K+ Channel and Gating Regulation by G Proteins, PIP2, and Sodium. *Cell* **2011**, *147* (1), 199−208.
(40) Šali, A.; Blundell, T. L. Comparative protein modelling by satisfaction of spatial restraints. *J. Mol. Biol.* **1993**, *234* (3), 779−815.
(41) Whorton, M. R.; MacKinnon, R. X-ray structure of the mammalian GIRK2-[bgr][ggr] G-protein complex. *Nature* **2013**, *498* (7453), 190−197.

DOI: 10.1021/acs.molpharmaceut.5b00942
Mol. Pharmaceutics 2016, 13, 2263−2273

(42) Fiser, A.; Sali, A. ModLoop: automated modeling of loops in protein structures. *Bioinformatics* **2003**, *19* (18), 2500−1.
(43) Grubmüller, H.; Groll, V. *Solvate: A Program To Create Atomic Solvent Models*; Max Planck Institute for Biophysical Chemistry, 1996. http://www.mpibpc.mpg.de/grubmueller/solvate.
(44) Lupyan, D.; Mezei, M.; Logothetis, D. E.; Osman, R. A molecular dynamics investigation of lipid bilayer perturbation by PIP 2. *Biophys. J.* **2010**, *98* (2), 240−247.
(45) Klauda, J. B.; Venable, R. M.; Freites, J. A.; O'Connor, J. W.; Tobias, D. J.; Mondragon-Ramirez, C.; Vorobyov, I.; MacKerell, A. D.; Pastor, R. W. Update of the CHARMM All-Atom Additive Force Field for Lipids: Validation on Six Lipid Types. *J. Phys. Chem. B* **2010**, *114* (23), 7830−7843.
(46) Brooks, B.; Brooks, C.; MacKerell, A.; Nilsson, L.; Petrella, R.; Roux, B.; Won, Y.; Archontis, G.; Bartels, C.; Boresch, S.; et al. CHARMM: the biomolecular simulation program. *J. Comput. Chem.* **2009**, *30* (10), 1545−1614.
(47) Jorgensen, W. L.; Chandrasekhar, J.; Madura, J. D.; Impey, R. W.; Klein, M. L. Comparison of simple potential functions for simulating liquid water. *J. Chem. Phys.* **1983**, *79* (2), 926−935.
(48) Noskov, S. Y.; Berneche, S.; Roux, B. Control of ion selectivity in potassium channels by electrostatic and dynamic properties of carbonyl ligands. *Nature* **2004**, *431* (7010), 830−834.
(49) Phillips, J. C.; Braun, R.; Wang, W.; Gumbart, J.; Tajkhorshid, E.; Villa, E.; Chipot, C.; Skeel, R. D.; Kalé, L.; Schulten, K. Scalable molecular dynamics with NAMD. *J. Comput. Chem.* **2005**, *26* (16), 1781−1802.
(50) Darden, T.; York, D.; Pedersen, L. Particle mesh Ewald: An N·log(N) method for Ewald sums in large systems. *J. Chem. Phys.* **1993**, *98* (12), 10089.
(51) Chovancova, E.; Pavelka, A.; Benes, P.; Strnad, O.; Brezovsky, J.; Kozlikova, B.; Gora, A.; Sustr, V.; Klvana, M.; Medek, P.; et al. CAVER 3.0: a tool for the analysis of transport pathways in dynamic protein structures. *PLoS Comput. Biol.* **2012**, *8* (10), e1002708.
(52) Sievers, F.; Wilm, A.; Dineen, D.; Gibson, T. J.; Karplus, K.; Li, W.; Lopez, R.; McWilliam, H.; Remmert, M.; Soding, J.; Thompson, J. D.; Higgins, D. G. Fast, scalable generation of high-quality protein multiple sequence alignments using Clustal Omega. *Mol. Syst. Biol.* **2011**, *7* (1), 539−539.
(53) Baker, N. A.; Sept, D.; Joseph, S.; Holst, M. J.; McCammon, J. A. Electrostatics of nanosystems: Application to microtubules and the ribosome. *Proc. Natl. Acad. Sci. U. S. A.* **2001**, *98* (18), 10037−10041.
(54) Cheng, A. C.; Coleman, R. G.; Smyth, K. T.; Cao, Q.; Soulard, P.; Caffrey, D. R.; Salzberg, A. C.; Huang, E. S. Structure-based maximal affinity model predicts small-molecule druggability. *Nat. Biotechnol.* **2007**, *25* (1), 71−75.
(55) Liang, J.; Woodward, C.; Edelsbrunner, H. Anatomy of protein pockets and cavities: Measurement of binding site geometry and implications for ligand design. *Protein Sci.* **1998**, *7* (9), 1884−1897.
(56) Coleman, R. G.; Burr, M. A.; Souvaine, D. L.; Cheng, A. C. An intuitive approach to measuring protein surface curvature. *Proteins: Struct., Funct., Genet.* **2005**, *61* (4), 1068−1074.
(57) Kaczmarski, J. A.; Corry, B. Investigating the size and dynamics of voltage-gated sodium channel fenestrations. *Channels* **2014**, *8* (3), 264−277.
(58) Barber, A. F.; Carnevale, V.; Raju, S. G.; Amaral, C.; Treptow, W.; Klein, M. L. Hinge-bending motions in the pore domain of a bacterial voltage-gated sodium channel. *Biochim. Biophys. Acta, Biomembr.* **2012**, *1818* (9), 2120−2125.
(59) Corry, B.; Lee, S.; Ahern, C. A. Pharmacological insights and quirks of bacterial sodium channels. In *Voltage Gated Sodium Channels*; Springer, 2014; pp 251−267.
(60) Yang, T.; Smith, J. A.; Leake, B. F.; Sanders, C. R.; Meiler, J.; Roden, D. M. An Allosteric Mechanism for Drug Block of the Human Cardiac Potassium Channel KCNQ1. *Mol. Pharmacol.* **2013**, *83* (2), 481−489.
(61) Lenaeus, M. J.; Burdette, D.; Wagner, T.; Focia, P. J.; Gross, A. Structures of KcsA in Complex with Symmetrical Quaternary Ammonium Compounds Reveal a Hydrophobic Binding Site. *Biochemistry* **2014**, *53* (32), 5365−5373.

DOI: 10.1021/acs.molpharmaceut.5b00942
Mol. Pharmaceutics 2016, 13, 2263−2273

3.3 Exploring the Dynamics of the TWIK-1 Channel, *Biophysical Journal*, 2016

3.3.1 Authorship and Permissions

<table>
<tr><td colspan="10">This declaration concerns the article entitled</td></tr>
<tr><td colspan="10">Exploring the dynamics of the TWIK-1 Channel</td></tr>
<tr><td colspan="10">Publication status (tick one)</td></tr>
<tr><td>Draft manuscript</td><td></td><td>Submitted</td><td></td><td>In review</td><td></td><td>Accepted</td><td></td><td>Published</td><td>✓</td></tr>
<tr><td>Publication details</td><td colspan="9">*Biophysical Journal*, 2016, 111 (4), 775-784
DOI: 10.1016/j.bpj.2016.07.009
Received: 30 December 2015
Accepted: 11 July 2016
Published online: 23 August 2016

This article is available under the Creative Commons Attribution License (CC BY): https://creativecommons.org/licenses/by/4.0/</td></tr>
<tr><td>Candidates contribution to the paper (detailed and also given as a percentage)</td><td colspan="9">The candidate contributed to/considerably contributed/predominantly executed the…
Formulation of ideas (50%):
V. Oakes and C. Domene contributed equally.

Design of methodology (25%):
V. Oakes and C. Domene contributed equally.

Experimental work (100%):
TWIK-1 simulation and analysis was performed by V.Oakes.

Presentation of data in journal format (80%):
V. Oakes: Main author of manuscript and supporting information.
S. Furini: Critically assessed and revised the manuscript.
C. Domene: Critically assessed and revised the manuscript.</td></tr>
<tr><td>Statement from Candidate</td><td colspan="9">This paper reports on original research I conducted during the period of my Higher Degree by Research candidature.</td></tr>
<tr><td>Signed</td><td colspan="5"></td><td>Date</td><td colspan="3"></td></tr>
</table>

Biophysical Journal
Article

Exploring the Dynamics of the TWIK-1 Channel

Victoria Oakes,[1] Simone Furini,[2] David Pryde,[3] and Carmen Domene[1,4,*]
[1]Department of Chemistry, King's College London, London, United Kingdom; [2]Department of Medical Biotechnologies, University of Siena, Siena, Italy; [3]Worldwide Medicinal Chemistry, Pfizer Neuroscience and Pain Research Unit, Cambridge, United Kingdom; and [4]Chemistry Research Laboratory, Mansfield Road, University of Oxford, Oxford, United Kingdom

ABSTRACT Potassium channels in the two-pore domain family (K2P) have various structural attributes that differ from those of other K^+ channels, including a dimeric assembly constituted of nonidentical domains and an expansive extracellular cap. Crystallization of the prototypical K2P channel, TWIK-1, finally revealed the structure of these characteristics in atomic detail, allowing computational studies to be undertaken. In this study, we performed molecular-dynamics simulations for a cumulative time of ~1 μs to discern the mechanism of ion transport throughout TWIK-1. We observed the free passage of ions beneath the extracellular cap and identified multiple high-occupancy sites in close proximity to charged residues on the protein surface. Despite the overall topological similarity of the x-ray structure of the selectivity filter to other K^+ channels, the structure diverges significantly in molecular-dynamics simulations as a consequence of nonconserved residues in both pore domains contributing to the selectivity filter (T118 and L228). The behavior of such residues has been linked to channel inactivation and the phenomenon of dynamic selectivity, where TWIK-1 displays robust Na^+ inward flux in response to subphysiological K^+ concentrations.

INTRODUCTION

The two-pore domain K^+ family (K2P) forms a structurally and functionally distinct class of K^+ channels. These channels are responsible for background leak K^+ currents that stabilize the negative resting potential of the cell, and also play roles in ion homeostasis, hormone secretion, cell development, and excitability (1). K2P channels can be modulated by a vast array of regulatory stimuli, such as pH (2), temperature (3), mechanical stress (4), the presence of polyunsaturated fatty acids (5), and volatile anesthetics (6). The expression of these channels in the heart and brain has also led to increased exploration of their therapeutic potential for the treatment of various neuronal and cardiac disorders (5,7).

K2P channels assemble as a dimer of dimers, with each subunit containing four transmembrane helices (H1–H4) and two pore loops (P1 and P2). The recent crystallization of multiple K2P channels (TWIK-1 (8), TRAAK (9,10), and TREK-2 (11)) has greatly advanced our understanding of this unique architecture, exhibiting various conserved features throughout the family. For example, an extracellular cap (EC) between H1 and P1 is present, extending 35 Å above the transmembrane helices, with the apex of each subunit connected by a disulphide bond. An unrestricted pathway at the cytoplasmic entrance is also observed throughout, revealing apertures of comparable dimension to other K^+ channels that are considered open. This is in line with experimental studies suggesting that structural changes at or near the selectivity filter (SF) form the predominant gating mechanism across the K2P family, which shares its canonical structure with other K^+ channel families.

With regard to the electrophysiological properties of the K2P channels, in asymmetrical K^+ concentrations, almost all K2P subfamilies (TREK, TALK, TASK, THIK, and TRESK) conform to the typical properties of leak K^+ currents, demonstrating outward (or open) rectification. The functional properties of the TWIK family have remained elusive due to low levels of activity recorded in physiological K^+ gradients (12). This phenomenon was originally attributed to the sumoylation of a lysine residue in the C-terminal domain, which could be inactivated by a single-point mutation (13). However, this was later disproved as the primary mechanism of TWIK-1 silencing (14). The mutation of consecutive isoleucine residues in the C-terminal domain was found to induce strong expression of TWIK-1 in the cell membrane (14); however, meager currents were still recorded relative to other K2P channels in the same conditions (15,16). Such observations led to the proposal that the prohibition of ionic current is an inherent property of TWIK-1 (17). Furthermore, reports have suggested that TWIK-1 does not exhibit such open rectification. Various mutant

Submitted December 30, 2015, and accepted for publication July 11, 2016.
*Correspondence: carmen.domene@kcl.ac.uk
Editor: Emad Tajkhorshid.
http://dx.doi.org/10.1016/j.bpj.2016.07.009

channels were found to both increase the conductance and shift the rectification properties to those of other K2P channels, indicating a convoluted regulation mechanism.

In particular, TWIK-1 was the first channel to display variable selectivity in response to external stimuli such as lowered K^+ concentrations (18), increased NH_4^+ and Rb^+ concentrations (19), and acidification (20). Hypokalemia (when extracellular K^+ concentrations are lower than 3.5 mM) is observed in up to 20% of hospitalized patients and has been associated with an increased risk of sudden cardiac arrest (21). The adjusted selectivity of TWIK-1 in these conditions indicates the presence of an inward Na^+ current in response to the Na^+ concentration gradient, and this property is known to depolarize cardiomyocytes and potentially contribute to cardiac arrhythmia (7,22). As a consequence, TWIK-1 has emerged as a putative drug target for antiarrhythmic drugs (23). In-depth exploration of the molecular determinants of conduction, selectivity, and gating in TWIK-1 will likely contribute to the development of targeted therapies.

Previous molecular-dynamics (MD) studies of TWIK-1 identified a hydrophobic cuff in the inner pore that is responsible for a cyclical dewetting process and consequently an unfavorable barrier to conduction (24). This effect was suggested to be influenced by the presence of lipid molecules in proximal fenestrations (25), and was supported by studies involving gain-of-function mutagenesis of such residues to hydrophilic components (24). However, the behavior of the SF and its implications for the mechanism of conduction, selectivity, and gating have not yet been examined. Therefore, we conducted an MD study utilizing the crystal structure of TWIK-1 to obtain insight into these phenomena.

MATERIALS AND METHODS

System setup

The crystal structure of TWIK-1 was retrieved from the Protein Data Bank (PDB: 3UKM) at a resolution of 3.4 Å (residues 19–288) (8). Five potassium ions were resolved in the crystal structure in the internal SF sites (S1–S4) and S0, suggesting that the structure is representative of an open, conductive state. Three of these ions were kept in positions S0, S2, and S4, and those in positions S1 and S3 were converted to water molecules to represent one of the low-energy conformations identified in previous studies (26). Crystallographic waters were kept. Missing loops were modeled using Modloop (27) and combined with the crystal structure. N- and C-termini were acetylated and methylated, respectively. Residues C69 of opposing subunits were linked by a disulfide bond. Default protonation states were used for ionizable residues, supported by PropKa calculations (28). SOLVATE1.0 was used to solvate the protein and fill cavities present in the structure. A preequilibrated lipid bilayer of 1-palmitoyl-2-oleoyl-*sn*-glycero-3-phosphocholine (POPC) molecules was used. The protein was aligned to the bilayer normal and inserted into the membrane. All lipid molecules within 1.2 Å of protein atoms were removed. The combined system was then solvated to produce a rectangular water box of dimensions $93 \times 93 \times 118$ Å. Potassium and chloride ions were added to neutralize the system to a biologically relevant ion concentration (150 mM) using the Autoionize Plugin of VMD (29). All water molecules deemed as overlapping (distance < 1.2 Å) with the protein, lipids, and ions were removed, resulting in a system size of ~90,000 atoms. Trajectories of 200 ns were produced and denoted as HSE (δ position in H122 protonated, D230 unprotonated), HSEP (δ position in H122 protonated, D230 protonated), HSD (ε position in H122 protonated, D230 unprotonated), HSDP (ε position in H122 protonated, D230 protonated), HSP (both δ and ε positions in H122 protonated, D230 unprotonated), and HSPP (both δ and ε positions in H122 protonated, D230 protonated).

MD simulations

NAMD2.9 was employed to calculate trajectories (30). We used the CHARMM36 force field for the protein, CHARMM36 for lipids (31), the TIP3P model for water (32), and the CHARMM NBFIX parameters for ions (33,34). The particle mesh Ewald method was used for the treatment of periodic electrostatic interactions, with an upper threshold of 1 Å for grid spacing (35). Electrostatic and van der Waals forces were calculated every time step. A cutoff distance of 12 Å was used for van der Waals forces. A switching distance of 10 Å was chosen to smoothly truncate the nonbonded interactions. Only atoms in a Verlet pair list with a cutoff distance of 13.5 Å (reassigned every 20 steps) were considered (36). The SETTLE algorithm was used to constrain all bonds involving hydrogen atoms, to allow the use of a 2 fs time step throughout the simulation (37). The Nose-Hoover-Langevin piston method was employed to control the pressure with a 200 fs period, 50 fs damping constant, and a desired value of 1 atmosphere (38,39). The system was coupled to a Langevin thermostat to sustain a temperature of 310 K throughout, to maintain the model membrane above its gel transition temperature.

Equilibration protocol

The systems were subjected to 1000 steps of minimization and equilibrated for a total of 3.5 ns. The duration of each equilibration step was 500 ps with a gradual reduction of restraints throughout: 1) protein atoms, ions in the SF, lipid headgroups, and water molecules within protein cavities restrained; 2) protein atoms, ions in the SF, and water molecules within protein cavities restrained; 3) protein atoms and ions in the SF restrained; 4) protein backbone atoms, SF atoms, and ions in the SF restrained; 5) SF atoms and ions in the SF restrained; 6) SF backbone atoms and ions in the SF restrained; and 7) SF ions restrained only.

RESULTS AND DISCUSSION

K2P channels exhibit a unique architecture (illustrated in Fig. 1 *A*) formed from the assembly of two identical subunits (denoted A and B). Each subunit consists of two nonidentical pore domains, with the former including an expansive EC. Despite the substantial structural variations, TWIK-1 displays the archetypal conductive SF structure, which is highly conserved in numerous human and bacterial K^+-channel crystal structure analogs (Fig. 2 *A*). Backbone carbonyls from each subunit and pore domain within the subunits assemble in a cage-like structure to form four adjacent binding sites (S1–S4) that are capable of binding dehydrated K^+ ions. Additional sites are capable of binding partially hydrated species at the intracellular (SC) and extracellular (S0) exits. The sequence is divergent from the signature sequence TXGYG, where X represents any hydrophobic amino acid; P1 is TTGYG and P2 is TIGLG. On closer inspection, a degree of asymmetry is observed in the pore; the distance between the T118 (P1) carbonyls is

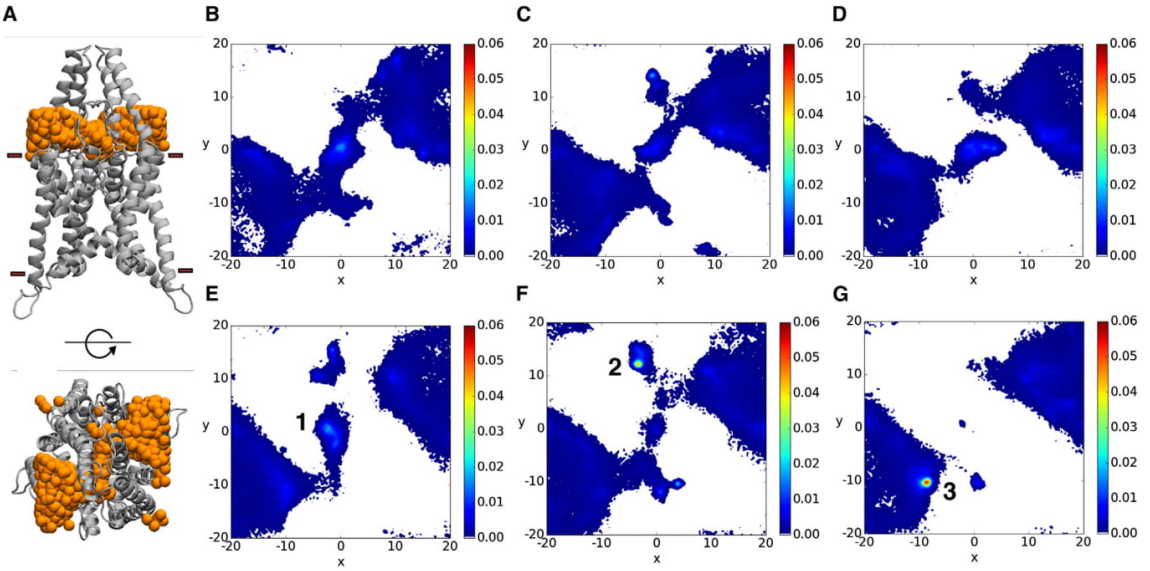

FIGURE 1 Extracellular ion transport pathways in TWIK-1. (*A*) Side view (*upper panel*) and top view (*bottom panel*) of the region between the EC (G80) and the SF (G121), where the position of K^+ ions (*orange spheres*) was tracked. (*B–G*) Color maps showing the position of extracellular ions entering the filter region in simulations HSE, HSD, HSP, HSEP, HSDP, and HSPP, respectively. Ion positions were measured as the *x* and *y* coordinates of the center of mass and then discretized into bins of 0.5 Å. To see this figure in color, go online.

4.3 Å, compared with 4.8 Å between I226 (P2) atoms. Furthermore, the SF is known to be influenced by external pH, with ionizable residues present at the top of the SF in both P1 and P2. H122, in particular, has been established as the putative proton sensor in TWIK-1, as well as in the K2P channels TASK-1 and TASK-3, that responds to changes in extracellular pH (17). How these features influence the dynamics of the SF and hence ion permeation on

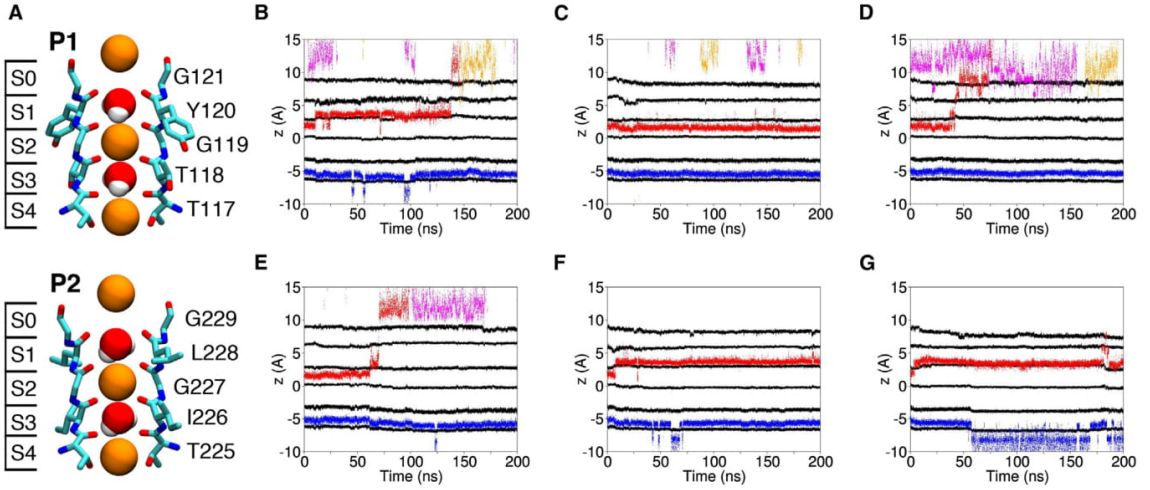

FIGURE 2 (*A*) Crystal structure of the P1 and P2 domains of the TWIK-1 SF, with the initial ion configuration used in all simulations. Definitions of the binding sites are provided on the left. The SF residues T117–G121 and T225–G229 are displayed in licorice representation, with van der Waals spheres representing ions and water molecules. Oxygen, nitrogen, carbon, sodium, and potassium atoms are shown in red, blue, cyan, yellow, and orange, respectively. (*B–G*) Ion trajectories in simulations HSE (*B*), HSD (*C*), HSP (*D*), HSEP (*E*), HSDP (*F*), and HSPP (*G*). The black traces correspond to the center of mass of the oxygen atoms of the SF residues that contribute to the binding sites. The blue, red, yellow, and pink trajectories correspond to the trajectories of individual K^+ ions. Representative snapshots of each ion configuration can be found in Fig. S3. To see this figure in color, go online.

an atomistic level is currently unknown. To address this issue, we performed multiple independent MD simulations to gain insight into the properties of the TWIK-1 SF, as outlined in Materials and Methods.

In all systems, the root mean-square deviations of the transmembrane domain (Fig. S1 in the Supporting Material) and the EC (Fig. S2) show initial jumps associated with the release of restraints present in the initial equilibration procedure, and remain under 2.5 Å and 3.5 Å, respectively, throughout, suggesting that the channel is stable and representative of the determined structure. It is well established in the literature that cytoplasmic gating does not modulate activity in K2P channels. In agreement with this, the cytoplasmic gate does not undergo any significant constriction throughout our simulations, and the slide helix remains parallel to the membrane normal.

Ion transport to the SF

K2P channels possess an extracellular domain that is distinct from other K^+ channel families, extending ~35 Å above the transmembrane domain. The geometry of this region imposes obvious steric constraints on the diffusion pathway to the central pore (Fig. 1 *A*). In addition, the residual composition is predominantly negatively charged, providing a sink for surrounding cations. To gain insight into the transport of ions in this region, we tracked the x and y positions of ions entering the region between the SF and the turret above, excluding occupancy of the S0–S4 sites. The bounding box was defined by z coordinates of the Cα atoms of G80 in the EC and residue G121 at the mouth of the SF, with the x-y coordinates restricted by the region occupied by the transmembrane helices. Density plots of ion distribution, displayed in Fig. 1, *B–F*, show that bidirectional diffusion of ions occurs through side portals of the protruding domain. Negligible diffusion is seen in Fig. 1 *G*, corresponding to the HSPP simulation in which both H122 and D230 are protonated.

The density plots in Fig. 1 pinpoint three unique regions of increased ion density. First, the region above the SF, denoted 1 in Fig. 1 *E*, is consistently a high-occupancy region, with the exception of the HSPP simulation. The charged nature of the SF and above extracellular helices, in addition to contacts with surrounding residues, all contribute to binding in this region, with subtle differences dependent on the filter conformation. A central site can be occupied between the carbonyls of G121 and G229 in both subunits, at the upper bounds of the S0 site. Additional instances are also observed in which ions can be found in off-axis sites interacting with H122 (protonated in the δ or ε position), G121, G229, D230 (unprotonated), S86 (EC), or N87 (EC) residues.

A site was identified in the HSDP simulation (labeled 2 in Fig. 1 *F*) occupying a region directly behind the P1 SF sequence, with ions predominantly interacting with N101, H122, N242, and E235. An additional site in close proximity to this (denoted 3 in Fig. 1 *G*) was also found in the HSPP simulation. This site is present between the P1 SF sequence and P-loop helix, and is defined by direct interactions with E207 (H3-P2 loop), V232 (P2-H4 loop), E235 (P2-H4 loop), and extracellular water molecules. The close proximity of these sites to the SF may have implications for the conformation of the SF and hence ion permeation.

Ion-binding sites in the SF

To probe the behavior of ions within the SF, we tracked the positions of the four ions in contact with the SF for the longest period of time (Fig. 2, *B–G*) and analyzed their behavior. No complete permeation events were observed within any trajectory. However, individual ion movements provide insight into the stability of the K^+ binding sites and the behavior of ions within them. A comparison of the conduction profiles of all of the simulations reveals that the S2–S4 K^+ configuration, as well as the structure observed in the crystallographic data, shows variable stability in the TWIK-1 SF and is sustained for ~5–200 ns. This is in spite of the absence of a concentration gradient or an applied voltage.

With the exception of HSPP, the ion occupying the S4 site is generally stagnant for the timescale of our simulations in the absence of additional ions, due to the consistent coordination to backbone carbonyls and side-chain hydroxyl groups of T117 and T225, resulting in a coordination number of 7 or 8 throughout. In contrast, the ion that originally occupies S2 is subject to reduced coordination at both the upper and lower bounds of the site, and abstraction from this site is observed in all simulations except HSD. T118 in P1 shows increased conformational freedom, resulting in prolonged periods where ion contacts cannot be formed and hence elevation of the ion in the site, which consequently reduces the coordinating ability of I226 in the equivalent position in P2. Additionally, structural changes originating from the top of the P2 SF sequence also lead to reduced coordination of G227, further contributing to the instability of the occupying ion. In the case of HSD, conformational changes at the top of the P1 domain of the SF result in a constriction at the S0 site and the removal of multiple carbonyls from the S1 site, rendering the S2 site the most favorable for an ion in this region of the SF. Qualitatively, these observations are in agreement with the crystallographic data, which demonstrate ion density in S1 to S4 sites.

In the HSE, HSDP, and HSPP simulations, the S1–S4 conformation is sustained for ~100–200 ns. Due to the increased conformational freedom of the upper region of the filter in both the P1 and P2 domains, the ion in S1 is subject to coordination by carbonyls from two G119 residues. The remaining contributions come from Y120 and G227 residues and additional water molecules depending on the conformation of the SF, which generally exhibits a full

coordination shell despite divergence from the canonical structure. Furthermore, transient constrictions in the S0 region of the P1 domain, similar to those observed in the HSD simulation, likely contribute to ion maintenance in this site, and expulsion to the extracellular solution is only permitted in the absence of these constrictions.

Structure of the SF

Experimental evidence indicates that the K^+ channel SF can adopt multiple conformations in addition to the stereotypical conductive conformation (40). Certain voltage-gated K^+ channels have shown Na^+ conductance in the absence of internal K^+ ions, suggesting that the SF can adopt different open conformations with shifting selectivity (41–46). In the case of TWIK-1, inward rectification of Na^+ and outward rectification of K^+ have been measured in low extracellular K^+ concentrations and acidic conditions, even though it exhibits the attributes of a highly selective channel in normal physiological conditions (18), albeit with low conductance properties. These results indicate that TWIK-1 has at least three distinct SF conformations: one conductive, one inactivated, and one with altered selectivity properties. Therefore, we focused our attention on characterizing the conformations of the TWIK-1 SF in response to the range of ionic configurations we identified.

The crystal structure is representative of a typical conductive conformation that consists of four contiguous binding sites and is capable of providing a full coordination shell to dehydrated K^+ ions (47). This structure is observed initially in the MD trajectories (Fig. 3 *A*) but diverges rapidly in all simulations to a number of conformations that contain defective coordination sites yet maintain the general framework of the SF and can be considered partially conductive. This is due to an amalgamation of distinctive P1 and P2 conformations (Fig. 3 *B*). The disparity compared with the typical structure in P1 is localized in the region of T118, which exhibits rotational freedom, causing lateral expansion of the S2 and S3 sites. Crystallization of the noninactivating E71A KcsA mutant revealed remarkable similarities to the structure of P1 in this region (48). In the P2 domain, the canonical structure is lost in the upper region, with residue D230 exhibiting a dynamic behavior, both in protonated and unprotonated forms. A consequence of this higher mobility is a reduced ion coordination by protein atoms in binding sites S0–S2. The functional state of this conformation cannot be attained in our simulations, but as all sites remain viable to accommodate K^+ ions, it is likely that conduction, even if less favorable, can still occur in this state. This is observed in all simulations except HSD, where a constriction in the S0 site is observed in the P1 domain (Fig. 3 *C*), occluding water and ions from entering the SF from this angle for the remainder of the simulation. The predominance of such states throughout the simulation may have implications for the low conductance properties of TWIK-1 relative to other K2P channels.

The vacancy of both the central S2 and S3 sites induces conformations in which the S2 site is physically occluded by backbone rearrangements of SF residues (Fig. 3 *D*). In the HSE and HSP simulations, this occurs by movement of T118 and G119 in P1, whereas in the HSEP and HSPP simulations, this state is observed in I226 and G227 in P2. In these configurations, ions and water molecules are excluded from the S2 site for the remainder of the simulation. The S4 and S3 sites are maintained, with diffuse S0 and S1 sites containing multiple molecules as in the previous conformation. The constriction of the filter shares similar attributes with the crystal structure of KcsA in low K^+ concentrations, where the SF is blocked by a constriction involving V76 and G77 residues, and V76 is oriented away from its optimal position (49). This was confirmed to be nonconductive (50–52) and suggested to be representative of a C-type inactivated state (53). It must be noted that this state is stable on a millisecond timescale, which is unattainable during our simulations; therefore, it is possible that this conformation is an intermediary state that can block

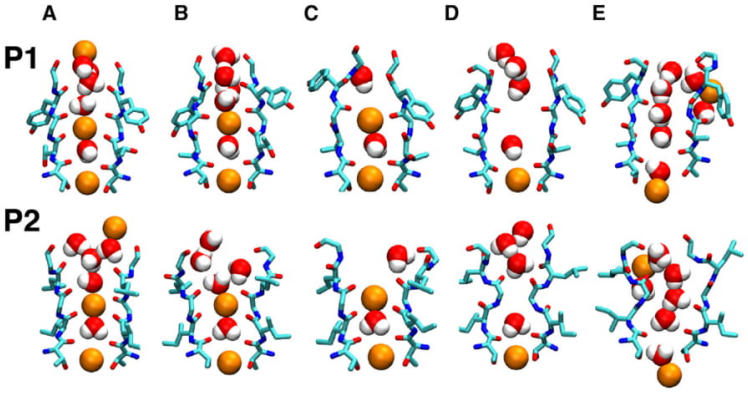

FIGURE 3 Snapshots of the identified SF conformations. The SF residues T117–G121 and T225–G229 are displayed in licorice representation, with van der Waals spheres representing ions and water molecules, and oxygen, nitrogen, carbon, sodium, and potassium atoms shown in red, blue, cyan, yellow, and orange, respectively. (*A*) HSD, 10 ns. (*B*) HSDP, 5 ns. (*C*) HSD, 200 ns. (*D*) HSEP, 200 ns. (*E*) HSPP, 200 ns. To see this figure in color, go online.

permeation transiently, but does not represent the typical inactivated state.

Finally, in the HSPP simulation, a novel, to our knowledge, structure of the SF was observed in which all binding sites were depleted of ions but the SF remained open (Fig. 3 *E*). Previous computational studies suggested the existence of a pathway behind the SF (54) for water transport in collapsed K^+ channels (55). However, these results demonstrate an atomistic representation of the K^+ SF that can stably occupy water in the absence of ions and potentially allow water permeation directly through the SF. These observations provide insight into the unique behavior of the SF of TWIK-1 as a consequence of a single sequence difference in each domain.

Structural changes in P1

Compelling experimental evidence suggests that the hydrogen (H)-bond network behind the SF plays an integral role in determining the structure of the SF, influenced by the presence of structural water molecules and the orientation of local residues (56). Therefore, we analyzed the atomic interactions that stabilized the observed conformations. An examination of T118 is of particular importance due to its confirmed role in the variable selectivity of TWIK-1 in response to low extracellular K^+ concentrations (18). To understand the interrelation between the behavior of this residue and the ionic configurations, we characterized its conformation throughout our simulations using the Ψ (backbone) and X (side chain) dihedral angles (Fig. 4, *A* and *B*). Overall, the Ψ backbone conformations could be prorated into seven clusters, with Ψ values centered at approximately −95°, −45°, 20°, 65°, 110°, 140°, and 170°. These clusters were denoted I–VII in ascending order. In each cluster, the side-chain dihedral angle X could occupy three rotameric states, g+, g−, and t, corresponding to average X angles of 36°, −41°, and −176°, respectively (57). These conformations will be referred to by these classifications henceforth, and the structures of the most highly populated conformations are shown in Fig. 4 *B*.

Conformation II (g−) is representative of the crystal structure with the carbonyls poised for ion binding, and therefore can be considered to be conductive. This conformation is one of the least populated conformations in our simulations, displaying a complex H-bond network as a means of stabilization for a fully conductive filter. T118 and G119 act as H-bond donors to the T113 carbonyl on the pore helix, and the T118 side chain is capable of H-bonding with both S116 and S222 side chains. The remaining filter residues interact with up to two structured water molecules, which in turn contact the side chains of T113, H122, and T123.

In the additional T118 conformations we identified, the backbone carbonyl deviates from this orientation; hence, the extent to which T118 can bind permeant ions in S2 and S3 is compromised. Conformation IV (g−) represents a flipped state, with the carbonyl perpendicular to the pore axis. Further rotation of T118 results in a blocked conformation, V (g−). Backbone atoms in this region physically occlude the permeation axis, resulting in complete removal of the S2 site and blockage of the SF. Such conformations have been established as part of the normal functioning of K^+ channels via MD simulations, depending on the ion occupation of the SF. The H-bond network is highly conserved with regard to conformation II (g−), with minimal reorientations involving the T113 carbonyl and water molecules that now interact with the T118 backbone. In conformation III (t), the carbonyl is rotated ~75° relative to the crystal structure, displaying an H-bond between the side-chain hydroxyl and backbone carbonyl of T118, and

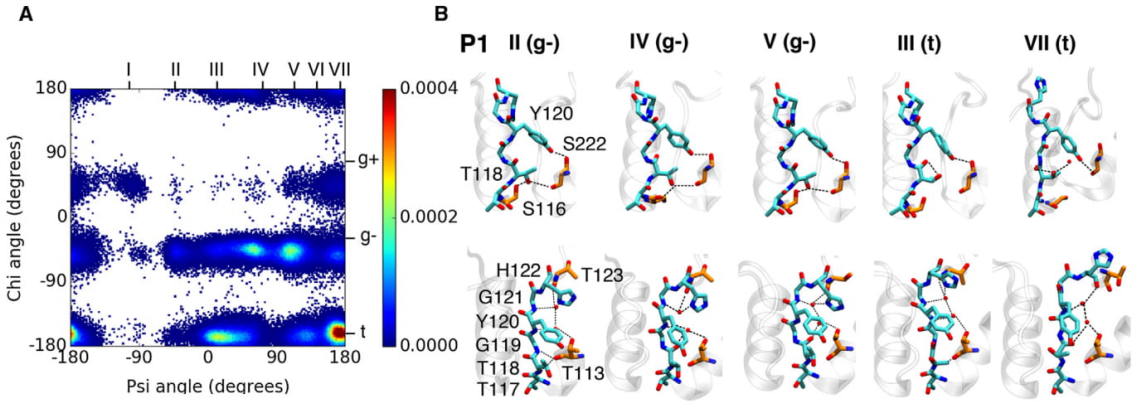

FIGURE 4 (*A*) Heat map of Ψ and X angles of T118 throughout all simulations. (*B*) Snapshots of the full P1 SF in the most populated T118 conformations (from left to right): II (g−)/conductive, IV (g−)/flipped, V (g−)/inactivated, III (t)/open conformation (I), and VII (t)/open conformation with H122 in the up state. The upper and lower panels represent the front and side views of the SF, respectively. SF residues T117–H122 and H-bond partner residues S113, T123, and S222 are shown in cyan and orange, respectively, with red spheres representing water molecules. To see this figure in color, go online.

conserved H-bonding properties elsewhere. As hydrophobic residues usually occupy this position, this conformation appears to be unique to TWIK-1 and, to the best of our knowledge, has not been characterized in previous computational studies.

A prerequisite of the H-bond network described in these conformations is that H122 must be in a so-called down state, where the histidine ring is embedded in the small cavity behind the SF. It must be noted, therefore, that H122 can also occupy an up state, with the ring displaying enhanced flexibility above the filter. In this case, extracellular water molecules penetrate the region previously occupied by the H122 side chain, and interact with selectivity filter residues to stabilize similar conformations. An additional conformation is also observed in which T118 is in the region of the Ramachandran plot corresponding to a β-sheet, with the T118 side chain occupying the pore and H-bonding with surrounding water molecules. In this case, H122 is primarily in the up state, and is predominant throughout our simulations.

In both conformations III (t) and VII (t), coordinating atoms in the S2 and S3 sites are removed, providing a direct link between the behavior of T118 and the structure of the TWIK-1 SF. The S2 site has been identified as the most selective site in K^+ channels; therefore, these conformations may represent a potentially nonselective state, as shown experimentally in reduced K^+ concentrations and extracellular pH (18,20). The importance of the so-called pH sensor, H122, for the different conformations of P1 suggests a further association between the latter stimulus and the dynamic selectivity phenomenon.

Structural changes in P2

The P2 sequence in TWIK-1 is also not conserved with respect to other K^+ channels, since the representative TXGYG sequence is constituted of TIGLG in this channel. The sampled conformations of this domain display a variable H-bond network involving water molecules and pore helix (Y217 and I221), SF (I226, G227, and G229), and loop (D230 and Y231) residues. Favorable hydrophobic interactions between the bulky side chains of I226 and L228 can also be identified. The lower region of the P2 filter domain (S2–S4) is highly conserved with respect to other K^+ channels and thus exhibits paramount stability relative to P1, demonstrating only conductive and constricted conformations. With regard to the upper region of the filter, the preservation of the S0–S2 sites is dependent on the maintenance of interactions between Y217 and D230 (Fig. 5). Detachment of these residues (in both protonation states) propagates structural changes throughout the SF, notably rotation of L228 and G229, resulting in numerous structural variants in which the upper sites are removed and incapable of ion binding. Most commonly, the behavior of this region is largely determined by dynamic interactions

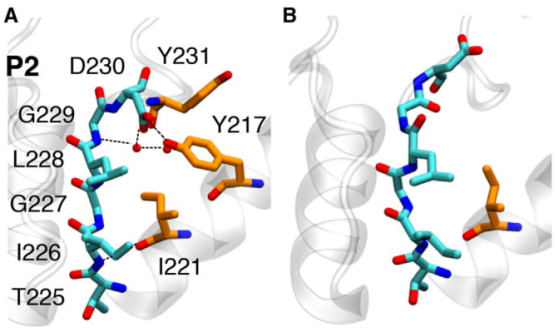

FIGURE 5 Snapshots of the observed P2 conformations in licorice representation, using the coloring scheme defined in Fig. 2 for P2 residues, and the carbon atoms of additional H-bonding residues shown in orange. (*A*) Conductive conformation. (*B*) Conformation with S2–S4 sites maintained, with disruption in the upper sites. To see this figure in color, go online.

with surrounding water molecules and cations, as well as transient interactions with K131.

Comparison with other K^+ channels

Investigations of SF dynamics have focused largely on the prokaryotic K^+ channel, KcsA. The crystal structure of KcsA exhibits a complex network of H-bonds involving contributions from the SF (G77, Y78, and G79), adjacent pore helices (W67 and E71), the succeeding extracellular loop (D80), and an adjacent water molecule, stabilizing the conductive conformation of the filter (49). In the nonconductive case, a reorganized H-bond arrangement was observed that was devoid of direct E71-Y78 and E71-G77 interactions, which were replaced by three structured water molecules behind the SF, the presence of which is thought to control the recovery from slow inactivation (58). A multitude of structural, functional, and computational investigations have since indicated that the W67, E71, D80 triad is crucial in determining the degree to which C-type inactivation occurs (48,59,60). Crystal structures of the E71A mutant provided an atomistic description of a noninactivating SF. The nonflipped state showed remarkable similarities to the conductive state of KcsA in spite of low K^+ concentrations. Remarkably, the W67-D80 interaction was maintained. In contrast, W67 and D80 occupy alternative conformational states in the flipped state, with the latter extending above the SF, resulting in a novel, to our knowledge, SF framework in which the S2 and S3 sites are merged due to rotations of V76.

Residues that occupy equivalent positions in TWIK-1 play an integral role in the conformations we observed, despite their low conservation. In P1, T113 and H122 occupy the positions of E71 and D80 in KcsA, undergoing interactions with each other and SF residues mediated by water molecules. This network, in addition to specific T118 interactions, typically serves to maintain conductive

and nonconductive states with the SF, and it also stabilizes partially conductive conformations. These open states epitomize the flipped E71A mutant, with T118 and H122 mimicking the flexible nature of V76 and D80, respectively. In P2, the W67-D80 interaction is conserved in Y217 and D230 in the conductive conformation, but is primarily detached in the remaining conformations, with swelled S0 and S1 sites. This is consistent with the position of L228, where KcsA contains Y78, suggesting that the presence of this residue may destabilize this region.

To assess whether the dynamics we observed in the SF are unique to TWIK-1, we aligned multiple sequences constituting the SF and the surrounding environment (Fig. 6), and compared interactions that are known to stabilize the SF. In Kv1.2, which is representative of the voltage-gated K^+ channel family, residues D379 and W366 are integral and display exact conservation with D80 and W67 in KcsA, respectively. In Kir2.2, which is representative of the inward-rectifying K^+ channel family, a salt-bridge between E139 (conserved with E71) and R149 is responsible for maintenance of the conductive SF structure. This suggests that TWIK-1 cannot be likened to such channel families. With regard to other K2P channels, TRAAK and TREK-2 demonstrate highly conserved sequences in the pore region but diverge from TWIK-1 with regard to the T118, H122, and L228 positions, which contain I, N, and F residues, respectively. This is consistent with our proposal that the variability of the SF structure originates from these residues, and supports experimental evidence indicating that TWIK-1 is also atypical within the K2P family with regard to its conduction properties.

CONCLUSIONS

Throughout our computational study, we gained insights into the highly dynamic behavior of the TWIK-1 SF. Multiple K^+ ions can occupy alternate sites in the SF, bound in a typical cage-like manner to surrounding carbonyl atoms; however, we find the behavior of SF is disparate from that previously recorded.

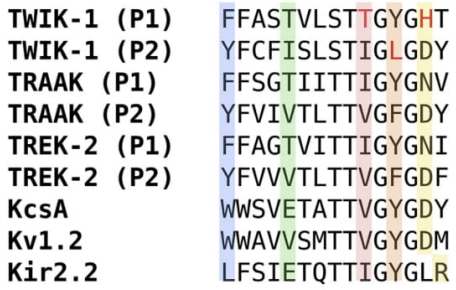

FIGURE 6 Sequence alignment of the SF region with multiple K^+ channels. P1 and P2 denote the nonidentical domains observed in K2P channels. To see this figure in color, go online.

The divergence of the SF in comparison with other K^+ channels is exemplified at the S2 site, with diverse behaviors from both nonconserved P domains in the SF converging here. We identified multiple conformations in P1 that exhibited lateral expansion of the S2 and S3 sites, primarily depending on the conformational state of T118. Introduction of this residue into other K2P channels induced the dynamic-selectivity phenomenon observed in subphysiological conditions in native TWIK-1 channels; therefore, it is possible that such conformations may have varied selectivity properties. The dependence on the surrounding H-bond network, in particular the behavior of H122, raises the possibility that external stimuli, such as K^+ concentration and pH, can be translated to structural changes in the SF. In addition, we observed a widening at the extracellular mouth of the P2 domain, removing the upper sites in the SF. The protonation state of the residues of the selectivity was extensively tested. With the exception of a single simulation (with H122 protonated in the δ position and the unprotonated state of D230), ions were always observed to leave the binding site S2. Upon exclusion of ions from S2, we observed additional conformational states that physically blocked the SF, similar to what was observed in KcsA in low K^+ concentrations. Finally, in a simulation in which both H122 and D230 were in protonated forms and both ions were lost from the filter, the SF remained in an open conformation and all sites were filled with water molecules. TWIK-1 is the first channel, to our knowledge, to display such noninactivating characteristics in a computational simulation.

Overall, these results shed light on the conduction properties of TWIK-1, which exhibits low levels of activity in physiological conditions, yet a robust inward Na^+ current in subphysiological K^+ concentrations and upon acidification. The connection between such properties and the paradoxical depolarization of cardiomyocytes has potential implications for the development of channel-based therapies for associated cardiac disorders.

SUPPORTING MATERIAL

Three figures are available at http://www.biophysj.org/biophysj/supplemental/S0006-3495(16)30540-9.

AUTHOR CONTRIBUTIONS

V.O. performed the modeling and analyzed the data. V.O., S.F., and C.D. interpreted the data and wrote the manuscript. D.P. critically revised the manuscript.

ACKNOWLEDGMENTS

We thank ARCHER, the UK National Supercomputing Service (http://www.archer.ac.uk); the Hartree Centre; and the National Service for Computational Chemistry Software for providing computational resources.

This work was supported by the Biotechnology and Biological Sciences Research Council and Pfizer Neusentis.

REFERENCES

1. Enyedi, P., and G. Czirják. 2010. Molecular background of leak K+ currents: two-pore domain potassium channels. *Physiol. Rev.* 90: 559–605.
2. Sandoz, G., D. Douguet, …, F. Lesage. 2009. Extracellular acidification exerts opposite actions on TREK1 and TREK2 potassium channels via a single conserved histidine residue. *Proc. Natl. Acad. Sci. USA.* 106:14628–14633.
3. Kang, D., C. Choe, and D. Kim. 2005. Thermosensitivity of the two-pore domain K^+ channels TREK-2 and TRAAK. *J. Physiol.* 564:103–116.
4. Maingret, F., M. Fosset, …, E. Honoré. 1999. TRAAK is a mammalian neuronal mechano-gated K^+ channel. *J. Biol. Chem.* 274:1381–1387.
5. Lesage, F., F. Maingret, and M. Lazdunski. 2000. Cloning and expression of human TRAAK, a polyunsaturated fatty acids-activated and mechano-sensitive K^+ channel. *FEBS Lett.* 471:137–140.
6. Patel, A. J., E. Honoré, …, M. Lazdunski. 1999. Inhalational anesthetics activate two-pore-domain background K^+ channels. *Nat. Neurosci.* 2:422–426.
7. Es-Salah-Lamoureux, Z., D. F. Steele, and D. Fedida. 2010. Research into the therapeutic roles of two-pore-domain potassium channels. *Trends Pharmacol. Sci.* 31:587–595.
8. Miller, A. N., and S. B. Long. 2012. Crystal structure of the human two-pore domain potassium channel K2P1. *Science.* 335:432–436.
9. Brohawn, S. G., J. del Mármol, and R. MacKinnon. 2012. Crystal structure of the human K2P TRAAK, a lipid- and mechano-sensitive K^+ ion channel. *Science.* 335:436–441.
10. Brohawn, S. G., E. B. Campbell, and R. MacKinnon. 2014. Physical mechanism for gating and mechanosensitivity of the human TRAAK K^+ channel. *Nature.* 516:126–130.
11. Dong, Y. Y., A. C. W. Pike, …, E. P. Carpenter. 2015. K2P channel gating mechanisms revealed by structures of TREK-2 and a complex with Prozac. *Science.* 347:1256–1259.
12. Lesage, F., E. Guillemare, …, J. Barhanin. 1996. TWIK-1, a ubiquitous human weakly inward rectifying K^+ channel with a novel structure. *EMBO J.* 15:1004–1011.
13. Rajan, S., L. D. Plant, …, S. A. Goldstein. 2005. Sumoylation silences the plasma membrane leak K^+ channel K2P1. *Cell.* 121:37–47.
14. Feliciangeli, S., M. P. Tardy, …, F. Lesage. 2010. Potassium channel silencing by constitutive endocytosis and intracellular sequestration. *J. Biol. Chem.* 285:4798–4805.
15. Goldstein, S. A., L. A. Price, …, M. H. Pausch. 1996. ORK1, a potassium-selective leak channel with two pore domains cloned from Drosophila melanogaster by expression in Saccharomyces cerevisiae. *Proc. Natl. Acad. Sci. USA.* 93:13256–13261.
16. Ben-Abu, Y., Y. Zhou, …, O. Yifrach. 2009. Inverse coupling in leak and voltage-activated K^+ channel gates underlies distinct roles in electrical signaling. *Nat. Struct. Mol. Biol.* 16:71–79.
17. Chatelain, F. C., D. Bichet, …, F. Lesage. 2012. TWIK1, a unique background channel with variable ion selectivity. *Proc. Natl. Acad. Sci. USA.* 109:5499–5504.
18. Ma, L., X. Zhang, and H. Chen. 2011. TWIK-1 two-pore domain potassium channels change ion selectivity and conduct inward leak sodium currents in hypokalemia. *Sci. Signal.* 4:ra37.
19. Ma, L., Y. P. Xie, …, H. Chen. 2012. Silent TWIK-1 potassium channels conduct monovalent cation currents. *Biophys. J.* 102: L34–L36.
20. Ma, L., X. Zhang, …, H. Chen. 2012. Acid-sensitive TWIK and TASK two-pore domain potassium channels change ion selectivity and become permeable to sodium in extracellular acidification. *J. Biol. Chem.* 287:37145–37153.
21. Paice, B. J., K. R. Paterson, …, D. H. Lawson. 1986. Record linkage study of hypokalaemia in hospitalized patients. *Postgrad. Med. J.* 62:187–191.
22. Schaefer, T. J., and R. W. Wolford. 2005. Disorders of potassium. *Emerg. Med. Clin. North Am.* 23:723–747., viii–ix., (viii–ix.).
23. Schmidt, C., F. Wiedmann, …, D. Thomas. 2013. Class I antiarrhythmic drugs inhibit human cardiac two-pore-domain K^+ ($K2_{2p}$) channels. *Eur. J. Pharmacol.* 721:237–248.
24. Aryal, P., F. Abd-Wahab, …, S. J. Tucker. 2014. A hydrophobic barrier deep within the inner pore of the TWIK-1 K2P potassium channel. *Nat. Commun.* 5:4377.
25. Aryal, P., F. Abd-Wahab, …, S. J. Tucker. 2015. Influence of lipids on the hydrophobic barrier within the pore of the TWIK-1 K2P channel. *Channels (Austin).* 9:44–49.
26. Aqvist, J., and V. Luzhkov. 2000. Ion permeation mechanism of the potassium channel. *Nature.* 404:881–884.
27. Fiser, A., and A. Sali. 2003. ModLoop: automated modeling of loops in protein structures. *Bioinformatics.* 19:2500–2501.
28. Li, H., A. D. Robertson, and J. H. Jensen. 2005. Very fast empirical prediction and rationalization of protein pKa values. *Proteins.* 61: 704–721.
29. Humphrey, W., A. Dalke, and K. Schulten. 1996. VMD: visual molecular dynamics. *J. Mol. Graph.* 14:33–38., 27–28.
30. Phillips, J. C., R. Braun, …, K. Schulten. 2005. Scalable molecular dynamics with NAMD. *J. Comput. Chem.* 26:1781–1802.
31. Klauda, J. B., R. M. Venable, …, R. W. Pastor. 2010. Update of the CHARMM all-atom additive force field for lipids: validation on six lipid types. *J. Phys. Chem. B.* 114:7830–7843.
32. Jorgensen, W. L., J. Chandrasekhar, …, M. L. Klein. 1983. Comparison of simple potential functions for simulating liquid water. *J. Chem. Phys.* 79:926–935.
33. Beglov, D., and B. Roux. 1994. Finite representation of an infinite bulk system: solvent boundary potential for computer simulations. *J. Chem. Phys.* 100:9050–9063.
34. Luo, Y., and B. Roux. 2010. Simulation of osmotic pressure in concentrated aqueous salt solutions. *J. Phys. Chem. Lett.* 1:183–189.
35. Darden, T., D. York, and L. Pedersen. 1993. Particle mesh Ewald: an N•log(N) method for Ewald sums in large systems. *J. Chem. Phys.* 98:10089–10092.
36. Verlet, L. 1967. Computer "experiments" on classical fluids. I. Thermodynamical properties of Lennard-Jones molecules. *Phys. Rev.* 159:98.
37. Miyamoto, S., and P. A. Kollman. 1992. SETTLE: an analytical version of the SHAKE and RATTLE algorithm for rigid water models. *J. Comput. Chem.* 13:952–962.
38. Feller, S. E., Y. Zhang, …, B. R. Brooks. 1995. Constant pressure molecular dynamics simulation: the Langevin piston method. *J. Chem. Phys.* 103:4613–4621.
39. Martyna, G. J., D. J. Tobias, and M. L. Klein. 1994. Constant pressure molecular dynamics algorithms. *J. Chem. Phys.* 101:4177–4189.
40. Hoshi, T., and C. M. Armstrong. 2013. C-type inactivation of voltage-gated K^+ channels: pore constriction or dilation? *J. Gen. Physiol.* 141:151–160.
41. Kiss, L., J. LoTurco, and S. J. Korn. 1999. Contribution of the selectivity filter to inactivation in potassium channels. *Biophys. J.* 76:253–263.
42. Korn, S. J., and S. R. Ikeda. 1995. Permeation selectivity by competition in a delayed rectifier potassium channel. *Science.* 269:410–412.
43. Wang, Z., X. Zhang, and D. Fedida. 2000. Regulation of transient Na+ conductance by intra- and extracellular K+ in the human delayed rectifier K^+ channel Kv1.5. *J. Physiol.* 523:575–591.
44. Starkus, J. G., L. Kuschel, …, S. H. Heinemann. 1997. Ion conduction through C-type inactivated Shaker channels. *J. Gen. Physiol.* 110:539–550.

45. Starkus, J. G., L. Kuschel, …, S. H. Heinemann. 1998. Macroscopic Na+ currents in the "Nonconducting" Shaker potassium channel mutant W434F. *J. Gen. Physiol.* 112:85–93.

46. Gang, H., and S. Zhang. 2006. Na^+ permeation and block of hERG potassium channels. *J. Gen. Physiol.* 128:55–71.

47. Doyle, D. A., J. Morais Cabral, …, R. MacKinnon. 1998. The structure of the potassium channel: molecular basis of K^+ conduction and selectivity. *Science.* 280:69–77.

48. Cordero-Morales, J. F., L. G. Cuello, …, E. Perozo. 2006. Molecular determinants of gating at the potassium-channel selectivity filter. *Nat. Struct. Mol. Biol.* 13:311–318.

49. Zhou, Y., J. H. Morais-Cabral, …, R. MacKinnon. 2001. Chemistry of ion coordination and hydration revealed by a K^+ channel-Fab complex at 2.0 A resolution. *Nature.* 414:43–48.

50. Domene, C., and S. Furini. 2009. Dynamics, energetics, and selectivity of the low-K^+ KcsA channel structure. *J. Mol. Biol.* 389:637–645.

51. Domene, C., M. L. Klein, …, M. Parrinello. 2008. Conformational changes and gating at the selectivity filter of potassium channels. *J. Am. Chem. Soc.* 130:9474–9480.

52. Cuello, L. G., V. Jogini, …, E. Perozo. 2010. Structural basis for the coupling between activation and inactivation gates in K^+ channels. *Nature.* 466:272–275.

53. Cuello, L. G., V. Jogini, …, E. Perozo. 2010. Structural mechanism of C-type inactivation in K^+ channels. *Nature.* 466:203–208.

54. Furini, S., O. Beckstein, and C. Domene. 2009. Permeation of water through the KcsA K^+ channel. *Proteins.* 74:437–448.

55. Hoomann, T., N. Jahnke, …, P. Pohl. 2013. Filter gate closure inhibits ion but not water transport through potassium channels. *Proc. Natl. Acad. Sci. USA.* 110:10842–10847.

56. Raghuraman, H., S. M. Islam, …, E. Perozo. 2014. Dynamics transitions at the outer vestibule of the KcsA potassium channel during gating. *Proc. Natl. Acad. Sci. USA.* 111:1831–1836.

57. van der Kamp, M. W., R. D. Schaeffer, …, V. Daggett. 2010. Dynameomics: a comprehensive database of protein dynamics. *Structure.* 18:423–435.

58. Ostmeyer, J., S. Chakrapani, …, B. Roux. 2013. Recovery from slow inactivation in K^+ channels is controlled by water molecules. *Nature.* 501:121–124.

59. Cordero-Morales, J. F., V. Jogini, …, E. Perozo. 2007. Molecular driving forces determining potassium channel slow inactivation. *Nat. Struct. Mol. Biol.* 14:1062–1069.

60. Cordero-Morales, J. F., V. Jogini, …, E. Perozo. 2011. A multipoint hydrogen-bond network underlying KcsA C-type inactivation. *Biophys. J.* 100:2387–2393.

3.4 Post-Commentary

3.4.1 Conclusions

Structural and dynamic properties of the K2P channel TWIK-1 have been investigated, in comparison to other K^+ channels of known structure. By examining a series of equilibrium simulations of K^+ channels from the K_{2P}, K_{IR} and K_V subfamilies, the size, location and residual composition of the fenestration regions was assessed. Crucially, this analysis revealed that the fenestrations identified in TWIK-1 could theoretically accommodate small-drug molecules, whereas the fenestrations located in $K_V1.2$ and $K_{IR}3.2$ were much smaller, and hence inaccessible.

This publication has contributed to a flourishing research field, examining the practicability of fenestrations as drug-binding sites and access pathways to binding sites on the protein interior, in the K^+-channel family. It has been cited in several reviews related to the topic and in recent studies scrutinizing the role of pore and fenestration sites in other K_V and K_{2P} channels.[1-5] At the time of writing, lateral fenestrations have been exposed in high-resolution crystal structures of several members of the K_{2P} family: TWIK-1,[6] TRAAK,[7] TREK-2[8] and TREK-1.[9] Furthermore, simulations using a homology model of TASK-1 identified a fenestration binding site for highly potent TASK-1 blocker A1899,[10] suggesting drug binding to fenestrations are a common feature within this family.

Drug design efforts are generally focused towards identifying compounds that exhibit high-affinity binding to a specific target, and negligible binding to other proteins which may cause adverse side-effects.[11] Considering this outlook, the next logical step is to compare the behaviour of fenestrations within the K2P channel family. Several simulation protocols would be suitable to follow this line of inquiry: (i) equilibrium MD simulations of various K2P channels with K2P channel blockers to identify binding sites and the associated entry route, and (ii) biased MD simulations, such as metadynamics, to calculate the binding affinities of such sites and the energy barriers associated with access through the fenestration regions in multiple K2P channels. Metadynamics has proven successful to confirm that anesthetic (benzocaine) and anti-epileptic (phenytoin) can enter the central cavity of Na_VAb through the fenestration region, with entrance of phenytoin associated with greater energy barriers.[12] Information of this kind may be exploited to aid drug development strategies to design state or subtype-selective drug compounds for the K2P channel family.

Following on from this, the dynamics of other unique structural characteristics of the TWIK-1 channel (selectivity filter and extracellular cap) were examined. Distorted selectivity filter conformations were routinely observed in MD simulations, originating from the presence of molecular non-conserved selectivity filter residues (T118 and L228). Since publication, the

findings of this paper have been supported by ion-exchange-induced difference infrared spectroscopy measurements, flux assays and further computational analysis performed by Tsukamoto et al.[13] In this study, the selectivity filters of highly selective T118I and L228F TWIK-1 mutant channels,[14,15] which display the canonical selectivity sequence in the P1 and P2 domains, respectively, are shown to exhibit greater K^+ affinity. Moreover, evidence is presented that the selectivity filter is flexible enough to accommodate larger ions, specifically Rb^+ and Cs^+, in a disordered manner in the wild-type TWIK-1 channel. Finally, the H-bond characteristics detailed in the study are reproduced using alternative forcefield and simulation parameters. The publication has also been cited in a publication using similar analyses to examine the behaviour of the selectivity filter in the ether-à-go-go (EAG) K^+ channel.[16]

Further study of conduction in the TWIK-1 channel is somewhat limited by the lack of available experimental information concerning the behaviour of the channel in physiological K^+ gradients.[17] Additional work, both experimental and computational, is now required to identify stimuli which promote conduction in TWIK-1. Identification of structural characteristics which stabilize specific selectivity filter conformations of TWIK-1, would enable further computational studies to take place. In the absence of a steadfast selectivity filter conformation for the TWIK-1 channel, the use of free-energy methods to probe the permeation mechanism in this K^+ channel was considered unfeasible at this time. In recognition of this, we turned our attentions towards the archetypal K^+ channel, KcsA, in the following chapter.

3.4.2 References

(1) Gianti, E.; Carnevale, V. Chemical and Biochemical Approaches for the Study of Anesthetic Function, *Methods Enzymol*., **2018**, 602, 25.

(2) Kudaibergenova, M.; Perissinotti, L. L.; Noskov, S. Y. Lipid roles in hERG function and interactions with drugs. *Neurosci. Lett.* **2018**.

(3) Chen, R.; Chung, S. H. Inhibition of Voltage-Gated K^+ Channel Kv1.5 by Antiarrhythmic Drugs. *Biochemistry* **2018,** *57* (18), 2704.

(4) Wen, P.-C.; Mahinthichaichan, P.; Trebesch, N.; Jiang, T.; Zhao, Z.; Shinn, E.; Wang, Y.; Shekhar, M.; Kapoor, K.; Chan, C. K.et al. Microscopic view of lipids and their diverse biological functions. *Curr. Opin. Struc. Biol.* **2018,** *51*, 177.

(5) Ramirez, D.; Arevalo, B.; Martinez, G.; Rinne, S.; Sepulveda, F. V.; Decher, N.; Gonzalez, W. Side Fenestrations Provide an "Anchor" for a Stable Binding of A1899 to the Pore of TASK-1 Potassium Channels. *Mol. Pharmaceut.* **2017,** *14* (7), 2197.

(6) Miller, A. N.; Long, S. B. Crystal Structure of the Human Two-Pore Domain Potassium Channel K2P1. *Science* **2012,** *335* (6067), 432.

(7) Brohawn, S. G.; Campbell, E. B.; MacKinnon, R. Physical mechanism for gating and mechano sensitivity of the human TRAAK K^+ channel. *Nature* **2014,** *516* (7529), 126.

(8) Dong, Y. Y.; Pike, A. C. W.; Mackenzie, A.; McClenaghan, C.; Aryal, P.; Dong, L.; Quigley, A.; Grieben, M.; Goubin, S.; Mukhopadhyay, S.et al. K2P channel gating mechanisms revealed by structures of TREK-2 and a complex with Prozac. *Science* **2015,** *347* (6227), 1256.

(9) Lolicato, M.; Arrigoni, C.; Mori, T.; Sekioka, Y.; Bryant, C.; Clark, K. A.; Minor, D. L. K(2P)2.1 (TREK-1)-activator complexes reveal a cryptic selectivity filter binding site. *Nature* **2017,** *547* (7663), 364.

(10) Ramirez, D.; Arevalo, B.; Martinez, G.; Rinne, S.; Sepulveda, F. V.; Decher, N.; Gonzalez, W. Side Fenestrations Provide an "Anchor" for a Stable Binding of A1899 to the Pore of TASK-1 Potassium Channels. *Mol. Pharmaceut.* **2017,** *14* (7), 2197.

(11) Huggins, D. J.; Sherman, W.; Tidor, B. Rational Approaches to Improving Selectivity in Drug Design. *J. Med. Chem.* **2012,** *55* (4), 1424.

(12) Martin, L. J.; Corry, B. Locating the Route of Entry and Binding Sites of Benzocaine and Phenytoin in a Bacterial Voltage Gated Sodium Channel. *PLOS Comput. Biol.* **2014,** *10* (7), 12.

(13) Tsukamoto, H.; Higashi, M.; Motoki, H.; Watanabe, H.; Ganser, C.; Nakajo, K.; Kubo, Y.; Uchihashi, T.; Furutani, Y. Structural properties determining low K^+ affinity of the selectivity filter in the TWIK1 K^+ channel. *J. Biol. Chem.* **2018,** *293* (18), 6969.

(14) Ma, L. Q.; Zhang, X. X.; Chen, H. J. TWIK-1 Two-Pore Domain Potassium Channels Change Ion Selectivity and Conduct Inward Leak Sodium Currents in Hypokalemia. *Sci. Signal.* **2011,** *4* (176), 10.

(15) Chatelain, F. C.; Bichet, D.; Douguet, D.; Feliciangeli, S.; Bendahhou, S.; Reichold, M.; Warth, R.; Barhanin, J.; Lesage, F. TWIK1, a unique background channel with variable ion selectivity. *P. Natl. Acad. Sci. USA* **2012,** *109* (14), 5499.

(16) Bernsteiner, H.; Brundl, M.; Stary-Weinzinger, A. Dynamics of the EAG1 K^+ channel selectivity filter assessed by molecular dynamics simulations. *Biochem. Bioph. Res. Co.* **2017,** *484* (1), 107.

(17) Lesage, F.; Guillemare, E.; Fink, M.; Duprat, F.; Lazdunski, M.; Romey, G.; Barhanin, J. TWIK-1, a ubiquitous human weakly inward rectifying K+ channel with a novel structure. *EMBO J.* **1996,** *15* (5), 1004.

4. Molecular Determinants of Conduction in the KcsA K^+-Channel

4.1 Commentary

4.1.1 Introduction

High-resolution crystal structures are now available for three major classes of K^+ channels in eukaryotes: voltage-gated (K_V),[1] inward-rectifying (K_{IR})[2] and two-pore domain (K_{2P}).[3] However, the prokaryotic K^+ channel, KcsA from *Streptomyces lividans*, has traditionally been the focus of simulation studies, since the structure of its pore domain was first resolved at high-resolution in 1998.[4] Equilibrium and non-equilibrium simulations have been utilised to model processes including, but not limited to, ion conduction through the selectivity filter, inactivation of the selectivity filter, and drug and lipid binding.

Umbrella sampling simulations have been employed in a multitude of computational studies to calculate the potential of mean force (PMF) of ion transport across the KcsA selectivity filter.[5-7] Previous efforts have exclusively used the wild-type channel, focusing on the viability of the two proposed mechanisms of conduction. In the last two decades, the structure and electrophysiology of KcsA channels with a single mutation has been investigated by a number of research groups. Of interest to us, mutant channels with the S4 site substituted (T75C and T75A mutations) displayed reduced single-channel conductances, relative to the wild-type channel.[8,9] In the accompanying high-resolution crystal structures of these channels, the selectivity filter structure was almost indistinguishable to the wild-type channel. On the basis of this, the structures of T75C and T75A KcsA mutant channels were considered suitable candidates for umbrella sampling simulations of ion translocation through the selectivity filter. The manuscript presented in section 4.2 details the output of such calculations, examining the importance of the S4 site to the permeation process. This communication builds on insights from the previous chapter regarding the behaviour of individual residues in the K^+-channel selectivity filter.

Historically, the KcsA channel has also acted as the central model to understand the molecular determinants of inactivation in K^+-channels.[10-12] C-type inactivation refers to the process in which conduction is impeded as a result of conformational transitions at the selectivity filter. This phenomenon has been reported in eukaryotic voltage-gated K^+-channels,[13,14] in addition to the bacterial channel KcsA. Structures of KcsA exhibiting pinched selectivity filter conformations,[10,15] have been proposed to represent the C-type inactivated state, although this has been disputed in some publications.[16,17] C-type inactivation can be modulated by the functional state of the cytoplasmic gate,[2] membrane composition[18] and other factors.[19,20] The specific influence of the anionic phospholipid phosphatidic acid on the inactivation properties of KcsA is currently under investigation by our experimental collaborators at Miguel Hernandez

University of Elche. In the joint publication presented hereafter, a molecular mechanism coupling lipid-binding and selectivity filter dynamics is proposed, taking into account electrophysiological, NMR and MD simulation results of wild-type KcsA and several channel mutants.

To conclude our investigation into the behaviour of the KcsA channel selectivity filter, we examined two additional factors, described in section 4.3. Firstly, the presence of anionic lipids in non-annular sites affects the energetics of ion permeation. Secondly, ion permeation is also affected by deprotonation of E71, which alters the conformation and electrostatics of residues directly behind the selectivity filter.[21] To this end, umbrella sampling simulations were performed using a similar protocol to that described in section 4.2. Together, these results advocate that the primary role of anionic lipids lies in the inactivation process.

In this chapter, I have performed and analysed all the simulation data presented here, aided by C. Domene and S. Furini, who have published extensively on conduction in KcsA and other ion channels.[5,21] Experimental work in section 4.3 has been performed by external collaborators (see section 4.3.1).

4.1.2 References

(1) Long, S. B.; Campbell, E. B.; MacKinnon, R. Voltage sensor of Kv1.2: Structural basis of electromechanical coupling. *Science* **2005,** *309* (5736), 903.

(2) Nishida, M.; MacKinnon, R. Structural basis of inward rectification: Cytoplasmic pore of the G protein-gated inward rectifier GIRK1 at 1.8 angstrom resolution. *Cell* **2002,** *111* (7), 957.

(3) Miller, A. N.; Long, S. B. Crystal Structure of the Human Two-Pore Domain Potassium Channel K2P1. *Science* **2012,** *335* (6067), 432.

(4) Doyle, D. A.; Cabral, J. M.; Pfuetzner, R. A.; Kuo, A. L.; Gulbis, J. M.; Cohen, S. L.; Chait, B. T.; MacKinnon, R. The structure of the potassium channel: Molecular basis of K+ conduction and selectivity. *Science* **1998,** *280* (5360), 69.

(5) Furini, S.; Domene, C. Atypical mechanism of conduction in potassium channels. *P. Natl. Acad. Sci. USA* **2009,** *106* (38), 16074.

(6) Berneche, S.; Roux, B. Energetics of ion conduction through the K^+ channel. *Nature* **2001,** *414* (6859), 73.

(7) Heer, F. T.; Posson, D. J.; Wojtas-Niziurski, W.; Nimigean, C. M.; Berneche, S. Mechanism of activation at the selectivity filter of the KcsA K+ channel. *Elife* **2017,** *6*, 18.

(8) Zhou, M.; MacKinnon, R. A mutant KcsA K+ channel with altered conduction properties and selectivity filter ion distribution. *J. Mol. Biol.* **2004,** *338* (4), 839.

(9) Labro, A. J.; Cortes, D. M.; Tilegenova, C.; Cuello, L. G. Inverted allosteric coupling between activation and inactivation gates in K^+ channels. *P. Natl. Acad. Sci. USA* **2018,** *115* (21), 5426.

(10) Cuello, L. G.; Jogini, V.; Cortes, D. M.; Perozo, E. Structural mechanism of C-type inactivation in K^+ channels. *Nature* **2010,** *466* (7303), 203.

(11) Pan, A. C.; Cuello, L. G.; Perozo, E.; Roux, B. Thermodynamic coupling between activation and inactivation gating in potassium channels revealed by free energy molecular dynamics simulations. *J. Gen. Physiol.* **2011,** *138* (6), 571.

(12) Cordero-Morales, J. F.; Jogini, V.; Lewis, A.; Vasquez, V.; Cortes, D. M.; Roux, B.; Perozo, E. Molecular driving forces determining potassium channel slow inactivation. *Nat. Struct. Mol. Biol.* **2007,** *14* (11), 1062.

(13) Hoshi, T.; Zagotta, W. N.; Aldrich, R. W. 2 Types of inactivation in shaker k+ channels - effects of alterations in the carboxy-terminal region. *Neuron* **1991,** *7* (4), 547.

(14) Choi, K. L.; Aldrich, R. W.; Yellen, G. Tetraethylammonium blockade distinguishes two inactivation mechanisms in voltage-activated K^+ channels. *P. Natl. Acad. Sci. USA* **1991,** *88* (12), 5092.

(15) Zhou, Y. F.; Morais-Cabral, J. H.; Kaufman, A.; MacKinnon, R. Chemistry of ion coordination and hydration revealed by a K^+ channel-Fab complex at 2.0 angstrom resolution. *Nature* **2001,** *414* (6859), 43.

(16) Devaraneni, P. K.; Komarov, A. G.; Costantino, C. A.; Devereaux, J. J.; Matulef, K.; Valiyaveetil, F. I. Semisynthetic K^+ channels show that the constricted conformation of the selectivity filter is not the C-type inactivated state. *P. Natl. Acad. Sci. USA* **2013,** *110* (39), 15698.

(17) Hoshi, T.; Armstrong, C. M. C-type inactivation of voltage-gated K+ channels: Pore constriction or dilation? *J. Gen. Physiol.* **2013,** *141* (2), 151.

(18) Marius, P.; Zagnoni, M.; Sandison, M. E.; East, J. M.; Morgan, H.; Lee, A. G. Binding of anionic lipids to at least three nonannular sites on the potassium channel KcsA is required for channel opening. *Biophys. J.* **2008,** *94* (5), 1689.

(19) Levy, D. I.; Deutsch, C. Recovery from C-type inactivation is modulated by extracellular potassium. *Biophys. J.* **1996,** *70* (2), 798.

(20) Perez-Cornejo, P. H^+ ion modulation of C-type inactivation of Shaker K+ channels. *Pflug. Arch. Eur. J. Phy.* **1999,** *437* (6), 865.

(21) Berneche, S.; Roux, B. The ionization state and the conformation of Glu-71 in the KcsA K^+ channel. *Biophys. J.* **2002,** *82* (2), 772.

(22) Furini, S.; Domene, C. On Conduction in a Bacterial Sodium Channel. *PLOS Comput. Biol.* **2012,** *8* (4), 7.

4.2 Effect of Mutagenesis in the K^+ Selectivity Filter on the Mechanism of Ion Permeation

4.2.1 Authorship and Permissions

<table>
<tr><td colspan="10">This declaration concerns the article entitled</td></tr>
<tr><td colspan="10">Effect of Mutagenesis in the K^+ Selectivity Filter on the Mechanism of Ion Permeation</td></tr>
<tr><td colspan="10">Publication status (tick one)</td></tr>
<tr><td>Draft manuscript</td><td>✓</td><td>Submitted</td><td></td><td>In review</td><td></td><td>Accepted</td><td></td><td>Published</td><td></td></tr>
<tr><td>Publication details</td><td colspan="9">Not Applicable</td></tr>
<tr><td>Candidates contribution to the paper (detailed and also given as a percentage)</td><td colspan="9">The candidate contributed to/considerably contributed/predominantly executed the…
Formulation of ideas (50%):
V. Oakes and C. Domene contributed equally.

Design of methodology (50%):
V. Oakes and C. Domene contributed equally.

Experimental work (80%):
V.Oakes: Performed simulations and analysis
S. Furini: Provided analysis tools for weighted-histogram analysis method

Presentation of data in journal format (80%):
V. Oakes: Main author of manuscript and supporting information.
S. Furini: Critically assessed and revised the manuscript and supporting information.
C. Domene: Critically assessed and revised the manuscript and supporting information.</td></tr>
<tr><td>Statement from Candidate</td><td colspan="9">This paper reports on original research I conducted during the period of my Higher Degree by Research candidature.</td></tr>
<tr><td>Signed</td><td colspan="5"></td><td>Date</td><td colspan="3"></td></tr>
</table>

4.2.2 Manuscript

Effect of Mutagenesis in the K^+ Selectivity Filter on the Mechanism of Ion Permeation

Victoria Oakes[1], Simone Furini[2] and Carmen Domene[1,3]

[1]Department of Chemistry, University of Bath, Claverton Down, Bath, BA2 7AY, UK

[2]Department of Medical Biotechnologies, University of Siena, Siena, Italy

[3]Department of Chemistry, University of Oxford, Oxford, OX1 3TA, UK

Abstract

The behaviour of the K^+ channel selectivity filter has been studied intensively in the previous two decades. Biased molecular dynamics methodologies, such as umbrella sampling, have proven to be invaluable to assess the energetics of ion translocation of across the K^+ channel selectivity filter. Here, the potential of mean force of ion permeation is calculated in KcsA mutant channels, where the threonine side-chain in position 75 is mutated to alanine or cysteine. The results provide insights into the significance of threonine in this position, revealing the effect of substitution on the alternate mechanisms of conduction proposed in the literature, involving either water or vacant sites.

Introduction

The first high-resolution crystal structure of a prokaryotic K^+ channel, KcsA from *Streptomyces lividans*, revealed the atomic configuration of the K^+ channel pore domain.[1] This assembly, which is generally conserved in eukaryotic K^+ channels, is formed from the symmetrical arrangement of four subunits, containing two transmembrane α-helices connected by a re-entrant pore loop. The pore loop contains a pore helix and the highly conserved selectivity filter structure. The selectivity filter is a critical determinant of ion permeation, selectivity (discrimination between ionic species) and inactivation (blockage of ionic current at the level of the filter) processes in K^+ channels.

The canonical sequence, TVGYG, from each subunit form four contiguous binding sites (S1-S4) at the extracellular side of the channel (Figure 1A-B).[1,2] Sites S1-S3 are enclosed by the backbone carbonyl groups of the selectivity sequence, which can accommodate single dehydrated K^+ ions. The S4 site is unique in that it is forged from carbonyl (upper) and hydroxyl (lower) groups from the initial threonine residue yet exhibits analogous occupancy. In addition, sites have been determined above and below the selectivity filter, at the extracellular mouth (S0) and in the central cavity (S_{CAV}), respectively.[2]

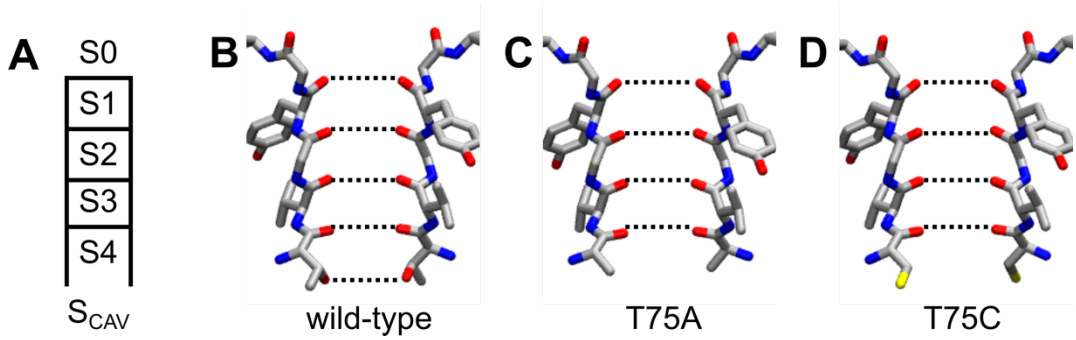

Figure 1. (A) Definition of selectivity binding sites. Structure of the selectivity filter in the (B) wild-type, (C) T75A and T75C KcsA channels. Carbon, oxygen and nitrogen atoms are shown in grey, red and blue, respectively.

Various electrophysiological studies of KcsA mutants have been performed to discern the importance of individual selectivity filter sites with regards to the rate of conduction, inactivation and recovery from inactivation.[3-6] Ion occupancy of the S1-S3 sites can be tuned by synthetic substitution of individual amide bonds to ester linkages, translating to functional effects in the inactivation process.[4,5] Using this protocol, the inactivation rate and rate of recovery from inactivation were diminished on removal of the S2 and S3 sites respectively, whereas negligible effects for both phenomenon were observed for S1. Side-chain substitutions have also been examined to perturb the S4 site. The T75G KcsA channel exhibited a minor reduction in the inactivation rate, but a major decline in the rate of recovery from inactivation.[5] On the contrary, the T75A KcsA channel completely abolished channel inactivation, as a result of an inversion of the allosteric coupling between the upper and lower gates.[6]

Thus far, the conduction properties have been characterised for two KcsA mutant channels, where the threonine side-chain forming the S4 site has been substituted. The conductance of the T75C/A108S double mutant (at 200 mV) was reported to decrease by a factor of ~2-4, relative to the wild-type (at 180 mV), in a concentration-dependent manner.[3] Moreover, the recorded conductance of the non-inactivating T75A mutant channel was reduced by a factor of ~17, relative to the wild-type, at a potential of +100 mV.[6] Although macroscopic currents have also been determined for the T75G mutant channel, detailed information regarding this is not included in the relevant publication.[5] Consequently, we sought to understand the rationale behind the drastic reduction in conduction rates on mutation of the S4 site. To this end, high-resolution crystal structures of T75C (PDB ID 1S5H; closed state)[3] and T75A (PDB ID 6BY3; open state)[6] were utilized to perform umbrella sampling calculations, in order to simulate conduction through the altered selectivity filter and evaluate the energy of this process. The structure of the selectivity filter in the mutant channels under investigation is displayed in Figure 1C and D.

The microscopic mechanism of conduction has been under intense scrutiny since the publication of the initial KcsA structure.[1] Initial reports from crystallographic information and

computational experiments supported a process involving both K^+ ions and water molecules.[1,7-9] In this mechanism, referred to as KWK or 'soft' knock-on mechanism, K^+ ions and water molecules occupy alternative sites in the selectivity filter, occupying either S2/S4 or S1/S3 configurations. Following this, ion transport occurs by coordinated movements between these sites, prompted by an incoming intracellular ion.[10] This is supported by various independent computational studies which have calculated the maximum energetic barrier of process in the 2-3 kcal/mol range,[7,8,10] the associated transport of water molecules in K^+ channels reported experimentally,[11,12] and two-dimensional infrared spectroscopy.[13] An alternative mechanism of conduction involving vacant sites, has also been proposed by Furini and Domene, exhibiting similar energetics.[10] In this mechanism, known as the KK or 'hard' knock-on mechanism, the selectivity filter can accommodate two or three K^+ ions simultaneously, in adjacent sites or separated by empty sites. In this way, direct electrostatic repulsion drives permeation. Evidence supporting this rationale has gained traction in recent years, as a result of extensive unbiased MD simulations in voltage conditions, and re-examination of the initial electron density profiles within the same study.[14] Both schemes are considered in the context of this study.

Materials and Methods

Model Setup

High-resolution crystal structures of T75C (PDB ID 1S5H; closed state)[3] and T75A (PDB ID 6BY3; open state)[6] were used as the atomic coordinates of the mutant channels. Residues 26-114 and 26-121 were used for the T75C and T75A mutant channels, respectively. N- and C-termini were acetylated and methylated respectively. The amino acid E71 of KcsA is modelled in the protonated state to form a diacid hydrogen bond with D80.[15] Default ionisation states were used for the remaining amino acids. Four water molecules were placed at the back of the selectivity filter, in agreement with crystallographic data and previous molecular dynamics (MD) simulations. SOLVATE 1.0 was used to solvate internal cavities of the protein. The structures were aligned perpendicular to the bilayer and inserted into a neutral membrane containing 1-palmitoyl-2-oleoyl-sn-glycero-3-phosphocholine (POPC) molecules. The VMD solvate plugin was then used to create a cubic water box around the membrane-protein system.[16] The overlapping water and lipid molecules around the ion channel structure were removed with the cut-off distance (1.2 Å). Potassium and chloride ions were added using Autoionize Plugin of VMD to neutralise the systems and obtain a concentration of 150 mM.16 The final system size was approximately 90,000 atoms.

Molecular Dynamics Simulations

MD simulations were performed with version NAMD 2.12.[17] CHARMM36 parameters were used for the protein and lipids,[18] the TIP3P model was used for water,[19] and the CHARMM NBFIX parameters for ions. The particle mesh Ewald method was used for the treatment of periodic electrostatic interactions, with an upper threshold of 1 Å for grid spacing.[20]

Electrostatic and van der Waals forces were calculated every time step. A cutoff distance of 12 Å was used for van der Waals forces. A switching distance of 10 Å was chosen to smoothly truncate the non-bonded interactions. Only atoms in a Verlet pair list with a cutoff distance of 13.5 Å (reassigned every 20 steps) were considered. The SETTLE algorithm was used to constrain all bonds involving hydrogen atoms, to allow the use of a 2 fs time step throughout the simulation.[21] MD simulations were performed in the NPT ensemble. The Nose-Hoover-Langevin piston was employed to control the pressure with a 200 fs period, 50 fs damping constant, and the desired value of 1 atmosphere.[22,23] The system was coupled to a Langevin thermostat to sustain a temperature of 300 K throughout. In the equilibration process, the same protocol was used for all of the systems. The systems were subjected to 10,000 steps of minimization, with harmonic constraints (force constant 20 kcal $mol^{-1}Å^{-2}$) on protein atoms, lipid headgroups and crystallographic water and ions. Harmonic restraints were gradually reduced to a force constant of 2 kcal $mol^{-1}Å^{-2}$ and removed in consecutive steps from the lipid headgroups, protein side-chains and protein backbone over the course of a 3.5 ns trajectory. Unbiased MD simulations were then performed for 20 ns to equilibrate the system. Coordinates and velocities from this point were used as the starting point for subsequent biased simulations.

Umbrella Sampling Simulations

Umbrella sampling has been used to calculate the potential of mean force of ion translocation through the mutated KcsA selectivity filter. Ion permeation involving three ions was examined, simulating the events connecting the S_{CAV}/S3/S1 and S3/S1/S_{EC} configurations, with either a water molecule (KWK mechanism) or a gap (KK mechanism) in the S2 site. The initial and final configurations are considered to be equivalent, and thus the energetics obtained are representative of the permeation of a single ion. The three ions are denoted K1 (exterior ion), K2 (central ion) and K3 (interior ion). Two biasing potentials were initialized, acting on the K3 ion and the center of mass of the K1 and K2 ions. Individual simulations were predominantly spaced 0.5 Å apart, adopting a force constant of 20 kcal $mol^{-1}Å^{-2}$ for the harmonic potential. In the extremities of K1 (extracellular) and K3 (intracellular), windows were spaced 1 Å apart, adopting a force constant of 10 kcal $mol^{-1}Å^{-2}$ for the harmonic potential. In a single scenario (T75C-KK), the chosen collective variables resulted in degenerate states, thus it was performed using three biasing potentials on the center of mass of the individual ions. Ions were moved to their starting configurations during an initial 10 ps trajectory, with weak restraints were applied to the backbone atoms of residues E71 to D80. Simulations of 500 ps were then performed for each configuration. The positions of water molecules in the selectivity filter were monitored throughout, and simulations exhibiting water molecules with unconventional behaviour were removed from subsequent analysis. The initial 100 ps of the trajectories were considered as equilibration and also removed. The weighted histogram analysis method was used to unbias the data and obtain the PMF in two (T75C-KWK, T75A-KWK, T75A-KK) or three-dimensions (T75C-KK).[24] Error estimates were obtained by calculating PMF profiles for 100 ps portions of the trajectory and combining them.

It should be noted here, that differences in the activation gate are neglected, on the basis of structural studies of voltage-gated K^+ channels which exhibit comparable ion occupancies in the crystal structures of representative open-conductive and closed-conductive states.[25,26] Furthermore, substitution of T75 position has dramatic consequences on the coupling of the activation-inactivation gates.[6] Therefore, further mutations in this position in either of structures used would likely destabilize the channel structure.

Results

KWK Mechanism

Firstly, the long-established KWK mechanism in the T75A and T75C mutant channels is investigated, denoted T75A-KWK and T75C-KWK, respectively. In the following discussion, it can be assumed that all selectivity filter sites are filled with K^+ ions or water molecules. The 2D PMF of the T75A mutant channel (Figure 2A) exhibits three minima corresponding to S1/S3, S0/S2, S0/S2/$S3_B$ and S2/$S3_B$ configurations, where B represents the lower boundary of the site. The S1/S3 site is the most thermodynamically stable and progression of ions from S1/S3 to S0/S2 poses the largest barrier to conduction (~5 kcal/mol), where the behaviour of the third ion is omitted. This mechanism is inconsistent with the traditional KWK mechanism, which involves S1/S3/$S4_B$ and S0/S2/S4 configurations. It is therefore apparent that elimination of the S4 site abolishes the knock-on effect of the intracellular ion and increases the maximum barrier to conduction. Following evolution of the S0/S2 configuration, the remainder of the permeation event can be completed with low energetic barriers (~2 kcal/mol) on approach of the third ion.

In contrast to the above, the wild-type and T75C mutant channel differ primarily by the electrostatics of the S4 site, as threonine and cysteine are similar sizes. In the 2D PMF of the T75C channel (Figure 2B), configurations S1/S3/S_{CAV}, S0/S2/S_{CAV}, S0/S2/S4 and S2/S3 represent minima in the conduction mechanism. Expectantly, the S4 site is restored, though the $S4_B$ site remains unviable. S0/S2/S4 constitutes the lowest energy state, followed by S1/S3/S_{CAV}, the energy of which fluctuates in a ~2kcal/mol range dependent on the position of the ion in the central cavity. Similar to the T75A mutant channel, conduction is initiated interchange between S1/S3 to S0/S2 configurations. In this case, the barrier to this process is at a minimum (~3-4 kcal/mol), when the cavity ion is approximately 6 Å below the S3 site. Movement of this ion towards the S4 site, requires an additional 3 kcal/mol. Overall, transition from S0/S2/S4 and S2/S3 limits conduction to the greatest extent, with a calculated barrier in excess of 6 kcal/mol.

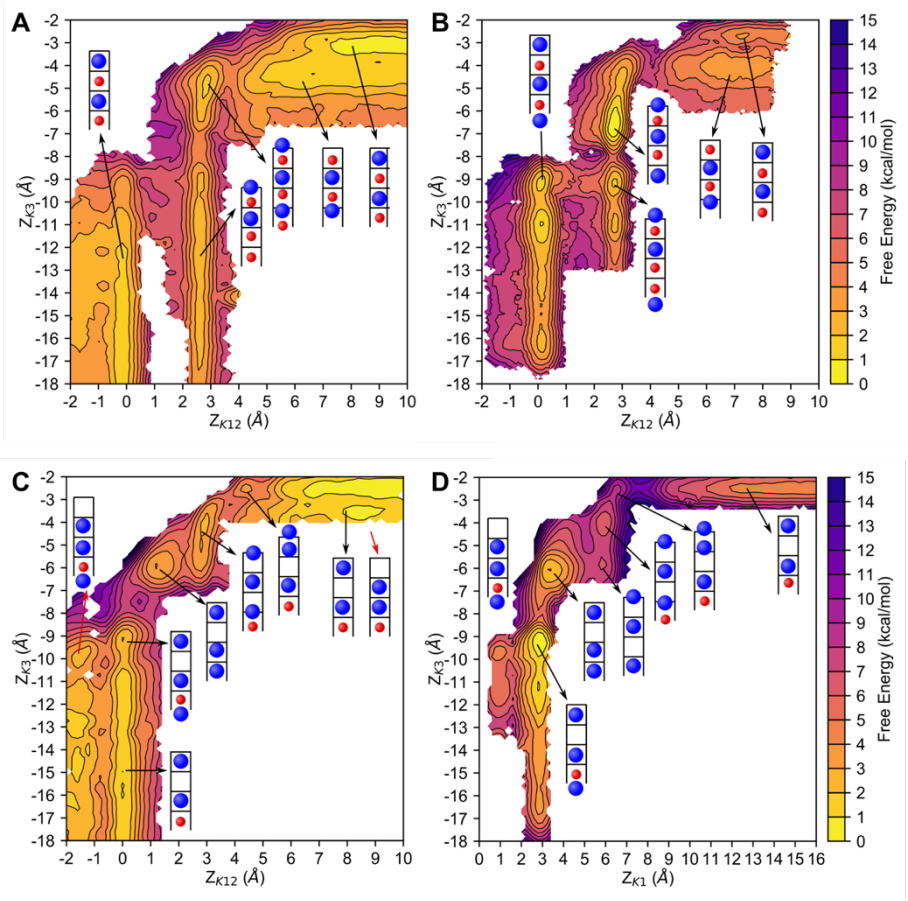

Figure 2. PMF profiles of (A) T75A-KWK, (B) T75C-KWK, (C) T75A-KK and (D) T75C-KK simulations, obtained using umbrella sampling. Figure 2D is a projection onto two collective variables, derived from the 3D-PMF calculated directly from the simulation. Ion configurations are represented using a simplified representation of the selectivity filter, defined in Figure 1A, with K^+ ions and water molecules shown as blue and red spheres, respectively.

KK Mechanism

Next, the energetics of the KK mechanism in the T75A and T75C mutant channels is evaluated, denoted T75A-KK and T75-KK, respectively. Here, sites not occupied by K^+ ions are empty unless specifically mentioned. In the T75A mutant channel, four minima can be identified on the permeation pathway in the 2D PMF corresponding to configurations: S1/S3/S_{CAV}, S1/S2/S4, S0/S2/S3 and S0/S1/S3 (Figure 2C). Minima representing S2/S3/S_{CAV} configurations, are also found. S1/S3 and S2/S3 configurations are similar in energy and separated by low energy barriers (~2kcal/mol); thus, it is likely S3/S2 can unwittingly evolve from S3/S1 but does not necessarily play a direct role in conduction. The energy of certain selectivity filter configurations varies dependent on the position of the ion in the central cavity. The maximum barrier to conduction (5 kcal/mol) arises from the progression of one ion from the cavity to S4, and the accompanying movement of a second ion from S3 to S2. The remaining energetic barriers are of the order of 1-3kcal/mol, however intermediary steps with direct ion-ion

interactions (S1/S2/S4, S0/S2/S3 and S0/S1/S3) are visibly higher in energy than the initial S1/S3 state.

In the 3D PMF of the T75C channel mutant (Figure 2D), an additional minimum is observed representing a S0/S2/S4 configuration, which is similar in energy to S0/S2/S3. In this case, however, S0/S2/S4, S0/S2/S3 and S0/S1/S3, forms part of the elevated region of the PMF, although S1/S2/S4 is excluded. As a result, high energy barriers (between 5-6 kcal/mol) are realized in three separate regions of the PMF: 1) entrance of ion to S4 from the cavity, when other ions occupy S1 and S3, 2) movement of ion to S0 from S1, when other ions occupy S2 and S4, and 3) a concerted movement of ions in from S2 and S0, to S1 and S_{EC}, respectively, to return to the S1/S3 starting conformation. Moreover, the energy barrier of the backward transition of movement 3) is in excess of 7kcal/mol. It should be noted that the marked stability of the cavity site is a result of occupation of the S4 site by a water molecule, intersecting the cavity and S3 ions.

Discussion

By using umbrella sampling simulations, the PMF for both KK and KWK mechanisms in the T75A and T75C mutant channels has been evaluated. From these, the maximum barrier to conduction has been calculated for all scenarios to be in the range 5-7 kcal/mol. This is a significant increase from values calculated for the wild-type KcsA channel, which is frequently cited as 2-3 kcal/mol,[7,8,10] justifying the diminished conductances recorded experimentally.[3,6]

The increased barriers can be attributed to differences in the observed mechanisms of conduction, as a result of tuning the properties of the S4 site. For example, the threonine-cysteine substitution maintains a comparable side-chain volume yet transforms the electrostatic properties, rendering the $S4_B$ site inhospitable. On the other hand, both side-chain volume and polarity are reduced on substitution of threonine to alanine, which merges the S4 site with the central cavity, effectively removing both S4 and $S4_B$ regions. In the KWK mechanism, the difference is stark. In the absence of the $S4_B$ site, in both T75A and T75C, the approach of an intracellular K^+ ion, to promote the concerted movement of ions from S1/S3 to S0/S2 in the KWK mechanism, is unworkable. Thus, removal of threonine in this scenario eliminates the long-established “knock-on” aspect of conduction. In the KK mechanism, the sequence of atomic movements is unchanged, however two-ion configurations are evidently more favorable than those with three ions. This observation is in agreement with experimental work which documents a reduction in the total ion occupancy of the T75C filter to less than two (~1.7).[3]

Subsequently, it is of interest to examine if the calculated PMF profiles can rationalize the ion occupancies approximated from the crystal structure of the T75C channel.[3] In the mutated filter, the ion occupancies of S2 and S4 are diminished, whilst those in S1 and S3 are basically sustained. In the accompanying publication, Zhou and Mackinnon contemplate this in terms of the KWK mechanism, suggesting that the S1/S3 configuration may be more energetically

favorable than the S2/S4 configuration in the mutant channel. However, in the PMF profile of this process (T75C-KWK), configurations involving S2 are energetically equivalent to those that involve S1 and S3, and in fact, the S0/S2/S4 configuration is found to be the most thermodynamically stable, advocating that this is not the case. What is more, the free energy of the S1/S3/$S_{CAV(-9.0)}$ configuration in the PMF profile of the KK mechanism is at least 2-6 kcal/mol lower than other configurations involving the S2 site, with energetic barriers of ~5 kcal/mol to evolve from this. Considering this model, it can be suggested that the S1/S3 configuration, where the S2 site is vacant, is primarily responsible for the elevated electron densities in S1/S3. It then follows that the S2 density may arise from either S1/S2/S4 (KK mechanism) or S0/S2/S4 (KWK mechanism), although this is inconsistent with the absence of electron density in S4. With this in mind, we cannot fully interpret the reported ion occupancies.

Finally, we remark on the significance of the ion in the central cavity of the T75C channel. Our PMF profiles reveal several minima in the central cavity which overlap well with the electron density presented in the crystal structure and stabilize certain selectivity filter configurations. It is interesting to note that the S1/S3/$S_{CAV(-9.0)}$ configuration, in the KK mechanism, includes a water molecule in the region considered as S4, inferring that a potential hybrid pathway, involving both vacant and hydrated sites may exist. Investigation of this in the future may provide further insights into the K^+ channel conduction mechanism.

Conclusions

In this study, umbrella sampling simulations have been performed to evaluate the potential of mean force of KcsA mutant channels, where the S4 site is substituted. Substitution of the threonine residue to hydrophobic residues of differing sizes (alanine and cysteine) notably increases the maximum barrier to ion permeation, in line with the reduced conductance rates obtained from single-channel recordings in prior experimental studies. Moreover, insights are provided into the deviant ion occupancies reported for the T75C mutant channel, indicating the dominant mechanism of conduction in this channel involves vacant sites in the selectivity filter.

References

(1) Doyle, D. A.; Cabral, J. M.; Pfuetzner, R. A.; Kuo, A. L.; Gulbis, J. M.; Cohen, S. L.; Chait, B. T.; MacKinnon, R. The structure of the potassium channel: Molecular basis of K+ conduction and selectivity. *Science* **1998,** *280* (5360), 69.

(2) Zhou, Y. F.; Morais-Cabral, J. H.; Kaufman, A.; MacKinnon, R. Chemistry of ion coordination and hydration revealed by a K^+ channel-Fab complex at 2.0 angstrom resolution. *Nature* **2001,** *414* (6859), 43.

(3) Zhou, M.; MacKinnon, R. A mutant KcsA K^+ channel with altered conduction properties and selectivity filter ion distribution. *J. Mol Biol.* **2004,** *338* (4), 839.

(4) Devaraneni, P. K.; Komarov, A. G.; Costantino, C. A.; Devereaux, J. J.; Matulef, K.; Valiyaveetil, F. I. Semisynthetic K^+ channels show that the constricted conformation of the selectivity filter is not the C-type inactivated state. *P. Natl. Acad. Sci. USA* **2013,** *110* (39), 15698.

(5) Matulef, K.; Annen, A. W.; Nix, J. C.; Valiyaveetil, F. I. Individual Ion Binding Sites in the K^+ Channel Play Distinct Roles in C-type Inactivation and in Recovery from Inactivation. *Structure* **2016,** *24* (5), 750.

(6) Labro, A. J.; Cortes, D. M.; Tilegenova, C.; Cuello, L. G. Inverted allosteric coupling between activation and inactivation gates in K^+ channels. *P. Natl. Acad. Sci. USA* **2018,** *115* (21), 5426.
(7) Aqvist, J.; Luzhkov, V. Ion permeation mechanism of the potassium channel. *Nature* **2000,** *404* (6780), 881.
(8) Berneche, S.; Roux, B. Energetics of ion conduction through the K^+ channel. *Nature* **2001,** *414* (6859), 73.
(9) Morais-Cabral, J. H.; Zhou, Y. F.; MacKinnon, R. Energetic optimization of ion conduction rate by the K^+ selectivity filter. *Nature* **2001,** *414* (6859), 37.
(10) Furini, S.; Domene, C. Atypical mechanism of conduction in potassium channels. *P. Natl. Acad. Sci. USA* **2009,** *106* (38), 16074.
(11) Miller, C. Coupling of water and ion fluxes in a k+-selective channel of sarcoplasmic-reticulum. *Biophys. J.* **1982,** *38* (3), 227.
(12) Alcayaga, C.; Cecchi, X.; Alvarez, O.; Latorre, R. Streaming potential measurements in Ca^{2+}-activated K^+ channels from skeletal and smooth-muscle - coupling of ion and water fluxes. *Biophys. J.* **1989,** *55* (2), 367.
(13) Kratochvil, H. T.; Carr, J. K.; Matulef, K.; Annen, A. W.; Li, H.; Maj, M.; Ostmeyer, J.; Serrano, A. L.; Raghuraman, H.; Moran, S. D.et al. Instantaneous ion configurations in the K^+ ion channel selectivity filter revealed by 2D IR spectroscopy. *Science* **2016,** *353* (6303), 1040.
(14) Kopfer, D. A.; Song, C.; Gruene, T.; Sheldrick, G. M.; Zachariae, U.; de Groot, B. L. Ion permeation in K^+ channels occurs by direct Coulomb knock-on. *Science* **2014,** *346* (6207), 352.
(15) Berneche, S.; Roux, B. The ionization state and the conformation of Glu-71 in the KcsA K+ channel. *Biophys. J.* **2002,** *82* (2), 772.
(16) Humphrey, W.; Dalke, A.; Schulten, K. VMD: Visual molecular dynamics. *J. Mol. Graph* **1996,** *14* (1), 33.
(17) Phillips, J. C.; Braun, R.; Wang, W.; Gumbart, J.; Tajkhorshid, E.; Villa, E.; Chipot, C.; Skeel, R. D.; Kale, L.; Schulten, K. Scalable molecular dynamics with NAMD. *J. Comput. Chem.* **2005,** *26* (16), 1781.
(18) Klauda, J. B.; Venable, R. M.; Freites, J. A.; O'Connor, J. W.; Tobias, D. J.; Mondragon-Ramirez, C.; Vorobyov, I.; MacKerell Jr, A. D.; Pastor, R. W. Update of the CHARMM all-atom additive force field for lipids: validation on six lipid types. *J. Phys. Chem. B* **2010,** *114* (23), 7830.
(19) Jorgensen, W. L.; Chandrasekhar, J.; Madura, J. D.; Impey, R. W.; Klein, M. L. Comparison of simple potential functions for simulating liquid water. *J. Chem. Phys.* **1983,** *79* (2), 926.
(20) Darden, T.; York, D.; Pedersen, L. Particle mesh Ewald: An N·log(N) method for Ewald sums in large systems. *J. Chem. Phys.* **1993,** *98* (12), 10089.
(21) Miyamoto, S.; Kollman, P. A. SETTLE: an analytical version of the SHAKE and RATTLE algorithm for rigid water models. *J. Comput. Chem.* **1992,** *13* (8), 952.
(22) Feller, S. E.; Zhang, Y.; Pastor, R. W.; Brooks, B. R. Constant pressure molecular dynamics simulation: the Langevin piston method. *J. Chem. Phys.* **1995,** *103* (11), 4613.
(23) Martyna, G. J.; Tobias, D. J.; Klein, M. L. Constant pressure molecular dynamics algorithms. *J. Chem. Phys.* **1994,** *101* (5), 4177.
(24) Kumar, S.; Bouzida, D.; Swendsen, R. H.; Kollman, P. A.; Rosenberg, J. M. The weighted histogram analysis method for free-energy calculations on biomolecules .1. the method. *J. Comput. Chem.* **1992,** *13* (8), 1011.
(25) Jiang, Y. X.; Lee, A.; Chen, J. Y.; Ruta, V.; Cadene, M.; Chait, B. T.; MacKinnon, R. X-ray structure of a voltage-dependent K^+ channel. *Nature* **2003,** *423* (6935), 33.
(26) Long, S. B.; Tao, X.; Campbell, E. B.; MacKinnon, R. Atomic structure of a voltage-dependent K^+ channel in a lipid membrane-like environment. *Nature* **2007,** *450* (7168), 376.

4.3 Modulation of the KcsA potassium channel by anionic phospholipids: role of the non-annular arginines

4.3.1 Authorship and Permissions

<table>
<tr><td colspan="10">This declaration concerns the article entitled</td></tr>
<tr><td colspan="10">Modulation of the KcsA potassium channel by anionic phospholipids: role of the non-annular arginines</td></tr>
<tr><td colspan="10">Publication status (tick one)</td></tr>
<tr><td>Draft manuscript</td><td>✓</td><td>Submitted</td><td></td><td>In review</td><td></td><td>Accepted</td><td></td><td>Published</td><td></td></tr>
<tr><td>Publication details</td><td colspan="9">Not Applicable</td></tr>
<tr><td>Candidates contribution to the paper (detailed and also given as a percentage)</td><td colspan="9">The candidate contributed to/considerably contributed/predominantly executed the…

Formulation of ideas:
Experimental (50%): J. A. Poveda, A. M. Giudici, M. L. Renart, O. Millet, A. Morales and J. González-Ros
Computational (50%): V. Oakes (50%) and C. Domene (50%)

Design of methodology:
Experimental (50%): J. A. Poveda, A. M. Giudici, M. L. Renart, O. Millet, A. Morales and J. González-Ros
Computational (50%): V. Oakes (50%) and C. Domene (50%)

Experimental work:
Experimental (50%): J. A. Poveda, A. M. Giudici, M. L. Renart, O. Millet, A. Morales and J. González-Ros
Computational (50%): V. Oakes (100%)

Presentation of data in journal format (40%):
V.Oakes and J. A. Poveda contributed equally to composing the manuscript. All other authors critically revised the manuscript.</td></tr>
<tr><td>Statement from Candidate</td><td colspan="9">This paper reports on original research I conducted during the period of my Higher Degree by Research candidature.</td></tr>
<tr><td>Signed</td><td colspan="5"></td><td>Date</td><td colspan="3"></td></tr>
</table>

4.3.2 Manuscript

Modulation of the KcsA potassium channel by anionic phospholipids: Role of the non-annular arginines

José A. Poveda,[1] Victoria Oakes,[2]* A. Marcela Giudici,[1]* M. Lourdes Renart,[1] Oscar Millet,[3] Andrés Morales,[4] Simone Furini,[5] Carmen Domene[2,6] and José M. González-Ros,[1]*

[1]Instituto de Biología Molecular y Celular, Universidad Miguel Hernández, Elche, E-03202 Alicante, Spain

[2]Department of Chemistry, University of Bath, Claverton Down, Bath, BA2 7AY, UK

[3]Structural Biology Unit, CICbioGUNE, Bizkaia Technology Park, Derio, 48160 Vizcaya, Spain

[4]Departamento de Fisiología, Genética y Microbiología, Universidad de Alicante, E-03080 Alicante, Spain.

[5]Department of Medical Biotechnologies, University of Siena, Siena, Italy

[6]Department of Chemistry, University of Oxford, Oxford OX1 3TA, UK

*These authors contributed equally to this work

Abstract

The role of two arginine residues R64 and R89 present at the non-annular lipid binding sites of the K^+-channel KcsA on the modulation of channel activity by anionic lipids, has been investigated using a combined molecular biology, electrophysiology, NMR spectroscopy and molecular dynamics (MD) simulations approach. We have worked with the wild-type KcsA and with different arginine mutant channels reconstituted into membranes containing increasing amounts of the anionic lipid PA (phosphatidic acid). The characterization of these samples allows us to propose a molecular mechanism of the modulatory process, which determines the functional state of the channel selectivity filter. In summary, we reveal a critical interaction between D80, a component of the "inactivation triad", and R89, a non-annular arginine, which can be modulated by non-annular lipids and mutations in the position of R64. The efficacy of this mechanism is dependent on the stability of the lipid bound to the non-annular lipid site and is therefore intensified in the presence of negatively charged lipid headgroups, such as PA, which thrive on the positive charge of the non-annular arginines.

Introduction

Membrane lipids modulate the structure and function of many integral membrane proteins and such effect can be carried out basically by two ways: **i)** directly, through lipid binding to specific sites on the membrane protein and **ii)** indirectly, by changing physical properties of the membrane bilayer. In the former, specific binding sites for lipids at transmembrane segments of the proteins are classified as annular or non-annular, depending on their lipid selectivity and binding affinity. Non-annular lipid binding sites are usually located at clefts between adjacent different subunits of the membrane proteins and although there are several examples of lipid modulation through these non-annular sites,[1-5] the exact mechanisms through which the bound lipids exert such modulatory function remains elusive.

Ion channels are of the essence to many physiological and pathological processes and constitute an important pharmacological target. Many studies have shown an influence of lipids on the structure and function of different ion channels and non-annular lipid binding sites have been identified as key elements in this modulation.[1] This is the case of KcsA, a prokaryotic potassium channel that serves as a reference for the potassium ion channel superfamily due to the high homology with its eukaryotic counterparts. Anionic lipids have been shown to modulate KcsA in different manners and are required for channel function. For instance, anionic lipids increase ion channel conductance and open probability,[6,7] provide stability to the tetrameric channel against thermal or chemical denaturation[8-10] and enable its *in vitro* proper folding,[11] although it is still unclear how and where anionic lipids exert such effects.

From the structural view point, KcsA is a homotetramer in which the four subunits are disposed around a central pore. Each subunit contains a N-terminal cytoplasmic domain followed by a first transmembrane segment (TM1), then, a tilted short pore helix, the selectivity filter, a second transmembrane segment (TM2) and finally, a C-terminal cytoplasmic domain (Figure 1). The selectivity filter, with the sequence TVGYG unmistakable homologous to the eukaryotic K^+ channels, provides a stack of ion binding sites contributed by the backbone carbonyl oxygens to which potassium ions bind in a dehydrated form. Flow of ions through this channel is controlled by the opening and closing of two different gates for ions. The inner gate is formed by the crossing of a cytoplasmic bundle of helices near the C-terminal ends of each subunit. A pH drop initiates a conformational movement of such helical bundle, allowing the formation of an aperture that communicates the pore with the cytoplasmic solution. On the other hand, the outer gate is formed by the selectivity filter itself at the extracellular side of the protein and is stabilized in the open conformation while the inner gate is closed. However, when the inner gate opens, the extracellular outer gate is destabilized as to enter the inactivated conformation, where the passage of ions through the selectivity filter is impeded. This process is similar to the C-type inactivation in many eukaryotic ion channels, which makes KcsA a good model to study this important phenomenon. A complex web of H-bonds implicating several water molecules and

different residues behind the selectivity filter, particularly the so-called inactivation triad E71-D80-W67, have been identified as clue elements in the channel inactivation process.[12-19]

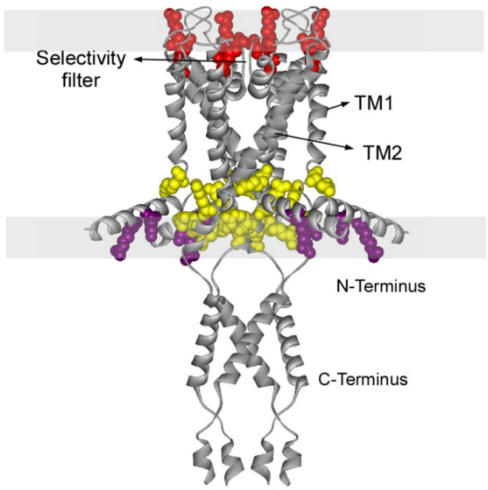

Figure 1. Schematic representation of the KcsA structure (PDB 1F6G) indicating potential binding regions for anionic lipids. For the sake of clarity, only two out of the four KcsA subunits have been drawn. The N-terminal R11 and K14 residues (violet); the arginine residues 27, 117, 121 and 122 (yellow) situated at the cytoplasmic side close to the C-terminal; and the arginine residues present at the non-annular site R64 and R89A (red), are depicted like spheres. The location of important domains of KcsA such as the selectivity filter, the N- and C-terminus and the transmembrane segments TM1 and TM2 is also indicated.

A further examination of the KcsA crystal structure reveals that it contains non-covalently bound lipid[20,21] that co-crystallizes with the protein and has been identified as phosphatidylglycerol (PG).[22] The crystallographic evidence and other studies[23] conclude that the PG binding sites in KcsA have the features of "non-annular" sites,[1] i.e., a deep cleft on the protein surface, between the pore helix and TM2 of adjacent subunits. These sites bind "in vitro" other anionic phospholipids besides PG and contain two cationic arginine residues (R64 and R89) at the most extracellular side of the cleft, which are believed to be essential for binding of anionic phospholipids with high selectivity and affinity.[6,23-26] Moreover, it has been proposed that at least three of the four non-annular binding sites in KcsA should be occupied by anionic lipids for the channel to open.[6] Additionally, these non-annular sites are proposed to be involved in protein-protein interactions leading to the formation of KcsA clusters, which show an activity pattern very different from that of the isolated KcsA channel.[27] Therefore, competing lipid-protein and protein-protein interactions involving these non-annular sites seem important factors to determine the behavior of the KcsA channel.

Besides the role of R64 and R89 at the non-annular sites, other protein domains containing basic amino acid residues have been proposed to be potential sites for anionic lipid binding: i) the N-terminal R11 and K14 residues and ii) the arginine residues 27, 117, 121 and 122 located at the cytoplasmic side, close to the C-terminal segment (Figure 1). In the latter, anionic lipid binding

increases the stability of the channel protein against chemical denaturation.[8] In the former, binding of anionic lipids reportedly induces a conformational change at the N-terminus that stabilizes the open conformation of the inner gate, resulting in an increase in the open channel probability and conductance.[7]

In this work, we have studied the role of the two arginine residues, R64 and R89, present at the non-annular lipid binding sites, on the modulation of KcsA activity by anionic lipids. To do so, we have worked with the wild-type KcsA and with different arginine mutant channels reconstituted into membranes containing increasing amounts of the anionic lipid PA (phosphatidic acid). The analysis of single-channel and macroscopic currents, complemented with NMR and molecular dynamics (MD), enable us to propose a molecular mechanism encompassing the whole process, from the binding of anionic lipids to the non-annular sites, to the structural consequences on the inactivating triad and on the selectivity filter, which finally determine the functional state of the channel.

Materials and Methods

Asolectin (L-α-Phosphatidylcholine from soybean type 2-S) was purchased from Sigma. PA, L-α-phosphatidic acid (egg chicken) from Avanti Polar Lipids, DDM from Calbiochem, and Bio-Beads SM-2 from Bio-Rad.

Cloning and mutagenesis of KcsA

The pT7-837KcsA containing the R64A-KcsA gene mutant was kindly donated by Professor A. Killian (Utrecht University, Holland). The R89A-KcsA mutant was obtained through site-directed mutagenesis, using the wild-type gene inserted into the pQE30 (Qiagen) plasmid as a template. The R64L and the R64,89A-KcsA double mutant were obtained using the pT7-837 KcsA containing the R64A gene mutant as a template and the oligonucleotides:
5'-ACGTATCCGCTTGCGCTGTGGTG-3'(sense) and
5'-CACCACAGCGCAAGCGGATACGT-3' (antisense) or
5′-TGACTCTGTGGGGCGCACTCGTGGCCGTGGTGGTGAT-3′ (sense) and
5′-ATCACCACCACGGCCACGAGTGCGCCCCACAGAGTCAC-3′ (antisense) (Invitrogen).
All mutations were confirmed by sequencing.

Overexpression and purification of KcsA

Expression of the wild-type protein and the R89A mutant were performed in *Escherichia coli* M15 (pRep4) cells, whereas the R64L, R64A and R64,89A mutants were expressed in *E. coli* strain BL21(λDE3) (Molina et al., 2004). For the NMR experiments, the cells were first cultured in 5 ml of LB medium supplemented with antibiotics until an OD_{600} of 0.4 was reached. This culture was diluted into 400 ml of M9 minimum medium, supplemented with thiamine, biotin and antibiotics and incubated at 37°C until an OD_{600} of 0.6 was reached and finally transferred into M9 minimum medium containing 1 g/L $^{15}NH_4Cl$ (Cambridge Isotope

Laboratories) to reach again a OD_{600} of 0.6. In all cases, protein purification was performed essentially as previously described,[28] except that the purification buffer contained 10 mM HEPES, pH 7.5, 100 mM KCl and 5 mM DDM. The higher concentration of DDM used now is aimed to reduce the formation of KcsA clusters (see below). Yields ranging 1-2 mg of purified, DDM-solubilized, tetrameric KcsA per liter of culture were routinely obtained. Protein concentrations were determined from the absorbance at 280 nm, using a molar extinction coefficient of 34,950 $M^{-1}cm^{-1}$ for the KcsA monomer.[11] The purified protein batches were also analyzed by polyacrylamide gel electrophoresis in the presence of sodium dodecyl sulfate.[28]

Reconstitution of KcsA and preparation of giant liposomes

Wild-type KcsA and mutant channels were reconstituted in asolectin lipid vesicles, with or without an additional 25 or 50 % (by weight) of PA. In order to prepare the vesicles, the required amount of lipid was dissolved in chloroform:methanol (2:1, by volume). Then, solvents were removed using a rotary evaporator and vacuum. The dried lipid films at 20 mg/ml were resuspended in 10 mM HEPES (pH 7.0), 100 mM KCl and stored in liquid nitrogen. Before use, defrosted lipid suspensions were diluted at 5 mg/ml, then vortexed and sonicated to clarity.

To further prevent clustering of KcsA, the reconstitution step at a low lipid-protein ratio (5:1 w/w) was avoided.[27,29] Instead, DDM-solubilized KcsA at approximately 1 mg/ml was added drop by drop to the lipid solution while being vortexed, to give a lipid to KcsA tetramer ratio of 100:1 or 1000:1 (by weight) for macroscopic or single-channel current recordings, respectively. The mixture was incubated for at least 30 minutes at room temperature. Then, the detergent was removed using Bio-Beads SM-2 (Bio-Rad laboratories) as described previously (Giudici et al., 2013). After discarding the Bio-Beads, the reconstituted KcsA liposome suspensions were collected by centrifugation (60 minutes at 300,000 x g) and finally suspended in 10 mM HEPES (pH 7.0), 100 mM KCl to a lipid concentration of 0.1 mg/µl. Samples were stored at -80 ºC.

In order to form multilamellar giant liposomes, a drop of the above reconstituted liposomes was placed on a glass slide and dried overnight in a desiccator chamber at 4ºC and then rehydrated with 20 µl of 10 mM HEPES (pH 7.0), yielding giant liposomes suitable for patch-clamp experiments after a few hours of rehydration (Riquelme et al., 1990).

Electrophysiological Recordings

Inside-out patch clamp recordings[30] were performed on excised patches from giant liposomes, using an automated patch clamp system (Nanion Technologies, Germany) equipped with an external perfusion device. Gigaseals were obtained on NPC-1 borosilicate glass chips (Nanion Technologies, Germany) with resistances of 3-5 MΩ. Negative pressure was applied to place a giant liposome on the aperture of the chip and form a planar lipid bilayer in the aperture (Kreir et al., 2008). After a stable seal was formed, the remaining liposomes were washed away with the corresponding intracellular buffer. Currents were recorded using an EPC-10 amplifier (HEKA Electronic, Lambrecht/Pfalzt, Germany), at a gain of 50 mV/pA. Data were digitized at a sampling rate of 10 kHz or 40 kHz (the latter only when recording +150 mV continuous pulses) and low-pass filtered to 2 or 8 kHz (Bessel filter, HEKA amplifier), respectively. Afterwards, the recordings were analyzed with Clampfit 10.3 (Molecular Devices, Axon Instruments). All measurements were taken at room temperature, with the extracellular solution containing 10 mM HEPES buffer (pH 7), 100 mM KCl and the intracellular solution 10 mM MES buffer (pH 4), 100 mM KCl.

For the recording of macroscopic currents, chips with a resistance of 2–3.5 MΩ were used. Currents were elicited in response to pH jumps from 7.0 (10 mM HEPES buffer, 100 mM KCl) to 4.0 (10 mM MES buffer, 100 mM KCl) using the perfusion system, with the membrane held at +150 mV. Maximum currents observed ranged between 250 and 2500 pA.

Kinetic Analysis

Preprocessing. Kinetic analysis of single-channel recordings was done as detailed by others (Chakrapani et al., 2007a), using the QuB suite of programs (www.qub.buffalo.edu). The recordings were initially examined to eliminate those portions containing anomalous noise and overlapping channel activity. Then, they were idealized into open and close transitions using SKM, a segmental k-means algorithm based on hidden Markov modeling procedure at full bandwidth.[31,32] Histograms of the closed and open intervals from the whole recordings, using a logarithmic abscissa and square root ordinate,[33] were fitted to a linear scheme of four closed and one open states using a maximum likelihood criteria after imposing a dead time of 25–75 μs (Chakrapani et al., 2007a).[34,35]

Isolation of Bursts. This process was also done as in (Chakrapani et al., 2007a). Briefly, a closed-state interval longer that a critical duration (t_{crit}) determines when a burst of activity ends and a new one starts. Once a continuous trace is idealized and its corresponding histogram calculated and fitted to the linear scheme (see above), t_{crit} was estimated as the intersection of areas between the second and third closed state durations. Isolated bursts likely arise from the activity of a single channel, which minimizes the total number of misclassified events (Jackson et al., 1983). The mean duration of open and closed times within the burst were estimated by averaging the corresponding idealized dwell times. Then, bursts were classified into low,

intermediate and high mean open probability, restricting the quantitative kinetic modeling studies to the latter ones, because of their predominance and larger homogeneity. Rate constants were estimated from the dwell-time distributions of the intraburst closed and open intervals using an interval-based maximum likelihood method with an incorporated first order corrections for missed events (25–75 μs).[31,32,36,37]

Molecular dynamics simulations

The closed (PDB ID 1K4C) crystal structure of KcsA was retrieved from the Protein Data Bank and resolved residues 26 to 114 were used for subsequent modelling.[20] R64A, R64L and R89A mutant channels were generated using the Mutator plugin of VMD.[38] N- and C-termini were acetylated and methylated respectively. The amino acid E71 of KcsA is modelled in the protonated state to form a diacid hydrogen bond with D80.[39] Default ionisation states were used for the remaining amino acids. Four water molecules were placed at the back of the selectivity filter, in agreement with crystallographic data and previous molecular dynamics (MD) simulations. SOLVATE 1.0 was used to solvate internal cavities of the protein. The structures were aligned perpendicular to the bilayer and inserted into two membrane systems: a neutral membrane containing 1-palmitoyl-2-oleoyl-sn-glycero-3-phosphocholine (POPC) molecule and a charged membrane constituted of POPC and 1-palmitoyl-2-oleoyl phosphatidic acid (POPA) molecules in a 3:1 ratio, with x and y dimensions of 96 Å.[40-42] The VMD solvate plugin was then used to create a rectangular water box around the membrane-protein system.[38] The overlapping water and lipid molecules around the ion channel structure were removed with the cut-off distance (1.2 Å). Potassium and chloride ions were added using Autoionize Plugin of VMD to neutralise the systems and obtain a concentration of 150 mM.[38] The final system size was approximately 90,000 atoms.

MD simulations were performed with NAMD 2.12.[43] CHARMM36 parameters were used for the protein and lipids,[44] the TIP3P model was used for water,[45] and the CHARMM NBFIX parameters for ions. The particle mesh Ewald method was used for the treatment of periodic electrostatic interactions, with an upper threshold of 1 Å for grid spacing.[46] Electrostatic and van der Waals forces were calculated every time step. A cutoff distance of 12 Å was used for van der Waals forces. A switching distance of 10 Å was chosen to smoothly truncate the non-bonded interactions. Only atoms in a Verlet pair list with a cutoff distance of 13.5 Å (reassigned every 20 steps) were considered. The SETTLE algorithm was used to constrain all bonds involving hydrogen atoms, to allow the use of a 2 fs time step throughout the simulation.[47] MD simulations were performed in the NPT ensemble. The Nose-Hoover-Langevin piston was employed to control the pressure with a 200 fs period, 50 fs damping constant, and the desired value of 1 atmosphere.[48,49] The system was coupled to a Langevin thermostat to sustain a temperature of 300 K throughout. In the equilibration process, the same protocol was used for all of the systems. The systems were subjected to 10,000 steps of minimization, with harmonic constraints (force constant 20 kcal/mol/Å^2) on protein atoms, lipid headgroups and

crystallographic water and ions. Harmonic restraints were gradually reduced to a force constant of 2 kcal/mol/Å^2 and removed in consecutive steps from the lipid headgroups, protein side-chains and protein backbone over the course of a 3.5 ns trajectory.

NMR spectroscopy

Two-dimensional ^{1}H,^{15}N-HSQC (Heteronuclear Single Quantum Correlation spectroscopy) experiments were recorded on an 800 MHz Bruker Advance III spectrometer at 298 K for 5h, using detergent-solubilized ^{15}N isotopically enriched protein samples of KcsA (50 µM, tetramer) in 10 mM HEPES, pH 7.5, 100 mM KCl, 5 mM DDM. In all experiments 1024x200 points where collected and water suppression was achieved using WATERGATE. Chemical Shift Perturbation (CSP) of the arginine guanidino side chain region was used to determine the putative Arg residues from the channel that are interacting with the lipid (PA or PC) at a molar ratio of protein:lipid 1:3 (egg PA) or 1:5 (egg PC). Chemical shift perturbations were observed in the fast exchange regime and the signal corresponding to Nε-Hε of R64 was chosen as binding reporter.

Results

Macroscopic KcsA currents

Macroscopic KcsA currents elicited by rapidly changing the pH from neutral to acidic at the intracellular side of the channel, have been recorded in macro patches containing a large number of KcsA channels (Figure 2). K^+ currents were not observed at the starting neutral pH, which is consistent with the absence of KcsA clusters from these samples[29] and suggests that the currents observed upon activation by the pH jump result from the added contributions of individual KcsA channels. Our perfusion system is not fast enough to acquire reliable data on the very rapid, pH-induced channel activation, but the slower inactivation process that follows can be properly recorded. Figure 2A shows that KcsA reconstituted in asolectin lipids inactivates at a rate similar to that reported by others,[35] with a halflife of around one second when fitted to a single exponential. Figure 2A also shows that addition of the anionic lipid PA to the asolectin lipid drastically slowed down current inactivation, with no significant differences between 25 or 50% of PA added to the lipid matrix.

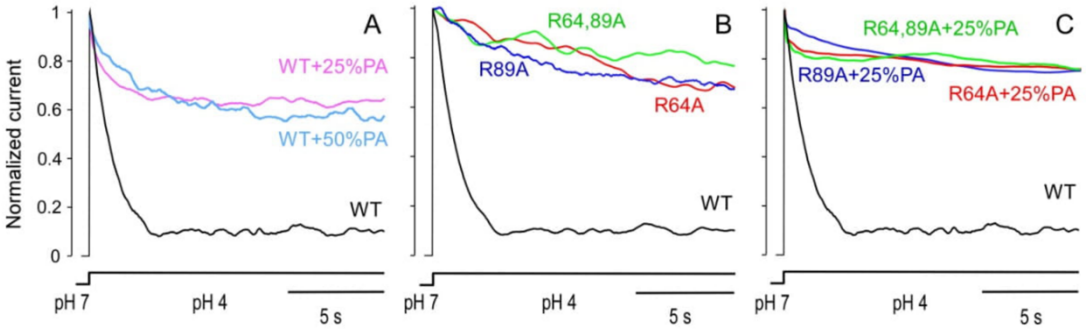

Figure 2. Macroscopic inactivation of KcsA. Normalized macroscopic currents elicited by fast pH jumps (pH 7 to 4) are shown. Each trace is the average from three to five different experiments. (A) Influence of anionic phospholipid on KcsA inactivation. K^+ currents were recorded from macropatches of wild-type KcsA reconstituted in plain asolectin lipids (WT), asolectin lipids with an added 25% of egg PA (WT+25%PA) or asolectin lipids with an added 50% of egg PA (WT+50%PA). (B) Effects of R64A, R89A and R64,89A KcsA mutations on channel inactivation upon reconstitution of the arginine mutant channels in plain asolectin lipids. (C) Effects of adding 25% PA to the reconstituted asolectin lipid matrix of the arginine mutants mentioned above. The holding potential in all these experiments was +150 mV.

Since the non-annular sites at the extracellular side of the protein, particularly the arginines at positions 64 and 89, have been proposed as key elements for the binding of anionic lipids (see Introduction), similar experiments were conducted with arginine to alanine mutants of KcsA at such positions (R64A, R89A and the double mutant R64,89A-KcsA). Figure 2B shows that the effects on the inactivation rate of any of such mutants reconstituted in plain asolectin lipids are qualitatively similar to those caused on the wild type channel by addition of PA to the membrane matrix, that is, the rate of inactivation markedly decreases in all cases. This is similar to that reported previously for the R64A mutant.[13] Noticeably, the addition of PA to the reconstituted, slowly inactivating mutant channels has no further effects on the inactivation rates of these channels (Figure 2C).

Single-channel measurements

Single-channel experiments were also performed with the wild-type and mutant channels from above. In these experiments, a larger lipid/protein ratio was used in the reconstitution step to disperse the channels within the bilayer and favor individual channel recordings (see Methods). In our hands, as in the early report by Schrempf's group (Meuser et al., 1999), the wild-type KcsA reconstituted in asolectin lipids shows a high degree of heterogeneity in the observed potassium currents. Figure 3A is a representative example of a long recording taken at +150 mV, showing bursts of activity with different amplitudes. Such a variability is always present in different samples prepared independently or even within the same membrane patch. Figure 3B, upper panel, shows in more detail the prevailing currents from wild-type KcsA reconstituted in plain asolectin lipids, which correspond to conductance values ranging 30 to 100 pS and have the common feature of exhibiting low open probabilities ($NP_0 \leq 0.2$). The amplitude distribution (Figure 3C, upper panel) shows that the most frequently observed current under these conditions is that of approximately 9 pA (60 pS) and its I/V plot (Figure 4) has a characteristic sigmoid-like pattern with inward and outward rectification, as reported by others.[50]

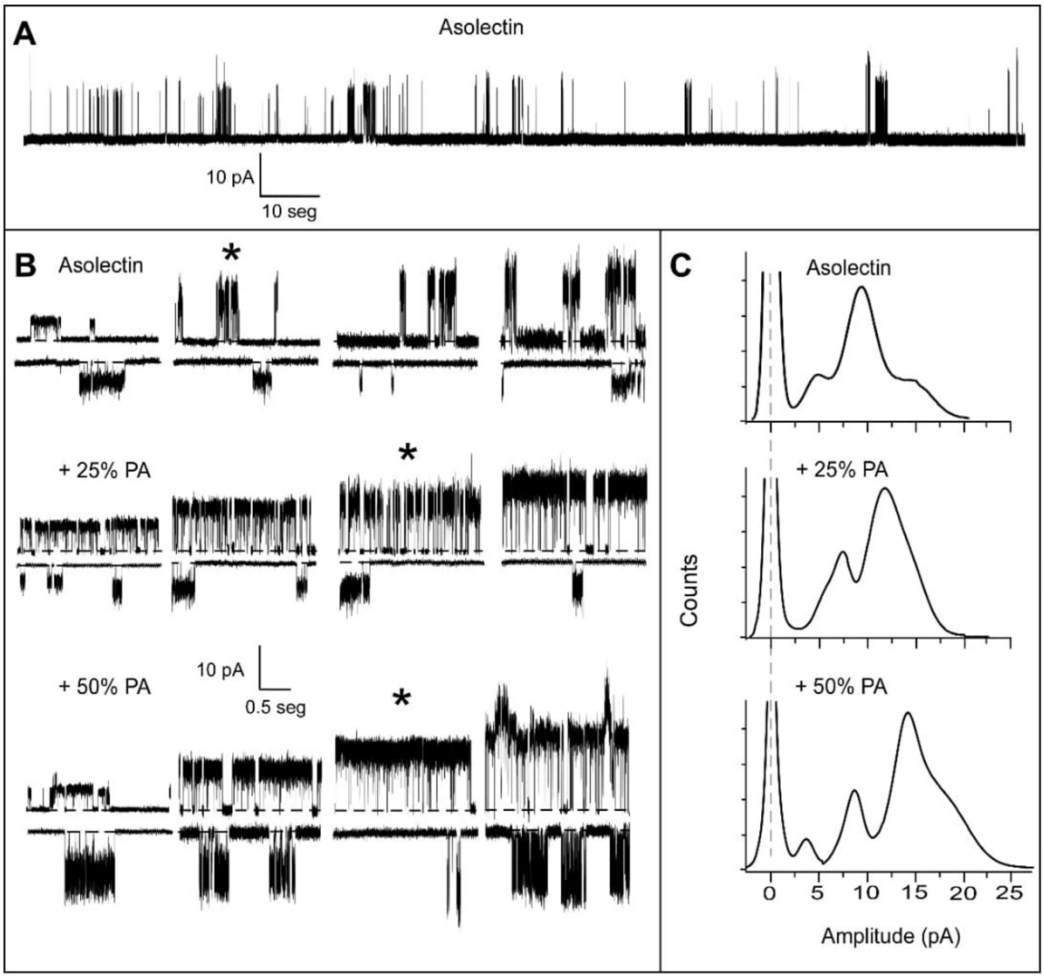

Figure 3. Effect of the anionic phospholipid lipid PA on wild-type KcsA single channel currents. Panel A shows a long, representative recording taken at +150 mV from a membrane patch containing wild-type KcsA reconstituted in plain asolectin lipids. The recording serves to illustrate heterogeneous bursts of channel activity with different amplitudes throughout. Out of that heterogeneity, panel B shows in more detail shorter recordings of the different currents at +150 and -150 mV found for the wild-type channel reconstituted in plain asolectin lipids (upper traces) or in asolectin supplemented with 25% (mid traces) or 50% (lower traces) PA. The asterisks indicate the prevalent, most frequently found current for each experimental condition. Panel C shows the amplitude histograms for the currents found under the different reconstitution conditions from above and illustrates that the amplitude of the most frequently found currents increases as the percentage of added PA is increased. The histograms shown are the summation of 9 to 15 individual histograms from different samples.

As to the recordings taken at negative potentials (Figure 3B, lower traces in upper panel), it is observed that channel openings are scarce, very noisy and quite heterogeneous in terms of current intensity, which is in agreement with previous reports (LeMasurier et al., 2001; Chakrapani et al., 2007a) and precluded further analysis.[34,50]

Figure 3 also shows that adding PA to the reconstituted asolectin lipid bilayer has two main effects on the single-channel recordings taken at +150 mV. Figure 3B, midle and lower traces, show that although the heterogeneity in the population of currents is still maintained in presence of added PA, the predominant currents are now those with higher amplitudes. Indeed, 12 pA (80 pS) and 15 pA (100 pS) are now the most frequently observed currents in 25% and 50% added PA, respectively (Figure 3C). Such predominant currents still maintain the rectification seen in plain asolectin, regardless of the PA content (Figure 4). Second and most noticeable, addition of PA to the reconstituted matrix, either at 25% or 50% with respect to the asolectin lipids, causes a large increase in the open probability ($NP_0 \geq 0.8$). This has been observed previously[6,7,51] and seems consistent with the marked decrease in the inactivation rates seen in the above recordings from macro-patches. Finally, the lower traces in Figure 3B show that at negative potentials, the addition of PA to the reconstituted bilayer produces only small changes relative to the asolectin control sample. The observed currents remain heterogeneous and the openings are very noisy and maintain a low open probability. At these negative potentials, the only parameter affected by PA addition in a somewhat clear manner is the intensity of the prevailing current, which is enhanced in the sample containing the highest amount of PA tested.

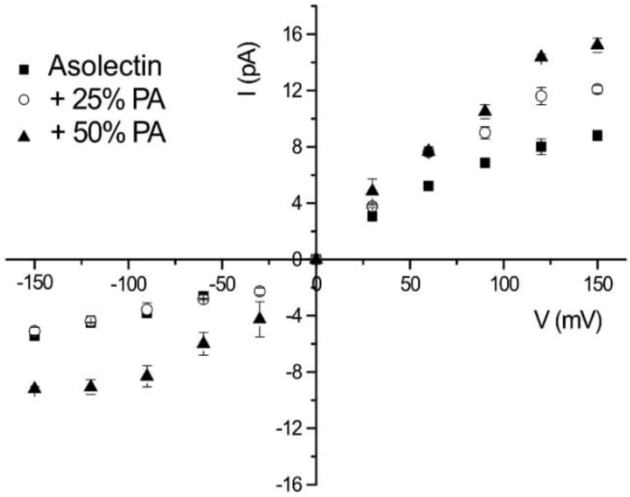

Figure 4. I/V curves of wild-type KcsA single channel currents. The figure shows the I/V curves for the most frequently found currents under the different reconstitution conditions specified in Figure 3. In addition to the already mentioned increase in current amplitude caused by the added PA, the figure shows that the rectification seen in plain asolectin remains regardless of the added PA content. Data points and error bars are the average and s.e.m. of 10 to15 different samples.

The KcsA arginine to alanine mutants (Figure 5) show a much higher open probability at positive voltages compared to the single channel recordings from the wild-type channel, regardless of whether or not different amounts of PA were added to the asolectin lipid matrix. Again, this seems consistent with the marked decrease observed in the inactivation rates of these mutants (Figure 2). As in the wild-type channel, the mutants also exhibit a high degree of

heterogeneity in the observed potassium currents (not shown). Figure 5 shows that the prevailing currents in these mutant channels exhibit higher amplitudes than those of the wild-type channel in asolectin. Such an increase in the current amplitudes resemble that observed when PA is added to the asolectin matrix containing the wild-type channel (Figure 3C). Nonetheless, in contrast to the wild-type channel, addition of PA to the reconstituted mutants results in little (only in the R64A-KcsA mutant) or no effects on further increasing the amplitudes of the most frequently observed currents which, additionally, show now an essentially ohmic behavior (Figure 5).

As to the observations at negative voltages in the arginine mutants, the recordings maintain a pattern similar to that of the wild-type, being essentially undistinguishable among the different mutants and remaining practically unaltered when PA was added to the reconstituted lipid matrix (Figure 5, lower traces in each panel).

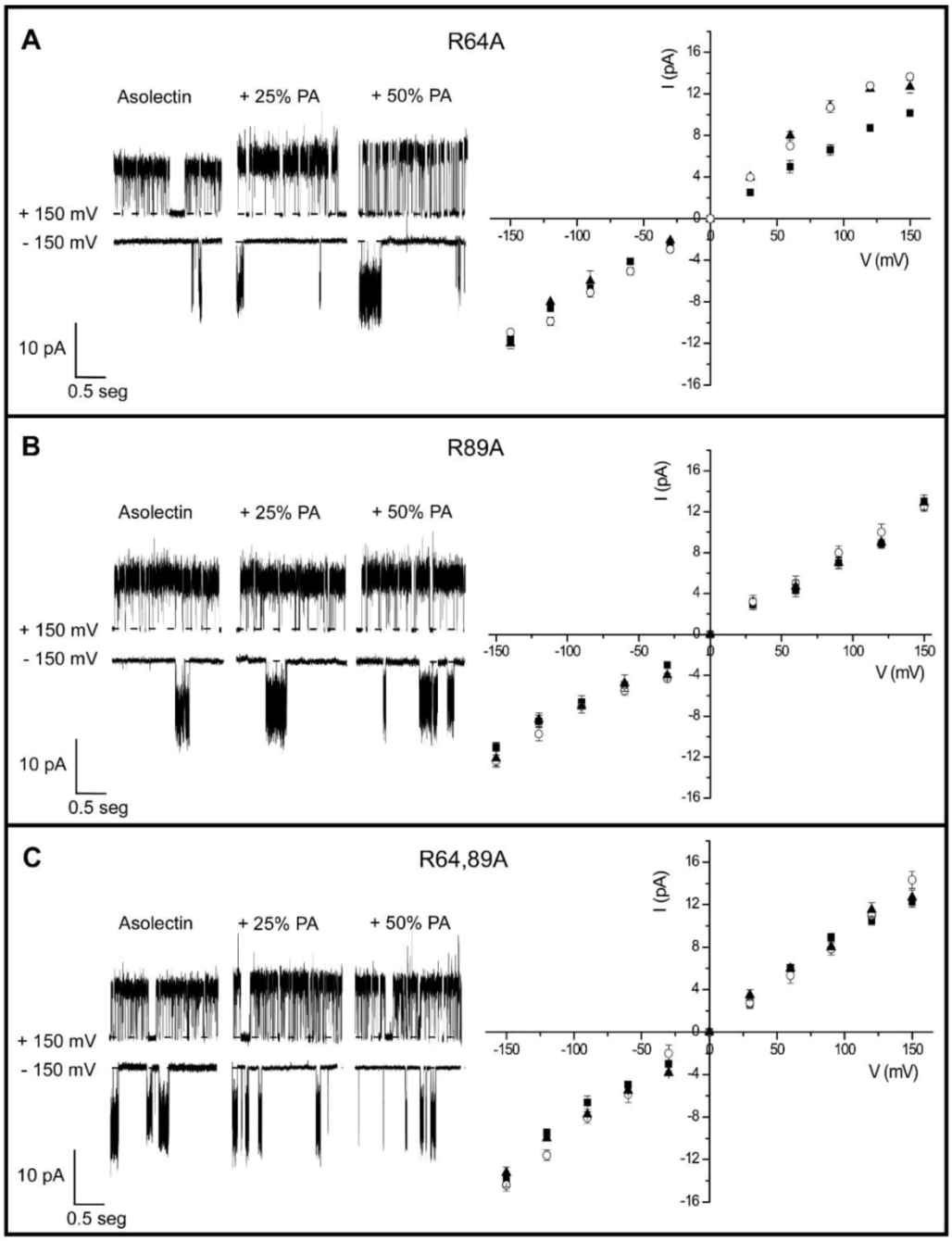

Figure 5. Effects of added PA on single channel currents from arginine to alanine mutants of KcsA reconstituted in asolectin lipids. Only the most frequently found, prevalent current from the recordings of each of the mutants at +150 and -150 mV are included in the figure. Compared to the wild-type channel in plain asolectin in Figure 3B, all arginine to alanine mutants exhibit much higher open probabilities and higher amplitudes. Also, in contrast to the wild-type channel, addition of 25 or 50% PA to the reconstituted bilayers results in little (only in the R64A-KcsA mutant at positive voltages) or no effects on further increasing the current amplitudes. Moreover, I/V curves to the right in each panel show an essentially ohmic behavior for all three mutants. Symbols used in this Figure are as in Figure 4. Data points and error bars are the average and s.e.m. of 10 to 15 different samples.

Gating kinetics

In an attempt to further characterize the effects of PA on channel activity and the role of the non-annular arginines in this process, an analysis of the kinetic behavior of KcsA at the single-channel level under steady-state inactivation conditions, at pH 4, was performed. Gating kinetics of wild-type KcsA is highly complex and its underlying mechanisms are not yet well understood.[35] There are different patterns of bursts and a large variation in the open probability and mean open and closed times from patch to path.[34,52] Additionally, the low open probability under steady-state inactivation conditions makes it difficult to know the exact number of channels present in the patch. To partly circumvent these issues, kinetic analysis was restricted to isolated bursts, which most likely correspond to single channel activity, from the prevailing current in the continuous recordings. Moreover, such intraburst activity has been associated to conformational fluctuations at the selectivity filter (outer gate), independently of inner gate events,[35] which facilitates the interpretation of the results. Finally, the analysis was confined to recordings obtained at +150 mV, both because this is the condition used in the inactivation experiments and also because at this potential the channel showed the larger open probability and the effect of lipids was more pronounced, as shown above.

The kinetic analysis for all the samples follows the approach used by Chakrapani and coworkers.[35] Once the appropriate τ_{crit} (see Materials and Methods) was obtained, bursts were isolated and classified according to their intraburst open probability into low (LPo; Po<0.4), intermediate (0.4<Po<0.8) and high modes (HPo; Po>0.8). In order to study a more homogenous population, the kinetic analysis was further restricted to the open and close dwell-time histograms of HPo isolated bursts, which indeed are the most frequently observed. Relative to the distribution of closed lifetimes, Figure 6 shows that similarly to previous reports on the wild type channel in asolectin, it can be reasonably described by two components, which were assigned to a flickering and an intermediate short-lived inactivated states that KcsA would enter once it opens by acidic pH and from which the channel would recover quickly.[35] Also, Figure 6 shows that the open lifetime histogram in this case can be described by just a single component.[35,52] When comparing these data with those from the arginine to alanine channel mutants or from the wild-type channel in presence of PA, the most noticeable change detected in the histograms refers to a shift observed in the distribution of open events to longer lifetimes, which seems consistent with the slower inactivation exhibited by all these samples. To quantify these changes, the events within the bursts were fit to a kinetic model consisting of the above two closed states (the flickering and the intermediate) and one open state (Chakrapani et al., 2007a), according to:

$$I_f \underset{k_f}{\overset{k_{-f}}{\rightleftharpoons}} O \underset{k_{-i}}{\overset{k_i}{\rightleftharpoons}} I_i$$

where O represents the open state, I_f and I_i are the inactivated flickering and intermediate states and k_f, k_i, k_{-f} and $k_{-i,}$ are the corresponding closing and opening rate constants, respectively. The

solid lines on top of the histograms in Figure 6 shows that such kinetic model fits reasonably well to the experimental data. Moreover, the right column in Figure 6 shows that the closing rate constants, k_f and k_i, estimated from the fits, are clearly diminished in the wild-type channel with added PA or in the arginine channel mutants relative to that of wild-type-KcsA in asolectin. These changes seem consistent with the observed increase in the mean open time (Figure 6, right column), and with the decrease in the rate of inactivation in those samples (Fig. 2).

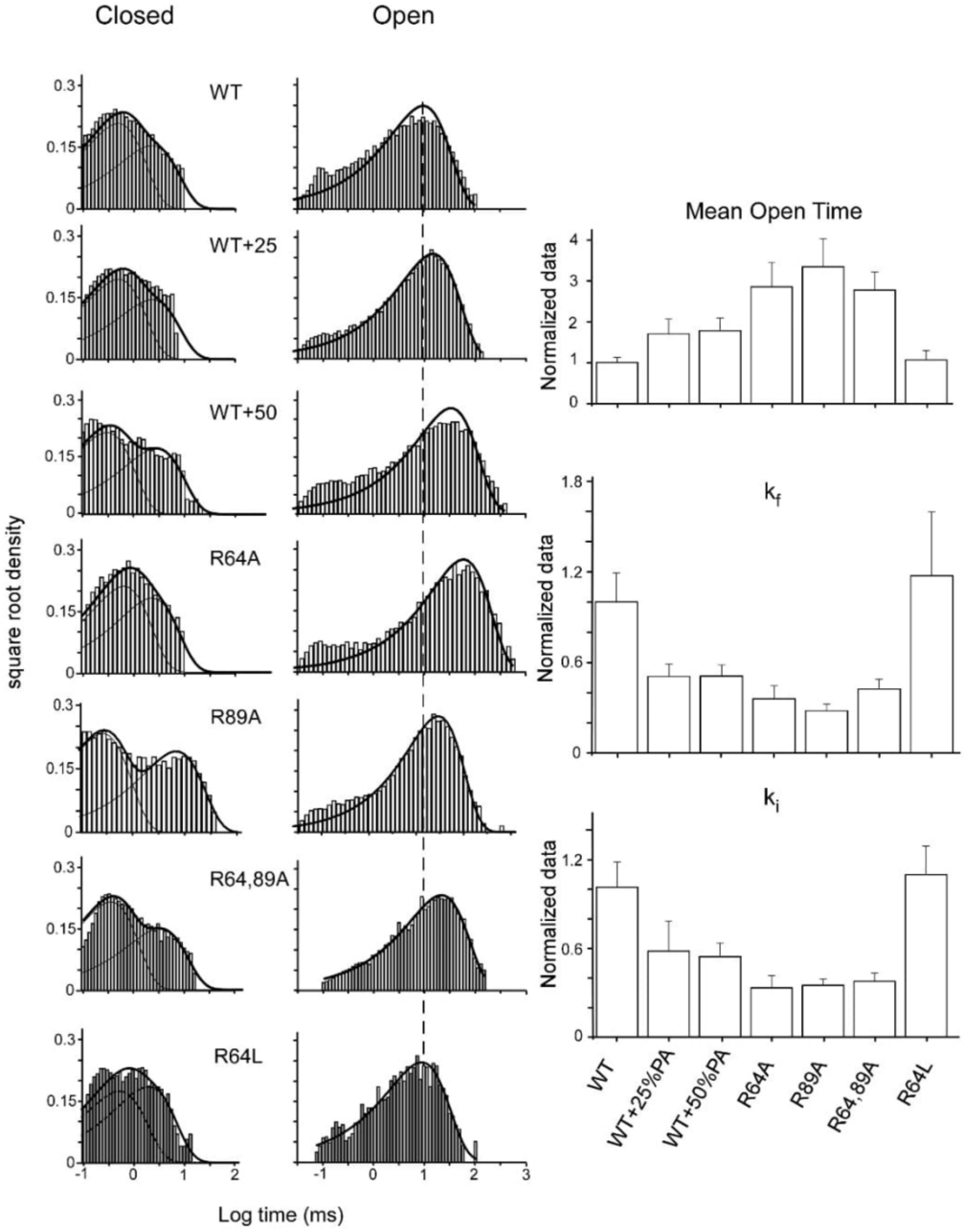

Figure 6. Kinetic behaviour of KcsA is modulated by PA and non-annular arginine mutations (A) Representative dwell time distribution of closed and open events within bursts identified using t_{crit}, (see Methods section). The solid line denotes the density function calculated by fitting the data to two closed and one open state model (see text). (B) Kinetic parameters derived from

the above fitting. k_f and k_i refer to the flickering and intermediate closing rate constants, respectively (see text). Data are the mean values ± s.e.m. of 4 to 7 different samples.

Side chain charge versus size in determining the behavior of arginine mutants

From the above results it follows that mutation to alanine of any of the two non-annular arginines strongly alters the activity pattern of KcsA and minimizes the effects of PA seen on the wild-type channel. Being a positively-charged residue, it is tempting to assume that it is the loss of such charges that determines the behavior of the arginine mutants. Nonetheless, an arginine to alanine mutation changes not only the charge, but also the size of the side chain to the much shorter alanine, which might bear on the mobility of such residue within the protein structure or on its ability to reach out for interacting counterparts. Thus, we prepared R64L and R89L-KcsA mutants, since the leucine side chain is also non-charged, but larger than that of alanine. Unfortunately, only the R64L mutant could be expressed as a tetrameric channel protein in our expression system and therefore, the experiments that followed were done only with this latter channel. Figure 7A shows that in sharp contrast to the arginine to alanine mutants, the R64L mutant inactivates quite rapidly as evidenced in macro-patch recordings, in a manner practically undistinguishable to that seen in the wild-type channel. Moreover, addition of PA to the asolectin lipid matrix does not modify appreciably the observed inactivation rate. Single-channel experiments also show that the R64L mutant has an activity pattern similar to that of the wild-type channel (Figure 7B), i.e., characterized by a low open probability. Moreover, kinetic analysis of the R64L mutant channel, also included in Figure 6 to facilitate comparison, yields short opening times and high closing rate constants, essentially identical to those of the wild-type channel. It should be emphasized that R89 is still present in the R64L mutant and therefore, all the effects reported for this mutant are due to the substitution by leucine of just a single arginine residue.

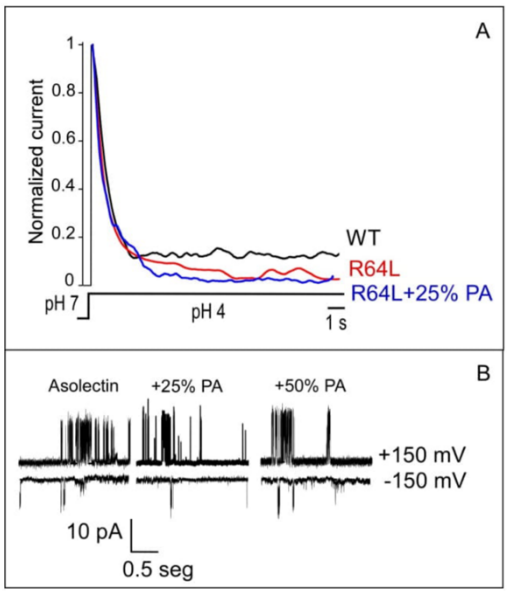

Figure 7. Salient features of R64L-KcsA mutant K^+ currents. Panel A shows normalized macroscopic currents at a holding potential of +150 mV from fast pH jumps (pH 7 to 4) in macropatches containing the mutant channel reconstituted in plain asolectin lipids with or without added PA. The behavior of the wild-type KcsA channel reconstituted in plain asolectin under comparable experimental conditions, has been added for comparison. Each trace is the average from three different experiments. Panel B shows representative single channel recordings at +150 and -150 mV of the prevalent current from this mutant channel reconstituted in plain asolectin with or without added PA.

NMR measurements of phospholipid binding

The interaction between PA and the KcsA channel was further investigated using NMR spectroscopy in detergent-solubilized samples. NMR is a suitable technique to determine intermolecular interactions with atomic resolution and a ^{15}N-labeled sample of KcsA was used to monitor the NHε moiety of the guanidino group of the arginine side chains, whose chemical shift is located in a particularly clean region of the ^{1}H,^{15}N-HSQC (Figure 8, blue contours). Actually, this region is very crowded, consistent with the abundant Arg residues that belong to the KcsA channel. The two terminal R189 and R190 are more flexible and they are tentatively assigned to the most intense signals of the spectrum, while R89 and R64 are unequivocally assigned after recording the ^{1}H,^{15}N-HSQC spectra of the R89A- and R64A-KcsA mutant channels. Addition of PC does not cause noticeable chemical shifts of any of the spectral signals. On the contrary, the presence of added PA results in significant chemical shifts affecting several arginine side chains. Remarkably, R64 shifts about 0.5 ppm in the ^{15}N dimension, reflecting a change in the chemical environment of the residue as a consequence of interaction with the anionic phospholipid. Due to signal overlap, R89 cannot be equally monitored.

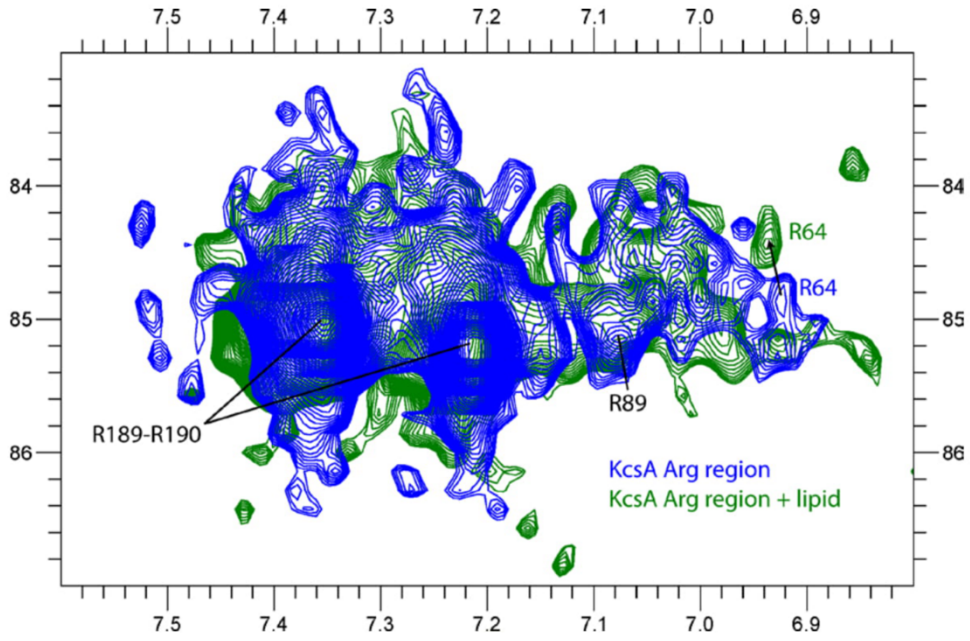

Figure 8. Solution NMR spectroscopy. Guanidino region of the $^{1}H,^{15}N$-HSQC spectra of detergent-solubilized wild type KcsA in the absence of any ligand (blue contours) and in the presence of three equivalents of PA (green contours). The assigned residues are indicated in black arrows.

Structural basis of lipid modulation of KcsA inactivation

The KcsA channel filter is comprised of four ion-binding sites, formed by a tetrameric arrangement of backbone carbonyl atoms of residues T75 to G79, in addition to the side-chain of T75, and an external site. The canonical conformation of the selectivity filter is stabilized by H-bonding with surrounding amino acids. Residues Y78 (selectivity filter) and D80 (pore loop) H-bond with residue E71 (pore helix), whilst D80 also H-bonds with W67. Structured water molecules also contribute to the structural integrity of this region. W67-Y78-D80 have been termed the "inactivation triad" in view of their critical role in this process.[15] Our attentions are focused towards the molecular behaviour of this region in order to understand the initial steps of the inactivation process, and how membrane lipids may be involved.

MD simulations of KcsA in a closed state (PDB 1K4C) were performed in zwitterionic (PC) and mixed zwitterionic/anionic (PC/PA) lipid bilayers. Such lipid bilayers are expected to yield a non-functional (PC) and a functional (the PA/PC mixture) KcsA channel, respectively, upon reconstitution of the purified protein. At the outset, simulations were initiated from a random lipid configuration (see Methods), denoted ^{n}WT-PA or ^{n}WT-PC where n indicates the replica. Over the course of these simulations, performed in duplicate, both zwitterionic and charged lipid molecules were observed to occupy a non-annular binding site, on the interface between two adjacent subunits. The cleft is lined with hydrophobic residues from TM1 (L40), the pore helix (P63, L66 and W67) and TM2 (L86, C90 and V93), with the lipid headgroup capable of interacting with charged and polar residues in the immediate locale (T61, R64 and R89). The

observed site is in agreement with those previously postulated by computation,[6,23,24] and regions of electron density assigned as lipid molecules in crystal structures of KcsA.[22] On account of this, additional simulations were performed with lipids bound into the four identical non-annular binding sites, denoted ^{n}WT-PA4 or ^{n}WT-PC4, where n indicates the replica. The binding pose used for each lipid was extracted from the most highly populated cluster observed in the replica 1 and docked into each site. Marius and coworkers previously posited that occupancy of at least three sites was obligatory for KcsA activation by anionic lipid PG, giving credence to the initial model utilized here.[6] A summary of all the simulations performed can be found in Table 1.

Table 1. Summary of simulations performed

System	Bilayer Composition	Notation	Non-Annular Lipids?	Replica	Length (ns)
WT	PA/PC	WT-PA	N	1	400
				2	200
		WT-PA_4	Y	1	400
				2	200
				3	200
				4	150
				5	150
	PC	WT-PC	N	1	400
				2	200
		WT-PC_4	Y	1	400
				2	200
				3	200
				4	150
				5	150
R64A	PA/PC	R64A-PA	N	1	100
		R64A-PA_4	Y	1	250
	PC	R64A-PC	N	1	100
		R64A-PC_4	Y	1	250
R64L	PA/PC	R64L-PA	N	1	100
		R64L-PA_4	Y	1	250
	PC	R64L-PC	N	1	100
		R64L-PC_4	Y	1	250
R89A	PA/PC	R89A-PA	N	1	100
		R89A-PA_4	Y	1	200
	PC	R89A-PC	N	1	100
		R89A-PC_4	Y	1	200

Striking differences in the inactivation triad environment are observed on comparison of the WT (wild type) channel when non-annular lipids are present, relative to when they are absent (Figure 9). In the first replica of the simulation of the wild type KcsA in the PA membrane, ^{1}WT-PA, persistent H-bonds are formed between non-annular arginine R89, and triad residue D80 for between ~40-80% of the simulation in all tetramer subunits (Figure 9A and Figure S1). In contrast, in WT-PA_4 simulations, the equivalent interaction frequency reaches a maximum of ~20% in all subunits. This can be attributed to preferred H-bonding between R89 and the negatively charged PA headgroup in the adjacent site. Bound PA typically exhibits a stable and persistent binding pose is observed in which an ester oxygen atom at the apex of an acyl chain H-bonds to R89, whilst the phosphate oxygen atoms of the headgroup H-bond to R64. The

frequency of these H-bonds is generally in excess of 80% in at least three non-annular sites. Moreover, phosphate oxygen atoms are also capable of simultaneously H-bonding T61, and the T61-PA H-bond frequencies are observed to be between 50-60% (Table S1). Overall, each non-annular lipid is involved in approximately 2.5 H-bonds at one time.

In contrast, the H-bond frequencies between zwitterionic lipid, PC, and the equivalent protein residues are highly variable (T61 0-80%, R64 40-90% and R89 30-90%). In three out of five replicas, the proposed D80-R89 interaction is absent (H-bond frequency < 20%) in all subunits; in the remaining two replicas, this interaction is predominant (H-bond frequency > 50%) in one or two subunits. Representative examples of both scenarios are shown in Figure 9B. In the latter case, these instances correlate with diminished H-bonding with PC. It is therefore more probable that the D80-R89 interaction will form when the non-annular lipid species is PC rather than PA. The two possible scenarios described are shown in Figure 9A and B.

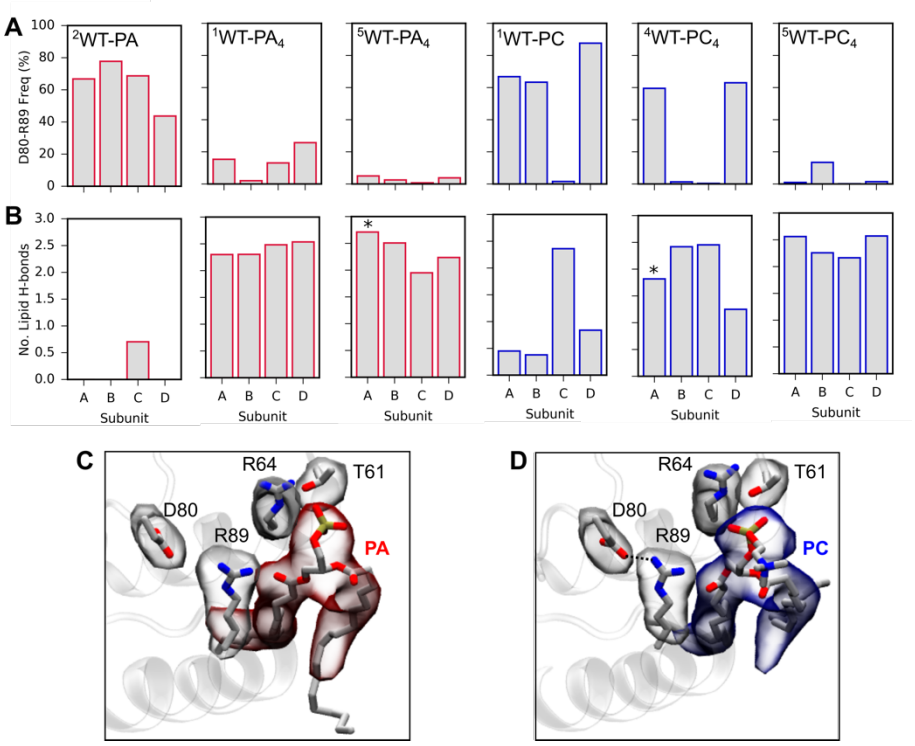

Figure 9. (A) D80-R89 interaction frequency in WT-KcsA simulations. (B) Average number of lipid H-bonds in WT-KcsA simulations, calculated using a 3.5 Å distance cutoff between polar atoms and 35° cutoff for the acceptor-donor-hydrogen angle. (C) Dominant H-bond configuration of non-annular PA, which disrupts D80-R89 interactions. (D) Example of a H-bond scenario where D80 and R89 interact in spite of bound PC. For (C-D) the simulation and subunit shown is marked with an asterisk in (A-B). Data for the remaining simulations can be found in Figure S1.

To test this hypothesis, the equivalent simulation protocol was utilized for KcsA mutants R64A and R64L, and the prevalence of the D80-R89 H-bond was monitored in the resulting trajectories (Figure 10A). On all accounts, the H-bond frequency, averaged over all subunits,

was fewer in the KcsA-R64A simulation than the corresponding KcsA-R64L simulation, corroborating our proposal. This effect can be ascribed to the bulkiness of the leucine sidechain, which induces a shift in R89 towards D80, demonstrated in Figure 10A. Furthermore, the D80-R89 H-bond frequency was attenuated to the greatest extent when non-annular lipids are bound.

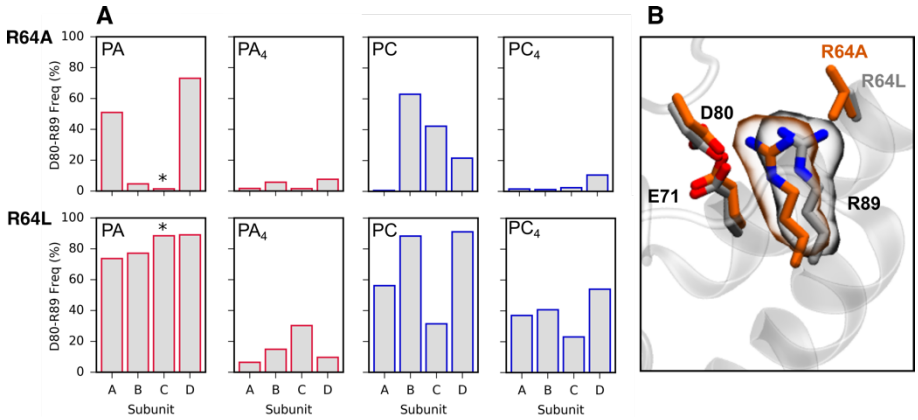

Figure 10. (A) D80-R89 hydrogen bond frequency in R64A-KcsA and R64L-KcsA simulations. (B) Depiction of opposing scenarios in R64 mutant channels. The specific simulation and subunit shown is marked with an asterisk in (A).

When the arginine at position 89 is mutated to alanine, an alternative scenario is presented. In this case, the removal of arginine, can destabilize the conformation of W67, resulting in its detachment from D80. This movement coincides with the breakage of the E71-D80 H-bond, culminating in complete disruption of the inactivation triad (Table 2). This can be attributed to the negligible size of the alanine side-chain, suggesting the residue at position 89 is important to reinforce the conformation of the inactivation triad and maintain its stability. This effect is observed irrespective in neutral and anionic lipid bilayers, with and without bound non-annular lipids.

Table 2. Lifetime of inactivation triad, calculated as the period of time when both triad interactions (W67-D80) are intact.

Simulation	Lifetime (ns)			
	A	B	C	D
R89A-PA	100	30	33	59
R89A-PA_4	200	1	34	88
R89A-PC	14	11	100	00
R89A-PC_4	52	55	5	50

In addition to the effects described on the inactivation triad, it is interesting to note that there are instances in the WT channel where water molecules can access the region behind the selectivity filter. Entrance of water molecules is initiated by separation of W67 and L81 (Table 3), which are in close contact in the crystal structure. This pathway can remain open with time enabling frequent in and out water transitions or close after a short period, trapping water molecules. Considering R64 and W67 interact closely with both L81 and non-annular lipids, it is

conceivable that non-annular lipids may modulate the conformational freedom of L81, and hence acts as a tap, governing water accessibility to this region.

Table 3. Frequency of W67-L81 opening in simulations with the wild type KcsA. It should be noted that each replica has a different simulation time, see Table 1.

Simulation	W67-L81 Open Frequency (%)			
	A	B	C	D
[1]WT-PA	77	14	66	42
[2]WT-PA	0	1	24	47
[1]WT-PA_4	2	14	8	0
[2]WT-PA_4	26	3	30	0
[3]WT-PA_4	1	10	2	7
[4]WT-PA_4	0	2	4	3
[5]WT-PA_4	1	22	48	38
[1]WT-PC	0	31	2	0
[2]WT-PC	25	0	11	0
[1]WT-PC_4	0	65	30	50
[2]WT-PC_4	1	4	3	1
[3]WT-PC_4	2	7	1	8
[4]WT-PC_4	0	68	3	4
[5]WT-PC_4	3	5	90	13

Discussion

This work aims to shed further light on the modulation of KcsA function by anionic lipids and to decipher the role on such process of the so called non-annular arginine residues, R64 and R89. Our results show that addition of the anionic lipid PA to the asolectin lipid matrix containing the reconstituted KcsA drastically changes the behavior of the wild-type channel at the single-channel level, causing a slowdown of the closing rates and consequently, an increase in the mean open time and the open probability. Such alterations would be expected to result in a decrease in the channel inactivation rate, as it is indeed observed experimentally in our macroscopic current measurement in presence of added PA.

Effects akin to those are observed when either one or the two arginines are mutated to alanine, in the absence of added anionic lipids. Studies using the single arginine to alanine mutants (R64A or R89A-KcsA) show that a single arginine is not enough to retain the inactivation features of the wild type channel and thus arginines at both positions are required for that purpose. In stark contrast with this, the arginine to leucine R64L mutant shows that the bulkier leucine side chain, although uncharged, could substitute R64 in maintaining the inactivation features of the wild-type channel. This suggests that the interactions leading to alteration of the channel inactivation features by the arginines are to some extent non-electrostatic in nature. Moreover, in spite of their different behaviour, neither the arginine to alanine mutants, nor the R64L mutant show additional alterations in the inactivation rate when in the presence of anionic phospholipids.

In line with previous postulates referred in the Introduction,[10,20,21,23,26] we interpret our electrophysiological results of the WT channel as a consequence of electrostatic interactions between the arginines and anionic lipids bound to the non-annular sites. This receives support

from NMR data which unequivocally demonstrates that at least R64 is specifically involved in binding the anionic PA. Although it should be noted that this experimental system consisted of detergent-solubilized protein and added lipid. Moreover, our MD simulations predict that R64, R89 and other surrounding residues such as T61, are involved in persistent binding of the anionic phospholipid head group to the non-annular sites.

Since channel inactivation is considered to be controlled by the inactivation triad, it is expected that the specific binding of charged phospholipids, affects the inactivation triad in some manner, either directly or indirectly. This notion is supported by evidence that the mutation of residues constituting the triad[13,15] results in a slowdown of the inactivation process very similar to that reported here when anionic lipids are present and the arginines are mutated to alanine. Our MD simulations reveal that non-annular lipids are pivotal to the inhibition of direct D80-R89 interactions. Moreover, our simulations of the R64A and R64L bolster opposing effects, with regards to D80-R89, in keeping with the divergent inactivation rates reported in this study. With this in mind, we advocate that the attachment of R89 to D80, strengthens the E71-D80 bond, which is conducive to KcsA inactivation.

This is in accord with prior MD simulations of KcsA with anionic lipid PG,[26] conflicting with alternative proposals that simple electrostatic attractions between potassium ions and anionic phospholipids increase the potassium concentration locally and cause the observed larger currents.[53,54] Unorthodoxly, the simulations disclose that the inactivation triad is completely disrupted in the R89A mutant, due to the absence of stabilizing interactions between the bulky arginine side-chain and the tryptophan ring typically in position 67. Therefore, this data provides evidence that both the size and charge of both non-annular arginines are critical to the configuration of the inactivation triad, and hence the inactivation rates of KcsA.

Since the non-annular arginines appear as the relevant sites for the functional modulation of the KcsA channel by anionic phospholipids, it should be taken into account that there are four equivalent, non-annular lipid binding sites per channel and a pertinent question would be, how many of such sites need to be occupied by the bound lipids to exert their effects on the inactivation rate? Previous proposals suggest that occupation of at least three equivalent non-annular sites is necessary for channel opening,[6] although the differences in experimental conditions makes difficult the extrapolation to our system. Furthermore, coarse-grained simulations observed minimal binding affinity to a single site when the remaining three sites are occupied, suggesting occupation of three sites is optimum.[26]We observed saturation of the lipid effects on inactivation at 25% of PA added to the asolectin matrix, but the asolectin lipids themselves already contain an approximately 10% of different anionic lipids,[55] plus those retained bound at the non-annular sites of KcsA upon its purification. In our simulated bilayers used for the MD study, the four non-annular sites in each channel remain lipid-bound during the time course of the simulation. However, it is possible that on extended timescales, expulsion of phospholipid molecules from some of such sites could take place. Indeed, although speculative,

our simulation results insinuate that full occupancy of non-annular sites may not be required, considering zwitterionic phospholipid PC is also capable of perturbing the D80-R89 interaction, albeit to a lesser extent.

Finally, we consider the surmised water access pathway between the extracellular solution and region containing the inactivation triad. The relevance of water molecules behind the KcsA selectivity filter has earned significant interest in recent years. Extensive unbiased MD simulations of the low K^+ structure (PDB 1K4D) revealed the containment of three structured water molecules buried behind the selectivity filter, as the principal determinant in the slow recovery rate of the pinched structure of the KcsA selectivity filter, considered as a non-conductive, 'C-type inactivated' state.[17] The timescales of water release and re-entry vary by an order of magnitude, reported as ~10-15 μs and ~80-100 ns respectively, with access governed by Y82 in this case. Long residence times were later confirmed by solid state NMR.[56] Moreover, the observed structured water network was resolved in the recent high-resolution structure of the fast-inactivating KcsA-Y82A mutant, which displays accelerated C-type inactivated gating (Cordero-Morales et al., 2006b),[13] confirming the importance of these molecules in the magnitude and rate of inactivation and the role of Y82 in this process.[57] Considering these results and the data presented in this manuscript, it is tempting to speculate that both L81 and Y82 can act independently to govern water access to the cavity behind the selectivity filter. Moreover, the proposed relevance of interactions at the extracellular loops on the ion conduction properties of KcsA has received support from a previous report on this matter.[58] Moreover, probing the effects of anionic lipids on the stability of KcsA functional states,[51] the same authors provided evidence that the lipid-protein-interface at this region is critical in stabilizing the open-activated channel structure.

The overall conclusion from the above paragraphs is that the inactivation properties of KcsA are determined by the interaction between the inactivation triad with the non-annular arginines. The presence of phospholipids bound at non-annular sites, can prevent such interactions, providing the molecular basis of how lipids modulate channel inactivation. It should be noted, however, that this proposal is based on the comparison between macroscopic inactivation and single-channel measurements made at an acidic pH and at a positive holding potential, and data from MD simulations, which are obtained at neutral pH and in the absence of any electrical gradient, based on KcsA crystals obtained in analogous conditions. In fact, single channel recordings at negative voltages from both the wild-type channel and arginine to alanine mutants, in the presence of added PA, are similar to those from wild-type channel in plain asolectin, i.e. very few and short apertures, consistent with the maintenance of fast inactivation under these conditions. This can be rationalized by considering that at hyperpolarizing potentials the E71-D80 interaction is enhanced, as a result of the voltage-dependent orientation of the E71 residue,[59] D80 or R89, considering the results present here. It is worth noting, the only reported case in which inactivation at negative voltages can be removed is that of the E71A mutant.[59]

The prokaryotic KcsA is often considered a simplified version of eukaryotic potassium channel counterparts and therefore, we search for similarities at putative non-annular lipid binding sites in different eukaryotic channels. An equivalent to R89 is conserved in many K^+ channels (mostly as either an arginine or a lysine), but that equivalent to R64 is conserved only in a few instances, such as the human Kv5.1 channel, where a glutamine residue is found at that position.[60] Thus, it is conceivable that some eukaryotic potassium channels should be able to bind anionic phospholipids to these sites and behave similarly to KcsA in terms of its functional modulation.

In summary, our tenet is that the type of phospholipid headgroup bound at the non-annular KcsA sites determines the conformation of R89. To be more specific, non-annular lipids hinder formation of direct interactions between D80 and R89 bond in WT KcsA, which directly affects the efficaciousness of the inactivation triad, hence impeding the initial steps of inactivation. According to the MD simulations, anionic lipids (PA) bind securely to non-annular sites, as a result of persistent H-bonding with T61, R64 and R89, stubbornly inhibiting this interaction. On the other hand, the H-bonding attributes of zwitterionic lipids (PC) are more variable, and thus the interaction is more likely to form. Functionally, these predictions are likely to explain the observed decrease in the selectivity filter closing rate and increase of the mean open time observed experimentally, when the concentration of PA is increased in WT systems. This hypothesis is supported by simulations of R64-KcsA mutants, which exert opposing effects on conformation of R89, in agreement with the electrophysiological results demonstrating paradoxical inactivation profiles. Overall, our results reveal the critical role of non-annular arginines in the KcsA inactivation process, by the coordinated binding of non-annular lipids.

References

(1) Lee, A. G. How lipids affect the activities of integral membrane proteins. *Biochim. Et Biophy. Acta-Biomembranes* **2004,** *1666* (1-2), 62.

(2) Marsh, D. Protein modulation of lipids, and vice-versa, in membranes. *Biochimica Et Biophysica Acta-Biomembranes* **2008,** *1778* (7-8), 1545.

(3) Phillips, R.; Ursell, T.; Wiggins, P.; Sens, P. Emerging roles for lipids in shaping membrane-protein function. *Nature* **2009,** *459* (7245), 379.

(4) Poveda, J. A.; Giudici, A. M.; Renart, M. L.; Molina, M. L.; Montoya, E.; Fernandez-Carvajal, A.; Fernandez-Ballester, G.; Encinar, J. A.; Gonzalez-Ros, J. M. Lipid modulation of ion channels through specific binding sites. *Biochim. Et Biophy. Acta-Biomembranes* **2014,** *1838* (6), 1560.

(5) Poveda, J. A.; Giudici, A. M.; Renart, M. L.; Morales, A.; Gonzalez-Ros, J. M. Towards understanding the molecular basis of ion channel modulation by lipids: Mechanistic models and current paradigms. *Biochim. Et Biophy. Acta-Biomembranes* **2017,** *1859* (9), 1507.

(6) Marius, P.; Zagnoni, M.; Sandison, M. E.; East, J. M.; Morgan, H.; Lee, A. G. Binding of anionic lipids to at least three nonannular sites on the potassium channel KcsA is required for channel opening. *Biophys. J.* **2008,** *94* (5), 1689.

(7) Iwamoto, M.; Oiki, S. Amphipathic antenna of an inward rectifier K+ channel responds to changes in the inner membrane leaflet. *P. Natl. Acad. Sci. USA* **2013,** *110* (2), 749.

(8) Raja, M.; Spelbrink, R. E. J.; de Kruijff, B.; Killian, J. A. Phosphatidic acid plays a special role in stabilizing and folding of the tetrameric potassium channel KcsA. *Febs Let.* **2007,** *581* (29), 5715.

(9) Raja, M. The Role of Extramembranous Cytoplasmic Termini in Assembly and Stability of the Tetrameric K^+-Channel KcsA. *J. Memb. Biol.* **2010,** *235* (1), 51.
(10) Triano, I.; Barrera, F. N.; Renart, M. L.; Molina, M. L.; Fernandez-Ballester, G.; Poveda, J. A.; Fernandez, A. M.; Encinar, J. A.; Ferrer-Montiel, A. V.; Otzen, D.et al. Occupancy of Nonannular Lipid Binding Sites on KcsA Greatly Increases the Stability of the Tetrameric Protein. *Biochemistry* **2010,** *49* (25), 5397.
(11) Barrera, F. N.; Renart, M. L.; Poveda, J. A.; De Kruijff, B.; Killian, J. A.; Gonzalez-Ros, J. M. Protein self-assembly and lipid binding in the folding of the potassium channel KcsA. *Biochemistry* **2008,** *47* (7), 2123.
(12) Bhate, M. P.; McDermott, A. E. Protonation state of E71 in KcsA and its role for channel collapse and inactivation. *P. Natl. Acad. Sci. USA* **2012,** *109* (38), 15265.
(13) Cordero-Morales, J. F.; Cuello, L. G.; Zhao, Y. X.; Jogini, V.; Cortes, D. M.; Roux, B.; Perozo, E. Molecular determinants of gating at the potassium-channel selectivity filter. *Nat. Struct. Mol. Biol.* **2006,** *13* (4), 311.
(14) Cordero-Morales, J. F.; Jogini, V.; Lewis, A.; Vasquez, V.; Cortes, D. M.; Roux, B.; Perozo, E. Molecular driving forces determining potassium channel slow inactivation. *Nat. Struct. Mol. Biol.* **2007,** *14* (11), 1062.
(15) Cordero-Morales, J. F.; Jogini, V.; Chakrapani, S.; Perozo, E. A Multipoint Hydrogen-Bond Network Underlying KcsA C-Type Inactivation. *Biophys. J.* **2011,** *100* (10), 2387.
(16) Imai, S.; Osawa, M.; Mita, K.; Toyonaga, S.; Machiyama, A.; Ueda, T.; Takeuchi, K.; Oiki, S.; Shimada, I. Functional Equilibrium of the KcsA Structure Revealed by NMR. *J. Biol Chem.* **2012,** *287* (47), 8.
(17) Ostmeyer, J.; Chakrapani, S.; Pan, A. C.; Perozo, E.; Roux, B. Recovery from slow inactivation in K^+ channels is controlled by water molecules. *Nature* **2013,** *501* (7465), 5.
(18) Raghuraman, H.; Islam, S. M.; Mukherjee, S.; Roux, B.; Perozo, E. Dynamics transitions at the outer vestibule of the KcsA potassium channel during gating. *P. Natl. Acad. Sci. USA* **2014,** *111* (5), 1831.
(19) Rotem, D.; Mason, A.; Bayley, H. Inactivation of the KcsA potassium channel explored with heterotetramers. *J. Gen. Physiol.* **2010,** *135* (1), 29.
(20) Zhou, Y. F.; Morais-Cabral, J. H.; Kaufman, A.; MacKinnon, R. Chemistry of ion coordination and hydration revealed by a K^+ channel-Fab complex at 2.0 angstrom resolution. *Nature* **2001,** *414* (6859), 43.
(21) Valiyaveetil, F. I.; Zhou, Y. F.; Mackinnon, R. Lipids in the structure, folding, and function of the KcsA K^+ channel. *Biochemistry* **2002,** *41* (35), 10771.
(22) Demmers, J. A. A.; van Dalen, A.; de Kruijff, B.; Heck, A. J. R.; Killian, J. A. Interaction of the K+ channel KcsA with membrane phospholipids as studied by ESI mass spectrometry. *Febs Lett.* **2003,** *541* (1-3), 28.
(23) Deol, S. S.; Domene, C.; Bond, P. J.; Sansom, M. S. P. Anionic phospholipid interactions with the potassium channel KcsA: Simulation studies. *Biophys. J.* **2006,** *90* (3), 822.
(24) Marius, P.; Alvis, S. J.; East, J. M.; Lee, A. G. The interfacial lipid binding site on the potassium channel KcsA is specific for anionic phospholipids. *Biophys. J.* **2005,** *89* (6), 4081.
(25) Marius, P.; de Planque, M. R. R.; Williamson, P. T. F. Probing the interaction of lipids with the non-annular binding sites of the potassium channel KcsA by magic-angle spinning NMR. *Biochim. Et Biophy. Acta-Biomembranes* **2012,** *1818* (1), 90.
(26) Weingarth, M.; Prokofyev, A.; van der Cruijsen, E. A. W.; Nand, D.; Bonvin, A.; Pongs, O.; Baldus, M. Structural Determinants of Specific Lipid Binding to Potassium Channels. *J. Am. Chem. Soc.* **2013,** *135* (10), 3983.
(27) Molina, M. L.; Giudici, A. M.; Poveda, J. A.; Fernandez-Ballester, G.; Montoya, E.; Renart, M. L.; Fernandez, A. M.; Encinar, J. A.; Riquelme, G.; Morales, A.et al. Competing Lipid-Protein and Protein-Protein Interactions Determine Clustering and Gating Patterns in the Potassium Channel from Streptomyces lividans (KcsA). *J. Biol. Chem.***2015,** *290* (42), 25745.
(28) Molina, M. L.; Encinar, J. A.; Barrera, F. N.; Fernandez-Ballester, G.; Riquelme, G.; Gonzalez-Ros, J. M. Influence of C-terminal protein domains and protein-lipid interactions on tetramerization and stability of the potassium channel KcsA. *Biochemistry* **2004,** *43* (47), 14924.

(29) Molina, M. L.; Barrera, F. N.; Fernandez, A. M.; Poveda, J. A.; Renart, M. L.; Encinar, J. A.; Riquelme, G.; Gonzalez-Ros, J. M. Clustering and coupled gating modulate the activity in KcsA, a potassium channel model. *J. Biol.Chem.* **2006,** *281* (27), 18837.
(30) Hamill, O. P.; Marty, A.; Neher, E.; Sakmann, B.; Sigworth, F. J. Improved patch-clamp techniques for high-resolution current recording from cells and cell-free membrane patches. *Pflug. Arch. Eur. J. Phy.* **1981,** *391* (2), 85.
(31) Qin, F.; Auerbach, A.; Sachs, F. Estimating single-channel kinetic parameters from idealized patch-clamp data containing missed events. *Biophys. J.* **1996,** *70* (1), 264.
(32) Qin, F.; Auerbach, A.; Sachs, F. Maximum likelihood estimation of aggregated Markov processes. *P. Roy. Soc. B.* **1997,** *264* (1380), 375.
(33) Sigworth, F. J.; Sine, S. M. Data transformations for improved display and fitting of single-channel dwell time histograms. *Biophys. J.* **1987,** *52* (6), 1047.
(34) Chakrapani, S.; Cordero-Morales, J. F.; Perozo, E. A quantitative description of KcsA Gating I: Macroscopic currents. *J. Gen. Phys.* **2007,** *130* (5), 465.
(35) Chakrapani, S.; Cordero-Morales, J. F.; Perozo, E. A quantitative description of KcsA Gating II: Single-channel currents. *J. Gen. Phys.* **2007,** *130* (5), 479.
(36) Horn, R.; Lange, K. Estimating kinetic constants from single channel data. *Biophys. J.* **1983,** *43* (2), 207.
(37) Roux, B.; Sauve, R. A General-solution to the time interval omission problem applied to single channel analysis. *Biophys. J.* **1985,** *48* (1), 149.
(38) Humphrey, W.; Dalke, A.; Schulten, K. VMD: Visual molecular dynamics. *J. Mol. Graph.* **1996,** *14* (1), 33.
(39) Berneche, S.; Roux, B. The ionization state and the conformation of Glu-71 in the KcsA K^+ channel. *Biophys. J.* **2002,** *82* (2), 772.
(40) Jo, S.; Kim, T.; Iyer, V. G.; Im, W. CHARMM-GUI: a web-based graphical user interface for CHARMM. *J. Comput. Chem.* **2008,** *29* (11), 1859.
(41) Jo, S.; Lim, J. B.; Klauda, J. B.; Im, W. CHARMM-GUI Membrane Builder for Mixed Bilayers and Its Application to Yeast Membranes. *Biophys. J.* **2009,** *97* (1), 50.
(42) Wu, E. L.; Cheng, X.; Jo, S.; Rui, H.; Song, K. C.; Dávila-Contreras, E. M.; Qi, Y.; Lee, J.; Monje-Galvan, V.; Venable, R. M. CHARMM-GUI Membrane Builder toward realistic biological membrane simulations. *J. Comput. Chem.* **2014,** *35* (27), 1997.
(43) Phillips, J. C.; Braun, R.; Wang, W.; Gumbart, J.; Tajkhorshid, E.; Villa, E.; Chipot, C.; Skeel, R. D.; Kale, L.; Schulten, K. Scalable molecular dynamics with NAMD. *J. Comput. Chem.* **2005,** *26* (16), 1781.
(44) Klauda, J. B.; Venable, R. M.; Freites, J. A.; O'Connor, J. W.; Tobias, D. J.; Mondragon-Ramirez, C.; Vorobyov, I.; MacKerell Jr, A. D.; Pastor, R. W. Update of the CHARMM all-atom additive force field for lipids: validation on six lipid types. *J. Phys. Chem. B* **2010,** *114* (23), 7830.
(45) Jorgensen, W. L.; Chandrasekhar, J.; Madura, J. D.; Impey, R. W.; Klein, M. L. Comparison of simple potential functions for simulating liquid water. *J. Chem. Phys.* **1983,** *79* (2), 926.
(46) Darden, T.; York, D.; Pedersen, L. Particle mesh Ewald: An N·log(N) method for Ewald sums in large systems. *J. Chem. Phys.* **1993,** *98* (12), 10089.
(47) Miyamoto, S.; Kollman, P. A. SETTLE: an analytical version of the SHAKE and RATTLE algorithm for rigid water models. *J. Comput. Chem.* **1992,** *13* (8), 952.
(48) Feller, S. E.; Zhang, Y.; Pastor, R. W.; Brooks, B. R. Constant pressure molecular dynamics simulation: the Langevin piston method. *J. Chem. Phys.* **1995,** *103* (11), 4613.
(49) Martyna, G. J.; Tobias, D. J.; Klein, M. L. Constant pressure molecular dynamics algorithms. *J. Chem. Phys.* **1994,** *101* (5), 4177.
(50) LeMasurier, M.; Heginbotham, L.; Miller, C. KcsA: It's a potassium channel. *J. Gen. Phys.* **2001,** *118* (3), 303.
(51) van der Cruijsen, E. A. W.; Prokofyev, A. V.; Pongs, O.; Baldus, M. Probing Conformational Changes during the Gating Cycle of a Potassium Channel in Lipid Bilayers. *Biophys. J.* **2017,** *112* (1), 99.
(52) Chakrapani, S.; Cordero-Morales, J. F.; Jogini, V.; Pan, A. C.; Cortes, D. M.; Roux, B.; Perozo, E. On the structural basis of modal gating behavior in K+ channels. *Nat. Struct. Mol. Biol.* **2011,** *18* (1), 67.
(53) Chung, S. H.; Allen, T. W.; Kuyucak, S. Modeling diverse range of potassium channels with brownian dynamics. *Biophys. J.* **2002,** *83* (1), 263.

(54) Nimigean, C. M.; Chappie, J. S.; Miller, C. Electrostatic tuning of ion conductance in potassium channels. *Biochemistry* **2003,** *42* (31), 9263.
(55) McCormick, J. I.; Johnstone, R. M. Volume enlargement and recovery of na+-dependent amino-acid transport in proteoliposomes derived from ehrlich ascites cell-membranes. *J. Biol. Chem.* **1988,** *263* (17), 8111.
(56) Weingarth, M.; van der Cruijsen, E. A. W.; Ostmeyer, J.; Lievestro, S.; Roux, B.; Baldus, M. Quantitative Analysis of the Water Occupancy around the Selectivity Filter of a K+ Channel in Different Gating Modes. *J. Am. Chem. Soc.* **2014,** *136* (5), 2000.
(57) Cuello, L. G.; Cortes, D. M.; Perozo, E. The gating cycle of a K+ channel at atomic resolution. *Elife* **2017,** *6*, 17.
(58) van der Cruijsen, E. A. W.; Nand, D.; Weingarth, M.; Prokofyev, A.; Hornig, S.; Cukkemane, A. A.; Bonvin, A.; Becker, S.; Hulse, R. E.; Perozo, E.et al. Importance of lipid-pore loop interface for potassium channel structure and function. *P. Natl. Acad. Sci. USA* **2013,** *110* (32), 13008.
(59) Cordero-Morales, J. F.; Cuello, L. G.; Perozo, E. Voltage-dependent gating at the KcsA selectivity filter. *Nat. Struct. Mol. Biol.* **2006,** *13* (4), 319.
(60) McCoy, J. G.; Nimigean, C. M. Structural correlates of selectivity and inactivation in potassium channels. *Biochim. Et Biophy. Acta-Biomembranes* **2012,** *1818* (2), 272.

4.4 Effect of Anionic Lipids on Ion Permeation through K^+ Channels

4.4.1 Authorship and Permissions

<table>
<tr><td colspan="10">This declaration concerns the article entitled</td></tr>
<tr><td colspan="10">Effect of Anionic Lipids on Ion Permeation through K^+-Channels</td></tr>
<tr><td colspan="10">Publication status (tick one)</td></tr>
<tr><td>Draft manuscript</td><td>✓</td><td>Submitted</td><td></td><td>In review</td><td></td><td>Accepted</td><td></td><td>Published</td><td></td></tr>
<tr><td>Publication details</td><td colspan="9">Not Applicable</td></tr>
<tr><td>Candidates contribution to the paper (detailed and also given as a percentage)</td><td colspan="9">The candidate contributed to/considerably contributed/predominantly executed the…
Formulation of ideas (50%):
V. Oakes and C. Domene contributed equally.

Design of methodology (50%):
V. Oakes and C. Domene contributed equally.

Experimental work (80%):
V. Oakes: Performed simulations and analysis
S. Furini: Provided analysis tools for weighted-histogram analysis method

Presentation of data in journal format (80%):
V. Oakes: Main author of manuscript and supporting information.
S. Furini: Critically assessed and revised the manuscript and supporting information.
C. Domene: Critically assessed and revised the manuscript and supporting information.</td></tr>
<tr><td>Statement from Candidate</td><td colspan="9">This paper reports on original research I conducted during the period of my Higher Degree by Research candidature.</td></tr>
<tr><td>Signed</td><td colspan="5"></td><td>Date</td><td colspan="3"></td></tr>
</table>

4.4.2 Manuscript

Effect of Anionic Lipids on Ion Permeation through K^+-Channels

Victoria Oakes[1], Simone Furini[2] and Carmen Domene[1,3]

[1]Department of Chemistry, University of Bath, Claverton Down, Bath, BA2 7AY, UK

[2]Department of Medical Biotechnologies, University of Siena, Siena, Italy

[3]Department of Chemistry, University of Oxford, Oxford, OX1 3TA, UK

Abstract

K^+-channels are responsible for the efficient and selective conduction of K^+ ions across the plasma membrane. The bacterial channel KcsA has historically been used to characterize various aspects of K^+ conduction via computational means. The energetic barriers associated with ion translocation across the KcsA selectivity filter have been computed in various studies, leading to the proposal of two alternate mechanisms of conduction. Thus far, the effect of several features of the KcsA channel structure on the ion conduction have not been characterized. Here, the potential of mean force of K^+ permeation is evaluated for KcsA in lipid bilayers containing anionic lipids, which is known to increase the conductance of the channel. In addition, the effect of the protonation/deprotonation of residue E71, which directly interacts with the selectivity filter sequence, is assessed. Both conduction mechanisms are considered throughout. The results obtained provide novel insights into the molecular functioning of the K^+ selectivity filter.

Introduction

The plasma membrane is a critical regulator of ion channel function. Various membrane lipids have been shown to exert an effect on ion channels from a diverse range of families, including cholesterol, and several types of phospholipids (such as phosphatidylinositol 4,5-bisphosphate) and sphingolipids (such as sphingosine-2-phosphate).[1-3] Membrane lipids can regulate ion channel activity by several mechanisms among which are: 1) direct binding to specific sites on the channel surface, 2) perturbation of the physical properties of the phospholipid bilayer, and 3) modulation of complex formation with other protein assemblies.

In the K^+-channel family, the regulation of several channel types by membrane lipids has been investigated, including inward-rectifying and voltage-gated K^+-channels.[1,4,5] In KcsA, a bacterial K^+-channel, it has been shown that anionic phospholipids are instrumental to channel function. For instance, the conductance and open probability of KcsA is increased in the

presence of anionic lipids.[6,7] Moreover, anionic lipids enhance the structural stability of KcsA, in conditions of thermal or chemical denaturation.[8-10] In addition, correct folding *in vitro* is assisted by anionic lipids.[11] However, the exact role of anionic lipids in these processes remains unclear.

The landmark crystal structure of KcsA revealed the structure of the K^+-channel pore domain in atomic detail.[12] The homotetramer is formed from the assembly of four identical subunits, each containing two transmembrane helices, connected by a loop which converges at the center of the channel. The pore-loop, as this is known, contains an α-helix and the selectivity filter sequence (TVGYG), which is conserved in prokaryotic and eukaryotic K^+-channels.[13,14] This region is responsible for permitting fast and efficient permeation of K^+ ions, whilst excluding other ionic species. A symmetric arrangement of the backbone carbonyl groups of the selectivity filter sequence and the side-chain of the included threonine form four adjacent binding sites, which can accommodate dehydrated K^+ ions (Figure 1A). During outward rectification, ions enter from the cytoplasm to a water-filled cavity in the center of the membrane, ions can penetrate the selectivity filter before exiting to the periplasm. Ion conduction is regulated at the lower gate (by opening and closing of the transmembrane helices) and the upper gate (by activation and inactivation of the selectivity filter). It is, therefore, possible that anionic lipids can act at two distinct sites to modulate ion conductance in KcsA.

Several clues into the mechanism of lipid regulation have been gained from the abundance of high-resolution structural information available for the KcsA channel. Re-examination of an early KcsA structure has disclosed the location of a binding site for anionic lipid POPG (1-palmitoyl-2-oleoyl-sn-glycero-3-phosphoglycerol), in a cleft at the interface between adjacent subunits, and in close proximity to the selectivity filter.[15-17] In these sites, typically referred to as "non-annular sites",[18] several arginine residues are thought to be involved in the selective, high-affinity binding of phospholipids.[4,6,19-21] The behaviour of non-annular arginines has been directly implicated in the dynamics of selectivity filter residues,[21] providing a plausible mechanism of action of anionic lipids on the selectivity filter. Marius et al suggest that the inhabitance of three or four identical sites by anionic lipids is a prerequisite for channel opening.[6] What is more, the occupation of non-annular sites has been shown to encourage the formation of KcsA clusters, which exhibit altered conduction properties than isolated channels.[22]

In this work, the energetics of ion conduction through the KcsA selectivity filter, in zwitterionic and mixed anionic/zwitterionic lipid bilayers, is evaluated using umbrella sampling simulations. The relationship between anionic lipids and the rate of permeation through the conductive K^+-channel selectivity filter has not yet been examined via computational means. This is supplemented by analogous calculations, where the protonation state of neighbouring residue E71 is modified, which increases the negative charge density directly behind the selectivity filter and alters the conformation of proximal residues. The data obtained provide important

insights into the molecular functioning of the selectivity filter in response to the introduction of anionic components.

Materials and Methods

Model Setup

Coordinates from the high-resolution crystal structure of KcsA in a closed-state (PDB ID 1K4C) (residues 26-114) was used to model the channel.[15] This particular structure was used to allow direct comparison with previous studies.[23] N- and C-termini were acetylated and methylated respectively. The amino acid E71 of KcsA is modelled in the protonated state to form a diacid hydrogen bond with D80,[24] as well as the deprotonated state. Default ionisation states were used for the remaining amino acids. Four water molecules were placed at the back of the selectivity filter, in agreement with crystallographic data and previous molecular dynamics (MD) simulations.[25] SOLVATE 1.0 was used to solvate internal cavities of the protein. The structures were aligned perpendicular to the bilayer and inserted into two membrane systems: 1) a neutral membrane containing 1-palmitoyl-2-oleoyl-sn-glycero-3-phosphocholine (POPC) molecule and 2) a charged membrane constituted of POPC and 1-palmitoyl-2-oleoylphosphatidylserine (POPS) molecules in a 3:1 ratio, which were generated using the CHARMM-GUI online server.[26-28] The VMD solvate plugin was then used to create a cubic water box around the membrane-protein system.[29] The overlapping water and lipid molecules around the ion channel structure were removed with the cut-off distance 1.2 Å. Potassium and chloride ions were added using Autoionize Plugin of VMD to neutralise the systems up to a concentration of 150 mM.[29] The final system size was approximately 90,000 atoms.

Molecular Dynamics Simulations

MD simulations were performed with version NAMD 2.12.[30] CHARMM36 parameters were used for the protein and lipids,[31] the TIP3P model was used for water,[32] and the CHARMM NBFIX parameters for ions. The particle mesh Ewald method was used for the treatment of periodic electrostatic interactions, with an upper threshold of 1 Å for grid spacing.[33] Electrostatic and van der Waals forces were calculated every time step. A cutoff distance of 12 Å was used for van der Waals forces. A switching distance of 10 Å was chosen to smoothly truncate the non-bonded interactions. Only atoms in a Verlet pair list with a cutoff distance of 13.5 Å (reassigned every 20 steps) were considered. The SETTLE algorithm was used to constrain all bonds involving hydrogen atoms, to allow the use of a 2 fs time step throughout the simulation.[34] MD simulations were performed in the NPT ensemble. The Nose-Hoover-Langevin piston was employed to control the pressure with a 200 fs period, 50 fs damping constant, and the desired value of 1 atmosphere.[35,36] The system was coupled to a Langevin thermostat to sustain a temperature of 300 K throughout. In the equilibration process, the same protocol was used for all of the systems. The systems were subjected to 10,000 steps of minimization, with harmonic constraints (force constant 20 kcal $mol^{-1}Å^{-2}$) on protein atoms,

lipid headgroups and crystallographic water and ions. Harmonic restraints were gradually reduced to a force constant of 2 kcal $mol^{-1}Å^{-2}$ and removed in consecutive steps from the lipid headgroups, protein side-chains and protein backbone over the course of a 3.5 ns trajectory. Initial 500 ns unbiased MD simulations identified binding of charged and zwitterionic phospholipids in non-annular sites on the interface between two adjacent subunits. On account of this, analogous systems were then prepared and equilibrated with full occupancy of the four non-annular binding sites, in consideration of previous observations.[6] Coordinates and velocities after 20 ns of unconstrained MD simulations from these systems were used as the starting point for subsequent biased simulations. A summary of the systems is provided in Table 1.

Table 1. Summary of simulations performed. PC and PS refers to the type of lipid, P and D to the protonated or not nature of E71, and finally W and G refer to the conduction mechanism either with water or gaps in between K^+ ions.

Bilayer Composition	E71 Protonation State	Permeation Mechanism	Notation
POPC	Protonated	KWK	PC-PW
		KK	PC-PG
	Deprotonated	KWK	PC-DW
		KK	PC-DW
POPS+POPC	Protonated	KWK	PS-PW
		KK	PS-PG
	Deprotonated	KWK	PS-DW
		KK	PS-DW

Umbrella Sampling Simulations

Umbrella sampling has been used to calculate the potential of mean force of ion translocation through the KcsA selectivity filter. Ion permeation involving four ions was examined. To simulate the KWK mechanism (where water molecules fill sites not containing K^+ ions), the events connecting the S0/S2/S4/S_{CAV} and S_{EC}/S0/S2/S4/ configurations were examined, with water molecules in remaining sites. To simulate the KK mechanism (where sites not containing K^+ ions are empty), the events connecting the S1/S2/S4/S_{CAV} and S_{EC}/S1/S2/S4/ were examined. The initial and final configurations are considered to be equivalent. The ions considered are denoted K1 (exterior ion), K2 (central ion 1), K3 (central ion 2) and K4 (interior ion). Three biasing potentials were initialized, acting on the K1 ion, the K4 ion and the center of mass of the K2 and K3 ions. Individual simulations were predominantly spaced 1 Å apart, adopting a force constant of 10 kcal $mol^{-1}Å^{-2}$ for the harmonic potential. In the barrier regions, additional windows with a force constant of 20 kcal $mol^{-1}Å^{-2}$ for the harmonic potential were used. In two scenarios (PC-DG and PC-PG), the chosen collective variables resulted in degenerate states; alternative biasing potentials acted upon the K1 ion, the K2 ion and the center of mass of both K3 and K4 ions were tested. The results for these simulations are not included as additional work is required to obtain a converged PMF in these cases. At the start of each window, ions were manually moved to their starting configurations. Simulations of 500 ps were then

performed for each configuration. The positions of water molecules in the selectivity filter were monitored throughout, and simulations exhibiting water molecules with unconventional behaviour were removed from subsequent analysis. The initial 100 ps of the trajectories were considered as equilibration and also removed. The weighted histogram analysis method was used to unbias the data and obtain the PMF in three or four (PC-DG and PC-PG) dimensions,[37] which were then projected onto two-dimensions for visualization. Error estimates were obtained by calculating PMF profiles for 100 ps portions of the trajectory and combining them.

Results

Umbrella sampling simulations have been used to calculate the energetics of ion conduction through the KcsA selectivity filter. Three independent parameters have been modified in order to assess their effect: 1) membrane composition, 2) E71 deprotonation state, and 3) ion permeation mechanism (KK vs. KWK mechanisms), resulting in eight independent systems. Umbrella sampling simulations were initiated from unbiased and unrestrained MD simulations of the systems following a 20 ns equilibration period. In this time period, deprotonation of E71 disrupts the hydrogen-bond network behind the selectivity filter, involving W67, E71, Y78, D80 residues and a structured water molecule. This is associated with the entrance of various water molecules into the region behind the selectivity filter. The specific simulation frame used to seed the umbrella sampling simulations are shown in Figure 1B-D, demonstrating the hydrogen-network. The results are organised by conduction mechanism to avoid repetition.

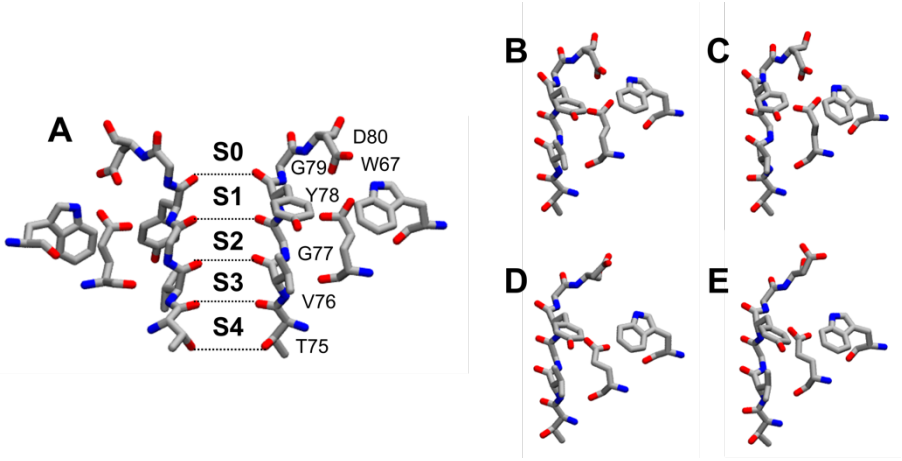

Figure 1. Structure of the KcsA selectivity filter in (A) the initial crystal structure and (B) PS-PW, (C) PC-PW, (D) PS-DW and (E) PC-DW simulations. In (A), the main selectivity filter binding sites are labelled, along with relevant residues. Water molecules are excluded for clarity. Individual K^+ binding sites are defined in Figure 1A.

KWK Mechanism

In the KWK mechanism of conduction, K^+ ions occupy nonadjacent sites in selectivity filter (i.e. S2/S4 or S1/S3), interspersed by water molecules. Ion transport occurs by concerted

transitions between these configurations, associated with an incoming intracellular ion, and an outgoing extracellular ion.[23] This has been supported by prior computational[23,25,38,39] and experimental studies.[40-42] The potential of mean force for the KWK mechanism can be found in Figure 2A-D. In this case, the calculated energetic barriers are generally consistent for the initial movement of ions through the selectivity filter, irrespective of the protonation state of E71 (Table 2). Overall, an energetic cost of 3-4 kcal/mol is associated with loss of the exterior ion from S0 (transition I→II), as well as the attachment of the cavity ion to the lower border of the S4 site (denoted $S4_B$ from this point forward) and the concurrent movement of selectivity filter ions from S2/S4 to S1/S3. The subsequent ion movements to reformed to S0/S2/S4 configuration poses the highest barrier to conduction, approximately of the order of 5 kcal/mol, with the exception of PC-DW. In this case, the barrier increases to ~5 kcal/mol when the extracellular ion is in alternate positions.

Consequences of E71 deprotonation can be detected in the PMF profiles calculated for the PC-PW and PC-DW systems. Here, the position of the minima describing the $S1/S3/S4_B$ configuration are altered, owing to the preferred position of the ion in the S1 site. In PC-PW, the minimum at position -1.0, -9.0 in the Z_{K23}, Z_{K4} projection shown in Figure 1B, depicts the preferred binding of the S1 ion at the S1/S2 boundary, in close proximity with the carbonyl atoms of G77. In contrast, the minimum is shifted upwards in PC-DW, identified at position 0.0, -8.5. This position is more in line with 'typical' K^+ binding in the selectivity filter, where the ion settles centrally in contact distance with carbonyl groups from both G77 and Y78. This can be easily rationalized by considering the altered orientation and charge of E71. When protonated, the conformation of E71 is locked by coexistent hydrogen bonds with Y78 and D80, which in turn hydrogen bonds with W67. When deprotonated, the aforementioned hydrogen bond network is ruptured; instead, negatively charged E71 is oriented between the amide groups of G77 and Y78. It can be surmised that the increased charge density and rotation of the E71 side tampers with the energetics of the S1 site. It is interesting to note that this effect is silenced in simulations containing anionic lipids (PS-PW and PS-DW), and the entire S1 site is hospitable. In PS-DW, the E71-Y78 hydrogen bond can be maintained, even though D80 is detached.

Table 2. Energetic barriers (>1 kcal/mol) calculated from US simulations for the KWK mechanism.

Simulation	Energy Barrier (kcal/mol ± SD)		
	I → II	**II → III**	**II → III**
PS-PW	4.2 ± 0.6	3.6 ± 0.9	4.8 ± 1.2
PC-PW	3.7 ± 0.8	3.3 ± 0.8	5.5 ± 0.9
PS-DW	3.4 ± 0.9	2.7 ± 0.9	5.2 ± 1.0
PC-DW	3.0 ± 0.8	3.0 ± 0.3	1.9 ± 1.0

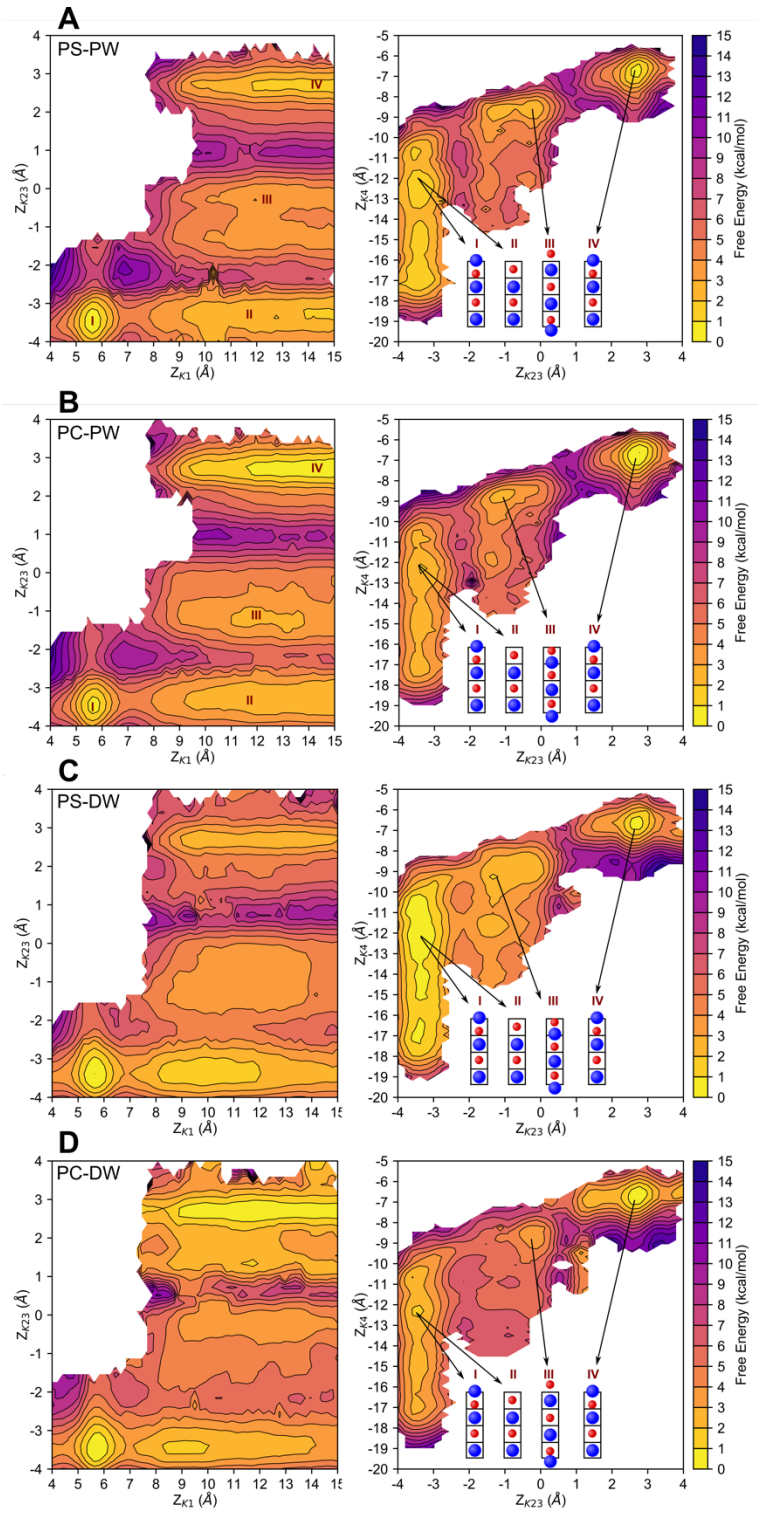

Figure 3. PMF profiles for (A) PS-PW, (B) PC-PW, (C) PS-DW and (D) PC-DW umbrella sampling simulations. The ion configurations are shown in a simplified representation of the selectivity filter. K^+ ions and water molecules are displayed as blue and red spheres, respectively. It should be noted that four ions are tracked in all cases but are not shown in the configuration when they are distant from the selectivity filter.

KK Mechanism

An alternative mechanism of conduction has also been proposed, excluding the involvement of water molecules.[23] In this mechanism, the selectivity filter also contains two or three K^+ ions simultaneously, whilst the remaining sites are vacant, and direct ion-ion repulsion is responsible for low-energy conduction. The potential of mean force for the KK mechanism can be found in Figure 3A-B.

Negligible differences are seen in the energetic barriers for ion permeation, via this mechanism, when E71 is protonated. Energetic costs of ion exit to the extracellular solution (transitions I → II and II → III) and entrance from the central cavity (transitions III → IV) are between 3-4 kcal/mol. After this point, the computed barriers are of the order of 1kcal/mol, roughly equivalent to the reported errors. The equivalent information for PS-DG and PC-DG is not included, as additional work is required to obtain the PMF for these systems. In this conduction mechanism, the exact sequence of movements during ion translocation diverges when the protonation state of E71 is modified. When E71 is deprotonated, a configuration involving ions in the adjacent S2/S3 sites emerges, which is absent when E71 is protonated. This is likely because the heightened negative charge density in this region, increasing the tendency of positively charged ions to enter such conformations. This minimum is considerably more pronounced in PS-DW relative to PC-DW, originating from the differing orientations of deprotonated E71.

Table 3. Energetic barriers (>1 kcal/mol) calculated from US simulations for KK mechanism.

Simulation	Energy Barrier (kcal/mol ± SD)		
	I → II	**II → III**	**III → IV**
PS-PG	3.8 ± 0.3	4.0 ± 0.5	3.0 ± 0.9
PC-PG	2.3 ± 0.2	4.1 ± 0.5	3.7 ± 0.9

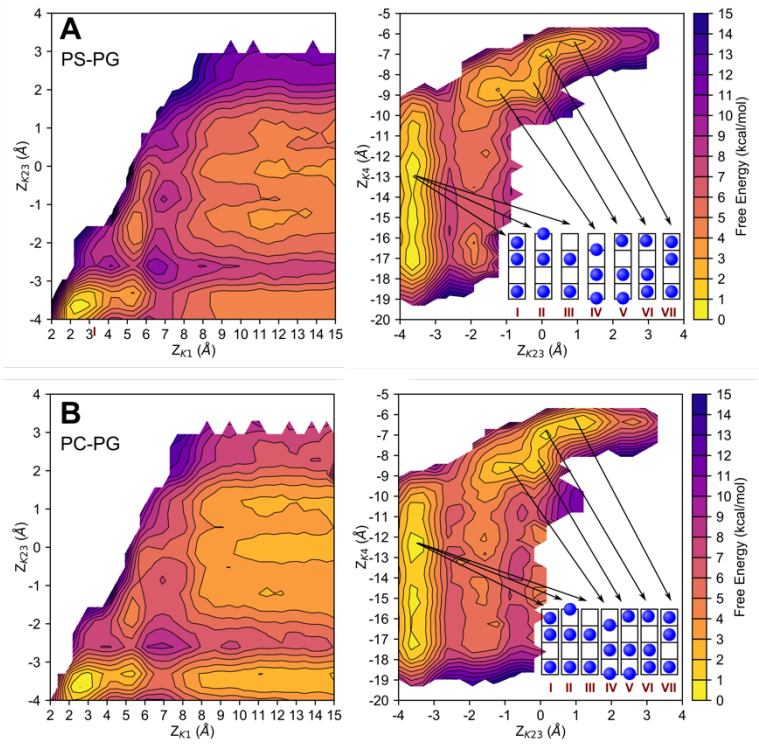

Figure 3. PMF profiles for (A) PS-PG and (B) PC-PG umbrella sampling simulations. The ion configurations are shown in a simplified representation of the selectivity filter. K^+ ions and water molecules are displayed as blue and red spheres, respectively. It should be noted that four ions are tracked in all cases but are not shown in the configuration when they are distant from the selectivity filter.

Discussion

The umbrella sampling technique is an established method to characterize PMF of ion transport across the KcsA selectivity filter, in both the KK and KWK mechanisms. In several studies, the maximum energy barrier for the KWK mechanism has been calculated to be in the range between 2-3 kcal/mol range.[23,38,39] However, a recent study (utilizing the same closed KcsA structure) has reported larger energy barriers of approximately 6 kcal/mol, corresponding to the transition between S1/S3/$S4_B$ and S0/S2/S4 transitions,[43] similar to the PMFs presented in this study. By comparison with an artificial open-state structure (formed from combination of an open-state structure and the closed-state selectivity filter), the authors of this study advocate that opening of the intracellular gate enable greater fluctuations in the selectivity filter, transforming the selectivity filter from a prohibitive closed state to a permissible open state. In opposition to this, our results recommend that ions are more likely to traverse the selectivity filter in the closed-state structure (PDB 1K4C: used in both studies)[15] via the KK mechanism.

Several other important conclusions can be drawn from this work. Somewhat surprisingly, differences in membrane composition have a negligible impact to the maximum barrier to conduction, in the canonical structure of the selectivity filter. Moreover, the energetics of the

KWK mechanism are also unaffected by deprotonation of E71, and disruption of the related hydrogen-bond network. The KcsA conduction cycle is typically considered to be a four-site, containing closed-inactivated, closed-activated, open-activated and open-inactivated structures. The selectivity filter structure observed in the crystal structure is traditionally considered to be the active, conductive form of the selectivity filter. However, our observations suggest that additional conformations, where E71 is deprotonated, can permit conduction at a similar rate, and therefore may be of physiological relevance. In addition, the orientation of E71 is able to tune the occupancy of individual binding sites in the selectivity filter. Individual sites in K^+-channel selectivity filter have previously been shown to be critical for K^+ selectivity,[44] the rate of inactivation and recovery from it,[45,46] and maintaining the structural stability of the filter.[47] With this in mind, additional effects such as these should be examined in considering the aspects examined here.

Conclusions

In this study, umbrella sampling simulations have been used to compute the energetics of ion permeation through the KcsA selectivity filter, via two mechanisms of conduction involving either water or vacant sites. The effect of membrane composition (specifically anionic lipids) and E71 deprotonation state are assessed, serving as contemporary aspects of this work. The information gained brings to light several novel prospects concerning the behaviour of the KcsA selectivity filter: 1) anionic lipids do not affect the conduction rates of K^+ through the canonical selectivity filter structure, 2) selectivity filter conformations involving the deprotonated E71 residue may be actively involved in the K^+ conduction cycle, and 3) the occupancies of individual selectivity filter sites are affected by the orientation/charge of membrane composition. In future studies, the effect of membrane lipid on aspects of gating and selectivity should be examined.

References

(1) Rosenhouse-Dantsker, A.; Mehta, D.; Levitan, I. Regulation of Ion Channels by Membrane Lipids. *Comp. Physiol.* **2012,** *2* (1), 31.

(2) Levitan, I.; Singh, D. K.; Rosenhouse-Dantsker, A. Cholesterol binding to ion channels. *Front. in Physiol.* **2014,** *5*, 14.

(3) Coyan, F. C.; Loussouarn, G. Cholesterol regulation of ion channels: Crosstalk in proteins, crosstalk in lipids. *Channels* **2013,** *7* (6), 415.

(4) Deol, S. S.; Domene, C.; Bond, P. J.; Sansom, M. S. P. Anionic phospholipid interactions with the potassium channel KcsA: Simulation studies. *Biophys. J.* **2006,** *90* (3), 822.

(5) Domene, C.; Bond, P. J.; Deol, S. S.; Sansom, M. S. P. Lipid/protein interactions and the membrane/water interfacial region. *J. Am. Chem. Soc.* **2003,** *125* (49), 14966.

(6) Marius, P.; Zagnoni, M.; Sandison, M. E.; East, J. M.; Morgan, H.; Lee, A. G. Binding of anionic lipids to at least three nonannular sites on the potassium channel KcsA is required for channel opening. *Biophys. J.* **2008,** *94* (5), 1689.

(7) Iwamoto, M.; Oiki, S. Amphipathic antenna of an inward rectifier K+ channel responds to changes in the inner membrane leaflet. *P. Natl. Acad. Sci. USA* **2013,** *110* (2), 749.

(8) Raja, M.; Spelbrink, R. E. J.; de Kruijff, B.; Killian, J. A. Phosphatidic acid plays a special role in stabilizing and folding of the tetrameric potassium channel KcsA. *Febs Lett.* **2007,** *581* (29), 5715.

(9) Raja, M. The Role of Extramembranous Cytoplasmic Termini in Assembly and Stability of the Tetrameric K+-Channel KcsA. *J. Memb. Biol.* **2010,** *235* (1), 51.
(10) Triano, I.; Barrera, F. N.; Renart, M. L.; Molina, M. L.; Fernandez-Ballester, G.; Poveda, J. A.; Fernandez, A. M.; Encinar, J. A.; Ferrer-Montiel, A. V.; Otzen, D.et al. Occupancy of Nonannular Lipid Binding Sites on KcsA Greatly Increases the Stability of the Tetrameric Protein. *Biochemistry* **2010,** *49* (25), 5397.
(11) Barrera, F. N.; Renart, M. L.; Poveda, J. A.; De Kruijff, B.; Killian, J. A.; Gonzalez-Ros, J. M. Protein self-assembly and lipid binding in the folding of the potassium channel KcsA. *Biochemistry* **2008,** *47* (7), 2123.
(12) Doyle, D. A.; Cabral, J. M.; Pfuetzner, R. A.; Kuo, A. L.; Gulbis, J. M.; Cohen, S. L.; Chait, B. T.; MacKinnon, R. The structure of the potassium channel: Molecular basis of K+ conduction and selectivity. *Science* **1998,** *280* (5360), 69.
(13) Smart, O. S.; Goodfellow, J. M.; Wallace, B. A. The pore dimensions of gramicidin A. *Biophys. J.* **1993,** *65* (6), 2455.
(14) Heginbotham, L.; Lu, Z.; Abramson, T.; MacKinnon, R. Mutations in the K^+ channel signature sequence. *Biophys. J.* **1994,** *66* (4), 1061.
(15) Zhou, Y. F.; Morais-Cabral, J. H.; Kaufman, A.; MacKinnon, R. Chemistry of ion coordination and hydration revealed by a K^+ channel-Fab complex at 2.0 angstrom resolution. *Nature* **2001,** *414* (6859), 43.
(16) Valiyaveetil, F. I.; Zhou, Y. F.; Mackinnon, R. Lipids in the structure, folding, and function of the KcsA K^+ channel. *Biochemistry* **2002,** *41* (35), 10771.
(17) Demmers, J. A. A.; van Dalen, A.; de Kruijff, B.; Heck, A. J. R.; Killian, J. A. Interaction of the K+ channel KcsA with membrane phospholipids as studied by ESI mass spectrometry. *Febs Lett.* **2003,** *541* (1-3), 28.
(18) Lee, A. G. How lipids affect the activities of integral membrane proteins. *Biochim. Et Biophy. Acta-Biomembranes* **2004,** *1666* (1-2), 62.
(19) Marius, P.; Alvis, S. J.; East, J. M.; Lee, A. G. The interfacial lipid binding site on the potassium channel KcsA is specific for anionic phospholipids. *Biophys. J.* **2005,** *89* (6), 4081.
(20) Marius, P.; de Planque, M. R. R.; Williamson, P. T. F. Probing the interaction of lipids with the non-annular binding sites of the potassium channel KcsA by magic-angle spinning NMR. *Biochim. Et Biophy. Acta-Biomembranes* **2012,** *1818* (1), 90.
(21) Weingarth, M.; Prokofyev, A.; van der Cruijsen, E. A. W.; Nand, D.; Bonvin, A.; Pongs, O.; Baldus, M. Structural Determinants of Specific Lipid Binding to Potassium Channels. *J. Am. Chem. Soc* **2013,** *135* (10), 3983.
(22) Molina, M. L.; Encinar, J. A.; Barrera, F. N.; Fernandez-Ballester, G.; Riquelme, G.; Gonzalez-Ros, J. M. Influence of C-terminal protein domains and protein-lipid interactions on tetramerization and stability of the potassium channel KcsA. *Biochemistry* **2004,** *43* (47), 14924.
(23) Furini, S.; Domene, C. Atypical mechanism of conduction in potassium channels. *P. Natl. Acad. Sci. USA* **2009,** *106* (38), 16074.
(24) Berneche, S.; Roux, B. The ionization state and the conformation of Glu-71 in the KcsA K+ channel. *Biophys. J.* **2002,** *82* (2), 772.
(25) Domene, C.; Sansom, M. S. P. Potassium channel, ions, and water: Simulation studies based on the high resolution X-ray structure of KcsA. *Biophys. J.* **2003,** *85* (5), 2787.
(26) Jo, S.; Kim, T.; Iyer, V. G.; Im, W. CHARMM-GUI: a web-based graphical user interface for CHARMM. *J. Comput. Chem.* **2008,** *29* (11), 1859.
(27) Jo, S.; Lim, J. B.; Klauda, J. B.; Im, W. CHARMM-GUI Membrane Builder for Mixed Bilayers and Its Application to Yeast Membranes. *Biophys. J.* **2009,** *97* (1), 50.
(28) Wu, E. L.; Cheng, X.; Jo, S.; Rui, H.; Song, K. C.; Dávila-Contreras, E. M.; Qi, Y.; Lee, J.; Monje-Galvan, V.; Venable, R. M. CHARMM-GUI Membrane Builder toward realistic biological membrane simulations. *J. Comput. Chem.* **2014,** *35* (27), 1997.
(29) Humphrey, W.; Dalke, A.; Schulten, K. VMD: Visual molecular dynamics. *J. Mol. Graph.* **1996,** *14* (1), 33.
(30) Phillips, J. C.; Braun, R.; Wang, W.; Gumbart, J.; Tajkhorshid, E.; Villa, E.; Chipot, C.; Skeel, R. D.; Kale, L.; Schulten, K. Scalable molecular dynamics with NAMD. *J. Comput. Chem.* **2005,** *26* (16), 1781.
(31) Klauda, J. B.; Venable, R. M.; Freites, J. A.; O'Connor, J. W.; Tobias, D. J.; Mondragon-Ramirez, C.; Vorobyov, I.; MacKerell Jr, A. D.; Pastor, R. W. Update of the CHARMM

all-atom additive force field for lipids: validation on six lipid types. *J. Phys. Chem. B* **2010,** *114* (23), 7830.
(32) Jorgensen, W. L.; Chandrasekhar, J.; Madura, J. D.; Impey, R. W.; Klein, M. L. Comparison of simple potential functions for simulating liquid water. *J. Chem. Phys.* **1983,** *79* (2), 926.
(33) Darden, T.; York, D.; Pedersen, L. Particle mesh Ewald: An N·log(N) method for Ewald sums in large systems. *J. Chem. Phys.* **1993,** *98* (12), 10089.
(34) Miyamoto, S.; Kollman, P. A. SETTLE: an analytical version of the SHAKE and RATTLE algorithm for rigid water models. *J. Comput. Chem.* **1992,** *13* (8), 952.
(35) Feller, S. E.; Zhang, Y.; Pastor, R. W.; Brooks, B. R. Constant pressure molecular dynamics simulation: the Langevin piston method. *J. Chem. Phys.* **1995,** *103* (11), 4613.
(36) Martyna, G. J.; Tobias, D. J.; Klein, M. L. Constant pressure molecular dynamics algorithms. *J. Chem. Phys.* **1994,** *101* (5), 4177.
(37) Kumar, S.; Bouzida, D.; Swendsen, R. H.; Kollman, P. A.; Rosenberg, J. M. The weighted histogram analysis method for free-energy calculations on biomolecules .1. the method. *J. Comput. Chem.* **1992,** *13* (8), 1011.
(38) Aqvist, J.; Luzhkov, V. Ion permeation mechanism of the potassium channel. *Nature* **2000,** *404* (6780), 881.
(39) Berneche, S.; Roux, B. Energetics of ion conduction through the K+ channel. *Nature* **2001,** *414* (6859), 73.
(40) Miller, C. Coupling of water and ion fluxes in a K^+-selective channel of sarcoplasmic-reticulum. *Biophys. J.* **1982,** *38* (3), 227.
(41) Alcayaga, C.; Cecchi, X.; Alvarez, O.; Latorre, R. Streaming potential measurements in Ca^{2+}-activated K^+ channels from skeletal and smooth-muscle - coupling of ion and water fluxes. *Biophys. J.* **1989,** *55* (2), 367.
(42) Kratochvil, H. T.; Carr, J. K.; Matulef, K.; Annen, A. W.; Li, H.; Maj, M.; Ostmeyer, J.; Serrano, A. L.; Raghuraman, H.; Moran, S. D.et al. Instantaneous ion configurations in the K^+ ion channel selectivity filter revealed by 2D IR spectroscopy. *Science* **2016,** *353* (6303), 1040.
(43) Heer, F. T.; Posson, D. J.; Wojtas-Niziurski, W.; Nimigean, C. M.; Berneche, S. Mechanism of activation at the selectivity filter of the KcsA K+ channel. *Elife* **2017,** *6*, 18.
(44) Noskov, S. Y.; Roux, B. Importance of hydration and dynamics on the selectivity of the KcsA and NaK channels. *J. Gen. Physiol.* **2007,** *129* (2), 135.
(45) Devaraneni, P. K.; Komarov, A. G.; Costantino, C. A.; Devereaux, J. J.; Matulef, K.; Valiyaveetil, F. I. Semisynthetic K^+ channels show that the constricted conformation of the selectivity filter is not the C-type inactivated state. *P. Natl. Acad. Sci. USA* **2013,** *110* (39), 15698.
(46) Matulef, K.; Annen, A. W.; Nix, J. C.; Valiyaveetil, F. I. Individual Ion Binding Sites in the K+ Channel Play Distinct Roles in C-type Inactivation and in Recovery from Inactivation. *Structure* **2016,** *24* (5), 750.
(47) Oakes, V.; Furini, S.; Pryde, D.; Domene, C. Exploring the Dynamics of the TWIK-1 Channel. *Biophys. J.* **2016,** *111* (4), 775.

4.5 Commentary

4.5.1 Conclusion

In this chapter, factors influencing K^+ conduction and blockage of K^+ conduction (inactivation) in the KcsA channel selectivity filter. In the first manuscript presented in this section (section 4.2), umbrella sampling simulations have been used to calculate the potential of mean force associated with the translocation of K^+ ions in KcsA channels where the threonine side-chain in position 75 is mutated to alanine or cysteine Two 'knock-on' mechanisms of conduction were modelled, involving water (KWK or 'soft' knock-on mechanism) or vacant sites (KK or 'hard' knock-on mechanism).[1] In the former, the approach of ions from the cavity no longer initiates a concerted movement of ions, eliminating the well-known "knock-on" aspect of conduction. In the latter, configurations involving more than two ions are disfavoured. Further umbrella sampling simulations in other mutant KcsA channels (i.e. T75G, V76ester, G77ester, Y78ester)[3,4] would strengthen the data already provided.

In the second manuscript, (section 4.3) a combined molecular biology, electrophysiology, NMR spectroscopy and molecular dynamics approach was used to evaluate the effect of anionic lipids on wild-type and KcsA mutant channels (residues in position 64 and 89). Both non-annular anionic lipids and mutations in non-annular sites were found to diminish the inactivation process experimentally. The simulation results attribute this effect to interactions between R89 and D80, a component of the "inactivation triad", and R89, a non-annular arginine, which can be modulated by non-annular lipids and mutations in the position of R64.

Various computational and electrophysiological experiments can be designed to test the proposals presented in this work. Inactivation rates, for example, could be measured for further mutant channels. For example, we suggest that R89 stabilises the inactivation triad, which could be tested by combination with mutations that favour inactivation.[5] Furthermore, positions R64 and R89 could be mutated to a larger range of amino acids, to further pinpoint the role of the non-annular arginines. From a computational viewpoint, the length of the simulations (200 ns) prohibits the calculation of typical lipid diffusion rates; this could be improved by extension of the current simulations or by performing analogous coarse-grained simulations.[6] Alternatively, biased simulation methodologies can be used to calculate free-energy of binding the selected lipids in non-annular sites, which may provide a compromise between the necessary computational resources and level of detail required for the final analysis. Calculation of binding free-energy of the lipids in mutated non-annular sites (R64 and R89) would also be useful to assess the importance of non-annular arginines to lipid binding.

In the final manuscript (section 4.4), the potential of mean force of K^+ conduction, via umbrella sampling, has been calculated for wild-type KcsA with anionic and zwitterionic lipids bound in non-annular sites previously identified. In these situations, the calculated energetic barriers are more favourable in the KK mechanism.[1] Moreover, the effect of the protonation/deprotonation

of residue E71, which directly interacts with the selectivity filter, is assessed using the same protocol, revealing negligible differences.

To continue this work, analogous simulations are being performed for KcsA conformations, identified in previous unbiased simulations (section 4.3), where R89 is directly interacting with D80. Such simulations will enable further comparison of the energetic barriers associated with permeation and the relative occupancies of individual filter sites, when positively-charged arginine side-chains are introduced in close proximity to the selectivity filter. Previously, synthetic substitutions of amide bonds to ester linkages, in selectivity filter residues, have been shown to alter ion occupancy of the S1-S3 sites, altering the rates of inactivation and recovery from inactivation.[3,4] Considering this, the suggested simulations have the potential to provide further additional insight into the attenuated inactivation processes in wild-type KcsA channels, when anionic lipids are present.

Overall, our data reveals various novel insights into the functioning of the KcsA channel selectivity filter, which is structurally conserved across the K^+ channel family. The potential of mean force profiles calculated in different lipid compositions with E71 protonated or deprotonated, and those calculated when individual sites are mutated, contribute to the ongoing debate concerning the underlying K^+ conduction mechanism in K^+ channels. Furthermore, insights into the role of membrane lipids in selectivity filter inactivation have been provided. It should be noted that the inactivation process is not unique to the prokaryotic KcsA channel; several eukaryotic K_V channels have been observed to inactivate at the selectivity filter.[7,8] Moreover, inactivation in K_V channels can also be modulated by membrane phospholipids; for example, $K_V2.1$ is regulated by PIP_2.[9] Therefore, investigations, such as those performed in this chapter, also provide insight into the behaviour of other inactivating channels, such as eukaryotic K_V channels.

4.5.2 References

(1) Furini, S.; Domene, C. Atypical mechanism of conduction in potassium channels. *P. Natl. Acad. Sci. USA* **2009,** *106* (38), 16074.

(2) Devaraneni, P. K.; Komarov, A. G.; Costantino, C. A.; Devereaux, J. J.; Matulef, K.; Valiyaveetil, F. I. Semisynthetic K^+ channels show that the constricted conformation of the selectivity filter is not the C-type inactivated state. *P. Natl. Acad. Sci. USA* **2013,** *110* (39), 15698.

(3) Matulef, K.; Annen, A. W.; Nix, J. C.; Valiyaveetil, F. I. Individual Ion Binding Sites in the K+ Channel Play Distinct Roles in C-type Inactivation and in Recovery from Inactivation. *Structure* **2016,** *24* (5), 750.

(4) Cuello, L. G.; Cortes, D. M.; Perozo, E. The gating cycle of a K+ channel at atomic resolution. *Elife* **2017,** *6*, 17.

(5) Sengupta, D.; Chattopadhyay, A. Identification of Cholesterol Binding Sites in the Serotonin(1A) Receptor. *J.Phys. Chem. B* **2012,** *116* (43), 12991.

(6) Bahring, R.; Barghaan, J.; Westermeier, R.; Wollberg, J. Voltage sensor inactivation in potassium channels. *Front. Pharmacol.* **2012,** *3*, 8.

(7) Hoshi, T.; Armstrong, C. M. C-type inactivation of voltage-gated K+ channels: Pore constriction or dilation? *J. Gen. Physiol.* **2013,** *141* (2), 151.

(8) Delgado-Ramirez, M.; De Jesus-Perez, J. J.; Arechiga-Figueroa, I. A.; Arreola, J.; Adney, S. K.; Villalba-Galea, C. A.; Logothetis, D. E.; Rodriguez-Menchaca, A. A. Regulation of Kv2.1 channel inactivation by phosphatidylinositol 4,5-bisphosphate. *Sci. Rep. UK* **2018,** *8*, 13.

5 Prediction of Functional Binding Sites in the TRPV1 Ion Channel

5.1 Commentary

5.5.1 Introduction

The existence of a biological assembly which elicits a functional response to capsaicin, the central ingredient of the chilli pepper, was inferred by several studies before its eventual cloning in 1997.[1,2] It is now known that the non-selective cation channel TRPV1, otherwise known as vanilloid receptor 1 (VR1) or the capsaicin receptor, is responsive to a broad-range of factors, including noxious chemical and thermal stimuli.[3] Emanating from this, TRPV1 functions as a vital sensor for pain and is a prominent target in the development of novel analgesics.[4-6] Thus far, TRPV1 inhibitors have demonstrated limited success as pharmaceuticals, owing to adverse side effects relating to the heat sensation.[7] Understanding the structural and functional components of TRPV1 activation are, therefore, of the utmost importance for future developmental efforts.

Structures of TRPV1 in multiple activation states revealed several important features of the activation process.[8,9] Of note, the structure of the capsaicin binding site was disclosed, and the effects of capsaicin binding localised in the lower pore region of the channel was ascertained. Moreover, TRPV1 structures determined in lipid nanodiscs revealed a binding site for PIP_2, a known TRPV1 modulator, which overlaps with the putative capsaicin binding site.[10] The availability of various TRPV1 structures has also triggered a myriad of computational studies, further addressing questions of TRPV1 functionality. Previous work in our research group has characterised the probable binding mode of capsaicin,[11] transmembrane binding sites for volatile general anesthetic molecules[12] and the permeation mechanism of cations through the selectivity filter.[13] The aim of this chapter is to locate the site of several novel TRPV1 regulators, which have been recently identified by our experimental collaborators. The insights gained contribute to our current understanding of how ion channels function on a molecular level.

5.5.2 References

(1) Caterina, M. J.; Schumacher, M. A.; Tominaga, M.; Rosen, T. A.; Levine, J. D.; Julius, D. The capsaicin receptor: a heat-activated ion channel in the pain pathway. *Nature* **1997,** *389* (6653), 816.

(2) Yang, F.; Zheng, J. Understand spiciness: mechanism of TRPV1 channel activation by capsaicin. *Protein Cell* **2017,** *8* (3), 169.

(3) Venkatachalam, K.; Montell, C. TRP Channels. *Ann. Rev. Biochem.* **2007,** *76*, 387.

(4) Tominaga, M.; Caterina, M. J.; Malmberg, A. B.; Rosen, T. A.; Gilbert, H.; Skinner, K.; Raumann, B. E.; Basbaum, A. I.; Julius, D. The cloned capsaicin receptor integrates multiple pain-producing stimuli. *Neuron* **1998,** *21* (3), 531.

(5) Tominaga, M.; Julius, D. Capsaicin receptor in the pain pathway. *Jpn J. Pharmacology* **2000,** *83* (1), 20.

(6) Julius, D. TRP channels and pain. *Annu. Rev. Cell. Dev. Biol.* **2013**, *29*, 355.

(7) Carnevale, V.; Rohacs, T. TRPV1: A Target for Rational Drug Design. *Pharmaceuticals* **2016,** *9* (3), 20.

(8) Liao, M.; Cao, E.; Julius, D.; Cheng, Y. Structure of the TRPV1 ion channel determined by electron cryo-microscopy. *Nature* **2013,** *504* (7478), 107.

(9) Cao, E.; Liao, M.; Cheng, Y.; Julius, D. TRPV1 structures in distinct conformations reveal mechanisms of activation. *Nature* **2013,** *504* (7478), 113.

(10) Gao, Y.; Cao, E. H.; Julius, D.; Cheng, Y. F. TRPV1 structures in nanodiscs reveal mechanisms of ligand and lipid action. *Nature* **2016,** *534* (7607), 347.

(11) Darre, L.; Domene, C. Binding of Capsaicin to the TRPV1 Ion Channel. *Mol. Pharm.* **2015,** *12* (12), 4454.

(12) Jorgensen, C.; Domene, C. Location and Character of Volatile General Anesthetics Binding Sites in the Transmembrane Domain of TRPV1. *Mol. Pharm.* **2018,** *15* (9), 3920.

(13) Darre, L.; Furini, S.; Domene, C. Permeation and Dynamics of an Open-Activated TRPV1 Channel. *J. Mol. Biol.* **2015,** *427* (2), 537.

5.2 Oxytocin Modulates Nociception as an Agonist of Pain-Sensing TRPV1, *Cell Rep*. 2017

5.2.1 Authorship and Permissions

<table>
<tr><td colspan="9">This declaration concerns the article entitled</td></tr>
<tr><td colspan="9">Oxytocin Modulates Nociception as an Agonist of Pain-Sensing TRPV1</td></tr>
<tr><td colspan="9">Publication status (tick one)</td></tr>
<tr><td>Draft manuscript</td><td></td><td>Submitted</td><td></td><td>In review</td><td></td><td>Accepted</td><td></td><td>Published</td><td>✓</td></tr>
<tr><td>Publication details</td><td colspan="8">*Cell Rep*. 2017, 21(6), 1681–1691

DOI: 10.1016/j.celrep.2017.10.063

Received: 17 February 2017
Accepted: 16 October 2017
Published online: 7 November 2017
This article is available under the Creative Commons Attribution License (CC BY): https://creativecommons.org/licenses/by/4.0/</td></tr>
<tr><td>Candidates contribution to the paper (detailed and also given as a percentage)</td><td colspan="8">The candidate contributed to/considerably contributed/predominantly executed the…

Experimental work (75%): Y. Nersesyan, L. Demirkhanyan, D. Cabezas-Bratesco, R. Kusuda, T. Dawson, X. Sun, C. Cao, A. Cohen, B. Chelluboina, K. Kumar Veeravalli,[1] K. Zimmermann, S. Brauchi, and E. Zakharian

Computational work (25%): V. Oakes and C. Domene

Formulation of ideas (Computational: 50%):
V. Oakes and C. Domene contributed equally.
Design of methodology (Computational: 50%):
V. Oakes and C. Domene contributed equally.
Experimental work (Computational: 100%):
V. Oakes: Performed simulations and analysis
Presentation of data in journal format (15%):
E. Zakharian: Main author of manuscript and supporting information.

V. Oakes: Main author of text and figures relating to computational work.
All authors critically revised the manuscript.</td></tr>
<tr><td>Statement from Candidate</td><td colspan="8">This paper reports on original research I conducted during the period of my Higher Degree by Research candidature.</td></tr>
<tr><td>Signed</td><td colspan="5"></td><td>Date</td><td colspan="2"></td></tr>
</table>

Oxytocin Modulates Nociception as an Agonist of Pain-Sensing TRPV1

Yelena Nersesyan,[1] Lusine Demirkhanyan,[1] Deny Cabezas-Bratesco,[2] Victoria Oakes,[3] Ricardo Kusuda,[4,5] Tyler Dawson,[1] Xiaohui Sun,[1,6] Chike Cao,[7] Alejandro Martin Cohen,[8] Bharath Chelluboina,[1] Krishna Kumar Veeravalli,[1] Katharina Zimmermann,[4] Carmen Domene,[3,9] Sebastian Brauchi,[2] and Eleonora Zakharian[1,10,*]

[1]Department of Cancer Biology and Pharmacology, University of Illinois College of Medicine, 1 Illini Drive, Peoria, IL 61605, USA
[2]Instituto de Fisiologia, Facultad de Medicina, Universidad Austral de Chile, and Millennium Nucleus of Ion Channels-Associated Diseases (MiNICAD), Valdivia 5110566, Chile
[3]Department of Chemistry, King's College London, Britannia House, 7 Trinity Street, London, SE1 1DB, UK
[4]Department of Anesthesia, Friedrich-Alexander University Erlangen-Nürnberg, Krankenhausstrasse 12, 91054 Erlangen, Germany
[5]Department of Pharmacology, Ribeirão Preto Medical School, University of São Paulo, Av. Bandeirantes 3900, 14049-900 Ribeirão Preto, Brazil
[6]College of Pharmaceutical Sciences, Soochow University, Suzhou, Jiangsu 215123, China
[7]Ion Channel Research Unit, Duke University Medical Center, Durham, NC 27710, USA
[8]Department of Biochemistry and Molecular Biology, Faculty of Medicine, Dalhousie University, 5850 College Street, P.O. Box 15000, Halifax, NS B3H 4R2, Canada
[9]Chemistry Research Laboratory, Mansfield Road, University of Oxford, Oxford, OX1 3TA, UK
[10]Lead Contact
*Correspondence: zakharel@uic.edu
https://doi.org/10.1016/j.celrep.2017.10.063

SUMMARY

Oxytocin is a hormone with various actions. Oxytocin-containing parvocellular neurons project to the brainstem and spinal cord. Oxytocin release from these neurons suppresses nociception of inflammatory pain, the molecular mechanism of which remains unclear. Here, we report that the noxious stimulus receptor TRPV1 is an ionotropic oxytocin receptor. Oxytocin elicits TRPV1 activity in native and heterologous expression systems, regardless of the presence of the classical oxytocin receptor. In TRPV1 knockout mice, DRG neurons exhibit reduced oxytocin sensitivity relative to controls, and oxytocin injections significantly attenuate capsaicin-induced nociception in *in vivo* experiments. Furthermore, oxytocin potentiates TRPV1 in planar lipid bilayers, supporting a direct agonistic action. Molecular modeling and simulation experiments provide insight into oxytocin-TRPV1 interactions, which resemble DkTx. Together, our findings suggest the existence of endogenous regulatory pathways that modulate nociception via direct action of oxytocin on TRPV1, implying its analgesic effect via channel desensitization.

INTRODUCTION

Oxytocin is a versatile hormone with various physiological actions. The wide range of oxytocin-elicited effects include stimulation of uterine smooth muscle contraction to facilitate labor, induction of lactation, and expression of complex social and bonding behaviors related to reproduction and care for offspring (Carter, 2014). Oxytocin is produced in the brain in the hypothalamic paraventricular (PVN), supraoptic (SON), and intermediate accessory nuclei (Sawchenko and Swanson, 1983). Magnocellular neurons release oxytocin into the bloodstream (Scharrer and Scharrer, 1940) and also innervate various regions of the brain, including the nucleus accumbens (Ross et al., 2009) and the central nucleus of the amygdala (Knobloch et al., 2012). The brainstem and various regions of the spinal cord (Swanson and Sawchenko, 1983) are innervated by oxytocin-containing parvocellular neurons, and the secreted neuropeptide modulates nociception via targeting C-type fibers in the dorsal root ganglion (DRG) (Juif and Poisbeau, 2013).

Many activities of oxytocin are accomplished through the canonical oxytocin receptor (OXTR), a G-protein-coupled receptor that is present in neural tissues, uterus, and breast (Gimpl and Fahrenholz, 2001). However, not all oxytocin-provoked actions have been linked to its cognate receptor. For example, oxytocin is present at distinctly high levels in brain regions that lack OXTR (Gimpl and Fahrenholz, 2001). Among oxytocin actions is the regulation of Ca^{2+} fluxes. These responses can involve (i) OXTR-mediated signaling via $G\alpha_{q/11}$ that stimulates release of Ca^{2+} from internal stores and (ii) the influx of extracellular Ca^{2+}. The latter mechanism is dependent upon the extracellular Ca^{2+} concentrations, which suggested the participation of voltage-gated or ligand-coupled channels (Sanborn et al., 1998).

Here, we aimed to identify the receptor responsible for an ionotropic oxytocin effect. Our data indicate that oxytocin directly targets the pain receptor, TRPV1 (transient receptor potential vanilloid 1), a non-selective Ca^{2+}-permeable cation channel. TRPV1 is expressed in afferent somatosensory neurons and along the spinal cord. The original discovery of the TRPV1 channel as a heat and capsaicin receptor validated the existence of

nociceptive neural circuitry that mitigates awareness of noxious stimulus exposure (Caterina et al., 1997; Julius, 2013).

In this work, using native and heterologous expression systems, we find that oxytocin-elicited Ca^{2+} responses are mediated through TRPV1 channels. This activity is consistently observed in TRPV1-expressing cells, regardless of the presence of OXTR. Furthermore, DRG neurons isolated from the TRPV1-deficient mice displayed reduced oxytocin sensitivity in comparison to the wild-type and other controls. Planar lipid bilayer experiments confirmed that oxytocin can directly activate the TRPV1 channel. Molecular modeling indicated that, similarly to the tarantula double knot toxin (DkTx), oxytocin interacts with TRPV1 at the extracellular domain leading to channel gating. Together, our results provide solid evidence that oxytocin is a direct TRPV1 agonist. These results imply that oxytocin-induced suppression of nociception might be achieved directly through potentiation of the pain receptor TRPV1, causing analgesia upon the desensitization of the channel.

RESULTS

Oxytocin Elicits Ca^{2+} Influx through TRPV1 Channels

To assess the mechanism of oxytocin-induced anti-nociception, we tested whether it exerts any action on pain-sensing TRPV1. To test the effects of oxytocin on TRPV1 channels, initial experiments used a heterologous expression system, HEK293 cells, to stably express the channel. Oxytocin concentrations used were in the low micromolar range, which matches some physiological conditions. In the neurosecretory granules of the posterior pituitary, oxytocin is present at high concentrations (>100 μM) and is complexed to its carrier protein neurophysin (Gimpl and Fahrenholz, 2001; Ludwig and Leng, 2006). Upon secretion, oxytocin concentrations can range from tens to hundreds of micromolar (Gimpl and Fahrenholz, 2001; Ludwig and Leng, 2006). In contrast, in cerebrospinal fluid, oxytocin is present in low picomolar concentrations, while plasma oxytocin can reach hundreds of picomolar (Kendrick et al., 1991; Winslow et al., 2003).

Under these experimental conditions, oxytocin induced rapid Ca^{2+} influx in cells stably expressing TRPV1 (Figures 1A and 1B), albeit modest in comparison to capsaicin. This effect was not observed in HEK293 cells, used as a control (Figures 1B and 1E). The observed TRPV1 responses displayed a rapid desensitization, which was noticeable during the individual and sequential oxytocin applications (Figure 1B). Co-application of capsaicin with oxytocin elicited a stronger Ca^{2+} response, indicating a cumulative effect of both compounds (Figures 1A and 1B). However, the co-application also exhibited a more rapid "run-down" in comparison to the control (Figures 1A and 1B). Importantly, the oxytocin-evoked activity was abolished (1) with the pre-application of TRPV1 antagonist capsazepine or (2) upon introduction of TRPV1-specific small interfering RNA (siRNA) (Figures 1C, 1D, and S1). The Ca^{2+} imaging performed on the HEK293 cells is summarized in Figure 1F.

Interesting, pre-activation of TRPV1 using capsaicin provoked stronger responses to oxytocin (Figure S2). Under these experimental conditions, oxytocin elicited TRPV1 responses beginning at low picomolar concentrations (Figure S2). Similar channel behavior was observed when oxytocin was applied after potentiating TRPV1 with a low-pH pulse (pH 4.5 or 5.5; data not shown). These results indicated that oxytocin potency to TRPV1 increases when the channel is present in its active/open state. It is tempting to speculate that these conditions are physiologically relevant, reflecting increased oxytocin affinity to the channel following TRPV1 potentiation by inflammatory stimuli.

To determine whether oxytocin-evoked Ca^{2+} responses are mediated through the OXTR or vasopressin 1a receptors, we tested these responses using G-protein-coupled receptor inhibitors. Cells treated with the PLC inhibitor U73122, its negative control U73343 (following the protocol described previously [Horowitz et al., 2005; Thyagarajan et al., 2009]), or the oxytocin receptor (OXTR) inhibitor atosiban displayed no differences in the oxytocin-induced responses (Figure S3).

Next, we tested TRPV1 responses using neuronal F-11 cells. Transiently expressing TRPV1 F-11 cells promptly responded to oxytocin (Figure 1). Unlike HEK293, TRPV1-F-11 cells demonstrated more sustained activity and less desensitization (Figures 1G and 1H). Since the neuronal F-11 cells could also endogenously express the canonical oxytocin receptor, we again tested whether or not OXTR mediates the oxytocin-elicited Ca^{2+} signals using OXTR-specific siRNA. No difference occurred in the magnitude or kinetics of oxytocin-induced responses (Figures 1G, 1H, and S1), whereas F-11 cells transfected with control pcDNA vector were essentially unresponsive to all the stimuli (Figure 1I). The summary of Ca^{2+} influx in F-11 cells is presented in Figure 1J.

We next examined oxytocin-evoked activity using DRG neurons isolated from the wild-type (WT) and TRPV1 knockout (TRPV1-KO, referred to as TRPV1$^{-/-}$) mice (Figures 2A–2G). In the majority of experiments, DRG neurons that were sensitive to oxytocin were also sensitized by capsaicin. A few exceptions were noted when the initial oxytocin-elicited responses were of higher magnitude and were further desensitized to subsequent applications of capsaicin or oxytocin (Figure 2A). DRG neurons transiently expressing TRPV1 channels were sensitive to both agonists (Figure 2B).

On average, we found no essential differences between genders. In WT female mice, oxytocin-sensitive DRGs comprised ~22%, and male neurons comprised ~26% (Figure 2G). In contrast, only a few DRG neurons isolated from TRPV1-KO animals exhibited oxytocin sensitivity, comprising ~5% responsive neurons obtained from female mice and ~2.2% from the males (Figures 2C, 2D, and 2G). We hypothesized that these residual Ca^{2+} signals were mediated through the other oxytocin receptors present in DRG neurons, including OXTR, vasopressin 1a receptors (V1aR), or some other receptors. Notably, these residual Ca^{2+} responses were kinetically slower compared to the WT mice, which could reflect G-protein-mediated Ca^{2+} release from intracellular stores (Figures 2A and 2C). Rescuing TRPV1 expression in TRPV1-KO DRG neurons by transiently expressing the channel recovered their responses to both agonists (Figure 2E).

Alternatively, we tested whether other pain receptors such as TRPA1 or TRPM8 are implicated in oxytocin-elicited activity. However, DRG neurons from TRPA1-KO and TRPM8-KO mice displayed similar sensitivity to oxytocin as those obtained from the WT (Figure S4).

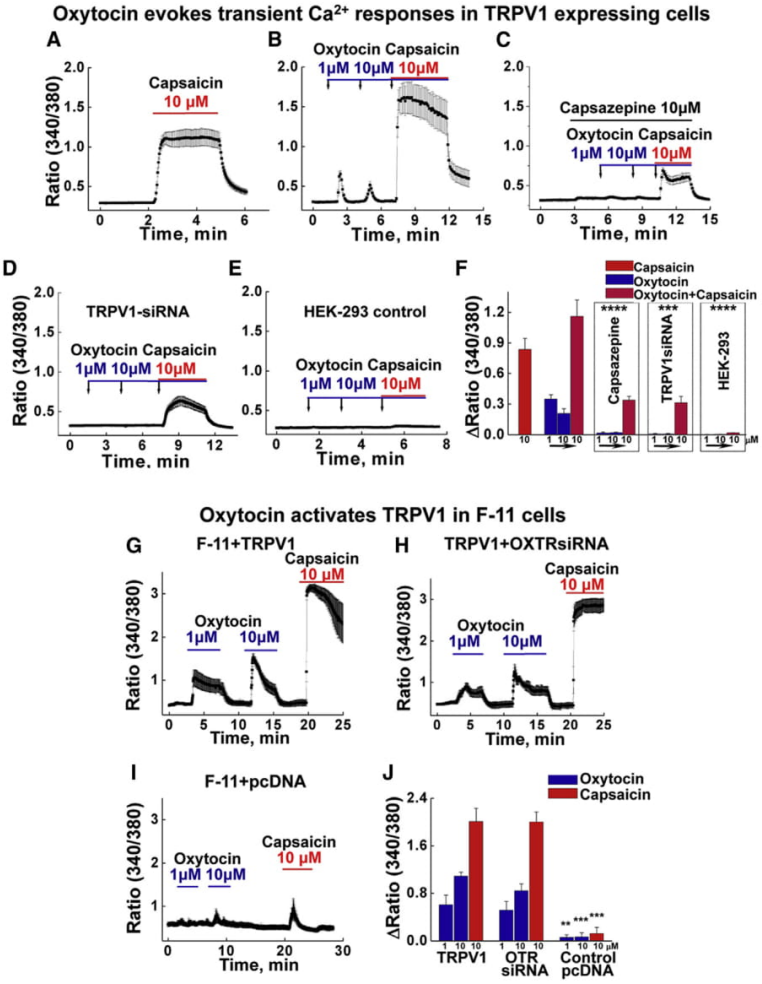

Figure 1. Oxytocin Evokes TRPV1 Activity in HEK293 Cells Stably Expressing the Channel

(A) Control experiment with 10 μM capsaicin-induced TRPV1 activation ($n_{exp.}$ = 6; n_{cells} = 81).

(B) Subsequent applications of 1 μM and 10 μM of oxytocin, followed by 10 μM capsaicin, elicited transient Ca^{2+} responses with oxytocin but a cumulative effect in the presence of both compounds ($n_{exp.}$ = 9; n_{cells} = 96).

(C) Capsazepine significantly inhibited both the oxytocin- and oxytocin/capsaicin-induced responses ($n_{exp.}$ = 6; n_{cells} = 84); p values in comparison to those of the control in (B) are the following: 1 μM oxytocin, p = 1.6E−7; 10 μM oxytocin, p = 9.3E−7; 10 μM oxytocin/capsaicin, p = 4.25E−7).

(D) Co-expression of TRPV1-specific siRNA (0.75 μg) and GFP (0.25 μg) significantly inhibited all the responses ($n_{exp.}$ = 6; n_{cells} = 66); p values in comparison to those of the control in (B) are the following: 1 μM oxytocin, p = 1.24E−4; 10 μM oxytocin, p = 3.58E−4; 10 μM oxytocin/capsaicin, p = 8.19E−4).

(E) Control HEK293-cell non-expressing TRPV1 channels show no responses to any of the agonists ($n_{exp.}$ = 4; n_{cells} = 100); p values in comparison to those of the control in (B) are the following: 1 μM oxytocin, p = 1.04E−11; 10 μM oxytocin, p = 1.16E−9; 10 μM oxytocin/capsaicin, p = 1.88E−13).

(F) The summary presents the means under all the conditions.

Oxytocin elicits TRPV1 responses in F-11 neuronal cells transiently expressing the channel.

(G) Oxytocin- and capsaicin-induced responses on F-11 cells with transiently expressed TRPV1 (0.5 μg) and GFP (0.15 μg) ($n_{exp.}$ = 6; n_{cells} = 71).

(H) Oxytocin- and capsaicin-induced responses on F-11 cells with transiently expressed TRPV1 (0.5 μg), GFP (0.15 μg), and OXTR siRNA (0.4 μg) ($n_{exp.}$ = 6; n_{cells} = 60).

(I) Oxytocin- and capsaicin-induced responses on F-11 cells with transiently expressed empty pcDNA vector (0.5 μg) and GFP (0.15 μg) ($n_{exp.}$ = 6; n_{cells} = 48); p values in comparison to those of TRPV1/GFP-expressing cells are the following: 1 μM oxytocin, p = 0.009; 10 μM oxytocin, p = 2.1E−6; 10 μM oxytocin/capsaicin, p = 2.5E−9).

(J) The summary presents the means of Ca^{2+} responses obtained under all the conditions.

All error bars represent ±SEM. *p < 0.05, **p < 0.01, ***p <0.001, and ****p < 0.0001.

Together, these results suggest that the DRG sensitivity to oxytocin is, in large part, mediated through TRPV1 channels.

Oxytocin Evokes TRPV1 Channel Activation in Whole-Cell Patch Clamp

Next, we assessed the effect of oxytocin on TRPV1 activity using an electrophysiological approach. We found that oxytocin application elicited current potentiation in whole-cell patch-clamp recordings performed on HEK293 cells expressing TRPV1 (Figures 3A–3D). The channel current showed an outward rectification similar to that of capsaicin-evoked currents. However, the maximal response against oxytocin (10 μM) was modest compared to that of capsaicin (1 μM) (Figure 3A). The conductance versus voltage relation was similar under both conditions (conductance/voltage [GV] curves), suggesting that differences in the current density are associated with differences in the desensitization induced by these agonists. In fact, oxytocin strongly desensitized the channel, while the observed desensitization for capsaicin was only partial (Figure 3B). Desensitization observed in the context of the intact cells impeded our ability to obtain the full dose-response curve, as concentrations over 30 μM rapidly inactivated the elicited current (Figure 3D).

Oxytocin Directly Activates TRPV1 in Planar Lipid Bilayers

The use of cellular systems to decipher direct agonistic actions of hormones can be complicated by the presence of various signaling pathways that give rise to intermediate effects. Thus,

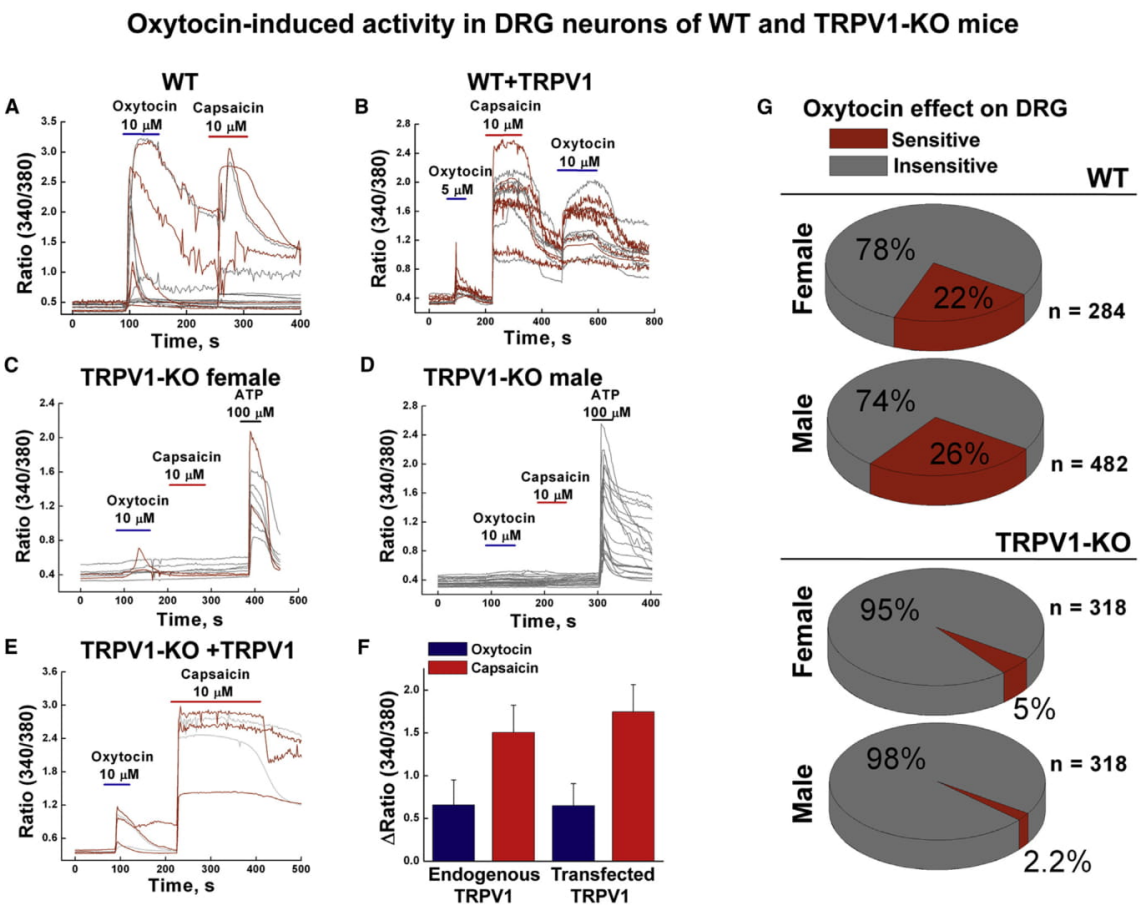

Figure 2. Oxytocin Sensitivity Is Diminished in DRG Neurons Isolated from TRPV1-Deficient Mice

(A) Oxytocin- and capsaicin-elicited Ca^{2+} responses in DRG neurons obtained from the WT mice (number of experiments [$n_{exp.}$] = 33).

(B) Oxytocin- and capsaicin-elicited Ca^{2+} responses in the WT DRG neurons transiently expressing TRPV1 (3 μg) together with GFP (0.5 μg), ($n_{exp.}$ = 6).

(C and D) show oxytocin and capsaicin sensitivity of DRG neurons obtained from TRPV1-KO (C) female ($n_{exp.}$ = 21) and (D) male ($n_{exp.}$ = 21) mice, respectively.

(E) Oxytocin- and capsaicin-induced responses obtained from the TRPV1-KO ($^{-/-}$) DRG neurons transiently expressing TRPV1 (3 μg) along with GFP (0.5 μg), ($n_{exp.}$ = 6).

(F) Summary of oxytocin- and capsaicin-induced responses obtained from WT and WT with transiently expressed TRPV1 channels.

(G) Pie graphs present distribution of the oxytocin-sensitive and oxytocin-insensitive DRG neurons isolated from the WT female (n_{cells} = 284), WT male (n_{cells} = 482), TRPV1-KO female (n_{cells} = 318), and TRPV1-KO male (n_{cells} = 318) mice.

All error bars represent ±SEM.

to validate direct actions of oxytocin on TRPV1, we used planar lipid bilayers to characterize oxytocin-induced channel activity.

For these experiments, the TRPV1 protein was purified and incorporated into bilayers as described previously (Lukacs et al., 2013; Sun and Zakharian, 2015). Protein purity was validated using liquid chromatography-mass spectrometry (LC-MS/MS). Distinct TRPV1 peptides were identified at high abundance (Figure S5; Table S1). After incorporating TRPV1 in the bilayers, we found that oxytocin activates the channel directly, similar to the other known agonists, heat (Sun and Zakharian, 2015) and capsaicin (Lukacs et al., 2013). Likewise, TRPV1 opening required the presence of phosphatidylinositol-4,5-bisphosphate (PIP_2) (Figures 4 and S6).

Oxytocin-induced TRPV1 opening demonstrated distinct current rectification and profound voltage dependence. These features were evident in the single-channel conductance and the open probability (Figures 4A–4D). The channel exhibited the outward current with the mean slope conductance of ~81 pS, while the inward current was ~20 pS (Figures 4A and 4C). In addition, oxytocin-evoked TRPV1 openings showed strong voltage dependence, with marked low open probability obtained at negative voltages and an exponentially increasing open

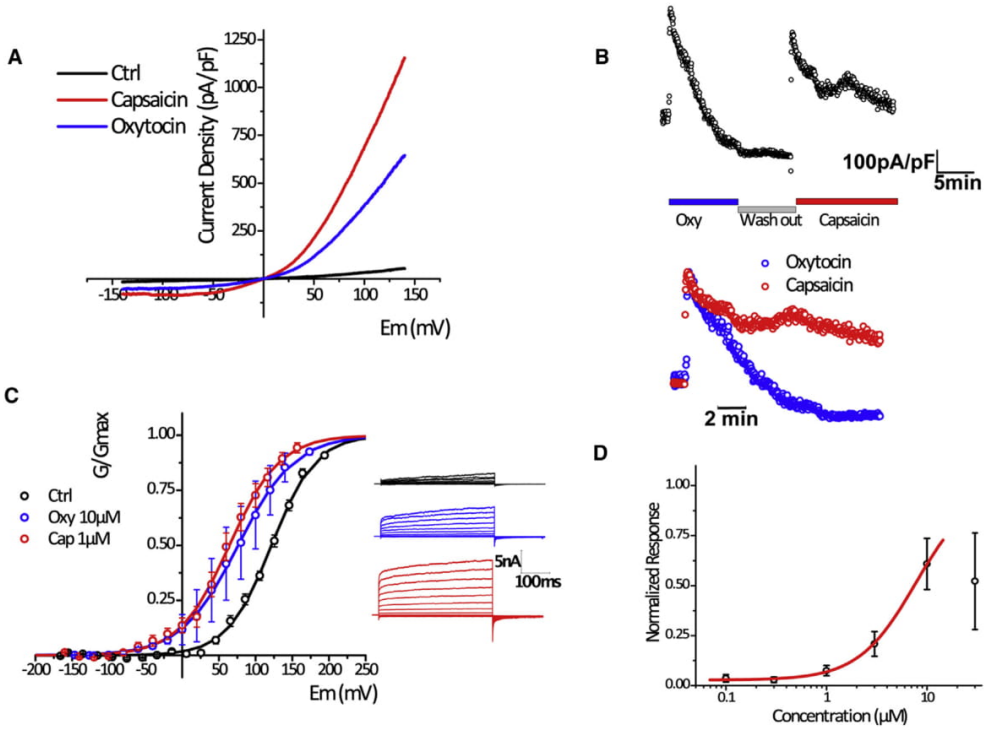

Figure 3. Oxytocin Potentiates TRPV1 Currents in Whole-Cell Patch-Clamp Recordings

(A) Current-voltage (I-V) relations obtained from voltage ramps from −140 mV to +140 mV in the presence of vehicle (black), 10 μM oxytocin (blue) or 1 μM capsaicin (red). EM, membrane electric potential.

(B) Top: time course of representative 10 μM oxytocin and 1 μM capsaicin responses. Bottom: the overlay of normalized responses showing differences in the desensitization kinetics.

(C) Left: G-V curves were obtained by plotting peak tail currents at −100 mV in response to voltage-activated steady-state currents from −160 mV to +160 mV in 20-mV increments: voltage for half-maximal activation of a channel (Vm) values for control, 121.66 ± 14.29 (n = 12); for oxytocin, 64.22 ± 8.96 (n = 12); and for capsaicin, 76.25 ± 21.03 (n = 4); charge z for control, 0.85 ± 0.07 (n = 12); for oxytocin, 0.75 ± 0.06 (n = 12); and for capsaicin, 0.67 ± 0.108 (n = 4). Right: representative traces obtained in transfected cells subjected to voltage steps in control conditions (black) or in the presence of 10 μM oxytocin (blue) or 1 μM capsaicin (red).

(D) Dose-response curve fitted to concentrations <30 μM. EC_{50} = 7.74 ± 8.5; h = 1.5 ± 0.6.

All error bars represent ±SEM.

probability at positive potentials (Figures 4A, 4B, and 4D). In planar lipid bilayers, oxytocin activated TRPV1 with a half-maximal effective concentration (EC_{50}) of ~0.32 μM (Figure 4E).

The comparison of oxytocin-evoked TRPV1 activity to that of capsaicin demonstrated that both conductance values of capsaicin-induced inward and outward currents were greater than that of oxytocin by about 20 and 22 pS, respectively (Figure 4F). The open probability of the channel was similar at negative voltages with both agonists, whereas the open probability was greater at positive voltages for capsaicin-evoked TRPV1 activity (Figure 4G).

In summary, the planar lipid bilayer experiments confirmed that oxytocin is a direct TRPV1 agonist, and this activity can occur independent of any other intermediate signaling pathway.

Identification of an Oxytocin-Binding Site

To investigate the interaction between oxytocin and the TRPV1 ion channel at the atomic level, computational studies were performed on the TRPV1 homotetramer. To that end, oxytocin molecules were docked onto the pore loop region of structures representing the open and closed states of the channel, and MD simulations of the resulting complexes were performed (see Experimental Procedures). Negligible binding to the closed state was observed.

In contrast, the open state (denoted simulation Pep1) interacted with a single oxytocin molecule via its extracellular pore loop. The interaction persisted for approximately 200 ns, with the most prevalent binding pose (clustered using a 3-Å root-mean-square deviation [RMSD] criterion) observed for 80 ns. In a further simulation (denoted simulation Pep2) with four oxytocin molecules initiated from this binding pose, interaction with a single oxytocin peptide persisted for the duration of the 200-ns trajectory, with a stable binding pose observed for 150 ns (Figures 5A–5E).

The identified binding site lies on the external surface of the transmembrane domain, in the interfacial region between two

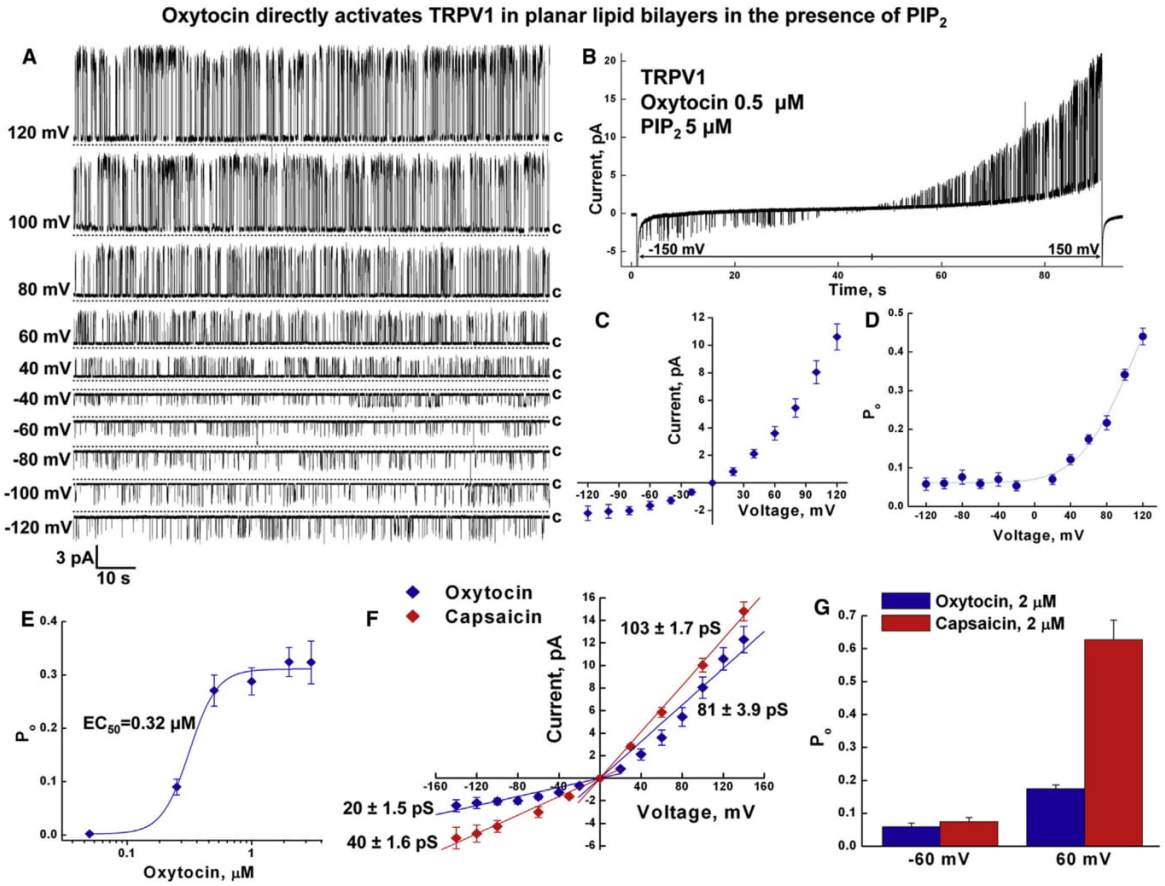

Figure 4. Oxytocin Directly Activates TRPV1 in Planar Lipid Bilayers in the Presence of PIP_2

(A) Representative single-channel current traces of oxytocin-induced (0.5 μM) TRPV1 obtained in the presence of PIP_2 (5 μM); voltages are indicated on the left.

(B) Representative ramp recording obtained at −150 to +150 mV.

(C and D) Graphs demonstrate current voltage relationship (C) and voltage dependence (D) of oxytocin-induced TRPV1; n = 12.

(E) Dose response of oxytocin-TRPV1 activation; EC_{50} = 0.316 μM ± 0.02 μM.

(F) Current voltage relationship of oxytocin- and capsaicin-induced TRPV1 channels.

(G) Capsaicin induces higher open probability of TRPV1 outward channel activity, as indicated by open probability differences of oxytocin-elicited (2 μM) and capsaicin-elicited (2 μM) openings at −60 and +60 mV.

All error bars represent ±SEM.

adjacent subunits. The predicted binding site is illustrated in Figure 5E. The extension of this computational analysis and further discussion of the influence on the TRPV1 activation state are presented in the Supplemental Information (see also Figure S7).

Oxytocin Interaction with TRPV1: Similarity with Other Agonists

Next, we compared the TRPV1 activation of oxytocin to that of the tarantula toxin DkTx. The latter has been studied extensively using both experimental and computational approaches (Bae et al., 2016; Bohlen et al., 2010). Mutations I599A, F649A, A657P, and F659A inhibit channel activation by DkTx, whereas V595A and T695A attenuate channel activation to a lesser extent (Bohlen et al., 2010). Conversely, Y631A enhanced activation by DkTx (Bohlen et al., 2010). The atomic model of TRPV1 in complex with DkTx, determined by Bae et al., advocated that some of the residues, Y631, F649, A657, and T650, were in direct contact with the toxin (Bae et al., 2016). Remarkably, such interactions are replicated in the model of oxytocin-bound TRPV1, thus suggesting that oxytocin may activate TRPV1 via a pathway similar to that of DkTx. Furthermore, our simulations revealed direct engagement between oxytocin and A649 in both *apo* and *holo* TRPV1 structures, identifying an explicit pathway by which oxytocin could modulate the behavior of this region and potentiate TRPV1.

To validate the TRPV1-oxytocin-binding site derived from computational analysis, we altered the most promising target

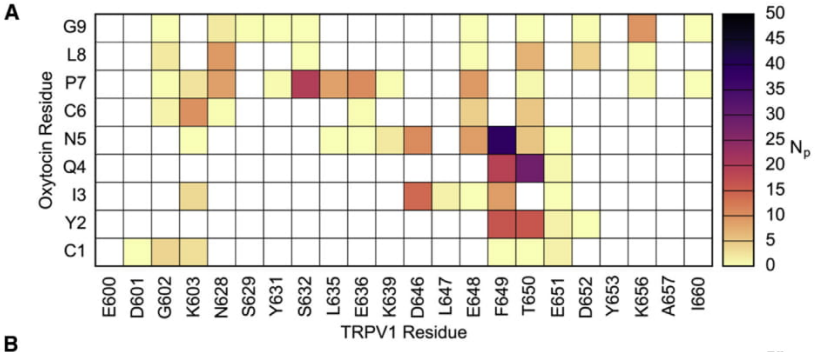

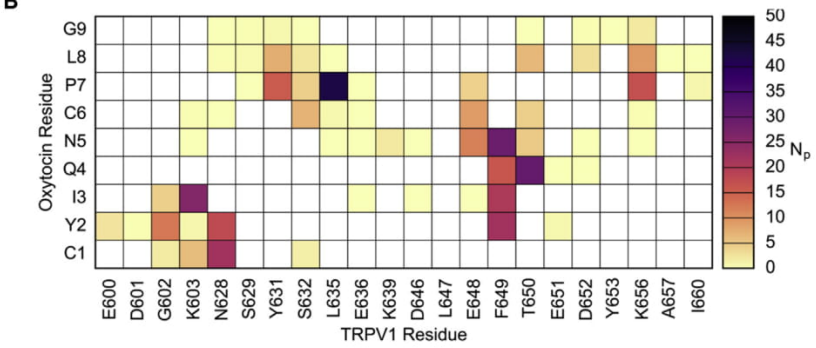

C

TRPV1 Residue	Oxytocin Residue	
	1	2
K603		I3
N628		C1 Y2
Y631		P7
S632	P7	
L635		P7
F649	Y2 Q4 N5	I3 Q4 N5
T650	Y2 Q4	Q4
K656		P7

D

TRPV1 Residue	Oxytocin Residue	% H-bonds	
		1	2
$E600_{SC}$	$Y2_{SC}$	0.0	47.0
$G602_{BB}$	$Y2_{BB}$	0.0	57.3
$G602_{BB}$	$I3_{BB}$	0.0	28.8
$E648_{BB}$	$N5_{SC}$	68.5	53.7
$F649_{BB}$	$Q4_{SC}$	16.4	25.2
$T650_{SC}$	$Q4_{BB}$	79.3	28.9

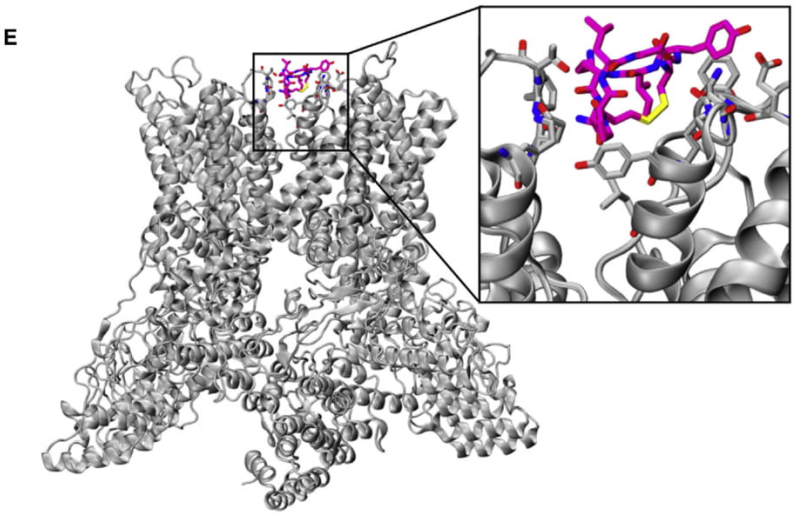

(legend on next page)

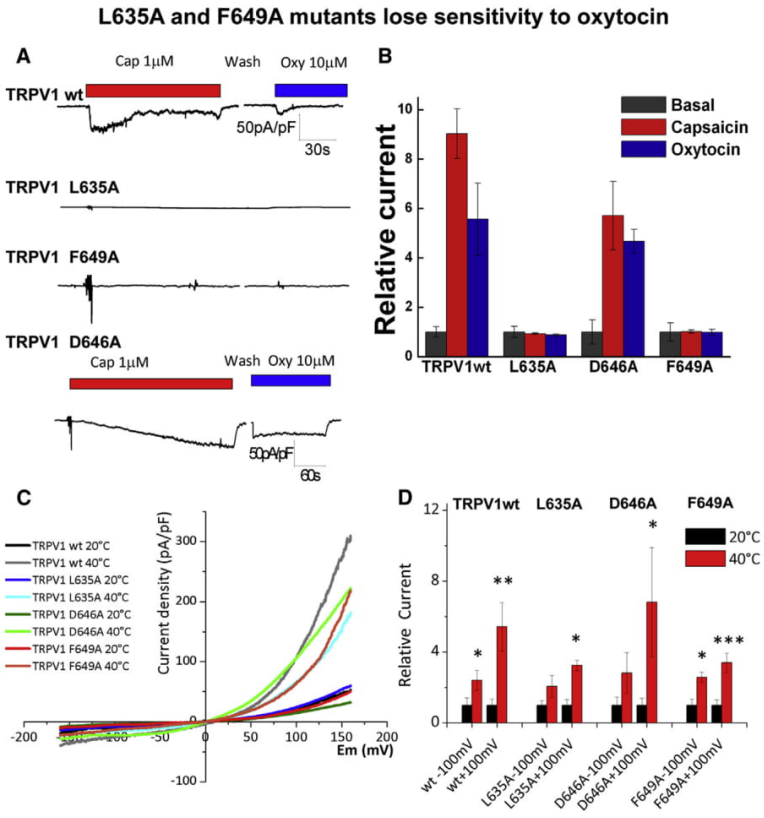

Figure 6. L635A and F649A Mutants Lose Sensitivity to Oxytocin

Patch-clamp recording show the current obtained from the wild-type TRPV1 and mutants. (A) demonstrates representative whole-cell currents recorded by using gap-free protocol with a holding potential at −70 mV. Traces are shown in current densities (picoamperes per picofarad; pA/pF). (B) presents the summary of the relative to control current of TRPV1 wt, L635A, D646A, and F649A constructs obtained upon application of 1 μM capsaicin and 10 μM oxytocin, n = 5 for each construct. (C) displays voltage ramp recordings of heat-induced potentiation of the wild-type TRPV1 and the mutants upon exposure to 40°C pulses. The summary of the heat-induced activities is presented in (D). *p < 0.05, **p < 0.01, ***p < 0.001. All error bars represent ±SEM.

residues by mutagenesis and tested their function. Patch-clamp recordings showed that L635A and F649A TRPV1 mutants completely lose their sensitivity to oxytocin. Surprisingly, they were also insensitive to capsaicin (Figures 6A and 6B) but displayed potentiation by heat (Figures 6C and 6D). Conversely, D646A mutation did not alter the sensitivity of TRPV1 to oxytocin (Figure 6A). Together, these experiments are consistent with the hypothesis that oxytocin interacts with TRPV1 via L635 and F649.

Oxytocin Reduces Capsaicin-Induced Aversive Behavior in Mice

In conclusion, our findings suggest that oxytocin suppresses nociception via activation and desensitization of the polymodal TRPV1 channels in nociceptors. To test this hypothesis, we performed *in vivo* experiments to quantify nocifensive behavior in mice subsequent to oxytocin and capsaicin application. Oxytocin alone did not provoke any noticeable aversive response in mice. However, co-application of oxytocin with capsaicin significantly induced analgesia over the capsaicin-evoked pain stimuli (Figure 7). Together, these results support a direct link between oxytocin and antinociception via TRPV1 activity modulation.

DISCUSSION

Physiological Implication of Oxytocin in Pain Modulation via TRPV1

Oxytocin is a highly abundant neurohypophysial peptide. Its prevalent site of expression is localized to the magnocellular neurons of the hypothalamic paraventricular and supraoptic nuclei (see, for review, Gimpl and Fahrenholz, 2001). Magnocellular oxytocin neurons of these nuclei innervate the forebrain and intensely release the hormone to the systemic circulation from the posterior pituitary in response to a variety of stimuli. The parvocellular oxytocin neurons further project to the brainstem and spinal cord, where the hormone was shown to modulate inflammatory pain processing (Eliava et al., 2016). Furthermore, this neuropeptide is also synthesized in peripheral tissues, such as uterus, placenta, amnion, *corpus luteum*, testis, and heart (Gimpl and Fahrenholz, 2001).

Physiologic roles of oxytocin range from various modalities of neuroendocrine reflexes to the complex social and bonding behaviors related to reproduction and care of offspring. It is now well established that oxytocin facilitates reproduction in all vertebrates (Gimpl and Fahrenholz, 2001). A well-known action of the hormone is the stimulation of milk ejection that was confirmed on

Figure 5. Modeling and Molecular Dynamics Stimulations Display Oxytocin-TRPV1-Interacting Site

(A–E) Contact map displaying the number of interacting atom pairs (N_P) between TRPV1 and oxytocin in simulation Pep1 (A) and Pep2 (B), averaged over the simulation length, using a 4-Å cutoff. The prominent interactions (defined as $N_P > 15$) are summarized in (C). The occurrence of hydrogen bonds is displayed in (D). In (E), a new cartoon representation of the TRPV1 system, in complex with oxytocin is illustrated; oxytocin and interacting TRPV1 residues are displayed in licorice representation.

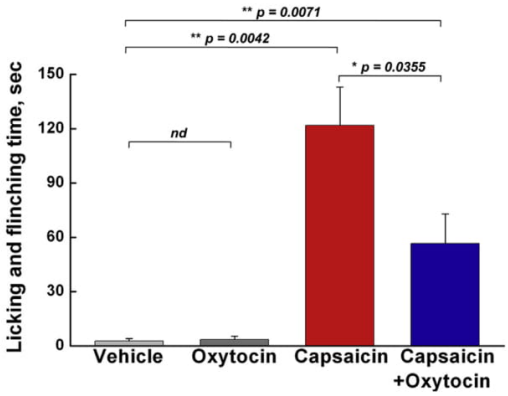

Figure 7. Oxytocin Reduces Capsaicin-Induced Aversive Behavior in Mice

Mouse hindpaws were intracutaneously injected under light sevoflurane anesthesia with the vehicle (n = 3), oxytocin (4 μg per paw; n = 3), capsaicin (1.6 μg per paw; n = 6), or a combination of capsaicin and oxytocin (4 μg per paw; n = 6), and nocifensive behavior was quantified as the time spent licking and flinching. Columns represent the amount of time (in seconds) animals spent licking and flinching the injected paw during the 30-min observation period following the injection (mean ± SEM; p value according to Student's t test). nd, not determined. All error bars represent ±SEM.

the model of oxytocin-deficient mice. The role of oxytocin in parturition is also established, although it involves more complex regulatory mechanisms. Some evidence indicates that, from the paraventricular nuclei of the hypothalamus, oxytocin can reach the central amygdala, where the hormone modulates emotion-related centers of the amygdala and brainstem (Stoop, 2012). Many oxytocin actions have been well characterized by the function of its classical receptor OXTR, a class I G-protein-coupled receptor that is differentially expressed in various tissues (Gimpl and Fahrenholz, 2001). The expression of the oxytocin receptor in the uterus and hypothalamus is strongly correlative with the presence of sex hormones, particularly estrogens. The estrogen receptors were shown to play the role of transcription factors of OXTR and are required for its expression mediated by estrogen binding (Young et al., 1998). Some oxytocin actions, however, imply OXTR-independent mechanisms.

Among its many activities, oxytocin is known to be involved in nociception and pain responses. These involve both peripheral components (Juif and Poisbeau, 2013) and central components (González-Hernández et al., 2014; Juif et al., 2013). Importantly, oxytocin neurons project directly into the C-type fibers of DRG (Juif and Poisbeau, 2013). In an animal model, oxytocin release suppresses nociception and induces analgesia by specifically affecting inflammatory pain pathways (Eliava et al., 2016). The oxytocin neuronal circuitry appears to occur via a dual process, by (1) releasing oxytocin from axons onto sensory spinal cord neurons and inhibiting their activity and (2) indirectly stimulating oxytocin release from supraoptic neurons into the periphery (Eliava et al., 2016). Thus, oxytocin modulates pain by reaching the spinal cord through fast neuronal projections and slower peripheral pathways (Eliava et al., 2016). Likewise, analgesic actions of oxytocin have been documented for migraine patients treated with intranasal oxytocin administration (Wang et al., 2013). One aspect of oxytocin-promoted pain regulation involves endogenous analgesia (González-Hernández et al., 2014). However, it is still debatable as to whether this effect is mediated through the OXTR, V1aR, or some other receptor, as the majority of these studies have been based upon pharmacological approaches using either OXTR or V1aR antagonists (for a review, see González-Hernández et al., 2014).

Also important is the effect of oxytocin on thermoregulation. Similarly to capsaicin (Kobayashi et al., 1998), peripheral administration of oxytocin induces strong hypothermia (Hicks et al., 2014). Hence, in addition to analgesia, our finding suggests a possible molecular mechanism for oxytocin-induced hypothermia.

The results reported here suggest that several oxytocin effects may be mediated by interaction with the TRPV1 pain receptor. TRPV1 is a well-investigated receptor in the pain pathway. The original discovery of TRPV1's role in nociception inspired the development of novel classes of analgesic drugs (Caterina et al., 1997; Julius, 2013). Furthermore, TRPV1 serves as a molecular marker for the nociceptive neuronal circuitry that enables sensation of noxious heat, protons, neurogenic inflammation, and thermal hyperalgesia (Julius, 2013). Profound TRPV1 expression in C-fibers contributes to the signaling associated with acute and chronic pain conditions and could be implicated in various pathophysiological conditions such as arthritis, pancreatitis, migraine headache, and others.

Indeed, the expression of TRPV1 in trigeminal afferent neurons of *dura mater* suggested a plausible linkage of the channel actions to migraine (Huang et al., 2012; Shimizu et al., 2007). More evidence for this relationship was suggested by the effect of capsaicin on dilation of dural vessels (Akerman et al., 2003) and induction of trigeminal ganglion neuronal activity (Iwashita et al., 2013). However, the mechanisms by which TRPV1 contributes to initiating or propagating the neuronal signaling related to migraine are poorly understood (for a review, see Dussor et al., 2014). Our discovery of oxytocin as an endogenous agonist for the TRPV1 channel may shed more light onto the regulatory mechanisms that underlie physiology and pathology related to headaches and chronic migraine development.

The ability of oxytocin to modulate nociception is most likely achieved by activation of TRPV1, followed by its marked desensitization. Such mechanism is evident in nocifensive mice behavior, where oxytocin attenuates capsaicin-evoked nociceptive response (Figure 7). This is consistent with the fact that therapeutic targeting of TRPV1 has been primarily advanced via exogenous agonists that lead to prompt channel desensitization. These treatment options are traditionally based on capsaicin-containing remedies, such as capsaicin cream or high-concentration capsaicin patches (Dussor et al., 2014). Intranasal capsaicin administration has also been tested in treating migraine; similar to another TRPV1 agonist civanide, capsaicin reduced the frequency of cluster headache attacks (Diamond et al., 2000; Fusco et al., 2003). In contrast, attempts to identify effective and safe TRPV1 antagonists have been stymied by numerous complications, including dysregulation of internal body temperature. In this light, identifying the endogenous

mechanisms of TRPV1 potentiation and desensitization by oxytocin along with the patterns of expression and their functional relationship within the neuronal network offers a valuable asset to pain regulation.

EXPERIMENTAL PROCEDURES

For detailed methods, see the Supplemental Information.

Cell Culture

HEK293 cells were maintained in minimal essential medium (MEM) as previously described (Zakharian et al., 2009). F-11 cells were cultured in DMEM/F12 medium as previously described (Zakharian et al., 2009). Mouse DRG neurons were cultured in primary neuron basal medium (PNBM), (Lonza, Allendale, NJ).

Whole-Cell Patch-Clamp Recordings

The whole-cell patch-clamp experiments were performed as previously described (Yudin et al., 2011; Zakharian et al., 2009). HEK293T cells were cotransfected with rTRPV1 and EGFP with Lipofectamine 2000 according to the manufacturer's protocol. Whole-cell patch-clamp recordings were performed 48–72 hr post-transfection at room temperature.

Intracellular Ca^{2+} Measurements

Ca^{2+} measurements were performed as previously described (Zakharian et al., 2009).

Preparation of the TRPV1 Protein from HEK Cells

TRPV1 protein isolation was performed as previously described (Sun and Zakharian, 2015; Zakharian et al., 2010). TRPV1 was purified by immunoprecipitation with anti-Myc-IgG conjugated to A/G protein magnetic beads (Pierce, Thermo Scientific, Milwaukee, WI). For the planar lipid bilayer experiments, the protein was eluted with Myc-peptide (150 μg/mL).

Planar Lipid Bilayer Measurements

Planar lipid bilayer measurements and temperature studies were performed as previously described (Sun and Zakharian, 2015; Zakharian, 2013; Zakharian et al., 2010).

Animal Studies

Age-matched male and female wild-type and $TRPV1^{-/-}$, $TRPA^{-/-}$, and $TRPM8^{-/-}$ mice were purchased from Jackson Laboratory (Maine, USA).

SUPPLEMENTAL INFORMATION

Supplemental Information includes Supplemental Experimental Procedures, seven figures, and one table and can be found with this article online at https://doi.org/10.1016/j.celrep.2017.10.063.

AUTHOR CONTRIBUTIONS

Y.N., L.D., D.C.-B., V.O., R.K., X.S., C.C., A.M.C., and E.Z. conducted experiments. Y.N., L.D., and E.Z. conducted imaging experiments. D.C.-B. conducted electrophysiological experiments, using whole-cell patch clamp. L.D., Y.N., T.D., and X.S. conducted electrophysiological experiments, using lipid bilayers. V.O. performed computational studies and analysis. L.D. conducted western blotting experiments. R.K. performed mouse behavioral experiments. E.Z. conducted experiments on protein isolation for mass spectrometry, and A.M.C. performed mass spectrometry experiments and their analysis. B.C. helped with the mouse tissue-isolation experiments. C.C. performed molecular biology studies. K.K.V. contributed reagents and material. Y.N., L.D., D.C.-B., V.O., R.K., X.S., A.M.C., K.Z., C.D., S.B., and E.Z. analyzed data. K.Z. designed and supervised mouse behavioral experiments. C.D. designed and supervised computational studies and simulation analysis. S.B. designed and supervised patch-clamp experiments. Y.N. and E.Z. designed the study, and E.Z. supervised the experiments. E.Z. wrote the manuscript, with the contributions of Y.N., C.D., K.Z., and S.B. All authors critically read and edited the manuscript.

ACKNOWLEDGMENTS

We deeply appreciate the commitment of Dr. Liskin Swint-Kruse and her immense help in critical reading of the manuscript and fruitful suggestions. We are grateful to Angela Daniels for her exceptional help with the animal experiments.

This work was initially supported by the NIH through grant R01GM098052 to E.Z. C.D. and V.O. acknowledge the PRACE initiative for awarding the access to computational resources in ARCHER—the UK National Supercomputing Service (http://www.archer.ac.uk), the PDC Centre for High Performance Computing (PDC-HPC), CINECA, and the Jülich Supercomputing Center. V.O. was supported by BB/L015269/1 from the Biotechnology and Biological Sciences Research Council and Pfizer Neusentis. S.B. was supported by Anillo Científico ACT-1401. S.B. is a part of CISNe-UACh and UACh Program for Cell Biology.

Received: February 17, 2017
Revised: August 21, 2017
Accepted: October 16, 2017
Published: November 7, 2017

REFERENCES

Akerman, S., Kaube, H., and Goadsby, P.J. (2003). Vanilloid type 1 receptors (VR1) on trigeminal sensory nerve fibres play a minor role in neurogenic dural vasodilatation, and are involved in capsaicin-induced dural dilation. Br. J. Pharmacol. *140*, 718–724.

Bae, C., Anselmi, C., Kalia, J., Jara-Oseguera, A., Schwieters, C.D., Krepkiy, D., Won Lee, C., Kim, E.-H., Kim, J.I., Faraldo-Gómez, J.D., and Swartz, K.J. (2016). Structural insights into the mechanism of activation of the TRPV1 channel by a membrane-bound tarantula toxin. eLife *5*, e11273.

Bohlen, C.J., Priel, A., Zhou, S., King, D., Siemens, J., and Julius, D. (2010). A bivalent tarantula toxin activates the capsaicin receptor, TRPV1, by targeting the outer pore domain. Cell *141*, 834–845.

Carter, C.S. (2014). Oxytocin pathways and the evolution of human behavior. Annu. Rev. Psychol. *65*, 17–39.

Caterina, M.J., Schumacher, M.A., Tominaga, M., Rosen, T.A., Levine, J.D., and Julius, D. (1997). The capsaicin receptor: a heat-activated ion channel in the pain pathway. Nature *389*, 816–824.

Diamond, S., Freitag, F., Phillips, S.B., Bernstein, J.E., and Saper, J.R. (2000). Intranasal civamide for the acute treatment of migraine headache. Cephalalgia *20*, 597–602.

Dussor, G., Yan, J., Xie, J.Y., Ossipov, M.H., Dodick, D.W., and Porreca, F. (2014). Targeting TRP channels for novel migraine therapeutics. ACS Chem. Neurosci. *5*, 1085–1096.

Eliava, M., Melchior, M., Knobloch-Bollmann, H.S., Wahis, J., da Silva Gouveia, M., Tang, Y., Ciobanu, A.C., Triana Del Rio, R., Roth, L.C., Althammer, F., et al. (2016). A new population of parvocellular oxytocin neurons controlling magnocellular neuron activity and inflammatory pain processing. Neuron *89*, 1291–1304.

Fusco, B.M., Barzoi, G., and Agrò, F. (2003). Repeated intranasal capsaicin applications to treat chronic migraine. Br. J. Anaesth. *90*, 812.

Gimpl, G., and Fahrenholz, F. (2001). The oxytocin receptor system: structure, function, and regulation. Physiol. Rev. *81*, 629–683.

González-Hernández, A., Rojas-Piloni, G., and Condés-Lara, M. (2014). Oxytocin and analgesia: future trends. Trends Pharmacol. Sci. *35*, 549–551.

Hicks, C., Ramos, L., Reekie, T., Misagh, G.H., Narlawar, R., Kassiou, M., and McGregor, I.S. (2014). Body temperature and cardiac changes induced by peripherally administered oxytocin, vasopressin and the non-peptide oxytocin receptor agonist WAY 267,464: a biotelemetry study in rats. Br. J. Pharmacol. *171*, 2868–2887.

Horowitz, L.F., Hirdes, W., Suh, B.C., Hilgemann, D.W., Mackie, K., and Hille, B. (2005). Phospholipase C in living cells: activation, inhibition, Ca2+ requirement, and regulation of M current. J. Gen. Physiol. *126*, 243–262.

Huang, D., Li, S., Dhaka, A., Story, G.M., and Cao, Y.Q. (2012). Expression of the transient receptor potential channels TRPV1, TRPA1 and TRPM8 in mouse trigeminal primary afferent neurons innervating the dura. Mol. Pain *8*, 66.

Iwashita, T., Shimizu, T., Shibata, M., Toriumi, H., Ebine, T., Funakubo, M., and Suzuki, N. (2013). Activation of extracellular signal-regulated kinase in the trigeminal ganglion following both treatment of the dura mater with capsaicin and cortical spreading depression. Neurosci. Res. *77*, 110–119.

Juif, P.E., and Poisbeau, P. (2013). Neurohormonal effects of oxytocin and vasopressin receptor agonists on spinal pain processing in male rats. Pain *154*, 1449–1456.

Juif, P.E., Breton, J.D., Rajalu, M., Charlet, A., Goumon, Y., and Poisbeau, P. (2013). Long-lasting spinal oxytocin analgesia is ensured by the stimulation of allopregnanolone synthesis which potentiates GABA(A) receptor-mediated synaptic inhibition. J. Neurosci. *33*, 16617–16626.

Julius, D. (2013). TRP channels and pain. Annu. Rev. Cell Dev. Biol. *29*, 355–384.

Kendrick, K.M., Keverne, E.B., Hinton, M.R., and Goode, J.A. (1991). Cerebrospinal fluid and plasma concentrations of oxytocin and vasopressin during parturition and vaginocervical stimulation in the sheep. Brain Res. Bull. *26*, 803–807.

Kobayashi, A., Osaka, T., Namba, Y., Inoue, S., Lee, T.H., and Kimura, S. (1998). Capsaicin activates heat loss and heat production simultaneously and independently in rats. Am. J. Physiol *275*, R92–R98.

Knobloch, H.S., Charlet, A., Hoffmann, L.C., Eliava, M., Khrulev, S., Cetin, A.H., Osten, P., Schwarz, M.K., Seeburg, P.H., Stoop, R., and Grinevich, V. (2012). Evoked axonal oxytocin release in the central amygdala attenuates fear response. Neuron *73*, 553–566.

Ludwig, M., and Leng, G. (2006). Dendritic peptide release and peptide-dependent behaviours. Nat. Rev. Neurosci. *7*, 126–136.

Lukacs, V., Rives, J.M., Sun, X., Zakharian, E., and Rohacs, T. (2013). Promiscuous activation of transient receptor potential vanilloid 1 (TRPV1) channels by negatively charged intracellular lipids: the key role of endogenous phosphoinositides in maintaining channel activity. J. Biol. Chem. *288*, 35003–35013.

Ross, H.E., Cole, C.D., Smith, Y., Neumann, I.D., Landgraf, R., Murphy, A.Z., and Young, L.J. (2009). Characterization of the oxytocin system regulating affiliative behavior in female prairie voles. Neuroscience *162*, 892–903.

Sanborn, B.M., Dodge, K., Monga, M., Qian, A., Wang, W., and Yue, C. (1998). Molecular mechanisms regulating the effects of oxytocin on myometrial intracellular calcium. Adv. Exp. Med. Biol. *449*, 277–286.

Sawchenko, P.E., and Swanson, L.W. (1983). The organization of forebrain afferents to the paraventricular and supraoptic nuclei of the rat. J. Comp. Neurol. *218*, 121–144.

Scharrer, E., and Scharrer, B. (1940). Secretory cells within the hypothalamus. Res. Publ. Assoc. Res. Nerv. Ment. Dis. *20*, 170–194.

Shimizu, T., Toriumi, H., Sato, H., Shibata, M., Nagata, E., Gotoh, K., and Suzuki, N. (2007). Distribution and origin of TRPV1 receptor-containing nerve fibers in the dura mater of rat. Brain Res. *1173*, 84–91.

Stoop, R. (2012). Neuromodulation by oxytocin and vasopressin. Neuron *76*, 142–159.

Sun, X., and Zakharian, E. (2015). Regulation of the temperature-dependent activation of transient receptor potential vanilloid 1 (TRPV1) by phospholipids in planar lipid bilayers. J. Biol. Chem. *290*, 4741–4747.

Swanson, L.W., and Sawchenko, P.E. (1983). Hypothalamic integration: organization of the paraventricular and supraoptic nuclei. Annu. Rev. Neurosci. *6*, 269–324.

Thyagarajan, B., Benn, B.S., Christakos, S., and Rohacs, T. (2009). Phospholipase C-mediated regulation of transient receptor potential vanilloid 6 channels: implications in active intestinal Ca2+ transport. Mol. Pharmacol. *75*, 608–616.

Wang, Y.L., Yuan, Y., Yang, J., Wang, C.H., Pan, Y.J., Lu, L., Wu, Y.Q., Wang, D.X., Lv, L.X., Li, R.R., et al. (2013). The interaction between the oxytocin and pain modulation in headache patients. Neuropeptides *47*, 93–97.

Winslow, J.T., Noble, P.L., Lyons, C.K., Sterk, S.M., and Insel, T.R. (2003). Rearing effects on cerebrospinal fluid oxytocin concentration and social buffering in rhesus monkeys. Neuropsychopharmacology *28*, 910–918.

Young, L.J., Wang, Z., Donaldson, R., and Rissman, E.F. (1998). Estrogen receptor alpha is essential for induction of oxytocin receptor by estrogen. Neuroreport *9*, 933–936.

Yudin, Y., Lukacs, V., Cao, C., and Rohacs, T. (2011). Decrease in phosphatidylinositol 4,5-bisphosphate levels mediates desensitization of the cold sensor TRPM8 channels. J. Physiol. *589*, 6007–6027.

Zakharian, E. (2013). Recording of ion channel activity in planar lipid bilayer experiments. Methods Mol. Biol. *998*, 109–118.

Zakharian, E., Thyagarajan, B., French, R.J., Pavlov, E., and Rohacs, T. (2009). Inorganic polyphosphate modulates TRPM8 channels. PLoS ONE *4*, e5404.

Zakharian, E., Cao, C., and Rohacs, T. (2010). Gating of transient receptor potential melastatin 8 (TRPM8) channels activated by cold and chemical agonists in planar lipid bilayers. J. Neurosci. *30*, 12526–12534.

5.3 Prediction of the Interfacial Region in the Proposed TRPV1-PKR Complex

5.3.1 Authorship and Permissions

<table>
<tr><td colspan="9">This declaration concerns the article entitled</td></tr>
<tr><td colspan="9">Prediction of the Interfacial Region in the Proposed TRPV1-PKR Complex</td></tr>
<tr><td colspan="9">Publication status (tick one)</td></tr>
<tr><td>Draft manuscript</td><td>✓</td><td>Submitted</td><td></td><td>In review</td><td></td><td>Accepted</td><td></td><td>Published</td><td></td></tr>
<tr><td>Publication details</td><td colspan="8">Not Applicable</td></tr>
<tr><td>Candidates contribution to the paper (detailed and also given as a percentage)</td><td colspan="8">The candidate contributed to/considerably contributed/predominantly executed the…

This partial manuscript is a contribution to a collaboration with the research group of Guilherme Lucas at the University of São Paulo. The full manuscript is currently being prepared.

Formulation of ideas (50%):
V. Oakes and C. Domene contributed equally.

Design of methodology (50%):
V. Oakes and C. Domene contributed equally.

Experimental work (Computational: 100%):
V. Oakes: Performed simulations and analysis

Presentation of data in journal format (15%):
V. Oakes: Main author of text and figures relating to computational work.
C. Domene critically revised the manuscript.</td></tr>
<tr><td>Statement from Candidate</td><td colspan="8">This paper reports on original research I conducted during the period of my Higher Degree by Research candidature.</td></tr>
<tr><td>Signed</td><td colspan="5"></td><td>Date</td><td colspan="2"></td></tr>
</table>

5.3.2 Manuscript

Prediction of the Interfacial Region in the Proposed TRPV1-PKR Complex

Victoria Oakes[1] and Carmen Domene[1,2]

[1]Department of Chemistry, University of Bath, Claverton Down, Bath, BA2 7AY, UK

[2]Department of Chemistry, University of Oxford, Mansfield Road, Oxford, OX1 3TA, Oxford, UK

Introduction

Protein kinases play a pivotal role in cellular function by appending phosphate groups to protein substrates and initiating signal transduction pathways. Double-stranded (ds) RNA-dependent protein kinase, also known as protein kinase R (PKR) is a serine/threonine protein kinase. PKR is historically known for its role in inhibition of the translation factor eIF2α.[1] X-ray crystal structures of the PKR-eIF2α complex have provided critical insights into this process.[2]

PKR is constituted of two functionally distinct domains, an N-terminal dsRNA binding domain and a C-terminal domain, typical of protein kinases, containing two lobes linked by a short segment.[2] The N-terminal lobe (residues 258-369) is composed of a twisted five-strand antiparallel β-sheet, flanked by helices; the C-terminal lobe (residues 370-551) contains two antiparallel β-strands and eight α-helices. Of these, residues 432-458 form the activation segment. PKR activity is strictly dependent on homodimerization of both kinase and RNA-binding domains, and autophosphorylation of residue T446 in the so-called activation loop.[3] This process is triggered by binding of double-stranded RNA, as well as PACT and heparin ligands.[4,5] PKR is activated not only by double-stranded RNA presented by viruses, but also pro-inflammatory mediators, growth factors and cytokines.[6,7] Thus, PKR has been proposed to participate in several cellular processes including immune responses, cell growth control, apoptosis, and metabolic stress.[8] These results have advocated a broader role for PKR in the regulation of transcription and signal transduction associated with diverse pathological processes, including chronic pain.

Experimental Background

Recently, a series of experiments have been performed to explore the involvement of PKR in chronic pain (Guilherme Lucas et al, personal communication). Immunohistochemistry revealed constitutively phosphorylated T466 PKR in the spinal cord dorsal horn where nociceptive messages are primarily released to the central nervous system. However, 3 days after CFA-induced peripheral inflammation the phosphorylated form of PKR was significantly increased in the spinal dorsal horn ipsilateral to the inflamed paw. In the DRG neurons, PKR is co-localized

with TRPV1, and $NaV_{1.8}$ ion channels. In addition, neurons, but not astrocytes or microglia cells, exhibit enhanced phosphorylation of PKR throughout the dorsal horn. Behaviorally, spinal inhibition of PKR significantly reduced inflammatory pain hypersensitivity in a concentration-dependent manner. At 5 μM, PKR inhibitor completely reversed thermal hyperalgesia. Conversely, PKR inhibitor per se induced no change on the paw withdrawal latency after noxious stimulus. In addition, inflammatory thermal hyperalgesia, but not mechanical allodynia, was completely abolished in PKR knockout (PKR-/-) mice whereas paw edema remained unaltered as compared with wild-type animals.

PKR has been shown to phosphorylate a number of substrates such as mitogen activated protein kinases (MAPKs), the nuclear factor-kappaB (NF-κB) , and the α subunit of eukaryotic initiation factor 2 (eIF2α).[9] As MAPK p38, JNK, and ERK1,2 as well as NF-κB phosphorylation have also been reported to be increased in the spinal dorsal horn during peripheral inflammation,[10-12] the question of whether inhibition of PKR prevents activation of these signaling pathways under persistent inflammatory condition was examined. Intrathecal administration of PKR inhibitor (5μM) completely reversed p38 and JNK phosphorylation in the dorsal horn during chronic inflammation, but had no effect on ERK1,2 activity. PKR has also been shown to activate NF-κβ family of transcription factors through interaction with and activation of the IKK complex.[13] NFκβ is required for the transcriptional activation of a variety of genes regulating inflammatory responses of cells and is highly activated in the spinal dorsal horn under inflammatory conditions.[12] Inhibition of spinal PKR activity significantly reduced IKK phosphorylation induced by chronic inflammation. The most well characterized substrate for PKR, eIF2α, was also investigated, where PKR prevents mRNA translation and produces an antiviral response.[14] Peripheral inflammation induced no change on eIF2α phosphorylation in the dorsal horn and PKR inhibition has no effect on basal eIF2α activity suggesting that antiviral and pronociceptive effects of PKR are mediated by distinct signaling pathways.

Next, the experiments addressed if nociception induced by central inflammatory mediators requires PKR-dependent intracellular signaling. PKR has been reported to signal downstream of a number of cytokines including tumor necrosis factor-α (TNF-α),[15] interleukin 1β (IL-1β),[16] and Interferon-γ (IFN-γ)[17] which also mediate a marked hypernociception when intrathecally administrated.[18,19,20] Thus, thermal hyperalgesia induced by TNF-α, IL-1β, NGF (nerve growth factor) and LPS (Lipopolysaccharides) was inhibited by systemic administration of PKR inhibitor (100μg/Kg, i.p.).

Combined, these findings show that PKR is a critical mediator of chronic inflammatory pain acting through p38, JNK, and NFκB signaling pathways. Thermal hypersensitivity is primarily mediated by TRPV1, $NaV_{1.7}$ and $NaV_{1.8}$ ion channels, and therefore they are potential targets of PKR activity.

Simulation Objectives

To investigate this proposal, docking calculations and molecular dynamics (MD) simulations have been performed to classify potential PKR interaction sites and phosphorylation sites on TRPV1. For this purpose, the activated PKR structure (PDB ID 2A1A)[2] and an open-state TRPV1 structure (PDB ID 5IRX, resolution 2.95 Å)[29] are utilized to resemble the anticipated conformational states when in action.

Several other protein kinases are known to alter the functional properties of TRPV1; protein kinases A and C (PKA and PKC) are known to curtail desensitization of TRPV1, the process by which ion channels close upon continual exposure to chemical or physical stimuli, and hence potentiate TRPV1 activation.[21,22] PKA and PKC act through distinct serine/threonine phosphorylation sites in the intracellular ankyrin-repeat domain of TRPV1, many of which have been isolated (Table 1). Identification of additional phosphorylation sites will guide aid future investigation into the behaviour of TRPV1 and protein kinases, and their interrelationship.

Table 1. Reported phosphorylation sites of TRPV by protein kinases.

Kinase	Receptor	Residue (hTRPV1)	Reference
PKA	TRPV1	S117	23
		T145	24
		T371	21,24
		S502	24,25
PKC		S502	26
		T705	27
		S801	26,28

Methods

Docking Calculations

Docking can be undertaken via a template-based or direct approach. Direct methods endeavor to identify thermodynamically favorable complexes by algorithmically evaluating the free-energy and then performing minimization to obtain the estimated free-energy minima.[30] Here, two protein-protein docking web-servers based on direct methods, GRAMM-X[31,32] and ClusPro,[33] have been used to perform TRPV1-PKR docking.

The structures of the open-state TRPV1 channel determined by single-particle cryo-electron microscopy in lipid nanodiscs (PDB: 5IRX, resolution 2.95 Å) states were used to model the ion channel containing residues 111 to 751.[29] The double-knot toxin (DkTx) and the vanilloid resiniferatoxin (RTx) were removed from the open state. For PKR, the structure of the PKR kinase-domain in complex with eIF2α was utilized as the initial model, with eIF2α removed.[2] Missing residues were modelled using Modloop.[34] Both structures were input into the servers, with no restraints. The output was curated to include only complexes where PKR predominantly

interacted with the intracellular domain, and to recognize degenerate binding modes originating from the presence of four identical monomers in the channel.

Molecular Dynamics Simulations

To prepare the TRPV1-PKR complexes for simulation, the N- and C- termini of both proteins were acetylated and methylated respectively and default protonation states used for ionizable residues.[35] SOLVATE1.0 was used to fill the internal cavities of the proteins, which were inserted into a pre-equilibrated lipid bilayer of 1-palmitoyl-2-oleoyl-sn-glycero-3-phosphocholine (POPC) molecules, generated using the Membrane Plugin of VMD.[36] The systems were then solvated to produce a cubic water box, and NaCl was added, using the Autoionise Plugin of VMD, to neutralize and mimic the biological ionic concentration of 150 mM.[21] The resulting system size was between 400,000-500,000 atoms dependent on the position of the docked PKR in each of the binding poses.

NAMD2.12 was employed to perform MD simulations.[37] The CHARMM36 force field (with the CMAP correction) was used to describe the TRPV1 channel and the PKR protein, CHARMM36 for lipids,[38] TIP3P[39] model for water, and standard ion parameters.[40] The Particle Mesh Ewald method was used for the treatment of periodic electrostatic interactions, with an upper threshold of 1 Å for grid spacing.[41] Electrostatic and van der Waals forces were calculated every timestep. A cut-off distance of 12 Å was used for Van der Waals forces. A switching distance of 10 Å was chosen to smoothly truncate the non-bonded interactions. Only atoms in a Verlet pair list with a cut-off distance of 13.5 Å (reassigned every 20 steps) were considered.[42] The SETTLE algorithm was used to constrain all bonds involving hydrogen atoms to allow the use of a 2 fs time step throughout the simulation.[43] The Nose-Hoover-Langevin piston method was employed to control the pressure with a 200 fs period, 50 fs damping constant and a desired value of 1 atmosphere.[44,45] The system was coupled to a Langevin thermostat to sustain a temperature of 310 K throughout.

The system was coupled to a Langevin thermostat to sustain a temperature of 310 K throughout. Initially, the systems were subject to 10,000 steps of minimization with the protein backbone atoms restrained, and subsequently equilibrated for a total of 2.5 ns. Each equilibration step was undertaken for 500 ps, with restraints removed systematically: (i) lipid tails, (ii) water and lipid headgroups, (iv) protein side-chain atoms.

Results and Discussion

Docking calculations successfully identified a number of TRPV1-PKR complexes with PKR bound in the intracellular domain. The most highly populated clusters were extracted and subjected to molecular simulation to assess the stability of the complex and identify influential interaction pairs. Three complexes were investigated in total (displayed in Figure 1) from the ClusPro (POSE 1 & 3) and GRAMM-X (POSE 2) outputs.

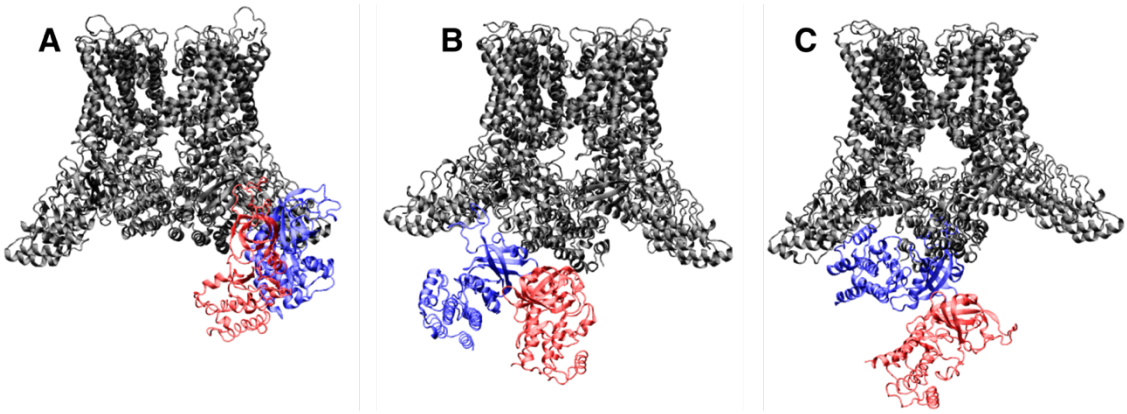

Figure 1. TRPV1-PKR complexes: (A) POSE 1, (B) POSE 2 and (C) POSE 3. TRPV1 is shown in grey, and the two subunits of the PKR dimer are shown in red and blue.

POSE 1

MD simulations 250 ns in length have been performed. The TRPV1 ankyrin-repeat domain (ARD), present intracellularly (residues 101–364), is comprised of six ankyrin repeats (AR1-6), each formed of a pair of antiparallel α helices followed by a "finger" loop. In this case, the PKR dimer interacts with two TRPV1 subunits, via PKR residues E269, K291, E303, K314, D370, R409, K440-R447 and S461-D464 (Figure 2). These residues interact with TRPV1 residues from AR1 (L111, D119, Q123 and E128), AR6 (P360, E361 and R363) and residues in the C-terminal intracellular domain (F730, T731, K735, D736 and D737). D370 (PKR)-R138 (TRPV1), D464 (PKR)-R363 (TRPV1) and R447 (PKR)-E361 (TRPV1) contribute the most extensive interactions. This configuration allows T731 to form contacts with the activation loop (432-458), in close proximity to T446 (PKR), the critical residue for autophosphorylation of PKR, providing a potential target residue for PKR. Residues S116 and T322 are also in the vicinity of PKR in this pose.

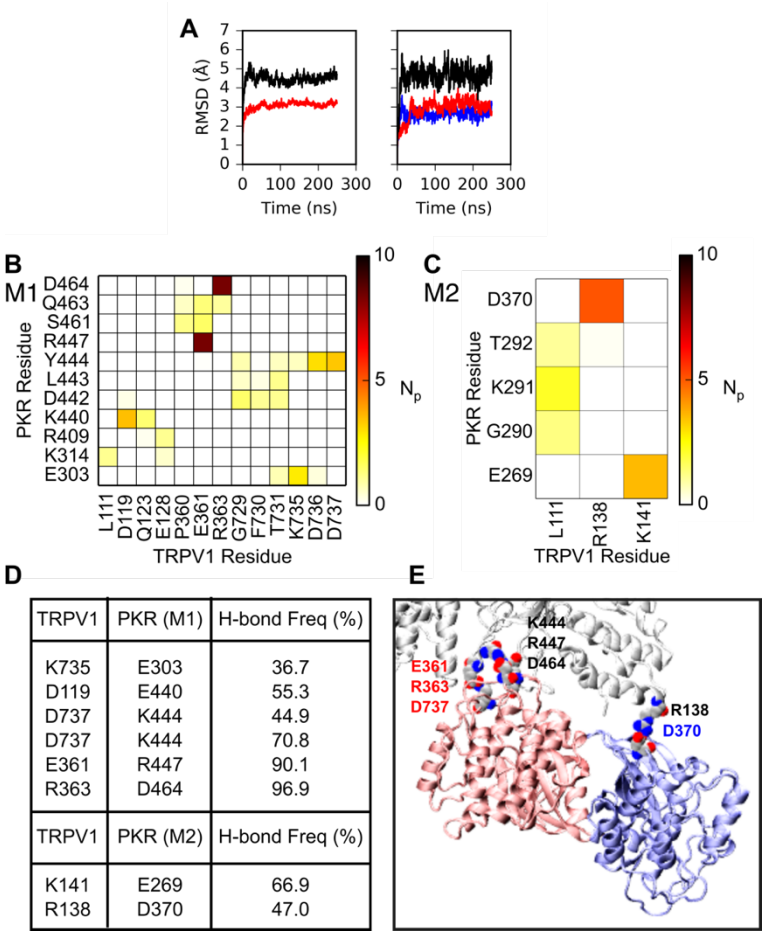

TRPV1	PKR (M1)	H-bond Freq (%)
K735	E303	36.7
D119	E440	55.3
D737	K444	44.9
D737	K444	70.8
E361	R447	90.1
R363	D464	96.9
TRPV1	**PKR (M2)**	**H-bond Freq (%)**
K141	E269	66.9
R138	D370	47.0

Figure 2. Dynamics of POSE 1 simulation. (A: left) RMSD of TRPV1, the TM and IC/TM domains are shown in black and red, respectively. (A: right) RMSD of PKR, the dimer is shown in black, and monomer 1 and 2 are shown separately in blue and red, respectively. (B-C) Contact map displaying the number of interacting atom pairs (N_P) between TRPV1 and PKR (monomer 1 in B and 2 in C), averaged over the simulation length (4Å cut-off and including heavy atoms only). (D) Percentage frequency of hydrogen bond formation (3.5 Å distance and 35° angle cut-off) between specified residue pairs, calculated over the whole trajectory. (E) Position of critical residues, which have over 70% H-bond frequency and/or are involved in at least 4 atomic interaction pairs. Monomer 1 and 2 are shown in blue and red, respectively.

POSE 2

MD simulations 350 ns in length have been performed. Here, PKR residues between 330-360 on both subunits and residues 255-265 on a single subunit interact with TRPV1 (Figure 3). TRPV1 interactions are spread across ARD1, ARD2, ARD3, ARD4, ARD5 and the C-terminus. In this conformation, TRPV1 serine/threonine residues are inaccessible from the PKR activation loop.

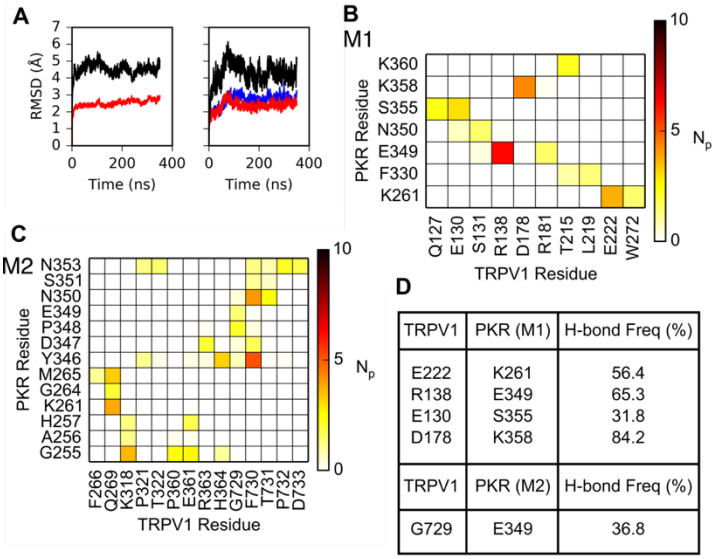

TRPV1	PKR (M1)	H-bond Freq (%)
E222	K261	56.4
R138	E349	65.3
E130	S355	31.8
D178	K358	84.2
TRPV1	PKR (M2)	H-bond Freq (%)
G729	E349	36.8

Figure 3. Dynamics of POSE 2 simulation. (A: left) RMSD of TRPV1, the TM and IC/TM domains are shown in black and red, respectively. (A: right) RMSD of PKR, the dimer is shown in black, and monomer 1 and 2 are shown separately in blue and red, respectively. (B-C) Contact map displaying the number of interacting atom pairs (N_P) between TRPV1 and PKR (monomer 1 in B and 2 in C), averaged over the simulation length (4Å cut-off and including heavy atoms only). (D) Percentage frequency of hydrogen bond formation (3.5 Å distance and 35° angle cut-off) between specified residue pairs, calculated over the whole trajectory. (E) Position of critical residues, which have over 70% H-bond frequency and/or are involved in at least 4 atomic interaction pairs. Monomer 1 and 2 are shown in blue and red, respectively.

POSE 3

MD simulations 600 ns in length have been performed, with the corresponding results presented in Figure 4. The results suggest PKR residues in the regions, 303-304, 335-360, 446-466 and 486-506 interact with TRPV1. The latter region overlaps with the eIF2α-binding consensus motif (V484-E490).[46] In this case, S271 is in contact distance of the activation loop, providing another potential target residue for PKR.

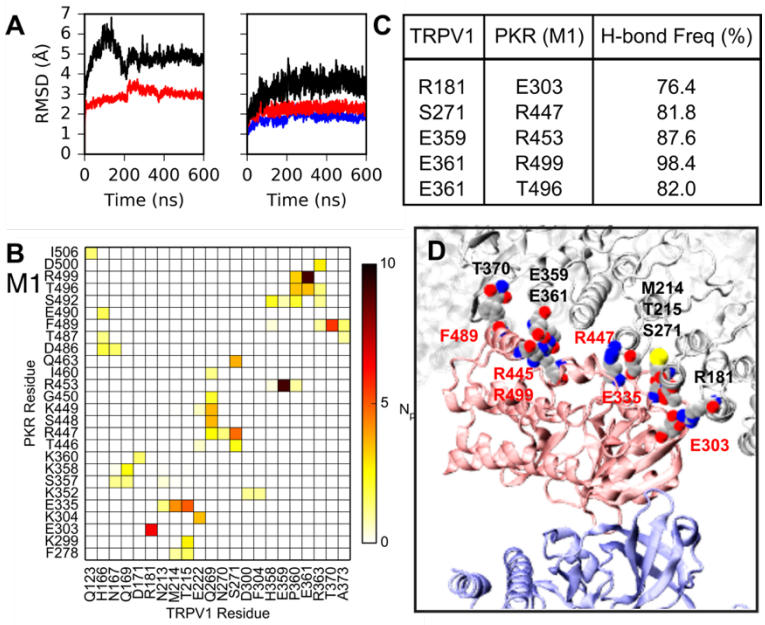

TRPV1	PKR (M1)	H-bond Freq (%)
R181	E303	76.4
S271	R447	81.8
E359	R453	87.6
E361	R499	98.4
E361	T496	82.0

Figure 4. Dynamics of POSE 1 simulation. (A: left) RMSD of TRPV1, the TM and IC/TM domains are shown in black and red, respectively. (A: right) RMSD of PKR, the dimer is shown in black, and monomer 1 and 2 are shown separately in blue and red, respectively. (B-C) Contact map displaying the number of interacting atom pairs (N_P) between TRPV1 and PKR (monomer 1 in B and 2 in C), averaged over the simulation length (4Å cut-off and including heavy atoms only). (D) Percentage frequency of hydrogen bond formation (3.5 Å distance and 35° angle cut-off) between specified residue pairs, calculated over the whole trajectory. (E) Position of critical residues, which have over 70% H-bond frequency and/or are involved in at least 4 atomic interaction pairs. Monomer 1 and 2 are shown in blue and red, respectively.

Conclusions

Extensive experimental findings have shown that PKR is a critical mediator of chronic inflammatory pain acting through p38, JNK, and NFκB signaling pathways. Thermal hypersensitivity is primarily mediated by TRPV1, $NaV_{1.7}$ and $NaV_{1.8}$ ion channels; therefore, such channels have been suggested as potential targets of PKR activity.

To explore this hypothesis, docking calculations and MD simulations have been performed to characterise possible PKR interaction and phosphorylation sites in the intracellular domain of

TRPV1. Overall, three interaction models for the TRPV1-PKR complex have been tested; two models contain direct interactions between the activation segment (residues 432-458) and the intracellular TRPV1 results. These results reveal several potential candidates for phosphorylation by PKR, and thereby suggest a potential mechanism by which PKR affects the functional properties of TRPV1. This information can now be used by our collaborators to assess the effect of PKR in selected TRPV1 mutants and evaluate the importance of such residues in the physiology of the TRPV1 ion channel.

The importance of PKR-mediated signaling for development of inflammatory pain conditions disclosed in this project provide new insights on underlying mechanisms participating in neuronal sensitization and may raise new strategies for the establishment of antinociceptive treatments. The increasing availability of high-resolution structures of TRP and related channels implicated in nociceptive pathways will also aid the development of analgesic compounds in the future.

References

(1) Williams, B. R. G. Role of the double-stranded RNA-activated protein kinase (PKR) in cell regulation. *Biochem. Soc. T.* **1997,** *25* (2), 509.

(2) Dar, A. C.; Dever, T. E.; Sicheri, F. Higher-order substrate recognition of eIF2 alpha by the RNA-dependent protein kinase PKR. *Cell* **2005,** *122* (6), 887.

(3) Taylor, S. S.; Haste, N. M.; Ghosh, G. PKR and eIF2 alpha: Integration of kinase dimerization, activation, and substrate docking. *Cell* **2005,** *122* (6), 823.

(4) Anderson, E.; Pierre-Louis, W. S.; Wong, C. J.; Lary, J. W.; Cole, J. L. Heparin Activates PKR by Inducing Dimerization. *J. Mol. Biol.* **2011,** *413* (5), 973.

(5) Dong, Y. Y.; Pike, A. C. W.; Mackenzie, A.; McClenaghan, C.; Aryal, P.; Dong, L.; Quigley, A.; Grieben, M.; Goubin, S.; Mukhopadhyay, S.et al. K2P channel gating mechanisms revealed by structures of TREK-2 and a complex with Prozac. *Science* **2015,** *347* (6227), 1256.

(6) Leaman, D. W.; Salvekar, A.; Patel, R.; Sen, G. C.; Stark, G. R. A mutant cell line defective in response to double-stranded RNA and in regulating basal expression of interferon-stimulated genes. *Proc. Nat. Acad. Sci. USA* **1998,** *95* (16), 9442.

(7) Garcia, M. A.; Gil, J.; Ventoso, I.; Guerra, S.; Domingo, E.; Rivas, C.; Esteban, M. Impact of protein kinase PKR in cell biology: from antiviral to antiproliferative action. *Microbiol. Mol. Biol. R.* **2006,** *70* (4), 1032.

(8) Tan, S. L.; Katze, M. G. The emerging role of the interferon-induced PKR protein kinase as an apoptotic effector: A new face of death? *J. Interf. Cytok. Res.* **1999,** *19* (6), 543.

(9) Ji, R. R.; Samad, T. A.; Jin, S. X.; Schmoll, R.; Woolf, C. J. p38 MAPK activation by NGF in primary sensory neurons after inflammation increases TRPV1 levels and maintains heat hyperalgesia. *Neuron* **2002,** *36* (1), 57.

(10) Gao, Y. J.; Ji, R. R. Light touch induces ERK activation in superficial dorsal horn neurons after inflammation: involvement of spinal astrocytes and JNK signaling in touch-evoked central sensitization and mechanical allodynia. *J. Neurochem.* **2010,** *115* (2), 505.

(11) Silva, A. M.; Whitmore, M.; Xu, Z.; Jiang, Z. F.; Li, X. X.; Williams, B. R. G. Protein kinase R (PKR) interacts with and activates mitogen-activated protein kinase kinase 6 (MKK6) in response to double-stranded RNA stimulation. *J. Biol. Chem.* **2004,** *279* (36), 37670.

(12) Zamanian-Daryoush, M.; Mogensen, T. H.; DiDonato, J. A.; Williams, B. R. G. NF-kappa B activation by double-stranded-RNA-activated protein kinase (PKR) is mediated through NF-kappa B-inducing kinase and I kappa B kinase. *Mol. Cell. Biol.* **2000,** *20* (4), 1278.

(13) Lee, K. M.; Kang, B. S.; Lee, H. L.; Son, S. J.; Hwang, S. H.; Kim, D. S.; Park, J. S.; Cho, H. J. Spinal NF-kB activation induces COX-2 upregulation and contributes to inflammatory pain hypersensitivity. *Eur. J. Neurosci.* **2004,** *19* (12), 3375.
(14) Sadler, A. J.; Williams, B. R. G. Structure and function of the protein kinase R. *Interferon* **2007,** *316*, 253.
(15) Takada, Y.; Ichikawa, H.; Pataer, A.; Swisher, S.; Aggarwal, B. B. Genetic deletion of PKR abrogates TNF-induced activation of I kappa B alpha kinase, JNK, Akt and cell proliferation but potentiates p44/p42 MAPK and p38 MAPK activation. *Oncogene* **2007,** *26* (8), 1201.
(16) Boo, K. H.; Yang, J. S. Intrinsic Cellular Defenses against Virus Infection by Antiviral Type I Interferon. *Yonsei Med. J.* **2010,** *51* (1), 9.
(17) Balachandran, S.; Barber G.N. PKR in Innate Immunity, Cancer, and Viral Oncolysis. In: Fisher P.B. (eds) Cancer Genomics and Proteomics. *Methods in MolecularBiology™,* **2007**, *383*.
(18) Zhang, L.; Berta, T.; Xu, Z. Z.; Liu, T.; Park, J. Y.; Ji, R. R. TNF-alpha contributes to spinal cord synaptic plasticity and inflammatory pain: Distinct role of TNF receptor subtypes 1 and 2. *Pain* **2011,** *152* (2), 419.
(19) Narita, M.; Shimamura, M.; Imai, S.; Kubota, C.; Yajima, Y.; Takagi, T.; Shiokawa, M.; Inoue, T.; Suzuki, M.; Suzuki, T. Role of interleukin-1 beta and tumor necrosis factor-alpha-dependent expression of cyclooxygenase-2 mRNA in thermal hyperalgesia induced by chronic inflammation in mice. *Neuroscience* **2008,** *152* (2), 477.
(20) Vikman, K. S.; Siddall, P. J.; Duggan, A. W. Increased responsiveness of rat dorsal horn neurons in vivo following prolonged intrathecal exposure to interferon-gamma. *Neuroscience* **2005,** *135* (3), 969.
(21) Mohapatra, D. P.; Nau, C. Regulation of Ca^{2+}-dependent desensitization in the vanilloid receptor TRPV1 by calcineurin and cAMP-dependent protein kinase. *J. Biol. Chem.* **2005,** *280* (14), 13424.
(22) Studer, M.; McNaughton, P. A. Modulation of single-channel properties of TRPV1 by phosphorylation. *J. of Physiol-London* **2010,** *588* (19), 3743.
(23) Bhave, G.; Zhu, W. G.; Wang, H. B.; Brasier, D. J.; Oxford, G. S.; Gereau, R. W. cAMP-dependent protein kinase regulates desensitization of the capsaicin receptor (VR1) by direct phosphorylation. *Neuron* **2002,** *35* (4), 721.
(24) Rathee, P. K.; Distler, C.; Obreja, O.; Neuhuber, W.; Wang, G. K.; Wang, S. Y.; Nau, C.; Kress, M. PKA/AKAP/VR-1 module: A common link of G(s)-mediated signaling to thermal hyperalgesia. *J. Neurosci.* **2002,** *22* (11), 4740.
(25) Zhang, X. M.; Li, L.; McNaughton, P. A. Proinflammatory mediators modulate the heat-activated ion channel TRPV1 via the scaffolding protein AKAP79/150. *Neuron* **2008,** *59* (3), 450.
(26) Numazaki, M.; Tominaga, T.; Toyooka, H.; Tominaga, M. Direct phosphorylation of capsaicin receptor VR1 by protein Kinase C epsilon and identification of two target serine residues. *J. Biol. Chem.* **2002,** *277* (16), 13375.
(27) Li, L.; Hasan, R.; Zhang, X. M. The Basal Thermal Sensitivity of the TRPV1 Ion Channel Is Determined by PKC beta II. *J. Neurosci.* **2014,** *34* (24), 8246.
(28) Lee, J.; Chung, M. K.; Ro, J. Y. Activation of NMDA receptors leads to phosphorylation of TRPV1 S800 by protein kinase C and A-Kinase anchoring protein 150 in rat trigeminal. *Biochem. and Bioph. Res. Co.* **2012,** *424* (2), 358.
(29) Gao, Y.; Cao, E. H.; Julius, D.; Cheng, Y. F. TRPV1 structures in nanodiscs reveal mechanisms of ligand and lipid action. *Nature* **2016,** *534* (7607), 347.
(30) Vajda, S.; Kozakov, D. Convergence and combination of methods in protein-protein docking. *Curr. Opin. in Struc. Biol.* **2009,** *19* (2), 164.
(31) Tovchigrechko, A.; Vakser, I. A. Development and testing of an automated approach to protein docking. *Proteins* **2005,** *60* (2), 296.
(32) Tovchigrechko, A.; Vakser, I. A. GRAMM-X public web server for protein-protein docking. *Nucleic Acids Res.* **2006,** *34*, W310.
(33) Kozakov, D.; Hall, D. R.; Xia, B.; Porter, K. A.; Padhorny, D.; Yueh, C.; Beglov, D.; Vajda, S. The ClusPro web server for protein-protein docking. *Nature Protocols* **2017,** *12* (2), 255.
(34) Fiser, A.; Sali, A. ModLoop: automated modeling of loops in protein structures. *Bioinformatics* **2003,** *19* (18), 2500.

(35) Li, H.; Robertson, A. D.; Jensen, J. H. Very fast empirical prediction and rationalization of protein pKa values. *Proteins* **2005,** *61* (4), 704.
(36) Humphrey, W.; Dalke, A.; Schulten, K. VMD: Visual molecular dynamics. *J. Mol. Graphics* **1996,** *14* (1), 33.
(37) Phillips, J. C.; Braun, R.; Wang, W.; Gumbart, J.; Tajkhorshid, E.; Villa, E.; Chipot, C.; Skeel, R. D.; Kale, L.; Schulten, K. Scalable molecular dynamics with NAMD. *J. Comput. Chem.* **2005,** *26* (16), 1781.
(38) Klauda, J. B.; Venable, R. M.; Freites, J. A.; O'Connor, J. W.; Tobias, D. J.; Mondragon-Ramirez, C.; Vorobyov, I.; MacKerell Jr, A. D.; Pastor, R. W. Update of the CHARMM all-atom additive force field for lipids: validation on six lipid types. *J. Phys. Chem.* B **2010,** *114* (23), 7830.
(39) Jorgensen, W. L.; Chandrasekhar, J.; Madura, J. D.; Impey, R. W.; Klein, M. L. Comparison of simple potential functions for simulating liquid water. *J. Chem. Physics* **1983,** *79* (2), 926.
(40) Beglov, D.; Roux, B. Finite representation of an infinite bulk system: Solvent boundary potential for computer simulations. *J. Chem. Physics* **1994,** *100* (12), 9050.
(41) Darden, T.; York, D.; Pedersen, L. Particle mesh Ewald: An N·log(N) method for Ewald sums in large systems. *J. Chem. Physics* **1993,** *98* (12), 10089.
(42) Verlet, L. Computer" experiments" on classical fluids. I. Thermodynamical properties of Lennard-Jones molecules. *Phys. Rev.* **1967,** *159* (1), 98.
(43) Miyamoto, S.; Kollman, P. A. SETTLE: an analytical version of the SHAKE and RATTLE algorithm for rigid water models. *J. Comput. Chem.* **1992,** *13* (8), 952.
(44) Feller, S. E.; Zhang, Y.; Pastor, R. W.; Brooks, B. R. Constant pressure molecular dynamics simulation: the Langevin piston method. *J. Chem. Physics* **1995,** *103* (11), 4613.
(45) Martyna, G. J.; Tobias, D. J.; Klein, M. L. Constant pressure molecular dynamics algorithms. *J. Chem. Physics* **1994,** *101* (5), 4177.
(46) Liu, M. S.; Wang, D.; Morimoto, H.; Yim, H. C. H.; Irving, A. T.; Williams, B. R. G.; Sadler, A. J. Molecular dynamics reveal a novel kinase-substrate interface that regulates protein translation. *J. Mol. Cell Biol.* **2014,** *6* (6), 473.

5.4 Commentary

5.4.1 Conclusions

The non-selective cation channel TRPV1 is most well-known for its action as a sensor for pain, heat and capsaicin, the active ingredient in the chilli pepper. In the pharmaceutical industry, TRPV1 is a leading target in the development of pain-relief treatments.[1-3] In order to progress in this area, adverse side effects associated with known TRPV1 inhibitors must be eliminated.[4] Therefore, investigations are required to comprehensively assess the diverse range of physiological stimuli which activate TRPV1 channels *in vivo* and understand how such processes take place on a molecular level. In this chapter, two combined experimental and molecular modelling studies have been presented, which reveal two novel TRPV1 activators and the associated binding sites on the TRPV1 channel surface.

Firstly, TRPV1 is shown to act as an ionotropic oxytocin receptor in cells, potentiating TRPV1 function in cells and lipid bilayers in the absence of the classical oxytocin receptor. In addition, oxytocin induces rapid desensitisation of capsaicin-induced nociception. This research feeds into recent efforts to develop exogenous agonists, which accelerate desensitisation of the channel,[5-7] as opposed to TRPV1 antagonists, which have been correlated with many complications, such as disruption of thermoregulation.[4] The associated MD simulations reveal an extracellular binding site, which overlaps with the DkTx binding site revealed by high-resolution structural information,[8] which is then confirmed by mutagenesis studies. This data may be exploited to advance therapeutic targeting of TRPV1, by developing agonists which target the specific locale in the extracellular region.

Following this, TRPV1 is pinpointed as a potential target of PKR activity, a serine/threonine kinase which is shown to be critical mediator of chronic inflammatory pain. Additional MD simulations reveal two potential intracellular binding sites, where the PKR 'activation loop' is in close contact to serine and/or threonine residues, suggesting several sites which may be vulnerable to phosphorylation. Further experimental work is now required to corroborate these proposals. To the best of my knowledge, this manuscript represents the first simulation study to evaluate the molecular interactions between TRPV channels and protein kinases, in order to predict intracellular phosphorylation sites. The docking and simulation protocol followed could be applied in future studies of TRPV1 with other protein kinases, known to act through distinct serine/threonine phosphorylation sites in the intracellular ankyrin-repeat domain of TRPV1 (PKA and PKC).[9-15]

5.4.2 References

(1) Tominaga, M.; Caterina, M. J.; Malmberg, A. B.; Rosen, T. A.; Gilbert, H.; Skinner, K.; Raumann, B. E.; Basbaum, A. I.; Julius, D. The cloned capsaicin receptor integrates multiple pain-producing stimuli. *Neuron* **1998,** *21* (3), 531.

(2) Tominaga, M.; Julius, D. Capsaicin receptor in the pain pathway. *Jpn J. Pharmacology* **2000,** *83* (1), 20.

(3) Julius, D. TRP channels and pain. *Annu. Rev. Cell. Dev. Biol.* **2013**, *29*, 355.

(4) Carnevale, V.; Rohacs, T. TRPV1: A Target for Rational Drug Design. *Pharmaceuticals* **2016,** *9* (3), 20.

(5) Dussor, G.; Yan, J.; Xie, J. Y.; Ossipov, M. H.; Dodick, D. W.; Porreca, F. Targeting TRP Channels For Novel Migraine Therapeutics. *ACS Chem. Neuro.* **2014,** *5* (11), 1085.

(6) Diamond, S.; Freitag, F.; Phillips, S. B.; Bernstein, J. E.; Saper, J. R. Intranasal civamide for the acute treatment of migraine headache. *Cephalalgia* **2000,** *20* (6), 597.

(7) Fusco, B. M.; Barzoi, G.; Agro, F. Repeated intranasal capsaicin applications to treat chronic migraine. *Brit. J. Anaesth.* **2003,** *90* (6), 812.

(8) Cao, E. H.; Liao, M. F.; Cheng, Y. F.; Julius, D. TRPV1 structures in distinct conformations reveal activation mechanisms. *Nature* **2013,** *504* (7478), 113.

(9) Mohapatra, D. P.; Nau, C. Regulation of Ca^{2+}-dependent desensitization in the vanilloid receptor TRPV1 by calcineurin and cAMP-dependent protein kinase. *J. Biol. Chem.* **2005,** *280* (14), 13424.

(10) Bhave, G.; Zhu, W. G.; Wang, H. B.; Brasier, D. J.; Oxford, G. S.; Gereau, R. W. cAMP-dependent protein kinase regulates desensitization of the capsaicin receptor (VR1) by direct phosphorylation. *Neuron* **2002,** *35* (4), 721.

(11) Rathee, P. K.; Distler, C.; Obreja, O.; Neuhuber, W.; Wang, G. K.; Wang, S. Y.; Nau, C.; Kress, M. PKA/AKAP/VR-1 module: A common link of G(s)-mediated signaling to thermal hyperalgesia. *J. Neurosci.* **2002,** *22* (11), 4740.

(12) Zhang, X. M.; Li, L.; McNaughton, P. A. Proinflammatory mediators modulate the heat-activated ion channel TRPV1 via the scaffolding protein AKAP79/150. *Neuron* **2008,** *59* (3), 450.

(13) Numazaki, M.; Tominaga, T.; Toyooka, H.; Tominaga, M. Direct phosphorylation of capsaicin receptor VR1 by protein kinase C epsilon and identification of two target serine residues. *J. Biol. Chem.* **2002,** *277* (16), 13375.

(14) Li, L.; Hasan, R.; Zhang, X. M. The Basal Thermal Sensitivity of the TRPV1 Ion Channel Is Determined by PKC beta II. *J. Neurosci.* **2014,** *34* (24), 8246.

(15) Lee, J.; Chung, M. K.; Ro, J. Y. Activation of NMDA receptors leads to phosphorylation of TRPV1 S800 by protein kinase C and A-kinase anchoring protein 150 in rat trigeminal. *Biochem. and Bioph. Res. Co.* **2012,** *424* (2), 358.

6 Cholesterol Interaction with Membrane Proteins

6.1 Commentary

6.1.1 Introduction

In the final chapter of this thesis, I digress from the study of ion channels and delve into the behaviour of G-protein coupled receptors (GPCRs). Here, the topic of focus is the behaviour of serotonin (5-hydroxytryptamine: 5-HT) receptors in response to the presence of membrane cholesterol.

Cholesterol is a major constituent of the cell membrane, directly binding to membrane proteins and also regulating the physical properties of the membrane. As a consequence, the exact mechanism of cholesterol modulation of membrane proteins has been difficult to decipher.[1] In the context of GPCRs, this is further complicated by the spectrum of functional responses cholesterol can elicit. In the 5-HT_{1A} receptor, cholesterol is reported to affect receptor stability,[2] ligand binding affinity[3,4] and the formation of dimers and higher-order oligomers.[5] Stereoisomers of cholesterol, and closely related sterol molecules, have emerged as valuable chemical probes to distinguish between specific and non-specific effects, in both ion channels and membrane proteins.[6] Many studies have also scrutinized the behaviour of the 5-HT_{1A} receptor in response to such molecules.[3,7,8]

Prior to this investigation, information concerning the site of cholesterol binding in receptors in the 5-HT receptor family has been limited to homology models of the 5-HT_{1A} receptor and the biologically relevant isomer of cholesterol.[9] Moreover, assessment of indirect affects is omitted. To pursue this further, we have used a two-pronged approach to evaluate the ramifications of membrane cholesterol on two 5-HT receptors, where structures have now been resolved experimentally (5-HT_{1B} and 5-HT_{2B}).[10,11] In the first instance, the membrane properties of mixed cholesterol-phospholipid bilayers, containing several stereoisomers of cholesterol, have been examined. Following this, simulations of the 5-HT_{1B} and 5-HT_{2B} receptors in the aforementioned bilayers have been performed, in an attempt to ascertain the location and relevance of specific binding sites in these receptors. The protocol used here is analogous to the approach employed in section 4.3 to identify binding sites for anionic lipids in KcsA. The output from these calculations has resulted in two separate publications given in section 6.2 and 6.3, respectively.

6.1.2 References

(1) Gimpl, G. Interaction of G protein coupled receptors and cholesterol. *Chem. Phys. Lipids* **2016,** *199*, 61.

(2) Saxena, R.; Chattopadhyay, A. Membrane cholesterol stabilizes the human serotonin(1A) receptor. *BBA-Biomembranes* **2012,** *1818* (12), 2936.

(3) Jafurulla, M.; Rao, B. D.; Sreedevi, S.; Ruysschaert, J. M.; Covey, D. F.; Chattopadhyay, A. Stereospecific requirement of cholesterol in the function of the serotonin1A receptor. *Biochim. Biophys. Acta* **2014,** *1838* (1 Pt B), 158.

(4) Chattopadhyay, A.; Jafurulla, M.; Kalipatnapu, S.; Pucadyil, T. J.; Harikumar, K. G. Role of cholesterol in ligand binding and G-protein coupling of serotonin(1A) receptors solubilized from bovine hippocampus. *Biochem. Bioph. Res. Co.* **2005,** *327* (4), 1036.

(5) Paila, Y. D.; Kombrabail, M.; Krishnamoorthy, G.; Chattopadhyay, A. Oligomerization of the Serotonin(1A) Receptor in Live Cells: A Time-Resolved Fluorescence Anisotropy Approach. *J. Phys. Chem. B* **2011,** *115* (39), 11439.

(6) Levitan, I.; Singh, D. K.; Rosenhouse-Dantsker, A. Cholesterol binding to ion channels. *Front. Physiol.* **2014,** *5*, 14.

(7) Singh, P.; Saxena, R.; Paila, Y. D.; Jafurulla, M.; Chattopadhyay, A. Differential effects of cholesterol and desmosterol on the ligand binding function of the hippocampal serotonin(1A) receptor: Implications in desmosterolosis. *BBA-Biomembranes* **2009,** *1788* (10), 2169.

(8) Singh, P.; Jafurulla, M.; Paila, Y. D.; Chattopadhyay, A. Desmosterol replaces cholesterol for ligand binding function of the serotonin(1A) receptor in solubilized hippocampal membranes: Support for nonannular binding sites for cholesterol? *BBA-Biomembranes* **2011,** *1808* (10), 2428.

(9) Sengupta, D.; Chattopadhyay, A. Identification of Cholesterol Binding Sites in the Serotonin(1A) Receptor. *J. Phys. Chem. B* **2012,** *116* (43), 12991.

(10) Wacker, D.; Wang, C.; Katritch, V.; Han, G. W.; Huang, X. P.; Vardy, E.; McCorvy, J. D.; Jiang, Y.; Chu, M. H.; Siu, F. Y.et al. Structural Features for Functional Selectivity at Serotonin Receptors. *Science* **2013,** *340* (6132), 615.

(11) Wang, C.; Jiang, Y.; Ma, J. M.; Wu, H. X.; Wacker, D.; Katritch, V.; Han, G. W.; Liu, W.; Huang, X. P.; Vardy, E.et al. Structural Basis for Molecular Recognition at Serotonin Receptors. *Science* **2013,** *340* (6132), 610.

6.2 Stereospecific Interactions of Cholesterol in a Model Cell Membrane: Implications for the Membrane Dipole Potential, *J Membr Biol*. 2018.

6.2.1 Authorship and Permissions

<table>
<tr><td colspan="9">This declaration concerns the article entitled</td></tr>
<tr><td colspan="9">Stereospecific Interactions of Cholesterol in a Model Cell Membrane: Implications for the Membrane Dipole Potential</td></tr>
<tr><td colspan="9">Publication status (tick one)</td></tr>
<tr><td>Draft manuscript</td><td></td><td>Submitted</td><td></td><td>In review</td><td></td><td>Accepted</td><td></td><td>Published</td><td>✓</td></tr>
<tr><td>Publication details</td><td colspan="8">*J Membr Biol*. 2018, 251(3), 507-519
DOI: 10.1007/s00232-018-0016-0.
Epub 2018

Published online: 30 Jan 2018</td></tr>
<tr><td>Candidates contribution to the paper (detailed and also given as a percentage)</td><td colspan="8">The candidate contributed to/considerably contributed/predominantly executed the…
Formulation of ideas (50%):
V. Oakes and C. Domene contributed equally.

Design of methodology (25%):
V. Oakes and C. Domene contributed equally.

Experimental work (100%):
Simulation and analysis was performed by V.Oakes.

Presentation of data in journal format (80%):
V. Oakes: Main author of manuscript and supporting information.
C. Domene: Critically assessed and revised the manuscript.</td></tr>
<tr><td>Statement from Candidate</td><td colspan="8">This paper reports on original research I conducted during the period of my Higher Degree by Research candidature.</td></tr>
<tr><td>Signed</td><td colspan="4"></td><td>Date</td><td colspan="3"></td></tr>
</table>

6.2.2 Manuscript

Stereospecific Interactions of Cholesterol in a Model Cell Membrane: Implications for the Membrane Dipole Potential

Victoria Oakes[1] *& Carmen Domene*[1,2]

[1]Department of Chemistry, Claverton Drive, University of Bath, Bath BA2 7AY, UK

[2]Chemistry Research Laboratory, Mansfield Road, University of Oxford, Oxford, OX1 3TA, UK

Abstract

Cholesterol is a major constituent of the plasma membrane in higher-order eukaryote organisms. The effect of cholesterol on the structure and organisation of cell membranes has been studied extensively by both experimental and computational means. In recent years, a wealth of data has been accumulated illustrating how subtle differences in the structure of cholesterol equate to considerable changes in the physical properties of the membrane. The effect of cholesterol stereoisomers, in particular, has been established, identifying a direct link with the activity of specific membrane proteins. In this study, we perform extensive molecular dynamics simulations of phospholipid bilayers containing three isomers of cholesterol, the native form (*nat*-cholesterol), the enantiomer of the native form (*ent*-cholesterol), and an epimer of cholesterol that differs by the orientation of the polar hydroxyl group (*epi*-cholesterol). Based on these simulations, an atomic-level description of the stereospecific cholesterol-phospholipid interactions is provided, establishing a potential mechanism for the perturbation of membrane properties, specifically the membrane dipole potential.

Introduction

Phospholipid bilayers serve as the fundamental scaffold of all biological membranes, forming a barrier between the cell interior and the surrounding environment. Integral membrane proteins are responsible for the controlled passage of substances across this barrier. Cholesterol is particularly abundant in the plasma membrane of higher-order eukaryotes, and is an important requirement for the functioning of a diverse range of membrane proteins, whilst acting as a crucial regulator of membrane fluidity.[1] As a result, the specific effect of cholesterol on the structure of a phospholipid bilayer has been under discussion for much of the last century.[2] Arguably the most striking response to membrane cholesterol is the ‘condensing effect’, whereby the area per lipid molecule is noticeably lower than would be observed during ideal mixing, and the membrane thickness is increased concordantly, indicating changes in lipid organisation.[3]

In recent years, significant interest has been focused toward characterising the physical effect of naturally occurring cholesterol analogues, as well as synthetic cholesterol isomers and derivatives on lipid membranes. The native form of cholesterol (*nat*-cholesterol) is an asymmetric amphiphilic molecule, composed of a hydroxyl group attached to a tetracyclic sterane backbone, exhibiting a smooth α face and rough β face (Fig. 1A). The enantiomer of *nat*-cholesterol (*ent*-cholesterol) is the non-superimposable mirror image (Fig. 1B), exhibiting physiochemical properties indistinguishable to native cholesterol, except for the rotation of plane-polarised light.[4-7] Subtle changes in cholesterol membrane structure have been shown to exert profound effects on innate physiochemical properties. Certain attributes are known to significantly diverge in membranes containing related cholesterol molecules, including but not limited to *epi*-cholesterol, a stereoisomer of cholesterol, which differs in the orientation of the hydroxyl group (Fig. 1C), and 7-dehydrocholesterol and desmosterol, cholesterol precursors that differ by a double bond.[8-13] Membrane dipole potential, the potential difference within the membrane bilayer, exemplifies this phenomenon. A significant increase in dipole potential is observed upon cholesterol replenishment of both model and natural membranes, a lesser increase when 7-dehydrocholesterol and desmosterol are present, whilst replacement with *epi*-cholesterol causes the dipole potential to decrease, thus demonstrating that this property is highly dependent on the exact cholesterol structure.[14-17] The molecular mechanism underlying the regulation of membrane dipole potential via cholesterol and related molecules is currently unclear, however.

It has also been demonstrated that variations in cholesterol structure can modulate the functioning of specific membrane proteins, including but not limited to inwardly rectifying potassium channel Kir2.1,[18] ligand-gated ion channel receptor $GABA_A$[19] and G-protein coupled receptor 5-HT_{1A}.[20] Membrane cholesterol has been suspected to regulate membrane proteins by a direct mechanism, where direct coordination of cholesterol provokes conformational changes in the receptor, or an indirect mechanism, by modifying the membrane properties. Unnatural isomers, *ent*- and *epi*-cholesterol, have proven to be useful experimental probes to determine the exactitude of the interaction of cholesterol with such membrane proteins, and consequently the mechanism of cholesterol action.[6, 18-21] *Ent*-cholesterol, in particular, is a useful candidate to elucidate specific cholesterol effects, as the membrane properties are unchanged.

To elucidate how cholesterol and related molecules evoke differences in the physical properties of the membrane and the dynamics of membrane proteins, a high-resolution description of the specific interactions is required. As a consequence, molecular dynamics (MD) simulations have become an established method to typify the impact of cholesterol on membrane lipids and proteins, in atomic detail.[22-24] In this study, we have performed all-atom MD simulations of phospholipid bilayers containing 30% *nat*-, *ent*- and *epi*-cholesterol, as well as a 100% phospholipid bilayer, in order to determine the atomic behaviour of the cholesterol isomers. The simulations were 500 ns in length, significantly improving the timescale of prior MD

simulations examining the dynamics of *epi*-cholesterol, which were executed for 2 ns.[25] Key biophysical properties, including area per lipid, cholesterol tilt-angle and solvent-accessible-surface area, as well as the identity of crucial cholesterol-phospholipid interactions, were derived from the simulations. The results indicate potential mechanisms by which *epi*-cholesterol influences the membrane dipole potential and interfere with the functioning of membrane proteins. This is particularly relevant for the functioning of 5-HT_{1A} receptor, as ligand binding is abated in the presence of the *epi*-cholesterol.[20]

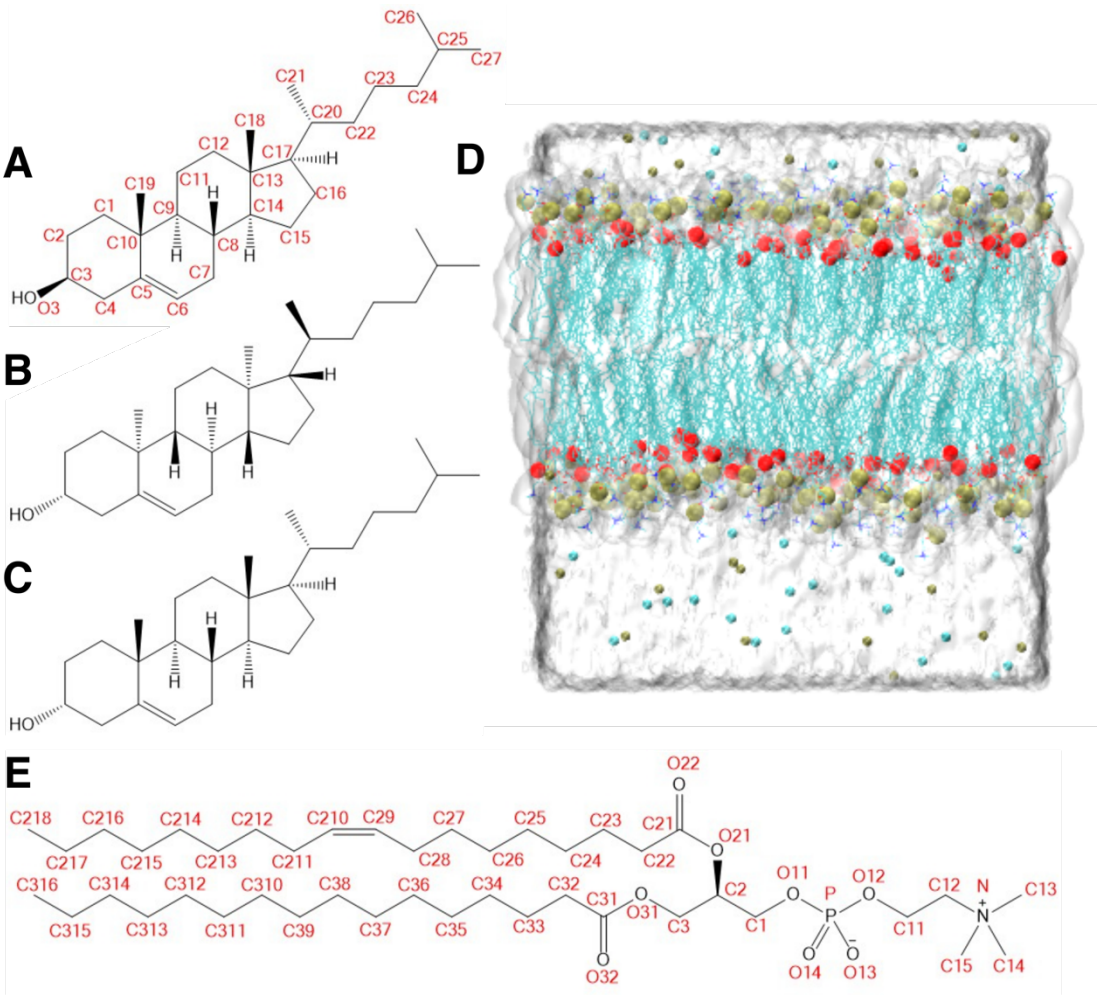

Figure 1. Chemical structure of (A) *nat*-cholesterol, (B) *ent*-cholesterol and (C) *epi*-cholesterol molecules, with atom naming used in this study labelled in red. (D) Representative snapshot of a simulation system: a lipid bilayer is solvated in a water box with a final concentration of 150 mM final of KCl. Phosphate atoms of the phospholipid molecules, and oxygen atoms of the cholesterol molecules are represented by a brown and red spheres, respectively, to indicate the position of the headgroups. Carbon atoms are shown in cyan. (E) Chemical structure of POPC, with atom naming used in this study labelled in red.

Methods

System Setup

Membranes containing 1- palmitoyl-2-oleoyl-sn-glycero-3-phosphocholine (POPC) molecules and *nat*-cholesterol molecules were generated using the CHARMM-GUI Membrane Builder.[26] [27] [28] The POPC membrane contained 244 POPC molecules, and the mixed bilayer contained 196 POPC molecules and 84 cholesterol molecules which represents ~30% cholesterol content to mimic known experimental conditions. The mixed POPC/*nat*-cholesterol membrane was then modified to generate additional membranes containing the epimer and enantiomer of cholesterol (topology and parameters employed are available upon request). The combined system was then solvated to produce a rectangular water box of dimensions (92 x 92 x 80) $Å^3$. K^+ and Cl^- ions were added using the Autoionise Plugin of VMD, to neutralise the system and obtain a 150 mM concentration.[29] The final systems contained approximately 60,000 atoms, and can be seen in Fig. 1D.

Molecular Dynamics Simulations

NAMD2.9 was employed to perform molecular dynamics (MD) simulations of the systems throughout.[30] CHARMM36 parameters were used for phosholipids[31], with standard parameters for ions[32] and the TIP3P[33] model for water. The modified CHARMM36 parameters by Lim et al were used for *nat*-cholesterol, *ent*- and *epi*-cholesterol molecules.[34] All systems were equilibrated using the documented CHARMM-GUI protocol.[27] Unrestrained dynamics for each system was then performed in the NPT ensemble for 500 ns. The Particle Mesh Ewald method was used for the treatment of full-system periodic electrostatic interactions; interactions were evaluated every second timestep with a value of 1 Å to determine grid spacing.[35] Short-range electrostatic and van der Waals forces were calculated every timestep and up to a cut-off distance of 12 Å. A switching distance of 10 Å was chosen to smoothly truncate the non-bonded interactions. Only atoms in a Verlet pair list within a cut-off distance of 13.5 Å were considered, with the list reassigned every 20 steps.[36] To allow the use of a 2 fs timestep, the SETTLE algorithm was used to make water molecules rigid, and the SHAKE algorithm was used to constrain all other bonds involving hydrogen atoms, utilizing a rigid tolerance of $1x10^{-5}$ Å.[37] The Nose-Hoover-Langevin piston was employed to control the pressure with a 200 fs period, 50 fs damping constant and a desired value of 1 atmosphere.[38] [39] The systems were coupled to a Langevin thermostat to sustain a temperature of 298 K throughout, in line with the experimental conditions used for radiolabel binding assays by Jafurulla et al.[20]

Trajectory Analysis

The atom names of the cholesterol and POPC molecules referred to in the following text are defined Fig. 1. MEMBPLUGIN was used to perform analyses of (1) membrane thickness, (2) area per lipid, (3) the carbon-deuterium (SCD) order parameter, (4) lipid tilt angle, and (5) lipid interdigitation.[40] To begin with, the membrane thickness was calculated as the distance between the projected mass distributions of the P atoms in the phospholipid headgroups in the upper and lower leaflets. To calculate the area per lipid, the simulation box was divided into a Voronoi

diagram, based on the coordinates of atom O3 in cholesterol molecules and atoms C2, C21 and C31 in POPC molecules (See Fig. 1A and 1D for notation), and the resulting area of the polygons was evaluated, for each bilayer leaflet. The SCD order parameter was calculated as $S_{CD} = -\frac{1}{2}\langle 3\cos^2\theta - 1\rangle$, to gauge the motility of the C-H bonds on the phospholipid acyl chains.[41] The tilt angle was calculated as the angle between the vector defined by the C10 and C13 cholesterol atoms and the bilayer normal, which is aligned to the z-axis throughout the simulation trajectories. The degree of acyl chain interdigitation was measured via a coordination-based fraction, obtained by evaluating the number of heavy atoms within 4 Å (default value) of atoms in the opposing leaflets.[40] Density profiles were calculated using the Density Profile Tool of VMD.[42] The solvent-accessible surface area and radial distribution functions were also calculated using built-in VMD tools. Further analysis was performed using in-house TCL scripts. A 4 Å distance cut-off was used for the calculation of intermolecular charge pairs and atomic interaction pairs between heavy atoms. A 3.5 Å distance and 35° angle cut-off was used for the calculation of H-bonding. The lifetime of *epi*-cholesterol dimers was calculated by considering the period between H-bond formation and disruption of the H-bond for a minimum of 0.5 ns. Reformation after this interval is considered as a new dimer, and hence lifetime. The initial 200 ns of the simulation trajectories were considered as an equilibration period, following assessment of the fluctuations of the membrane thickness and area per lipid (Table S1). These properties were regarded as converged by 500 ns, thus all analysis is performed on the 200-500 ns time interval. Electrostatic potential of the simulation system was calculated using the "PMEpot" plugin of VMD, following the methodology of Aksimentiev and Schulten.[43]

Results

In the first instance, global membrane properties have been calculated to elucidate the differences detectable using the MD simulation protocol described in this study, and the conformance of such results with known experimental data. In the POPC simulation, the membrane thickness and the area per lipid (Fig. S1) are calculated as 40 ± 1 Å and 63 ± 1 Å^3 respectively (Table 1), in close agreement with accepted experimental values.[44] The addition of cholesterol causes a net reduction of total bilayer area, with the overall average area per lipid in the system reducing to 45 ± 1 Å^3 in CHL and 46 ± 1 Å^3 in ENT, characteristic of the well-known condensing effect of cholesterol.[3] This effect is slightly offset in EPI, with an overall average area per lipid of 48 ± 1 Å^3, primarily as a result of an increased area of POPC molecules (Table 1). Correspondingly, an increase in membrane thickness is observed in CHL (46 ± 1 Å), ENT (46 ± 1 Å) and to a lesser degree in EPI (45 ± 1 Å). The extent to which the components of the upper and lower leaflets overlap, known as lipid interdigitation, are expectantly inversely correlated, displaying an increase in interdigitation alongside a decrease in thickness (Table 1).

Table 1. Summary of key membrane physical properties (± SD) obtained from MD simulations on the 200-500 ns time interval.

		POPC	CHL	ENT	EPI
Thickness (Å)	POPC	39.8 ± 0.9	46.3 ± 0.9	45.9 ± 0.9	44.8 ± 1.0
	Sterol	-	35.7 ± 0.8	35.6 ± 0.7	33.2 ± 0.8
Area per Lipid ($Å^3$)	POPC+Sterol	62.5 ± 1.2	45.4 ± 0.7	45.9 ± 0.7	47.4 ± 0.9
	POPC	62.5 ± 0.9	53.3 ± 0.7	53.9 ± 0.6	55.7 ± 0.8
	Sterol	-	27.2 ± 0.8	27.0 ± 0.8	28.1 ± 1.1
Tilt Angle (°)	Sterol	-	14.4 ± 1.2	15.3 ± 1.2	19.0 ± 1.5
Interdigitation (%)		5.6 ± 0.4	3.4 ± 0.2	3.5 ± 0.2	3.8 ± 0.2

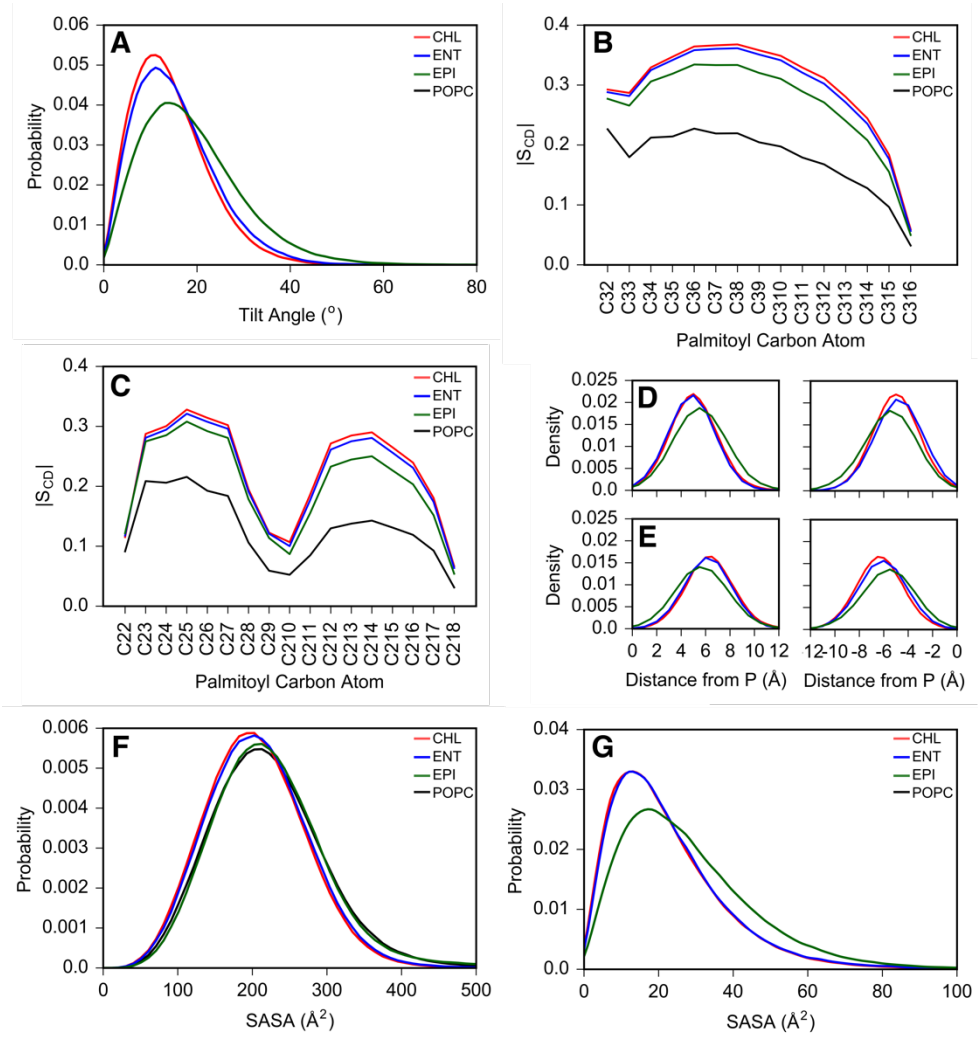

Figure 2. (A) Distribution of cholesterol tilt angles, normalized to 1 with a bin width of 1. SCD order parameter of (B) 16:0 saturated acyl chain at the glycerol *sn1* position (C3) and (C) 18:1 unsaturated acyl chain at the glycerol *sn2* position (C2). Mass density profiles of cholesterol (D) C3 and (E) O3 atoms, in the lower (left) and upper (right) leaflets, following alignment of the POPC phosphate atoms, normalized to 1 with a bin width of 0.5. SASA per (F) POPC and (G) cholesterol molecule, normalized to 1 with a bin width of 10 and 1 respectively. CHL, ENT, EPI and POPC simulations are displayed in red, blue, green and black respectively.

Such differences in the membrane physical properties arise from differences in the position and orientation of cholesterol in the bilayer, and the synergistic interaction with other bilayer components.[45] Cholesterol tilt angle is an important quantity, which is closely related to the ability of cholesterol to order its environment.[46] In this example, CHL and ENT display the narrowest distribution of tilt angles, with mean values of 14 ± 1 ° and 15 ± 1 °, respectively, representing a conformation almost parallel to the bilayer normal (Fig. 2A). The distribution of tilt angles in EPI is noticeably more spread, with an increased mean of 19 ± 2 °. This effect is reflected in the calculated S_{CD} order parameter, which is commonly used as a measure of lipid tail organisation, and can be directly compared to experimentation.[47-49] Overall, S_{CD} values increase in the cholesterol-containing bilayers, relative to POPC alone (Fig. 2B-C), indicative of the ordering effect of cholesterol that is well established in the literature.[50] This effect has been attributed to lipid packing around the rigid cholesterol frame. EPI exerts a weaker ordering effect overall, relative to CHL and ENT, with the greatest differences observed in the saturated regions of the acyl chains. These results contribute to a wealth of previous literature, which note the specificity of membrane ordering with regards the atomic structure of cholesterol.[51]

To directly compare the position of the cholesterol hydrophobic ring system and the hydrophilic hydroxyl group in the membrane, the mass density profiles of the C3 and O3 atoms (defined in Fig. 1A), following alignment of PC phosphate atoms, can be calculated (Fig. 2D-E). The C3-O3 maxima of EPI overlap at ~5.5 Å resulting from the axial conformation of the hydroxyl group, suggesting that whilst C3 adopts a shallower position in the membrane (~6 Å in CHL and ENT) whilst O3 is more buried (~5 Å in CHL and ENT).

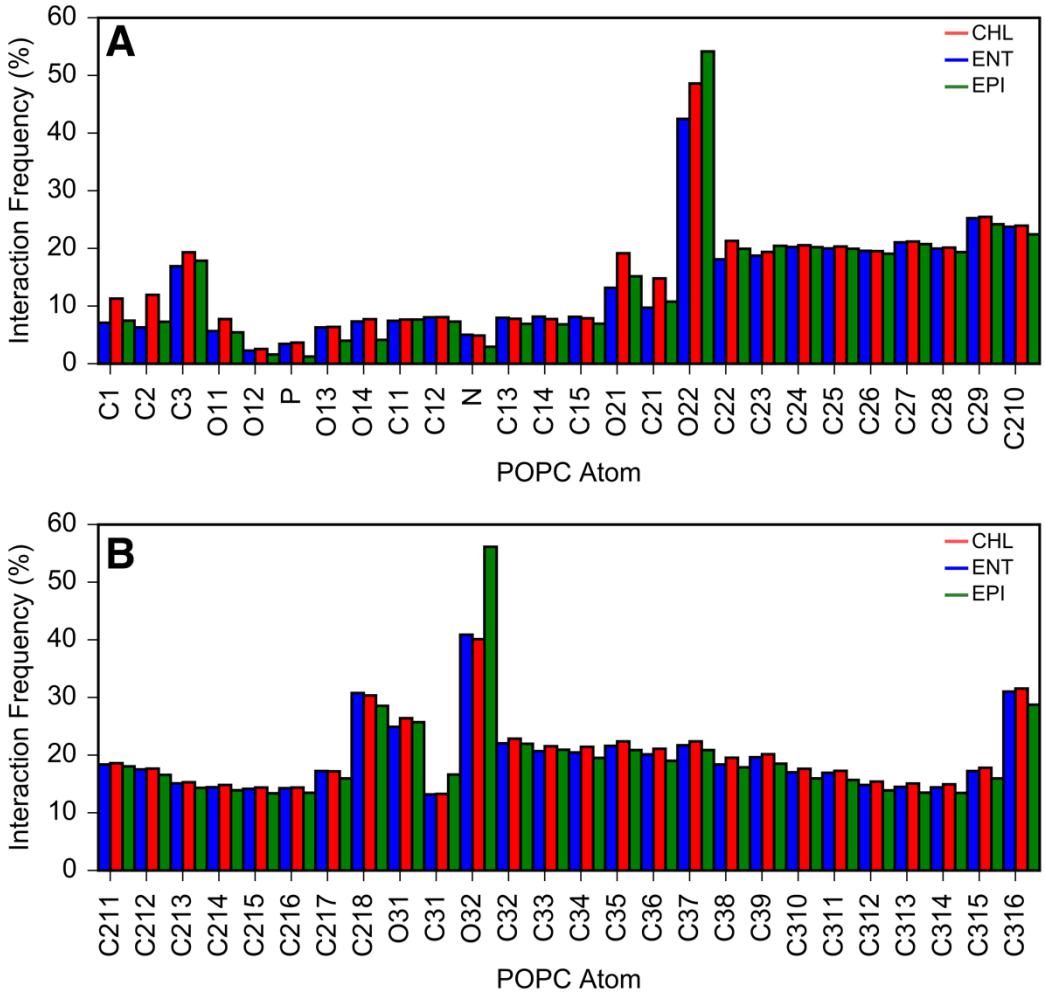

Figure 3. (A-B) Average interaction frequency between cholesterol and POPC atoms (specified). Interactions are calculated using a 4 Å criterion between heavy atoms.

To assess how this altered position affects the organisation of the membrane on an atomic-level, the average interaction frequency between individual POPC and cholesterol atoms has been calculated (Fig. 3). In general, headgroup atoms exhibit an average interaction frequency of ~0-10% of POPC, whilst tail atoms and those in the linker region, display average interaction frequencies in the 10-30% range, with EPI consistently presenting lower values. The carbonyl groups of the ester linkages (O22 and O32) are the exceptions to this, with average interaction frequencies in excess of 40% and elevated average interaction frequencies in EPI (54%, 56%) are relative to CHL (42%, 41%) and ENT (49%, 40%). The observed net increases can be attributed to enhanced interactions with C1, C5, C6 and C7 atoms, offsetting the reduced contact interface with O3.

To assess the impact of such differences at the membrane-water interface, the solvent accessible surface area (SASA) per molecule has been calculated for POPC and each sterol species (Fig. 2F-G and Table 2). The SASA of POPC in a single component membrane is calculated as ~220 $Å^3$, which reduces by ~15 $Å^3$ in CHL, 12 $Å^3$ in ENT and remarkably increases by ~5 $Å^3$ in EPI,

despite a decrease in the area per lipid for all cholesterol isomers relative to POPC-only. These observations provide evidence that SASA, and hence POPC-solvent interactions, are modulated by specific lipid-cholesterol interactions. It is interesting to note that the hydration of POPC headgroups decreases by ~4% in CHL and ENT, and 2% in EPI, as calculated from the individual RDFs of all POPC atoms (Fig. S2).

Table 2. Average SASA (± SD) of membrane lipids (the standard error of reported values is less than 0.1)

SASA (Å^2)	**POPC**	**CHL**	**ENT**	**EPI**
POPC	220 ± 75	205 ± 67	208 ± 68	225 ± 81
Sterol	-	22 ± 16	23 ± 16	28 ± 18

With regard to the SASA of cholesterol, CHL (22 Å^3) and ENT (23 Å^3) display similar values, increasing to 28 Å^3 in EPI (Table 2). This increase can be attributed to numerous effects, such as the increased area per cholesterol and tilt angle, the elevated position in the membrane and exposure of ring atoms as a result of the orientation of the hydroxyl group. The net increase in hydration in EPI is ~10%, relative to CHL and ENT, as calculated from the individual RDFs of all cholesterol atoms (Fig. S3). It is worth noting that a decrease is observed for O3, signalling that interactions with hydrophobic atoms are solely responsible for the observed increase. This will likely perturb the electrostatics of the cholesterol-water interfacial region.

H-bonding is a further important feature of the membrane-water interface. Approximately, all CHL and ENT molecules participate in at least one H-bond, via the cholesterol hydroxyl group, with 42% of molecules associated with PC headgroups and 60% of molecules H-bonding with water, in both cases. In contrast, 70% of EPI molecules are involved in H-bonding, as a result of diminished interactions with both PC headgroups (25%) and solvent (37%), and the evolution of cholesterol homo-dimers (8%). Dissection into the individual components of the PC headgroup (Fig. 4A, see Fig. 1D for atom names), identifies the largest reduction of H-bonding with atoms O13 (-3%) and O14 (-3%) in the phosphate group, and O22 (-6%) at the apex of the unsaturated acyl chain at the *sn2* acyl position, whilst H-bonding with O32 on the saturated acyl chain at the *sn1* position is generally conserved. The remaining reductions can be attributed to atoms C12, C13, C14, C15, O11 and O12. The total number of interactions with the cholesterol hydroxyl group displays an analogous pattern.

With regards to the hydration of the PC headgroups, approximately 18% of POPC molecules H-bond with CHL and ENT, whilst 10% H-bond with EPI. The reduction in PC-sterol H-bonds in EPI is overcompensated for by an increase in solvent H-bonds, resulting in a total of 9.4, 9.4 and 9.5 H-bonds per POPC molecule, in the CHL, ENT and EPI simulations respectively. Thus it is effectively unchanged by the presence of different cholesterol isomers. This is noticeably less than in the pure POPC membrane simulation (~10.3 H-bonds per POPC molecules), which

can largely be attributed to elevated H-bonding of phosphate oxygen atoms (O13 and O14; -32%), choline methyl groups (C13, C14, C15; -21%) and carbonyl atoms within the ester linkages (O22, O32; -20%) in the absence of cholesterol (Fig. 4B).

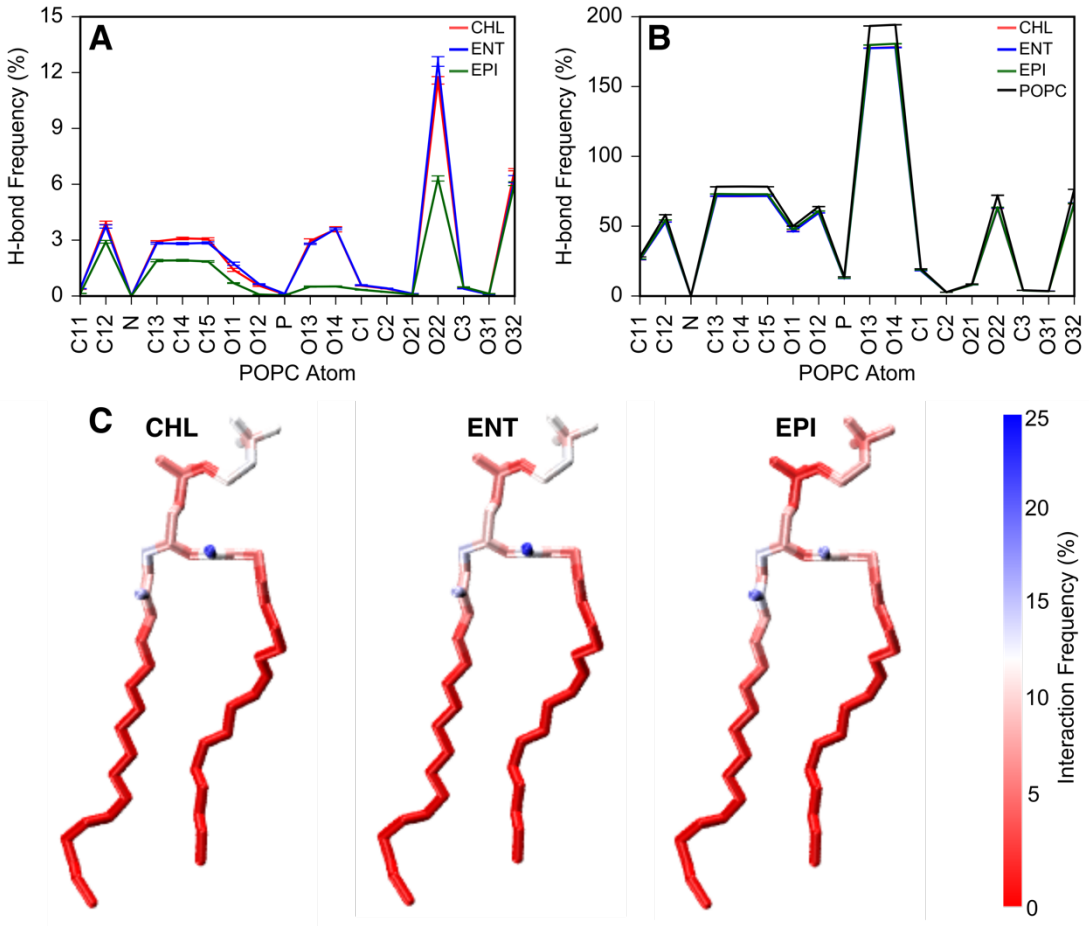

Figure 4. (A) Frequency of PC-sterol H-bonds, per cholesterol molecule. (B) Frequency of PC-water H-bonds, per POPC molecule. CHL, ENT, EPI and POPC simulations are displayed in red, blue, green and black respectively. (C) Licorice representation of a POPC molecule coloured according to the percentage interaction with the cholesterol hydroxyl group. A distance criterion of 4 Å between heavy atoms is used in this case.

Charge-pairs also contribute significantly to the dynamics of the membrane headgroup region. Intermolecular charge-pairs can be formed between the methyl groups of the positively charged choline moiety of PC, and negatively charged groups in cholesterol and PC headgroups, including the cholesterol hydroxyl (O3), the non-ester phosphate oxygen atoms (O13, O14) and the carbonyl atoms within the ester linkages at the apex of the acyl chains (O22, O32). The frequency of CHL-PC charge pairs is significantly perturbed in EPI, likely as a direct result of the orientation of the O3 hydroxyl (Fig. 5A). Relative to the POPC-only membrane, the number of PC-PC charge-pairs is increased by approximately 15%, 14% and 3%, in CHL, ENT and EPI respectively. The number of charge-pairs involving O13 and O14 (POPC < EPI < CHL ≈ ENT) is inversely correlated in the observed trend for the values calculated for the area per lipid

(POPC > EPI > CHL ≈ ENT) (Fig. 5B). It is apparent, however, that the distance between PC headgroups does not dictate the frequency of choline charge-pairs with O22 and O32 (Fig. 5C-D), and instead is likely directly influenced by the cholesterol headgroup. As a result, the number of charge-pairs for O22 displays the trend EPI ≈ POPC < CHL ≈ ENT, whilst the trend EPI < POPC ≈ CHL ≈ ENT is observed for O32. Thus, the increased frequency of O13/O14 choline charge-pairs in EPI, relative to POPC, is offset by the reduction in O32 choline charge-pairs, resulting in an overall pattern of EPI ≈ POPC < CHL ≈ ENT.

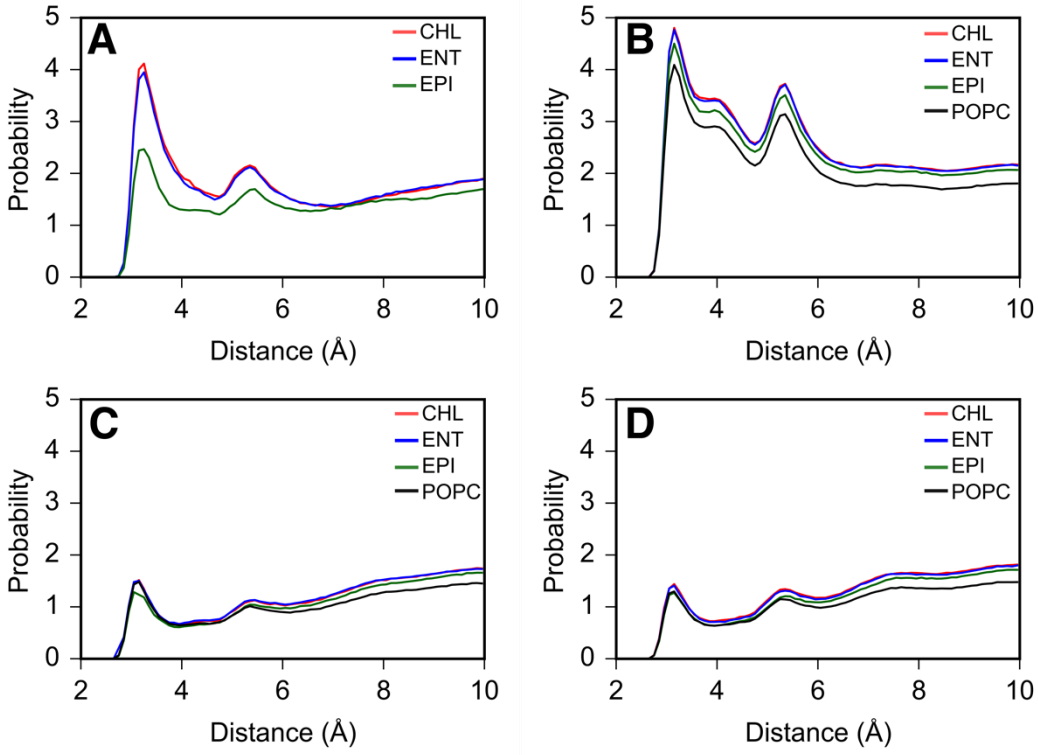

Figure 5. Radial distribution function of (A) cholesterol O3, (B) lipid O13/O14, (C) lipid O32, and (D) O22 atoms with C12, C13 and C14 atoms of the lipid headgroup choline region, to represent the distribution of intermolecular charge pairs. CHL, ENT, EPI and POPC simulations are displayed in red, blue, green and black respectively.

It is conceivable that a correlation exists between the formation of charge pairs between the choline methyl groups and the carbonyl oxygen atoms involved in the ester linkages, and the P^{+}-N^{-} dipole of the phospholipid headgroups. The average P^{+}-N^{-} vector relative to the bilayer normal is calculated as 68 ± 27° throughout, however, indicating this is not the case (Fig. 6A). Instead, it is apparent the charge density on the bilayer surface is significantly perturbed, demonstrated by the RDF of K^{+} and Cl^{-} ions with respect to phospholipid and cholesterol molecules (Fig. 6B and C, respectively). A maximum is observed at ~2.65 Å for K^{+} ions throughout, with the probability at this point following the trend: POPC (0.54) > ENT (0.45) > CHL (0.41) > EPI (0.17). In the case of Cl^{-}, a unique peak is observed at ~2.65 (0.05) which is absent elsewhere. The reduced density of cations, and concurrently, increased density of anions

on the bilayer surface reveals the elevated positive potential of the EPI bilayer surface, relative to CHL and ENT. This can also be illustrated by the electrostatic potential of the cholesterol isomers; considering the bilayer centre as 0 mV, CHL, ENT and EPI display values of -226 mV, -220 mV and -162 mV, respectively (Fig. 6D). The electrostatic potential of the complete CHL, ENT and EPI simulation systems vary to a lesser extent, with calculated values of -801 mV, -807 mV and -783 mV.

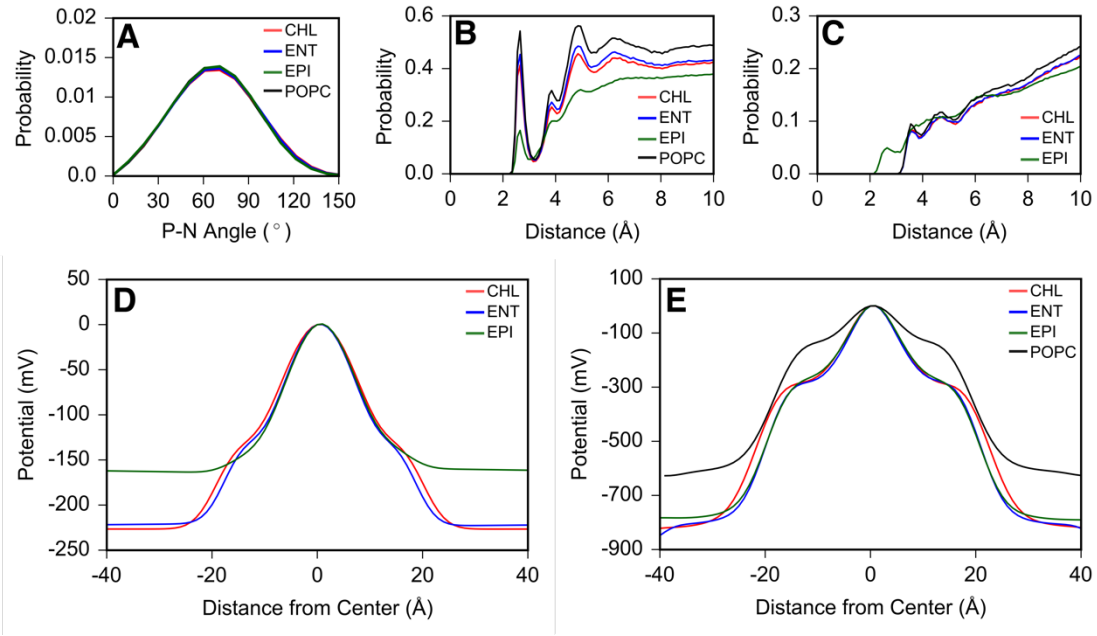

Figure 6. (A) Angle between P^+-N^- vector relative to the bilayer normal. Radial distribution function between (B) K^+ and (C) Cl^- ions and phospholipid and cholesterol molecules. Electrostatic potential of (D) cholesterol molecules and (E) the full simulation system, relative to the bilayer center. CHL, ENT, EPI and POPC simulations are displayed in red, blue, green and black respectively.

The nature of intermolecular cholesterol interactions is also worth considering. The calculated RDF of the cholesterol C3 atoms, up to a distance of 10 Å, is shown in Fig. 7A. According to this data, all cholesterol isomers are guaranteed to be within ~6.5 Å of another cholesterol molecule, yet the characteristics of cholesterol self-association are considerably different in EPI. The first RDF peak in CHL and ENT lies at 4 Å, whereas in EPI the first RDF peak ~5 Å and is approximately twice as probable, suggesting the alternative orientation of the hydroxyl group simultaneously acts as a spacer and a stabiliser. It should be noted that the concentration and initial configuration of cholesterol isomers is identical between simulations, and thus differences can be predominantly attributed to this feature. These results are consistent with the noticeable population of intermolecular cholesterol H-bonds identified in EPI by prior H-bond analysis, calling attention to the evolution of novel cholesterol dimers in this case. Using H-bond frequency as an indicator of dimer formation, the average lifetime of *epi*-cholesterol dimers has been calculated as 0.9 ± 1.1 ns, with a maximum lifetime of ~11 ns (Fig. 7B).

Characterisation of the interfacial region between two bound molecules (Fig. 7C) reveals the crucial interactions are localised in the hydroxyl region, with the oxygen interacting with ~4 atoms on the adjacent molecule simultaneously; the most probable interactions in descending order are O3, C3, C6 and C1 (Fig. 7D).

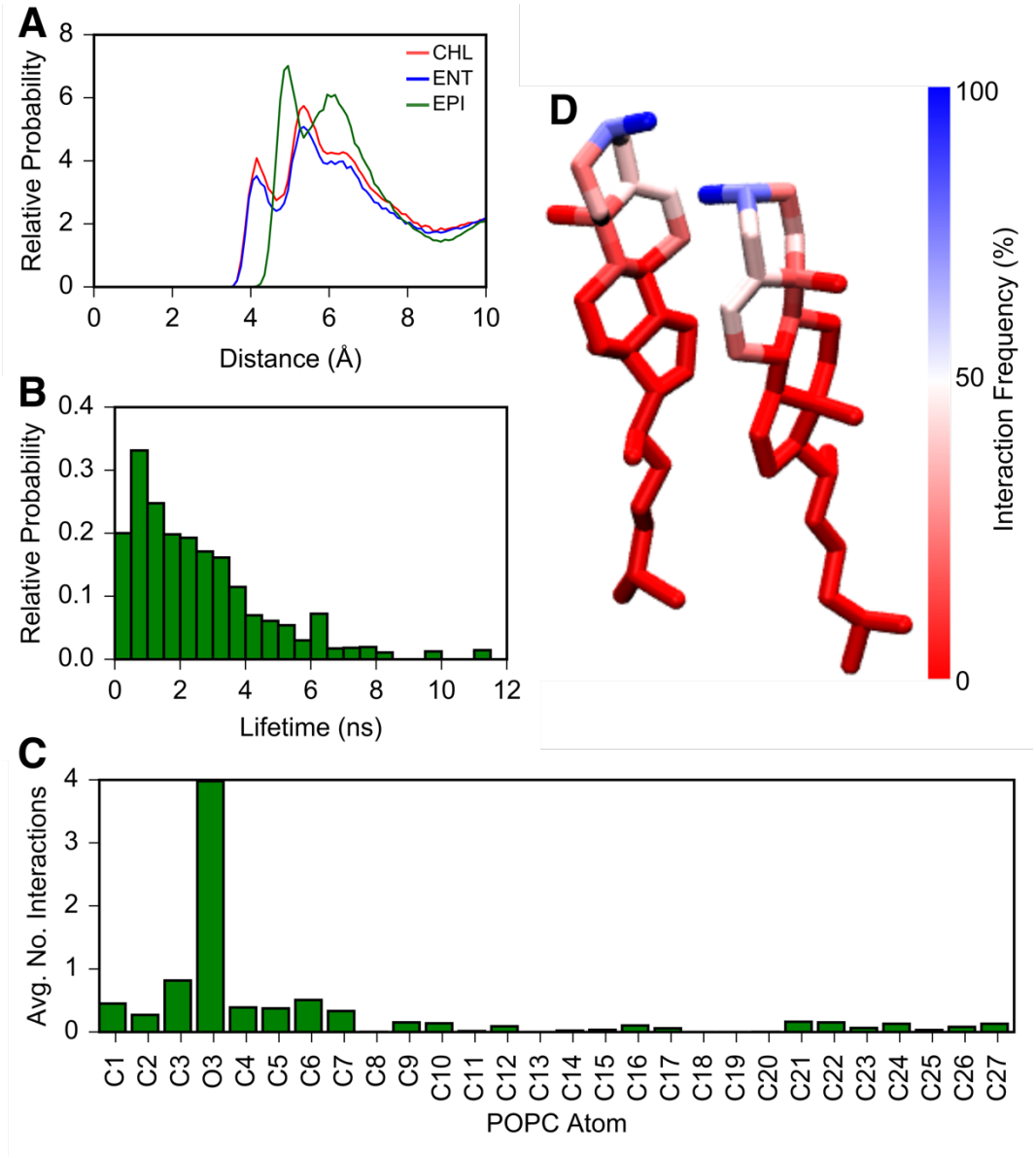

Figure 7. (A) RDF of cholesterol C3 atoms. CHL, ENT and EPI systems are shown in red, blue and black respectively. (B) Weighted histogram of dimer lifetime calculated as the continuous occurrence of inter-cholesterol H-bonds. (C) Average number of interaction pairs between epi-cholesterol molecules exclusively involved in dimers (D) Interaction frequency between a hydroxyl O3 and an adjacent epi-cholesterol molecule.

Discussion

Of the cholesterol isomers in this study, *nat*-cholesterol exhibits the greatest influence on the physical properties of the membrane, almost exactly replicated by its enantiomer. *Epi*-

cholesterol, on the other hand, exerts a weaker ordering effect as represented by the S_{CD} order parameter, manifesting in a decrease in bilayer thickness. Such deviations can be attributed to adjustment of the position and tilt angle of *epi*-cholesterol in the phospholipid bilayer, and modification of the cholesterol surface available to interact with other cholesterol and phospholipid molecules.

The simulations presented here establish a direct link between the isomerisation of the cholesterol hydroxyl group and the occurrence of novel cholesterol oligomer conformations, specifically *epi*-cholesterol dimers stabilised by intermolecular H-bonding. Despite significant interest in cholesterol aggregation and raft formation, experimental evidence concerning the existence of cholesterol dimers is negligible. Face-to-face dimers, stabilised by van der Waals interactions between the cholesterol α-faces, were first proposed by Martin and Yeagle,[52] and have been examined in detail in recent years by computational means.[53] A study by Bandara et al, using unbiased MD simulations, calculated dimer lifetime at the order of hundreds of picoseconds, with instances of a nanosecond lifetime more prevalent at higher cholesterol and sphingomyelin concentrations.[53] Furthermore, Andoh and coworkers used thermodynamic integration to calculate the free-energy profile of cholesterol dimerization.[54] Cholesterol molecules separated by ~10-15 Å and interspersed by POPC acyl tails displayed an attractive interaction, with a well depth of -3.5 kJ mol^{-1}. This value approximates to a thermal energy of ~310 K, highlighting the temperature dependence of the dimerization process.[54] Additional computational studies have noted the instability of artificial aggregates that rapidly dissociate to approximately monomeric units,[55] and the increased likelihood of cholesterol aggregates at elevated concentrations,[56] as well as the direct observation of raft formation in both all-atom and coarse-grained MD simulations.[22, 57-59] In this case, it is apparent the H-bonding properties of *epi*-cholesterol significantly enhance the stability of the dimer, resulting in an average lifetime at least one order of magnitudes greater than those previously calculated. The increased frequency of such assemblies inadvertently reduces the availability of the cholesterol α-face, which forms the dimer interface, and can therefore modify the molecular interaction between other cholesterol and phospholipid molecules, as well as membrane proteins. A growing number of studies predicate a direct relationship between membrane cholesterol and GPCR oligomerisation,[60-62] with the involvement of the face-to-face dimer in the formation of a GPCR functional dimer postulated in earlier works.[63] It is therefore conceivable that evolved *epi*-cholesterol dimer species may directly interact with membrane proteins, translating as the observed functional changes. In the 5-HT_{1A} receptor, for example, the binding affinity of extracellular ligands is directly related to the presence of specific cholesterol isomers, *nat*- and *ent*- cholesterol in solubilized native hippocampal membranes.[20] Specific interactions between cholesterol and the 5-HT_{1A} receptor will be explored in future computational studies.

Bandari and coworkers have identified a close correlation between the activity of the 5-HT_{1A} receptor and the membrane dipole potential.[17] Dipole potential has been implicated in the

modulation of channel gating in voltage-gated ion channels,[64] the formation of lipid rafts,[65] the clustering and ligand binding affinity of receptor tyrosine kinases[65] and the mechanism of anaesthetic action, and other small molecules.[66]

The membrane dipole potential emanates from the ordered orientation of lipid headgroups and associated water dipoles in the polar region separating the hydrocarbon interior from the solvent.[67] Regulation of membrane dipole potential by cholesterol has been ascribed to a number of factors, including (1) reorientation of the P^+-N^- dipole in the phospholipid headgroup towards the membrane plane, (2) membrane condensation, resulting in increased charge density, (3), an ordered water network in the interfacial region, and (4) the inherent dipole of cholesterol molecule itself.[14, 64] These hypotheses will be discussed in relation to the known experimental trend for the bilayer compositions under investigation: *epi*-cholesterol (~338 mV) < POPC-only (~369 mV) < *ent*-cholesterol (~480 mV) < *nat*-cholesterol (~500 mV).[17]

Immediately, it can be proposed that conformational changes in the phospholipid headgroup do not contribute to modification of the dipole potential in phospholipid-cholesterol bilayers, as negligible differences are observed in the behaviour of the P^+-N^- dipole. The orientation of the P^+-N^- dipole has been proposed as a significant contributor to the difference in dipole potential observed between PC and PE headgroups, as well as the dynamics of the interfacial water.[68] The PE P^+-N^- dipole is thought to occupy a position more parallel to the membrane, relative to PC, maintain optimal contacts with the phospholipid acyl chains. Concurrently, the negative contribution to the dipole potential is reduced, resulting in a more positive overall value. This theory is supported by quadrupole splitting of NMR spectra of deuterated phospholipids, but not applicable in the context of this study.

Evidence has been provided in this study that the inherent dipole moment of cholesterol provides a positive contribution to the membrane dipole potential. Notably, we demonstrate that the observed augmentation is dampened in the presence of *epi*-cholesterol, providing a less positive increase to the dipole potential. In a previous study examining cholesterol and four derivatives (6-ketocholestanol, 4-cholesten-3-one, coprostanol, and 5-cholesten-3β-ol-7-one), 10-30% of the total change in the dipole potential was attributed to the intrinsic dipole moments of the molecules.[14] The authors credit the additional increase to membrane condensation and modifications in water penetration of the membrane. For the cholesterol isomers examined here, the calculated area per lipid is similar in the cholesterol isomers examined, indicating an equable increase in dipole potential as a result of higher packing.[69] The relationship between headgroup hydration is more complex, however. The interaction of water with phospholipid bilayers has been investigated in detail in numerous studies;[70-73] revealing water molecules specifically oriented parallel to the bilayer normal, with hydrogen atoms directed towards the membrane, thus providing positive contributions to the dipole potential.[64] In theory, therefore, further hydration will increase the membrane dipole potential, whilst disruption will decrease it. Using MD simulations Villareal and coworkers attributed the observed changes in dipole

potential of DMPC membranes in the presence of trehalose to replacement of lipid-water H-bonds with lipid-trehalose H-bonds, despite maintenance of the overall number of H-bonds.[74] Overall, we observe the loss of a single H-bond between POPC molecules and water molecules when cholesterol isomers are included in the bilayer systems, with a further H-bond replaced with *nat*- and *ent*-cholesterol hydroxyl groups, and to a lesser extent with *epi*-cholesterol. We must also note the additional loss of H-bonding between *epi*-cholesterol and water, despite increased hydration, relative to *nat*-cholesterol and *ent*-cholesterol. As a consequence, it is apparent cholesterol isomers modulate the behaviour of interfacial water molecules in the presence of distinct cholesterol isomers, and hence the effective dielectric constant of the interfacial region. However, it is difficult to establish the exact contribution to the dipole potential, relative to the cholesterol-free bilayer.

Finally, differential ion binding to phospholipid headgroups is also exposed within this study, highlighting further divergence in the interfacial region. In general, physiologically relevant cations, Na^+, K^+ and Ca^{2+} are known to bind to carbonyl and phosphate atoms in phospholipid molecules, whilst Cl^- ions remain loosely associated to the bilayer surface, generating an effectively positive charged surface, and biasing other interactions in the interfacial region.[75-77] Magarkar and colleagues uncovered an inverse correlation between cholesterol concentration and Na^+ binding, parallel to reductions in the positive surface potential, using a combination of computational and experimental means.[78] Such changes were attributed to the replacement of high affinity phospholipid binding sites with low affinity cholesterol binding sites, preferred interactions between phospholipids and cholesterol and increased hydrophobicity of the membrane. This is supported by recent reports utilizing atomic force microscopy and Kelvin force microscopy indicating distinct regions of electric surface potential directly associated with cholesterol nanodomain formation.[79] Further to this, data from Lairion and Disalvo indicates that the dipole and surface potentials of bilayers are interdependent.[80] In this case, subsidence of cation (K^+) binding is intensified when *epi*-cholesterol is present, signalling the greatest displacement of the membrane surface potential to less positive values, and imposing further variance to the membrane dipole potential.

Overall, interpretation of the data presented in this study reveals that the intricate balance between membrane condensation, the dipole moment of sterol molecules, and the behaviour of interfacial water molecules ions underlie the observed differences in the membrane dipole potential in cholesterol-containing bilayers. The influence of the P^+-N^- vector can be discounted in the context of this study.

Conclusions

Using extensive MD simulations, totalling 2 μs, the behaviour of *epi*-cholesterol in an unsaturated phospholipid bilayer has been characterised, and compared to *nat*-cholesterol and

ent-cholesterol, as well as a cholesterol-free phospholipid bilayer. Slight differences in membrane thickness, area per lipid, interdigitation fraction and S_{CD} order parameter are observed, relative to *nat*-cholesterol and *ent*-cholesterol which display identical properties throughout, in agreement with experimental studies. This can be attributed to minor deviations of the position and tilt angle of *epi*-cholesterol, as well as an observable population of long-lasting *epi*-cholesterol dimers, which are directly stabilised by H-bonding of the axial hydroxyl group on the cholesterol α-face.

Noteworthy variations are evident in the membrane-water interfacial region when *epi*-cholesterol is present, with the phospholipid SASA and interaction profile more closely resembling that of a cholesterol-free membrane. Following this, we have considered in detail how the divergent atomic-level interactions directly influence the dipole potential of the membrane and provide a comprehensive mechanism for the action of cholesterol in this respect.

The membrane dipole potential is known to regulate transport processes, directly through the plasma membrane and also via embedded proteins. Consequently, understanding how the membrane dipole potential is modulated by various factors, such as the inclusion of small molecules, is of intense interest in the pharmaceutical industry. Therefore, it is desired that the outcomes of this study provide crucial insights in this area and contribute to our current understanding of the behaviour and role of the cholesterol in the cell membrane.

References

(1) Ikonen, E. Cellular cholesterol trafficking and compartmentalization. *Nat. Rev. Mol. Cell. Bio*. **2008,** *9* (2), 125.

(2) Leathes, J. B. Croonian Lectures On the role of fats in vital phenomena. *The Lancet 205* (5304), 853.

(3) McConnell, H. M.; Radhakrishnan, A. Condensed complexes of cholesterol and phospholipids. *Biochim. Biophys. Acta* **2003,** *1610* (2), 159.

(4) Westover, E. J.; Covey, D. F.; Brockman, H. L.; Brown, R. E.; Pike, L. J. Cholesterol depletion results in site-specific increases in epidermal growth factor receptor phosphorylation due to membrane level effects. Studies with cholesterol enantiomers. *J. Biol. Chem.* **2003,** *278* (51), 51125.

(5) Westover, E. J.; Covey, D. F. The enantiomer of cholesterol. *J. Memb. Biol.* **2004,** *202* (2), 61.

(6) Covey, D. F. ent-Steroids: novel tools for studies of signaling pathways. *Steroids* **2009,** *74* (7), 577.

(7) Mannock, D. A.; McIntosh, T. J.; Jiang, X.; Covey, D. F.; McElhaney, R. N. Effects of natural and enantiomeric cholesterol on the thermotropic phase behavior and structure of egg sphingomyelin bilayer membranes. *Biophys. J.* **2003,** *84* (2 Pt 1), 1038.

(8) Demel, R. A.; Bruckdorfer, K. R.; van Deenen, L. L. M. Structural requirements of sterols for the interaction with lecithin at the air-water interface. *BBA-Biomembranes* **1972,** *255* (1), 311.

(9) Dufourc, E. J.; Parish, E. J.; Chitrakorn, S.; Smith, I. C. P. Structural and dynamical details of cholesterol-lipid interaction as revealed by deuterium NMR. *Biochemistry* **1984,** *23* (25), 6062.

(10) Murari, R.; Murari, M. P.; Baumann, W. J. Sterol orientations in phosphatidylcholine liposomes as determined by deuterium NMR. *Biochemistry* **1986,** *25* (5), 1062.

(11) Cheetham, J. J.; Wachtel, E.; Bach, D.; Epand, R. M. Role of the stereochemistry of the hydroxyl group of cholesterol and the formation of nonbilayer structures in phosphatidylethanolamines. *Biochemistry* **1989,** *28* (22), 8928.
(12) Liu, Y.; Chipot, C.; Shao, X.; Cai, W. The effects of 7-dehydrocholesterol on the structural properties of membranes. *Phys. Biol.* **2011,** *8* (5), 056005.
(13) Huster, D.; Scheidt, H. A.; Arnold, K.; Herrmann, A.; Müller, P. Desmosterol May Replace Cholesterol in Lipid Membranes. *Biophys. J.* **2005,** *88* (3), 1838.
(14) Starke-Peterkovic, T.; Turner, N.; Vitha, M. F.; Waller, M. P.; Hibbs, D. E.; Clarke, R. J. Cholesterol Effect on the Dipole Potential of Lipid Membranes. *Biophys. J.* **2006,** *90* (11), 4060.
(15) Haldar, S.; Kanaparthi, R. K.; Samanta, A.; Chattopadhyay, A. Differential effect of cholesterol and its biosynthetic precursors on membrane dipole potential. *Biophys. J.* **2012,** *102* (7), 1561.
(16) Singh, P.; Haldar, S.; Chattopadhyay, A. Differential effect of sterols on dipole potential in hippocampal membranes: Implications for receptor function. *BBA-Biomembranes* **2013,** *1828* (3), 917.
(17) Bandari, S.; Chakraborty, H.; Covey, D. F.; Chattopadhyay, A. Membrane dipole potential is sensitive to cholesterol stereospecificity: Implications for receptor function. *Chem. Phys. Lipids* **2014,** *184*, 25.
(18) D'Avanzo, N.; Hyrc, K.; Enkvetchakul, D.; Covey, D. F.; Nichols, C. G. Enantioselective Protein-Sterol Interactions Mediate Regulation of Both Prokaryotic and Eukaryotic Inward Rectifier K^+ Channels by Cholesterol. *PLOS One* **2011,** *6* (4), e19393.
(19) Sooksawate, T.; Simmonds, M. A. Influence of membrane cholesterol on modulation of the GABA(A) receptor by neuroactive steroids and other potentiators. *Brit. J. Pharmacol.* **2001,** *134* (6), 1303.
(20) Jafurulla, M.; Rao, B. D.; Sreedevi, S.; Ruysschaert, J. M.; Covey, D. F.; Chattopadhyay, A. Stereospecific requirement of cholesterol in the function of the serotonin1A receptor. *Biochim. Biophys. Acta* **2014,** *1838* (1 Pt B), 158.
(21) Kristiana, I.; Luu, W.; Stevenson, J.; Cartland, S.; Jessup, W.; Belani, J. D.; Rychnovsky, S. D.; Brown, A. J. Cholesterol through the looking glass: ability of its enantiomer to also elicit homeostatic responses. *J. Biol. Chem.* **2012**.
(22) Berkowitz, M. L. Detailed molecular dynamics simulations of model biological membranes containing cholesterol. *BBA-Biomembranes* **2009,** *1788* (1), 86.
(23) Sengupta, D.; Chattopadhyay, A. Molecular dynamics simulations of GPCR-cholesterol interaction: An emerging paradigm. *Biochim. Biophys. Acta* **2015,** *1848* (9), 1775.
(24) Grouleff, J.; Irudayam, S. J.; Skeby, K. K.; Schiott, B. The influence of cholesterol on membrane protein structure, function, and dynamics studied by molecular dynamics simulations. *Biochim. Biophys. Acta* **2015**.
(25) Róg, T.; Pasenkiewicz-Gierula, M. Effects of Epicholesterol on the Phosphatidylcholine Bilayer: A Molecular Simulation Study. *Biophys. J.* **2003,** *84* (3), 1818.
(26) Jo, S.; Kim, T.; Iyer, V. G.; Im, W. CHARMM-GUI: a web-based graphical user interface for CHARMM. *J. Comput. Chem.* **2008,** *29* (11), 1859.
(27) Jo, S.; Lim, J. B.; Klauda, J. B.; Im, W. CHARMM-GUI Membrane Builder for Mixed Bilayers and Its Application to Yeast Membranes. *Biophys. J.* **2009,** *97* (1), 50.
(28) Wu, E. L.; Cheng, X.; Jo, S.; Rui, H.; Song, K. C.; Dávila-Contreras, E. M.; Qi, Y.; Lee, J.; Monje-Galvan, V.; Venable, R. M. CHARMM-GUI Membrane Builder toward realistic biological membrane simulations. *J. Comput. Chem.* **2014,** *35* (27), 1997.
(29) Humphrey, W.; Dalke, A.; Schulten, K. VMD: Visual molecular dynamics. *J. Mol. Graph* **1996,** *14* (1), 33.
(30) Phillips, J. C.; Braun, R.; Wang, W.; Gumbart, J.; Tajkhorshid, E.; Villa, E.; Chipot, C.; Skeel, R. D.; Kale, L.; Schulten, K. Scalable molecular dynamics with NAMD. *J. Comput. Chem.* **2005,** *26* (16), 1781.
(31) Klauda, J. B.; Venable, R. M.; Freites, J. A.; O'Connor, J. W.; Tobias, D. J.; Mondragon-Ramirez, C.; Vorobyov, I.; MacKerell Jr, A. D.; Pastor, R. W. Update of the CHARMM all-atom additive force field for lipids: validation on six lipid types. *J. Phys. Chem. B* **2010,** *114* (23), 7830.

(32) Noskov, S. Y.; Berneche, S.; Roux, B. Control of ion selectivity in potassium channels by electrostatic and dynamic properties of carbonyl ligands. *Nature* **2004,** *431* (7010), 830.
(33) Jorgensen, W. L.; Chandrasekhar, J.; Madura, J. D.; Impey, R. W.; Klein, M. L. Comparison of simple potential functions for simulating liquid water. *J. Chem. Phys* **1983,** *79* (2), 926.
(34) Lim, J. B.; Rogaski, B.; Klauda, J. B. Update of the Cholesterol Force Field Parameters in CHARMM. *The J. Phys. Chem.B* **2012,** *116* (1), 203.
(35) Darden, T.; York, D.; Pedersen, L. Particle mesh Ewald: An N·log(N) method for Ewald sums in large systems. *J. Chem. Phys* **1993,** *98* (12), 10089.
(36) Verlet, L. Computer" experiments" on classical fluids. I. Thermodynamical properties of Lennard-Jones molecules. *Phys. Rev.* **1967,** *159* (1), 98.
(37) Miyamoto, S.; Kollman, P. A. SETTLE: an analytical version of the SHAKE and RATTLE algorithm for rigid water models. *J. Comput. Chem.* **1992,** *13* (8), 952.
(38) Feller, S. E.; Zhang, Y.; Pastor, R. W.; Brooks, B. R. Constant pressure molecular dynamics simulation: the Langevin piston method. *J. Chem. Phys.* **1995,** *103* (11), 4613.
(39) Martyna, G. J.; Tobias, D. J.; Klein, M. L. Constant pressure molecular dynamics algorithms. *J. Chem. Phys.* **1994,** *101* (5), 4177.
(40) Guixa-Gonzalez, R.; Rodriguez-Espigares, I.; Ramirez-Anguita, J. M.; Carrio-Gaspar, P.; Martinez-Seara, H.; Giorgino, T.; Selent, J. MEMBPLUGIN: studying membrane complexity in VMD. *Bioinformatics* **2014,** *30* (10), 1478.
(41) Vermeer, L. S.; de Groot, B. L.; Reat, V.; Milon, A.; Czaplicki, J. Acyl chain order parameter profiles in phospholipid bilayers: computation from molecular dynamics simulations and comparison with 2H NMR experiments. *Eur. Biophys. J.* **2007,** *36* (8), 919.
(42) Giorgino, T. Computing 1-D atomic densities in macromolecular simulations: The density profile tool for VMD. *Comput. Phys. Commun.* **2014,** *185* (1), 317.
(43) Aksimentiev, A.; Schulten, K., Imaging α-Hemolysin with Molecular Dynamics: Ionic Conductance, Osmotic Permeability, and the Electrostatic Potential Map. *Biophysical journal 88* (6), 3745-3761.
(44) Kučerka, N.; Nieh, M.-P.; Katsaras, J. Fluid phase lipid areas and bilayer thicknesses of commonly used phosphatidylcholines as a function of temperature. *BBA-Biomembranes* **2011,** *1808* (11), 2761.
(45) Olsen, B. N.; Schlesinger, P. H.; Ory, D. S.; Baker, N. A. 25-Hydroxycholesterol Increases the Availability of Cholesterol in Phospholipid Membranes. *Biophys. J.* **2011,** *100* (4), 948.
(46) Aittoniemi, J.; Róg, T.; Niemelä, P.; Pasenkiewicz-Gierula, M.; Karttunen, M.; Vattulainen, I. Tilt: Major Factor in Sterols' Ordering Capability in Membranes. *J. Phys. Chem. B* **2006,** *110* (51), 25562.
(47) Oldfield, E.; Meadows, M.; Rice, D.; Jacobs, R. Spectroscopic studies of specifically deuterium labeled membrane systems. Nuclear magnetic resonance investigation of the effects of cholesterol in model systems. *Biochemistry* **1978,** *17* (14), 2727.
(48) Urbina, J. A.; Pekerar, S.; Le, H.-b.; Patterson, J.; Montez, B.; Oldfield, E. Molecular order and dynamics of phosphatidylcholine bilayer membranes in the presence of cholesterol, ergosterol and lanosterol: a comparative study using 2H-, 13C- and 31P-NMR spectroscopy. *BBA-Biomembranes* **1995,** *1238* (2), 163.
(49) Jacobs, R.; Oldfield, E. Deuterium nuclear magnetic resonance investigation of dimyristoyllecithin--dipalmitoyllecithin and dimyristoyllecithin--cholesterol mixtures. *Biochemistry* **1979,** *18* (15), 3280.
(50) Róg, T.; Pasenkiewicz-Gierula, M.; Vattulainen, I.; Karttunen, M. Ordering effects of cholesterol and its analogues. *BBA-Biomembranes* **2009,** *1788* (1), 97.
(51) Kulig, W.; Tynkkynen, J.; Javanainen, M.; Manna, M.; Rog, T.; Vattulainen, I.; Jungwirth, P. How well does cholesteryl hemisuccinate mimic cholesterol in saturated phospholipid bilayers? *J. Mol. Modeling* **2014,** *20* (2), 2121.
(52) Martin, R. B.; Yeagle, P. L. Models for lipid organization in cholesterol-phospholipid bilayers including cholesterol dimer formation. *Lipids* **1978,** *13* (9), 594.

(53) Bandara, A.; Panahi, A.; Pantelopulos, G. A.; Straub, J. E. Exploring the structure and stability of cholesterol dimer formation in multicomponent lipid bilayers. *J. Comput. Chem.* **2017,** *38* (16), 1479.
(54) Andoh, Y.; Oono, K.; Okazaki, S.; Hatta, I. A molecular dynamics study of the lateral free energy profile of a pair of cholesterol molecules as a function of their distance in phospholipid bilayers. *J. Chem. Phys* **2012,** *136* (15), 155104.
(55) Dai, J.; Alwarawrah, M.; Huang, J. Instability Of Cholesterol Clusters In Lipid Bilayers And The Cholesterol's Umbrella Effect. *J. Phys. Chem. B* **2010,** *114* (2), 840.
(56) O'Connor, J. W.; Klauda, J. B. Lipid Membranes with a Majority of Cholesterol: Applications to the Ocular Lens and Aquaporin 0. *J. Phys. Chem. B* **2011,** *115* (20), 6455.
(57) Pandit, S. A.; Bostick, D.; Berkowitz, M. L. Complexation of Phosphatidylcholine Lipids with Cholesterol. *Biophys. J.* **2004,** *86* (3), 1345.
(58) Marrink, S. J.; de Vries, A. H.; Tieleman, D. P. Lipids on the move: Simulations of membrane pores, domains, stalks and curves. *BBA-Biomembranes* **2009,** *1788* (1), 149.
(59) Davis, R. S.; Sunil Kumar, P. B.; Sperotto, M. M.; Laradji, M. Predictions of Phase Separation in Three-Component Lipid Membranes by the MARTINI Force Field. *The J. Phys. Chem.B* **2013,** *117* (15), 4072.
(60) Gahbauer, S.; Böckmann, R. A. Membrane-Mediated Oligomerization of G Protein Coupled Receptors and Its Implications for GPCR Function. *Front. Physiol.* **2016,** *7*, 494.
(61) Prasanna, X.; Chattopadhyay, A.; Sengupta, D. Cholesterol Modulates the Dimer Interface of the β(2)-Adrenergic Receptor via Cholesterol Occupancy Sites. *Biophys. J.* **2014,** *106* (6), 1290.
(62) Prasanna, X.; Sengupta, D.; Chattopadhyay, A. Cholesterol-dependent Conformational Plasticity in GPCR Dimers. *Sci. Rep.* **2016,** *6*, 31858.
(63) Fantini, J.; Barrantes, F. J. How cholesterol interacts with membrane proteins: an exploration of cholesterol-binding sites including CRAC, CARC, and tilted domains. *Front. Physiol.* **2013,** *4*, 31.
(64) Pearlstein, R. A.; Dickson, C. J.; Hornak, V. Contributions of the membrane dipole potential to the function of voltage-gated cation channels and modulation by small molecule potentiators. *BBA- Biomembranes* **2017,** *1859* (2), 177.
(65) Kovács, T.; Batta, G.; Zákány, F.; Szöllősi, J.; Nagy, P. The dipole potential correlates with lipid raft markers in the plasma membrane of living cells. *Journal of Lipid Research* **2017**.
(66) Davis, B. M.; Brenton, J.; Davis, S.; Shamsher, E.; Sisa, C.; Grgic, L.; Cordeiro, M. F. Modulation of the membrane dipole potential: a prospective mechanism to differentiate anaesthetic/non-anaesthetic activity and a tool to assess susceptibility. *J. Lipid Res.* **2017**.
(67) Gawrisch, K.; Ruston, D.; Zimmerberg, J.; Parsegian, V. A.; Rand, R. P.; Fuller, N. Membrane dipole potentials, hydration forces, and the ordering of water at membrane surfaces. *Biophys. J.* **1992,** *61* (5), 1213.
(68) Starke-Peterkovic, T.; Clarke, R. J., Effect of headgroup on the dipole potential of phospholipid vesicles. *Euro. Biophys. J.* **2009,** *39* (1), 103.
(69) Clarke, R. J., Effect of lipid structure on the dipole potential of phosphatidylcholine bilayers. *BBA - Biomembranes* **1997,** *1327* (2), 269-278.
(70) Re, S.; Nishima, W.; Tahara, T.; Sugita, Y., Mosaic of Water Orientation Structures at a Neutral Zwitterionic Lipid/Water Interface Revealed by Molecular Dynamics Simulations. *J. Phys. Chem. Lett.* **2014,** *5* (24), 4343-4348.
(71) Abd Halim, K. B.; Koldso, H.; Sansom, M. S. P., Interactions of the EGFR juxtamembrane domain with PIP2-containing lipid bilayers: Insights from multiscale molecular dynamics simulations. *Biochim. Biophys. Acta* **2015,** *1850* (5), 1017-25.
(72) Krylov, N. A.; Pentkovsky, V. M.; Efremov, R. G., Nontrivial Behavior of Water in the Vicinity and Inside Lipid Bilayers As Probed by Molecular Dynamics Simulations. *ACS Nano* **2013,** *7* (10), 9428-9442.
(73) Davis, J. E.; Rahaman, O.; Patel, S., Molecular Dynamics Simulations of a DMPC Bilayer Using Nonadditive Interaction Models. *Biophys. J. 96* (2), 385-402.

(74) Villarreal, M. A.; Díaz, S. B.; Disalvo, E. A.; Montich, G. G., Molecular Dynamics Simulation Study of the Interaction of Trehalose with Lipid Membranes. *Langmuir* **2004,** *20* (18), 7844-7851.
(75) Berkowitz, M. L.; Bostick, D. L.; Pandit, S., Aqueous Solutions next to Phospholipid Membrane Surfaces: Insights from Simulations. *Chem. Rev.* **2006,** *106* (4), 1527-1539.
(76) Stępniewski, M.; Bunker, A.; Pasenkiewicz-Gierula, M.; Karttunen, M.; Róg, T., Effects of the Lipid Bilayer Phase State on the Water Membrane Interface. *J. Phys. Chem. B* **2010,** *114* (36), 11784-11792.
(77) Magarkar, A.; Karakas, E.; Stepniewski, M.; Róg, T.; Bunker, A., Molecular Dynamics Simulation of PEGylated Bilayer Interacting with Salt Ions: A Model of the Liposome Surface in the Bloodstream. *J. Phys. Chem. B* **2012,** *116* (14), 4212-4219.
(78) Magarkar, A.; Dhawan, V.; Kallinteri, P.; Viitala, T.; Elmowafy, M.; Róg, T.; Bunker, A., Cholesterol level affects surface charge of lipid membranes in saline solution. *Sci. Rep. UK* **2014,** *4*, 5005.
(79) Drolle, E.; Bennett, W. F. D.; Hammond, K.; Lyman, E.; Karttunen, M.; Leonenko, Z., Molecular dynamics simulations and Kelvin probe force microscopy to study of cholesterol-induced electrostatic nanodomains in complex lipid mixtures. *Soft Matter* **2017,** *13* (2), 355-362.
(80) Lairion, F.; Disalvo, E. A., Effect of Dipole Potential Variations on the Surface Charge Potential of Lipid Membranes. *J. Phys. Chem. B* **2009,** *113* (6), 1607-1614.

6.3 Influence of Cholesterol and its Stereoisomers on Members of the Serotonin Receptor Family

6.3.1 Authorship and Permissions

<table>
<tr><td colspan="9">This declaration concerns the article entitled</td></tr>
<tr><td colspan="9">Influence of cholesterol and its stereoisomers on members of the serotonin receptor family</td></tr>
<tr><td colspan="9">Publication status (tick one)</td></tr>
<tr><td>Draft manuscript</td><td></td><td>Submitted</td><td></td><td>In review</td><td></td><td>Accepted</td><td>✓</td><td>Published</td><td></td></tr>
<tr><td>Publication details</td><td colspan="8">Journal of Molecular Biology</td></tr>
<tr><td>Candidates contribution to the paper (detailed and also given as a percentage)</td><td colspan="8">The candidate contributed to/considerably contributed/predominantly executed the…
Formulation of ideas (50%):
V. Oakes and C. Domene contributed equally.

Design of methodology (25%):
V. Oakes and C. Domene contributed equally.

Experimental work (100%):
Simulation and analysis was performed by V.Oakes.

Presentation of data in journal format (80%):
V. Oakes: Main author of manuscript and supporting information.
C. Domene: Critically assessed and revised the manuscript.</td></tr>
<tr><td>Statement from Candidate</td><td colspan="8">This paper reports on original research I conducted during the period of my Higher Degree by Research candidature.</td></tr>
<tr><td>Signed</td><td colspan="5"></td><td>Date</td><td colspan="2"></td></tr>
</table>

This is the author accepted manuscript of an article published in final form in Journal of Molecular Biology and available online via: https://doi.org/10.1016/j.jmb.2019.02.030

6.3.2 Manuscript

Influence of cholesterol and its stereoisomers on members of the serotonin receptor family

Victoria Oakes[1] *and Carmen Domene*[1,2*]

[1]Department of Chemistry, University of Bath, Claverton Down, Bath, BA2 7AY, UK

[2]Department of Chemistry, University of Oxford, Oxford, OX1 3TA, Oxford, UK

Abstract

Despite the ubiquity of cholesterol within the cell membrane, the mechanism by which it influences embedded proteins remains elusive. Numerous GPCRs exhibit dramatic responses to membrane cholesterol, with regards to the ligand-binding affinity and functional properties, including the 5-HT receptor family. Here, we use over 25 μs of unbiased atomistic MD simulations to identify cholesterol interaction sites in the 5-HT_{1B} and 5-HT_{2B} receptors and evaluate their impact on receptor structure. Susceptibility to membrane cholesterol is shown to be subtype-dependent and determined by the quality of interactions between the extracellular loops. Charged residues are essential to maintain the arrangement of the extracellular surface in 5-HT_{2B}; in the absence of such interactions, the extracellular surface of the 5-HT_{1B} is malleable, populating a number of distinct conformations. Elevated-cholesterol density near transmembrane helix 4 is considered to be conducive to the conformation of extracellular loop 2. Occupation of this site is also shown to be stereospecific, illustrated by differential behaviour of *nat*-cholesterol isomers, *ent*- and *epi*-cholesterol. In simulations containing the endogenous agonist, serotonin, cholesterol binding at transmembrane helix 4 biases bound serotonin molecules towards an unexpected binding mode in the extended binding pocket. The results highlight the capability of membrane cholesterol to influence the mobility of the extracellular surface in the 5-HT_1 receptor family and manipulate the architecture of the extracellular ligand-binding pocket.

Introduction

G-protein coupled receptors (GPCRs) play a fundamental role in the transmission of extracellular stimuli to the cell interior, participating in a broad spectrum of physiological processes being the most prominent target of clinically approved drugs.[1] GPCRs are seven-helix transmembrane proteins (TM1-7), which can exist in a variety of conformational states. The evolution of active, inactive and intermediate states is promoted by small-molecule binding in the core of the transmembrane bundle, typically accessible from the extracellular medium.

Activating ligands, known as agonists, stabilize conformations capable of G-protein coupling, eliciting a response within the cell.

In recent years, membrane composition has emerged as an important factor in the drug-binding properties of GPCRs. Cholesterol,[2] sphingolipids[3] and phospholipid[4] have been shown to modulate the activity of GPCRs; the ligand-binding affinity is a crucial property that can be regulated by cholesterol in both positive and negative manners.[5-7] However, the mechanism by which cholesterol modulates protein structure and function is largely unknown.[8] One theory suggests cholesterol acts by varying the physical properties of the membrane, which then influences the conformation of the protein. An alternative rationale proposes that cholesterol binds directly to specific sites on the protein surface, acting as an allosteric modulator. A third proposition suggests that cholesterol facilitates interactions with a third party which biases the activation state. Of course, the possibility also exists that these effects are not mutually exclusive, and a combinatory approach occurs.

Cholesterol exhibits an asymmetric structure formed from the isooctyl chain planar attached to the rigid polycylic sterane backbone. The latter comprises a smooth α face and rough β face, and a polar hydroxyl moiety at the apex. A single cholesterol isomer occurs naturally, although eight stereocenters exist in the molecule (Scheme 1). Biological systems are capable of discriminating between stereoisomers of substrates and can therefore be classified as stereospecific. This is typically discussed in terms of enzyme catalysis. However, this trait has been established for various membrane proteins, regarding both agonists and allosteric modulators, such as membrane cholesterol. Subsequently, cholesterol isomers have emerged as valuable probes to distinguish between specific and non-specific effects of cholesterol in membrane proteins, and to scrutinize the level of specificity required action.[9] *Epi*-cholesterol, which bears a distinct orientation of the hydroxyl group (Scheme 1), has been used widely, on the basis it forms analogous structured lipid domains[10] and induces a similar level of membrane fluidity.[11] However, other properties, such as the area per lipid and cholesterol tilt angle, are known to diverge,[12] hence it is possible that both direct and indirect mechanisms of cholesterol are involved in modulation by *epi*-cholesterol. For this reason, it has been somewhat superseded by *ent*-cholesterol, the enantiomer of cholesterol (Scheme 1), which is considered to mimic the physiochemical membrane properties more closely.[13] Experiments utilizing these analogues have successfully implicated stereospecific binding of cholesterol in the regulation of various membrane proteins.[14-19]

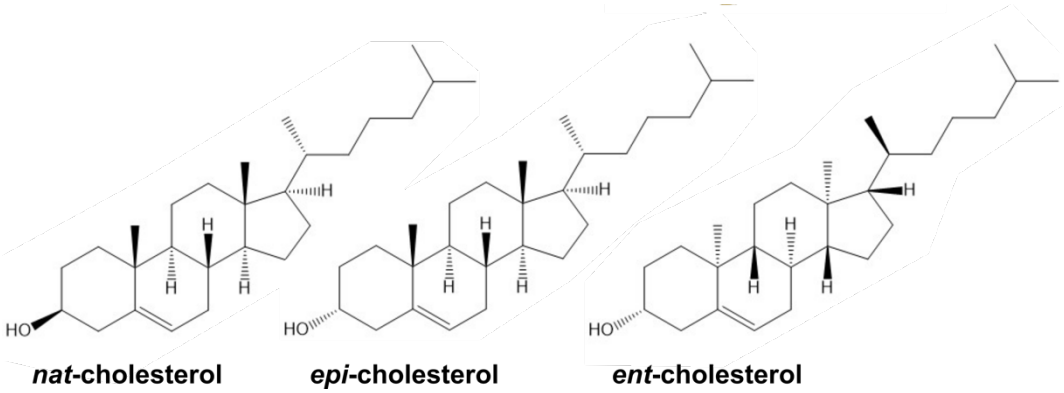

Scheme 1. Chemical structures of cholesterol isomers considered in this study.

Identification of specific cholesterol binding sites in GPCRs has been accomplished by a number of methods. Several general cholesterol interaction motifs have been proposed and identified in GPCRs by sequence alignment,[20,21] including the cholesterol recognition/interaction amino acid consensus (CRAC) motif,[22] constituted of the sequence L/V-X_{1-5}-Y-X_{1-5}-K/R (where X can represent any amino acid), and the inverted form of the CRAC motif,[23] termed the CARC motif, where the central tyrosine can also be occupied by a phenylalanine residue in the CRAC domain. High-resolution structural information of multiple GPCRs (A_{2A} adenosine,[24] β1-adrenergic,[25] β2-adrenergic,[26,27] 5-HT_{2B}[28] and metabotropic glutamate type 1[29] receptors) in complex with cholesterol molecules, has revealed a number of specific cholesterol interaction sites, such as cholesterol consensus motif (CCM), a groove region between TM2 and TM4 constituted of highly conserved residues $Y^{2.41}$,$K/R^{4.39-4.43}$, $I/V/L^{4.46}$ and $W/Y^{4.50}$ (labeled using the Ballesteros-Weinstein numbering scheme, which is a generic numbering scheme for class A GPCR's).[27] Further to this, molecular dynamics (MD) simulations have become an established tool to identify high- and low-affinity cholesterol interaction sites on GPCRs and evaluate the potential consequences on protein structure and dynamics.[30-33]

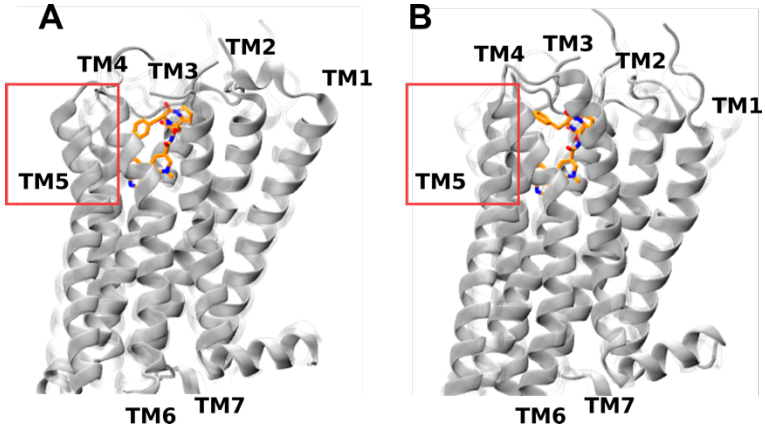

Figure 1. Crystal structures of the (A) 5-HT_{1B} (PDB ID: 4IAR) and (B) 5-HT_{2B} (PDB ID: 4IB4) receptors. Each transmembrane helix (TM) is labelled. Ergotamine is displayed with carbon, oxygen and nitrogen atoms in orange, red and blue respectively. The alternate conformations of the TM5 helix are displayed within the red boxes.

The serotonin (5-HT) receptor family spans seven receptor subfamilies (5-HT_{1-7}), classified by structural and functional similarities. The serotonin (5-HT) receptor family spans seven receptor subfamilies (5-HT_{1-7}), classified by structural and functional similarities. All serotonin receptors are GPCRs, with the exception of the 5-HT_3 receptor, which is a ligand-gated ion channel. 5-HT receptors have been associated with medical conditions, including neurological disorders, such as Alzheimer's disease, depression and schizophrenia. [34,35]

Significant experimental and computational efforts have been focused towards characterizing the functional response of the 5-HT_{1A} receptor to cholesterol.[36-38] Solubilized native hippocampal membranes exhibit diminished ligand binding, which can be restored on the addition of membrane cholesterol or its enantiomer (*ent*-cholesterol).[39] However, replenishment with closely related molecules, such as *epi*-cholesterol (a diastereoisomer of cholesterol)[39] fail to restore binding properties. Curiously, cholesterol depletion enhances ligand binding activity in neuronal cells, when examining the same agonist as prior experiments.[40] Disparate effects are also observed when considering biosynthetic precursors, differing to cholesterol by a double bond, and various experimental procedures are used.[41,42] Alongside this, simulation methodologies have been utilized to identify cholesterol interaction sites on homology models of the 5-HT_{1A} receptor, in the absence of high-resolution structural information of this subtype.[43]

In milestone publications, the crystal structures of related 5-HT_{1B} and 5-HT_{2B} receptors in complex with ergotamine, and dihydroergotamine in the former, were disclosed. These structures revealed insights into the molecular determinants of subtype selectivity and biased signaling (Figure 1A-B).[44,45] The 5-HT receptors exhibit analogous orthosteric binding pockets, with 70% of residues completely conserved (residues 3.32, 3.37, 5.46, 6.48, 6.51, 6.52 and 7.43 in the Ballesteros-Weinstein numbering scheme), and another 10% displaying conservative mutations (3.33). As a consequence, subtype selectivity is attributed to the deviations in the extended binding pocket, constituted of residues from the second extracellular loop (ECL2) and the extracellular termini of TM3 and TM5-7. Most notably, an outward movement of TM5 in the 5-HT_{1B} receptor increases the volume of the canonical binding pocket, relative to the 5-HT_{2B} receptor, enabling inhabitance of bulkier ligands (Figure 1). This is demonstrated by the reported potencies of triptan molecules in wild-type 5-HT_{1B} and 5-HT_{2B}, and 5-HT_{2B} mutants, reported in the same study.

Considering the available structural information for the 5-HT_{1B} and 5-HT_{2B} receptors, and the reported cholesterol-dependence of the closely-related 5-HT_{1A} receptor, we hypothesized that membrane composition may actuate the conformation of TM4-5, and the attached ECL2, in the 5-HT receptor family, which translates to diversity in the framework of the orthosteric and/or extending binding pockets. To investigate this scenario, we performed extensive unbiased MD simulations of the high-resolution crystal structures of the 5-HT_{1B} (PDB ID 4IAR) and 5-HT_{2B} receptors (PDB ID 4IB4) in POPC bilayers with 0% and 30% cholesterol concentrations. We

also examined *ent*-cholesterol and *epi*-cholesterol, to delineate stereospecific cholesterol binding sites, considering the response of the 5-HT_{1A} receptor to these molecules.[39] Previous crystallographic and NMR studies of several class A GPCRs have demonstrated ligand-specific governance of the extracellular loop structure.[46-49] Thus, the 5-HT receptors of interest were simulated in the *apo* state, initially, to eliminate potential bias arising from the ligand identity.

Methods

Membrane Preparation

Bilayers containing 1-palmitoyl-2-oleoyl-sn-glycero-3-phosphocholine (POPC) molecules and *nat*-cholesterol molecules were generated using the CHARMM-GUI Membrane Builder.[50-52] The cholesterol-free bilayers contained 244 POPC molecules, with 196 POPC molecules and 84 *nat*-cholesterol molecules used for the cholesterol-enriched bilayers content. The mixed POPC/*nat*-cholesterol membrane was then modified to generate additional membranes containing the *ent*- and *epi*-cholesterol. All membranes were then equilibrated using the documented CHARMM-GUI protocol, and a production run was performed for 50 ns.[51] The membrane cholesterol in each bilayer was then transformed into the remaining isomers to provide three initial configurations of cholesterol in the membrane, labelled 1-3.

5-HT Receptor Modeling

The crystal structures of the 5-HT_{1B} receptor (PDB ID: 4IAR) and 5-HT_{2B} receptor (PDB ID: 4IB4) were used to prepare the initial models.[28,53] In both cases, the third intracellular loop (residues L240 to M305 in 5-HT_{1B} and Y249 to V313 in 5-HT_{2B}) between helices 5 and 6 was replaced by the engineered BRIL[54] loop for the purpose of crystallization, and was removed. The bound agonist, ergotamine, and lipid molecules present in the crystal structure were also removed to allow for unbiased detection of lipid binding sites. Missing loops (191 to 196 and 340 to 344 in the 5-HT_{1B} receptor) were replaced using the Modloop protocol,[55] neutral caps were used on the termini and default protonation states were used for ionizable residues. Additional simulations were initiated with docked 5-hydroxytryptamine (5-HT), which is otherwise known as serotonin. Two conformations of serotonin were utilized to initiate independent simulations, consistent with the ergotamine binding pose observed in the crystal structure (Figure 2A). In conformation 1 (Figure 2B), the indole nitrogen of serotonin is positioned to H-bond with the T134 side-chain, and the amine tail is positioned to interact with D129. In conformation 2 (Figure 2C), serotonin is flipped so that the hydroxyl group on the six-membered indole ring can interact with the T134 side-chain, whilst the amine tail can still interact with D129.

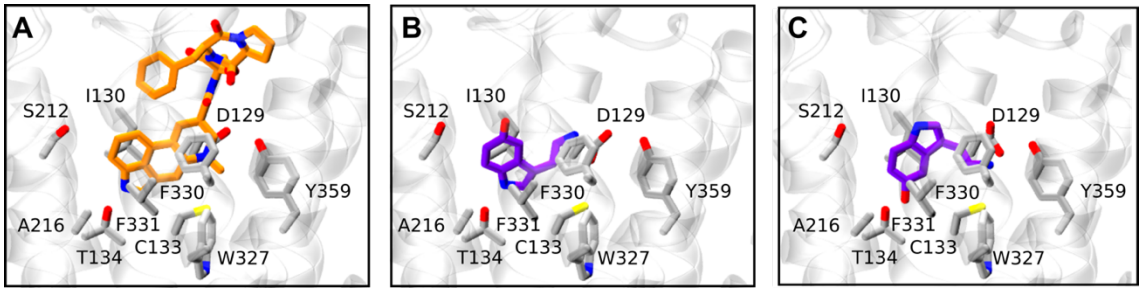

Figure 2. (A) Ergotamine binding pose (orange molecule) in the 5-HT_{1B} receptor crystal structure (PDB ID 4IAR), (B) serotonin starting conformation 1, and (C) serotonin starting conformation 2. Residues forming the orthosteric binding site are shown and labelled. Oxygen and nitrogen atoms are displayed in red and blue, respectively. Carbon atoms are orange in ergotamine, purple in serotonin and grey in the receptor.

System Setup and Equilibration

Each receptor model was aligned into the bilayer normal and inserted into the pre-equilibrated lipid bilayers (Table 1). All lipid molecules within 1.2 Å of the protein were removed with final cholesterol content approximately 30% in mixed bilayers. The combined system was then solvated to produce a rectangular water box of dimensions (92 x 92 x 105) $Å^3$. Ions were added using the Autoionize Plugin of VMD, resulting in a final concentration of 150 mM.[56] After the removal of water molecules overlapping (distance < 1.2 Å) with the ions, lipids or protein atoms, the final system contained between 70,000 and 80,000 atoms. CHARMM22[54] parameters (with CMAP correction) were used for the protein, CHARMM36 for lipids,[57] CGenFF parameters for the serotonin ligand,[58,59] standard parameters for ions[60] and the TIP3P[61] model for water. NAMD2.9 was employed to calculate the dynamics of the systems throughout.[62] Initially, 10,000 steps of minimization were performed to remove steric clashes, followed by the progressive removal of constraints at 500 ps intervals to allow for gradual equilibration of the system. Constraints were released in the following order: (i) bulk water and lipid tails, (ii) lipid head groups, (iii) water molecules in protein cavities, and finally, (iv) protein side chains. Unrestrained dynamics was then undertaken in the NPT ensemble. The Particle Mesh Ewald method was used for the treatment of full-system periodic electrostatic interactions; interactions were evaluated every second timestep with a value of 1 Å to determine grid spacing.[63] Electrostatic and van der Waals forces were calculated every timestep and up to a cutoff distance of 12 Å. A switching distance of 10 Å was chosen to smoothly truncate the non-bonded interactions. Only atoms in a Verlet pair list within a cutoff distance of 13.5 Å were considered, with the list reassigned every 20 steps.[64] The SETTLE algorithm was used to constrain all bonds involving hydrogen atoms to allow the use of a 2 fs timestep.[65] The Nose-Hoover-Langevin piston method was employed to control the pressure with a 200 fs period, 50 fs damping constant and a desired value of 1 atmosphere. [66,67] The system was coupled to a Langevin thermostat to sustain a temperature of 298K throughout. A summary of the simulations performed can be found in Table 1.

Table 1. Summary of simulations included in this study.

Receptor	Membrane Composition			Ligand State	Replica	Simulation Length (ns)	Simulation Abbreviation
	% POPC	% Cholesterol	Isomer				
5-HT$_{1B}$	70	30	nat-cholesterol	-	1	600	CHL1$_{1B}$
				-	2	600	CHL2$_{1B}$
				-	3	600	CHL3$_{1B}$
	70	30	ent-cholesterol	-	1	600	ENT1$_{1B}$
				-	2	600	ENT2$_{1B}$
				-	3	600	ENT3$_{1B}$
	70	30	epi-cholesterol	-	1	600	EPI1$_{1B}$
				-	2	600	EPI2$_{1B}$
				-	3	600	EPI3$_{1B}$
	100	0	-	-	1	600	POPC1$_{1B}$
				-	2	600	POPC2$_{1B}$
5-HT$_{1B}$ + Ligand	70	30	nat-cholesterol	1	1	600	L1-CHL1$_{1B}$
				2	1	600	L2-CHL1$_{1B}$
				1	2	600	L1-CHL2$_{1B}$
				2	2	600	L2-CHL2$_{1B}$
				1	3	600	L1-CHL3$_{1B}$
				2	3	600	L2-CHL3$_{1B}$
	70	30	ent-cholesterol	1	1	600	L1-ENT1$_{1B}$
				2	1	600	L2-ENT1$_{1B}$
				1	2	600	L1-ENT2$_{1B}$
				2	2	600	L2-ENT2$_{1B}$
				1	3	600	L1-ENT3$_{1B}$
				2	3	600	L2-ENT3$_{1B}$
	70	30	ent-cholesterol	1	1	600	L1-EPI1$_{1B}$
				2	1	600	L2-EPI1$_{1B}$
				1	2	600	L1-EPI2$_{1B}$
				2	2	600	L2-EPI2$_{1B}$
				1	3	600	L1-EPI3$_{1B}$
				2	3	600	L2-EPI3$_{1B}$
	100	0	-	1	1	600	L1-POPC1$_{1B}$
				2	1	600	L2-POPC1$_{1B}$
				1	2	600	L1-POPC2$_{1B}$
				2	2	600	L2-POPC2$_{1B}$
				1	3	600	L1-POPC3$_{1B}$
				2	3	600	L2-POPC3$_{1B}$
5-HT$_{2B}$	70	30	nat-cholesterol		1	500	CHL1$_{2B}$
					2	500	CHL2$_{2B}$
					3	500	CHL3$_{2B}$
	70	30	ent-cholesterol		1	500	ENT1$_{2B}$
					2	500	ENT2$_{2B}$
					3	500	ENT3$_{2B}$
	70	30	epi-cholesterol		1	500	EPI1$_{2B}$
					2	500	EPI2$_{2B}$
					3	500	EPI3$_{2B}$
	100	0	-		1	500	POPC1$_{2B}$
					2	500	POPC2$_{2B}$

Results

Specific binding of membrane components in 5-HT$_{1B}$ receptor

Cholesterol hotspots on membrane proteins are routinely identified using classical MD simulations on extended timescales, akin to the simulations presented here. A random distribution of cholesterol molecules was utilized, with simulations initiated from three different random configurations, enabling the identification of cholesterol-binding sites in an unbiased manner. To determine potential interaction sites, the spatial distribution of the cholesterol headgroups was calculated in all simulations. We focus on the extracellular leaflet in the following text (Figure 3A and S1A in the Supplementary Information).

Three high-density cholesterol regions are observed in the extracellular leaflet of the 5-HT_{1B} receptor. S1 is a hydrophobic groove on TM2, with the polar cholesterol region also in contact distance of extracellular loop 1 (ECL1). Cholesterol molecules can also occupy a number of positions on the periphery of TM4, and in close proximity to extracellular loop 2 (ECL2). Interactions at this site typically involve two or more cholesterol molecules; this expansive region has been denoted S2. S3 encompasses the TM5-TM6 interface, with cholesterol positioning biased by the conformation of the extracellular end of these helices, as described in the following section. Out of these sites, the S2 site is reproduced in two out of three, *ent*-cholesterol simulations and all *epi*-cholesterol simulations. Additional positions on the receptor surface can also be occupied when the isomers are present; TM6 residues in the extracellular leaflet are one such site identified in three independent simulations (Figure S1). However, we note the timescales achieved in this study (~600 ns) prohibit exhaustive sampling of the receptor surface, and multiple association/disassociation events are not observed, hence meaningful occupation times of the cholesterol isomers in the identified hotspots cannot be extracted.

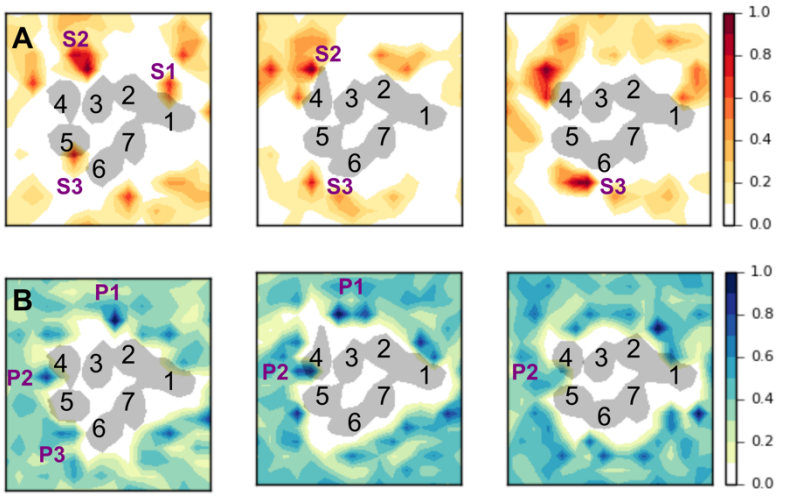

Figure 3. Interaction sites of membrane components. 2D density maps of (A) nat-cholesterol and (B) POPC, in three independent simulations of bilayers containing 30% nat-cholesterol. Bin dimensions of 4x4 Å are normalized so that the maximum density is 1. Sites observed in multiple simulations (including simulations with cholesterol isomers in Figure S1) and described in the text are labelled. Transmembrane helices are numbered from 1 to 7; cholesterol and POPC sites are labelled as SX or PX respectively, where X is an arbitrary number to distinguish individual sites.

In addition to the cholesterol interaction sites, we sought to ascertain if specific phospholipid binding sites also exist on the receptor surface, using the same methodology (Figure 3B and S1B). We identified two reproducible high-density sites (P1 and P2) in the extracellular leaflet. P2 is of interest, present at the TM4-5 interface, reproducible in all bilayers enriched with *nat*-cholesterol and isomeric forms. In this site, the phospholipid headgroup intercalates between ECL2 residues, which are initially beyond reach by membrane components. Occupation of this site can be evaluated using the contact distance between POPC molecules and residue P184

(Figure S2). This is determined by calculating the distance between the center of mass of all heavy atoms in both entities and identifying the minimum. In contrast, phospholipid molecules do not penetrate the ECL2 region consistently in both POPC-only bilayer simulations. In $CHL1_{1B}$, $ENT1_{1B}$ and $EPI2_{1B}$, POPC molecules are able to penetrate the TM4-TM5 interface, due to conformational changes in this region. This will be described in the following section.

Cholesterol tunes the extracellular surface in 5-HT_{1B} receptor

From this point forward, we refer to the second and third extracellular loops (ECL2 and ECL3) and the extracellular ends of the connected transmembrane helices (TM3-6) as the extracellular surface (ECS). The structure of the extracellular surface is a highly variable region, as shown by clustering the ECS conformations using a 2.5 Å criterion. Cluster population of the ECS is given in Table S1. Highly populated clusters are identified (> 70 % of simulation time) in all CHL_{1B} and $POPC_{1B}$ simulations. Visual inspection of the predominant clusters revealed that ECL2 can interact closely with the extracellular ends of TM5 and ECL3, or not at all, with the contact distance between hydrophobic residues V200/V201 (ECL2) and M337 (TM6) critical. We define these conformations as open or closed, pertaining to the minimum distance between all non-hydrogen atoms in V200/V201 and M337, using 4 Å as a cutoff, exhibited in Figure 4A and B, respectively. The retention of such conformations, and the frequency related structural characteristics, are summarized in Table 2. The time evolution of the ECS in all simulations is reported in Figure S2-4. Cholesterol-containing bilayers can stabilize open or closed conformations of the ECS. Closed conformations of the ECS prevail in the POPC-only bilayer simulations, entering this state consistently within a period of 150 ns. The closed state can also be stabilized by a salt-bridge between E198 and K341, as in $CHL3_{1B}$ (Table 2). In contrast, the absence of ECL2-TM6/ELC3 interactions in several simulations can mobilize ECL3 residues; F346, for example, can either remain buried in the surrounding bilayer or protrude into the extracellular solvent. The observed separation of ECL2 and ECL3 can also be accompanied by disruption of the initial conformations of the attached helices; TM5 (T209, V210 and T213) and TM6 residues (L335 and M338) dissociate, enabling the penetration of a proximal POPC molecule into this region, as mentioned earlier. This novel conformational change can be attributed to the continued close association between TM4/ECL2 residues (in the region of P183, P184 and F185) and ECL2 residues at the opposing end, particularly N202 (Figure S4).

Table 2. Summary of dynamics in ECL2 and surrounding regions in the 5-HT_{1B} receptor in all simulations presented. The values given are percentages of the total simulation time spent in a prototypical closed state of the EC loops. The criterion for each characteristic is given within the table.

Structural Feature	**ECL2-TM6 Hydrophobic Interactions**	**ECL2-ECL3 Salt Bridge Interactions**	**ECL3 Membrane Interactions**	**TM5-TM6 Interactions**	**ECL2-TM4 Interactions**
Criteria	**V200/V201-M337 Distance < 4 Å**	**E198-K341 Distance < 4 Å**	**F346 Solvent-Accessible Surface Area < 50 Å²**	**T209/V210/T213-L335 Distance < 5 Å**	**P184-N202 Distance > 4 Å**
$POPC1_{1B}$	88	14	100	100	97
$POPC2_{1B}$	82	13	100	82	96
$CHL1_{1B}$	1	0	18	3	9
$CHL2_{1B}$	3	0	5	100	59
$CHL3_{1B}$	67	55	100	100	73
$ENT1_{1B}$	1	0	100	17	9
$ENT2_{1B}$	60	10	43	100	55
$ENT3_{1B}$	49	0	1	100	34
$EPI1_{1B}$	35	2	13	100	56
$EPI2_{1B}$	0	0	97	1	82
$EPI3_{1B}$	81	1	0	100	69

Overall, simulations with *nat*-cholesterol are in qualitative agreement with its enantiomer, with the ECS exhibiting variable degrees of opening, both displaying enduringly open, closed or intermediate states, with transient periods of ECS closure. Further to this, TM5 and TM6 dissociate in a similar manner. In contrast, simulations with *epi*-cholesterol exhibit deviant behaviour; in $EPI1_{1B}$ and $EPI3_{1B}$ a closed ECS evolves after ~400 ns, persisting for the remainder of the 600-ns simulation. $EPI2_{1B}$, on the other hand, exhibits open forms of ECL2-ECL3 and TM5-6 from the outset (Figure S3).

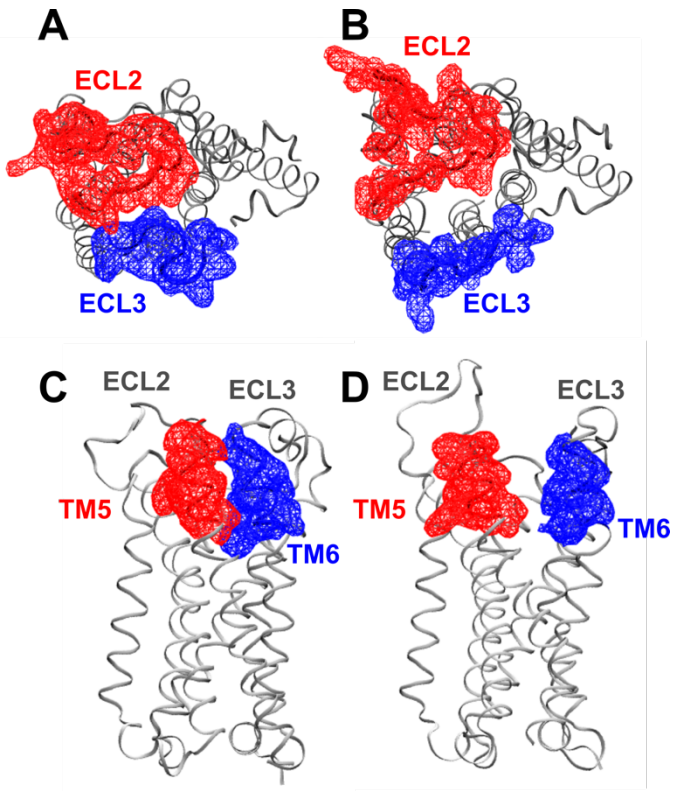

Figure 4. Dynamics of the extracellular surface. Representative structures of (A) closed (simulation POPC1_{1B}) and (B) open (simulation CHL1_{1B}) states of the ECS, displaying the density of residues 185-204 (red) and 338-349 (blue). Representative structures of (C) closed (simulation POPC1_{1B}) and (D) open (simulation CHL1_{1B}) TM5-TM6 helices, displaying the density of residues 205-213 (red) and 330-338 (blue). The density maps, shown as a wire mesh, are calculated using the VOLMAP plugin of VMD.

Stereospecific behavior of the TM3-4 site in the 5-HT$_{1B}$ receptor

From this point forward, we focus on CHL1_{1B}, ENT1_{1B} and EPI1_{1B} simulations, which are initiated from the same configuration of sterol molecules, displaying similar cholesterol occupancies as a result. In this case, the reported loop movements are not conserved when *epi*-cholesterol is present, despite occupation of molecules in the adjacent S2 site. Closure of the ECS in EPI1 at ~400 ns (Figure S3), follows destabilization of the P184-N202 interaction, in the 250-300 ns time period, which is maintained in CHL1 and ENT1 (Figure 5A). P184 resides at the TM4/ECL2 boundary; throughout, multiple sterol molecules inhabit the S2 region in close proximity to P184, interacting consistently with residues from TM3 (V120, F124, S127 and T131), TM4 (I178) and ECL2 (F185).

Differences can be observed in the binding poses of individual cholesterol molecules and attributed to the differential dynamics of this region. Sterol molecules in ENT1_{1B} and EPI1_{1B} penetrate deeper in the membrane, capable of H-bonding with T131 (TM4) (Figure 5B). In the latter case, this H-bond is formed in the initial stages of the simulation, and *epi*-cholesterol remains anchored in this position for the entirety of the simulation. In this pose, the smooth face

of *epi*-cholesterol stacks onto W174 (TM4); the hydroxyl headgroup H-bonds to T131 (TM3) and is surrounded by polar residues S127 (TM3) and S181 (TM4); the flexible tail extends to residues in TM2 (S90, V93 and L97) (Figure 5C, D). The headgroup of *ent*-cholesterol occupies the analogous region, with enhanced mobility, due to the orientation of the hydroxyl group on the rough face of cholesterol (Figure 5C, E). With this in mind, we postulate that the stability of cholesterol in this site is dependent on its exact structure, and that this region acts as a functional binding site in the 5-HT_{1B} receptor.

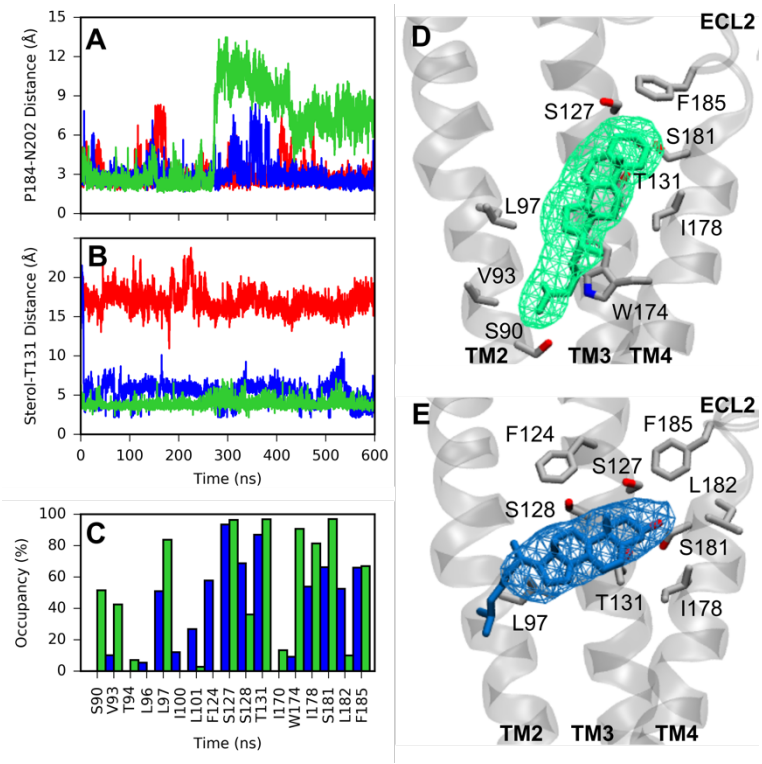

Figure 5. Comparison of 5-HT_{1B} receptor dynamics in $CHL1_{1B}$, $ENT1_{1B}$ and $EPI1_{1B}$ simulations. (A) Time evolution of P184-N202 contact distance, $CHL1_{1B}$, $ENT1_{1B}$ and $EPI1_{1B}$ simulations are displayed in red, blue and green respectively. (B) Time evolution of the minimum contact distance between cholesterol hydroxyl atoms and T131, colored as in (A). (C) Contact frequency of 5-HT_{1B} residues with stable ent- (blue) and epi- (green) cholesterol binding poses. Values are given as a percentage of total simulation time and calculated using a 5 Å criterion. (D-E) Position of deep epi- and ent-cholesterol molecules in the S2 site. Interacting 5-HT_{1B} residues are shown in licorice representation in grey.

Effect on ligand binding in the 5-HT_{1B} receptor

To discern the functional consequences of cholesterol binding to transmembrane helix 4, and the resulting conformational changes, we focused our attention towards the extracellular ligand-binding site. In the crystal structure of the 5-HT_{1B} receptor with bound ergotamine, which is used to construct our initial model, the planar ergoline moiety is embedded in the orthosteric binding pocket, a hydrophobic cleft composed of I130, C133, S212, A216, W327, F330 and

F331 residues. Binding is stabilized by (i) a H-bond between the indole nitrogen of ergotamine and the T134 side-chain, and (ii) a salt-bridge interaction between the amine tail of ergotamine and D129, which in turn is reinforced by H-bonding with Y359.

Additional simulations were performed with a 5-HT molecule, commonly known as serotonin, bound in the orthosteric binding site in two alternative conformations (see Methods), consistent with the interactions observed for ergotamine in the crystal structure. To distinguish between different open and closed states of the receptor, the extracellular surface (defined as residues 184 to 205 and 337 to 349), was clustered using a 2.5 A RMSD criterion (Table S1). The position of membrane cholesterol was monitored in the most highly populated cluster. The S2 site is occupied in 10 out of 18 independent simulations containing membrane cholesterol (L1-$CHL1_{1B}$, L2-$CHL1_{1B}$, L2-$CHL2_{1B}$, L2-$ENT1_{1B}$, L1-$ENT2_{1B}$, L2-$ENT2_{1B}$, L1-$EPI1_{1B}$, L2-$EPI1_{1B}$, L1-$EPI2_{1B}$ and L1-$EPI3_{1B}$). The position of the serotonin molecule was compared in ECS conformations from POPC-only simulations (denoted NoC), simulations with a mixed bilayer where S2 is occupied by cholesterol (denoted C_{S2}) and simulations with a mixed bilayer where S2 is not occupied by cholesterol (denoted C_{NoS2}). The density maps of cholesterol and serotonin, in the extracellular binding site are shown in Figure 6.

To illustrate the effect of cholesterol on extracellular ligands, we focus on the two most highly populated binding poses observed in the simulations, labelled Lig1 and Lig2 in Figure 6C-E. Remarkably, Lig1 is the only serotonin binding pose in the C_{S2} clusters. In the C_{NoS2} clusters, the serotonin density maximum is located in close proximity to the Lig1 position; overall, however, the serotonin position is more variable. Lig2 is a distinct maximum observed only in the NoC simulations, where serotonin resides deeper in the $5\text{-}HT_{1B}$ receptor, consistent with occupation of the orthosteric binding pocket. The contact frequency of $5\text{-}HT_{1B}$ receptor residues interacting with serotonin in conformations Lig1 and Lig2 were extracted from the L2-$CHL1_{1B}$ and L1-$POPC_{1B}$ simulations, respectively (Figure 6F-G). Important residues (contact frequency > 90 %) are shown in Table 3. These are consistent with experimental mutagenesis studies which reveal that binding of lysergic acid diethylamide (known as LSD), serotonin and ergotamine is completely abolished in D129A, I130A, C133A, and W327A and F330A mutants.[44,45] Overall, our results provide strong evidence that cholesterol binding influences the ligand binding characteristics of the 5-HT receptor.

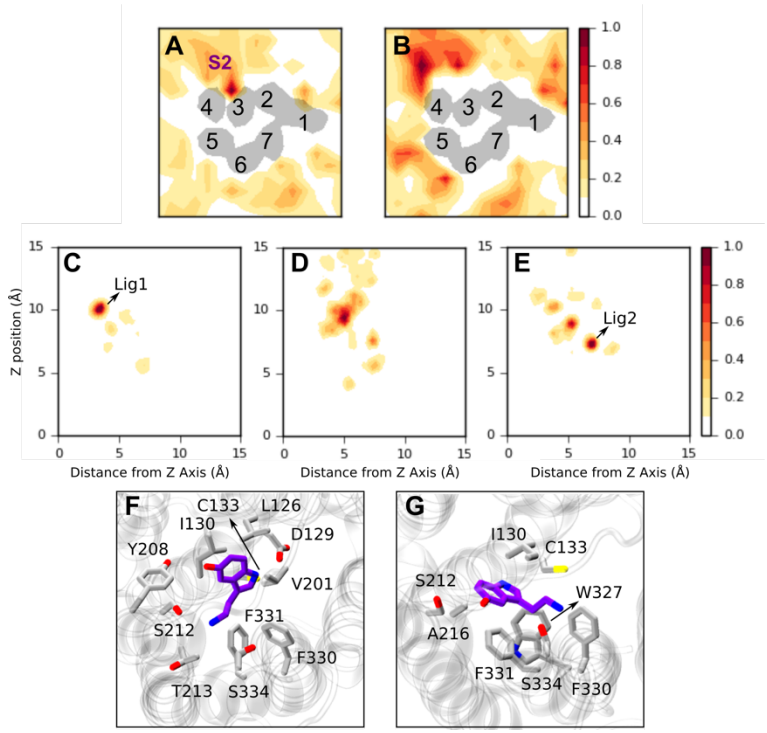

Figure 6. (A-B) Combined 2D density maps of the position of cholesterol isomers in C_{S2} and C_{NoS2} simulations respectively. Bin dimensions of 4x4 Å are normalized so that the maximum density is 1. Transmembrane helices are numbered from 1 to 7; site S2 is labelled. *(C-E)* Combined 2D density map of the position of the serotonin molecule in (C) C_{S2}, (D) C_{NoS2} and (E) NoC simulations (defined in the main text). Throughout, the serotonin position is measured as the z coordinate and the distance of this from the central axis (both of the center of mass of the indole ring axis) of the simulation box. (F) Representative frame of Lig1 binding pose from the L2-CHL1$_{1B}$ simulations and Lig2 binding pose from the L1-POPC$_{1B}$ simulation. Residues forming the orthosteric binding site are shown and labelled. Oxygen and nitrogen atoms are displayed in red and blue, respectively. Carbon atoms are purple in serotonin and grey in the receptor.

Table 3. Residues of 5-HT$_{1B}$ interacting with serotonin cluster poses Lig1 and Lig2. Residues included exhibit a contact frequency > 90 %, measured using a distance 5 Å criterion between the heavy atoms of the protein and ligand molecules.

Simulation	Serotonin Pose	Interacting Residues
L2-CHL1$_{1B}$	Lig1	L126 D129 I130 C133 V201 Y208 S212 T213 F330 F331 S334
L1-POPC$_{1B}$	Lig2	I130 C133 T134 S212 A216 W327 F330 F331 S334

Table 4. Residues of 5-HT$_{1B}$ which H-bond to the hydroxyl group of cholesterol molecules in the S2 (TM4) site. H-bond frequency is given as a percentage of the cluster measured; residues with H-bond frequency > 30% are shown.

Simulation	Residue	H-Bond Frequency (%)
L1-CHL1$_{1B}$	S127	48
	S128	64
L2-CHL1$_{1B}$	S127	63
L2-CHL2$_{1B}$	-	-
L2-ENT1$_{1B}$	T131	47
L1-ENT2$_{1B}$	D123	41
L2-ENT2$_{1B}$	R188	32
L1-EPI1$_{1B}$	S127	56
L2-EPI1$_{1B}$	-	-
L1-EPI2$_{1B}$	-	-
L1-EPI3$_{1B}$	-	-

Examining the S2 site more closely, the cholesterol molecules are seen to penetrate deep into the upper leaflet and hydrogen bond with S127 (L1-CHL1$_{1B}$, L2-CHL1$_{1B}$ and L1-EPI1$_{1B}$) or T131 (L2-ENT1$_{1B}$) (Table 4), in agreement with our *apo* state simulations. The interactions frequencies of the deep cholesterol binding sites are given for these simulations in Figure 7. In CHL$_{1B}$ simulations, the cholesterol molecule consistently interacts with L97, F124, S127, S128, T131, W174 and I178, for > 80 % of the 5-HT$_{1B}$ cluster frames. In addition, *nat*-cholesterol interacts with L182 in L1-CHL1$_{1B}$ and F185 in L2-CHL1$_{1B}$. In L1-EPI1$_{1B}$, where the hydroxyl group also H-bonds to S127, interactions with neither L182 and F185 are identified, although *epi*-cholesterol is more engaged with residues L101 and V175. In L2-ENT1$_{1B}$, persistent interactions (> 80 % of the cluster frames) are only observed with L97, D123, F124 and S127, highlighting the variability of *ent*-cholesterol in this site. This data suggests that cholesterol isomers interact differently with the TM4 surface, supporting our earlier postulate that the S2 site is stereospecific.

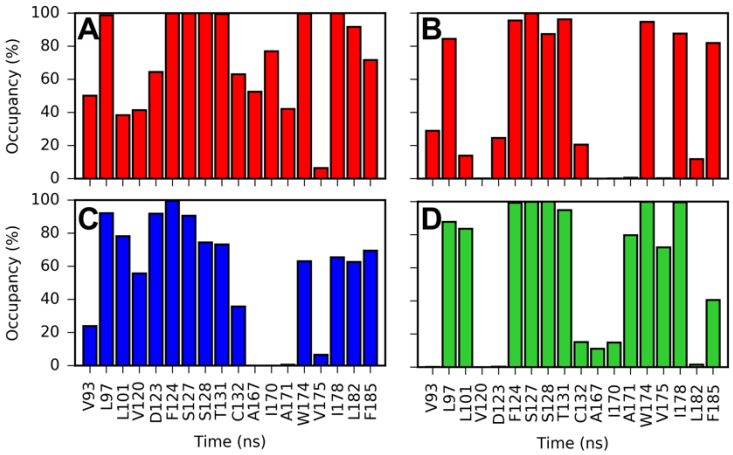

Figure 7. Contact frequency of 5-HT$_{1B}$ residues with stable *nat*- (red), *ent*- (blue) and *epi*- (green) cholesterol binding poses, in simulations (A) L1-CHL1$_{1B}$, (B) L2-CHL1$_{1B}$, (C) L2-ENT1$_{1B}$ and L1-EPI1$_{1B}$. Values are given as a percentage of total simulation time and calculated using a 5 Å criterion.

In several cases, a group of cholesterol molecules occupy the TM4 surface. This can be attributed to the high cholesterol concentration used in our simulations (30%). Under these circumstances, cholesterol molecules cover a larger region of the receptor surface and it becomes difficult to delineate stable binding poses and differences between individual cholesterol isomers.

Enhanced stability of ECL2 in the 5-HT_{2B} receptor

To determine if this mechanism of cholesterol is applicable to other 5-HT receptors, analogous simulations were performed for the 5-HT_{2B} receptor, as a crystal structure is available (PDB ID 4IB4). Here, cholesterol can populate the surface of all seven transmembrane helices in the extracellular leaflet to some extent (Figure 8). Five reproducible cholesterol hotspots have been identified: L1 (TM2), L2 (TM3), L3 (TM4-5), L4 (TM5-6) and L5 (TM7-1). The consequences of cholesterol binding in such positions are ambiguous, in this case. Here, ECL2 (G194 to R213) and ECL3 (L347 to T357) do not undergo significant conformational changes. The highly flexible region of ECL2 (T197 to I205) and ECL3 is flanked by multiple anchor points to surrounding transmembrane helices: (i) a disulfide bond between C128 (TM3) and C207 (ECL2) conserved in class A GPCRs, (ii) H-bonding between the backbone oxygen atom of K193 (TM4) and the sidechain of R213 (ECL2) and vice versa, (iii) a salt-bridge between K211 (ECL2) and D351 (ECL3), and, finally (iv) a hydrophobic cluster formed between V209 (ECL2) and residues from TM3 (L132, V136), TM4 (V190) and TM5 (F217). The dynamic interactions are prevalent in the simulations irrespective of the membrane composition, negating large-scale conformational changes in the extracellular ends of TM4, TM5 and TM6 (Table 5). These native contacts are conserved in the available structures of 5-HT_{2B} receptor,[44,45,49,68] with the exception of K211-D351 in the crystal structure of the 5-HT_{2B} receptor obtained using serial femtosecond crystallography at room temperature (PDB ID 4NC3), where the sidechain of K211 is unresolved.[69] This is consistent with our simulation data, where a frequency of interaction approximately between 70 and 95% is recorded in this case.

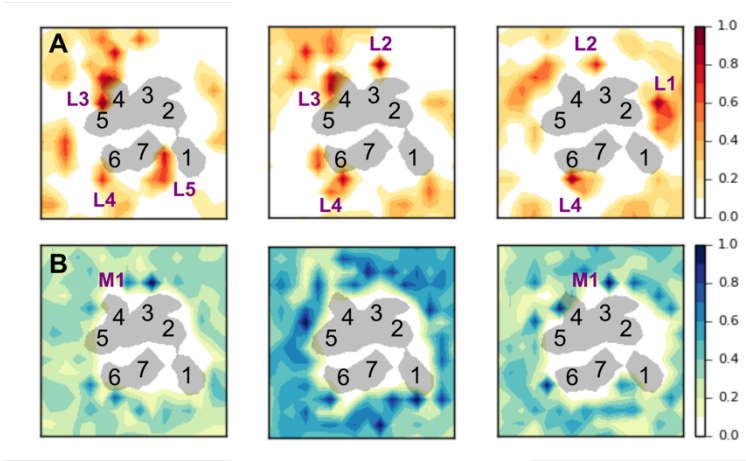

Figure 8. Interaction sites of membrane components on the 5-HT_{2B} receptor. 2D density maps of (A) nat-cholesterol and (B) POPC in three independent simulations of bilayers containing 30% cholesterol. Bin dimensions of 4x4 Å are normalized so that the maximum density is 1. Sites observed in multiple simulations (including simulations with cholesterol isomers in Figure S1) and described in the text are labelled. Transmembrane helices are numbered from 1 to 7; cholesterol and POPC sites are labelled as LX or MX respectively, where X is an arbitrary number to distinguish individual sites.

Table 5. Summary of dynamics in ECL2 and surrounding regions of the 5-HT_{2B} receptor. The values given are percentages of the total simulation time spent in a prototypical closed state of the ECS. The criterion for each characteristic is given within the table. The TM3/4/5 residues specified are in close contact, forming a hydrophobic cluster; therefore, this criteria is satisfied if V209 is within 5 Å of any of these residues.

Structural Feature	**TM4-ECL2 Salt Bridge**	**ECL2-ECL3 Salt Bridge**	**ECL2 –TM3/4/5 Hydrophobic Interactions**
Criteria	**K193-R213 Distance < 3.5 Å**	**K211-D351 Distance < 3.5 Å**	**V209- L132 (TM3)/V136 (TM3)/V190 (TM4)/F217(TM5) Distance < 5.0 Å**
$POPC1_{2B}$	100	77	99
$POPC2_{2B}$	100	87	99
$CHL1_{2B}$	100	71	100
$CHL2_{2B}$	100	86	100
$CHL3_{2B}$	100	96	100
$ENT1_{2B}$	100	68	100
$ENT2_{2B}$	100	79	100
$ENT3_{2B}$	100	88	100
$EPI1_{2B}$	100	72	100
$EPI2_{2B}$	100	92	100
$EPI3_{2B}$	100	80	99

Discussion

The bulk of specific cholesterol interaction sites identified by structural and simulation methodologies are situated so that the hydroxyl group inhabits the headgroup region of the membrane [8]. However, additional buried sites have also been exposed by computation.[70] In the

5-HT_{2B} receptor, cholesterol hotspots are shown on all of TM helices, occupying typical positions in the upper leaflet of the bilayer. In the 5-HT_{1B} receptor, we detect unparalleled high occupancy of the TM4 helix by membrane cholesterol in the upper leaflet. The TM4 helix includes the CARC motif[23] in the extracellular leaflet and the CCM[27] in the intracellular leaflet. Our simulations reveal that of several cholesterol molecules inhabiting this area, a single molecule can penetrate a deep cholesterol binding site on the TM3/4 helices, which can contain components of both canonical interaction motifs situated in this area. This is observed in multiple independent simulations for all three stereoisomers of cholesterol examined. Cholesterol molecules are able to hydrogen-bond with S127 or T131 several residues, exhibiting differential interactions with 5-HT_{1B} receptor residues in each case. With this in mind, we propose this region acts as a functional binding site in the 5-HT_{1B} receptor, with stereospecific properties. In compliance with this, high cholesterol density on TM4 (in the extracellular leaflet) is observed in coarse-grained simulations of the closely-related 5-HT_{1A} receptor.[31] This result is particularly important considering the known stereospecific requirement of cholesterol in the 5-HT_{1A} receptor.[39]

In support of this, we report reproducible conformational changes in the ECS, originating from residues in this region. The vulnerability of the TM4-ECL2 boundary in the 5-HT_{1B} receptor to cholesterol binding in this region, can be accredited to the presence of multiple proline residues (P183-P184), which are unable to adopt typical secondary structural components, and thus are inherently more flexible. This motif is conserved in all 5-HT_1 receptors; in 5-HT_2 receptors a hydrophobic residue is inserted in the middle of the analogous proline residues (P189-V190-P181 in 5-HT_{2B}), stabilizing this area to a greater extent. Considering the importance of such residues in the adjustability of ECL2 in the 5-HT_{1B} and 5-HT_{2B} receptors, it is conceivable that this region can act as a stereospecific cholesterol sensor in the 5-HT family, propagating changes through the ECS.

Interest in the behaviour of the highly variable ECS in GPCRs has grown in recent years, as a potential target for subtype-selective drugs.[29,71,72] In rhodopsin, ECL2 forms a steadfast cap over the covalently bound ligand.[73] However, in a number of class A GPCRs with diffusible ligands, the dependency of the ECL2 conformation on the chemical structure of the ligand has been demonstrated experimentally. In the β_2-adrenergic receptor, NMR spectroscopy revealed ligand-specific conformations of the ECS in the vicinity of a salt-bridge linking ECL2 and ECL3.[46] In the angiotensin type II receptor, cysteine accessibility experiments disclose open and closed conformations of ECL2, which can influence the dissociation rates of bound ligands.[47] In relation to 5-HT receptors, circular dichroism and steady-state fluorescence revealed variations in ECL2 conformation in the 5-HT_{4A}, resulting from binding of full, partial or inverse agonists.[48] Furthermore, in the 5-HT_{2B} receptor, the remarkably slow dissociation rates of the archetypal hallucinogen LSD have been attributed to an ECL2 lid revealed by the high-resolution structure of this complex.[49] Mutagenesis of one such residue, V209, dramatically altered LSD's binding kinetics in this case. Here, we demonstrate that cholesterol addition,

depletion or substitution_is able to bias the conformational states of ECL2 in the 5-HT_{1B}, providing a potential mechanism by which cholesterol and other membrane constituents can alter the ligand-binding properties of GPCRs.

It should be noted that the exact nature of cholesterol modulation on ligand binding affinity in the 5-HT_{1B} receptor cannot be ascertained from the data presented in this study. Nevertheless, our simulations expose a situation where the configuration of the extracellular binding site is altered in cholesterol-rich bilayers. In several independent simulations of the apo state, the orthosteric binding site is susceptible to lipid interactions, resulting from separation of the EC loops (ECL2 and ECL3) and the attached TM helices (TM5 and TM6). In simulations with serotonin, the ligand occupies an alternative binding site away from the orthosteric binding site, as a result of reorganization of ECL2. Coupling of the orthosteric binding pocket with the membrane milieu has been reported previously. In various cases, membrane-mediated pathways are required for ligands to circumnavigate closed ECS's, which prohibit transport between the extracellular binding pocket and solution. In the opsin receptor, TM5-6 and TM7-1 openings have been postulated to allow access to retinal,[74-76] and in the human free fatty-acid receptor 1 (known as FFAR1 or GPR40), the lipophilic agonist is proposed to traverse between an opening in TM3-4,[77] both as a result of closed ECL2 conformations. Similarly, an N-terminus fold obstructs the ECS in the S1P1 receptor, indicating ligand access occurs via TM7-1.[78] This multi-step process has been mapped by extensive unbiased MD simulations.[79] Moreover, it has recently been reported that membrane constituents can enter the orthosteric binding pocket via similar pathways. In the adenosine A_{2A} receptor, cholesterol is able to penetrate the protein core via TM5-6, effectively acting as a competitive inhibitor and abolishing binding of antagonist, ZM241385.[80] Overall, these studies substantiate our proposed response to specific cholesterol binding in 5-HT_{1B} receptor.

The indirect mechanism of cholesterol action has not been addressed thus far. The effect of cholesterol on the physical properties of model phospholipid bilayers have been studied intensively, with increased bilayer thickness and S_{CD} order parameters, as well as decreased area per lipid, consistently reported upon cholesterol enrichment.[81-84] Our previous work examined the molecular properties of *nat*-cholesterol, *ent*-cholesterol and *epi*-cholesterol in the phospholipid bilayers utilized here.[12] In general, *epi*-cholesterol exerted slightly weaker effects on bilayer properties, yet increased the solvent-accessible surface area of POPC molecules, relative to the cholesterol-free bilayer. In contrast, cholesterol-rich bilayers containing *nat*- and *ent*-cholesterol decreased this property. Considering this, we cannot completely rule out an indirect effect of cholesterol on the dynamics of the 5-HT_{1B} receptor. It is apparent, however, that the decisive conformational changes reported can be rationalized by stereospecific binding of cholesterol molecules to the receptor surface.

Finally, we acknowledge the increasing abundance of literature concerning the effect of cholesterol on the oligomerization properties of GPCRs. For example, coarse-grained MD simulations have shown that the dimer interface in the β2-adrenergic receptor is altered when

cholesterol concentration is increased.[85] Similar conclusions have since been reported for the 5-HT_{1A} receptor[86] and chemokine receptor type 4 using comparable methodologies.[87] The interrelationship between membrane cholesterol, receptor dimerization and the conformation of the extracellular surface may prove interesting in future studies.

Conclusions

In the current study, over 25 μs of unbiased MD simulations has been used to explore the relationship between membrane cholesterol in the 5-HT receptor family, specifically the 5-HT_{1B} and 5-HT_{2B} receptors. Our data suggests that the stability of the extracellular surface is subtype-dependent; the conformation of ECL2 in the 5-HT_{2B} receptor is maintained by a number of salt-bridges and hydrophobic interactions with sequentially distant regions of the protein. In the absence of such interactions in the 5-HT_{1B} receptor, ECL2 is unmistakably more mobile, populating a number of distinct conformations. In the latter case, we provide evidence that fluctuations in ECL2 are governed by occupation of the TM3 and TM4 surfaces by cholesterol molecules in the extracellular leaflet. Mobile residues at the TM4-ECL2 boundary are critical in this respect, interacting with both membrane cholesterol and residues at the other extreme of ECL2. Comparative analysis of cholesterol isomers demonstrates differential binding to this site, suggesting structural rearrangements in this region may be influenced by stereospecific binding of cholesterol. In addition, distinctive binding poses of serotonin are observed in simulations where cholesterol is bound in the suggested TM4 site, and where the TM4 site is unoccupied, providing a direct relationship between occupation of this site and ligand binding characteristics of the 5-HT_{1B} receptor. This data contributes to our understanding of how cholesterol and other membrane components modulate receptor function and might aid the development of targeted therapies of GPCRs, required for the treatment of numerous neurological disorders, such as depression and anxiety.

References

(1) Sriram, K.; Insel, P. A. G Protein-Coupled Receptors as Targets for Approved Drugs: How Many Targets and How Many Drugs? *Mol. Pharmacol.* **2018,** *93* (4), 251.

(2) Levitan, I.; Singh, D. K.; Rosenhouse-Dantsker, A. Cholesterol binding to ion channels. *Front. in Physiol.* **2014,** *5*, 14.

(3) Harikumar, K. G.; Puri, V.; Singh, R. D.; Hanada, K.; Pagano, R. E.; Miller, L. J. Differential effects of modification of membrane cholesterol and sphingolipids on the conformation, function, and trafficking of the G protein-coupled cholecystokinin receptor. *J. Biol. Chem.* **2005,** *280* (3), 2176.

(4) Dawaliby, R.; Trubbia, C.; Delporte, C.; Masureel, M.; Van Antwerpen, P.; Kobilka, B. K.; Govaerts, C. Allosteric regulation of G protein-coupled receptor activity by phospholipids. *Nat. Chem. Biol.* **2016,** *12* (1), 35.

(5) Pucadyil, T. J.; Chattopadhyay, A. Cholesterol modulates ligand binding and G-protein coupling to serotonin (1A) receptors from bovine hippocampus. *BBA-Biomembranes* **2004,** *1663* (1-2), 188.

(6) Pucadyil, T. J.; Chattopadhyay, A. Cholesterol modulates the antagonist-binding function of hippocampal serotonin(1A) receptors. *BBA-Biomembranes* **2005,** *1714* (1), 35.

(7) Chattopadhyay, A.; Jafurulla, M.; Kalipatnapu, S.; Pucadyil, T. J.; Harikumar, K. G. Role of cholesterol in ligand binding and G-protein coupling of serotonin(1A) receptors solubilized from bovine hippocampus. *Biochem Biophys. Res. Co.* **2005,** *327* (4), 1036.
(8) Gimpl, G. Interaction of G protein coupled receptors and cholesterol. *Chem. Phys. Lipids* **2016,** *199*, 61.
(9) Levitan, I.; Singh, D. K.; Rosenhouse-Dantsker, A. Cholesterol binding to ion channels. *Front. Physiol.* **2014,** *5*, 14.
(10) Xu, X. L.; London, E. The effect of sterol structure on membrane lipid domains reveals how cholesterol can induce lipid domain formation. *Biochemistry* **2000,** *39* (5), 843.
(11) Gimpl, G.; Burger, K.; Fahrenholz, F. Cholesterol as modulator of receptor function. *Biochemistry* **1997,** *36* (36), 10959.
(12) Oakes, V.; Domene, C. Stereospecific Interactions of Cholesterol in a Model Cell Membrane: Implications for the Membrane Dipole Potential. *J. Memb. Biol.* **2018,** *251* (3), 507.
(13) Westover, E. J.; Covey, D. F. The enantiomer of cholesterol. *J. Memb. Biol* **2004,** *202* (2), 61.
(14) Addona, G. H.; Sandermann, H.; Kloczewiak, M. A.; Miller, K. W. Low chemical specificity of the nicotinic acetylcholine receptor sterol activation site. *BBA-Biomembranes* **2003,** *1609* (2), 177.
(15) Sooksawate, T.; Simmonds, M. A. Effects of membrane cholesterol on the sensitivity of the GABA(A) receptor to GABA in acutely dissociated rat hippocampal neurones. *Neuropharmacology* **2001,** *40* (2), 178.
(16) Romanenko, V. G.; Rothblat, G. H.; Levitan, I. Sensitivity of volume-regulated anion current to cholesterol structural analogues. *J. Gen. Phys.* **2004,** *123* (1), 77.
(17) D'Avanzo, N.; Hyrc, K.; Enkvetchakul, D.; Covey, D. F.; Nichols, C. G. Enantioselective Protein-Sterol Interactions Mediate Regulation of Both Prokaryotic and Eukaryotic Inward Rectifier K+ Channels by Cholesterol. *PLOS One* **2011,** *6* (4), 7.
(18) Bukiya, A. N.; Belani, J. D.; Rychnovsky, S.; Dopico, A. M. Specificity of cholesterol and analogs to modulate BK channels points to direct sterol-channel protein interactions. *J. Gen. Phys.* **2011,** *137* (1), 93.
(19) Picazo-Juarez, G.; Romero-Suarez, S.; Nieto-Posadas, A.; Llorente, I.; Jara-Oseguera, A.; Briggs, M.; McIntosh, T. J.; Simon, S. A.; Ladron-de-Guevara, E.; Islas, L. D.et al. Identification of a Binding Motif in the S5 Helix That Confers Cholesterol Sensitivity to the TRPV1 Ion Channel. *J. Biol. Chem.* **2011,** *286* (28), 24966.
(20) Jafurulla, M.; Tiwari, S.; Chattopadhyay, A. Identification of cholesterol recognition amino acid consensus (CRAC) motif in G-protein coupled receptors. *Biochem. Bioph. Res. Co.* **2011,** *404* (1), 569.
(21) Fantini, J.; Barrantes, F. J. How cholesterol interacts with membrane proteins: an exploration of cholesterol-binding sites including CRAC, CARC, and tilted domains. *Front. Physiol.* **2013,** *4*, 9.
(22) Li, H.; Papadopoulos, V. Peripheral-type benzodiazepine receptor function in cholesterol transport. Identification of a putative cholesterol recognition/interaction amino acid sequence and consensus pattern. *Endocrinology* **1998,** *139* (12), 4991.
(23) Baier, C. J.; Fantini, J.; Barrantes, F. J. Disclosure of cholesterol recognition motifs in transmembrane domains of the human nicotinic acetylcholine receptor. *Sci. Rep.* **2011,** *1*.
(24) Liu, W.; Chun, E.; Thompson, A. A.; Chubukov, P.; Xu, F.; Katritch, V.; Han, G. W.; Roth, C. B.; Heitman, L. H.; Ijzerman, A. P.et al. Structural Basis for Allosteric Regulation of GPCRs by Sodium Ions. *Science* **2012,** *337* (6091), 232.
(25) Warne, T.; Moukhametzianov, R.; Baker, J. G.; Nehme, R.; Edwards, P. C.; Leslie, A. G.; Schertler, G. F.; Tate, C. G. The structural basis for agonist and partial agonist action on a beta(1)-adrenergic receptor. *Nature* **2011,** *469* (7329), 241.
(26) Cherezov, V.; Rosenbaum, D. M.; Hanson, M. A.; Rasmussen, S. G. F.; Thian, F. S.; Kobilka, T. S.; Choi, H.-J.; Kuhn, P.; Weis, W. I.; Kobilka, B. K.et al. High Resolution Crystal Structure of an Engineered Human β(2)-Adrenergic G protein-Coupled Receptor. *Science* **2007,** *318* (5854), 1258.
(27) Hanson, M. A.; Cherezov, V.; Roth, C. B.; Griffith, M. T.; Jaakola, V.-P.; Chien, E. Y. T.; Velasquez, J.; Kuhn, P.; Stevens, R. C. A specific cholesterol binding site is established by the 2.8 Å structure of the human β(2)-adrenergic receptor in an alternate crystal form. *Structure* **2008,** *16* (6), 897.

(28) Wang, C.; Jiang, Y.; Ma, J.; Wu, H.; Wacker, D.; Katritch, V.; Han, G. W.; Liu, W.; Huang, X. P.; Vardy, E.et al. Structural basis for molecular recognition at serotonin receptors. *Science* **2013,** *340* (6132), 610.
(29) Wu, H.; Wang, C.; Gregory, K. J.; Han, G. W.; Cho, H. P.; Xia, Y.; Niswender, C. M.; Katritch, V.; Meiler, J.; Cherezov, V.et al. Structure of a Class C GPCR Metabotropic Glutamate Receptor 1 Bound to an Allosteric Modulator. *Science* **2014,** *344* (6179), 58.
(30) Sengupta, D.; Chattopadhyay, A. Molecular dynamics simulations of GPCR-cholesterol interaction: An emerging paradigm. *BBA-Biomembranes* **2015,** *1848* (9), 1775.
(31) Sengupta, D.; Prasanna, X.; Mohole, M.; Chattopadhyay, A. Exploring GPCR-Lipid Interactions by Molecular Dynamics Simulations: Excitements, Challenges, and the Way Forward. *J. Phys. Chem. B* **2018,** *122* (22), 5727.
(32) Oakes, V.; Domene, C. In *Computational Tools for Chemical Biology*; The Royal Society of Chemistry, 2018.
(33) Jorgensen, C.; Oakes, V.; Domene, C. In *Membrane Organization and Dynamics*; Chattopadhyay, A., Ed.; Springer-Verlag Berlin: Berlin, 2017; Vol. 20.
(34) Ramírez, M. J. 5-HT(6)receptors and Alzheimer's disease. *Alzheimer's Res. Ther.* **2013,** *5* (2), 15.
(35) Akhondzadeh, S. The 5-HT hypothesis of schizophrenia. *IDrugs* **2001,** *4* (3), 295.
(36) Saxena, R.; Chattopadhyay, A. Membrane cholesterol stabilizes the human serotonin(1A) receptor. *BBA-Biomembranes* **2012,** *1818* (12), 2936.
(37) Shrivastava, S.; Pucadyil, T. J.; Paila, Y. D.; Ganguly, S.; Chattopadhyay, A. Chronic cholesterol depletion using statin impairs the function and dynamics of human serotonin(1A) receptors. *Biochemistry* **2010,** *49* (26), 5426.
(38) Paila, Y. D.; Murty, M. R.; Vairamani, M.; Chattopadhyay, A. Signaling by the human serotonin(1A) receptor is impaired in cellular model of Smith-Lemli-Opitz Syndrome. *Biochim. Biophys. Acta* **2008,** *1778* (6), 1508.
(39) Jafurulla, M.; Rao, B. D.; Sreedevi, S.; Ruysschaert, J. M.; Covey, D. F.; Chattopadhyay, A. Stereospecific requirement of cholesterol in the function of the serotonin1A receptor. *Biochim. Biophys. Acta* **2014,** *1838* (1 Pt B), 158.
(40) Prasad, R.; Paila, Y. D.; Chattopadhyay, A. Membrane cholesterol depletion enhances ligand binding function of human serotonin(1A) receptors in neuronal cells. *Biochem. Bioph. Res. Co.* **2009,** *390* (1), 93.
(41) Singh, P.; Saxena, R.; Paila, Y. D.; Jafurulla, M.; Chattopadhyay, A. Differential effects of cholesterol and desmosterol on the ligand binding function of the hippocampal serotonin(1A) receptor: Implications in desmosterolosis. *Biochim. Et Biophy. Acta-Biomembranes* **2009,** *1788* (10), 2169.
(42) Singh, P.; Jafurulla, M.; Paila, Y. D.; Chattopadhyay, A. Desmosterol replaces cholesterol for ligand binding function of the serotonin(1A) receptor in solubilized hippocampal membranes: Support for nonannular binding sites for cholesterol? *Biochim. Et Biophy. Acta-Biomembranes* **2011,** *1808* (10), 2428.
(43) Sengupta, D.; Chattopadhyay, A. Identification of Cholesterol Binding Sites in the Serotonin(1A) Receptor. *J. Phys. Chem. B* **2012,** *116* (43), 12991.
(44) Wacker, D.; Wang, C.; Katritch, V.; Han, G. W.; Huang, X. P.; Vardy, E.; McCorvy, J. D.; Jiang, Y.; Chu, M. H.; Siu, F. Y.et al. Structural Features for Functional Selectivity at Serotonin Receptors. *Science* **2013,** *340* (6132), 615.
(45) Wang, C.; Jiang, Y.; Ma, J. M.; Wu, H. X.; Wacker, D.; Katritch, V.; Han, G. W.; Liu, W.; Huang, X. P.; Vardy, E.et al. Structural Basis for Molecular Recognition at Serotonin Receptors. *Science* **2013,** *340* (6132), 610.
(46) Bokoch, M. P.; Zou, Y. Z.; Rasmussen, S. G. F.; Liu, C. W.; Nygaard, R.; Rosenbaum, D. M.; Fung, J. J.; Choi, H. J.; Thian, F. S.; Kobilka, T. S.et al. Ligand-specific regulation of the extracellular surface of a G-protein-coupled receptor. *Nature* **2010,** *463* (7277), 108.
(47) Unal, H.; Jagannathan, R.; Bhat, M. B.; Karnik, S. S. Ligand-specific Conformation of Extracellular Loop-2 in the Angiotensin II Type 1 Receptor. *J. Biol. Chem.* **2010,** *285* (21), 16341.
(48) Baneres, J. L.; Mesnier, D.; Martin, A.; Joubert, L.; Dumuis, A.; Bockaert, J. Molecular characterization of a purified 5-HT4 receptor - A structural basis for drug efficacy. *J. Biol. Chem.* **2005,** *280* (21), 20253.

(49) Wacker, D.; Wang, S.; McCorvy, J. D.; Betz, R. M.; Venkatakrishnan, A. J.; Levit, A.; Lansu, K.; Schools, Z. L.; Che, T.; Nichols, D. E.et al. Crystal Structure of an LSD-Bound Human Serotonin Receptor. *Cell* **2017,** *168* (3), 377.
(50) Jo, S.; Kim, T.; Iyer, V. G.; Im, W. CHARMM-GUI: a web-based graphical user interface for CHARMM. *J. Comput. Chem.* **2008,** *29* (11), 1859.
(51) Jo, S.; Lim, J. B.; Klauda, J. B.; Im, W. CHARMM-GUI Membrane Builder for Mixed Bilayers and Its Application to Yeast Membranes. *Biophys. J.* **2009,** *97* (1), 50.
(52) Wu, E. L.; Cheng, X.; Jo, S.; Rui, H.; Song, K. C.; Dávila-Contreras, E. M.; Qi, Y.; Lee, J.; Monje-Galvan, V.; Venable, R. M. CHARMM-GUI Membrane Builder toward realistic biological membrane simulations. *J. Comput. Chem.* **2014,** *35* (27), 1997.
(53) Wacker, D.; Wang, C.; Katritch, V.; Han, G. W.; Huang, X.-P.; Vardy, E.; McCorvy, J. D.; Jiang, Y.; Chu, M.; Siu, F. Y.et al. Structural Features for Functional Selectivity at Serotonin Receptors. *Science* **2013,** *340* (6132), 615.
(54) Li, H.; Robertson, A. D.; Jensen, J. H. Very fast empirical prediction and rationalization of protein pKa values. *Proteins* **2005,** *61* (4), 704.
(55) Fiser, A.; Sali, A. ModLoop: automated modeling of loops in protein structures. *Bioinformatics* **2003,** *19* (18), 2500.
(56) Humphrey, W.; Dalke, A.; Schulten, K. VMD: Visual molecular dynamics. *J. Mol. Graph* **1996,** *14* (1), 33.
(57) Klauda, J. B.; Venable, R. M.; Freites, J. A.; O'Connor, J. W.; Tobias, D. J.; Mondragon-Ramirez, C.; Vorobyov, I.; MacKerell Jr, A. D.; Pastor, R. W. Update of the CHARMM all-atom additive force field for lipids: validation on six lipid types. *J. Phys. Chem.B* **2010,** *114* (23), 7830.
(58) Vanommeslaeghe, K.; MacKerell, A. D. Automation of the CHARMM General Force Field (CGenFF) I: Bond Perception and Atom Typing. *J. Chem. Inf. Model.* **2012,** *52* (12), 3144.
(59) Vanommeslaeghe, K.; Raman, E. P.; MacKerell, A. D. Automation of the CHARMM General Force Field (CGenFF) II: Assignment of Bonded Parameters and Partial Atomic Charges. *J. Chem. Inf. Model.* **2012,** *52* (12), 3155.
(60) Noskov, S. Y.; Berneche, S.; Roux, B. Control of ion selectivity in potassium channels by electrostatic and dynamic properties of carbonyl ligands. *Nature* **2004,** *431* (7010), 830.
(61) Jorgensen, W. L.; Chandrasekhar, J.; Madura, J. D.; Impey, R. W.; Klein, M. L. Comparison of simple potential functions for simulating liquid water. *J. Chem. Phys* **1983,** *79* (2), 926.
(62) Phillips, J. C.; Braun, R.; Wang, W.; Gumbart, J.; Tajkhorshid, E.; Villa, E.; Chipot, C.; Skeel, R. D.; Kale, L.; Schulten, K. Scalable molecular dynamics with NAMD. *J. Comput. Chem.* **2005,** *26* (16), 1781.
(63) Darden, T.; York, D.; Pedersen, L. Particle mesh Ewald: An N·log(N) method for Ewald sums in large systems. *J. Chem. Phys* **1993,** *98* (12), 10089.
(64) Verlet, L. Computer" experiments" on classical fluids. I. Thermodynamical properties of Lennard-Jones molecules. *Phy. Rev.* **1967,** *159* (1), 98.
(65) Miyamoto, S.; Kollman, P. A. SETTLE: an analytical version of the SHAKE and RATTLE algorithm for rigid water models. *J. Comput. Chem.* **1992,** *13* (8), 952.
(66) Feller, S. E.; Zhang, Y.; Pastor, R. W.; Brooks, B. R. Constant pressure molecular dynamics simulation: the Langevin piston method. *J. Chem. Phys* **1995,** *103* (11), 4613.
(67) Martyna, G. J.; Tobias, D. J.; Klein, M. L. Constant pressure molecular dynamics algorithms. *J. Chem. Phys* **1994,** *101* (5), 4177.
(68) Ishchenko, A.; Wacker, D.; Kapoor, M.; Zhang, A.; Han, G. W.; Basu, S.; Patel, N.; Messerschmidt, M.; Weierstall, U.; Liu, W.et al. Structural insights into the extracellular recognition of the human serotonin 2B receptor by an antibody. *P. Natl. Acad. Sci. USA* **2017,** *114* (31), 8223.
(69) Liu, W.; Wacker, D.; Gati, C.; Han, G. W.; James, D.; Wang, D. J.; Nelson, G.; Weierstall, U.; Katritch, V.; Barty, A.et al. Serial Femtosecond Crystallography of G Protein-Coupled Receptors. *Science* **2013,** *342* (6165), 1521.
(70) Genheden, S.; Essex, J. W.; Lee, A. G. G protein coupled receptor interactions with cholesterol deep in the membrane. *BBA-Biomembranes* **2017,** *1859* (2), 268.
(71) Wheatley, M.; Wootten, D.; Conner, M. T.; Simms, J.; Kendrick, R.; Logan, R. T.; Poyner, D. R.; Barwell, J. Lifting the lid on GPCRs: the role of extracellular loops. *Brit. J. Pharmacology* **2012,** *165* (6), 1688.

(72) Conn, P. J.; Christopoulos, A.; Lindsley, C. W. Allosteric modulators of GPCRs: a novel approach for the treatment of CNS disorders. *Nat. Rev. Drug Discov.* **2009,** *8* (1), 41.
(73) Palczewski, K.; Kumasaka, T.; Hori, T.; Behnke, C. A.; Motoshima, H.; Fox, B. A.; Le Trong, I.; Teller, D. C.; Okada, T.; Stenkamp, R. E.et al. Crystal structure of rhodopsin: A G protein-coupled receptor. *Science* **2000,** *289* (5480), 739.
(74) Park, J. H.; Scheerer, P.; Hofmann, K. P.; Choe, H. W.; Ernst, O. P. Crystal structure of the ligand-free G-protein-coupled receptor opsin. *Nature* **2008,** *454* (7201), 183.
(75) Hildebrand, P. W.; Scheerer, P.; Park, J. H.; Choe, H. W.; Piechnick, R.; Ernst, O. P.; Hofmann, K. P.; Heck, M. A Ligand Channel through the G Protein Coupled Receptor Opsin. *PLOS One* **2009,** *4* (2), 9.
(76) Piechnick, R.; Ritter, E.; Hildebrand, P. W.; Ernst, O. P.; Scheerer, P.; Hofmann, K. P.; Heck, M. Effect of channel mutations on the uptake and release of the retinal ligand in opsin. *P. Natl. Acad. Sci. USA* **2012,** *109* (14), 5247.
(77) Srivastava, A.; Yano, J.; Hirozane, Y.; Kefala, G.; Gruswitz, F.; Snell, G.; Lane, W.; Ivetac, A.; Aertgeerts, K.; Nguyen, J.et al. High-resolution structure of the human GPR40 receptor bound to allosteric agonist TAK-875. *Nature* **2014,** *513* (7516), 124.
(78) Hanson, M. A.; Roth, C. B.; Jo, E. J.; Griffith, M. T.; Scott, F. L.; Reinhart, G.; Desale, H.; Clemons, B.; Cahalan, S. M.; Schuerer, S. C.et al. Crystal Structure of a Lipid G Protein-Coupled Receptor. *Science* **2012,** *335* (6070), 851.
(79) Stanley, N.; Pardo, L.; De Fabritiis, G. The pathway of ligand entry from the membrane bilayer to a lipid G protein-coupled receptor. *Sci. Rep. UK* **2016,** *6*, 9.
(80) Guixa-Gonzalez, R.; Albasanz, J. L.; Rodriguez-Espigares, I.; Pastor, M.; Sanz, F.; Marti-Solano, M.; Manna, M.; Martinez-Seara, H.; Hildebrand, P. W.; Martin, M.et al. Membrane cholesterol access into a G-protein-coupled receptor. *Nat. Comm.* **2017,** *8*, 12.
(81) McConnell, H. M.; Radhakrishnan, A. Condensed complexes of cholesterol and phospholipids. *BBA-Biomembranes* **2003,** *1610* (2), 159.
(82) Jedlovszky, P.; Mezei, M. Effect of cholesterol on the properties of phospholipid membranes. 1. Structural features. *J. Phys. Chem. B* **2003,** *107* (22), 5311.
(83) de Meyer, F.; Smit, B. Effect of cholesterol on the structure of a phospholipid bilayer. *P. Natl. Acad. Sci. USA* **2009,** *106* (10), 3654.
(84) Rog, T.; Pasenkiewicz-Gierula, M.; Vattulainen, I.; Karttunen, M. Ordering effects of cholesterol and its analogues. *BBA-Biomembranes* **2009,** *1788* (1), 97.
(85) Prasanna, X.; Chattopadhyay, A.; Sengupta, D. Cholesterol Modulates the Dimer Interface of the beta(2)-Adrenergic Receptor via Cholesterol Occupancy Sites. *Biophys. J.* **2014,** *106* (6), 1290.
(86) Prasanna, X.; Sengupta, D.; Chattopadhyay, A. Cholesterol-dependent Conformational Plasticity in GPCR Dimers. *Sci. Rep. UK* **2016,** *6*, 12.
(87) Pluhackova, K.; Gahbauer, S.; Kranz, F.; Wassenaar, T. A.; Bockmann, R. A. Dynamic Cholesterol-Conditioned Dimerization of the G Protein Coupled Chemokine Receptor Type 4. *PLOS Comput. Biol.* **2016,** *12* (11), 25.

6.4 Commentary

6.4.1 Conclusions

Cholesterol exhibits a diverse range of functions in the human body. Most commonly, cholesterol is known as a cause for heart disease; however, cholesterol serves a number of beneficial roles, for example, in the production of essential molecules (e.g. hormones) and as a critical component of the plasma membrane.[1] Cholesterol is especially abundant in the plasma membrane of higher-order eukaryotes, modulating the fluidity and rigidity of membrane lipids, and the behaviour of several classes of membrane protein.[2]

In this chapter, the effect of cholesterol on the structure of phospholipid bilayers (section 6.2) and GPCRs from the 5-HT receptor family (section 6.3), by using unbiased MD simulations. In both cases, the biological isomer of cholesterol (*nat*-cholesterol) is compared with stereoisomers (*ent*-cholesterol and *epi*-cholesterol) to evaluate the effect of subtle changes in cholesterol structure. In terms of bilayer structure, *nat*-cholesterol and *ent*-cholesterol are almost indistinguishable, whereas *epi*-cholesterol evokes differences in the membrane-water interfacial region. When considering the dynamics of membrane proteins, interactions between cholesterol isomers and transmembrane helices 3 and 4 in the extracellular leaflet are shown to bias the conformation of the extracellular loops in the 5-HT_{1B} receptor, in contrast to the 5-HT_{2B} receptor, which exhibits negligible conformational differences throughout the simulation trajectories. The enhanced stability of the 5-HT_{2B} extracellular surface is attributed to persistent interactions between independent loops. Together, these results provide information relevant to the effect of membrane cholesterol on the structure of phospholipid bilayers and membrane proteins, as well as specific insights into the molecular behaviour 5-HT receptors.

Experimental evidence regarding the behaviour of cholesterol and the GPCR systems investigated is currently unavailable. Therefore, experimental efforts are required to characterise the functional response of the 5-HT_{1B} and 5-HT_{2B} receptors to *nat*-cholesterol and its isomers; established experimental procedures are available for this purpose, as demonstrated for the closely related 5-HT_{1A} receptor.[3-9] To substantiate the specific proposals presented in this thesis, concerning the extracellular surface, ligand-binding affinities should be calculated in wild-type and mutant channels (specifically mutations within the extracellular loops), in the presence and absence of cholesterol. From a computational viewpoint, simulations of alternate 5-HT_{1B} and 5-HT_{2B} receptor structures, differing bound ligand identity and conformational state, may provide insight into the potential state-specific effects of cholesterol.[10-12] Furthermore, simulations of other 5-HT receptor structures, when the corresponding high-resolution structure become available, would provide a fuller picture of the molecular behaviour of this receptor family. This would be particularly informative for the 5-HT_{1A} receptor, where functional responses to cholesterol and its isomers have already been established.[3-9] 5-HT receptors are important drug targets for the treatment of psychological disorders. The 5-HT_{1B} receptor, in particular, has been

implicated in the action of antidepressants, obsessive-compulsive disorder, alcohol dependence, and cocaine dependence.[13] The 5-HT_{1B} partial agonist vortioxetine, for example, has been associated with a significant reduction in depression symptoms relative to patients given a placebo, albeit with an increased number of adverse reactions compared to those same patients.[14] Considering this, development of 5-HT_{1B} agonists, with increased efficacy and specificity, may provide significant advancements in anti-depressive treatments.[13] Structure-based computational methods are important in this respect, and have recently been employed for vortioxetine in the human serotonin transporter.[15] 5-HT_{1B} receptor conformations revealed by x-ray crystallography,[16] cryo-electron microscopy[10] and molecular dynamics simulations (such as those disclosed in this section), will likely inform this process in the future.

6.4.2 References

(1) Tabas, I. Cholesterol in health and disease. *J. Clin. Invest.* **2002**, *110* (5), 583.
(2) Ikonen, E. Cellular cholesterol trafficking and compartmentalization. *Nat. Rev. Mol. Cell. Bio.* **2008**, *9* (2), 125.
(3) Saxena, R.; Chattopadhyay, A. Membrane cholesterol stabilizes the human serotonin(1A) receptor. *BBA-Biomembranes* **2012**, *1818* (12), 2936.
(4) Shrivastava, S.; Pucadyil, T. J.; Paila, Y. D.; Ganguly, S.; Chattopadhyay, A. Chronic cholesterol depletion using statin impairs the function and dynamics of human serotonin(1A) receptors. *Biochemistry* **2010**, *49* (26), 5426.
(5) Paila, Y. D.; Murty, M. R.; Vairamani, M.; Chattopadhyay, A. Signaling by the human serotonin(1A) receptor is impaired in cellular model of Smith-Lemli-Opitz Syndrome. *Biochim. Biophys. Acta* **2008**, *1778* (6), 1508.
(6) Jafurulla, M.; Rao, B. D.; Sreedevi, S.; Ruysschaert, J. M.; Covey, D. F.; Chattopadhyay, A. Stereospecific requirement of cholesterol in the function of the serotonin1A receptor. *Biochim. Biophys. Acta* **2014**, *1838* (1 Pt B), 158.
(7) Prasad, R.; Paila, Y. D.; Chattopadhyay, A. Membrane cholesterol depletion enhances ligand binding function of human serotonin(1A) receptors in neuronal cells. *Biochem. Bioph. Res. Co.* **2009**, *390* (1), 93.
(8) Singh, P.; Saxena, R.; Paila, Y. D.; Jafurulla, M.; Chattopadhyay, A. Differential effects of cholesterol and desmosterol on the ligand binding function of the hippocampal serotonin(1A) receptor: Implications in desmosterolosis. *BBA-Biomembranes* **2009**, *1788* (10), 2169.
(9) Singh, P.; Jafurulla, M.; Paila, Y. D.; Chattopadhyay, A. Desmosterol replaces cholesterol for ligand binding function of the serotonin(1A) receptor in solubilized hippocampal membranes: Support for nonannular binding sites for cholesterol? *BBA-Biomembranes* **2011**, *1808* (10), 2428
(10) Garcia-Nafria, J.; Nehme, R.; Edwards, P. C.; Tate, C. G. Cryo-EM structure of the serotonin 5-HT1B receptor coupled to heterotrimeric G(o). *Nature* **2018**, *558* (7711), 620.
(11) Wacker, D.; Wang, S.; McCorvy, J. D.; Betz, R. M.; Venkatakrishnan, A. J.; Levit, A.; Lansu, K.; Schools, Z. L.; Che, T.; Nichols, D. E.et al. Crystal Structure of an LSD-Bound Human Serotonin Receptor. *Cell* **2017**, *168* (3), 377
(12) McCorvy, J. D.; Wacker, D.; Wang, S.; Agegnehu, B.; Liu, J.; Lansu, K.; Tribo, A. R.; Olsen, R. H. J.; Che, T.; Jin, J.et al. Structural determinants of 5-HT2B receptor activation and biased agonism. *Nat. Struct. Mol. Biol.* **2018**, *25* (9), 787.
(13) Tiger, M.; Varnas, K.; Okubo, Y.; Lundberg, J. The 5-HT1B receptor - a potential target for antidepressant treatment. *Psychopharmacology* **2018**, *235* (5), 1317.
(14) Berhan, A.; Barker, A. Vortioxetine in the treatment of adult patients with major depressive disorder: a meta-analysis of randomized double-blind controlled trials. *BMC Psychiatry* **2014**, *14*, 7
(15) Andersen, J.; Ladefoged, L. K.; Wang, D. Y.; Kristensen, T. N. B.; Bang-Andersen, B.; Kristensen, A. S.; Schiott, B.; Stromgaard, K. Binding of the Multimodal Antidepressant Drug Vortioxetine to the Human Serotonin Transporter. *ACS Chem. Neurosci.* **2015,** 6 (11), 1892.
(16) Wacker, D.; Wang, C.; Katritch, V.; Han, G. W.; Huang, X. P.; Vardy, E.; McCorvy, J. D.; Jiang, Y.; Chu, M. H.; Siu, F. Y.et al. Structural Features for Functional Selectivity at Serotonin Receptors. *Science* **2013**, *340* (6132), 615.

7 Conclusions and Future Outlook

7.1 Conclusions

At the start of 2019, over 870 three-dimensional structures unique membrane proteins had been resolved in high-resolution. Appropriately, the field of membrane protein simulations has expanded considerably. Owing to astronomical advances in computing hardware, the maximum timescales of membrane protein simulations that can be achieved with state-of-the-art technologies has surged from picoseconds to milliseconds, sanctioning the investigation of a wide-range of biological phenomenon.[1]

In this thesis, a range of classical MD simulations and umbrella sampling simulations have been performed to investigate the behaviour of several types of membrane proteins. A significant proportion of this research is devoted to analyses of K^+-channels, specifically TWIK-1 (section 1) and KcsA (section 2). KcsA has been used as a prototype for the molecular functioning of the K^+-channel, following the publication of various high-resolution structures in the period spanning 1998-2018.[2-4] In contrast, little is known about the structural attributes of the TWIK-1 channel, and the related K_{2P} channel family, which was first resolved at high-resolution in 2012.[5]

Firstly, the size, dynamics and residue composition of fenestrations in the TWIK-1 channel has been analysed and compared to $K_V1.2$ and $K_{IR}3.2$ channels, in order to assess the viability of such openings as drug access pathways in the K_{2P}, K_V and K_{IR} channel families, respectively. In agreement with structural information, only TWIK-1 exhibited 'open' fenestrations, affirming the potential role of fenestrations in the K_{2P} family. Detailed analysis of the TWIK-1 selectivity filter has also been undertaken, revealing radical differences in the conformation of the selectivity filter, originating from the presence of non-conserved residues in the selectivity filter sequence, and providing a rationale for the atypical conduction properties reported experimentally. For KcsA, the energetics of ion permeation has been calculated, in order to assess the effect of a number of properties: 1) mutation of a single site in the selectivity filter, 2) the presence of bound membrane lipids, and 3) the protonation state of E71, a residue directly behind the selectivity filter. Substitution of a specific threonine residue in the selectivity filter altered the energetics of ion entrance to the selectivity filter and ion occupancy of specific K^+ binding sites. Furthermore, a molecular mechanism coupling the behaviour of the selectivity filter and membrane lipids has been postulated, considering computational, electrophysiological and NMR results. The data presented provides novel insights into the conduction and inactivation process of KcsA, contributing the wealth of literature on the topic. In general, evidence has been provided for the critical role of specific residues in, and in close proximity, to the conserved selectivity filter sequence in K^+ channels.

From this point forward, our attentions were aimed at applying established simulation protocols to identify functional binding sites in novel structures of membrane proteins, to directly explain experimental phenomenon. In the TRPV1 ion channel, the prototypical TRP channel, an

extracellular binding site for oxytocin, neighbouring the selectivity filter, was indicated computationally, and subsequently confirmed by experimental mutagenesis. Moreover, an intracellular binding site for PKR has been proposed in TRPV1, awaiting experimental validation. Together, these results highlight the feasibility of combined docking and simulation studies, to predict complex protein-protein assemblies and aid in the interpretation of experimental results.

In the final chapter of this thesis, an atomic-level description of cholesterol, and related isomers, both in phospholipid bilayers and in complex with 5-HT_{1B} and 5-HT_{2B} receptors is provided. Computational studies of GPCR-cholesterol interactions are a burgeoning area of research and this study serves as the first to scrutinize cholesterol interactions in the 5-HT receptor family. A functional binding site in the 5-HT_{1B} is proposed, which is observed to alter the conformation of the extracellular surface of the receptor. The outcome of this study provides meaningful insights into the cholesterol-GPCR interaction, as well as the molecular functioning of the 5-HT_{1B} receptor.

Overall, several lines of enquiry have proven fruitful throughout this research. Firstly, description of the molecular behaviour of the selectivity filter and fenestration regions in K^+ channels; secondly, characterization of lipid-membrane protein complexes, and the associated effect on protein structure and dynamics; finally, prediction of membrane protein-protein complex interfaces. Studies of this nature contribute knowledge which cannot be easily obtained by experimental means, enrich our understanding of how membrane proteins function as highly capable transport apparatus and provide insights into how they are modulated by their environment and/or external stimuli.

7.2 Future Outlook

The results presented can be used to instruct future structure-based drug design efforts:

- Information regarding the size and characteristics of fenestrations in K_{2P} channels is useful to identify compounds that exhibit high-affinity binding to specific K_{2P} channels and achieve subtype selectivity.
- The K^+ selectivity filter is critical for enabling conduction in a highly selective manner, as well as blocking conduction (inactivation). Understanding of how it is modulated will allow the selectivity filter itself, and surrounding regions (i.e. lipid non-annular sites), to be targeted by drug compounds. This strategy is relevant in the context of inactivating channels, such as K_V channels.[6-9]
- Identification of a shared extracellular binding site in TRPV1 for oxytocin and DkTx[10] advocates that development of exogeneous agonists should be specifically targeted in this region. Interest in developing such agonists, which accelerate desensitisation of the channel, as antinociceptive treatments has surged recently,[11-13] as adverse side-effects associated with TRPV1 antagonists has become known.[14]

- Structure-based design strategies for GPCRs are heavily reliant on knowing the diverse-range of conformations involved in the activation cycle of a single receptor. The novel 5-HT_{1B} receptor conformations that have been identified, in response to cholesterol, supplement those revealed by x-ray crystallography[15] and cryo-electron microscopy[16] will likely contribute to this field in the future.

To close, the current state of the MD simulations discipline is considered. The recent growth of computing power has typically been exploited to increase the length of molecular dynamics simulations. Recently, several research groups have examined the reproducibility and convergence of individual molecular dynamics simulations.[17-19] It has been documented that the dynamic and structural properties of replicas (independent simulations using identical atomic coordinates and forcefield parameters) may diverge because of slight variations in the initial velocities of each simulation system, as well as differences related to the hardware and software used to produce the trajectories (e.g. floating-point precision, hardware architecture, compilation options, number of processors).[19] On this basis, it is possible that the outcome of a single simulation may not be representative of the underlying energy landscape. By comparing the standard analysis of a single long simulation trajectory versus multiple shorter replicas, Knapp et al advocate that at least 5-10 short replicas should be performed to increase the reliability of the data, and corresponding conclusions.[19] Therefore, in the future, researchers should carefully consider the compromise between simulation timescales and number of replicas, in order to maximise the probability of observing of important motions whilst ensuring reproducibility.

7.3 References

(1) Shaw, D. E.; Deneroff, M. M.; Dror, R. O.; Kuskin, J. S.; Larson, R. H.; Salmon, J. K.; Young, C.; Batson, B.; Bowers, K. J.; Chao, J. C.et al. Anton, a special-purpose machine for molecular dynamics simulation. *Commun. ACM* **2008,** *51* (7), 91.

(2) Doyle, D. A.; Cabral, J. M.; Pfuetzner, R. A.; Kuo, A. L.; Gulbis, J. M.; Cohen, S. L.; Chait, B. T.; MacKinnon, R. The structure of the potassium channel: Molecular basis of K+ conduction and selectivity. *Science* **1998,** *280* (5360), 69.

(3) Cuello, L. G.; Jogini, V.; Cortes, D. M.; Perozo, E. Structural mechanism of C-type inactivation in K+ channels. *Nature* **2010,** *466* (7303), 203.

(4) Cuello, L. G.; Cortes, D. M.; Perozo, E. The gating cycle of a K+ channel at atomic resolution. *Elife* **2017,** *6*, 17.

(5) Miller, A. N.; Long, S. B. Crystal Structure of the Human Two-Pore Domain Potassium Channel K2P1. *Science* **2012,** *335* (6067), 432.

(6) Bahring, R.; Barghaan, J.; Westermeier, R.; Wollberg, J. Voltage sensor inactivation in potassium channels. *Front. Pharmacol.* **2012,** *3*, 8.

(7) Hoshi, T.; Armstrong, C. M. C-type inactivation of voltage-gated K+ channels: Pore constriction or dilation? *J. Gen. Physiol.* **2013,** *141* (2), 151.

(8) Hoshi, T.; Zagotta, W. N.; Aldrich, R. W. 2 Types of inactivation in Shaker K+ Channels - effects of alterations in the carboxy-terminal region. *Neuron* **1991,** *7* (4), 547.

(9) Choi, K. L.; Aldrich, R. W.; Yellen, G. Tetraethylammonium blockade distinguishes two inactivation mechanisms in voltage-activated K^+ channels. *P. Natl. Acad. Sci. USA* **1991,** *88* (12), 5092.

(10) Cao, E. H.; Liao, M. F.; Cheng, Y. F.; Julius, D. TRPV1 structures in distinct conformations reveal activation mechanisms. *Nature* **2013,** *504* (7478), 113.

(11) Dussor, G.; Yan, J.; Xie, J. Y.; Ossipov, M. H.; Dodick, D. W.; Porreca, F. Targeting TRP Channels For Novel Migraine Therapeutics. *ACS Chem. Neuro.* **2014,** *5* (11), 1085.

(12) Diamond, S.; Freitag, F.; Phillips, S. B.; Bernstein, J. E.; Saper, J. R. Intranasal civamide for the acute treatment of migraine headache. *Cephalalgia* **2000,** *20* (6), 597.
(13) Fusco, B. M.; Barzoi, G.; Agro, F. Repeated intranasal capsaicin applications to treat chronic migraine. *Brit. J. Anaesth.* **2003,** *90* (6), 812.
(14) Carnevale, V.; Rohacs, T. TRPV1: A Target for Rational Drug Design. *Pharmaceuticals* **2016,** *9* (3), 20.
(15) Wacker, D.; Wang, C.; Katritch, V.; Han, G. W.; Huang, X. P.; Vardy, E.; McCorvy, J. D.; Jiang, Y.; Chu, M. H.; Siu, F. Y.et al. Structural Features for Functional Selectivity at Serotonin Receptors. *Science* **2013**, *340* (6132), 615.
(16) Garcia-Nafria, J.; Nehme, R.; Edwards, P. C.; Tate, C. G. Cryo-EM structure of the serotonin 5-HT1B receptor coupled to heterotrimeric G(o). *Nature* **2018**, *558* (7711), 620.
(17) Musiani, F.; Rossetti, G.; Capece, L.; Gerger, T. M.; Micheletti, C.; Varani, G.; Carloni, P. Molecular Dynamics Simulations Identify Time Scale of Conformational Changes Responsible for Conformational Selection in Molecular Recognition of HIV-1 Transactivation Responsive RNA. *J. Am. Chem. Soc.* **2014,** *136* (44), 15631.
(18) Galindo-Murillo, R.; Roe, D. R.; Cheatham, T. E. Convergence and reproducibility in molecular dynamics simulations of the DNA duplex d(GCACGAACGAACGAACGC). *BBA-Gen. Subjects* **2015,** *1850* (5), 1041.
(19) Knapp, B.; Ospina, L.; Deane, C. M. Avoiding False Positive Conclusions in Molecular Simulation: The Importance of Replicas. *J. Chem. Theory Comput.* **2018,** *14* (12), 6127.

Part III. Appendix

Appendix A: Supporting Information

A1 Lateral Fenestrations in K^+ Channels Explored using Molecular Dynamics Simulations, *Mol. Pharmaceutics*, 2016

SUPPORTING MATERIAL

Lateral fenestrations in K^+-channels explored using MD simulations

Christian Jorgensen,[a] Leonardo Darré,[a] Victoria Oakes,[a] Ruben Torella,[b] David Pryde[b] and Carmen Domene[a,c]*

[a]Department of Chemistry, King's College London, Britannia House, 7 Trinity Street, London SE1 1DB, UK
[b]Pfizer Neuroscience and Pain Research Unit, Worldwide Medicinal Chemistry, Portway Building, Granta Park, Great Abington, Cambridge CB21 6GS, U.K.
[c]Chemistry Research Laboratory, Mansfield Road, University of Oxford, Oxford OX1 3TA, UK

Figure S1. Protein stability. Backbone RMSD with respect to the crystal structure of each K^+ channel studied as a function of simulation time. (a) Kv.1.2, (b) Kir3.2/O, Kir3.2/C, (c) K2P1. Color code: (a) Kv1.2: pore (S5-6) and S4-S5 linker (Red), voltage domain and pore (S1-6) (Black), voltage domain (S1-4) (Blue); (b) Kir3.2: Kir3.2/open (Red), Kir3.2/closed (Black); (c) K2P1.1 backbone.

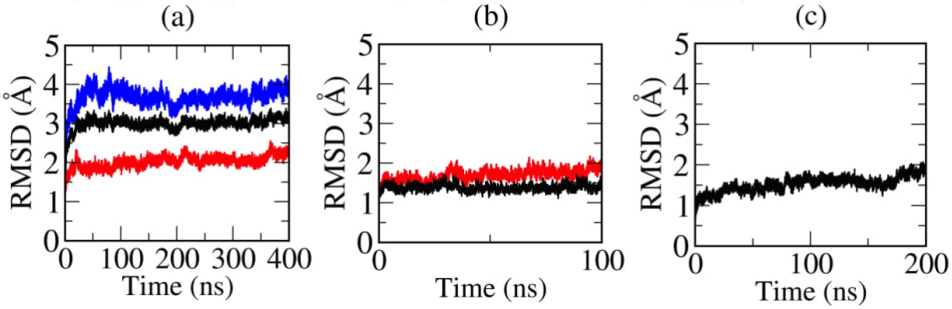

Figure S2. Bottleneck Radius (BR) distributions (normalised probabilities). Radii of each lateral fenestration bottleneck sampled during the MD simulations for (a) Kv1.2, (b) Kir3.2/O and (c) K2P1. Analysis performed on different timescales: 200 ns (Kv1.2 and TWIK-1), 100 ns (Kir3.2).

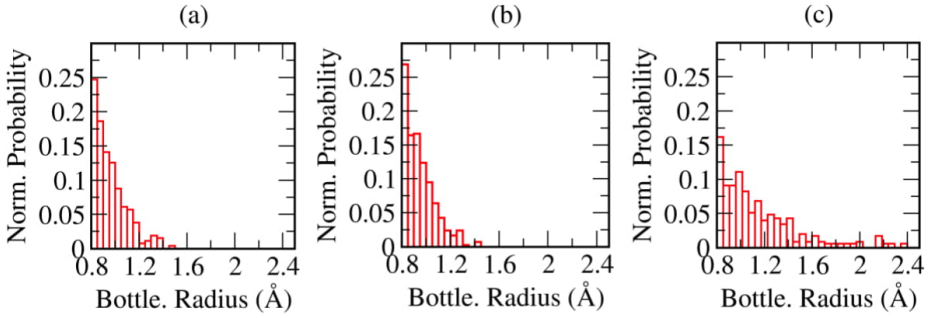

Figure S3. Electrostatic Potential (EP) iso-surface of lateral fenestrations using APBS v1.4. (a) Kv1.2 lining residues L328, I332, A397, V399, L400, T401, I402, A403, V406, P407, and V410, (b) Kir3.2 lining residues V188, N184, V183, G180, L179, T154, T153, E152, W106, T105, V104, Y102 and V101, and (c) TWIK-1 intra-chain fenestration residues T117, V139, I142, L146, S224, T225, M260, L261 and L264. EP gradient color scale red (-4) to blue (+4).

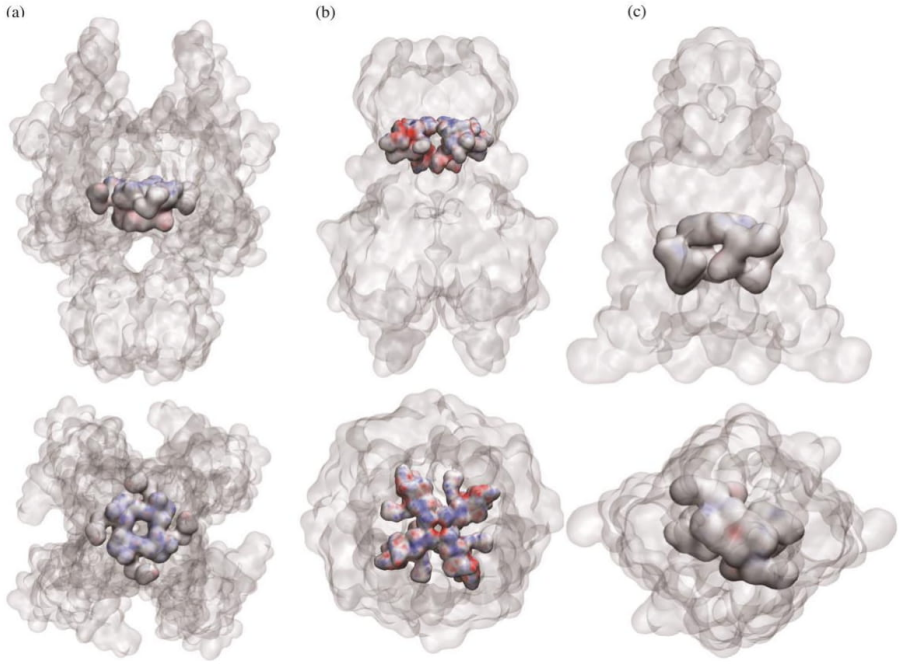

Figure S4. Electrostatic Potential (EP) iso-surface. (a) Kv1.2, (b) Kir3.2, (c) TWIK-1 with lateral fenestration positions indicated with arrows. EP gradient color scale red (-4) to blue (+4).

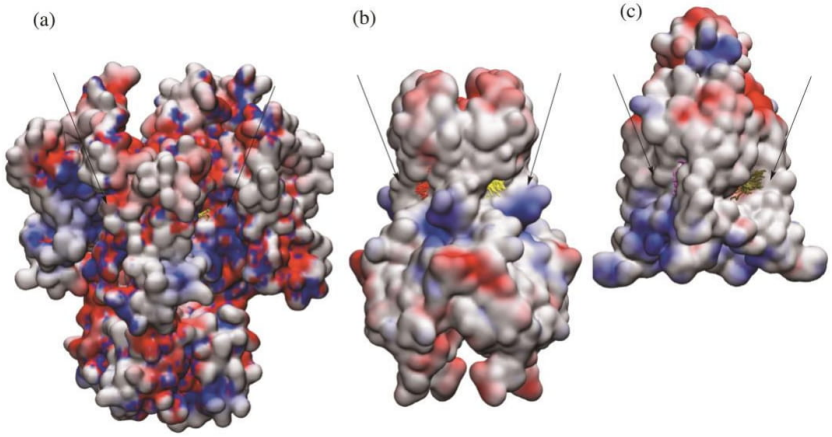

Figure S5. Lipid-protein interaction iso-surfaces. Lipids shown within 4 Å of fenestration lining residues for Kv1.2 (a) iso-0.1, (b) iso-0.2, (c) iso-0.4 surfaces; Kir3.2/O (d) iso-0.1, (e) iso-0.2 and (f) iso-0.4 surface; TWIK-1 fenestration 3,4 (upper), 1,2 (lower), (g) iso-0.1, (h) iso-0.2, (i) iso-0.4 surfaces. POPC lipids are shown in green. PIP-2 lipids in Kir3.2 are shown in blue.

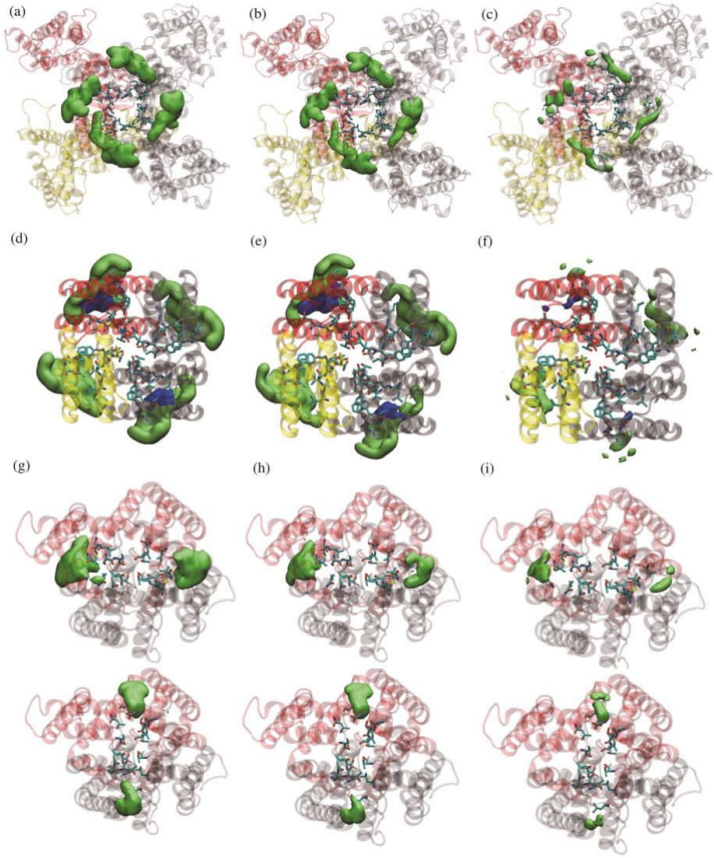

Table S1. Cavity analysis of the crystal structures TWIK-1 (PDB id 3UKM) and TREK-2 (Closed, C, state; PDB id 4XDJ) channels. Inter-chain lateral fenestrations between two nearby chains (A and B) analyzed using a clustering threshold of 8 Å. Length and bottleneck radius are specified in Å.

Channel	Fenestration ID	Bottleneck Radius (Å)	Length (Å)
TWIK-1	3	2.2	23
	4	0.9	22
TREK2/C	1	2.6	26
	2	2.6	27

Table S2. Lining residues (LR) consensus (Consens.) and bottleneck residues (BR) for each lateral fenestration (>90% of each fenestration). Open and closed channel conformations are indicated by O and C, respectively.

Channel	Fen.	Chain	Lining residues (LR)
Kir3.2/O	1	B	V^{101} Y^{102} V^{104} T^{105} W^{106} E^{152} T^{153} T^{154} L^{179} G^{180} I^{182} V^{183} N^{184} V^{188}
	2	D	V^{101} Y^{102} V^{104} T^{105} W^{106} F^{109} E^{152} T^{153} T^{154} L^{179} G^{180} S^{181} I^{182} V^{183} N^{184} V^{188}
	3	A	V^{101} Y^{102} V^{104} T^{105} W^{106} F^{109} E^{152} T^{153} T^{154} L^{179} G^{180} S^{181} V^{183} N^{184} V^{188}
	4	C	V^{101} Y^{102} V^{104} T^{105} W^{106} F^{108} F^{109} E^{152} T^{153} T^{154} L^{179} G^{180} S^{181} V^{183} N^{184} V^{188}
	Consens. (LR)		**V^{101} Y^{102} V^{104} T^{105} W^{106} E^{152} T^{153} T^{154} L^{179} G^{180} V^{183} N^{184} V^{188}**
	Consens. (BR)		**T^{105} G^{180} V^{183}**
Kir3.2/C	1	A	V^{101} $Y102$ T^{105} W^{106} E^{152} T^{153} T^{154} L^{179} G^{180} S^{181} V^{183} N^{184} V^{188}
	2	B	V^{101} Y^{102} V^{104} T^{105} W^{106} F^{108} F^{109} E^{152} T^{153} T^{154} L^{179} G^{180} S^{181} I^{182} V^{183} N^{184} V^{188}
	3	C	V^{101} Y^{102} V^{104} T^{105} W^{106} E^{152} T^{153} T^{154} L^{179} G^{180} S^{181} I^{182} V^{183} N^{184} V^{188}
	4	D	V^{101} V^{104} T^{105} F^{108} F^{109} E^{152} T^{153} T^{154} L^{179} G^{180} S^{181} V^{183} $N^{18S4}V^{188}$
	Consens. (LR)		**V^{101} T^{105} E^{152} T^{153} T^{154} L^{179} G^{180} S^{181} V^{183} N^{184} V^{188}**
	Consens. (BR)		**T^{105} G^{180} V^{183}**
Kv1.2	1	A/D	L^{328} I^{332} I^{396} A^{397} V^{399} L^{400} T^{401} I^{402} A^{403} V^{406} P^{407} I^{409} V^{410}
	2	B/C	L^{328} I^{332} L^{393} I^{396} A^{397} V^{399} L^{400} T^{401} I^{402} A^{403} V^{406} P^{407} V^{410}
	3	A/C	L^{328} I^{332} I^{396} A^{397} V^{399} L^{400} T^{401} I^{402} A^{403} V^{406} P^{407} I^{409} V^{410}
	4	B/D	L^{328} I^{332} A^{397} V^{399} L^{400} T^{401} I^{402} A^{403} V^{406} P^{407} I^{409} V^{410}
	Consens. (LR)		**L^{328} I^{332} A^{397} V^{399} L^{400} T^{401} I^{402} A^{403} V^{406} P^{407} V^{410}**
	Consens. (BR)		**L^{331} I^{396} I^{402} V^{406}**
TWIK-1	3	A/B	T^{117} V^{139} I^{142} L^{146} S^{224} T^{225} L^{257} M^{260} $L^{261}L^{264}$
	4	A/B	T^{117} V^{139} I^{142} L^{146} S^{224} T^{225} M^{260} $L^{261}L^{264}$
	Consens. (LR)		**T^{117} V^{139} I^{142} L^{146} S^{224} T^{225} M^{260} $L^{261}L^{264}$**
	Consens. (BR)		**V^{139} I^{142} P^{143} $F^{220}S^{224}$ M^{260} L^{264}**
	1	A	S^{116} T^{117} T^{145} L^{146} L^{149} T^{225} L^{254} L^{257}
	2	B	V^{27} S^{116} T^{117} T^{145} L^{146} L^{149} T^{225} L^{254} L^{257}
	Consens. (LR)		**S^{116} T^{117} T^{145} L^{146} L^{149} T^{225} L^{254} L^{257}**
	Consens. (BR)		**S^{116} T^{117} T^{145} L^{149} $L^{254}L^{257}$**
TREK2/C	1	A	T^{172} A^{193} I^{194} F^{195} $G^{196}I^{197}$ P^{198} G^{201} F^{202}
		B	V^{238} T^{241} I^{242} I^{245} C^{249} V^{253} V^{276} L^{279} T^{280} T^{281} L^{313} F^{316} A^{317} $A^{318}V^{319}$ L^{320} I^{323}
	2	A	T^{241} I^{242} I^{245} C^{249} V^{276} L^{279} T^{280} T^{281} L^{313} F^{316} A^{317} V^{319} L^{320} I^{323}
		B	T^{172} A^{193} I^{194} F^{195} $G^{196}I^{197}P^{198}$ G^{201}
	Consens. (LR)		**T^{172} A^{193} I^{194} F^{195} $G^{196}I^{197}P^{198}$ G^{201} T^{241} I^{242} I^{245} C^{249} V^{276} L^{279} T^{280} T^{281} L^{313} F^{316} A^{317} V^{319} $L^{320}I^{323}$**
	Consens. (BR)		**T^{172} $I^{197}P^{198}$ L^{279} T^{280} T^{281} L^{313} F^{316} A^{317} L^{320}**

Table S3. Cavity analysis as a function of time for Kv1.2. Analysis performed over 100, 200, and 400-ns trajectories. Data is provided for fenestration clusters 1 to 4 (clustering threshold of 8 Å). The percentage (%) of PDB snapshots analyzed with a bottleneck radius (BR) > 0.8 Å, id indicated, as well as the fenestration type (lateral intra or inter-chain). The average (Av.) and maximum (max.) bottleneck radius in Å, and the length of the fenestration are reported. Protein monomers are referred as A, B, C, and D.

Channel	Fenestration ID	% snapshots BR > 0.8 Å	Fenestration Type	Av. BR (Å)	Max BR (Å)	Length (Å)
Kv1.2 (100 ns)	1	48	Lateral-A/D	1.0 ± 0.1	1.3	23 ± 4
	2	72	Lateral-B/C	0.9 ± 0.1	1.5	25 ± 5
	3	76	Lateral-A/C	1.0 ± 0.1	1.2	26 ± 3
	4	56	Lateral-B/D	0.9 ± 0.1	1.1	23 ± 5
Kv1.2 (200 ns)	1	82	Lateral-A/D	1.0 ± 0.1	1.3	21 ± 4
	2	70	Lateral-B/C	1.0 ± 0.1	1.5	23 ± 4
	3	74	Lateral-A/C	1.0 ± 0.1	1.5	24 ± 3
	4	49	Lateral-B/D	0.9 ± 0.1	1.2	23 ± 4
Kv1.2 (400 ns)	1	73	Lateral-D	1.0 ± 0.1	1.4	22 ± 4
	2	63	Lateral-C	1.0 ± 0.1	1.5	25 ± 4
	3	65	Lateral-B	0.9 ± 0.1	1.5	25 ± 5
	4	56	Lateral-A	1.0 ± 0.3	3.5	25 ± 5

Table S4. Cavity analysis for the TWIK-1 channel as a function of time. Analysis is done over 100 and 200-ns trajectories. Data is provided for fenestration clusters 1 to 4 (clustering threshold of 8 Å). The percentage (%) of PDB snapshots analyzed with a bottleneck radius (BR) > 0.8 Å, id indicated, as well as the fenestration type (lateral interchain or intrasubunit). The average (Av.) and maximum (max.) bottleneck radius in Å, and the length of the fenestration are reported. Protein monomers are referred as A and B.

Channel	Fenestration ID	% snapshots BR > 0.8 Å	Fenestration Type	Av. BR (Å)	Max BR (Å)	Length (Å)
TWIK-1 (100 ns)	1	98	Lateral-A	1.1 ± 0.2	1.5	22 ± 2
	3	92	Lateral-A/B	1.6 ± 0.5	2.4	24 ± 2
	4	80	Lateral-A/B	1.1 ± 0.3	1.9	24 ± 2
	2	82	Lateral-B	0.9 ± 0.1	1.3	25 ± 2
TWIK-1 (200 ns)	1	97	Lateral-A	1.2 ± 0.2	1.6	22 ± 2
	3	90	Lateral-A/B	1.4 ± 0.5	2.5	24 ± 2
	4	80	Lateral-A/B	1.0 ± 0.2	1.9	26 ± 4
	2	83	Lateral-B	0.9 ± 0.1	1.3	26 ± 2

A.2 Exploring the Dynamics of the TWIK-1 Channel

SUPPLEMENTARY INFORMATION

Exploring the dynamics of the TWIK-1 channel

Victoria Oakes,[1] Simone Furini,[2] David Pryde,[3] Carmen Domene[1,4]

[1]Department of Chemistry, King's College London, Britannia House, 7 Trinity Street, London, SE1 1DB, UK.
[2]Department of Medical Biotechnologies, University of Siena, viale Mario Bracci 16, I-53100, Siena, Italy
[3]Worldwide Medicinal Chemistry, Pfizer Pfizer Neuroscience and Pain Research Unit, Portway Building, Granta Park, Great Abington, Cambridge CB21 6GS, UK
[4]Chemistry Research Laboratory, Mansfield Road, University of Oxford, Oxford, OX1 3TA, UK.

[1]Corresponding author: carmen.domene@kcl.ac.uk

Tel: +44 - (0) 2078483868

Figure S1. Root mean square deviation (RMSD) of the backbone of the transmembrane helices of TWIK-1 in simulations: (A) HSE, (B) HSEP, (C) HSD, (D) HSDP, (E) HSP and (F) HSPP.

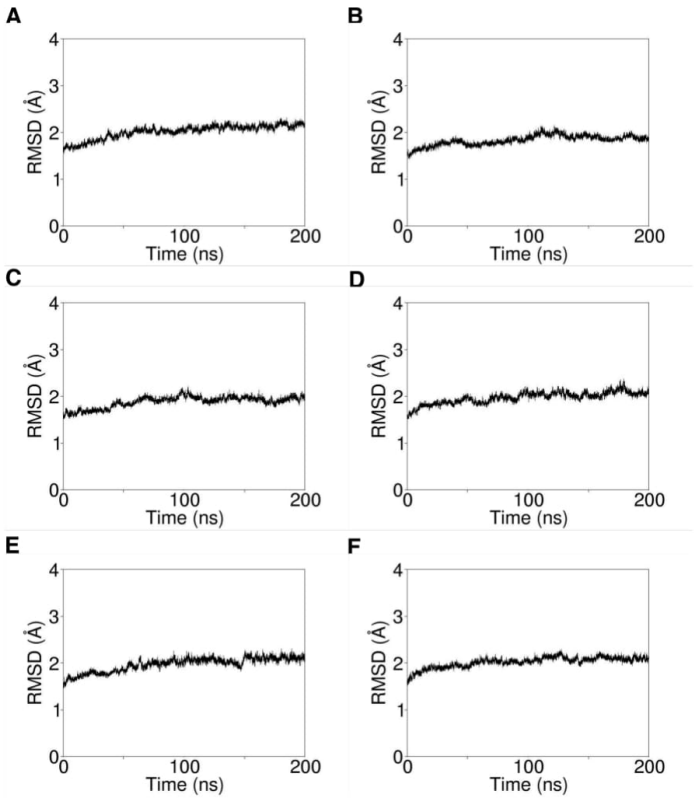

S2. Root mean square deviation (RMSD) of the extracellular cap
onding to residues S80 to D103 in simulations: (A) HSE, (B) HSEP, (C) HSD,
)P, (E) HSP and (F) HSPP.

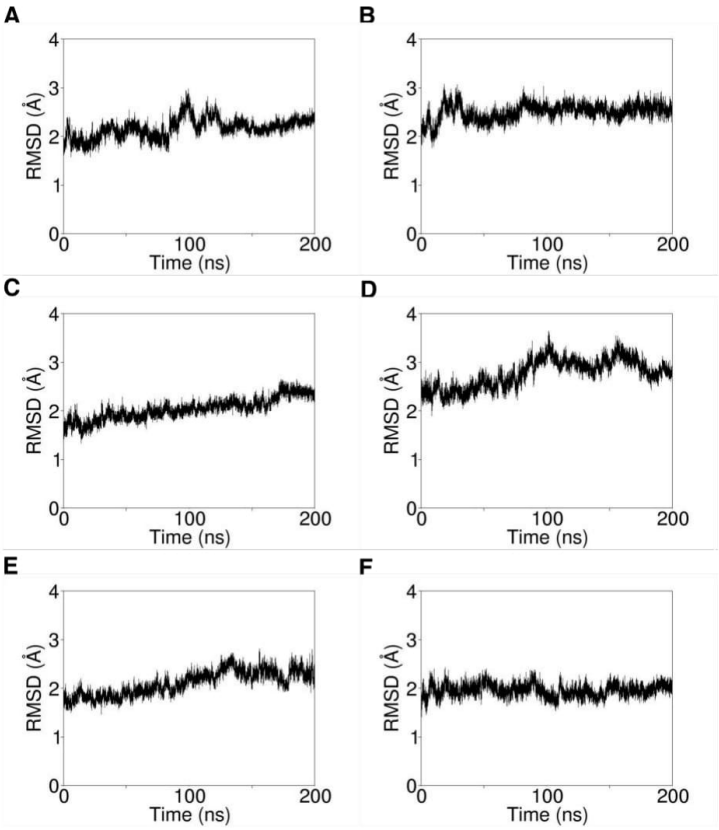

Figure S3. Representative snapshots of each ion configuration throughout simulations (A) HSE, (B) HSEP, (C) HSD, (D) HSDP, (E) HSP and (F) HSPP. The selectivity filter residues T117 to G121 and T225 to G229 are displayed in licorice representation, with Van der Waals spheres representing ions and water molecules, with oxygen, nitrogen, carbon, sodium and potassium atoms shown in red, blue, cyan, yellow and orange respectively.

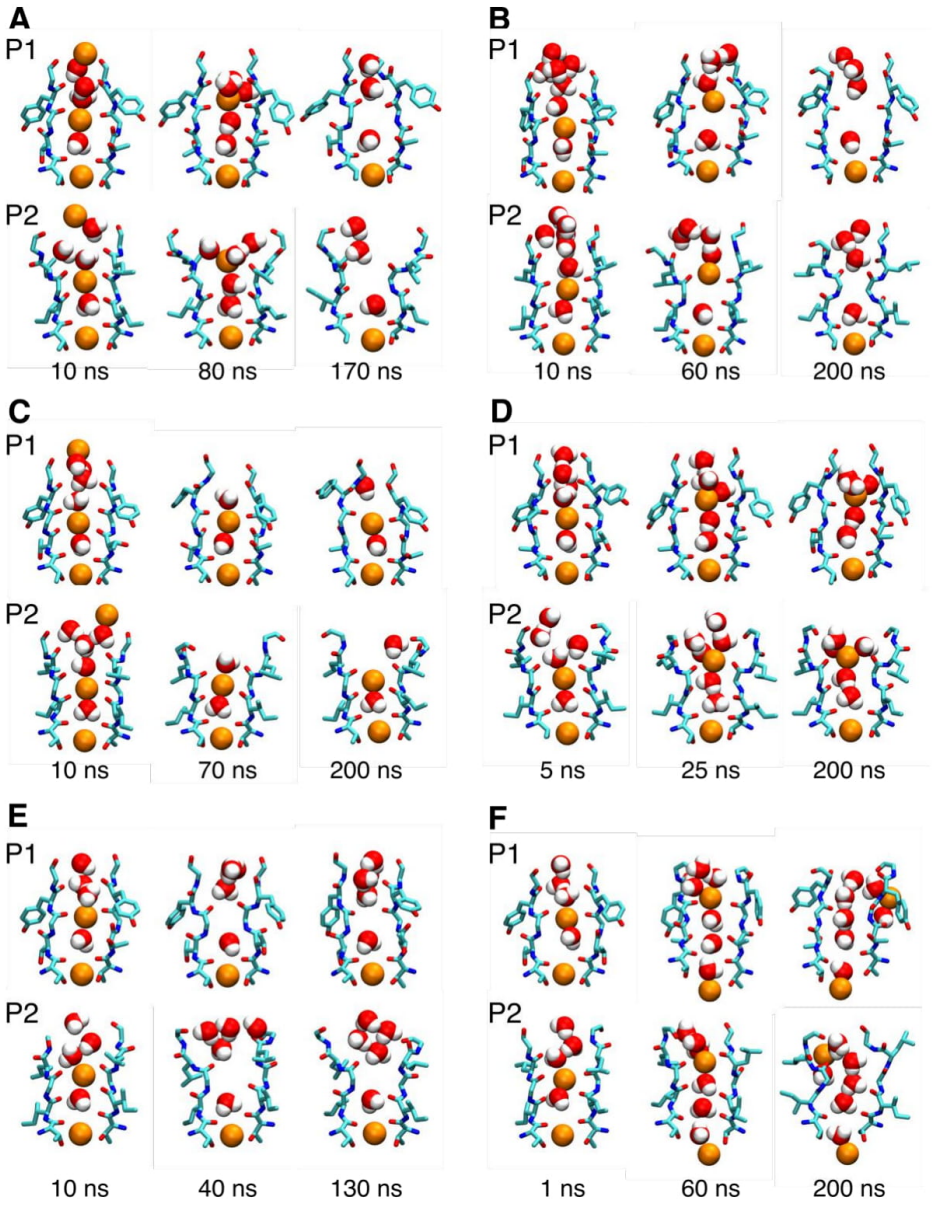

A.3 Modulation of the KcsA potassium channel by anionic phospholipids: role of the non-annular arginines

SUPPORTING INFORMATION

Modulation of the KcsA potassium channel by anionic phospholipids: Role of the non-annular arginines

José A. Poveda,[1] Victoria Oakes,[2]* A. Marcela Giudici,[1]* M. Lourdes Renart,[1] Oscar Millet,[3] Andrés Morales,[4] Simone Furini,[5] Carmen Domene[2,6] and José M. González-Ros,[1]*

[1]Instituto de Biología Molecular y Celular, Universidad Miguel Hernández, Elche, E-03202 Alicante, Spain

[2]Department of Chemistry, University of Bath, Claverton Down, Bath, BA2 7AY, UK

[3]Structural Biology Unit, CICbioGUNE, Bizkaia Technology Park, Derio, 48160 Vizcaya, Spain

[4]Departamento de Fisiología, Genética y Microbiología, Universidad de Alicante, E-03080 Alicante, Spain.

[5]Department of Medical Biotechnologies, University of Siena, Siena, Italy

[6]Department of Chemistry, University of Oxford, Oxford OX1 3TA, UK

Figure S1. MD simulations of WT KcsA. (A) D80-R89 interaction frequency in WT-KcsA (PC) simulations. (B) Average number of lipid H-bonds in WT-KcsA simulations (PC) calculated using a 3.5 Å distance cutoff between polar atoms and 35° cutoff for the acceptor-donor-hydrogen angle. (C-D) As for (A-B) with PA-containing bilayers.

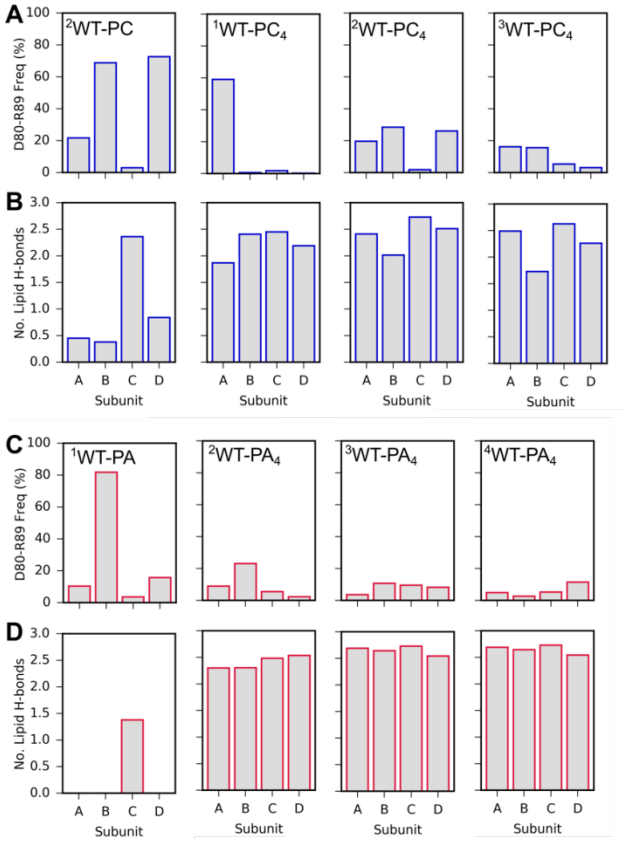

Table S1. H-bond frequency in KcsA WT simulations. H-bonds are calculated using a 3.5 Å distance cutoff between polar atoms and 35° cutoff for the acceptor-donor-hydrogen angle. PA and PC binding is colored red and blue, respectively.

Simulation	H-Bond Frequency (%)												Total Avg. H-bonds			
	T61				R64				R89							
	A	B	C	D	A	B	C	D	A	B	C	D	A	B	C	D
[1]WT-PA	36	2	42	24	47	34	48	0	30	0	31	0	1.3	0.5	1.4	0.2
[2]WT-PA	1	25	16	0	42	25	40	12	2	0	0	0	0.6	0.6	0.7	0.1
[1]WT-PA_4	30	52	51	82	87	71	88	92	85	82	75	58	2.7	2.5	2.6	2.7
[2]WT-PA_4	46	41	55	49	71	82	89	90	76	56	73	67	2.3	2.3	2.5	2.5
[3]WT-PA_4	46	58	71	46	89	90	89	84	86	73	75	83	2.7	2.6	2.7	2.5
[4]WT-PA_4	71	52	73	29	92	92	93	85	78	88	69	80	2.8	2.8	2.8	2.4
[5]WT-PA_4	80	48	51	84	94	77	40	57	60	85	72	60	2.7	2.5	1.9	2.2
[1]WT-PC	5	10	6	12	22	19	67	25	0	0	73	0	0.3	0.6	2.3	0.4
[2]WT-PC	42	14	39	14	3	18	67	50	0	0	81	0	0.4	0.4	2.4	0.4
[1]WT-PC_4	28	40	50	24	63	71	86	55	64	88	69	86	1.9	2.4	2.5	2.2
[2]WT-PC_4	53	41	53	55	73	61	87	86	79	66	85	65	2.4	2.0	2.7	2.5
[3]WT-PC_4	35	3	59	45	80	50	79	61	78	77	86	80	2.5	1.7	2.6	2.2
[4]WT-PC_4	41	42	49	31	63	67	68	41	49	87	78	31	1.8	2.4	2.5	1.2
[5]WT-PC_4	11	51	31	44	80	72	68	78	79	84	79	85	2.6	2.3	2.2	2.6

A4 Oxytocin Modulates Nociception as an Agonist of Pain-Sensing TRPV1, *Cell Reports*, 2017

Cell Reports, Volume *21*

Supplemental Information

Oxytocin Modulates Nociception

as an Agonist of Pain-Sensing TRPV1

Yelena Nersesyan, Lusine Demirkhanyan, Deny Cabezas-Bratesco, Victoria Oakes, Ricardo Kusuda, Tyler Dawson, Xiaohui Sun, Chike Cao, Alejandro Martin Cohen, Bharath Chelluboina, Krishna Kumar Veeravalli, Katharina Zimmermann, Carmen Domene, Sebastian Brauchi, and Eleonora Zakharian

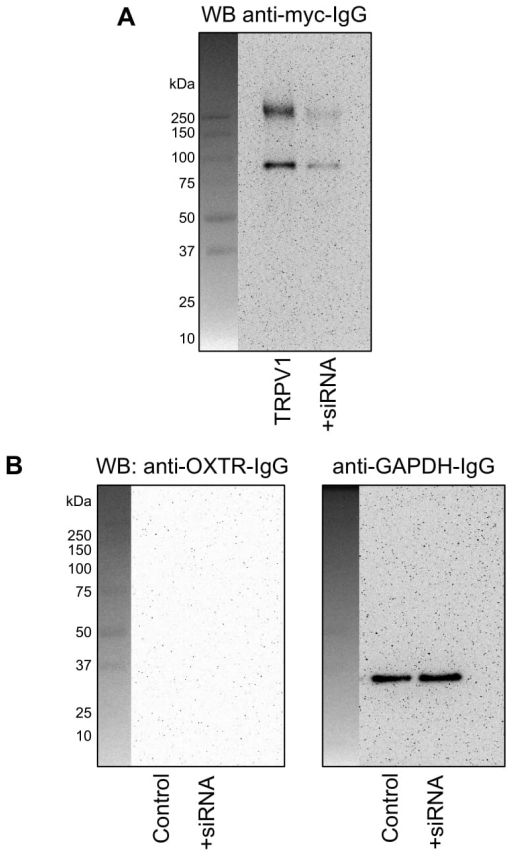

Figure S1: Protein expression levels after siRNA introduction. Related to Fig. 1.

A, Western blot (WB) displays TRPV1 protein expression levels in the control HEK-293 cells stably expressing TRPV1 and after introducing TRPV1-specific siRNA (Santa Cruz Biotechnology, Dallas, TX). The cells were transfected with 1 µg TRPV1-siRNA or control one using effectene reagent from Qiagen. After 44 h of growth, cells were washed once with PBS and detached from the plate by trypsin. Equal amounts of control and TRPV1-siRNA transfected cells ($1x10^5$ per sample) were used for WB detection of TRPV1. Cells were lyzed with 2X SDS-loading buffer, incubated at 95 °C bath for 15 minutes, and separated on 10% gel (BioRad). Blocking was done with 10 % milk for 1 h, following 2.5 h incubation with mouse anti-Myc antibody (4 µl per 8 ml of blocking buffer) and 1 h incubation with anti-mouse HRP-conjugated secondary antibodies, at room temperature. The chemiluminescence signals were obtained by using ECL Western Blotting Substrate (Thermo Scientific™ Pierce™).

B, WB was done to detect oxytocin receptor OXTR expression in the control F-11 cells and cells after introducing OXTR-specific siRNA (Santa Cruz Biotechnology, Dallas, TX). The cells were transfected with 1 µg OXTR-siRNA or control using effectene reagent from Qiagen. After 44 h of growth, cells were washed once with PBS and detached from the plate by trypsin. Equal amounts of control and OXTR-siRNA transfected cells ($1x10^5$ per sample) were used for WB detection of OXTR. We did not detect noticeable expression of OXTR levels in F-11 cells, which suggests that OXTR is present at low abundance levels (number of experiments n = 3). As a control we re-developed the WB with antibodies against GAPDH, which was detected at its predicted molecular mass of ~36 kDa.

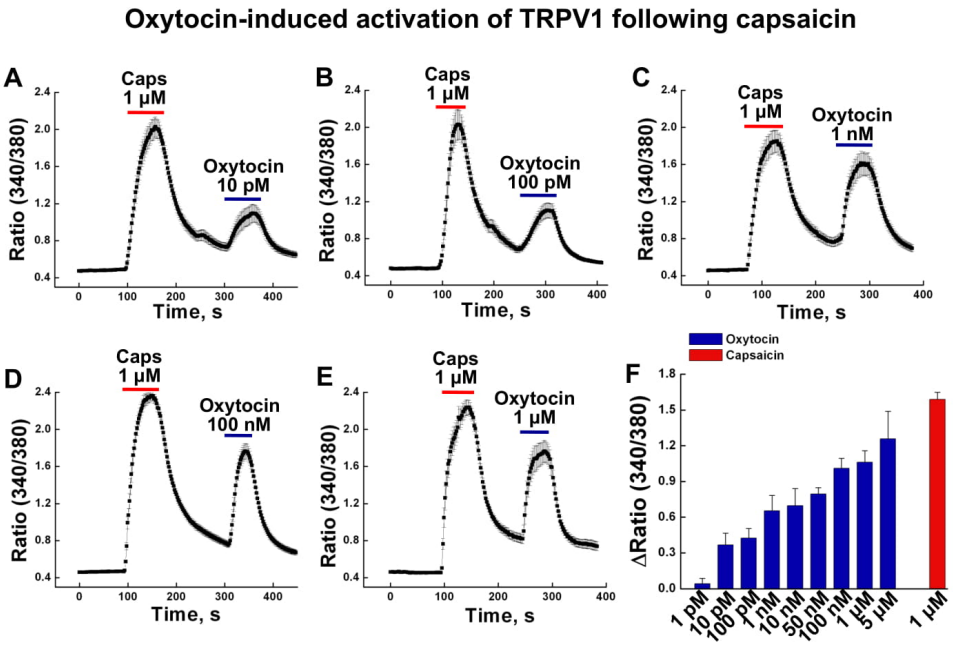

Figure S2: Oxytocin-induced potentiation of TRPV1 following capsaicin application. Related to Fig. 1.

Ca^{2+} imaging experiment performed on HEK-293 cells stably expressing TRPV1 channels: **A**, 10 pM oxytocin-induced activation of TRPV1 following 1 µM capsaicin application ($n_{exp.} = 3$, $n_{cells} = 71$). **B**, 100 pM oxytocin-induced TRPV1 response, following 1 µM capsaicin application ($n_{exp.} = 3$, $n_{cells} = 74$). **C**, 1 nM oxytocin-induced TRPV1 response, following 1 µM capsaicin application ($n_{exp.} = 3$, $n_{cells} = 64$). **D**, 100 nM oxytocin-induced TRPV1 response, following 1 µM capsaicin application ($n_{exp.} = 3$, $n_{cells} = 87$). **E**, 1 µM oxytocin-induced TRPV1 response, following 1 µM capsaicin application ($n_{exp.} = 3$, $n_{cells} = 80$). **F**, The summary presents the mean under all the conditions. All error bars stand for ±s.e.m.

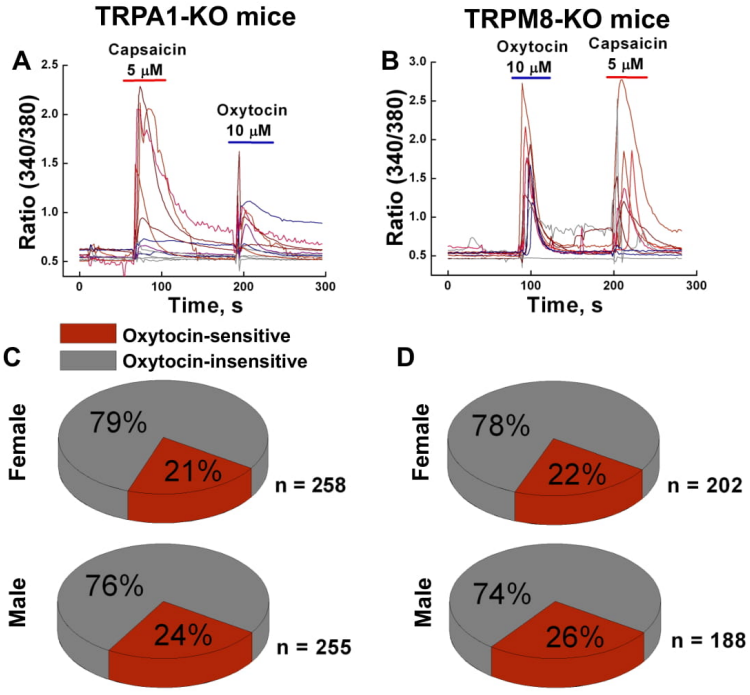

Figure S4: Oxytocin sensitivity in DRG neurons isolated from TRPA1$^{-/-}$ and TRPM8$^{-/-}$ mice. Related to Fig. 2.

A, Representative traces of the oxytocin- and capsaicin-elicited Ca^{2+} responses obtained from the DRG neurons of TRPA1$^{-/-}$ male mouse (a total number of measurements for both males and females $n_{exp.} = 18$). **B**, Representative traces of oxytocin- and capsaicin-elicited Ca^{2+} responses obtained from the DRG neurons of TRPM8$^{-/-}$ female mouse (a total number of measurements for both males and females $n_{exp.} = 24$). **C** and **D** panels show pie graphs of the distribution of the oxytocin-sensitive and oxytocin-insensitive DRG neurons isolated from the TRPA1$^{-/-}$-female ($n_{cells} = 258$), TRPA1$^{-/-}$-male ($n_{cells} = 255$), TRPM8$^{-/-}$-female ($n_{cells} = 202$), and TRPM8$^{-/-}$-male mice ($n_{cells} = 188$).

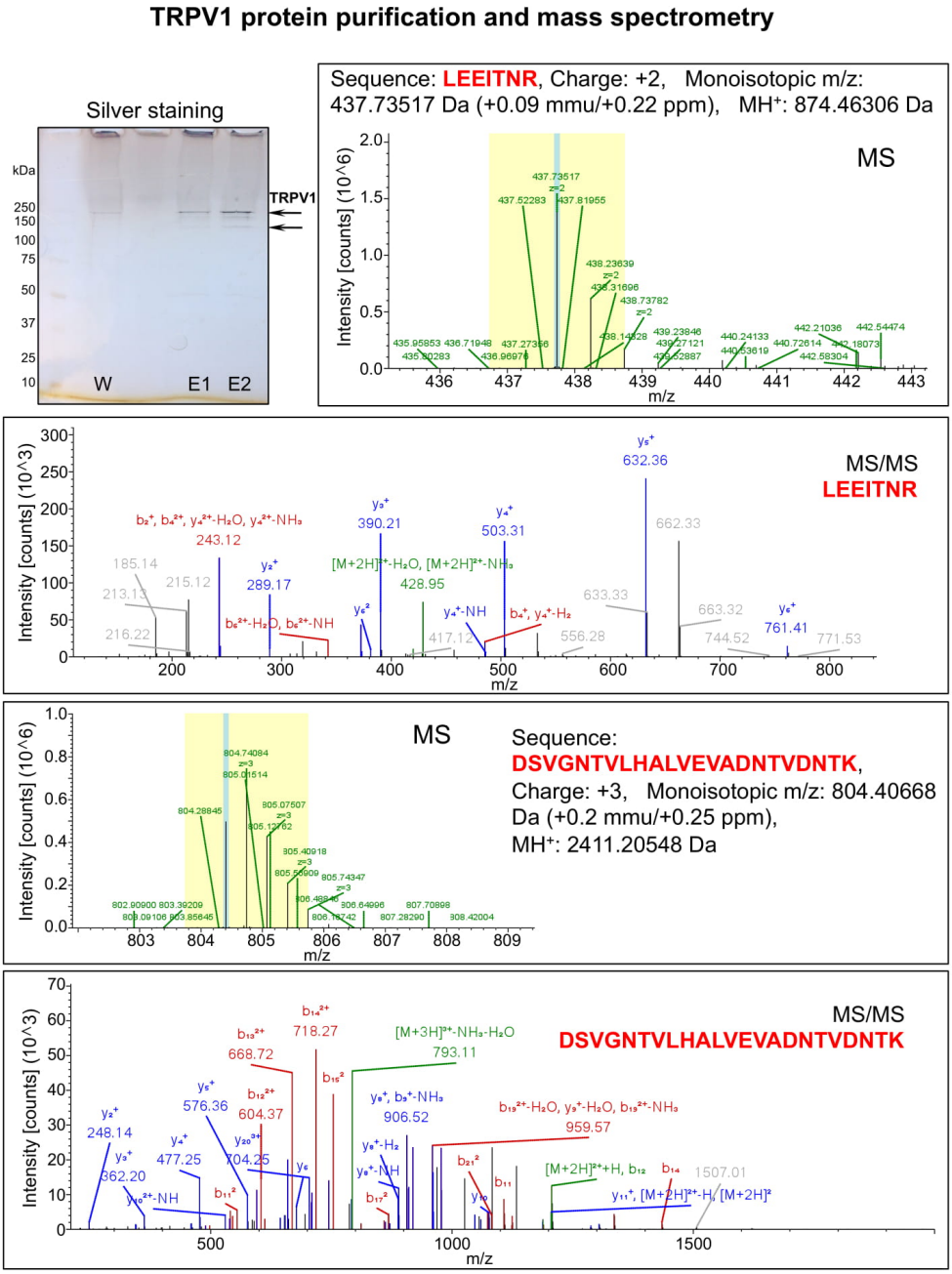

Figure S5: TRPV1 protein purification and mass spectrometry. Related to Fig. 4.

The Myc-tagged TRPV1 protein was purified by immunoprecipitation using monoclonal Myc-antibody (Sigma-Aldrich). Silver stained 10 % gel displays TRPV1 bands corresponding to the TRPV1 dimers and monomers, indicated by arrows. The letters indicate samples of wash (W), eluates (E), and left column presents markers. TRPV1 purified in the presence of 0.03% lauryl maltose neopentyl glycol (LMNG) preferably migrates on the gel in the form of dimers, and less in the form of monomers, for more details see (Lukacs et al., 2013).

The TRPV1 protein identity, prevalence, and purity in the obtained samples were validated using liquid chromatography mass spectrometric (LC-MS/MS) analysis. All bands present on the gel were excised and screened, where TRPV1 was present at the high abundance level. Representative MS and MS/MS spectra of the TRPV1 peptides are demonstrated in the figure.

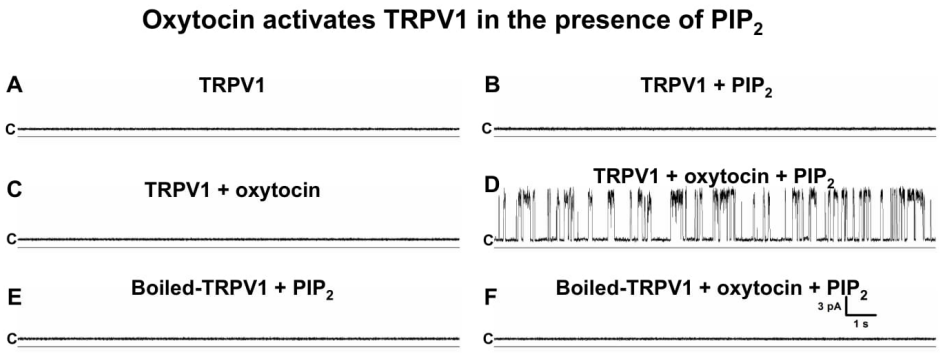

Figure S6: Oxytocin activates TRPV1 in the presence of PIP_2. Related to Fig. 4.

Representative TRPV1 channel traces obtained at different conditions in planar lipid bilayers. **A**, Representative traces of TRPV1 incorporated into planar lipid bilayers alone, and **B**, in the presence of PIP_2 (n = 25, with 2-5 h waiting time). **C**, TRPV1 incorporated in the bialyers in the presence of 0.5 µM oxytocin alone (n = 10, with at least 3 h waiting time), and **D,** after the addition of 5 µM PIP_2 (total number of events analyzed is 27,573; n = 13). Panels **E** and **F** demonstrate lack of TRPV1 channel activity in the presence of oxytocin and PIP_2 when the TRPV1 protein before incorporation to the bilayers was boiled for 30 min in the water bath (n = 5). All representative traces were obtained at 100 mV. The closed state indicated as letter "c" and is shown on the left of the traces.

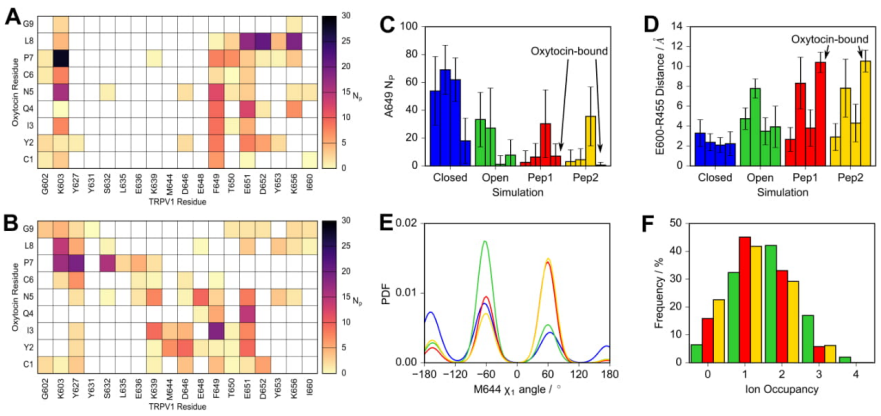

Figure S7: TRPV1-oxytocin interactions. **Related to Fig. 5.**

Contact maps displaying the number of interacting atom pairs (N_p) between TRPV1 and oxytocin in simulation Pep1 (**A**) and Pep2 (**B**), averaged over the simulation length, using a 4Å cut-off. **C**, Number of atomic interaction pairs between A649 and the other residues in the hydrophobic cluster. **D**, Minimum distance between E600 and E648 residues. In both, individual bars represent individual subunits in the TRPV1 channel, with those directly bound to oxytocin are shown. **E**, Probability density function of the M644 X_1 angle. **F**, Frequency distribution of the loading states of the SF2 site. Closed, Open, Pep1, and Pep2 simulations are shown in blue, green, red and yellow respectively.

Description	Coverage	# Peptides	# Unique Peptides
Transient receptor potential cation channel subfamily V member 1 OS=Rattus norvegicus GN=Trpv1	56.6307342	33	33
Keratin, type I cytoskeletal 10 OS=Homo sapiens GN=KRT10	45.2054795	25	21
Keratin, type II cytoskeletal 2 epidermal OS=Homo sapiens GN=KRT2	33.8028169	20	17
Keratin, type I cytoskeletal 9 OS=Homo sapiens GN=KRT9	33.2263242	9	9
Polyubiquitin-B (Fragment) OS=Homo sapiens GN=UBB	32.0388349	2	2
Protein S100-A7 OS=Homo sapiens GN=S100A7	30.6930693	3	3
Polyubiquitin-C (Fragment) OS=Homo sapiens GN=UBC	30.5970149	2	2
Lamin-B1 OS=Homo sapiens GN=LMNB1	29.5221843	14	14
Keratin, type II cytoskeletal 1 OS=Homo sapiens GN=KRT1	27.0186335	19	17
Trypsin OS=Sus scrofa	25.1082251	3	3
Histone H3.2 OS=Homo sapiens GN=HIST2H3A	23.5294117	1	1
Serine/threonine-protein kinase Nek3 (Fragment) OS=Homo sapiens GN=NEK3	18.2320442	1	1
Endoplasmin OS=Homo sapiens GN=HSP90B1	16.3138231	9	8
MICOS complex subunit MIC60 OS=Homo sapiens GN=IMMT	15.3305203	8	8
Keratin, type II cytoskeletal 6A OS=Homo sapiens GN=KRT6A	13.8297872	8	2
Heat shock protein HSP 90-beta OS=Homo sapiens GN=HSP90AB1	11.6022099	6	5
Ig gamma-2 chain C region OS=Homo sapiens GN=IGHG2	11.0429449	2	2
Keratin, type II cytoskeletal 5 OS=Homo sapiens GN=KRT5	11.0169495	7	1
Calnexin OS=Homo sapiens GN=CANX	9.96621626	4	4
60S ribosomal protein L3 OS=Homo sapiens GN=RPL3	8.43672456	2	2
Glial fibrillary acidic protein (Fragment) OS=Homo sapiens GN=GFAP	7.25806456	2	0
Hornerin OS=Homo sapiens GN=HRNR	7.22807015	3	3
Lysosome-associated membrane glycoprotein 2 OS=Homo sapiens GN=LAMP2	7.07317072	3	3
Keratin, type I cytoskeletal 16 OS=Homo sapiens GN=KRT16	5.72033893	3	2
Transitional endoplasmic reticulum ATPase OS=Homo sapiens GN=VCP	5.21091814	3	3
Cullin-1 OS=Homo sapiens GN=CUL1	4.89690726	1	1
Exocyst complex component 4 OS=Homo sapiens GN=EXOC4	3.90143732	1	1
Keratin, type II cytoskeletal 4 OS=Homo sapiens GN=KRT4	3.74531832	2	0
Keratin, type II cytoskeletal 80 OS=Homo sapiens GN=KRT80	2.43362839	1	1
Ceruloplasmin OS=Homo sapiens GN=CP	1.97183096	1	1
Leucine-rich PPR motif-containing protein, mitochondrial OS=Homo sapiens GN=LRPPRC	1.64992824	1	1

Table S1: The proteins identified using LC-MS/MS. Related to Figure 4.

The list of the proteins obtained from LC-MS/MS shows TRPV1 as the major protein purified from HEK-293 cells stably expressing the channel. The second group of abundant proteins includes keratins, as a typical contaminant factor during mass spectrometry. The peptide analysis was performed with the UniprotKB database, significance threshold $p < 0.05$, error range ±10 ppm. The TRPV1 protein was purified by immunoprecipitation with Myc antibodies.

Supplemental Information

Experimental Procedures

Computational studies: Influence on the TRPV1 activation state

Rearrangements in the outer pore region, encompassing the selectivity filter and adjacent extracellular loops, are a crucial attribute of TRPV1 activation, as evidenced by superposition of the apo and RTX/DkTx-bound structures. Three regions with marked differences are observed which show significant overlap with the oxytocin-binding site (Cao et al., 2013b): (1) A hydrophobic cluster constituted of residues V595, I599, T633, L637, F640, F649, T650, Y653, F659 and L663. The region is more compact in the *apo* state, relative to the RTX/DkTx-bound structure. (2) A charged cluster encompassing R455, K535, E600, and D654 residues. In the *apo* state, these residues are closely associated, whereas in the RTX/DkTx-bound structure, E600 is completely disengaged. (3) The selectivity filter (G643, M644, G645, D646). In the RTX/DkTx-bound structure, the selectivity filter is dilated and optimized for ion binding.

Accordingly, these regions were monitored throughout the simulation trajectories to assess the influence of oxytocin binding on the activation state of the receptor. F649 serves a dual-purpose as a key component of the hydrophobic cluster and oxytocin-binding interface. In the *apo* simulation, representative of the closed state, F649 forms frequent contacts with the hydrophobic residues, with an average of ~50 atomic pairs, and up to 140 formed at any time (Figure S7A). In the simulations initiated from the open state, F649 is predominantly detached from the cluster, but can spontaneously enter interacting conformations (Np > 20). When oxytocin is absent, two subunits have occupied the suggested closed state of the cluster; this is reduced to a single subunit when oxytocin is bound. Concurrently, the F649 residue in direct contact with oxytocin forms the lowest number of atomic contacts throughout, stabilizing the outer loop preceding S6 in a state representative of the open structure.

It is also apparent that oxytocin binding stabilizes surrounding loops in an open state, by interfering with cluster of charged residues R455, K535, E600, and D654. In the *apo* simulation, these residues are connected by salt-bridge interactions, with 2-4 Å between E600 and R455 (Figure S7B). In contrast, in the RTX/DkTx-bound structure, the charged entities of such residues are separated by approximately 10 Å. This distance is only maintained when E600 directly interacts with oxytocin, with frequent H-bonding observed with the Y2 residue of oxytocin in the Pep2 simulation. In the absence of an external binding partner, E600 is highly flexible and can spontaneously penetrate the charged cluster, forming the closed state.

Activation of TRPV1 is also accompanied by dilation of the selectivity filter, in order to cultivate ion permeation. The outward conduction mechanism can be described in terms of three binding sites; SC, the central cavity defined as the region in between residues I679 and Y671; SF1, localized on the carbonyl oxygen atoms of G643; and SF2, a region of high-field strength formed by negatively charged residues D646 and E648, and the carbonyl oxygen atoms of M644 and G645. Expansion of SF1 and SF2 are required to stimulate conduction, specifically via the distension of G643 carbonyl oxygen atoms and the downward movement of M644. The position of D646 is also optimized to facilitate ion coordination in the SF2 site.

The dynamics of the selectivity filter are seemingly perturbed in the SF2 locale as a result of oxytocin binding. Two rotameric states of M644 are observed in the *apo* and *holo* structures, displaying X_1 angles of -109 (up-state) and 39° (down-state) respectively. The up-state is prevalent in the presence of oxytocin (Figure S7C), whereas the unbound state predominantly occupies the down-state, suggesting oxytocin binding directly stabilizes this aspect of the open state selectivity filter. Although negligible differences are observed in the rotameric state of D646 residues, the occupancy of the SF2 site is markedly reduced when oxytocin is bound. The proportion of empty or singly occupied states is increased by 10-15 % in both oxytocin-bound simulations relative to the peptide-free simulation (Figure S7D), where doubly occupied states are most frequently observed.

The elevated occupancy of SF2 in the peptide-free simulation can be attributed to increased coordination of Na^+ ions to SF2 residues; in 45.7% of frames in the peptide-free simulations, bound ions interact with two or more SF2 residues, compared to 23.4% and 24.7% in the Pep1 and Pep2 simulations respectively. These coordination networks involve either D646 side-chains from adjacent subunits or D646 side-chains and M644/G645 backbone carbonyl atoms from the same subunit. It is possible that stabilization of the selectivity filter by oxytocin binding, as described previously, discourages the formation

of such networks and reduces the Na^+ binding affinity in this site. These observations suggest a direct link between oxytocin binding and permeation in the TRPV1 selectivity filter.

Mouse experiments

Adult male and female wild type, $TRPV1^{-/-}$, $TRPA1^{-/-}$, and $TRPM8^{-/-}$ mice were purchased from Jackson Laboratory, Maine, USA, and kept in the animal house located in the University of Illinois College of Medicine, as per protocols approved by the IACUC. The experiments were done under the protocol #627972. All the experiments were conducted using both genders at the age of 4-6 weeks old, to characterize their respective responsiveness to oxytocin. Mice were housed in a climate-controlled environment (22.8 ± 2.0 °C, 45–50% humidity) with a 12/12-light/dark cycle with access to designated diet and water *ad libitum*. All experiments were conducted at 22.8 ± 2.0 °C.

DRG neurons were isolated following the protocols (Malin et al., 2007; Sleigh et al., 2016), and maintained as we previously described (Cao et al., 2013a). Briefly, DRG neurons were cultured in the Primary Neuron Basal Medium, PNBM (Lonza Inc., Allendale, NJ). The fully supplemented medium contained 2 mM L-glutamine, 50 µg/ml gentamicin, 37 µg/ml amphotericin, and 2% NSF-1. For inhibition of Schwann cells and Glial cells, mitotic inhibitors were added to the medium (uridine 17.5 µg/ml and 5-fluoro-2-deoxyuridine 7.5 µg/ml). All the transfection experiments were done using Nucleofector(R) (Lonza), following the instructions from the manufacturer.

Cell culture

HEK-293 cells were maintained in minimal essential medium (MEM) solution (Invitrogen, San Diego, CA) supplemented with 10% fetal bovine serum (Invitrogen) and 1% penicillin/streptomycin. F-11 cells were cultured in DMEM/F12 medium +20% FBS, 0.2 mM L-glutamine, 100 µM sodium hypoxanthine, 400 nM aminopterin, 16 µM thymidine (HAT supplement), and penicillin/streptomycin at 37 °C, as previously described (Zakharian et al., 2009). The cells were transfected with the rat TRPV1 cDNA using the effectene reagent (Qiagen, Chatsworth, CA). The TRPV1 stable cell line was developed with TRPV1 tagged with *myc* on the N-terminus as previously described (Zakharian et al., 2009).

Intracellular Ca^{2+} measurements

The extracellular solution used in ratiometric $[Ca^{2+}]_i$ measurements contained (in mM) 137 NaCl, 5 KCl, 2 $CaCl_2$, 1 $MgCl_2$, 10 glucose and 10 HEPES, pH 7.4. Cells were incubated with 2 µM Fura-2 acetoxymethyl ester (Thermo Fisher Scientific, Waltham, MA) for 60 min at room temperature. The fluorescence signals of the cells grown on the coverslips were measured using alternating excitation at 340 and 380 nm and emission was detected at 510 nm. The ratio of fluorescence (340/380) was plotted against time. The obtained values of ratios from each coverslip were first analyzed and then the mean values of stimuli-induced signals were combined and statistically averaged values with mean errors were plotted in the summary graphs, the total number of measurements/cover slips (n) are indicated in the figure legend. The measurements were performed using a Photon Technology International (PTI) (Birmingham, NJ) imaging system mounted on Zeiss-AXIO Observed D1 microscope, equipped with a DeltaRAM excitation light source, or with a Ratiomaster 5 Imaging System (PTI) equipped with a Cool-snap HQ2 (Roper) Camera.

Whole-cell patch clamp recordings

The whole-cell patch clamp experiments were performed as previously described (Yudin et al., 2011; Zakharian et al., 2009). HEK-293T cells were cotransfected with rTRPV1 and eGFP with Lipofectamine 2000 according to manufacturer's protocol. Whole-cell patch clamp recordings were performed 48-72h post transfection at room temperature. The standard extracellular solution used in experiments contained (in mM) 135 NaCl, 5 KCl, 1 $MgCl_2$, 2 $CaCl_2$, 10 HEPES and 10 glucose, pH 7.4 (adjusted with NaOH). The pipette (intracellular) solution contained (in mM) 105 CsF, 35 NaCl, 8 KCl, 10 HEPES, 10 EGTA, pH 7.8 (adjusted with CsOH). Cell capacitance mean was 5.79±1pF, and access resistance <16MΩ. Data were acquired with an Axo-patch 200B amplifier (Molecular Devices), filtered with an 8-pole low-pass Bessel filter at 5 kHz and digitized at 10 kHz with a Digidata1320A interface and pClamp8.2 software (Molecular Devices). Pipettes were pulled from borosilicate glass and heat-polished to final resistances of 2-3.5MΩ. Currents are presented in terms of densities.

Preparation of the TRPV1 protein from HEK cells

HEK-293 cells stably expressing TRPV1 were grown to 70-80% confluence, washed, and collected with cold PBS. Cells were harvested and resuspended in NCB buffer, containing 500 mM NaCl, 50 mM NaH_2PO_4, 20 mM HEPES, 10% glycerol, pH 7.5, with addition of 1 mM of protease-inhibitor PMSF, 5 mM β-mercaptoethanol. Then the cells were lysed by freeze-thawing method and centrifuged at low speed to remove cell-debris and DNA. The supernatant was further centrifuged at 40,000 g for 2.5 h., and the pellet was resuspended in NCB buffer with addition of a protease inhibitor cocktail (Roche, Indianapolis, IN), 0.1% Nonidet P40 (Roche) and 0.5% dodecyl-maltoside (DDM) (CalBiochem). The suspension was incubated overnight at 4 °C on a shaker with gentle agitation and then centrifuged for 1 h. at 21,380 g. Further, the TRPV1 protein was purified by immuno-precipitation with anti-Myc-IgG conjugated to A/G protein magnetic beads (Pierce, Thermo Scientific), following the procedure provided by the manufacturer. All steps of purification were performed at 4 °C. For the planar lipid bilayers experiments the protein was eluted with Myc-peptide (150 μg/ml).

Mass spectrometry analysis

After the immunoprecipitation, TRPV1 prep was separated by SDS-PAGE and stained with coomassie blue. The bands was excised from the gel and digested with trypsin for mass spectrometry analysis according to Mann et al protocol (Shevchenko et al., 2006), with some modifications. Briefly, the gel bands were reduced with 0.5 M dithiothreitol and alkylated with 0.7 M iodoacetamide. Gel bands were digested with trypsin (Promega, Madison, WI) for 12 h at 37°C. Peptides were extracted from the gel bands with 100 μL of a 50% acetonitrile 5% formic acid solution. The extract was dried by vacuum centrifugation (SPD SpeedVac Thermo Electron Corp. Waltham, MA); the tryptic peptides were resuspended in 20 μL of a 3% acetonitrile, 0.5% formic acid solution.

Liquid chromatography-tandem mass mass spectrometry (LC-MS/MS) was performed using a nano flow liquid chromatography system (Ultimate3000, ThermoScientific) interfaced to a hybrid ion trap-orbitrap high-resolution tandem mass spectrometer (VelosPro, ThermoScientific) operated in data dependent acquisition (DDA) mode. Briefly, one micro-liter of each sample was injected onto a capillary column (4 μm Jupiter C18 manually packed on a 30 cm x 75um ID PicoFrit Column, New Objective) at a flow rate of 300 nl/min. Samples electro-sprayed at 1.2 kV using a dynamic nanospray ionization source. Chromatographic separation was carried out using 90 minute linear gradients (Mobile Phase A: 0.1% formic acid in MS-grade water, mobile phase B: 0.1% formic acid in MS-grade acetonitrile) from 3% B to 35% B over 60 minutes, then increasing to 95% B over 5 minutes. MS/MS spectra were acquired using both collision-induced dissociation (CID) and higher-energy collisional dissociation (HCD) for the top 15 peaks in the survey 30000-resolution MS scan. The .raw files were acquired (Xcalibur, ThermoFisher) and exported to Proteome Discoverer 2.0 (ThermoFisher) software for peptide and protein identification using SequestHT search algorithm (Full trypsin digestion with 2 maximum missed cleavages, 10 ppm precursor mass tolerance and 0.8 Da fragment mass tolerance). Database searching was done using the UniprotKB human database.

Planar lipid bilayer measurements

Planar lipid bilayers measurements were performed as previously described (Zakharian, 2013; Zakharian et al., 2010; Zakharian et al., 2009). Planar lipid bilayers were formed from a solution of synthetic 1-palmitoyl-2-oleoyl-glycero-3-phosphocoline (POPC) and 1-palmitoyl-2-oleoyl-glycero-3-phosphoethanolamine (POPE, Avanti Polar Lipids, Birmingham, AL) in ratio 3:1 in n-decane (Aldrich). The solution was used to paint a bilayer in an aperture of ~150μm diameter in a Delrin cup (Warner Instruments, Hamden, CT) between symmetric aqueous bathing solutions of 150 mM KCl, 0.02 mM $MgCl_2$, 1 μM $CaCl_2$, 20 mM Hepes, pH 7.2, at 22 °C. All salts were ultrapure (>99%) (Aldrich). Bilayer capacitances were in the range of 50-75 pF. After the bilayers were formed, the TRPV1 protein from micellar solution (20 ng/ml) was added by painting. Unitary currents were recorded with an integrating patch clamp amplifier (Axopatch 200B, Axon Instruments). The *trans* solution (voltage command side) was connected to the CV 201A head stage input, and the *cis* solution was held at virtual ground *via* a pair of matched Ag-AgCl electrodes. Currents through the voltage-clamped bilayers (background conductance < 1 pS) were filtered at the amplifier output (low pass, -3 dB at 10 kHz, 8-pole Bessel response). Data were secondarily filtered at 100 Hz through an 8-pole Bessel filter (950 TAF, Frequency Devices) and digitized at 1 kHz using an analog-to-digital converter (Digidata 1322A, Axon Instruments), controlled by pClamp10.3 software (Axon Instruments). Single-channel conductance events, all points' histograms, open

probability, and other parameters were identified and analyzed using the Clampfit10.3 software (Axon Instruments).

Defining the atomic interaction network between oxytocin and the TRPV1 ion channel

System Setup: The structures of the TRPV1 channel determined by single-particle cryo-electron microscopy in open (PDB: 3J5Q, resolution 3.8 Å) and closed (PDB: 3J5P, resolution 3.28 Å) states were used as atomic models of the system. To predict the sequence of the β-strand in the C-terminal domain (denoted 752-762 in the PDB model), all possible models of residues 720-751 were built and validated using FASTCONTACT, advocating that residues 741-751 are the likely occupants of the β-strand (Camacho and Zhang, 2005). This assignment was further supported by alignment with the TRPV2 channel, where the resolved structure demonstrates conserved residues in the analogous position (Zubcevic et al., 2016). The remaining missing loop in the C-terminal domain (residues 720 to 740), as well as the unresolved segment of the S2-S3 loop (503 to 507), were modelled using Modloop (Fiser and Sali, 2003). Thus, the final channel model contained residues 111 to 751, with the N- and C- termini acetylated and methylated respectively and default protonation states used for ionisable residues (Li et al., 2005). The double-knot toxin (DkTx) and the vanilloid resiniferatoxin (RTx) were removed from the open state. Structural alignment of DkTx and oxytocin was performed to predicate the binding site of oxytocin in the outer pore region, resulting in the placement of four oxytocin molecules in both open and closed systems. SOLVATE1.0 was used to fill the internal cavities of the proteins, which were inserted into a pre-equilibrated lipid bilayer of 1-palmitoyl-2-oleoyl-sn-glycero-3-phosphocholine (POPC) molecules, generated using the Membrane Plugin of VMD (Humphrey et al., 1996). The systems were then solvated to produce a cubic water box, and NaCl was added, using the Autoionise Plugin of VMD (Humphrey et al., 1996), to neutralize and mimic the biological ionic concentration of 150 mM. The resulting system size was approximately 300,000 atoms.

Initially, MD simulations of both the open and closed states of TRPV1 were performed for 200 ns. Prolonged oxytocin binding was observed in the open state, thus this simulation was extended for a further 100 ns. The predominant binding pose was replicated in each subunit in an independent simulation, 200 ns in length. A control simulation of TRPV1 in the open state, without oxytocin, was also performed for 200 ns, to assess the effect of bound oxytocin.

The FlexPepDock Server, a component of the Rosetta program, was used to predict further oxytocin-binding poses in the open and closed states (London et al., 2011; Raveh et al., 2010).

Molecular Dynamics (MD) Simulations

NAMD2.9 was employed to perform MD simulations (Phillips et al., 2005). The CHARMM22 force field (with the CMAP correction) was used to describe the TRPV1 channel and the oxytocin peptide, CHARMM36 for lipids,(Klauda et al., 2010) TIP3P(Jorgensen et al., 1983) model for water, and standard ion parameters.(Beglov and Roux, 1994) The Particle Mesh Ewald method was used for the treatment of periodic electrostatic interactions, with an upper threshold of 1 Å for grid spacing (Darden et al., 1993). Electrostatic and van der Waals forces were calculated every timestep. A cut-off distance of 12 Å was used for van der Waals forces. A switching distance of 10 Å was chosen to smoothly truncate the non-bonded interactions. Only atoms in a Verlet pair list with a cut-off distance of 13.5 Å (reassigned every 20 steps) were considered (Verlet, 1967). The SETTLE algorithm was used to constrain all bonds involving hydrogen atoms to allow the use of a 2 fs time step throughout the simulation (Miyamoto and Kollman, 1992). The Nose-Hoover-Langevin piston method was employed to control the pressure with a 200 fs period, 50 fs damping constant and a desired value of 1 atmosphere (Feller et al., 1995; Martyna et al., 1994). The system was coupled to a Langevin thermostat to sustain a temperature of 310 K throughout.

Equilibration Protocol

The systems were subject to 10,000 steps of minimization with the protein backbone atoms restrained, and subsequently equilibrated for a total of 2.5 ns. Each equilibration step was undertaken for 500 ps, with restraints removed systematically: (i) lipid tails, (ii) water and lipid headgroups, (iii) oxytocin molecules, (iv) TRPV1 side-chain atoms, and (v) TRPV1 backbone atoms of residues 720 to 740 and 503 to 507.

Nocifensive behavior in mice

Animals: Adult male C57BL/6J mice were used. Animals were housed in group cages in a temperature-controlled environment on a 12-hour light/dark cycle and supplied with water and food *ad libitum*. The experiments were performed according to the guideline of the International Association or the Study of Pain and approved by the internal review board of the university and the local district government.

Chemicals: The following chemicals were used: capsaicin (Sigma-Aldrich) and oxytocin (Cayman Chemical). Capsaicin was dissolved in ethanol for preparing concentrated stock solutions of 10 mM and working solution was diluted in saline prior to the use. Oxytocin was dissolved in *aqua destillata* to provide a stock solution of 1 mM kept at -20 ^{o}C in BSA pretreated Eppendorf cups and added to the capsaicin solution at its final concentration of 4 µg in 20 µL.

Behavior test: Animals were placed in an observation apparatus onto a transparent plexiglass surface with individual chambers of 9 x 9 x 15 cm. Mice were adapted to the equipment for one hour per day on 3 subsequent days previous to the behavioral test. Mice were anesthetized with 3% sevoflurane, and capsaicin (1.6 µg/paw in a volume of 20 µL) (Sakurada et al., 1992) or combination of capsaicin and oxytocin solution was injected intracutaneously into mice hind paw with a 100 µL Hamilton microsyringe and a 30 gauge needle. After the injection, animals (6 mice each time) were put in the observation apparatus, and their behavior was recorded from the bottom side with a high-resolution camera (C920 HD Pro Webcam, Logitech) for 30 minutes. Videos were analyzed offline with the experimenter blinded to the groups.

Statistical analysis

Statistical analysis was performed using Origin 9.0 software (Microcal Software Inc., Northampton, MA, USA). Statistical significance was calculated using one-way ANOVA followed by Fisher's LSD test, or Student's t-test and data were expressed as mean ± SEM. $P < 0.05$ was considered to be significant. In all figures, statistical significance is labeled the following way: *P <0.05, **P <0.01, ***P <0.001, and ****P <0.0001.

Supplementary References:

Beglov, D., and Roux, B. (1994). Finite representation of an infinite bulk system: Solvent boundary potential for computer simulations. The Journal of Chemical Physics *100*, 9050-9063.

Camacho, C.J., and Zhang, C. (2005). FastContact: rapid estimate of contact and binding free energies. Bioinformatics *21*, 2534-2536.

Cao, C., Yudin, Y., Bikard, Y., Chen, W., Liu, T., Li, H., Jendrossek, D., Cohen, A., Pavlov, E., Rohacs, T., *et al.* (2013a). Polyester modification of the mammalian TRPM8 channel protein: implications for structure and function. Cell reports *4*, 302-315.

Cao, E., Liao, M., Cheng, Y., and Julius, D. (2013b). TRPV1 structures in distinct conformations reveal activation mechanisms. Nature *504*, 113-118.

Darden, T., York, D., and Pedersen, L. (1993). Particle mesh Ewald: An N·log(N) method for Ewald sums in large systems. The Journal of Chemical Physics *98*, 10089-10092.

Feller, S.E., Zhang, Y., Pastor, R.W., and Brooks, B.R. (1995). Constant pressure molecular dynamics simulation: the Langevin piston method. The Journal of chemical physics *103*, 4613-4621.

Fiser, A., and Sali, A. (2003). ModLoop: automated modeling of loops in protein structures. Bioinformatics (Oxford, England) *19*, 2500-2501.

Humphrey, W., Dalke, A., and Schulten, K. (1996). VMD: Visual molecular dynamics. Journal of Molecular Graphics *14*, 33-38.

Jorgensen, W.L., Chandrasekhar, J., Madura, J.D., Impey, R.W., and Klein, M.L. (1983). Comparison of simple potential functions for simulating liquid water. The Journal of chemical physics *79*, 926-935.

Klauda, J.B., Venable, R.M., Freites, J.A., O'Connor, J.W., Tobias, D.J., Mondragon-Ramirez, C., Vorobyov, I., MacKerell Jr, A.D., and Pastor, R.W. (2010). Update of the CHARMM all-atom additive force field for lipids: validation on six lipid types. The journal of physical chemistry B *114*, 7830-7843.

Li, H., Robertson, A.D., and Jensen, J.H. (2005). Very fast empirical prediction and rationalization of protein pKa values. Proteins *61*, 704-721.

London, N., Raveh, B., Cohen, E., Fathi, G., and Schueler-Furman, O. (2011). Rosetta FlexPepDock web server--high resolution modeling of peptide-protein interactions. Nucleic acids research *39*, W249-253.
Lukacs, V., Rives, J.M., Sun, X., Zakharian, E., and Rohacs, T. (2013). Promiscuous activation of transient receptor potential vanilloid 1 (TRPV1) channels by negatively charged intracellular lipids: the key role of endogenous phosphoinositides in maintaining channel activity. J Biol Chem *288*, 35003-35013.
Malin, S.A., Davis, B.M., and Molliver, D.C. (2007). Production of dissociated sensory neuron cultures and considerations for their use in studying neuronal function and plasticity. Nat Protoc *2*, 152-160.
Martyna, G.J., Tobias, D.J., and Klein, M.L. (1994). Constant pressure molecular dynamics algorithms. The Journal of Chemical Physics *101*, 4177-4189.
Miyamoto, S., and Kollman, P.A. (1992). SETTLE: an analytical version of the SHAKE and RATTLE algorithm for rigid water models. J Comput Chem *13*, 952-962.
Phillips, J.C., Braun, R., Wang, W., Gumbart, J., Tajkhorshid, E., Villa, E., Chipot, C., Skeel, R.D., Kale, L., and Schulten, K. (2005). Scalable molecular dynamics with NAMD. Journal of computational chemistry *26*, 1781-1802.
Raveh, B., London, N., and Schueler-Furman, O. (2010). Sub-angstrom modeling of complexes between flexible peptides and globular proteins. Proteins *78*, 2029-2040.
Sakurada, T., Katsumata, K., Tan-No, K., Sakurada, S., and Kisara, K. (1992). The capsaicin test in mice for evaluating tachykinin antagonists in the spinal cord. Neuropharmacology *31*, 1279-1285.
Shevchenko, A., Tomas, H., Havlis, J., Olsen, J.V., and Mann, M. (2006). In-gel digestion for mass spectrometric characterization of proteins and proteomes. Nat Protoc *1*, 2856-2860.
Sleigh, J.N., Weir, G.A., and Schiavo, G. (2016). A simple, step-by-step dissection protocol for the rapid isolation of mouse dorsal root ganglia. BMC Res Notes *9*, 82.
Verlet, L. (1967). Computer" experiments" on classical fluids. I. Thermodynamical properties of Lennard-Jones molecules. Physical review *159*, 98.
Yudin, Y., Lukacs, V., Cao, C., and Rohacs, T. (2011). Decrease in phosphatidylinositol 4,5-bisphosphate levels mediates desensitization of the cold sensor TRPM8 channels. The Journal of physiology *589*, 6007-6027.
Zakharian, E. (2013). Recording of ion channel activity in planar lipid bilayer experiments. Methods in molecular biology *998*, 109-118.
Zakharian, E., Cao, C., and Rohacs, T. (2010). Gating of transient receptor potential melastatin 8 (TRPM8) channels activated by cold and chemical agonists in planar lipid bilayers. The Journal of neuroscience : the official journal of the Society for Neuroscience *30*, 12526-12534.
Zakharian, E., Thyagarajan, B., French, R.J., Pavlov, E., and Rohacs, T. (2009). Inorganic polyphosphate modulates TRPM8 channels. PLoS One *4*, e5404.
Zubcevic, L., Herzik Jr, M.A., Chung, B.C., Liu, Z., Lander, G.C., and Lee, S.-Y. (2016). Cryo-electron microscopy structure of the TRPV2 ion channel. Nat Struct Mol Biol *23*, 180-186.

SUPPLEMENTARY INFORMATION

Stereospecific Interactions of Cholesterol in a Model Cell Membrane: Implications for the Membrane Dipole Potential

Victoria Oakes[1] & Carmen Domene[1,2]

1. Department of Chemistry, 1 South Building, University of Bath, Bath BA2 7AY, UK

2. Chemistry Research Laboratory, Mansfield Road, University of Oxford, Oxford, OX1 3TA, UK

Text S1. Internal coordinates used to generate *nat*-cholesterol (CHL), *ent*-cholesterol (ENT) and *epi*-cholesterol (EPI). Modified values are displayed in red.

```
RESI CHL1
IC C1   C2   C3   C4    1.5383  110.44   55.92  110.66   1.5367
IC C4   C2   *C3  O3    1.5367  110.66  120.28  109.14   1.4158
IC O3   C2   *C3  H3    1.4158  109.14  118.92  109.40   1.1155
IC C2   C3   O3   H3'   1.5311  109.14  -58.51  105.39   0.9593
IC C2   C3   C4   C5    1.5311  110.66  -55.96  111.70   1.5156
IC C5   C3   *C4  H4A   1.5156  111.70  121.99  109.16   1.1099
IC H4A  C3   *C4  H4B   1.1099  109.16  115.03  107.34   1.1142
IC C3   C4   C5   C10   1.5367  111.70   54.04  115.09   1.5304
IC C10  C4   *C5  C6    1.5304  115.09 -177.32  121.28   1.3432
IC C4   C5   C6   C7    1.5156  121.28 -178.39  123.88   1.5018
IC C7   C5   *C6  H6    1.5018  123.88  177.19  119.54   1.1001
IC C5   C6   C7   C8    1.3432  123.88   14.50  112.36   1.5506
IC C8   C6   *C7  H7A   1.5506  112.36  122.18  110.84   1.1114
IC H7A  C6   *C7  H7B   1.1114  110.84  118.17  109.17   1.1124
IC C6   C7   C8   C14   1.5018  112.36 -165.89  110.02   1.5202
IC C14  C7   *C8  C9    1.5202  110.02  121.07  110.84   1.5327
IC C9   C7   *C8  H8    1.5327  110.84  119.34  108.18   1.1123
IC C7   C8   C14  C13   1.5506  110.02  179.73  115.21   1.5247
IC C13  C8   *C14 C15   1.5247  115.21  126.69  117.86   1.5382
IC C13  C8   *C14 H14   1.5247  115.21 -116.05  105.83   1.1205
IC C8   C14  C15  C16   1.5202  117.86 -163.10  103.40   1.5360
IC C16  C14  *C15 H15A  1.5360  103.40  117.45  109.62   1.1113
IC H15A C14  *C15 H15B  1.1113  109.62  121.32  111.94   1.1082
IC C14  C15  C16  C17   1.5382  103.40    7.85  106.79   1.5620
IC C17  C15  *C16 H16A  1.5620  106.79  118.96  109.25   1.1107
IC H16A C15  *C16 H16B  1.1107  109.25  120.76  111.65   1.1090
IC C13  C16  *C17 C20   1.5401  104.94  132.02  112.36   1.5633
IC C13  C16  *C17 H17   1.5401  104.94 -111.76  106.42   1.1153
IC C17  C14  *C13 C12   1.5401  100.27  122.68  106.98   1.5408
IC C12  C14  *C13 C18   1.5408  106.98  122.91  110.83   1.5518
IC C14  C13  C18  H18A  1.5247  110.83   60.33  111.48   1.1077
IC H18A C13  *C18 H18B  1.1077  111.48  119.80  110.01   1.1086
IC H18A C13  *C18 H18C  1.1077  111.48 -121.00  111.71   1.1067
IC C14  C13  C12  C11   1.5247  106.98   56.78  111.10   1.5422
IC C11  C13  *C12 H12A  1.5422  111.10  121.37  111.21   1.1067
IC H12A C13  *C12 H12B  1.1067  111.21  118.82  108.68   1.1119
IC C9   C12  *C11 H11A  1.5593  113.54  121.67  107.06   1.1093
IC H11A C12  *C11 H11B  1.1093  107.06  115.98  108.75   1.1100
IC C10  C8   *C9  H9    1.5531  112.73 -114.54  104.68   1.1185
IC C9   C5   *C10 C19   1.5531  111.91 -120.04  108.03   1.5524
IC C19  C5   *C10 C1    1.5524  108.03 -119.87  109.26   1.5579
IC C5   C10  C19  H19A  1.5304  108.03 -172.88  110.67   1.1082
IC H19A C10  *C19 H19B  1.1082  110.67  118.48  111.77   1.1080
IC H19A C10  *C19 H19C  1.1082  110.67 -120.66  110.97   1.1095
IC C2   C10  *C1  H1A   1.5383  114.55  122.42  109.26   1.1104
IC C2   C10  *C1  H1B   1.5383  114.55 -120.71  108.29   1.1134
IC C1   C3   *C2  H2A   1.5383  110.44  121.16  109.41   1.1119
IC H2A  C3   *C2  H2B   1.1119  109.41  118.30  109.70   1.1112
IC C16  C17  C20  C22   1.5620  112.36   55.21  110.55   1.5476
IC C22  C17  *C20 C21   1.5476  110.55  125.88  113.32   1.5349
IC C21  C17  *C20 H20   1.5349  113.32  118.87  107.27   1.1157
IC C17  C20  C21  H21A  1.5633  113.32   64.90  110.93   1.1077
IC H21A C20  *C21 H21B  1.1077  110.93 -121.00  110.41   1.1104
IC H21A C20  *C21 H21C  1.1077  110.93  118.40  111.29   1.1085
IC C17  C20  C22  C23   1.5633  110.55 -174.59  115.12   1.5394
IC C23  C20  *C22 H22A  1.5394  115.12  120.23  109.35   1.1116
IC H22A C20  *C22 H22B  1.1116  109.35  117.13  108.75   1.1121
IC C20  C22  C23  C24   1.5476  115.12  172.50  112.25   1.5377
IC C24  C22  *C23 H23A  1.5377  112.25  121.13  109.69   1.1108
IC H23A C22  *C23 H23B  1.1108  109.69  118.14  108.99   1.1129
IC C22  C23  C24  C25   1.5394  112.25 -176.23  114.06   1.5418
IC C25  C23  *C24 H24A  1.5418  114.06  120.56  108.44   1.1132
IC H24A C23  *C24 H24B  1.1132  108.44  117.11  109.39   1.1121
IC C23  C24  C25  C26   1.5377  114.06  174.26  111.24   1.5378
IC C26  C24  *C25 C27   1.5378  111.24  119.63  112.86   1.5381
IC C26  C24  *C25 H25   1.5378  111.24 -119.50  108.47   1.1151
IC C24  C25  C26  H26A  1.5418  111.24 -178.53  110.52   1.1105
IC H26A C25  *C26 H26B  1.1105  110.52  120.00  110.36   1.1105
IC H26A C25  *C26 H26C  1.1105  110.52 -120.09  110.33   1.1106
IC C24  C25  C27  H27A  1.5418  112.86 -178.28  110.40   1.1105
IC H27A C25  *C27 H27B  1.1105  110.40  119.95  110.31   1.1105
IC H27A C25  *C27 H27C  1.1105  110.40 -119.82  110.77   1.1097
```

```
IC C1   C2   C3   C4    1.5383  110.44  -55.92  110.66   1.5367
IC C4   C2   *C3  O3    1.5367  110.66 -120.28  109.14   1.4158
IC O3   C2   *C3  H3    1.4158  109.14 -118.92  109.40   1.1155
IC C2   C3   O3   H3'   1.5311  109.14   58.51  105.39   0.9593
IC C2   C3   C4   C5    1.5311  110.66   55.96  111.70   1.5156
IC C5   C3   *C4  H4A   1.5156  111.70 -121.99  109.16   1.1099
IC H4A  C3   *C4  H4B   1.1099  109.16 -115.03  107.34   1.1142
IC C3   C4   C5   C10   1.5367  111.70  -54.04  115.09   1.5304
IC C10  C4   *C5  C6    1.5304  115.09  177.32  121.28   1.3432
IC C4   C5   C6   C7    1.5156  121.28  178.39  123.88   1.5018
IC C7   C5   *C6  H6    1.5018  123.88 -177.19  119.54   1.1001
IC C5   C6   C7   C8    1.3432  123.88  -14.50  112.36   1.5506
IC C8   C6   *C7  H7A   1.5506  112.36 -122.18  110.84   1.1114
IC H7A  C6   *C7  H7B   1.1114  110.84 -118.17  109.17   1.1124
IC C6   C7   C8   C14   1.5018  112.36  165.89  110.02   1.5202
IC C14  C7   *C8  C9    1.5202  110.02 -121.07  110.84   1.5327
IC C9   C7   *C8  H8    1.5327  110.84 -119.34  108.18   1.1123
IC C7   C8   C14  C13   1.5506  110.02 -179.73  115.21   1.5247
IC C13  C8   *C14 C15   1.5247  115.21 -126.69  117.86   1.5382
IC C13  C8   *C14 H14   1.5247  115.21  116.05  105.83   1.1205
IC C8   C14  C15  C16   1.5202  117.86  163.10  103.40   1.5360
IC C16  C14  *C15 H15A  1.5360  103.40 -117.45  109.62   1.1113
IC H15A C14  *C15 H15B  1.1113  109.62 -121.32  111.94   1.1082
IC C14  C15  C16  C17   1.5382  103.40   -7.85  106.79   1.5620
IC C17  C15  *C16 H16A  1.5620  106.79 -118.96  109.25   1.1107
IC H16A C15  *C16 H16B  1.1107  109.25 -120.76  111.65   1.1090
IC C13  C16  *C17 C20   1.5401  104.94 -132.02  112.36   1.5633
IC C13  C16  *C17 H17   1.5401  104.94  111.76  106.42   1.1153
IC C17  C14  *C13 C12   1.5401  100.27 -122.68  106.98   1.5408
IC C12  C14  *C13 C18   1.5408  106.98 -122.91  110.83   1.5518
IC C14  C13  C18  H18A  1.5247  110.83  -60.33  111.48   1.1077
IC H18A C13  *C18 H18B  1.1077  111.48 -119.80  110.01   1.1086
IC H18A C13  *C18 H18C  1.1077  111.48  121.00  111.71   1.1067
IC C14  C13  C12  C11   1.5247  106.98  -56.78  111.10   1.5422
IC C11  C13  *C12 H12A  1.5422  111.10 -121.37  111.21   1.1067
IC H12A C13  *C12 H12B  1.1067  111.21 -118.82  108.68   1.1119
IC C9   C12  *C11 H11A  1.5593  113.54 -121.67  107.06   1.1093
IC H11A C12  *C11 H11B  1.1093  107.06 -115.98  108.75   1.1100
IC C10  C8   *C9  H9    1.5531  112.73  114.54  104.68   1.1185
IC C9   C5   *C10 C19   1.5531  111.91  120.04  108.03   1.5524
IC C19  C5   *C10 C1    1.5524  108.03  119.87  109.26   1.5579
IC C5   C10  C19  H19A  1.5304  108.03  172.88  110.67   1.1082
IC H19A C10  *C19 H19B  1.1082  110.67 -118.48  111.77   1.1080
IC H19A C10  *C19 H19C  1.1082  110.67  120.66  110.97   1.1095
IC C2   C10  *C1  H1A   1.5383  114.55 -122.42  109.26   1.1104
IC C2   C10  *C1  H1B   1.5383  114.55  120.71  108.29   1.1134
IC C1   C3   *C2  H2A   1.5383  110.44 -121.16  109.41   1.1119
IC H2A  C3   *C2  H2B   1.1119  109.41 -118.30  109.70   1.1112
IC C16  C17  C20  C22   1.5620  112.36  -55.21  110.55   1.5476
IC C22  C17  *C20 C21   1.5476  110.55 -125.88  113.32   1.5349
IC C21  C17  *C20 H20   1.5349  113.32 -118.87  107.27   1.1157
IC C17  C20  C21  H21A  1.5633  113.32  -64.90  110.93   1.1077
IC H21A C20  *C21 H21B  1.1077  110.93  121.00  110.41   1.1104
IC H21A C20  *C21 H21C  1.1077  110.93 -118.40  111.29   1.1085
IC C17  C20  C22  C23   1.5633  110.55  174.59  115.12   1.5394
IC C23  C20  *C22 H22A  1.5394  115.12 -120.23  109.35   1.1116
IC H22A C20  *C22 H22B  1.1116  109.35 -117.13  108.75   1.1121
IC C20  C22  C23  C24   1.5476  115.12 -172.50  112.25   1.5377
IC C24  C22  *C23 H23A  1.5377  112.25 -121.13  109.69   1.1108
IC H23A C22  *C23 H23B  1.1108  109.69 -118.14  108.99   1.1129
IC C22  C23  C24  C25   1.5394  112.25  176.23  114.06   1.5418
IC C25  C23  *C24 H24A  1.5418  114.06 -120.56  108.44   1.1132
IC H24A C23  *C24 H24B  1.1132  108.44 -117.11  109.39   1.1121
IC C23  C24  C25  C26   1.5377  114.06 -174.26  111.24   1.5378
IC C26  C24  *C25 C27   1.5378  111.24 -119.63  112.86   1.5381
IC C26  C24  *C25 H25   1.5378  111.24  119.50  108.47   1.1151
IC C24  C25  C26  H26A  1.5418  111.24  178.53  110.52   1.1105
IC H26A C25  *C26 H26B  1.1105  110.52 -120.00  110.36   1.1105
IC H26A C25  *C26 H26C  1.1105  110.52  120.09  110.33   1.1106
IC C24  C25  C27  H27A  1.5418  112.86  178.28  110.40   1.1105
IC H27A C25  *C27 H27B  1.1105  110.40 -119.95  110.31   1.1105
IC H27A C25  *C27 H27C  1.1105  110.40  119.82  110.77   1.1097
```

```
RESI EPI
IC C1   C2   C3   C4    1.5383  110.44   55.92  110.66   1.5367
IC C4   C2   *C3  O3    1.5367  110.66 -120.28  109.14   1.4158
IC O3   C2   *C3  H3    1.4158  109.14 -118.92  109.40   1.1155
IC C2   C3   O3   H3'   1.5311  109.14  -58.51  105.39   0.9593
IC C2   C3   C4   C5    1.5311  110.66  -55.96  111.70   1.5156
IC C5   C3   *C4  H4A   1.5156  111.70  121.99  109.16   1.1099
IC H4A  C3   *C4  H4B   1.1099  109.16  115.03  107.34   1.1142
IC C3   C4   C5   C10   1.5367  111.70   54.04  115.09   1.5304
IC C10  C4   *C5  C6    1.5304  115.09 -177.32  121.28   1.3432
IC C4   C5   C6   C7    1.5156  121.28 -178.39  123.88   1.5018
IC C7   C5   *C6  H6    1.5018  123.88  177.19  119.54   1.1001
IC C5   C6   C7   C8    1.3432  123.88   14.50  112.36   1.5506
IC C8   C6   *C7  H7A   1.5506  112.36  122.18  110.84   1.1114
IC H7A  C6   *C7  H7B   1.1114  110.84  118.17  109.17   1.1124
IC C6   C7   C8   C14   1.5018  112.36 -165.89  110.02   1.5202
IC C14  C7   *C8  C9    1.5202  110.02  121.07  110.84   1.5327
IC C9   C7   *C8  H8    1.5327  110.84  119.34  108.18   1.1123
IC C7   C8   C14  C13   1.5506  110.02  179.73  115.21   1.5247
IC C13  C8   *C14 C15   1.5247  115.21  126.69  117.86   1.5382
IC C13  C8   *C14 H14   1.5247  115.21 -116.05  105.83   1.1205
IC C8   C14  C15  C16   1.5202  117.86 -163.10  103.40   1.5360
IC C16  C14  *C15 H15A  1.5360  103.40  117.45  109.62   1.1113
IC H15A C14  *C15 H15B  1.1113  109.62  121.32  111.94   1.1082
IC C14  C15  C16  C17   1.5382  103.40    7.85  106.79   1.5620
IC C17  C15  *C16 H16A  1.5620  106.79  118.96  109.25   1.1107
IC H16A C15  *C16 H16B  1.1107  109.25  120.76  111.65   1.1090
IC C13  C16  *C17 C20   1.5401  104.94  132.02  112.36   1.5633
IC C13  C16  *C17 H17   1.5401  104.94 -111.76  106.42   1.1153
IC C17  C14  *C13 C12   1.5401  100.27  122.68  106.98   1.5408
IC C12  C14  *C13 C18   1.5408  106.98  122.91  110.83   1.5518
IC C14  C13  C18  H18A  1.5247  110.83   60.33  111.48   1.1077
IC H18A C13  *C18 H18B  1.1077  111.48  119.80  110.01   1.1086
IC H18A C13  *C18 H18C  1.1077  111.48 -121.00  111.71   1.1067
IC C14  C13  C12  C11   1.5247  106.98   56.78  111.10   1.5422
IC C11  C13  *C12 H12A  1.5422  111.10  121.37  111.21   1.1067
IC H12A C13  *C12 H12B  1.1067  111.21  118.82  108.68   1.1119
IC C9   C12  *C11 H11A  1.5593  113.54  121.67  107.06   1.1093
IC H11A C12  *C11 H11B  1.1093  107.06  115.98  108.75   1.1100
IC C10  C8   *C9  H9    1.5531  112.73 -114.54  104.68   1.1185
IC C9   C5   *C10 C19   1.5531  111.91 -120.04  108.03   1.5524
IC C19  C5   *C10 C1    1.5524  108.03 -119.87  109.26   1.5579
IC C5   C10  C19  H19A  1.5304  108.03 -172.88  110.67   1.1082
IC H19A C10  *C19 H19B  1.1082  110.67  118.48  111.77   1.1080
IC H19A C10  *C19 H19C  1.1082  110.67 -120.66  110.97   1.1095
IC C2   C10  *C1  H1A   1.5383  114.55  122.42  109.26   1.1104
IC C2   C10  *C1  H1B   1.5383  114.55 -120.71  108.29   1.1134
IC C1   C3   *C2  H2A   1.5383  110.44  121.16  109.41   1.1119
IC H2A  C3   *C2  H2B   1.1119  109.41  118.30  109.70   1.1112
IC C16  C17  C20  C22   1.5620  112.36   55.21  110.55   1.5476
IC C22  C17  *C20 C21   1.5476  110.55  125.88  113.32   1.5349
IC C21  C17  *C20 H20   1.5349  113.32  118.87  107.27   1.1157
IC C17  C20  C21  H21A  1.5633  113.32   64.90  110.93   1.1077
IC H21A C20  *C21 H21B  1.1077  110.93 -121.00  110.41   1.1104
IC H21A C20  *C21 H21C  1.1077  110.93  118.40  111.29   1.1085
IC C17  C20  C22  C23   1.5633  110.55 -174.59  115.12   1.5394
IC C23  C20  *C22 H22A  1.5394  115.12  120.23  109.35   1.1116
IC H22A C20  *C22 H22B  1.1116  109.35  117.13  108.75   1.1121
IC C20  C22  C23  C24   1.5476  115.12  172.50  112.25   1.5377
IC C24  C22  *C23 H23A  1.5377  112.25  121.13  109.69   1.1108
IC H23A C22  *C23 H23B  1.1108  109.69  118.14  108.99   1.1129
IC C22  C23  C24  C25   1.5394  112.25 -176.23  114.06   1.5418
IC C25  C23  *C24 H24A  1.5418  114.06  120.56  108.44   1.1132
IC H24A C23  *C24 H24B  1.1132  108.44  117.11  109.39   1.1121
IC C23  C24  C25  C26   1.5377  114.06  174.26  111.24   1.5378
IC C26  C24  *C25 C27   1.5378  111.24  119.63  112.86   1.5381
IC C26  C24  *C25 H25   1.5378  111.24 -119.50  108.47   1.1151
IC C24  C25  C26  H26A  1.5418  111.24 -178.53  110.52   1.1105
IC H26A C25  *C26 H26B  1.1105  110.52  120.00  110.36   1.1105
IC H26A C25  *C26 H26C  1.1105  110.52 -120.09  110.33   1.1106
IC C24  C25  C27  H27A  1.5418  112.86 -178.28  110.40   1.1105
IC H27A C25  *C27 H27B  1.1105  110.40  119.95  110.31   1.1105
IC H27A C25  *C27 H27C  1.1105  110.40 -119.82  110.77   1.1097
```

Table S1. Average membrane properties in specified time intervals (ns)

Bilayer thickness ± SD (Å)					
Simulation	**0-100**	**100-200**	**200-300**	**300-400**	**400-500**
POPC	39.8 ± 0.5	39.9 ± 0.5	39.5 ± 0.4	39.9 ± 0.4	39.7 ± 0.4
CHL	44.9 ± 1.2	45.8 ± 0.3	46.4 ± 0.4	46.6 ± 0.3	46.3 ± 0.4
ENT	45.0 ± 1.2	46.2 ± 0.3	45.6 ± 0.3	45.9 ± 0.4	46.1 ± 0.3
EPI	44.5 ± 1.0	45.0 ± 0.4	44.9 ± 0.3	44.8 ± 0.4	44.8 ± 0.3
Area per POPC molecule ± SD (Å)					
Simulation	**0-100**	**100-200**	**200-300**	**300-400**	**400-500**
POPC	62.4 ± 0.9	62.1 ± 0.9	63.0 ± 0.9	62.3 ± 0.8	62.7 ± 0.7
CHL	55.3 ± 2.1	54.0 ± 0.5	53.2 ± 0.6	52.7 ± 0.4	53.4 ± 0.7
ENT	55.2 ± 2.1	53.6 ± 0.5	54.5 ± 0.6	53.8 ± 0.7	53.7 ± 0.6
EPI	56.2 ± 1.7	55.3 ± 0.6	55.7 ± 0.6	56.1 ± 0.7	55.8 ± 0.7
Area per cholesterol molecule ± SD (Å)					
Simulation	**0-100**	**100-200**	**200-300**	**300-400**	**400-500**
CHL	28.3 ± 1.0	27.6 ± 0.7	26.8 ± 0.8	27.1 ± 0.6	26.9 ± 0.7
ENT	28.0 ± 1.2	26.7 ± 0.9	27.0 ± 0.7	27.2 ± 0.7	27.0 ± 0.7
EPI	28.2 ± 1.4	28.5 ± 1.0	28.3 ± 0.9	28.0 ± 0.9	28.7 ± 0.8

Figure S1. Area per lipid as a function of time. CHL, ENT, EPI and POPC simulations are displayed in red, blue, green and black respectively.

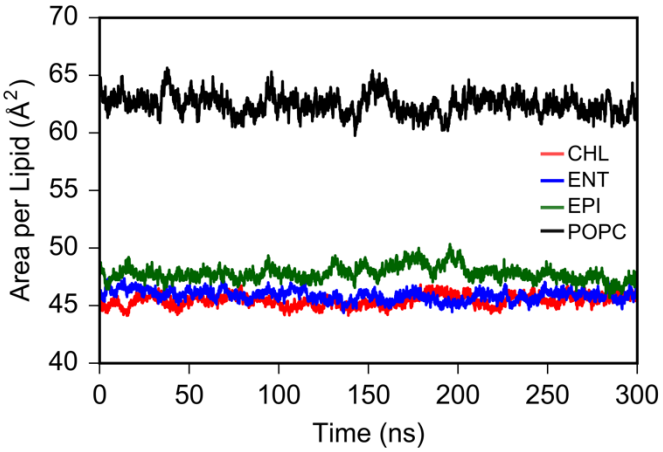

Figure S2. Radial distribution functions of POPC (A) O13/O14, (B) P, (C) C13/C14/C15, (D) N, (E) C12, (F) O11, (G) O12, (F) O22 and (H) O32 atoms with water. CHL, ENT, EPI and POPC simulations are displayed in red, blue, green and black respectively.

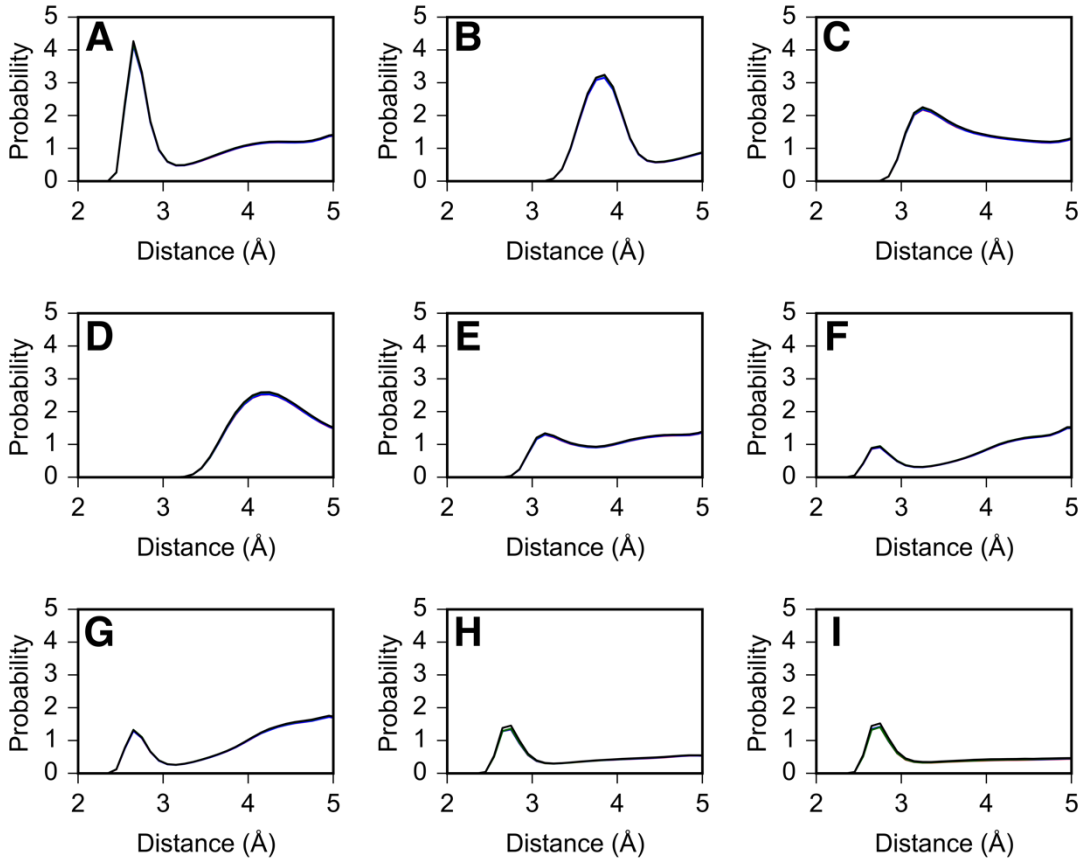

Figure S3. Radial distribution functions of cholesterol (A) O3, (B) C3, (C) C2, and (D) C4 atoms with water. CHL, ENT and EPI simulations are displayed in red, blue and green respectively. The red line (CHL) is directly underneath the green (ENT).

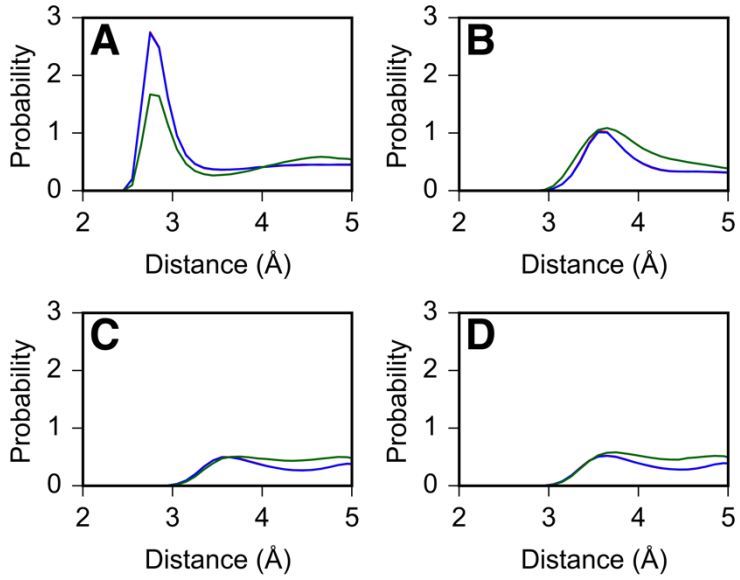

A.6 Influence of Cholesterol and its Stereoisomers on Members of the Serotonin Receptor Family

SUPPLEMENTARY INFORMATION

Influence of cholesterol and its stereoisomers on members of the 5-HT receptor family

Victoria Oakes[1] and Carmen Domene[1,2]

[1]Department of Chemistry, University of Bath, Claverton Down, Bath, BA2 7AY, UK, [2]Department of Chemistry, University of Oxford, Oxford, OX1 3TA, Oxford, UK

Figure S1. Interaction sites of membrane components in the 5-HT_{1B} receptor. 2D density maps of (A) POPC in $POPC1_{1B}$ and $POPC2_{1B}$, (B) ent-cholesterol and (C) POPC in $ENT1_{1B}$, $ENT2_{1B}$ and $ENT3_{1B}$, and (D) epi-cholesterol and (E) POPC in $EPI1_{1B}$, $EPI2_{1B}$ and $EPI3_{1B}$. Bin dimensions of 4 x 4 Å are normalized so that the maximum density is 1. Sites observed in multiple simulations (including simulations with cholesterol isomers in Figure S1) and described in the text are labelled. Transmembrane helices are numbered from 1 to 7; cholesterol and POPC sites are labelled as SX or PX respectively, where X is an arbitrary number to distinguish individual sites.

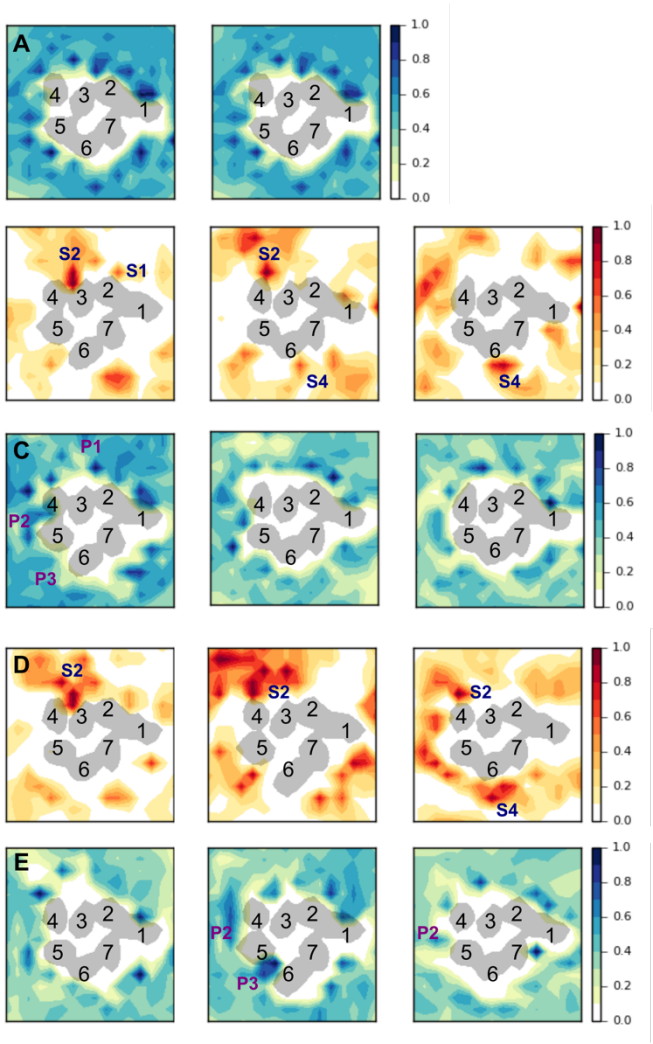

Figure S2. Minimum contact distance between amino acid P184 and membrane phospholipids, in (A) CHL_{1B}, (B) ENT_{1B}, (C) EPI_{1B} and (D) $POPC_{1B}$ simulations. This is determined by calculating the distance between the center of mass of all heavy atoms in both entities and identifying the minimum. Independent simulations 1, 2 and 3 are shown in red, blue and green respectively.

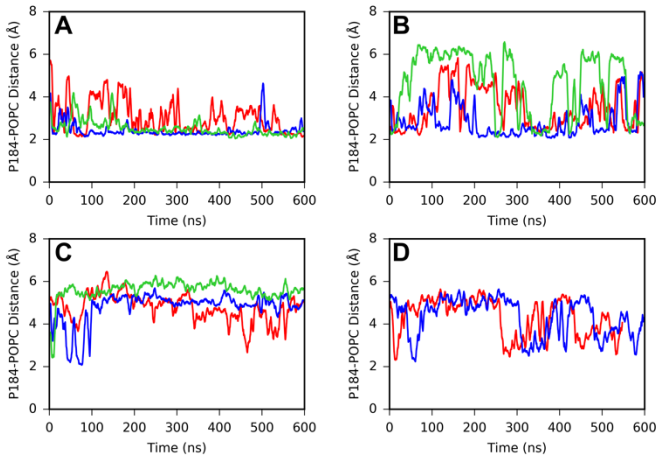

Figure S3. Minimum contact distance between extracellular loops, ECL2 (V200/V201) and ECL3 (M337), in (A) CHL_{1B}, (B) ENT_{1B}, (C) EPI_{1B} and (D) $POPC_{1B}$ simulations. This is determined by calculating the distance between the center of mass of all heavy atoms in both entities and identifying the minimum. Independent simulations 1, 2 and 3 are shown in red, blue and green respectively.

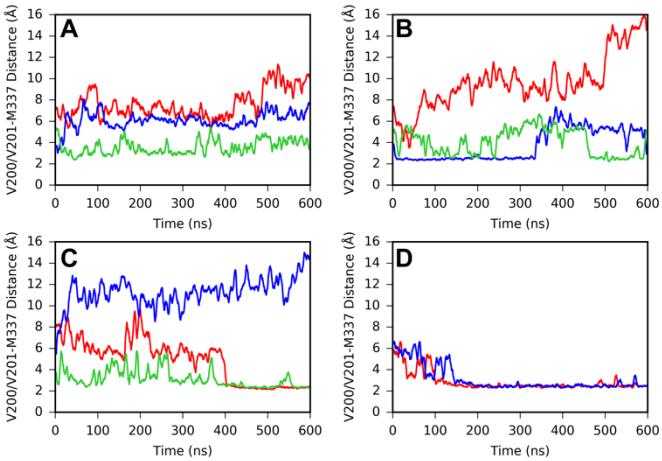

Figure S4. Minimum contact distance between residues P184 and N202 in ECL2, in (A) CHL_{1B}, (B) ENT_{1B}, (C) EPI_{1B} and (D) $POPC_{1B}$ simulations. This is determined by calculating the distance between the center of mass of all heavy atoms in both entities and identifying the minimum. Independent simulations are 1, 2 and 3 are shown in red, blue and green respectively.

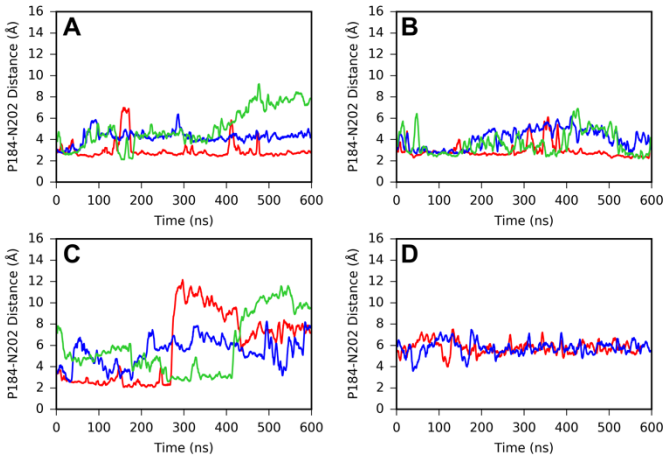

Figure S5. Interaction sites of membrane components in the 5-HT_{2B} receptor. 2D density maps of (A) POPC in $POPC1_{1B}$ and $POPC2_{1B}$, (B) ent-cholesterol and (C) POPC in $ENT1_{1B}$, $ENT2_{1B}$ and $ENT3_{1B}$, and (D) epi-cholesterol and (E) POPC in $EPI1_{1B}$, $EPI2_{1B}$ and $EPI3_{1B}$. Bin dimensions of 4 x 4 Å are normalized so that the maximum density is 1. Sites observed in multiple simulations (including simulations with cholesterol isomers in Figure S1) and described in the text are labelled. Transmembrane helices are numbered from 1 to 7; cholesterol and POPC sites are labelled as SX or PX respectively, where X is an arbitrary number to distinguish individual sites.

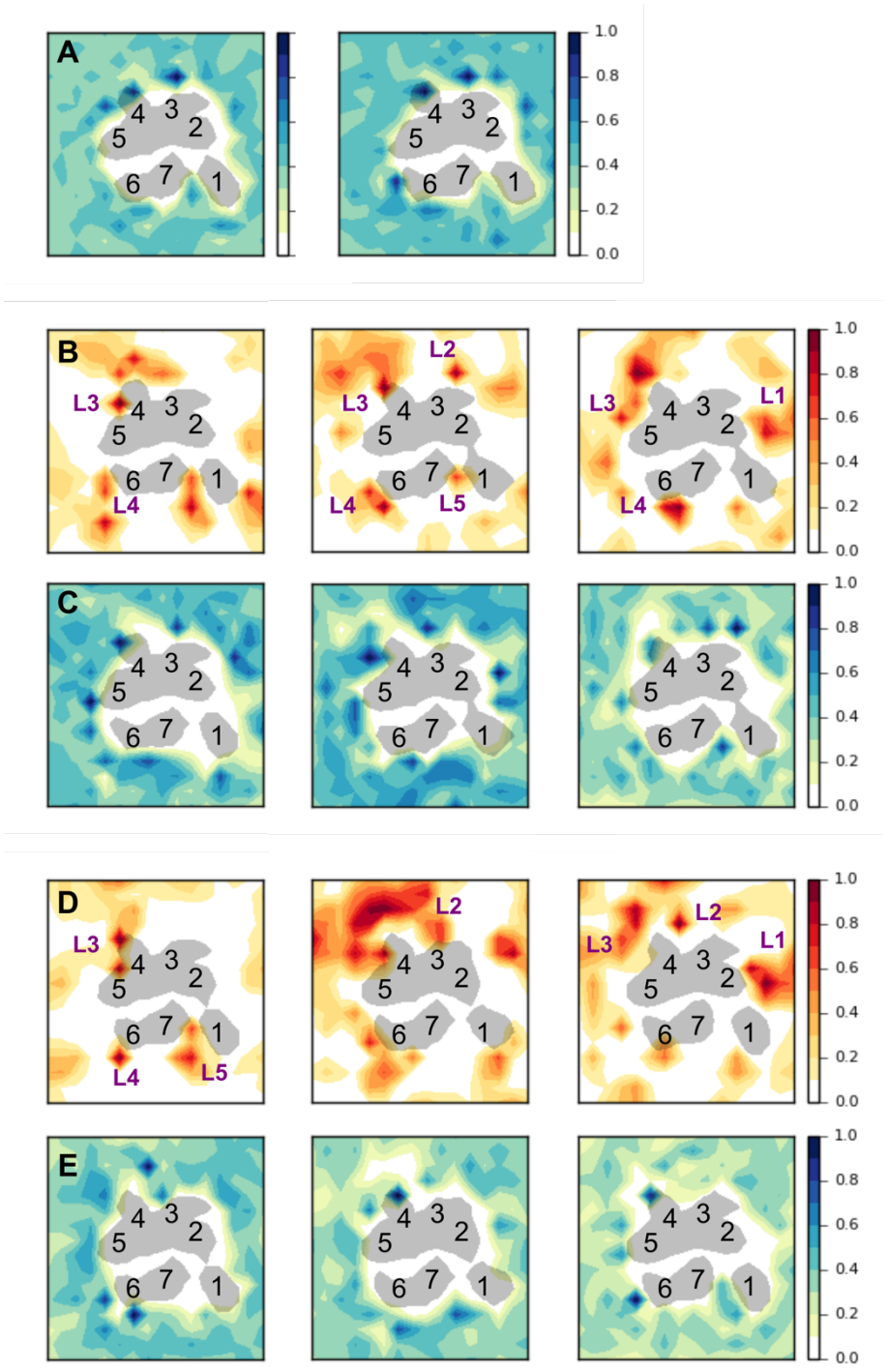

Table S1. Cluster analysis of the extracellular surface, defined as residues 184-205 and 337-349) using a 2.5 Å RMSD criteria. Representative structures of cluster 1 in $POPC1_{1B}$ and $CHL1_{1B}$ can be found in Figure 3.

Simulation Abbreviation	Cluster Frequency (%)	
	Cluster 1	Cluster 2
$CHL1_{1B}$	87	7
$CHL2_{1B}$	87	3
$CHL3_{1B}$	90	6
$ENT1_{1B}$	26	23
$ENT2_{1B}$	96	2
$ENT3_{1B}$	50	34
$EPI1_{1B}$	58	28
$EPI2_{1B}$	57	18
$EPI3_{1B}$	56	24
$POPC1_{1B}$	80	15
$POPC2_{1B}$	77	19
L1-$CHL1_{1B}$	78	7
L2-$CHL1_{1B}$	79	11
L1-$CHL2_{1B}$	71	8
L2-$CHL2_{1B}$	40	21
L1-$CHL3_{1B}$	70	8
L2-$CHL3_{1B}$	81	9
L1-$ENT1_{1B}$	74	10
L2-$ENT1_{1B}$	87	7
L1-$ENT2_{1B}$	39	26
L2-$ENT2_{1B}$	73	12
L1-$ENT3_{1B}$	82	12
L2-$ENT3_{1B}$	60	27
L1-$EPI1_{1B}$	51	37
L2-$EPI1_{1B}$	65	17
L1-$EPI2_{1B}$	56	22
L2-$EPI2_{1B}$	58	24
L1-$EPI3_{1B}$	70	9
L2-$EPI3_{1B}$	53	22
L1-$POPC1_{1B}$	78	8
L2-$POPC1_{1B}$	30	24
L1-$POPC2_{1B}$	35	32
L2-$POPC2_{1B}$	77	9
L1-$POPC3_{1B}$	45	25
L2-$POPC3_{1B}$	67	11

Appendix B: Additional Published Material

B1 Voltage-Gated Sodium Channels: Mechanistic Insights from Atomistic Molecular Dynamics Simulations, *Curr. Top. Memb.,* 2016

B.1.1 Authorship and Permissions

<table>
<tr><td colspan="10">This declaration concerns the article entitled</td></tr>
<tr><td colspan="10">Voltage-Gated Sodium Channels: Mechanistic Insights from Atomistic Molecular Dynamics Simulations</td></tr>
<tr><td colspan="10">Publication status (tick one)</td></tr>
<tr><td>Draft manuscript</td><td></td><td>Submitted</td><td></td><td>In review</td><td></td><td>Accepted</td><td></td><td>Published</td><td>✓</td></tr>
<tr><td>Publication details</td><td colspan="9">Current Topics in Membranes, 2016, 78, 183-241
DOI: doi: 10.1016/bs.ctm.2015.12.002
Online publication date: 14 March 2016</td></tr>
<tr><td>Candidates contribution to the paper (detailed and also given as a percentage)</td><td colspan="9">The candidate contributed to/considerably contributed/predominantly executed the…
Formulation of ideas (90%):
V. Oakes and C. Domene contributed to the content.

Design of methodology:
NA

Experimental work:
NA

Presentation of data in journal format (90%):
V. Oakes: Main author of manuscript
S. Furini: Critically assessed and appended manuscript
C. Domene: Critically assessed and appended manuscript</td></tr>
<tr><td>Statement from Candidate</td><td colspan="9">This paper reports on original research I conducted during the period of my Higher Degree by Research candidature.</td></tr>
<tr><td>Signed</td><td colspan="5"></td><td>Date</td><td colspan="3"></td></tr>
</table>

CHAPTER SEVEN

Voltage-Gated Sodium Channels: Mechanistic Insights From Atomistic Molecular Dynamics Simulations

V. Oakes*, S. Furini[§] and C. Domene*,[¶,1]
*King's College London, London, United Kingdom
[§]University of Siena, Siena, Italy
[¶]University of Oxford, Oxford, United Kingdom
[1]Corresponding author: E-mail: carmen.domene@kcl.ac.uk

Contents

Abstract

The permeation of ions and other molecules across biological membranes is an inherent requirement of all cellular organisms. Ion channels, in particular, are responsible for the conduction of charged species, hence modulating the propagation of electrical signals. Despite the universal physiological implications of this property, the molecular functioning of ion channels remains ambiguous. The combination of atomistic structural data with computational methodologies, such as molecular dynamics (MD) simulations, is now considered routine to investigate structure–function relationships in biological systems. A fuller understanding of conduction, selectivity,

Current Topics in Membranes, Volume 78
ISSN 1063-5823
http://dx.doi.org/10.1016/bs.ctm.2015.12.002

and gating, therefore, is steadily emerging due to the applicability of these techniques to ion channels. However, because their structure is known at atomic resolution, studies have consistently been biased toward K^+ channels, thus the molecular determinants of ionic selectivity, activation, and drug blockage in Na^+ channels are often overlooked. The recent increase of available crystallographic data has eminently encouraged the investigation of voltage-gated sodium (Na_V) channels via computational methods. Here, we present an overview of simulation studies that have contributed to our understanding of key principles that underlie ionic conduction and selectivity in Na^+ channels, in comparison to the K^+ channel analogs.

List of Abbreviations

PD	Pore domain
SF	Selectivity filter
TRP	Transient receptor potential
VGIC	Voltage-gated ion channel
VSD	Voltage sensor domain

1. INTRODUCTION

Ion channels are an important family of integral membrane proteins that are responsible for passive transport across biological membranes. Gene sequencing has identified over 400 alleged ion channels, yet only a fragment of these have been cloned, functionally tested, and crystallized (Bagal et al., 2013). Therefore, despite their ubiquitous distribution in tissues throughout all living organisms and their decisive roles in fundamental processes such as cell proliferation, nerve transmission, muscle contraction, sensory transduction and blood pressure regulation ion channels are considerably underexploited by targeted drug therapies (Bagal et al., 2013). Furthermore, conglomerates of ailments, known as "channelopathies," are the consequence of ion channel mutations and subsequent functional alterations (Zaydman, Silva, & Cui, 2012).

The widespread physiological implications of ion channels emanate from the modulation of electrical signals across the cellular membrane. This occurs by facilitating the passive diffusion of ionic species down their electrochemical gradient between periplasmic and cytoplasmic compartments. The permeation pathway is ordinarily "gated" on the application of external stimuli; for example, adjustment of transmembrane potentials (voltage-gated ion channels (VGIC)), ligand binding (ligand-gated ion channels), and mechanical stretch (mechanosensitive channels) can induce transformations

between open and closed states. A constricted region of the pore, known as the selectivity filter, imposes further restraints on conduction, by discrimination between ionic species. Selectivity, as this property is known, is responsible for K^+/Na^+ permeability ratios of 1000:1 and 1:8 in K^+ and Na^+ channels, respectively (Hille, 1992).

The understanding of such channel properties at the atomic level using computational techniques has traditionally been focused toward K^+ channels due to the availability of crystallographic data, while the principles determining conduction in Na^+ channels remain largely unsolved. The publication of the crystal structure of the Na_VAb α-subunit (Payandeh, Scheuer, Zheng, & Catterall, 2011), a mutated voltage-gated Na^+ channel from *Arcobacter butzleri* (Fig. 1A), and subsequent analogous structures from bacterial sources (Bagnéris et al., 2013; McCusker et al., 2012; Payandeh, Gamal El-Din, Scheuer, Zheng, & Catterall, 2012; Shaya et al., 2014) in the last 5 years has invigorated interest into the workings of Na^+ channels, resulting in numerous exploratory computational studies. In this chapter, we provide a comprehensive survey of the available X-ray crystal data and accompanying simulation studies that have been undertaken to discern the fundamental features regulating permeation and selectivity in Na^+ channels, with particular focus on voltage-gated sodium (Na_V) channels. The atomic structures of associated β-subunits have recently been determined (Gilchrist, Das, Van Petegem, & Bosmans, 2013; Namadurai et al., 2014), yet in this review, the focus is on the principal subunits (designated α or α1) which are responsible for the voltage-gated ion conductance, the defining characteristic of these proteins.

2. VOLTAGE-GATED SODIUM CHANNELS

Na_V channels form part of the VGIC family, which contains a variety of potassium, sodium, calcium, chloride, and transient receptor potential (TRP) ion channels, of which Na_V was the first to be cloned (Noda et al., 1984). Currently, based on common structural and functional properties, with distinct expression, regulatory, and pharmacological profiles, nine members of the Na_V family have been identified ($Na_V1.1$–$Na_V1.9$).

Na_V channels are critical for the generation of action potentials in neurons and other excitable cells. Most biological membranes experience a high-Na^+/low-K^+ concentration on the extracellular surface and a low-Na^+/high-K^+ concentration on the intracellular surface, generating

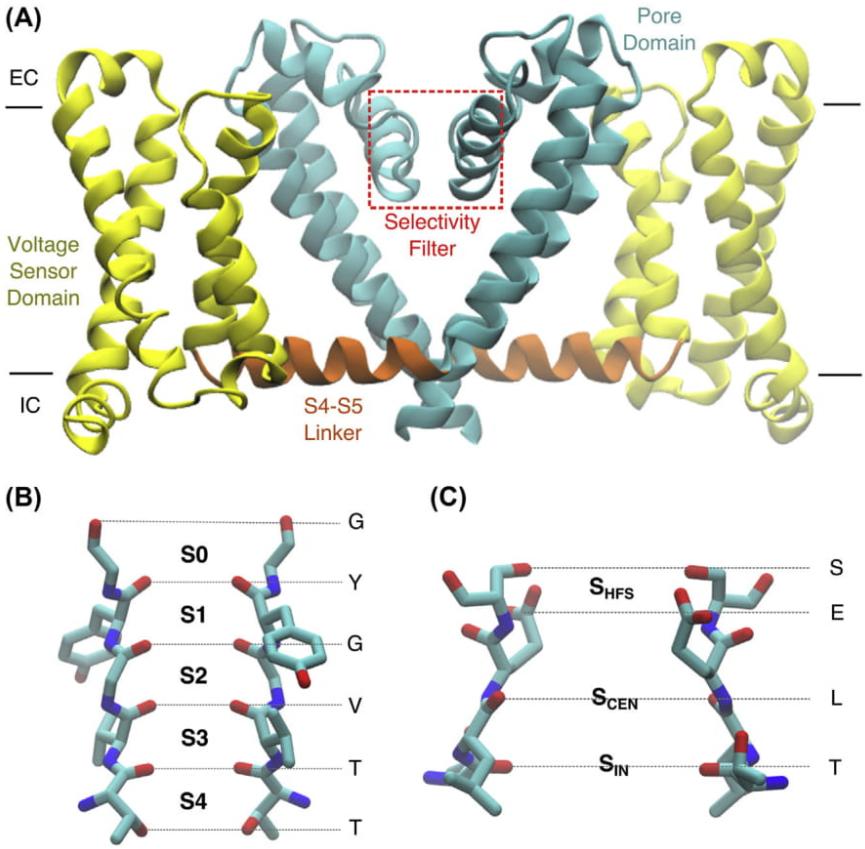

Figure 1 (A) Overall architecture of a voltage-gated ion channel as represented by the crystal structure of Na_VAb (PDB ID: 3RVY) in a closed conformation. Only two chains are shown for clarity. The voltage sensor domain (VSD) comprises transmembrane helices S1–S4, with S5 and S6 constituting the pore domain (PD) in cyan (light gray in print versions); the S4–S5 linker (in orange (gray in print versions)) is responsible for conferring conformational changes between the VSD and the PD on voltage activation. The selectivity filter is an integral part of the PD at the extracellular entrance to the pore. (B) Structure of a K^+ selective selectivity filter from the prototypical K^+ channel, KcsA (PDB ID: 1K4C). Binding sites are clearly defined by surrounding carbonyl oxygen atoms directed toward the pore axis. (C) Structure of a prototypical Na^+ selective selectivity filter from Na_VAb (PDB ID: 3RVY), with proposed binding sites labeled.

apt conditions for passive Na^+ influx and K^+ efflux in their respective channels. At typical negative resting potential (ie, −60 mV), both K_V and Na_V activation gates are closed. Under depolarizing conditions Na_V channels open, allowing diffusion of Na^+ ions through the central pore; this causes further depolarization inducing a large inward current. K_V channels respond

slower than Na_V channels to depolarization; therefore, delayed K^+ efflux is observed and an overall positive membrane potential results. At the peak of depolarization, repolarization is initiated by the inactivation of Na_V and the opening of K_V channels. By the generation of a nascent electrical signal in this way, VGICs initiate action potentials in excitable cells in various tissues in the heart, brain, and nervous system.

The expression on Na_V channels is not limited to excitable cells; the role of Na_V channels in astrocytes, NG2 cells, microglia, macrophages, and cancer cells is currently under investigation (Black & Waxman, 2013). The dysfunction of Na_V channels has been affiliated with a myriad of disorders such as pain, migraine, impaired movement, epilepsy, and cardiac arrhythmias (Mantegazza, Curia, Biagini, Ragsdale, & Avoli, 2010). Currently, treatment of these disorders is serviced by the binding of small organic molecules, such as local anesthetics, to block the channels (Bagal et al., 2013). However, due to the high structural and sequence homology (Fig. 2), subtype targeting can rarely be achieved, increasing the risk of inimical side effects (England & de Groot, 2009). Therefore, understanding of the molecular determinants of conduction, gating, and drug binding in ion channels is required to develop the next generation of subtype specific pharmaceuticals.

3. STRUCTURAL BASIS OF K^+ VERSUS Na^+ CONDUCTION

Hodgkin and Keynes provided the first insights into conduction in K^+ channels, proposing a "knock-on" mechanism of ionic conduction, associated with concerted transitions of individual ions in a single-file manner through a narrow pore (Hodgkin & Keynes, 1955). In addition, various theories for selectivity were proposed concerning the hydration free energy (Eisenman, 1962; Eisenman & Horn, 1983), coordination number, and the size difference of K^+ and Na^+ ions (Bezanilla & Armstrong, 1972). Furthermore, sequence analysis and complementary mutagenesis studies of K^+ channels identified a conserved sequence, TVGYG, which confers ionic selectivity, hence coined the selectivity filter (Heginbotham, Lu, Abramson, & MacKinnon, 1994; Smart, Goodfellow, & Wallace, 1993). The X-ray crystal structure of KcsA, from *Streptomyces lividans*, provided the first atomistic structural information, revealing key insights into the conduction/selectivity mechanisms of K^+ channels (Doyle et al., 1998). Developments concerning expression, purification, and crystallization of ion

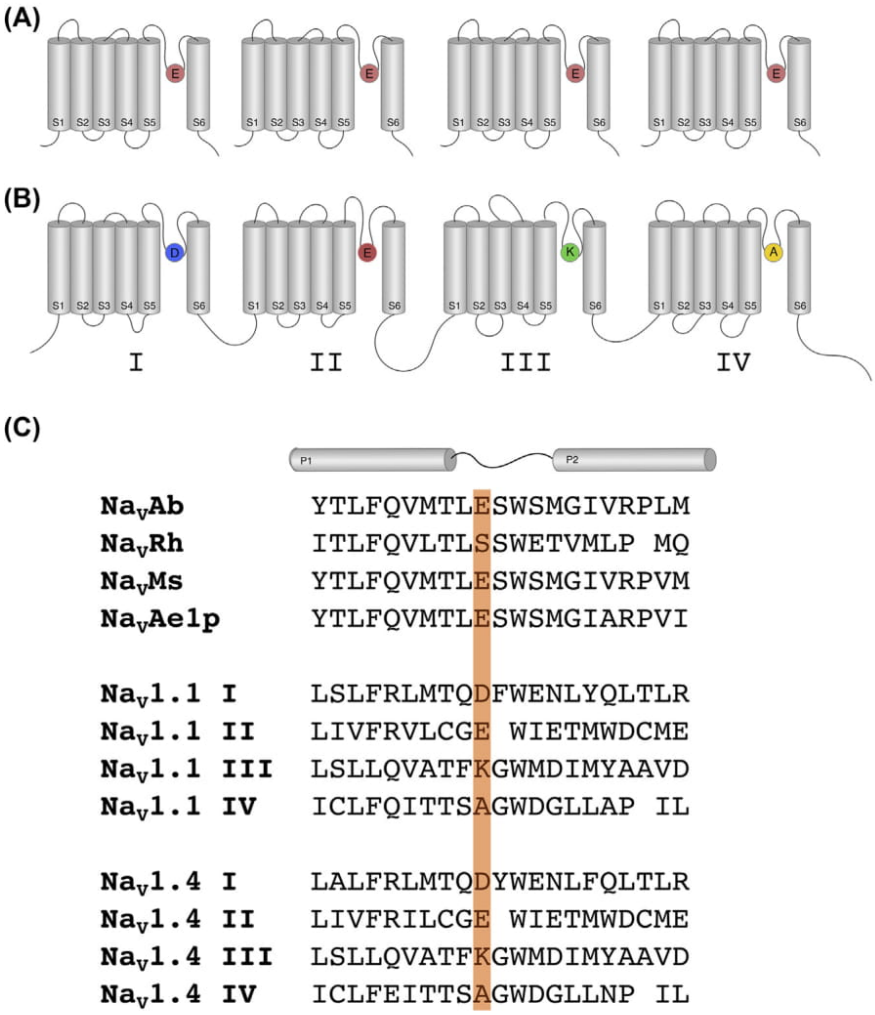

Figure 2 Topology and sequence data of voltage-gated sodium channels from prokaryotic and eukaryotic origins. (A) General representation of Na_V channel architecture from bacterial channels: four homologous subunits comprising voltage-sensor (S1—S4) and pore-forming (S5—S6) domains, containing the signature EEEE sequence, form the channel. (B) Eukaryotic channels share a similar tetrameric architecture, yet in a continuous polypeptide chain, with nonconserved sequences in individual domains. In this case, DEKA constitutes the characteristic SF ring, as illustrated in (C). Sequence alignments of the selectivity filter and surrounding pore domain in select bacterial (Na_VAb, Na_VRh, Na_VMs, NaVAe1p) and mammalian (Na_V1.1, Na_V1.4) channels; the signature SF sequence is highlighted in orange (light gray in print versions) (Payandeh & Minor, 2015).

channels have now lead to a wealth of available K^+ channel crystal structures (Brohawn, del Marmol, & MacKinnon, 2012; Doyle et al., 1998; Jiang et al., 2003; Kuo et al., 2003; Long, Campbell, & Mackinnon, 2005; Miller & Long, 2012). K^+ channels can exist in numerous activation states, most simply defined as open, closed, and inactivated. A range of these is sampled throughout these structures, providing additional clues into the gating mechanism of K^+ channels.

Throughout K^+ channels, a fundamental pore structure is conserved. The channel is formed from a symmetrical arrangement of four identical subunits composed of inner and outer transmembrane α-helices connected by a pore loop. The latter contains a pore helix and the signature selectivity sequence, TVGYG. A water-filled cavity, directly connected to the cytoplasm, is present underneath the selectivity filter to overcome large energetic barriers accompanying penetration of the hydrophobic core of the surrounding membrane by ionic species (Parsegian, 1969). In the open state of the channel, passage of ions is unrestricted from the cavity to the cytoplasm. In the closed state, the inner helices coalesce, via bending at a conserved glycine residue, preventing ion translocation and intra- and extracellular water exchange. A wide range of external stimuli modulates cytoplasmic gating of this sort, interceded by supplementary structural domains in some cases.

In K_V channels, an additional four transmembrane segments in each subunit comprise the voltage sensor domain (VSD), which regulates channel opening. The molecular basis of voltage sensing and gating was elucidated by the X-ray crystal structure of K_VAP from *Aeropyrum pernix* at 3.2 Å resolution with the isolated VSD at 1.9 Å (Jiang et al., 2003). The VSD segments, denoted S1–S4, arrange in an antiparallel α-helical bundle, attached to the "traditional" pore helices, S5–S6. Between four and seven repeat motifs containing a positively charged residue, ordinarily arginine, succeeded by two hydrophobic residues, constitutes the conserved S4 VSD segment that is deemed the activation gate (Stuhmer et al., 1989) The assemblages of charge clusters in this region stabilize S4 within the membrane and facilitate channel gating by interactions with S1–S3 (Long, Tao, Campbell, & MacKinnon, 2007). When stimulated by a change in the transmembrane voltage, movement of S4 prompts rearrangement of the pore-lining helices, via the S4–S5 linker, thus controlling the passage of ions.

Ion permeation, of ionic species other than K^+, is blocked at the selectivity filter. The KcsA structure revealed a selectivity filter optimized for favorable binding and efficient conduction of K^+ ions. In physiological K^+

concentrations, the selectivity filter residues arrange to form rings of carbonyl oxygen atoms directed toward the center of the pore axis (Fig. 1B). With the added contribution of threonine side-chain oxygen atoms, four adjoining sites are formed, namely S1−S4, which are able to bind dehydrated ions in a cage-like structure. Further binding sites for "partially" hydrated K^+ have been identified at the extracellular entrance (S0, S_{EXT}) and within the central cavity (S_C). Stabilization of ions in S_C is a consequence of the helix-dipole effect from the above pore helices (Aqvist, Luecke, Quiocho, & Warshel, 1991; Furini, Zerbetto, & Cavalcanti, 2007; Jogini & Roux, 2005). Specific salt bridges and hydrogen bonding with proximal helices and solvent generally stabilize the selectivity filter (Cordero-Morales, Jogini, Chakrapani, & Perozo, 2011). However, a further KcsA structure, in low K^+/high Na^+ concentrations, displayed significant distortions in the selectivity filter rendering the channel impermeable to K^+, Na^+, and even water (Zhou, Morais-Cabral, Kaufman, & MacKinnon, 2001). This structure has been associated with an inactivated state, reminiscent of C-type inactivation, a mechanism of gating characterized by conformational changes in the proximity of the selectivity filter which prevent conduction (Cuello, Jogini, Cortes, & Perozo, 2010).

In contrast to K_V channels, the molecular structure of eukaryotic Na_V channels remains uncharacterized. Crystallographic data of bacterial Na_V channels, of which the first structure, (mutant) Na_VAb, was published in 2011 (Payandeh et al., 2011) with numerous full length (Na_VRh, wild-type Na_VAb) (Bagnéris et al., 2013; Payandeh et al., 2012; Zhang et al., 2012) and pore-only structures to follow (Na_VMs, Na_VAe1p) (McCusker et al., 2012; Shaya et al., 2014), have provided, to date, the greatest molecular insights of Na_V channels at the atomic level.

Bacterial Na_V channels display a conserved structure similar to that of K^+ channels (Fig. 1A). As noted previously, four identical subunits arranged around a large central cavity that can accommodate and stabilize hydrated ions. The P-loop region contains a similar α-helix, with the addition of a unique second pore helix in an antiparallel configuration (Fig. 1A). The available structures display remarkable similarities with Cα superposition of monomer subunits comfortably under 1 Å in most cases (Payandeh & Minor, 2015), and only subtle differences in the symmetry of the pore helices with respect to the pore axis (Furini & Domene, 2013).

A novel finding in Na_VAb pore architecture is the presence of lateral openings, termed fenestrations, directly connecting the central pore to the surrounding membrane. In Na_VAb, membrane phospholipids penetrate these cavities, providing a further physical block to conduction in the pore

(Payandeh et al., 2011). Furthermore, these fenestrations may provide an additional entry route for small neutral or hydrophobic molecules and will therefore have implications for targeted channel blockage. Analogous fenestrations have recently been identified in multiple members of the two-pore domain K^+ channel (K_{2P}) family (Brohawn et al., 2012; Miller & Long, 2012).

The Na_V VSDs are analogous to those found in K_v channels. In Na_VAb, interactions of S4 with conserved intracellular and extracellular charge clusters suggest that the VSD is in an activated conformation (Payandeh et al., 2011). Therefore, Na_VAb is in a supposed "preopen" state in which the VSD is in an active state yet the cytoplasmic entrance is closed. Subtle differences in the conformational, and hence activation, state are observed throughout the available Na_V VSD structures; perspectives on voltage-sensing mechanisms as a consequence of these observations are outlined in a recent review by Payandeh and Minor (2015).

The resolved selectivity filter structure has also provided significant contributions to the understanding of Na^+ conduction. The sequence and structure is clearly divergent from K^+ channels, being notably wider and shorter, and comprised of four amino acids whose side chains partially line the pore (Fig. 1C). An arrangement of four glutamates, the so-called EEEE ring, forms the mouth of the selectivity filter in Na_VAb, consistent with experimental studies that implicated an anionic region of high-field strength (Hille, 1971, 1972) composed of Glu side chains (Heinemann, Terlau, Stuhmer, Imoto, & Numa, 1992; Sun, Favre, Schild, & Moczydlowski, 1997) in the selective conduction of Na^+ over K^+. The equivalent sequence in eukaryotic sodium channels, the DEKA motif, has also been affiliated with channel selectivity by mutagenesis studies (Favre, Moczydlowski, & Schild, 1996; Sun et al., 1997). Sequence alignments of the SF and surrounding PD in select bacterial (Na_VAb, Na_VRh, Na_VMs, Na_VAe1p) and mammalian ($Na_V1.1$, $Na_V1.4$) channels are shown in Fig. 2.

Na_VAb (with mutations I217C and M221C) and Na_VMs displayed symmetrical selectivity filter structures as above and are therefore considered conductive states. However, Na_VRh (Zhang et al., 2012) contains a dissimilar selectivity filter sequence, TLSSWE substituting TLESWS; therefore, the outer ring is comprised of serine residues, which adopt nonuniform conformations resulting in a 1−2 Å reduction in selectivity filter radii. Notable asymmetry is also observed in wild-type Na_VAb. Therefore, both are thought to correspond to inactivated states.

Despite the inability to resolve the location of Na^+ ions within the selectivity filter, on the basis of structural data three binding sites were proposed in Na_VAb. Firstly, the side chain of Glu177 (S_{HFS}) provides a negatively charged region at the extracellular entrance that can feasibly attract positively charged ions. Deeper sites formed of rings of carbonyl atoms from Leu76 (S_{CEN}) and Thr175 (S_{IN}) are proposed to form the remainder of the permeation pathway, with the latter sites potentially binding Na^+ ions via hydrogen bonding with a square array of water molecules forming the ions solvation shell. All binding sites are, therefore, amenable to hydrated ions, suggesting that in stark contrast to K^+ channels, sodium ions can traverse the entire length of the channel without full desolvation.

It is worth noting that all published structures to date are of prokaryotic origin; eukaryotic Na_V channels are comprised of a single polypeptide chain containing over ~2000 amino acids, arranged into four homologous transmembrane domains. A schematic representation of the basic topology of Na_V channels from prokaryotic and eukaryotic origins is presented in Fig. 2. The general representation of Na_V channel architecture from bacterial channels shows four homologous subunits comprising voltage-sensor (S1–S4) and pore-forming (S5–S6) domains, containing the signature EEEE sequence (Fig. 2). Further differences may be observed in eukaryotic species where the equivalent selectivity filter ring sequence is DEKA in contrast with EEEE (Na_VAb) and SSSS (Na_VRh). Note that eukaryotic channels share a similar tetrameric architecture, yet in a continuous polypeptide chain, with nonconserved sequences in individual domains. Therefore, crystallization of eukaryotic channels will markedly aid the advancement of this field.

4. OVERVIEW OF COMPUTATIONAL STUDIES

Crystallographic data essentially only provides static structural information, with limited indications of the operations in a biological setting. Therefore, computational studies utilizing molecular dynamics (MD) simulations are employed to supplement experimental data and gain time-dependent information on biological systems.

In MD simulations, integration of Newton's equations of motion, via an initial potential energy function, yields a trajectory containing the time evolution of the system. Accordingly, dynamical information can be gained at the atomistic level. The analytic expression for the energy, known as the *force field*, is composed of numerous functions approximating inter- and intramolecular energetic contributions. Various forms of this expression have been developed

for simulations of biological molecules, including, but not limited to, the CHARMM (Chemistry at Harvard Molecular Mechanics) (Brooks et al., 1983), AMBER (Assisted Model Building with Energy Requirement) (Cornell et al., 1995), GROMACS (Groningen Machine for Chemical Simulation) (Berendsen, van der Spoel, & van Drunen, 1995) and OPLS (Optimized Potentials for Liquid Simulations) (Jorgensen & Tirado-Rives, 1988) force fields. The availability of force field parameters for proteins, lipids, ions, and water, alongside defined protocols for the parameterization of novel drug molecules, equips the user with appropriate tools to study the behavior of ion channels embedded in model membranes and the identification of potential drug binding sites, for example.

The availability of accurate force fields is the first necessary condition for the analysis of ion conduction by atomistic simulations, the second one being the possibility to obtain statistically robust estimates of the conduction properties by sampling the ion configurations with MD trajectories. The most direct method to sample ion configurations in an MD trajectory is certainly to simulate the ion channel in the presence of an electrochemical driving force and to observe ion conduction as it happens. In simulations with periodic boundary conditions, a straightforward strategy for simulating the presence of a driving force is to apply a constant electric field in the direction orthogonal to the membrane (Gumbart, Khalili-Araghi, Sotomayor, & Roux, 2012). An alternative strategy is to include in the simulation domain two parallel lipid membranes, which divide the space in two separate compartments. In this way, it is possible to impose an electrochemical gradient between the two sides of each membrane by controlling the ion concentrations in the two compartments (Kutzner, Grubmüller, de Groot, & Zachariae, 2011). In order to analyze ion conduction by these strategies it is necessary to simulate trajectories sufficiently long to sample numerous conduction events. For a typical ion channel (conductance 10–50 pS) at physiological condition (membrane potential in the range ±100 mV) it is necessary to simulate tens of microseconds in order to obtain a statistically robust estimate of the conductance. A different approach for the analysis of the conduction properties of an ion channel is to estimate the potential of mean force (PMF) along a restricted set of reaction coordinates. Several algorithms exist to accelerate sampling along a predefined set of reaction coordinates. "Umbrella sampling" which uses a biased potential to transform a system between thermodynamic states has been widely used in the field of ion channels, but examples of applications of other approaches, such as metadynamics (Stock, Delemotte, Carnevale, Treptow, & Klein, 2013), adaptive

biasing force (Zuniga, Marquez, Gonzalez-Nilo, Chipot, Cid, Sepulveda, & Niemeyer, 2011), or steered-MD (Ngo, Stefanovski, Haas, & Farley, 2014) were also reported in the literature. Compared to the direct sampling of ion conduction in simulations with a driving force, the computational cost of PMF calculations might be significantly lower. However, these methods do not provide a direct estimate of the channel conductance, and the choice of the reaction coordinates might be critical.

MD simulations, and accompanying techniques, have become established methods to study K^+ channels in atomistic detail. We direct the reader to accomplished reviews (Furini & Domene, 2013; Roux, 2005) for an extensive overview of this field, yet we highlight a notable success in determining the conduction mechanism: the predominant selectivity filter conformations (Morais-Cabral, Zhou, & MacKinnon, 2001), w-S2-w-S4 and S1-w-S3-w, were identified in multiple MD simulations (Bernèche & Roux, 2000; Domene, Klein, Branduardi, Gervasio, & Parrinello, 2008; Domene & Sansom, 2003) and confirmed by free energy perturbation (FEP) techniques (Aqvist & Luzhkov, 2000) leading to the recognition of a "knock-on" mechanism, driven by the approach of K^+ from the central cavity and subsequent ion−ion repulsion, summarized in Fig. 3 (Morais-Cabral et al., 2001). Free energy calculations later showed that cation pairs moving through the selectivity filter without intervening water molecules are energetically feasible (Furini & Domene, 2009). In this mechanism, in addition to direct K^+−K^+ contacts, vacancies are also involved during the permeation event. A schematic representation of both mechanisms is illustrated in Fig. 3. FEP methods were also used to demonstrate a significant energetic preference for K^+ over Na^+ in the selectivity filter of K^+ channels (Berneche & Roux, 2001; Noskov & Roux, 2006). Specifically, S2 was identified as a highly selective, S1 and S3 displayed moderate selectivity whereas S4 provided a nonselective site, giving insights into the molecular determinants of selectivity in K^+ channels (Luzhkov & Åqvist, 2001).

Technical progressions concerning the development of parallel computing algorithms have resulted in an expansion of the phenomena that can be sampled throughout molecular simulations. D.E. Shaw and colleagues have been instrumental in enabling the performance of long-scale simulations of ion channels by the construction of the supercomputer Anton, which performs over an order of magnitude faster than any other machine utilizing an MD code. Simulations on an extended timescale under the influence of different membrane potentials have allowed the first direct observation of an ion channel gating transition (Jensen et al., 2012).

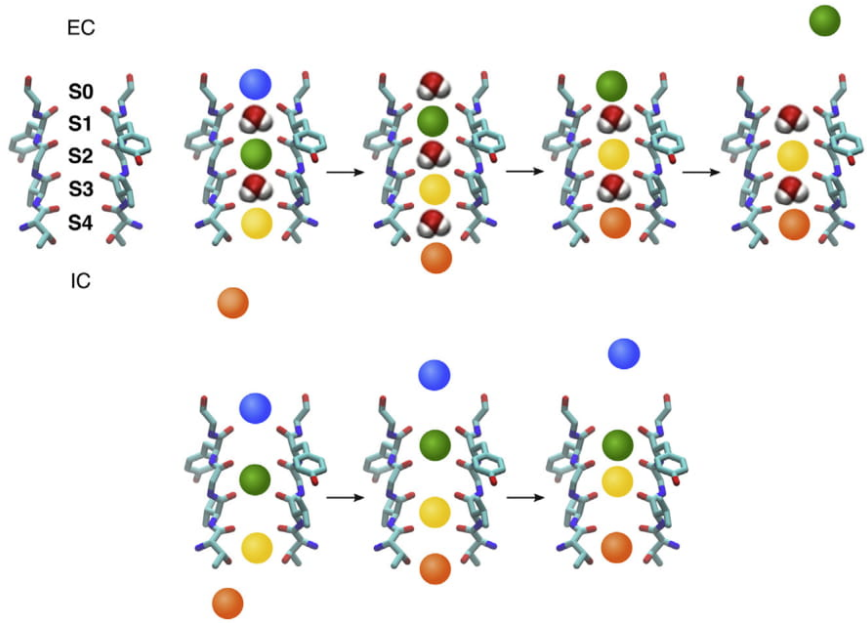

Figure 3 Proposed mechanisms of ion conduction in K^+ channels: (upper panel) chains of alternating K^+ ions and water molecules cross the selectivity filter, and/or (lower panel) cation move through the selectivity filter without intervening water molecules. Colored spheres represent individual K^+ ions. Approach of an ion from the central cavity prompts simultaneous ion movement throughout the selectivity filter, resulting in the exit of one ion that rapidly diffuses into the extracellular solution. The initial/final configuration of the selectivity filter was confirmed to be the most energetically favorable state using FEP methods (Aqvist & Luzhkov, 2000; Furini & Domene, 2009).

It is also worth noting that the Lennard–Jones interaction parameters in nonpolarizable *force fields* are derived from the standard Lorentz–Berthelot combination rule, optimized to emulate the free energies of ions in bulk water. As a consequence, in heterogeneous environments, such as the cell membrane, this method has inherent limitations. Therefore, the continued improvement of polarizable force fields will enhance the accuracy to which ion permeation can be simulated (Illingworth & Domene, 2009; Vanommeslaeghe & MacKerell, 2015; Xu et al., 2015).

4.1 Application to Na_V channels

Following the publication of the Na_VAb structure, numerous studies began to emerge in an attempt to identify the molecular determinants of Na^+ conduction mechanism, employing the vast range of available methods. In what

follows, an exhaustive review of the MD studies that have been published to date is provided, placing particular emphasis on the atomistic structure of the central pore that has key implications for conduction and selectivity.

The first published MD simulations demonstrated that the original Na_VAb structure was stable in the presence and absence of Na^+ ions (Carnevale, Treptow, & Klein, 2011). The cytoplasmic gate remained closed for the duration of the simulations; therefore, access to the central pore was limited to entrance at the periplasmic side via the selectivity filter. Observed ion dynamics confirmed earlier binding site predictions (Fig. 4). In Na^+ channels, binding sites for hydrated or partially hydrated sodium ions have been identified at the extracellular entrance (S_{HFS}) in the core region of the selectivity filer (S_{IN} and S_{CEN}) and within the central cavity (S_C). A considerable occupation time was observed at S_{HFS} ($\sim$10 ns), comprised of both symmetric and asymmetric conformations, with the former predominant. Electrostatic interactions with two opposite Glu177 residues, H-bonding between coordinating water molecules and remaining Glu177 residues, and further interactions with surrounding water stabilized ions in the on-axis binding mode. In contrast, the ion preferentially contacts one Glu177 and adjoined Ser178 in the off-axis mode at this site. The overall octahedral geometry mimics that observed in sodium hydrate crystals. Ions were observed to traverse deeper into the selectivity filter, mediated by surrounding water molecules to bind at S_{IN} via S_{CEN}, as postulated from the crystal structure. It is apparent that favorable binding sites are established on the basis of retaining a full hydration shell, with contributions from both water molecules and protein atoms in a manner consistent with K^+ conduction through Kv channels. In contrast, ions are partially hydrated throughout and interact in an asymmetric fashion to lining residues. Finally, water permeation is apparently uncoupled to the presence of bound species and therefore ion permeation. The nature of water transport in K^+ channels remains controversial in the

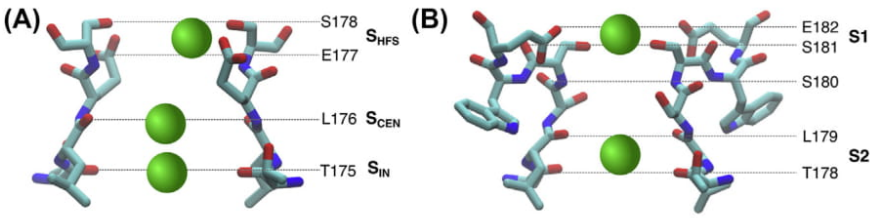

Figure 4 Binding sites in the selectivity filter of a Na^+ channel confirmed by MD simulations in (A) Na_VAb and (B) Na_VRh. Analogous binding sites as Na_VAb were also identified in Na_VMs.

literature, robust water flux has been observed in a K^+ depleted channel (Furini, Beckstein, & Domene, 2009), contrary to various accounts suggesting ions and water molecules are transported on a 1:1 ratio.

The Na_VAb binding sites of channels were also corroborated by the presence of defined energy minima in single and multiion PMF conduction profiles (Corry & Thomas, 2012; Furini & Domene, 2012) and various normal and long-scale MD simulations. A successive study provided insights into the stability of these binding sites; the overall selectivity filter structure remained remarkably similar in numerous ionic configurations, albeit a constriction of the pore in the presence of ions that can be attributed to favorable electrostatic interactions (Qiu, Shen, & Guo, 2012). This renders evidence the selectivity filter is stable independent of ionic occupancy, contrasting with K^+ channels that exhibit significant distortions in the absence of K^+ ions (Domene et al., 2008; Furini & Domene, 2009; Zhou et al., 2001).

Simulations of Na_V orthologs confirmed conserved selectivity filter binding sites across the bacterial Na_V family. The location and habitation of analogous binding sites observed in MD simulations of Na_VMs (Ke, Timin, & Stary-Weinzinger, 2014) is consistent with electron density detected in the Na_VMs crystal structure (McCusker et al., 2012). In Na_VRh, due to the nonconserved selectivity filter sequence, the characteristic inner "EEEE ring" and outer "SSSS ring" at the extracellular mouth are in reversed positions. Despite the supposed collapsed conformation of these residues, reorientation at the side chain of the inner ring (Ser181) leads to spontaneous opening of the selectivity filter in the first stages of the simulation (Zhang et al., 2013). Thereafter, occupation of binding sites at the vestibule (Ser181/Glu183 side chains: S1) and the inner of the selectivity filter (Thr178/Leu179 backbone carbonyls: S2) is observed.

To provide a feasible conduction pathway, an understanding of energetic barriers accompanying ionic movement, in addition to characterization of favorable binding sites is required. The application of free energy techniques to K^+ channels proved integral in elucidating the mechanism of K^+ conduction, therefore similar studies for Na_V emerged. Furthermore, long-scale MD simulations allow for the production of statistically significant conduction rates that can be validated against experimental single channel conductance measurements.

4.2 Single versus multiion conduction

The question of pore ion occupancy has ensued debate in the literature for many years, with flux measurements (Benos, Hyde, & Latorre, 1983) and

reversal potentials (Begenisich & Cahalan, 1980) suggesting independent and multiion movement respectively, with the latter supported by Brownian dynamics (Vora, Corry, & Chung, 2008). Therefore, single and multiion profiles of Na^+ conduction, utilizing the Na_VAb structure, emerged from numerous research groups (Corry & Thomas, 2012; Furini & Domene, 2012).

1D PMF profiles exploring movement of a single ion as a function of the pore axis follow the expected permeation pathway, subsequently occupying S_{HFS}, S_{CEN}, and S_{IN} until release into the central cavity. Due to the attractive interactions with the "EEEE ring", a deep energy well (between −5 kcal/mol (Corry, 2013) and −8 kcal/mol (Furini & Domene, 2012) relative to the extracellular solution) is observed at S_{HFS} corresponding to the off-axis binding mode described previously. Despite maintaining a full hydration shell throughout, penetration further into the selectivity filter is accompanied by an energetic barrier of ∼4 kcal/mol (Corry, 2013; Furini & Domene, 2012).

Multiion profiles demonstrated distinct differences; the presence of a second ion in close proximity to a bound ion in S_{HFS} significantly lowers the barrier for selectivity filter entrance. A further reduced energy well is also observed when both S_{CEN} and S_{HFS} are occupied. Therefore, the minimum energy pathway between initial (ions bound in the selectivity filter and external medium, denoted extracellular) and final states (ions bound in the selectivity filter and the central cavity, denoted intracellular) follows the multiion configurations: extracellular/S_{HFS}, S_{HFS}/S_{HFS}, S_{HFS}/S_{CEN}, S_{HFS}/S_{IN}, S_{HFS}/intracellular (Fig. 5). Considering this route, permeation can occur from the extracellular region into the central cavity with an energetic cost less than 3 kcal/mol. This value is consistent with the magnitude of energetic barriers previously determined for K^+ channels and the production of high flux rates (Aqvist & Luzhkov, 2000; Berneche & Roux, 2001).

Further efforts to characterize permeation through the Na_VAb selectivity filter were undertaken using metadynamics simulations (Stock, Delemotte, et al., 2013). Binding as a function of the radial distribution around the pore axis, as well as the distance along the pore axis, was taken into consideration to analyze previously unexplored two-ion configurations, and hence alternative conduction pathways. In particular, this allowed inspection of doubly occupied binding sites, a possible consequence of the wide selectivity filter.

Five local minima were recognized; potential wells, relative to the uppermost sampled state, of ∼−12 kcal/mol corresponded to occupancy of S_{HFS}/S_{CEN} and S_{CEN}/S_{CEN} whereas shallower regions between −7

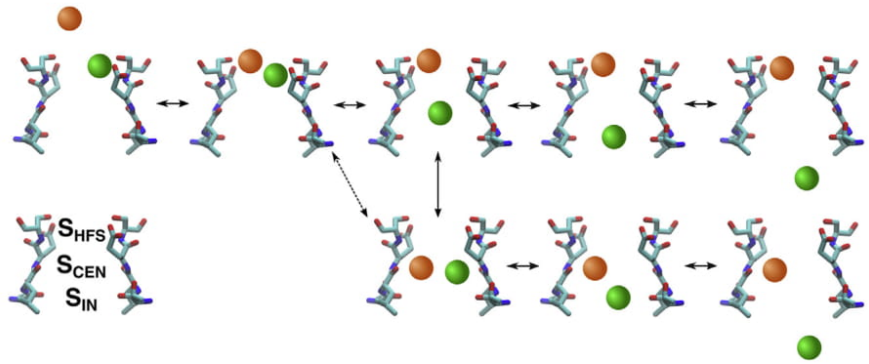

Figure 5 Proposed conduction pathways in the presence of two Na^+ ions in the selectivity filter. Selectivity filter residues are represented in licorice and Na^+ ions are orange (dark gray in print versions) and green (gray in print versions) spheres. 2D PMF profiles (Corry & Thomas, 2012; Furini & Domene, 2012) considering the position of individual ions along the pore axis, identified the minimum energy pathway following the sequence extracellular/S_{HFS}, S_{HFS}/S_{HFS}, S_{HFS}/S_{CEN}, S_{HFS}/S_{IN}, S_{HFS}/intracellular, represented in the upper array. Stock, Delemotte, et al. (2013) proposed an alternative mechanism with ions sequentially occupying extracellular/S_{HFS}, S_{HFS}/S_{HFS}, S_{HFS}/S_{CEN}, S_{CEN}/S_{CEN}, S_{CEN}/S_{IN}, and S_{HFS}/intracellular. The latter proved predominant in accompanying voltage-driven MD simulations.

and −9 kcal/mol coincided with S_{HFS}/S_{HFS}, S_{HSF}/S_{IN}, and S_{CEN}/S_{IN} configurations. These states form a complex network leading between the initial and final states of inward conduction, of which four are sampled in the minimum energy pathway (S_{HFS}/S_{HFS}, S_{HFS}/S_{CEN}, S_{CEN}/S_{CEN}, and S_{CEN}/S_{IN}). A direct S_{HFS}/S_{HFS} to S_{HFS}/S_{HFS} transition is also viable, in this case, illustrating transitions can be independent of the preceding ions, and conduction can occur via "knock-on" or "drive-by" mechanisms through the selectivity filter. These findings provide additional feasible routes to two-ion conduction, summarized in Fig. 5.

Overall, it is apparent that the conduction of a single Na^+ ion is promoted by the presence of additional ions. Weak coupling such as this can be described as a moderate version of the "knock-on" mechanism. Indications of a conserved mechanism throughout bacterial Na_V channels have been acknowledged. For example, in Na_VRh, FEP methods were used to determine if entrance to the outer state would destabilize ion binding at the inner site. Binding affinity was found to diminish from 3.7 kcal/mol to 2.6 kcal/mol, hence promoting onward conduction to the central cavity.

Throughout the examples described previously, further characterization of the permeation pathway succeeding the central cavity is restricted due to

the closed state of the Na_VAb structure. MD simulations in the same Stock, Delemotte, et al. (2013) study utilized an open-state structure of Na_VAb conferred from comparative studies of the available Na_VAb structure with activated-open and resting-closed states of $K_V1.2$ (Amaral, Carnevale, Klein, & Treptow, 2012) allowing for analysis of whole channel permeation. The onset of a hyperpolarized potential (−600 mV) to promote inward permeation events identified an average selectivity filter occupancy of ~1.8 ions throughout, providing further evidence that in the presence of a negative potential simultaneous binding of two ions is part of the normal functioning of the channel. Furthermore, ions were found to predominantly follow the minimum energy pathway identified in the previously described metadynamics calculations.

Similarly, simulations based on pore-only channel structure from Na_VMs (McCusker et al., 2012), containing an open activation gate, also identified an average selectivity filter occupancy of ~1.8 ions (Ulmschneider et al., 2013). Both single and multiion-binding events were observed, with the latter predominant; configurations with ions occupying an outer (extracellular site or S_{HFS}) and inner site (S_{CEN}, S_{IN} or an intermediate region 3 Å below S_{HFS}) monopolize approximately 70% of the simulation. The use of microsecond simulations, in combination with a constant electric field along the channel axis as in this study, allowed accurate estimation of conductance rate (34 ± 6 pS), in comparison to single channel conductance of transfected HEK cells (~33 pS) (Ulmschneider et al., 2013). This accordance with experimental data suggests that both conduction mechanisms are physiologically relevant, albeit to different extents. Furthermore, the rate of water transport was quantified of $\sim 3 \times 10^9\ s^{-1}$ in both directions, with a dwell time of two orders of magnitude less than Na^+ (<1 ns). In contrast to strongly coupled transport in K^+ channels (Alcayaga, Cecchi, Alvarez, & Latorre, 1989; Ando, Kuno, Shimizu, Muramatsu, & Oiki, 2005), this confirms earlier proposals that the permeation of water was uncoupled to that of ions in Na^+ channels.

Further large-scale MD simulations of the Na_VAb structure, totaling ~21.6 μs, in equilibrium conditions (under 0 mV), provided unique insights into selectivity filter occupancy and its relation to the conformational state of the selectivity filter, specifically the EEEE motif (Chakrabarti et al., 2013). These simulations displayed direct observations of "knock-on" and "knock-off" conduction events. Due to the closed nature of the channel, it is likely the occupation of the central cavity is higher than expected in an open-state structure in the presence of an electrochemical gradient.

Analysis of the selectivity filter alone confirmed an approximate 70% population of doubly occupied configurations; however, the identity of the remaining states digressed, with a triply occupied arrangement constituting 23%, increasing the average selectivity filter occupancy to 2.09 ± 0.05. The observed translocation kinetics has been attributed to the presence of highly degenerate ionic binding modes concerning the conformational isomerization of the EEEE ring. Glu177 side chains can either point out toward the extracellular vestibule or point in toward the selectivity filter pore. Inward facing conformations, referred to as "dunked" in this study, are shown to be favored in the presence of Na^+ and consequently promote Na^+ binding in the selectivity filter. The amalgamation of Na^+ ions and multiple carboxyl conformers leads to an extensive plethora of favorable states. Dynamic transitions between these ionic clusters occur on a $<$100 ps timescale and resembling that of a highly disordered liquid. The lack of preference for a particular state, and the separation by low-lying barriers, therefore promotes diffusion in the selectivity filter and high throughput Na^+ permeation. The authors suggest that voltage-driven nonequilibrium MD simulations may bias the dynamic behavior of the EEEE motif and discourage the occupation of degenerate conformational states in earlier studies, thereby overlooking this phenomenon.

Subsequently, Boiteux and coworkers identified a double potential well at S_{HFS} in PMF profiles, corresponding to available conformers of Glu177, reducing the barrier between selectivity filter sites (Boiteux, Vorobyov, & Allen, 2014). An average occupancy of 2.3 ions is reported in the selectivity filter, lending further evidence to a three-ion conduction mechanism in which the selectivity filter switches between one, two, and three-ion configurations facilitated by the isomerization of Glu177. In this case, three-ion binding events are promoted after the cleavage of H-bonding between Glu177 carbonyls and Ser178 hydroxyl groups, which restrict Glu177 movement during the first microsecond of the simulation. This remark illustrates that short scale MD simulations are also unlikely to sample this phenomena.

The coexistence of conduction mechanisms with two or three ions inside the selectivity filter was observed also in bias-exchange metadynamics simulations (Domene, Barbini & Furini, 2015). The significance of triply occupied states requires further investigation with regards to the possibility of contrasting mechanisms of Na^+ of inward and outward conduction. Comparative studies of Na_VAb (Stock, Delemotte, et al., 2013) and Na_VMs (Ke et al., 2014) channels under depolarized and hyperpolarized membrane

potentials, to emulate influx and efflux respectively, have therefore been undertaken to elucidate this proposal.

Both studies displayed an increased maximum barrier to conduction between S_{CEN} and S_{HFS}, (4.6 kcal/mol versus 0.4 kcal/mol and 2.1 kcal/mol versus 2.3 kcal/mol, respectively) with considerably higher dwell times in the selectivity filter (13.5 ± 0.6 ns versus 20.1 ± 1.1 ns) and hence lower flux rates (15 ± 3 pS versus ~27 ± 3 pS) in Na_VMs. Furthermore, an increased average occupancy of ~2.3 ions during efflux in comparison to ~1.8 ions during influx was observed in Na_VAb, thereby suggesting independent conduction mechanisms with the presence of a third ion more predominant in the outward direction (Stock, Delemotte, et al., 2013).

An additional "nudging" ion is observed to initiate the process in both systems. Therefore, to overcome the heightened barrier, this is considered to be an essential requirement. Moreover, in a Na_VMs study, reversible rotations of Glu177 residues play a pivotal role in efflux (Ke et al., 2014). A significantly larger proportion of flipped states is observed resulting in appreciable differences in the distribution of the ions throughout the selectivity filter (32 ± 5.9% versus 2.7 ± 0.5% for influx). Binding at S_{HFS} was found to be generally on-axis. Furthermore, S_{CEN} and an intermediate region below S_{HFS} were more densely populated. Additional simulations with a restrained "one-flip" ring conformation displayed increased efflux rates (relative to "no-flip" simulations), reiterating these proposals, yet appeared uncoupled to the Na^+ influx rate, disagreeing with Chakrabarti's earlier conclusions that this phenomenon was essential for the catalysis of Na^+ permeation regardless of the directionality (Chakrabarti et al., 2013). The discrepancies between previous studies are attributed to use of an open-state structure, as opposed to closed Na_VAb, which will induce repulsive effects when the central cavity is inhabited, in conjunction with the use of different force fields (Cordomí, Caltabiano, & Pardo, 2012).

4.3 Protonation state of Glu177

The conformational states of the EEEE signature sequence are further complicated by the prospect that one or more glutamate residues may be protonated. With potential implications for the electrostatics at the extracellular vestibule, and hence the ability to attract cations, and the overall structural stability of the selectivity filter and its enclosed binding sites, the dependency of the conduction mechanism on the protonation state requires thorough investigation.

Corry and Thomas (2012) calculated the 1D PMF profiles for Na_VAb with one and two Glu177 (in opposite side chains) residues protonated; the former exhibited a shallower, yet similar, profile with lower occupation of S_{HFS}, expected from the reduced negative potential of the selectivity filter. In contrast, when two protonated Glu177 residues are present, the ability of S_{HFS} to beckon Na^+ ions out of extracellular solution is diminished, in addition to an unexpectedly high energy at S_{CEN}, stunting Na^+ permeation.

Similar conclusions were reached from long-scale MD simulations (Boiteux et al., 2014), suggesting an essentially barrierless ($\sim$1.5 kcal/mol maximum barrier to conduction) multiion "knock-on" or "pass-by" mechanism is more likely in the fully charged state, promoted by repulsive interactions between charged side chains. The presence of one protonated glutamate, similarly, leads to a reduced charge density at the mouth of the selectivity filter. Rotational movements of Glu177 are integral in smoothing the energetic landscape and deeming conduction energetically feasible in this state, yet discourage three-ion events in the selectivity filter suggesting permeation occurs to a less extent. When two or more residues are protonated, hydrogen bonds between protonated and deprotonated glutamates occlude the permeation pathway causing significant barriers in the plane of the EEEE motif. Intrapore proton block such as this has been identified experimentally in $Na_V1.4$ (Khan, Kyle, Hanck, Lipkind, & Fozzard, 2006) and selected L-type Ca^{2+} channels (Chen, Bezprozvanny, & Tsien, 1996).

Overall, it is apparent that systems containing multiple protonated glutamates are unfeasible states for ion conduction; a fully charged EEEE ring is optimal for conduction; yet, the structural and functional state of Na_VAb containing a single uncharged Glu177 is presently dubious. An additional study by Furini, Barbini and Domene (2014) identified a noticeable increase in flexibility of the protonated glutamate relative to its deprotonated counterparts, residing in novel side chain conformations pointing toward S_{CEN} and laying at the back of the selectivity filter. As a consequence, structural fluctuations throughout the entire selectivity filter were experienced, with a substantial impact in both 1D and 2D PMF's, the energetics of which are likely to markedly impede ion flow. Recognized differences with prior microsecond simulations are attributed to allowed transitions to alternative metastable states that are unlikely to be sampled during typically short umbrella sampling trajectories, employed in this study. The appropriateness of these methods to the question in hand remains ambiguous; therefore, the physiological relevance of identified structural and permeation properties of a singly protonated Na_V selectivity filter cannot be delineated at present.

An interesting observation worth noting, however, is the extent to which structural changes at the selectivity filter are propagated throughout the entire pore domain. Restriction of the selectivity filter, in a singly protonated system, seemingly adjusts the cavity shape and the orientation of S6 (Boiteux et al., 2014). The observed bent conformation in S6, on the level of P200–T206, is parallel to that of an inactivated structure suggested by Payandeh et al. (2012). Such rapid conformational flux appears to be an inherent property of Na_V behavior on a microsecond timescale, potentially related to slow inactivation (millisecond to second).

Structural rearrangements in this region also have implications for fenestrations between the central core and the surrounding membrane. The size of these openings is directly related to the activation state of S6; specifically, the rotation of F203 of phenyl side chains reversibly blocks the pathway, consistent with experimental reports this residue is essential for inactivation and drug binding (Ahern, Eastwood, Dougherty, & Horn, 2008; Carboni, Zhang, Nepliouevа, Starmer, & Grant, 2005; Li, Galue, Meadows, & Ragsdale, 1999; Ragsdale, McPhee, Scheuer, & Catterall, 1994). The open fenestrations have a maximum ~4 Å width, feasible for the entry of lipophilic drugs (ie, local anesthetics), suggesting binding at this site may influence slow channel inactivation propagated through this region from the selectivity filter (Carboni et al., 2005; Chen et al., 2000; Li et al., 1999).

4.4 Selectivity of Na^+ over other monovalent and divalent ions

To elucidate the molecular determinants of selectivity in Na^+ channels, comparison of the energy profiles of Na^+ and K^+ was undertaken (Corry & Thomas, 2012; Furini & Domene, 2012). A similar landscape was observed, with elevated barriers at S_{HFS} and S_{CEN} of the order of 5–6 kcal/mol, independent of the presence of multiple ions.

Further analysis of the PMF displayed a similar binding affinity of both ions at S_{HFS}, due to flexibility and availability of water molecules, with a notable barrier to conduction arising in the plane of the Glu177 side chains. Corry et al. proposed a mechanism for this concerning the orientation of the proximal residues. The ideal geometry of S_{HFS} during a binding event involves a straight ion-water-carbonyl complex. However, the increased distance of direct coordination between K^+ and Glu177 means this conformation is improbable unless reorganization of the binding site occurs. Only slight differences in the binding site size are observed, between K^+ and Na^+,

insufficient for this purpose. Therefore, even though K^+ can fit through the pore with a full shell it is not in an optimum geometry.

This hypothesis was tested further by analysis of the relationship between selectivity and pore radius. The free energies of K^+, relative to Na^+, to travel through Glu177 ring of a model pore illustrated a lack of selectivity until bridging water molecules can no longer fit in plane of the pore, and a peak of selectivity at 6.3 Å, optimum for Na^+ and in plane binding of water molecules. Similar free energies are observed over a wide range of values, suggesting favorable conduction does not require specific alignment with the pore axis, as in K^+ channels.

In both studies (Corry & Thomas, 2012; Furini & Domene, 2012), the calculated energetic penalty of K^+ conduction through a Na_V channel was 3 kcal/mol, as opposed to 6 kcal/mol in the reverse situation of Na^+ conduction in K^+ channels. Therefore, the feasibility of K^+ conduction via this mechanism is consistent with the lower selectivity identified in Na_V channels compared to K^+ channels; K^+ channels select for K^+ ions at a rate of approximately 1000 to 1 whereas in Na^+ channels this is reduced to only 8 to 1.

The close relationship between Na^+ and Ca^{2+} selective channels complicates the situation of determining the origins of channel selectivity. A similar tetrameric architecture with each subunit containing six transmembrane helices and selectivity filter structure, in addition to interchangeable selectivity in both channel families on the mutation of selected selectivity filter residues, suggests only subtle differences in protein structure are responsible for the observed conduction ratios (Heinemann et al., 1992; Shaya et al., 2011; Sun et al., 1997; Yue, Navarro, Ren, Ramos, & Clapham, 2002). The similar ionic radii lead to proposals that selectivity is based on the inability of Na^+ channels to accommodate the increased charge density of Ca^{2+} (Corry, 2013).

Similarly to comparative simulations of Na^+ and K^+ described previously, off-axis binding modes between Glu177 and Ser178 are observed in the external site with Ca^{2+}, with an energetic barrier while penetrating the "EEEE ring" (Corry, 2013). A ~3 kcal/mol energetic penalty (1 kcal/mol for Na^+) is observed accompanying movement from the selectivity filter to central cavity, emphasizing an increased binding affinity for Ca^{2+} in this site. Furthermore, an additional barrier was identified deeper into the pore before reaching the central/internal sites, in contrast to Na^+ and K^+. An average lower coordination number observed at this position, and corresponding energies of dehydration of about 8 kcal/mol to reduce the coordination shell from seven to six, suggests the removal of water

moved back to its original orientation, with the second revolving further to accommodate ion translocation to S_{CEN} demonstrating the flexibility of this residue in this case. Similar potential wells are observed in PMF profiles of Na^+ (Ke et al., 2013), Na^+ and K^+ (Furini & Domene, 2012), and Ca^{2+} (Boiteux et al., 2014) yet absent in analogous calculations of Na^+, K^+, and Ca^{2+} permeation (Corry & Thomas, 2012) highlighting further contentions in the literature concerning the behavior of Glu177.

In Na_VRh, all simulations with variable concentrations of Ca^{2+} show persistent binding at S1; strong binding determined by electrostatic interactions with Glu183, as well as interactions with Ser180, results in an insurmountable energy barrier ($\sim$11.38 kcal/mol), hindering progression deeper in the selectivity filter (Zhang et al., 2013). Therefore, the authors suggest this site confers selectivity in Na_VRh. The binding mode of Na^+ at S1 is reflective of preferred interactions with Ser181; this conformation is unreachable when Ca^{2+} is bound, consistent with extracellular millimolar blockage of Na^+ current by Ca^{2+}. Simulations with ions beginning in the central cavity were used to examine binding in S2. Here, Ca^{2+} exists preferentially in the center, approximately equidistant from the eight surrounding carbonyls. In contrast, Na^+ binds off-axis, in close proximity to one or two of the carbonyls, occasionally jumping between positions, subsequently persuading asymmetric selectivity filter conformations. Elements of asymmetry are observed to some extent throughout the entire Na^+ translocation process, despite the homologous sequence present in all subunits. Relative to other bacterial Na_V channels, the selectivity filter sequence and asymmetric binding features of Na_VRh could be more applicable to mammalian Na_V channels, which contain nonconserved selectivity filter sequences; therefore, it is likely more studies utilizing this structure will emerge in the coming years.

5. CONCLUSIONS

In this review, we have primarily focused on the mechanisms of conduction and selectivity in Na^+ channels and a comparison with K^+ channels has been established. Aspects of voltage-gating and drug blockage have likewise been studied by computational methods to which numerous reviews are available (Bagnéris, Naylor, McCusker, & Wallace, 2015; Stock, Souza, & Treptow, 2013; Vargas et al., 2012). There is a general consensus about the main characteristics of ion conduction in bacterial Na^+ channels

molecules is a feasible explanation of the energy barrier. The lack of ion–protein interactions, from the selectivity filter lining residues, to compensate for the reduced ion–water interactions further substantiates this claim. Increased affinity for water binding in Ca^{2+} is also observed in the second solvation shell, likely propagating this effect further. The presence of a second ion lowers the maximum barrier to conduction between S_{HFS} and S_{CEN} to ~4.5 kcal/mol; therefore, an analogous weakly coupled "knock-on" mechanism is expected here. In a mixed ionic solution, barriers to Ca^{2+} conduction are slightly lower than those observed in the single-ion conduction. Na^{+} permeation, in the presence of bound Ca^{2+}, appears to be the most likely scenario in this case, however, despite an increased barrier in comparison to Na^{+} alone, suggesting the presence of Ca^{2+} diminishes Na^{+} conduction. This is consistent with experimental reports of Ca^{2+} obstruction (French, Worley, Wonderlin, Kularatna, & Krueger, 1994; Ravindran, Schild, & Moczydlowski, 1991; Yamamoto, Yeh, & Narahashi, 1984) albeit to a considerably lesser extent than predicted computationally (Ren et al., 2001). The disparity is likely due to the uniform protonation states of Glu177 residues and limitations regarding the use of nonpolarizable force fields for divalent cations (Bakó, Hutter, & Pálinkás, 2002; Bucher & Kuyucak, 2008).

Simulations undertaken simultaneously by Ke, Zangerl, and Stary-Weinzinger (2013) proposed contrasting conclusions. After a ~40 ns occupation of S_{HFS}, the ion entered an intermediate site below the EEEE ring, termed $S_{S178/L176}$ in this study, formed from the backbone nitrogen's of Ser178 and Leu176, for a further 55 ns. The single ion entered S_{CEN} thereafter, which is populated for the remainder of the simulation, excluding the entrance of further ions. The general landscape of the PMF energy profile is in general agreement with those calculated by the Corry group for single-ion conduction. An elevated barrier is observed in the plane of the EEEE ring, suggesting discrimination against Ca^{2+} may occur in this region due to size constraints in a similar mechanism proposed for K^{+} selectivity (Corry & Thomas, 2012). In addition, a significant barrier is observed after S_{CEN}, suggesting diffusion into the central cavity may be the rate-limiting step in the case of inward conduction of Ca^{2+}. The high binding affinity for S_{CEN} is consistent with crystallographic data of the closely related Na_VRh channel.

The presence of a potential well at $S_{S178/L176}$ requires further investigation; in this site, two rotated Glu177 residues bind Ca^{2+} to optimize the available electrostatic network. When the ion vacates this site, one glutamate

emerging from atomistic stimulations. Conduction requires the cooperative movement of at least two Na^+ ions across the selectivity filter of the channel. In sharp contrast to K^+ channels, the movements of the ions inside the selectivity filter of Na^+ channels are only loosely correlated, and the passage of water molecules is uncoupled from ion conduction. The central region of the selectivity filter can host a hydrated Na^+ ion but it cannot host a hydrated K^+ ion, which might explain the low selectivity of bacterial Na^+ channels for Na^+ ions over K^+ ions. In spite of this overall picture, there are still some controversial issues about the conformation of Glu177 and the number of ions involved in conduction events. Extensive atomistic simulations proved that the side chain of Glu177 is highly mobile, conferring a liquidlike nature to the selectivity filter of bacterial Na^+ channels. Instead, in other simulations of ion conduction, the side chain of Glu177 did not show significant deviations from the crystallographic structure. Therefore, the importance of the conformational states of Glu177 on ion conduction is still disputed. The movements of Glu177 can also modify the number of Na^+ ions inside the selectivity filter and consequently the number of ions involved in conduction events. Conduction mechanisms with two and three ions have been observed, and it has been proposed that inward and outward conduction might follow different routes, with the third ion possessing a more critical role in outward conduction. It is possible that several conduction mechanisms coexist for bacterial Na^+ channels, as it has been suggested for K^+ channels (Furini & Domene, 2009), and that the distribution of the conductive trajectories among these different mechanisms is influenced by the membrane potential and by the concentration of ions in the intracellular and extracellular compartments. These open questions can be investigated by atomistic simulations, and they will provide a description of ion conduction in bacterial Na^+ channels at an unprecedented level of detail.

ACKNOWLEDGMENTS

Work in the Domene lab is supported by the Hartree Center and the Engineering and Physical Sciences Research Council via the UK National Service for Computational Chemistry Software (NSCCS) and Archer. V.O is supported by a CASE studentship from the Biotechnology and Biological Sciences Research Council and Pfizer Neusentis.

REFERENCES

Ahern, C. A., Eastwood, A. L., Dougherty, D. A., & Horn, R. (2008). Electrostatic contributions of aromatic residues in the local anesthetic receptor of voltage-gated sodium channels. *Circulation Research, 102*(1), 86–94.

Alcayaga, C., Cecchi, X., Alvarez, O., & Latorre, R. (1989). Streaming potential measurements in Ca^{2+}-activated K^+ channels from skeletal and smooth muscle. Coupling of ion and water fluxes. *Biophysical Journal, 55*(2), 367–371.

Amaral, C., Carnevale, V., Klein, M. L., & Treptow, W. (2012). Exploring conformational states of the bacterial voltage-gated sodium channel NavAb via molecular dynamics simulations. *Proceedings of the National Academy of Sciences of the United States of America, 109*(52), 21336–21341.

Ando, H., Kuno, M., Shimizu, H., Muramatsu, I., & Oiki, S. (2005). Coupled K^+-water flux through the HERG potassium channel measured by an osmotic pulse method. *Journal of General Physiology, 126*(5), 529–538.

Aqvist, J., Luecke, H., Quiocho, F. A., & Warshel, A. (1991). Dipoles localized at helix termini of proteins stabilize charges. *Proceedings of the National Academy of Sciences of the United States of America, 88*(5), 2026–2030.

Aqvist, J., & Luzhkov, V. (2000). Ion permeation mechanism of the potassium channel. *Nature, 404*(6780), 881–884.

Bagal, S. K., Brown, A. D., Cox, P. J., Omoto, K., Owen, R. M., Pryde, D. C., & Swain, N. A. (2013). Ion channels as therapeutic targets: a drug discovery perspective. *Journal of Medicinal Chemistry, 56*(3), 593–624.

Bagnéris, C., DeCaen, P. G., Hall, B. A., Naylor, C. E., Clapham, D. E., Kay, C. W. M., & Wallace, B. A. (2013). Role of the C-terminal domain in the structure and function of tetrameric sodium channels. *Nature Communications, 4*.

Bagnéris, C., Naylor, C. E., McCusker, E. C., & Wallace, B. A. (2015). Structural model of the open–closed–inactivated cycle of prokaryotic voltage-gated sodium channels. *Journal of General Physiology, 145*(1), 5–16.

Bakó, I., Hutter, J., & Pálinkás, G. (2002). Car–Parrinello molecular dynamics simulation of the hydrated calcium ion. *Journal of Chemical Physics, 117*(21), 9838–9843.

Begenisich, T. B., & Cahalan, M. D. (1980). Sodium channel permeation in squid axons. I: reversal potential experiments. *Journal of Physiology, 307*, 217–242.

Benos, D. J., Hyde, B. A., & Latorre, R. (1983). Sodium flux ratio through the amiloride-sensitive entry pathway in frog skin. *Journal of General Physiology, 81*(5), 667–685.

Berendsen, H. J. C., van der Spoel, D., & van Drunen, R. (1995). GROMACS: a message-passing parallel molecular dynamics implementation. *Computer Physics Communications, 91*(1–3), 43–56.

Bernèche, S., & Roux, B. (2000). Molecular dynamics of the KcsA K^+ channel in a bilayer membrane. *Biophysical Journal, 78*(6), 2900–2917.

Berneche, S., & Roux, B. (2001). Energetics of ion conduction through the K^+ channel. *Nature, 414*(6859), 73–77.

Bezanilla, F., & Armstrong, C. M. (1972). Negative conductance caused by entry of sodium and cesium ions into the potassium channels of squid axons. *Journal of General Physiology, 60*(5), 588–608.

Black, J. A., & Waxman, S. G. (2013). Noncanonical roles of voltage-gated sodium channels. *Neuron, 80*(2), 280–291.

Boiteux, C., Vorobyov, I., & Allen, T. W. (2014). Ion conduction and conformational flexibility of a bacterial voltage-gated sodium channel. *Proceedings of the National Academy of Sciences of the United States of America, 111*(9), 3454–3459.

Brohawn, del Marmol, J., & MacKinnon, R. (2012). Crystal structure of the human K2P TRAAK, a lipid- and mechano-sensitive K^+ ion channel. *Science, 335*, 436–441.

Brooks, B. R., Bruccoleri, R. E., Olafson, B. D., States, D. J., Swaminathan, S., & Karplus, M. (1983). CHARMM: a program for macromolecular energy, minimization, and dynamics calculations. *Journal of Computational Chemistry, 4*(2), 187–217.

Bucher, D., & Kuyucak, S. (2008). Polarization of water in the first hydration shell of K^+ and Ca^{2+} ions. *Journal of Physical Chemistry B, 112*(35), 10786–10790.

Carboni, M., Zhang, Z. S., Neplioueva, V., Starmer, C. F., & Grant, A. O. (2005). Slow sodium channel inactivation and use-dependent block modulated by the same domain IV S6 residue. *Journal of Membrane Biology, 207*(2), 107–117.

Carnevale, V., Treptow, W., & Klein, M. L. (2011). Sodium ion binding sites and hydration in the lumen of a bacterial ion channel from molecular dynamics simulations. *Journal of Physical Chemistry Letters, 2*(19), 2504–2508.

Chakrabarti, N., Ing, C., Payandeh, J., Zheng, N., Catterall, W. A., & Pomès, R. (2013). Catalysis of Na^+ permeation in the bacterial sodium channel NaVAb. *Proceedings of the National Academy of Sciences of the United States of America, 110*(28), 11331–11336.

Chen, X. H., Bezprozvanny, I., & Tsien, R. W. (1996). Molecular basis of proton block of L-type Ca^{2+} channels. *Journal of General Physiology, 108*(5), 363–374.

Chen, Z., Ong, B.-H., Kambouris, N. G., Marbán, E., Tomaselli, G. F., & Balser, J. R. (2000). Lidocaine induces a slow inactivated state in rat skeletal muscle sodium channels. *Journal of Physiology, 524*, 37–49.

Cordero-Morales, J. F., Jogini, V., Chakrapani, S., & Perozo, E. (2011). A multipoint hydrogen-bond network underlying KcsA C-type inactivation. *Biophysical Journal, 100*(10), 2387–2393.

Cordomí, A., Caltabiano, G., & Pardo, L. (2012). Membrane protein simulations using AMBER force field and Berger lipid parameters. *Journal of Chemical Theory and Computation, 8*(3), 948–958.

Cornell, W. D., Cieplak, P., Bayly, C. I., Gould, I. R., Merz, K. M., Ferguson, D. M. … Kollman, P. A. (1995). A second generation force field for the simulation of proteins, nucleic acids, and organic molecules. *Journal of the American Chemical Society, 117*(19), 5179–5197.

Corry, B. (2013). Na^+/Ca^{2+} selectivity in the bacterial voltage-gated sodium channel NavAb. *PeerJ, 1*, e16.

Corry, B., & Thomas, M. (2012). Mechanism of ion permeation and selectivity in a voltage gated sodium channel. *Journal of the American Chemical Society, 134*(3), 1840–1846.

Cuello, L. G., Jogini, V., Cortes, D. M., & Perozo, E. (2010). Structural mechanism of C-type inactivation in K^+ channels. *Nature, 466*(7303), 203–208.

Domene, C., Barbini, P., & Furini, S. (2015). Bias-exchange metadynamics simulations: An efficient strategy for the analysis of conduction and selectivity in ion channels. *Journal of Chemical Theory and Computation, 11*(4), 1896–1906. http://dx.doi.org/10.1021/ct501053x.

Domene, C., Klein, M. L., Branduardi, D., Gervasio, F. L., & Parrinello, M. (2008). Conformational changes and gating at the selectivity filter of potassium channels. *Journal of the American Chemical Society, 130*(29), 9474–9480.

Domene, C., & Sansom, M. S. (2003). Potassium channel, ions, and water: simulation studies based on the high resolution X-ray structure of KcsA. *Biophysical Journal, 85*(5), 2787–2800.

Doyle, D. A., Morais Cabral, J., Pfuetzner, R. A., Kuo, A., Gulbis, J. M., Cohen, S. L. … MacKinnon, R. (1998). The structure of the potassium channel: molecular basis of K^+ conduction and selectivity. *Science, 280*(5360), 69–77.

Eisenman, G. (1962). Cation selective glass electrodes and their mode of operation. *Biophysical Journal, 2*, 259–323.

Eisenman, G., & Horn, R. (1983). Ionic selectivity revisited: the role of kinetic and equilibrium processes in ion permeation through channels. *Journal of Membrane Biology, 76*(3), 197–225.

England, S., & de Groot, M. J. (2009). Subtype-selective targeting of voltage-gated sodium channels. *British Journal of Pharmacology, 158*(6), 1413–1425.

Favre, I., Moczydlowski, E., & Schild, L. (1996). On the structural basis for ionic selectivity among Na^+, K^+, and Ca^{2+} in the voltage-gated sodium channel. *Biophysical Journal, 71*, 3110–3125.

French, R. J., Worley, J. F., Wonderlin, W. F., Kularatna, A. S., & Krueger, B. K. (1994). Ion permeation, divalent ion block, and chemical modification of single sodium channels. Description by single- and double-occupancy rate-theory models. *Journal of General Physiology, 103*, 447–470.

Furini, S., Barbini, P., & Domene, C. (2014). Effects of the protonation state of the EEEE motif of a bacterial Na(+)-channel on conduction and pore structure. *Biophysical Journal, 106*(10), 2175–2183. http://dx.doi.org/10.1016/j.bpj.2014.04.005.

Furini, S., Beckstein, O., & Domene, C. (2009). Permeation of water through the KcsA K^+ channel. *Proteins, 74*(2), 437–448.

Furini, S., & Domene, C. (2009). Atypical mechanism of conduction in potassium channels. *Proceedings of the National Academy of Sciences of the United States of America, 106*(38), 16074–16077.

Furini, S., & Domene, C. (2012). On conduction in a bacterial sodium channel. *PLoS Computational Biology, 8*(4), e1002476.

Furini, S., & Domene, C. (2013). K^+ and Na^+ conduction in selective and nonselective ion channels via molecular dynamics simulations. *Biophysical Journal, 105*(8), 1737–1745.

Furini, S., Zerbetto, F., & Cavalcanti, S. (2007). Role of the intracellular cavity in potassium channel conductivity. *Journal of Physical Chemistry B, 111*(50), 13993–14000.

Gilchrist, J., Das, S., Van Petegem, F., & Bosmans, F. (2013). Crystallographic insights into sodium-channel modulation by the β4 subunit. *Proceedings of the National Academy of Sciences of the United States of America, 110*(51), E5016–E5024.

Gumbart, J., Khalili-Araghi, F., Sotomayor, M., & Roux, B. (2012). Constant electric field simulations of the membrane potential illustrated with simple systems. *Biochim Biophys Acta, 1818*(2), 294–302.

Heginbotham, L., Lu, Z., Abramson, T., & MacKinnon, R. (1994). Mutations in the K^+ channel signature sequence. *Biophysical Journal, 66*(4), 1061–1067.

Heinemann, S. H., Terlau, H., Stuhmer, W., Imoto, K., & Numa, S. (1992). Calcium channel characteristics conferred on the sodium channel by single mutations. *Nature, 356*, 441–443.

Hille, B. (1971). The permeability of the sodium channel to organic cations in myelinated nerve. *Journal of General Physiology, 58*(6), 599–619.

Hille, B. (1972). The permeability of the sodium channel to metal cations in myelinated nerve. *Journal of General Physiology, 59*(6), 637–658.

Hille, B. (1992). *Ionic channels of excitable membranes* (2nd ed.). Sunderland, MA: Sinauer Associates Inc.

Hodgkin, A. L., & Keynes, R. D. (1955). The potassium permeability of a giant nerve fibre. *Journal of Physiology, 128*(1), 61–88.

Illingworth, C. J., & Domene, C. (2009). Many-body effects and simulations of potassium channels. *Proceedings of the Royal Society of London, Series A, 465*(2106), 1701–1716.

Jensen, M.Ø., Jogini, V., Borhani, D. W., Leffler, A. E., Dror, R. O., & Shaw, D. E. (2012). Mechanism of voltage gating in potassium channels. *Science, 336*(6078), 229–233.

Jiang, Y., Lee, A., Chen, J., Ruta, V., Cadene, M., Chait, B. T., & MacKinnon, R. (2003). X-ray structure of a voltage-dependent K^+ channel. *Nature, 423*(6935), 33–41.

Jogini, V., & Roux, B. (2005). Electrostatics of the intracellular vestibule of K^+ channels. *Journal of Molecular Biology, 354*(2), 272–288.

Jorgensen, W. L., & Tirado-Rives, J. (1988). The OPLS [optimized potentials for liquid simulations] potential functions for proteins, energy minimizations for crystals of cyclic peptides and crambin. *Journal of the American Chemical Society, 110*(6), 1657–1666.

Ke, S., Timin, E. N., & Stary-Weinzinger, A. (2014). Different inward and outward conduction mechanisms in NaVMs suggested by molecular dynamics simulations. *PLoS Computational Biology, 10*(7), e1003746.

Ke, S., Zangerl, E.-M., & Stary-Weinzinger, A. (2013). Distinct interactions of Na^+ and Ca^{2+} ions with the selectivity filter of the bacterial sodium channel NaVAb. *Biochemical and Biophysical Research Communications, 430*(4), 1272–1276.

Khan, A., Kyle, J. W., Hanck, D. A., Lipkind, G. M., & Fozzard, H. A. (2006). Isoform-dependent interaction of voltage-gated sodium channels with protons. *Journal of Physiology, 576*, 493–501.

Kuo, A., Gulbis, J. M., Antcliff, J. F., Rahman, T., Lowe, E. D., Zimmer, J., & Doyle, D. A. (2003). Crystal structure of the potassium channel KirBac1.1 in the closed state. *Science, 300*(5627), 1922–1926.

Kutzner, C., Grubmüller, H., de Groot, B. L., & Zachariae, U. (2011). Computational electrophysiology: The molecular dynamics of ion channel permeation and selectivity in atomistic detail. *Biophysical Journal, 101*(4), 809–817. http://dx.doi.org/10.1016/j.bpj.2011.06.010.

Li, H. L., Galue, A., Meadows, L., & Ragsdale, D. S. (1999). A molecular basis for the different local anesthetic affinities of resting versus open and inactivated states of the sodium channel. *Molecular Pharmacology, 55*(1), 134–141.

Long, S. B., Campbell, E. B., & Mackinnon, R. (2005). Crystal structure of a mammalian voltage-dependent Shaker family K^+ channel. *Science, 309*(5736), 897–903.

Long, S. B., Tao, X., Campbell, E. B., & MacKinnon, R. (2007). Atomic structure of a voltage-dependent K^+ channel in a lipid membrane-like environment. *Nature, 450*(7168), 376–382.

Luzhkov, V. B., & Åqvist, J. (2001). K^+/Na^+ selectivity of the KcsA potassium channel from microscopic free energy perturbation calculations. *BBA – Protein Structure and Molecular Enzymology, 1548*(2), 194–202.

Mantegazza, M., Curia, G., Biagini, G., Ragsdale, D. S., & Avoli, M. (2010). Voltage-gated sodium channels as therapeutic targets in epilepsy and other neurological disorders. *Lancet Neurology, 9*(4), 413–424.

McCusker, E. C., Bagneris, C., Naylor, C. E., Cole, A. R., D'Avanzo, N., Nichols, C. G., & Wallace, B. A. (2012). Structure of a bacterial voltage-gated sodium channel pore reveals mechanisms of opening and closing. *Nature Communications, 3*, 1102.

Miller, A. N., & Long, S. B. (2012). Crystal structure of the human Two–Pore domain potassium channel K2P1. *Science, 335*(6067), 432–436.

Morais-Cabral, J. H., Zhou, Y., & MacKinnon, R. (2001). Energetic optimization of ion conduction rate by the K^+ selectivity filter. *Nature, 414*(6859), 37–42.

Namadurai, S., Balasuriya, D., Rajappa, R., Wiemhöfer, M., Stott, K., Klingauf, J., & Jackson, A. P. (2014). Crystal structure and molecular imaging of the Nav channel β3 subunit indicates a trimeric assembly. *Journal of Biological Chemistry, 289*(15), 10797–10811.

Ngo, V., Stefanovski, D., Haas, S., & Farley, R. A. (2014). Non-equilibrium dynamics contribute to ion selectivity in the KcsA channel. *PLoS One, 9*(1), e86079. http://dx.doi.org/10.1371/journal.pone.0086079.

Noda, M., Shimizu, S., Tanabe, T., Takai, T., Kayano, T., Ikeda, T. … Numa, S. (1984). Primary structure of electrophorus electricus sodium channel deduced from cDNA sequence. *Nature, 312*(5990), 121–127.

Noskov, S. Y., & Roux, B. (2006). Ion selectivity in potassium channels. *Biophysical Chemistry, 124*(3), 279–291.

Parsegian, A. (1969). Energy of an ion crossing a low dielectric membrane: solutions to four relevant electrostatic problems. *Nature, 221*(5183), 844–846.

Payandeh, J., Gamal El-Din, T. M., Scheuer, T., Zheng, N., & Catterall, W. A. (2012). Crystal structure of a voltage-gated sodium channel in two potentially inactivated states. *Nature, 486*(7401), 135–139.

Payandeh, J., & Minor, D. L., Jr. (2015). Bacterial voltage-gated sodium channels (BacNaVs) from the soil, sea, and salt lakes enlighten molecular mechanisms of electrical signaling and pharmacology in the brain and heart. *Journal of Molecular Biology, 427*(1), 3–30.

Payandeh, J., Scheuer, T., Zheng, N., & Catterall, W. A. (2011). The crystal structure of a voltage-gated sodium channel. *Nature, 475*(7356), 353–358.

Qiu, H., Shen, R., & Guo, W. (2012). Ion solvation and structural stability in a sodium channel investigated by molecular dynamics calculations. *Biochimica et Biophysica Acta, 1818*(11), 2529–2535.

Ragsdale, D. S., McPhee, J. C., Scheuer, T., & Catterall, W. A. (1994). Molecular determinants of state-dependent block of Na^+ channels by local anesthetics. *Science, 265*(5179), 1724–1728.

Ravindran, A., Schild, L., & Moczydlowski, E. (1991). Divalent cation selectivity for external block of voltage-dependent Na^+ channels prolonged by batrachotoxin. Zn^{2+} induces discrete substates in cardiac Na^+ channels. *Journal of General Physiology, 97*(1), 89–115.

Ren, D., Navarro, B., Xu, H., Yue, L., Shi, Q., & Clapham, D. E. (2001). A prokaryotic voltage-gated sodium channel. *Science, 294*(5550), 2372–2375.

Roux, B. (2005). Ion conduction and selectivity in K^+ channels. *Annual Review of Biophysics and Biomolecular Structure, 34*(1), 153–171.

Shaya, D., Findeisen, F., Abderemane-Ali, F., Arrigoni, C., Wong, S., Nurva, S. R., & Minor, D. L., Jr. (2014). Structure of a prokaryotic sodium channel pore reveals essential gating elements and an outer ion binding site common to eukaryotic channels. *Journal of Molecular Biology, 426*(2), 467–483.

Shaya, D., Kreir, M., Robbins, R. A., Wong, S., Hammon, J., Brüggemann, A., & Minor, D. L. (2011). Voltage-gated sodium channel (NaV) protein dissection creates a set of functional pore-only proteins. *Proceedings of the National Academy of Sciences of the United States of America, 108*(30), 12313–12318.

Smart, O. S., Goodfellow, J. M., & Wallace, B. A. (1993). The pore dimensions of gramicidin A. *Biophysical Journal, 65*(6), 2455–2460.

Stock, L., Delemotte, L., Carnevale, V., Treptow, W., & Klein, M. L. (2013). Conduction in a biological sodium selective channel. *Journal of Physical Chemistry B, 117*(14), 3782–3789.

Stock, L., Souza, C., & Treptow, W. (2013). Structural basis for activation of voltage-gated cation channels. *Biochemistry, 52*(9), 1501–1513.

Stuhmer, W., Conti, F., Suzuki, H., Wang, X., Noda, M., Yahagi, N., & Numa, S. (1989). Structural parts involved in activation and inactivation of the sodium channel. *Nature, 339*(6226), 597–603.

Sun, Y. M., Favre, I., Schild, L., & Moczydlowski, E. (1997). On the structural basis for size-selective permeation of organic cations through the voltage-gated sodium channel. Effect of alanine mutations at the DEKA locus on selectivity, inhibition by Ca^{2+} and H^+, and molecular sieving. *Journal of General Physiology, 110*(6), 693–715.

Ulmschneider, M. B., Bagnéris, C., McCusker, E. C., DeCaen, P. G., Delling, M., Clapham, D. E. … Wallace, B. A. (2013). Molecular dynamics of ion transport through the open conformation of a bacterial voltage-gated sodium channel. *Proceedings of the National Academy of Sciences of the United States of America, 110*(16), 6364–6369.

Vanommeslaeghe, K., & MacKerell, A. D., Jr. (2015). CHARMM additive and polarizable force fields for biophysics and computer-aided drug design. *BBA, 1850*(5), 861–871.

Vargas, E., Yarov-Yarovoy, V., Khalili-Araghi, F., Catterall, W. A., Klein, M. L., Tarek, M., & Roux, B. (2012). An emerging consensus on voltage-dependent gating from computational modeling and molecular dynamics simulations. *Journal of General Physiology, 140*(6), 587–594.

Vora, T., Corry, B., & Chung, S. H. (2008). Brownian dynamics study of flux ratios in sodium channels. *European Biophysics Journal, 38*(1), 45–52.

Xu, P., Wang, J., Xu, Y., Chu, H., Liu, J., Zhao, M. … Li, G. (2015). Advancement of polarizable force field and its use for molecular modeling and design. In D. Wei, Q. Xu, T. Zhao, & H. Dai (Eds.), *Advance in structural bioinformatics* (Vol. 827, pp. 19–32). Netherlands: Springer.

Yamamoto, D., Yeh, J. Z., & Narahashi, T. (1984). Voltage-dependent calcium block of normal and tetramethrin-modified single sodium channels. *Biophysical Journal, 45*(1), 337–344.

Yue, L., Navarro, B., Ren, D., Ramos, A., & Clapham, D. E. (2002). The cation selectivity filter of the bacterial sodium channel, NaChBac. *Journal of General Physiology, 120*, 845–853.

Zaydman, M. A., Silva, J. R., & Cui, J. (2012). Ion channel associated diseases: overview of molecular mechanisms. *Chemical Reviews, 112*(12), 6319–6333.

Zhang, X., Ren, W., DeCaen, P., Yan, C., Tao, X., Tang, L., & Yan, N. (2012). Crystal structure of an orthologue of the NaChBac voltage-gated sodium channel. *Nature, 486*(7401), 130–134.

Zhang, X., Xia, M., Li, Y., Liu, H., Jiang, X., Ren, W., & Gong, H. (2013). Analysis of the selectivity filter of the voltage-gated sodium channel NavRh. *Cell Research, 23*(3), 409–422.

Zhou, Morais-Cabral, Kaufman, & MacKinnon. (2001). Chemistry of ion coordination and hydration revealed by a K^+ channel-Fab complex at 2.0 angstrom resolution. *Nature, 414*, 43–48.

Zuniga, L., Marquez, V., Gonzalez-Nilo, F. D., Chipot, C., Cid, L. P., Sepulveda, F. V., & Niemeyer, M. I. (Jan 25, 2011). Gating of a pH-sensitive K-2P potassium channel by an electrostatic effect of basic sensor residues on the selectivity filter. *PLoS One, 6*(1), e16141. http://dx.doi.org/10.1371/journal.pone.0016141.

B.2 Capturing the Molecular Mechanism of Anesthetic Action using Simulation Methods, *Chem. Rev.* (under review)

B.2.1 Authorship and Permissions

<table>
<tr><td colspan="10">This declaration concerns the article entitled</td></tr>
<tr><td colspan="10">Capturing the Molecular Mechanism of Anesthetic Action using Simulation Methods</td></tr>
<tr><td colspan="10">Publication status (tick one)</td></tr>
<tr><td>Draft manuscript</td><td></td><td>Submitted</td><td></td><td>In review</td><td></td><td>Accepted</td><td></td><td>Published</td><td>✓</td></tr>
<tr><td>Publication details</td><td colspan="9">Chem. Rev., Article ASAP
DOI: 10.1021/acs.chemrev.8b00366

Published online: 25 October 2018

Reprinted with permission from V. Oakes, and C. Domene, Chem. Reviews, 2018, Article ASAP. Copyright 2018 American Chemical Society.</td></tr>
<tr><td>Candidates contribution to the paper (detailed and also given as a percentage)</td><td colspan="9">The candidate contributed to/considerably contributed/predominantly executed the…
Formulation of ideas (90%):
V. Oakes and C. Domene contributed to the content.

Design of methodology:
NA

Experimental work:
NA

Presentation of data in journal format (90%):
V. Oakes: Main author of manuscript
C. Domene: Critically assessed and appended manuscript</td></tr>
<tr><td>Statement from Candidate</td><td colspan="9">This paper reports on original research I conducted during the period of my Higher Degree by Research candidature.</td></tr>
<tr><td>Signed</td><td colspan="4"></td><td>Date</td><td colspan="4"></td></tr>
</table>

CHEMICAL REVIEWS

Review

Cite This: Chem. Rev. XXXX, XXX, XXX−XXX

pubs.acs.org/CR

Capturing the Molecular Mechanism of Anesthetic Action by Simulation Methods

Victoria Oakes[†] and Carmen Domene*[,†,‡]

[†]Department of Chemistry, University of Bath, Claverton Down, Bath BA2 7AY, United Kingdom

[‡]Department of Chemistry, University of Oxford, Oxford OX1 3TA, United Kingdom

ABSTRACT: Significant computational efforts have been focused toward exposing the molecular mechanisms of anesthesia in recent years. In the past decade, this has been aided considerably by a momentous increase in the number of high-resolution structures of ion channels, which are putative targets for the anesthetic agents, as well as advancements in high-performance computing technologies. In this review, typical simulation methods to investigate the behavior of model membranes and membrane−protein systems are briefly reviewed, and related computational studies are surveyed. Both lipid- and protein-mediated mechanisms of anesthetic action are scrutinized, focusing on the behavior of ion channels in the latter case.

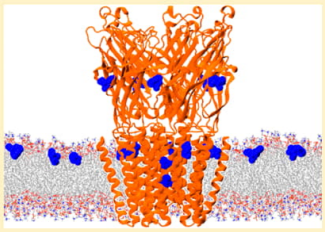

CONTENTS

1. INTRODUCTION

Anesthesia refers to a medically induced lack of sensation, enabling surgical procedures to take place in the absence of pain. During general anesthesia, the patient encounters a state of paralysis in the whole body, accompanied by unconsciousness. During local anesthesia, specific parts of the body are insensitive to pain, while patients are responsive. The identification of anesthetic molecules has revolutionized the medical industry, yet an in-depth understanding of the molecular mechanism of anesthetic action has not yet been achieved. Initial examinations by Meyer[1] and Overton[2] led to the proposal of a lipid-mediated mechanism for anesthesia. The early experimentalists revealed a notable correlation between anesthetic potency and solubility of molecules in oil, a lipidlike phase that is assumed to act as a simplified model of the membrane interior, advocating that anesthetics likely act via the plasma membrane. Studies of a variety of anesthetic compounds in an assortment of solvents have since been performed,[3,4] and the Meyer−Overton hypothesis was upheld for nearly a century, until a number of notable exceptions were revealed. For example, Koblin et al.[5,6] identified a series of polyhalogenated and perfluorinated compounds that displayed no anesthetic effect despite fulfilling the Meyer−Overton rule. On the other hand, the potency of short-chain 1-alkanols was markedly underestimated by the rule.[7]

Several alternatives have now been proposed to account for such exceptions. Pohorille et al.[8] identified an improved correlation when interfacial solubilities were used instead of bulk lipid solubilities, suggesting anesthetic compounds act at the lipid−water interface. Furthermore, Cantor[9,10] discussed various membrane properties that could potentially modify the activity of intrinsic membrane proteins, recognizing that the specific composition can influence the lateral pressure profile of the membrane. As the conformational equilibrium of membrane proteins is mechanically coupled to the lateral pressure profile, incorporation of compounds into the bilayer may therefore shift the activation state of membrane proteins such as ligand-gated ion channels.[9,11] The effect of stiffness and interfacial activity of anesthetic molecules on the pressure distributions was used in this context to predict the potency of alkanols previously classified as anomalous by the Meyer−Overton rule.[12]

As an alternative to the lipid-mediated theory, it has been postulated that anesthetics can act by directly binding to protein targets. Among early work, it was demonstrated that inhalational anesthetics directly inhibited the function of the

Special Issue: Biomembrane Structure, Dynamics, and Reactions

Received: June 10, 2018

DOI: 10.1021/acs.chemrev.8b00366
Chem. Rev. XXXX, XXX, XXX−XXX

enzyme firefly luciferase by competitive binding of the substrate.[13−15] Furthermore, anesthetics exerted an effect on soluble cytoplasmic proteins, such as protein kinase C.[16,17] Considerable efforts were then focused toward identifying specific protein targets. Nowadays, specific classes of membrane receptors and membrane channels are considered to be dominant targets for anesthetics. Targets include γ-aminobutyric acid A ($GABA_A$), glycine, nicotinic acetylcholine, glutamate, adenosine, and serotonin receptors, as well as voltage-gated, ATP-sensitive, and background potassium channels.[18] These proteins are generally considered to accommodate anesthetic molecules in pockets/cavities, which consequently modulate their structure and dynamics in a specific manner.[19] Thereupon, a legion of works has been published with the aim of classifying interaction sites and determining the repercussions of binding on the structure and dynamics of the protein.

Detailed understanding of membrane−ligand and membrane−protein interactions at an atomic level, and comprehension of the structural consequences of such binding, will greatly benefit future anesthetic drug design. In this review, we provide an overview of the achievements of computational tools for chemical biology in deciphering the molecular mechanism of anesthetic action. First, a brief overview of common simulation methods used for the study of biological systems is given in section 2, and then we explore how such methodologies have been used to investigate both lipid and protein mediated theories in sections 3 and 4. In the latter case, we focus on two types of membrane-channel systems, namely pentameric ligand-gated ion channels (section 4.1) and voltage-gated ion channels (section 4.2), which are both putative targets for anesthetics and have been studied extensively by computational means. We primarily focus on simulations based on high-resolution structural information, although homology models are mentioned where appropriate. Finally, a critical outlook on the state of the field will be sumarized in section 5.

2. COMMON SIMULATION METHODS

The broad range of tools for computational chemistry currently available enable researchers to study a considerable variety of properties. On the molecular level, molecular dynamics (MD) simulations are a popular method to analyze the dynamic behavior of chemical entities in atomic detail. A brief overview of MD simulations and related methods is provided in this section. Further information concerning the mathematical background can be found in various textbooks on the topic.[20−22] To perform MD simulations, the underlying potential energy of the system must be calculated in the first instance, via quantum or molecular mechanical methods. In the latter case, atoms and bonds are considered as balls and springs, respectively, and thus nuclear motion is evaluated by use of classical physics, and an analytical expression for the energy of a system, known as a force field, can be utilized. Inter- and intramolecular energetic terms, including bond stretching, angle bending, bond rotations, and nonbonded terms, contribute to the force field. This method in its simplest version neglects electronic properties such as polarizabilities but permits the evaluation of a significant number of properties. Classical MD simulations are particularly suited to the study of biological systems, such as membrane proteins, due to the large number of atoms that are involved and the resolution of the events under investigation.

In order to obtain information about time-dependent behavior, the motion of interacting particles is calculated by integrating Newton's equations of motion. The potential energy of the system, evaluated by use of the chosen force field, and the forces, evaluated by use of the negative gradient of the potential with respect to displacement in a specified direction, can be used to calculate the acceleration, and hence forecast the time evolution of the system, in the form of a trajectory. When a few atoms are involved, analytical solutions of the equations of motion can be accessed, generating a continuous trajectory over time. In larger systems, this is unworkable due to a many-body problem in force evaluations, arising from the existence of a continuous potential. Instead, finite difference methods can be used where forces are evaluated at discrete intervals (time steps) and assumed constant in the hiatus. By use of the positions, velocities, and forces of individual atoms at the current time step, the position and velocities at the following time step can be calculated. Forces are then recalculated, and the procedure is repeated until the desired time scale is reached.

Algorithms for classical MD simulations are implemented in a wide variety of software (NAMD,[23] AMBER,[24] and GROMACS,[25] for example), which are compatible with a broad range of biomolecular force fields (CHARMM,[26] AMBER,[27] OPLS,[28] etc.) Force fields generally differ in their functional form, parameterization protocol and parameters therein, and are generally obtained to accurately reproduce experimental and/or quantum mechanical data. Generally, individual terms for bond lengths and angles utilize simple harmonic potentials on the basis of an energetic penalty associated with a deviation from the equilibrium value.[26] To model the rotation of atoms, a torsional angle potential function is also typical with associated steric barriers. To obtain the energy of nonbonded interactions in additive force fields, fixed-point charges are assigned at the nuclei, and Coulomb and Lennard-Jones potentials are used to express electrostatic and van der Waals forces, respectively. In recent years, polarizable force fields have become available, which take into account charge polarization effects. Multiple schemes have been proposed to take into account charge fluctuations, induced by the presence of additional molecules.[29] The fluctuating charge model, the induced dipole model, and the Drude oscillator approach are respectively available via the CHeq force field,[30,31] AMOEBA,[32] and the CHARMM Drude polarizable force field.[33,34] Reference 32 is recommended as an encyclopedic update of the field.[35]

The time scales that can be achieved by classical MD simulations are limited by system size and the availability of computing resources and efficient simulation algorithms. Simulations from 100 ns to 1 μs are generally now routine for membrane protein systems with between 100 000 and 500 000 atoms. Simulations of this time and length scale are therefore suitable to study a broad spectrum of biological processes. The supercomputer Anton and optimized MD software developed by D. E. Shaw Research have enabled production of millisecond-long unbiased simulations, further extending the phenomena that can be considered.[36]

In parallel, various methods have been developed to enhance sampling by use of typical high-performance computing facilities. In coarse-grained (CG) molecular dynamics, a reduced representation is used; by treating a group of atoms as a single interaction site, the number of degrees of freedom in a simulation system is reduced, along with the calculation

DOI: 10.1021/acs.chemrev.8b00366
Chem. Rev. XXXX, XXX, XXX−XXX

Table 1. Survey of MD Simulation Studies Performed on Anesthetic Agents and Related Compounds[a]

	one-component bilayers				binary mixtures	
name	DOPC	DMPC	DPPC	POPC	other	
Local Anesthetics						
articaine		71−73		74		
benzocaine			75	76		64−66
benzyl alcohol		77			60	
bupivacaine				78		
etidocaine				79		
KP-23				80		
lidocaine		61, 73, 81, 82	83			
prilocaine				79, 84		
procaine		85	83			
tetracaine		85	83			
General Anesthetics						
alcohols	86	61, 87, 88	89		89	62, 67
chloroform	68, 90		91−94		90	68
diethyl ether			91, 93, 94			
enflurane			91, 93, 94			
halothane	95	63, 96−98	91, 93, 94, 99, 100	101	102	
desflurane				103		
isoflurane				103, 104		
ketamine					105	
propofol		106		103		
sevoflurane				103		
trichloroethylene	58					
xenon	69		57, 107		108, 109	
Nonimmobilizers						
hexafluoroethane		110, 111			102	

[a]Lipid types are abbreviated as follows: DOPC, 1,2-dioleoyl-*sn*-glycero-3-phosphocholine; DMPC, 1,2-dimyristoyl-*sn*-glycero-3-phosphocholine; DPPC, 1,2-dipalmitoyl-*sn*-glycero-3-phosphocholine; POPC, 1-palmitoyl-2-oleoyl-*sn*-glycero-3-phosphocholine.

expense of each time step. Furthermore, the time step of each iteration is increased, facilitating the simulation of larger systems with increased complexity. Several CG force fields have emerged in recent years that are suitable for the study of biological systems.[37−41]

Various methodologies also exist to calculate the free energy of relevant biological processes. Free-energy perturbation (FEP) is one such method, whereby unphysical alchemical transformations are performed to convert the system between thermodynamic states; free-energy differences can then be calculated by use of a thermodynamic cycle.[42,43] FEP is predominantly used to calculate relative binding affinities between related compounds, which is computationally inexpensive compared to calculating absolute binding affinities.[44] In this context, the free-energy difference of bound and unbound states is calculated as $\Delta G1 = M + L_1 \rightarrow ML_1$ and $\Delta G2 = M + L_2 \rightarrow ML_2$. The relative free energy of binding can be obtained from the relationship $\Delta(\Delta G) = \Delta G2 - \Delta G1$.

Several other algorithms exist that accelerate sampling along a predefined set of reaction coordinates, known as collective variables (CV), to overcome energetic barriers and evaluate the free energy of the chosen conformational transition, known as the potential of mean force (PMF). Umbrella sampling (US)[45] is a common enhanced sampling method in this field. To sample a specific transition, independent MD simulations are performed at energetically distinct regions of the potential energy surface, maintained by a biasing potential. These simulations, known as windows, are chosen to so that they overlap to some extent, and they can then be combined and unbiased by the weighted histogram analysis method (WHAM)[46,47] or umbrella integration, to obtain the underlying potential energy surface.[48]

In steered molecular dynamics (SMD) simulations, an external force is applied to an atom or group of atoms to overcome barriers and sample a specific process.[49] Relative free energies can then be obtained by Jarzynski's equality, which relates the free-energy difference between two thermodynamic states and work done for the interconversion between states.[50] In metadynamics,[51] a bias potential is also used to accelerate sampling along chosen CVs. Gaussian functions are added to CVs, which redirects the simulation away from low-energy configurational space that has been previously inhabited. In this manner, the system departs from local free-energy minima, exploring barrier regions and locating alternative thermodynamic states. Once the free-energy profile has been flattened, convergence can be achieved, and the free-energy profile can be reconstructed to provide an unbiased estimate of the landscape as a function of the CVs. The adaptive biasing force method (ABF)[52] is largely based on thermodynamic integration, whereby the instantaneous force along the reaction coordinate is evaluated directly and counteracted by an external biasing force of equal and opposite magnitude. This effectively provides a smooth energy landscape and uniform sampling, irrespective of energetic barriers, allowing accelerated dynamics.

Finally, we remark upon related methods that are applicable to the identification of binding sites in macromolecules. Molecular docking is an inexpensive tool to establish potential binding sites and predict the position, orientation, and binding

DOI: 10.1021/acs.chemrev.8b00366
Chem. Rev. XXXX, XXX, XXX−XXX

affinities of bound molecules. This is achieved by use of sampling algorithms to catalogue possible ligand−receptor conformations, which are then ranked by scoring functions. Commonplace sampling and scoring algorithms and tools to perform molecular docking are reviewed elsewhere in the literature.[53,54] It should be highlighted that molecular docking is not a simulation method and can be performed on a single core processor or via online servers. However, molecular docking is typically performed with a rigid receptor and a flexible ligand, neglecting changes in protein structure that may influence the conformation of the ligand. Therefore, the accuracy of this method is inherently limited in comparison to simulation methodologies.

Flooding is an alternative option with greater computational expense and accuracy. In this case, an excessive concentration of ligand is inserted in the solution surrounding the protein target and allowed to enter favorable positions over the course of an unbiased MD simulation trajectory.[55] This approach implicitly takes into account fluctuations in receptor and ligand dynamics.

3. ANESTHETIC INTERACTIONS WITH MEMBRANES

Investigations into the molecular mechanisms of anesthesia have historically been fixated on the interaction of anesthetic compounds and membranes, a legacy of the Meyer−Overton correlation. In the field of computation, initial studies followed this trend, with MD simulations becoming an established tool to investigate the atomic interaction between anesthetic agents and lipid bilayers, which act as a simplified model of the plasma membrane. Unbiased all-atom MD simulations have proven successful in characterizing the effect of anesthetics on the structural properties of lipid bilayers, with coarse-grained MD simulations used in a handful of cases.[56,57] One of the first simulation studies to compare bilayer properties in the presence and absence of an anesthetic, by Huang et al.[58] in 1995, inserted a single trichloroethylene molecule into a bilayer constituted of 24 DOPC (1,2-dioleoyl-*sn*-glycero-3-phosphocholine) molecules and an 8 Å layer of explicit water molecules to solvate the system. Moreover, enhanced-sampling methods are commonly used to calculate the free-energy profile of anesthetics crossing model membranes. In 1996, Pohorille et al.[59] calculated the first free-energy profiles of membrane crossing for anesthetics, using one molecule of the closely related trifluoroethane across a bilayer of 72 glycerol 1-monooleate molecules solvated by ∼1000 water molecules. In the two decades since the initial publication of these studies, significant advancements in computer software and hardware have enabled similar simulation protocols to be performed on larger systems with increased complexity on extended time scales. In several cases, such simulations have been used in conjunction with NMR,[60,61] small-angle neutron scattering,[62] and X-ray scattering[63] to determine the structural attributes of model membranes. An exhaustive list of publications of membrane−anesthetic simulations, categorized by compound and bilayer composition, can be found in Table 1. As is demonstrated, neutral one-component bilayers have primarily been used, although binary mixtures including charged species in symmetric or asymmetric distributions have now been reported.[62,64−68] The double bilayer system was also employed in a recent publication to impose a concentration gradient and promote permeation within unbiased MD simulations.[69] In this method, two bilayers are included in different planes of the z axis, to circumvent the effects of periodic boundary conditions, allowing different solute concentrations on alternate sides. Furthermore, analysis tools are now widely available, either within the simulation software itself, as implemented in GROMACS, for example,[25] or via additional plug-ins such as MEMBPLUGIN for VMD.[70] Structural characteristics that can easily be monitored include, but are not limited to, bilayer thickness, area per lipid, acyl chain segment order parameters, charge and mass density distribution, electrostatic potential, interdigitation fraction, water dipole orientation, hydrogen bonding, and lateral pressure profiles. Here, we review a number of common themes in the literature regarding anesthetic−membrane properties.

A number of molecules have been identified that are structurally related to anesthetic compounds but exhibit negligible anesthetic properties despite displaying similar solubilities and fulfilling the Meyer−Overton rule.[5,7,112] This has provoked considerable interest in differential responses of anesthetic and such nonimmobilizer molecules. Experimentally, it has been disclosed that anesthetic molecules modulate the orientational order of the hydrocarbon chains, whereas related nonimmobilizer molecules produce little or no response.[113,114] Observations from computation strongly agree with this postulate. Early calculations from Pohorille et al.[59,115,116] of both classes of molecule in a simple lipid bilayer revealed anesthetic molecules preferentially reside near the headgroup−water interface and nonimmobilizer analogues can penetrate into the hydrophobic membrane interior in nonspecific locations. MD simulations of halothane, in a saturated bilayer, confirmed this to be the case,[99,100] identifying a number of perturbations in the structure of the lipid bilayer, such as an increase in area per lipid, a change in the orientation of the headgroup dipole, and a decrease in the orientational order of the hydrocarbon chains, as predicted experimentally.[113,114] Such changes were then absent in the presence of the halothane analogue hexafluoroethane.[110,111] These experiments were then repeated with highly unsaturated lipid bilayers, which are often present in biological membranes.[102] The unsaturated systems displayed analogous distributions of compounds across the bilayer, with the exception of an additional minimum for halothane at the bilayer center, and exhibited similar effects on the electrostatic profiles. Overall, the associated studies advocate that anesthetic and nonimmobilizer molecules occupy distinct locales in lipid bilayers, irrespective of the degree of chain saturation, a phenomenon that may underlie the discrepant responses to chemically similar molecules biologically.

The protonation states of individual anesthetic molecules, which affect its biological activity, must be also considered, particularly for local anesthetics.[117] Comparative simulations between charged and uncharged forms of local anesthetic molecules have been reported in a number of cases, with observable differences shown. First, simulations of various neutral and charged KP-23 local anesthetics molecules in neutral and charged forms were performed.[118] Neutral molecules partitioned into the bilayer core whereas charged molecules self-condensed on the bilayer surface, consistent with experimental studies demonstrating differential intercalation.[119] In agreement with this, charged lidocaine molecules stably occupied the lipid headgroup region in a DMPC (1,2-dimyristoyl-*sn*-glycero-3-phosphocholine) bilayer primarily oriented parallel to the bilayer normal, whereas neutral molecules can penetrate further and move more freely in a perpendicular orientation.[81] In a subsequent study, the neutral

DOI: 10.1021/acs.chemrev.8b00366
Chem. Rev. XXXX, XXX, XXX−XXX

and charged lidocaine molecules were found to modify the electrostatic potential profiles to a similar extent, despite alternate positions and the associated effects. It was then suggested that changes of this magnitude (90 mV for 9 mol % lidocaine and 220 mV for 28 mol % lidocaine) could potentially alter the function of voltage-gated ion channels.[82] Under the same simulation protocol, articaine charged and uncharged molecules were observed to accumulate in analogous positions and crossing to a similar extent as those observed in lidocaine.[71] However, critical differences are observed in the orientation of the charged form, now parallel to the membrane surface, and the hydrogen bonding and diffusion attributes, resulting from an additional carbonyl group at the opposite end of the molecule, causing differential effects in the membrane physical properties. The effect on the electrostatic potential profile was also similar for both forms, again of the order of the transmembrane potential. What emerges from such studies is clear evidence that charged molecules preferentially bind to the headgroup regions whereas neutral molecules penetrate the hydrophobic region of the bilayers more readily. Consequentially, the impact of anesthetic intercalation on structural properties can differ.

Efforts have also been focused toward understanding the effects of pressure on general anesthesia, in order to rationalize the known pressure reversal, that is, the inverse correlation between pressure and anesthesic potency.[120,121] Computational simulations have been used to evaluate the effect of pressure on the behavior of anesthetic molecules, although other mechanisms of pressure modulation may exist in this context. Using halothane in artificially high concentrations (six times the clinical concentration), MD simulations by Chau et al.[96,98] revealed elevated aggregation of halothane at high pressures in DMPC bilayers. The authors suggest preferred accumulation disfavors binding of individual halothane to putative binding sites on intrinsic membrane proteins. At a lesser concentration (twice the clinical concentration) and using an alternative membrane (POPC, 1-palmitoyl-2-oleoyl-*sn*-glycero-3-phosphocholine), Tu et al.[101] disclosed halothane aggregation at 2×10^7 Pa but not at 4×10^7 Pa, consistent with conditions where pressure reversal is observed and inhibited. In contrast, such clustering of isoflurane molecules in lipid bilayers is not observed at elevated pressures, suggesting previous results may be isolated examples, and therefore an alternative mechanism may be in effect.[104] The question of pressure reversal will likely spawn numerous studies in the near future.

The noble gas xenon has been of considerable interest as a general anesthetic in recent years.[122−124] Although the clinical benefits of xenon have been known for decades,[125] the feasibility of the gas has been newly realized with lowered costs.[122] However, the mechanism of xenon remains elusive. Xenon is known to elicit a response in certain glutamatergic receptors,[126,127] nicotinic receptors,[128] and potassium channels,[129] yet it is ineffective on $GABA_A$ receptors,[126] a significant anesthetic target. Thus, computational efforts have been focused toward assessing the viability of the membrane-mediated mechanism of anesthetic action for xenon. The ramifications of xenon penetration on bilayer properties, pressure coupling, and comparative studies of similar chemical species lacking anesthetic activities have been extensively assessed in this case.

Initial simulations of xenon in POPC bilayers identified slight increases in the area per lipid, membrane thickness, and orientational order of the lipid tails, as a result of xenon occupation of the interfacial region and in the center of the bilayer.[107] In a POPE (1-palmitoyl-2-oleoyl-*sn*-glycero-3-phosphoethanolamine) bilayer, increases in the area and volume per lipid and decreases in the orientational order of acyl chains were observed in the presence of xenon alongside increased diffusivity of the lipid molecules.[109] Simulations conducted at a number of pressures (0.1, 10, 20, 35, and 50 MPa) reveal xenon molecules are pushed into the interface between the two bilayer leaflets at high pressures, which limits their diffusion. Comparable properties are observed in these bilayers and xenon-free bilayers at low pressure, advising that pressure reversal emanates from the elimination of diffusive xenon molecules in the membrane. Differential scanning calorimetry measurements combined with MD simulations confirmed favorable binding in the bilayer core, promoting straightening of the lipid tails concomitantly with increased headgroup spacing.[69] Biophysical properties were also perturbed, such as the decrease in phase-transition temperature and the lateral pressure profile in the headgroup region, adhering to the lipid-bilayer-mediated mechanism of general anesthesia proposed by Cantor.[130] This proposal was supported further by a comparative study of four noble gases (Ne, Ar, Kr, and Xe), which found that the degree of disruption of the membrane was dependent on the site of localization and correlated well with relative narcotic potencies.[108] Booker and Sum[69] hypothesize that the modified phase-transition temperature, lateral forces, and hydrophobic mismatch caused by accretion of xenon in the membrane can contribute to the conformational cycle of ion channels embedded in the membrane, providing multiple indirect mechanisms of action. The authors note that the suggested membrane-mediated mechanism for xenon likely contributes to an additional protein-mediated mechanism.

4. ANESTHETIC INTERACTIONS WITH ION CHANNELS

4.1. Pentameric Ligand-Gated Ion Channels or Cys-Loop Receptors

Ion channels facilitate the passive diffusion of ionic species down their electrochemical gradient between the extracellular medium and the cell cytoplasm. Permeation is controlled by the onset of various external stimuli, such as transmembrane voltage, heat, ligand binding, or mechanical stretch, and is responsible for regulating electrical signals across the cellular membrane. Pentameric ligand-gated ion channels (pLGICs) are responsible for the swift conversion of chemical signals to electrical impulses throughout the nervous system.[131] pLGICs from the Cys-loop receptor family have been identified as a putative target for general anesthetics at clinical concentrations, with the exact response, inhibition or potentiation, dependent on the channel type.[132,133]

Extensive work on nicotinic acetylcholine receptors revealed the overall structural assembly of pLGICs, containing five homologous or closely related heterologous subunits that assemble in a pentameric arrangement.[134] Each subunit contains N- and C-terminal extracellular domains and cytoplasmic and transmembrane domains.[134] Orthosteric and allosteric binding sites are located in the extracellular domain, alongside the characteristic Cys-loop, a 13-residue loop flanked by cysteine residues engaged in a disulfide bond.[135] The symmetry axis of the transmembrane domain constitutes the ion permeation pathway, formed from four transmembrane

DOI: 10.1021/acs.chemrev.8b00366
Chem. Rev. XXXX, XXX, XXX−XXX

segments (M1−M4); M2 lines the central pore, and a cytoplasmic domain of variable length intersects segments M3 and M4.

The discovery of prokaryotic homologues of pLGICs hastened the publication of high-resolution crystal structures of pLGICs: those from *Erwinia chrysanthemi* (ELIC)[136,137] and *Gloeobacter violaceus* (GLIC),[138,139] were the first to become available, representing closed and open states, respectively. The structures consist of a homologous transmembrane domain (M1−M4) and an expansive extracellular domain composed of five inner and three outer strands connected by loops forming a β-sandwich. The susceptibility of the prokaryotic homologue from *G. violaceus* (GLIC) to clinically relevant concentrations of general anesthetics has also been established.[140] Therefore, such structures provide a rational point to study the molecular mechanism of anesthetic action by computational means. Due to the number of simulation studies on the GLIC channel and the availability of high-resolution crystal structures, we will focus on this channel, although it should be noted that other Cys-loop receptors, such as the glycine receptor,[141−143] nicotinic acetylcholine receptor (nAChR),[144−146] GluCl channel,[147] and $GABA_A$[148−151] receptor, have been the subject of computational works, primarily by use of homology models.

Initial computational works utilizing the apo structures of GLIC aimed to identify anesthetic binding sites.[55] Brannigan et al.[55] performed a comparative study of isoflurane binding to nAChR and GLIC, implicating eight distinct sites throughout the transmembrane and extracellular domains and within the interfacial region between the two. Of potential functional relevance, the pore of both LGICs accommodates isoflurane dimers, which would impose a physical block to ion permeation, thus acting as an inhibitory site. Isoflurane also binds to the transmembrane (TM) domain of nAChR in intersubunit sites underneath the M2−M3 loop in nAChR, in agreement with earlier speculation from photoaffinity labeling.[152] The absence of such a site in GLIC leads the authors to postulate that this acts as a positively modulating site, rationalizing the increased sensitivity of GLIC to inhibition by anesthetics relative to nAChR.[140] Finally, novel intrasubunit sites in both nAChR α subunits and one GLIC α subunit were observed. It is speculated that residence of the α subunits, which determine agonist susceptibility, in a position behind the M2 helices, which are involved in channel opening, and parallel to the hydrophobic constriction could influence the active state of the receptor.

Various crystal structures have since been resolved of GLIC in complex with anesthetic molecules, including propofol,[153,154] desflurane,[153] bromoform,[154−156] ethanol,[155] and ketamine,[137] providing additional insights into sites in the transmembrane and extracellular domains and in the pore (Figure 1). A transmembrane anesthetic binding site was characterized in the 2011 structure of GLIC in complex with general anesthetics propofol and desflurane.[153] Here, the compounds occupy an intrasubunit crevice in the extracellular leaflet of the transmembrane domain, with residues from M1−M4 and the β6−β7 loop of the extracellular domain. Mutants T255A (in M3) and V242 M (in M2) displayed a marked, albeit distinct, response to propofol and desflurane, confirming the physiological importance of such a site. Increased propofol sensitivity was interpreted by MD simulations within the same study, as propofol percolated further into the cavity, becoming less mobile and intensifying interactions with residue 242 in mutant channels relative to the wild type.

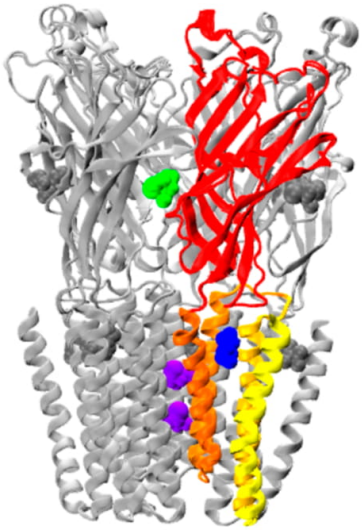

Figure 1. Positions of propofol (blue), isoflurane (purple), and ketamine (green) binding sites in GLIC/ELIC, obtained from PDB files 3P50,[153] 4Z90,[157] and 4F8H,[158] respectively. Transmembrane helices of a single subunit are colored yellow to orange, with the extracellular domain shown in red.

Using the crystallographic positions of desflurane as a reference and additional molecular docking calculations, Willenbring et al.[159] simulated isoflurane binding to GLIC to delineate the structural consequences of prolonged binding. Movement of isoflurane between sites promoted the breakage of intersubunit salt bridges in the extracellular domain, perturbing the quaternary structure and inward movement of the M2 helices, providing a mechanism by which isoflurane contributes to channel closure.

Subsequent MD simulations revealed loose binding of the resolved desflurane to the crystal structure site, which could dissociate in under 100 ns.[160] However, occupation of an adjacent site enhanced binding, suggesting that double occupation is required for desflurane to inhibit GLIC. Mutation in this site experimentally correlated with diminished binding in the crystal structure site, in agreement with this. The route of access of such sites is also exposed, with desflurane diffusing into and out of the site through the membrane, via the protein−membrane interfacial region.

Further to this, fluorescence quenching disclosed the presence of multiple binding sites for inhaled anesthetic halothane and the intravenous anesthetic thiopental in the transmembrane domain.[161] Simulations revealed a site in close proximity to N200, near M1 and the M2/3 loop, which was confirmed by mutagenesis of this residue and multiple additional sites. Some sites overlapped to some extent for the chemically distinct compounds and could therefore quench the same tryptophan residues. Halothane bound in the M1−M2/3 site stabilized the M2/3 loop while mobilizing the Cys-loop in the EC domain, two regions implicated in channel gating in pLGICs.[162−164] Binding of halothane near W160 at the extracellular domain−transmembrane domain interface disrupted critical salt bridges, such as D32−R192.[161,165]

DOI: 10.1021/acs.chemrev.8b00366
Chem. Rev. XXXX, XXX, XXX−XXX

Removal of the analogous salt bridges in other ligand-gated ion channels notably diminished the stability of the open state,[164,166,167] suggesting that occupation of this site may exert a similar effect in GLIC.

Transmembrane binding was also observed for propofol via flooding simulations using coarse-grained methods that accessed a multimicrosecond time scale.[168] GLIC channel dynamics with partial occupancy of propofol binding site were investigated by Mowrey et al.[169] Asymmetric states with one to three sites inhabited exhibited elevated channel dehydration relative to symmetric states with zero or five molecules bound. Conformational changes were observed in the asymmetric states, consistent with the known effects of asymmetric agonist binding in homo-pLGICs.[170−172]

With regard to a potential pore-binding site, crystal structures of GLIC bound to bromolidocaine, a lidocaine analogue, provided the first structural insights into a pore-binding site in pLGICs.[173] Computationally, isoflurane was also documented to pass through the closed hydrophobic gate,[159] in spite of dehydration of the central cavity, occupying a position between residues I233 and I240, supporting earlier theoretical and experimental evidence of pore-binding in GLIC.[55,173] LeBard et el.[174] performed a systematic study of binding to the GLIC pore, using monomers and dimers of both isoflurane and propofol, in addition to ethanol as a negative control. Isoflurane binding affinities, calculated via FEP, were contingent on the functional state of the pore, with a situation involving binding of two isoflurane molecules to the closed pore resembling the micromolar affinity determined experimentally and consistent with a pore-block mechanism. The determined affinities illustrated that the effect of propofol is overestimated when a pore-block mechanism is considered in isolation, and they support a mechanism where pore and allosteric sites exert competitive effects on the functional state of the channel.[175]

These conclusions were further supported by the high-resolution structure of ELIC cocrystallized with isoflurane, in both apo and agonist-bound forms, presumed to be in resting and desensitized activation states, respectively.[157] These structures show inhabitancy of two isoflurane molecules within the pore, with MD simulations in the same study revealing paramount stability in the ELIC resting state, as a result of observable changes in the pore radii along the channel. Nevertheless, the affinity for both states suggests isoflurane can act by stabilizing the closed channel and also obstructing the open channel. The structural and dynamical information presented throughout these works strongly supports a pore-binding mechanism of inhibition. Bromoform binding has also been observed in the pore of GLIC, experimentally and computationally.[155,156]

Finally, structural information has also revealed a binding site in the extracellular domain. The crystal structure of (*R*)-ketamine in complex with GLIC exhibits symmetric binding in extracellular intersubunit cavities.[137] MD simulations confirmed the observed stereospecifity of this site, with (*S*)-ketamine unable to interact with residue D154, which stably interacts with (*R*)-ketamine.[176] Notably, (*R*)-ketamine evolved into asymmetric binding poses over the course of the trajectories, in contrast to the known symmetric structures of pLGICs in complex with anesthetics.[137,153,155] Structural differences resulting from (*R*)-ketamine binding were propagated to the extracellular domain−transmembrane domain interface and to pore-lining helix M2, via either the pre-M1 region or the EC $\beta1-\beta2$ loop.[176,177] In coarse-grained simulations by Joseph and Mincer,[168] mentioned previously, propofol spontaneously occupied the crystallographic extracellular binding site, prompting asymmetric conformational changes in GLIC, transmitted through a similar allosteric network in the extracellular domain−transmembrane domain interface. The molecular mechanism of long-range allosteric coupling was further probed by coarse-grained MD simulations, using a novel elastic network model proposed by Li et al.[178]

Overall, a myriad of anesthetic binding sites have been proposed by both experimental and simulation methods for the GLIC channel. Consequently, uncovering the molecular mechanism of anesthetic action has proven difficult. Several studies of GLIC with a number of different anesthetics reported a degree of structural asymmetry during the inhibition of GLIC by anesthetics.

4.2. Voltage-Gated Ion Channels

The voltage-gated ion channel (VGIC) family that specifically conducts Na^+ (Na_V) and K^+ ions (K_V) implements critical actions in the generation and propagation of action potentials, and thus plays a crucial physiological role. VGICs are a common target for antiarrhythmic agents, local anesthetics, anticonvulsants, and pain therapeutics.[179,180] Anesthetics are known to block both Na_V and K_V currents at clinically relevant concentrations.[181,182] Various computational studies have been performed to investigate this phenomenon on a molecular level.

The first high-resolution structure of the pore domain of an ion channel, the KcsA channel from *Streptomyces lividans*, was revealed in 1998.[183] The protein is characterized by a symmetric tetrameric arrangement with each monomer containing two transmembrane α-helices and an intermittent pore loop. The pore loop contains the signature selectivity sequence, which determines the ionic permeability of the channel, and thus has become known as the selectivity filter.[184,185] Between the selectivity filter and the cytoplasm, a water-filled cavity is present to provide an ideal environment for ion transfer.[186] In K^+ channels, the selectivity filter is constituted of a conserved amino acid sequence arranged to form rings of oxygen atoms, which are able to bind dehydrated ions in a cagelike structure, in adjoining sites. In Na^+ channels, a ring of residues at the extracellular site forms the selectivity filter, although the identity of residues is more dependent on the specific channel. Atomistic structures of bacterial (K_VAP from *Aeropyrum pernix*)[187,188] and mammalian (K_V1.2)[189−192] K_V channels have since been obtained, illuminating the structure of voltage-sensor domains (VSD) and their interaction with the pore domain. In contrast, high-resolution crystallographic data for Na_V channels has been available only since 2011 from a number of bacterial sources: Na_VAb (*Arcobacter butzleri*),[193−196] Na_VRh (*Rickettsiales sp.* HIMB114),[197,198] Na_VMs (*Magnetococcus* sp.),[199−201] and Na_VAe1p (*Alkalilimnicola ehrlichii* sp. nov.).[202] These channels exhibit four identical subunits arranged symmetrically, each containing six transmembrane segments (S1−S6). Segments S1−S4 constitute the voltage-sensing domain, while S5 and S6 represent the pore domain, described previously. The behavior of the voltage sensor and pore domains are closely coupled, whereby movement of S4 (following a change in the transmembrane voltage) prompts rearrangement of the pore helices, via the S4−S5 linker, subsequently opening the

DOI: 10.1021/acs.chemrev.8b00366
Chem. Rev. XXXX, XXX, XXX−XXX

cytoplasmic gate. Recently, a cryoelectron microscopy structure of a eukaryotic Na_V channel, Na_VPs, at near-atomic resolution (3.8 Å), isolated from the American cockroach *Periplaneta americana*, has been published.[203] This channel is composed of a single polypeptide chain arranged into equivalent homologous transmembrane domains, as is the case for eukaryotic Na_V channels. The overall homology observed between known eukaryotic and prokaryotic structures advocates that bacterial analogues are suitable templates to study small-molecule inhibition of K_V and Na_V channels.

4.2.1. Sodium Channels. The therapeutic value of Na_V channel inhibitors is well-established, with antiarrhythmics, anticonvulsants, antidepressants, and antiepileptics known to block the Na_V channel pore. Various anesthetic agents, including but not limited to isoflurane,[204,205] lidocaine,[206] and bupivacaine,[206] are also known to modulate the entire mammalian Na_V channel family. The effect of local anesthetics on sodium currents was first acknowledged by Weidmann in 1955.[207] This idea was matured by various researchers into the 1970s, leading to the proposal of several mechanisms of anesthetic action on Na_V channels.[208] Making use of data on Na_V channel blockage by quarternary derivatives of lidocaine in myelinated nerves, Strichartz[209] established the concepts of tonic and use-dependent block, whereby drug molecules specifically bind to the closed and open state of the channel, respectively. At this time, factors including structure/protonation state of the molecule, mode of application, and membrane potential were found to alter the exact contribution of each mechanism to the observable response of individual anesthetics.[210] Nowadays, it is widely accepted that highly polar or charged compounds are effective during use-dependent block, traversing through a hydrophilic pathway, whereas neutral compounds are effective during tonic block, passing through a hydrophobic pathway when applied from either side of the membrane.[208,211]

The question of an alternative hydrophobic pathway was answered to some extent by the available structural information, which revealed lateral lipid-filled openings, termed fenestrations, directly connecting the central pore to the surrounding membrane, as illustrated in Figure 2. Considering this, computational methods have been used to investigate small-molecule binding sites in Na_V channels and potential access pathways for those within the pore.

One of the first prokaryotic Na_V channel to exhibit a response to anesthetics,[212] NaChBac, has been the subject of several computational works.[213,214] Homology models of NaChBac, based on a Na_VAb structure (PDB ID 3RVY) in combination with flooding simulations, were used to identify multiple binding sites for the general anesthetics isoflurane and sevoflurane.[213,214] Sites were located near the selectivity filter accessible from the extracellular solution, at the S4−S5 linker, in the central cavity, and at the entrance to the fenestration regions. The estimated binding affinities of the isoflurane interaction sites were calculated to be in the physiologically relevant range via FEP,[213] with those beneath the selectivity filter and near the S4−S5 linker later confirmed by NMR data.[215] Evidence for state-dependent binding of sevoflurane to the S4−S5 linker and selectivity filter site was also presented in a study by Barber et al.,[214] alongside a unique site in the deactivated state where the S6 helices coalesce. The specific locale of the observed isoflurane and sevoflurane binding sites suggests that general anesthetics may act by interfering with the selectivity filter or activation at the cytoplasmic S6 gate, or

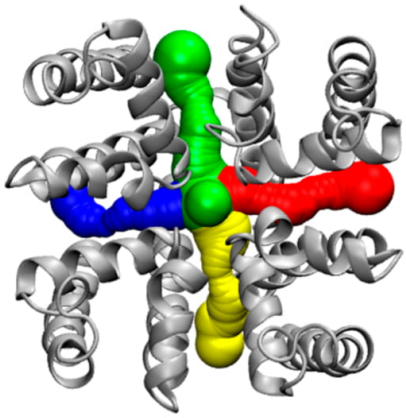

Figure 2. Pore structure of the Na_VMs channel, with the individual fenestrations colored in blue, red, yellow and green. Each of the four monomers is represented in gray. The view of the channel is perpendicular to the membrane plane.

by obstructing ion permeation within the pore, in a similar manner to local anesthetics in the latter case.[213] Isoflurane and sevoflurane molecules were able to enter the central cavity via fenestrations, bypassing the closed cytoplasmic gate. Entrance of such molecules was accompanied by displacement of fenestration-bound lipid molecules and expulsion of water molecules through the selectivity filter, with approximately six water molecules displaced by a single isoflurane in the pore. These observations demonstrated the capability of fenestrations to act as a hydrophobic pathway for small drugs such as isoflurane.[213]

Lending further support to this postulate, Kaczmarski and Corry[216] used unbiased MD simulations to analyze the behavior of fenestrations on the subunit interface between S5 and S6 helices in six bacterial Na_V channels and a homology model of Na_V1.4. The bottleneck radii of the fenestrations range in size from 1.6 to 2.2 Å with maximum radii between 2.6 to 2.8 Å, potentially tolerable for the passage of aromatic rings, a typical component of Na_V channel inhibitors. Fenestration size was determined by the identity (F203 in Na_VAb, whereas the equivalent positions in Na_VRh and Na_VMs are occupied by Ile and Met) and rotameric state of bottleneck residues and by the extent of lipid occupation, with local fluctuations typically observed on a nanosecond time scale. Following this, fenestration characteristics in the Na_V1.4 channel model varied as a result of sequential differences of the repeat sequences.

The location of small-molecule binding has also been of interest, utilizing the high-resolution structures of bacterial channels. Studies from independent research groups have identified two high-affinity binding sites for small neutral drugs, the local anesthetic benzocaine and the antiepileptic phenytoin, in the central cavity of Na_VAb, using unbiased and metadynamics simulations.[217] The observed binding occurs in two hydrophobic sites in the pore, in close proximity to the S6 gate and in a fenestration site, consistent with residues recognized in blocking of eukaryotic channels.[218] Using extensive equilibrium simulations, Boiteux and co-workers cite enhanced stability of the fenestration site as a result of π-stacking with F203; on the other hand, Martin and

DOI: 10.1021/acs.chemrev.8b00366
Chem. Rev. XXXX, XXX, XXX−XXX

Corry[217] advocate nonspecific hydrophobic interactions dominate binding in such sites, with the S6 site deemed more energetically favorable (by 3 kcal/mol) by use of metadynamics simulations. These results are in agreement with prior studies implicating multiple residues that are hydrophobic in nature in tonic block,[219] in stark contrast to use-dependent blockers, which rely on cationic interactions with aromatic residues.[219] Spontaneous translocation of benzocaine through the fenestrations is observed in the unbiased simulations, with low energy barriers of this route calculated by enhanced-sampling methods, confirming the fenestrations as a viable access route for the local anesthetic benzocaine. Unexpectedly, transfer of compounds through the closed cytoplasmic gate was noted to be viable in both studies. To imitate the eukaryotic Na_V channel pore, aromatic residues were introduced into the Na_VAb pore near the activation gate, pushing benzocaine and phenytoin toward the fenestration site whereas aromatic residues near the fenestrations imposed the opposite effect. Interestingly, the binding affinity increased in such channels.[220]

In the Na_VMs channel, Buyan et al.[221] characterized the transport and binding properties of a selection of physiologically active compounds, permanently neutral (benzocaine, lamotrigine, and carbamazepine) and protonatable (PF-5215786, PF-6305591, and lidocaine), in both neutral and charged states at pH 7, using unbiased MD simulations and replica exchange with a solute scaling/tempering method. Protonatable compounds penetrated the bilayer with ease in the neutral form relative to their charged protonated form advocating that such molecules relinquish their charge before entering the plasma membrane. Once within the lumen of Na_VMs, binding of neutral and charged molecules manifests at separate sites: neutral compounds primarily occupied the lower region of the pore, proximal to S6 residues, while charged compounds displayed prominent interactions with the selectivity filter. In the latter case, sodium currents were hampered by steric block and electrostatic repulsion with the bound molecule. This novel pore-blocking site correctly reproduces the position of resolved bromines in the crystallographic structure of Na_VMs with antagonist PF-5215786[200] and suggests that compounds reclaim their charge to exert an effect in the pore.

4.2.2. Potassium Channels. Both voltage-dependent and voltage-independent K^+ channels can be blocked by local anesthetics. Responses have been recorded for members of the two-pore domain[222] and inward rectifying channels.[223] An initial MD study of open and closed conformations of KirBac1.1 in the presence of halothane molecules demonstrated accumulation of halothane molecules at the cytoplasmic gate in the open state only.[224] Occupation of this region dampened movements of phenylalanine residues, which have previously been implicated in channel gating.[225] A similar mechanism whereby halothane moderates tryptophan fluctuations has been proposed by fluorescence experiments[226] and MD simulations alike.[227,228]

The potential role of K_V channels in the action of inhalational general anesthetics has been realized most recently,[229] with evidence accumulating from the 1990s.[230−234] A direct link between the application of isoflurane and the single-channel properties of *Drosophila* Shaker B K_V channel was first established by Li and Correa.[231] Inhibitory responses to general anesthetics (chloroform, halothane, isoflurane, and propofol) and short-chain alcohols have also been recorded for K-Shaw2, a distinct member of the *Drosophila* Shaker K_V channel family.[235−237] Distinctively, sevoflurane triggered activation of K-Shaw2.[238] Contrary to typical K^+ channels, K-Shaw2 is thought to undergo a simple activation cycle, involving only two[239,240] or three states.[238] Consolidation of the accrued data advocate that inhibitory compounds sustain closed states of the K^+ channel, whereas sevoflurane is proposed to eradicate unstable inactivated states that diverge from the activation pathway.[238]

In order to examine pore-binding sites in voltage-dependent channels, MD simulations of the open states of $K_V1.2$[190,191] and $K_{Ca}3.1$ (a homology model using the $K_V1.2$ structure) were performed with local anesthetic lidocaine and TRAM-34 initially inserted in the pore.[241] Both compounds occupy a conserved valine-alanine-valine motif in the pore in both channels, in close proximity to the selectivity filter, in agreement with interaction sites predicted for small-molecule binding in other K^+ channels.[242,243] K_d values were estimated as 20 μM (lidocaine−$K_V1.2$), 540 nM (TRAM-34−$K_V1.2$), and 10 nM (TRAM-34−$K_{Ca}3.1$), in broad agreement with experimentally determined values and the recorded ∼200-fold selectivity of TRAM-34 for $K_{Ca}3.1$ over $K_V1.2$.[244] The PMF profiles of ion permeation through $K_V1.2$ were then calculated, in order to delineate the functional consequences of pore binding to this site. The neutral form of lidocaine had a negligible effect on the calculated energetics, while the charged form imposed an energy barrier of the order of 6 kT, consistent with previous reports.[245] On the other hand, TRAM-34 prompted ion dehydration, inducing an energy barrier of ∼10 kT. As a consequence, lidocaine must be neutral to cross the membrane and enter the pore yet must be charged to exert an effect. In contrast, the neutral form of TRAM-34 is sufficient for both purposes, providing a potential scaffold for drugs that would remain active in acidic conditions typical of inflammation.

Various experimental results have also cited the involvement of the S4−S5 linker and the distal part of the S6 segment and adjacent helices in the inhibition of K-Shaw2 by general anesthetics.[236,237,246,247] The region is critical for coupling between the voltage-sensor and pore domains in the event of voltage activation, and it is therefore possible that anesthetic binding interferes with this phenomenon.[191,248] In order to provide a molecular description of this process, Barber et al.[249] performed a systematic alanine/valine mutagenesis scan of the S4−S5 linker and a segment of S6 on K-Shaw2, with associated electrophysiological experiments to delineate the consequences of such mutations on K-Shaw2 inhibition by 1-butanol and halothane. In conjunction with docking calculations and MD simulations, a putative anesthetic binding site was identified in the S4−S5 linker region, and residues critical for anesthetic binding allosteric coupling to the binding site and propagating structural changes to the cytoplasmic gate were determined. A molecular picture of closely associated yet distinct binding and effector sites emerged, beginning to unravel the determinants of anesthetic action in K-Shaw2.

Following this, the differential effects of several general anesthetics and the novel potentiator sevoflurane on $K_V1.2$ and $K_V1.2$-FRAKT chimera (where the S4−S5 linker was replaced with that from K-Shaw2) were characterized.[250] The output of such experiments demonstrated that discrete substitutions in the S4−S5 region can induce startling differences in the response of K_V channels to general anesthetics. More specifically, positive modulation of the $K_V1.2$ channel was

DOI: 10.1021/acs.chemrev.8b00366
Chem. Rev. XXXX, XXX, XXX−XXX

predominantly dependent on a single mutation, G329T, with the mutant response closely resembling that displayed by K-Shaw2. Docking and free-energy methods utilizing closed/resting and open/activated states[251,252] identified four sites in the wild type and G329T mutant: two involving the S4−S5 linker, one at the S5−S6 helical interface, and one in close proximity to the selectivity filter.[250] The selectivity filter sites displayed the highest affinity binding, and a single site at the S4−S5 linker displayed noticeable dependence on the active state. Identification of several sites in the linker region with low binding affinities is consistent with a multisite model for positive allosteric modulation of K_V channels by sevoflurane. Further evidence was provided on this subject by Stock et al.,[253] who proposed a novel theoretical framework to study concentration-dependent interactions of ligands to multiple saturable sites in membrane receptors, based on docking and FEP calculations.

5. OUTLOOK

The molecular mechanisms of anesthesia have been the source of significant debate since the turn of the 20th century. The Meyer−Overton hypothesis suggested anesthetic agents primarily act via the lipid membrane. However, various data have been interpreted to disprove it, motivating alternative postulates. The evolution of computational protocols over the last two decades has permitted the study of both membrane- and protein-mediated theories via molecular dynamics simulations, revealing dynamic characteristics of relevant biological processes at atomic resolution and applicable time scales.

Several lines of inquiry have provided notable success, such as the assessment of the modification of structural properties of lipid bilayers following anesthetic exposure and identification of anesthetic binding sites on intrinsic membrane proteins, most notably pentameric ligand-gated ion channels and voltage-gated cation channels. High-resolution structural information of bacterial analogues has proven indispensable in this case, providing a practical starting point for computational works. Concurrently, the publication of structures of pharmacologically relevant membrane proteins in the future will provide additional opportunities for researchers to perform simulation studies of this nature, for instance, in transient receptor potential channels.[254] Substantial advancements in high-performance computing facilities, simulation algorithms, and force fields required for the study of model membrane systems have also significantly contributed to the success of this field. Further improvements in computer hardware will likely be achieved at an unprecedented rate, continuously improving the time scales that can be reached by simulation methods.

Several pertinent questions remain to be addressed. Exactly how direct and indirect effects influence the activation state of known targets, and hence evoke a physiological response, has proven difficult to discern. Furthermore, detailed information regarding the subtype selectivity of known anesthetic compounds could be exploited to optimize compounds in the design of novel anesthetic compounds. It is likely that models accounting for the combined effect of small-molecule binding and membrane perturbations will emerge in the near future.

AUTHOR INFORMATION

Corresponding Author

*E-mail C.Domene@bath.ac.uk; tel +44 (0) 1225 386172.

ORCID

Carmen Domene: 0000-0001-7115-4232

Notes

The authors declare no competing financial interest.

Biographies

Victoria Oakes received an M.Chem. in chemistry from the University of Sheffield (U.K.) in 2014. In 2014, she joined the Domene group at King's College London and subsequently at the University of Bath to complete her Ph.D. in the modelling and simulation of membrane proteins. She was awarded a BBSRC-CASE studentship supported by Pfizer Neusentis.

Carmen Domene received her M.Chem. in chemistry from the University of Seville (Spain) and a Ph.D. in chemistry from the University of Exeter (U.K.), where she worked with Patrick Fowler and Paul Madden on modeling many-body effects in interionic interactions. She then moved to the University of Oxford as a postdoctoral fellow at the Laboratory of Molecular Biophysics, working on computer simulations of ion channels. From 2003 to 2011, she held a Royal Society University Research fellowship at the Physical and Theoretical Chemistry Laboratory of the University of Oxford, and she became a reader in computational chemistry at King's College London in 2012. From 2017, she is a full professor at the University of Bath (U.K.). Her current research involves probing the structure and dynamics of biomolecular systems using computer simulation techniques; systems of interest include enzymes, model membranes, and membrane-bound proteins.

ACKNOWLEDGMENTS

This work was supported by the Biotechnology and Biological Sciences Research Council and Pfizer Neusentis through a CASE studentship to V.O. This work was supported by the Royal Society through a Newton award.

REFERENCES

(1) Meyer, H. Zur Theorie Der Alkoholnarkose. *Naunyn-Schmiedeberg's Arch. Pharmacol.* **1899**, *42*, 109−118.

(2) Overton, C. E. *Studien Über Die Narkose Zugleich Ein Beitrag Zur Allgemeinen Pharmakologie* Gustav Fischer: Jena, Germany, 1901.

(3) Taheri, S.; Halsey, M. J.; Liu, J.; Eger, E. I.; Koblin, D. D.; Laster, M. J. What Solvent Best Represents the Site of Action of Inhaled Anesthetics in Humans, Rats, and Dogs. *Anesth. Analg.* **1991**, *72*, 627−634.

(4) Johansson, J. S.; Zou, H. Partitioning of Four Modern Volatile General Anesthetics into Solvents That Model Buried Amino Acid Side-Chains. *Biophys. Chem.* **1999**, *79*, 107−116.

(5) Koblin, D. D.; Chortkoff, B. S.; Laster, M. J.; Eger, E. I.; Halsey, M. J.; Ionescu, P. Polyhalogenated and Perfluorinated Compounds That Disobey the Meyer-Overton Hypothesis. *Anesth. Analg.* **1994**, *79*, 1043−1048.

(6) Koblin, D. D.; Chortkoff, B. S.; Laster, M. J.; Eger, E. I.; Halsey, M. J.; Ionescu, P. Nonanesthetic Polyhalogenated Alkanes and Deviations from the Meyer−Overton Hypothesis. *Progress in Anesthetic Mechanism, Vol 3, Special Issue, 1995*; Proceedings of the International Workshop on Anesthetic Mechanisms **1995**, pp 451−456.

(7) Fang, Z. X.; Laster, M. J.; Ionescu, P.; Koblin, D. D.; Sonner, J.; Eger, E. I.; Halsey, M. J. Effects of Inhaled Nonimmobilizer, Proconvulsant Compounds on Desflurane Minimum Alveolar

DOI: 10.1021/acs.chemrev.8b00366
Chem. Rev. XXXX, XXX, XXX−XXX

Anesthetic Concentration in Rats. *Anesth. Analg.* **1997**, *85*, 1149−1153.
(8) Pohorille, A.; Wilson, M. A.; New, M. H.; Chipot, C. Concentrations of Anesthetics across the Water-Membrane Interface; the Meyer-Overton Hypothesis Revisited. *Toxicol. Lett.* **1998**, *100*−*101*, 421−430.
(9) Cantor, R. S. Lipid Composition and the Lateral Pressure Profile in Bilayers. *Biophys. J.* **1999**, *76*, 2625−2639.
(10) Cantor, R. S. The Influence of Membrane Lateral Pressures on Simple Geometric Models of Protein Conformational Equilibria. *Chem. Phys. Lipids* **1999**, *101*, 45−56.
(11) Cantor, R. S. Lateral Pressures in Cell Membranes: A Mechanism for Modulation of Protein Function. *J. Phys. Chem. B* **1997**, *101*, 1723−1725.
(12) Cantor, R. S. Breaking the Meyer-Overton Rule: Predicted Effects of Varying Stiffness and Interfacial Activity on the Intrinsic Potency of Anesthetics. *Biophys. J.* **2001**, *80*, 2284−2297.
(13) Moss, G. W. J.; Lieb, W. R.; Franks, N. P. Anesthetic Inhibition of Firefly Luciferase, a Protein Model for General-Anesthesia, Does Not Exhibit Pressure Reversal. *Biophys. J.* **1991**, *60*, 1309−1314.
(14) Franks, N. P.; Jenkins, A.; Conti, E.; Lieb, W. R.; Brick, P. Structural Basis for the Inhibition of Firefly Luciferase by a General Anesthetic. *Biophys. J.* **1998**, *75*, 2205−2211.
(15) Franks, N. P.; Lieb, W. R. Do General Anaesthetics Act by Competitive Binding to Specific Receptors? *Nature* **1984**, *310*, 599−601.
(16) Hemmings, H. C.; Adamo, A. I. B. Effects of Halothane and Propofol on Purified Brain Protein-Kinase-C Activation. *Anesthesiology* **1994**, *81*, 147−155.
(17) Gomez, R. S.; Guatimosim, C.; Gomez, M. V. Mechanism of Action of Volatile Anesthetics: Role of Protein Kinase C. *Cell. Mol. Neurobiol.* **2003**, *23*, 877−885.
(18) Lugli, A. K.; Yost, C. S.; Kindler, C. H. Anaesthetic Mechanisms: Update on the Challenge of Unravelling the Mystery of Anaesthesia. *Eur. J. Anaesthesiol.* **2009**, *26*, 807−820.
(19) Eckenhoff, R. G.; Johansson, J. S. Molecular Interactions between Inhaled Anesthetics and Proteins. *Pharmacol. Rev.* **1997**, *49*, 343−367.
(20) Leach, A. *Molecular Modelling: Principles and Applications*; Pearson Prentice Hall: 2009.
(21) Cramer, C. J. *Essentials of Computational Chemistry: Theories and Models*, 2nd ed.; John Wiley & Sons: 2004.
(22) *Computational Biophysics of Membrane Proteins*; The Royal Society of Chemistry: 2016; DOI: 10.1039/9781782626695.
(23) Phillips, J. C.; Braun, R.; Wang, W.; Gumbart, J.; Tajkhorshid, E.; Villa, E.; Chipot, C.; Skeel, R. D.; Kale, L.; Schulten, K. Scalable Molecular Dynamics with NAMD. *J. Comput. Chem.* **2005**, *26*, 1781−1802.
(24) Case, D. A.; Cheatham, T. E., 3rd; Darden, T.; Gohlke, H.; Luo, R.; Merz, K. M., Jr.; Onufriev, A.; Simmerling, C.; Wang, B.; Woods, R. J. The Amber Biomolecular Simulation Programs. *J. Comput. Chem.* **2005**, *26*, 1668−1688.
(25) Van Der Spoel, D.; Lindahl, E.; Hess, B.; Groenhof, G.; Mark, A. E.; Berendsen, H. J. GROMACS: Fast, Flexible, and Free. *J. Comput. Chem.* **2005**, *26*, 1701−1718.
(26) Brooks, B. R.; Bruccoleri, R. E.; Olafson, B. D.; States, D. J.; Swaminathan, S.; Karplus, M. CHARMM: A Program for Macromolecular Energy, Minimization, and Dynamics Calculations. *J. Comput. Chem.* **1983**, *4*, 187−217.
(27) Cornell, W. D.; Cieplak, P.; Bayly, C. I.; Gould, I. R.; Merz, K. M.; Ferguson, D. M.; Spellmeyer, D. C.; Fox, T.; Caldwell, J. W.; Kollman, P. A. A Second Generation Force Field for the Simulation of Proteins, Nucleic Acids, and Organic Molecules. *J. Am. Chem. Soc.* **1995**, *117*, 5179−5197.
(28) Jorgensen, W. L.; Tirado-Rives, J. The OPLS [Optimized Potentials for Liquid Simulations] Potential Functions for Proteins, Energy Minimizations for Crystals of Cyclic Peptides and Crambin. *J. Am. Chem. Soc.* **1988**, *110*, 1657−1666.
(29) Vorobyov, I. V.; Anisimov, V. M.; MacKerell, A. D. Polarizable Empirical Force Field for Alkanes Based on the Classical Drude Oscillator Model. *J. Phys. Chem. B* **2005**, *109*, 18988−18999.
(30) Patel, S.; Brooks, C. L. CHARMM Fluctuating Charge Force Field for Proteins: I Parameterization and Application to Bulk Organic Liquid Simulations. *J. Comput. Chem.* **2004**, *25*, 1−16.
(31) Patel, S.; Mackerell, A. D., Jr.; Brooks, C. L., 3rd. CHARMM Fluctuating Charge Force Field for Proteins: II Protein/Solvent Properties from Molecular Dynamics Simulations Using a Non-additive Electrostatic Model. *J. Comput. Chem.* **2004**, *25*, 1504−1514.
(32) Shi, Y.; Xia, Z.; Zhang, J.; Best, R.; Wu, C.; Ponder, J. W.; Ren, P. Polarizable Atomic Multipole-Based AMOEBA Force Field for Proteins. *J. Chem. Theory Comput.* **2013**, *9*, 4046−4063.
(33) Lopes, P. E. M.; Huang, J.; Shim, J.; Luo, Y.; Li, H.; Roux, B.; MacKerell, A. D. Polarizable Force Field for Peptides and Proteins Based on the Classical Drude Oscillator. *J. Chem. Theory Comput.* **2013**, *9*, 5430−5449.
(34) Savelyev, A.; MacKerell, A. D., Jr. All-Atom Polarizable Force Field for DNA Based on the Classical Drude Oscillator Model. *J. Comput. Chem.* **2014**, *35*, 1219−1239.
(35) Lemkul, J. A.; Huang, J.; Roux, B.; MacKerell, A. D. An Empirical Polarizable Force Field Based on the Classical Drude Oscillator Model: Development History and Recent Applications. *Chem. Rev.* **2016**, *116*, 4983−5013.
(36) Shaw, D. E.; Maragakis, P.; Lindorff-Larsen, K.; Piana, S.; Dror, R. O.; Eastwood, M. P.; Bank, J. A.; Jumper, J. M.; Salmon, J. K.; Shan, Y.; et al. Atomic-Level Characterization of the Structural Dynamics of Proteins. *Science* **2010**, *330*, 341−346.
(37) Shelley, J. C.; Shelley, M. Y.; Reeder, R. C.; Bandyopadhyay, S.; Klein, M. L. A Coarse Grain Model for Phospholipid Simulations. *J. Phys. Chem. B* **2001**, *105*, 4464−4470.
(38) Shelley, J. C.; Shelley, M. Y.; Reeder, R. C.; Bandyopadhyay, S.; Moore, P. B.; Klein, M. L. Simulations of Phospholipids Using a Coarse Grain Model. *J. Phys. Chem. B* **2001**, *105*, 9785−9792.
(39) Marrink, S. J.; de Vries, A. H.; Mark, A. E. Coarse Grained Model for Semiquantitative Lipid Simulations. *J. Phys. Chem. B* **2004**, *108*, 750−760.
(40) Lopez, C. A.; Sovova, Z.; van Eerden, F. J.; de Vries, A. H.; Marrink, S. J. Martini Force Field Parameters for Glycolipids. *J. Chem. Theory Comput.* **2013**, *9*, 1694−1708.
(41) Saunders, M. G.; Voth, G. A. Coarse-Graining Methods for Computational Biology. *Annu. Rev. Biophys.* **2013**, *42*, 73−93.
(42) Zwanzig, R. W. High-Temperature Equation of State by a Perturbation Method. I. Nonpolar Gases. *J. Chem. Phys.* **1954**, *22*, 1420−1426.
(43) Beveridge, D. L.; DiCapua, F. M. Free Energy Via Molecular Simulation: Applications to Chemical and Biomolecular Systems. *Annu. Rev. Biophys. Biophys. Chem.* **1989**, *18*, 431−492.
(44) Wang, L.; Wu, Y. J.; Deng, Y. Q.; Kim, B.; Pierce, L.; Krilov, G.; Lupyan, D.; Robinson, S.; Dahlgren, M. K.; Greenwood, J.; et al. Accurate and Reliable Prediction of Relative Ligand Binding Potency in Prospective Drug Discovery by Way of a Modern Free-Energy Calculation Protocol and Force Field. *J. Am. Chem. Soc.* **2015**, *137*, 2695−2703.
(45) Torrie, G. M.; Valleau, J. P. Monte Carlo Free Energy Estimates Using Non-Boltzmann Sampling: Application to the Sub-Critical Lennard-Jones Fluid. *Chem. Phys. Lett.* **1974**, *28*, 578−581.
(46) Kumar, S.; Rosenberg, J. M.; Bouzida, D.; Swendsen, R. H.; Kollman, P. A. The Weighted Histogram Analysis Method for Free-Energy Calculations on Biomolecules. I. The Method. *J. Comput. Chem.* **1992**, *13*, 1011−1021.
(47) Souaille, M.; Roux, B. t. Extension to the Weighted Histogram Analysis Method: Combining Umbrella Sampling with Free Energy Calculations. *Comput. Phys. Commun.* **2001**, *135*, 40−57.
(48) Kästner, J.; Thiel, W. Bridging the Gap between Thermodynamic Integration and Umbrella Sampling Provides a Novel Analysis Method: "Umbrella Integration. *J. Chem. Phys.* **2005**, *123*, 144104.

DOI: 10.1021/acs.chemrev.8b00366
Chem. Rev. XXXX, XXX, XXX−XXX

(49) Park, S.; Schulten, K. Calculating Potentials of Mean Force from Steered Molecular Dynamics Simulations. *J. Chem. Phys.* **2004**, *120*, 5946−5961.
(50) Park, S.; Khalili-Araghi, F.; Tajkhorshid, E.; Schulten, K. Free Energy Calculation from Steered Molecular Dynamics Simulations Using Jarzynski's Equality. *J. Chem. Phys.* **2003**, *119*, 3559−3566.
(51) Furini, S.; Domene, C. Computational Studies of Transport in Ion Channels Using Metadynamics. *Biochim. Biophys. Acta, Biomembr.* **2016**, *1858*, 1733−1740.
(52) Darve, E.; Pohorille, A. Calculating Free Energies Using Average Force. *J. Chem. Phys.* **2001**, *115*, 9169−9183.
(53) Meng, X. Y.; Zhang, H. X.; Mezei, M.; Cui, M. Molecular Docking: A Powerful Approach for Structure-Based Drug Discovery. *Curr. Comput.-Aided Drug Des.* **2011**, *7*, 146−157.
(54) Pagadala, N. S.; Syed, K.; Tuszynski, J. Software for Molecular Docking: A Review. *Biophys. Rev.* **2017**, *9*, 91−102.
(55) Brannigan, G.; LeBard, D. N.; Henin, J.; Eckenhoff, R. G.; Klein, M. L. Multiple Binding Sites for the General Anesthetic Isoflurane Identified in the Nicotinic Acetylcholine Receptor Transmembrane Domain. *Proc. Natl. Acad. Sci. U. S. A.* **2010**, *107*, 14122−14127.
(56) Pickholz, M.; Giupponi, G. Coarse Grained Simulations of Local Anesthetics Encapsulated into a Liposome. *J. Phys. Chem. B* **2010**, *114*, 7009−7015.
(57) Pickholz, M.; Saiz, L.; Klein, M. L. Concentration Effects of Volatile Anesthetics on the Properties of Model Membranes: A Coarse-Grain Approach. *Biophys. J.* **2005**, *88*, 1524−1534.
(58) Huang, P.; Bertaccini, E.; Loew, G. H. Molecular-Dynamics Simulation of Anesthetic-Phospholipid Bilayer Interactions. *J. Biomol. Struct. Dyn.* **1995**, *12*, 725−754.
(59) Pohorille, A.; Cieplak, P.; Wilson, M. A. Interactions of Anesthetics with the Membrane-Water Interface. *Chem. Phys.* **1996**, *204*, 337−345.
(60) Ahumada, H.; Montecinos, R.; Tieleman, D. P.; Weiss-Lopez, B. E. Orientation and Dynamics of Benzyl Alcohol and Benzyl Alkyl Ethers Dissolved in Nematic Lyotropic Liquid Crystals. H-2 NMR and Molecular Dynamics Simulations. *J. Phys. Chem. A* **2005**, *109*, 6644−6651.
(61) Castro, V.; Stevensson, B.; Dvinskikh, S. V.; Hogberg, C. J.; Lyubartsev, A. P.; Zimmermann, H.; Sandstrom, D.; Maliniak, A. NMR Investigations of Interactions between Anesthetics and Lipid Bilayers. *Biochim. Biophys. Acta, Biomembr.* **2008**, *1778*, 2604−2611.
(62) Klacsova, M.; Bulacu, M.; Kucerka, N.; Uhrikova, D.; Teixeira, J.; Marrink, S. J.; Balgavy, P. The Effect of Aliphatic Alcohols on Fluid Bilayers in Unilamellar DOPC Vesicles - a Small-Angle Neutron Scattering and Molecular Dynamics Study. *Biochim. Biophys. Acta, Biomembr.* **2011**, *1808*, 2136−2146.
(63) McCarthy, N. L. C.; Brooks, N. J.; Tyler, A. I. I.; ElGamacy, M.; Welche, P. R. L.; Payne, M. C.; Chau, P. L. A Combined X-Ray Scattering and Simulation Study of Halothane in Membranes at Raised Pressures. *Chem. Phys. Lett.* **2017**, *671*, 21−27.
(64) Porasso, R. D.; Bennett, W. F. D.; Oliveira-Costa, S. D.; Cascales, J. J. L. Study of the Benzocaine Transfer from Aqueous Solution to the Interior of a Biological Membrane. *J. Phys. Chem. B* **2009**, *113*, 9988−9994.
(65) Cascales, J. J. L.; Costa, S. D. O.; Porasso, R. D. Thermodynamic Study of Benzocaine Insertion into Different Lipid Bilayers. *J. Chem. Phys.* **2011**, *135*, No. 135103.
(66) Cascales, J. J. L.; Costa, S. D. O. Effect of the Interfacial Tension and Ionic Strength on the Thermodynamic Barrier Associated to the Benzocaine Insertion into a Cell Membrane. *Biophys. Chem.* **2013**, *172*, 1−7.
(67) Polley, A.; Vemparala, S. Partitioning of Ethanol in Multi-Component Membranes: Effects on Membrane Structure. *Chem. Phys. Lipids* **2013**, *166*, 1−11.
(68) Reigada, R. Atomistic Study of Lipid Membranes Containing Chloroform: Looking for a Lipid-Mediated Mechanism of Anesthesia. *PLoS One* **2013**, *8*, No. e52631.
(69) Booker, R. D.; Sum, A. K. Biophysical Changes Induced by Xenon on Phospholipid Bilayers. *Biochim. Biophys. Acta, Biomembr.* **2013**, *1828*, 1347−1356.
(70) Guixa-Gonzalez, R.; Rodriguez-Espigares, I.; Ramirez-Anguita, J. M.; Carrio-Gaspar, P.; Martinez-Seara, H.; Giorgino, T.; Selent, J. Membplugin: Studying Membrane Complexity in VMD. *Bioinformatics* **2014**, *30*, 1478−1480.
(71) Mojumdar, E. H.; Lyubartsev, A. P. Molecular Dynamics Simulations of Local Anesthetic Articaine in a Lipid Bilayer. *Biophys. Chem.* **2010**, *153*, 27−35.
(72) Amjad-Iranagh, S.; Yousefpour, A.; Haghighi, P.; Modarress, H. Effects of Protein Binding on a Lipid Bilayer Containing Local Anesthetic Articaine, and the Potential of Mean Force Calculation: A Molecular Dynamics Simulation Approach. *J. Mol. Model.* **2013**, *19*, 3831−3842.
(73) Saeedi, M.; Lyubartsev, A. P.; Jalili, S. Anesthetics Mechanism on a DMPC Lipid Membrane Model: Insights from Molecular Dynamics Simulations. *Biophys. Chem.* **2017**, *226*, 1−13.
(74) Skjevik, A. A.; Haug, B. E.; Lygre, H.; Teigen, K. Intramolecular Hydrogen Bonding in Articaine Can Be Related to Superior Bone Tissue Penetration: A Molecular Dynamics Study. *Biophys. Chem.* **2011**, *154*, 18−25.
(75) Bernardi, R. C.; Pascutti, P. G. Hybrid Qm/Mm Molecular Dynamics Study of Benzocaine in a Membrane Environment: How Does a Quantum Mechanical Treatment of Both Anesthetic and Lipids Affect Their Interaction. *J. Chem. Theory Comput.* **2012**, *8*, 2197−2203.
(76) Martin, L. J.; Chao, R.; Corry, B. Molecular Dynamics Simulation of the Partitioning of Benzocaine and Phenytoin into a Lipid Bilayer. *Biophys. Chem.* **2014**, *185*, 98−107.
(77) Cascales, J. J. L.; Cifre, J. G. H.; de la Torre, J. G. Anaesthetic Mechanism on a Model Biological Membrane: A Molecular Dynamics Simulation Study. *J. Phys. Chem. B* **1998**, *102*, 625−631.
(78) Martini, M. F.; Pickholz, M. Molecular Dynamics Study of Uncharged Bupivacaine Enantiomers in Phospholipid Bilayers. *Int. J. Quantum Chem.* **2012**, *112*, 3341−3345.
(79) Pickholz, M.; Fraceto, L. F.; de Paula, E. Preferential Location of Prilocaine and Etidocaine in Phospholipid Bilayers: A Molecular Dynamics Study. *Synth. Met.* **2009**, *159*, 2157−2158.
(80) Pasenkiewicz-Gierula, M.; Rog, T.; Grochowski, J.; Serda, P.; Czarnecki, R.; Librowski, T.; Lochynski, S. Effects of a Carane Derivative Local Anesthetic on a Phospholipid Bilayer Studied by Molecular Dynamics Simulation. *Biophys. J.* **2003**, *85*, 1248−1258.
(81) Hogberg, C. J.; Maliniak, A.; Lyubartsev, A. P. Dynamical and Structural Properties of Charged and Uncharged Lidocaine in a Lipid Bilayer. *Biophys. Chem.* **2007**, *125*, 416−424.
(82) Hogberg, C. J.; Lyubartsev, A. P. Effect of Local Anesthetic Lidocaine on Electrostatic Properties of a Lipid Bilayer. *Biophys. J.* **2008**, *94*, 525−531.
(83) Zapata-Morin, P. A.; Sierra-Valdez, F. J.; Ruiz-Suarez, J. C. The Interaction of Local Anesthetics with Lipid Membranes. *J. Mol. Graphics Modell.* **2014**, *53*, 200−205.
(84) Pickholz, M.; Fraceto, L. F.; de Paula, E. Distribution of Neutral Prilocaine in a Phospholipid Bilayer: Insights from Molecular Dynamics Simulations. *Int. J. Quantum Chem.* **2008**, *108*, 2386−2391.
(85) Jalili, S.; Saeedi, M. Study of Procaine and Tetracaine in the Lipid Bilayer Using Molecular Dynamics Simulation. *Eur. Biophys. J.* **2017**, *46*, 265−282.
(86) Kondela, T.; Gallova, J.; Hauss, T.; Barnoud, J.; Marrink, S. J.; Kucerka, N. Alcohol Interactions with Lipid Bilayers. *Molecules* **2017**, *22*, No. 2078.
(87) Griepernau, B.; Leis, S.; Schneider, M. F.; Sikor, M.; Steppich, D.; Bockmann, R. A. 1-Alkanols and Membranes: A Story of Attraction. *Biochim. Biophys. Acta, Biomembr.* **2007**, *1768*, 2899−2913.
(88) Griepernau, B.; Bockmann, R. A. The Influence of 1-Alkanols and External Pressure on the Lateral Pressure Profiles of Lipid Bilayers. *Biophys. J.* **2008**, *95*, 5766−5778.
(89) Terama, E.; Ollila, O. H. S.; Salonen, E.; Rowat, A. C.; Trandum, C.; Westh, P.; Patra, M.; Karttunen, M.; Vattulainen, I.

DOI: 10.1021/acs.chemrev.8b00366
Chem. Rev. XXXX, XXX, XXX−XXX

Influence of Ethanol on Lipid Membranes: From Lateral Pressure Profiles to Dynamics and Partitioning. *J. Phys. Chem. B* **2008**, *112*, 4131−4139.
(90) Reigada, R. Influence of Chloroform in Liquid-Ordered and Liquid-Disordered Phases in Lipid Membranes. *J. Phys. Chem. B* **2011**, *115*, 2527−2535.
(91) Darvas, M.; Hoang, P. N. M.; Picaud, S.; Sega, M.; Jedlovszky, P. Anesthetic Molecules Embedded in a Lipid Membrane: A Computer Simulation Study. *Phys. Chem. Chem. Phys.* **2012**, *14*, 12956−12969.
(92) Vorobyov, I.; Bennett, W. F. D.; Tieleman, D. P.; Allen, T. W.; Noskov, S. The Role of Atomic Polarization in the Thermodynamics of Chloroform Partitioning to Lipid Bilayers. *J. Chem. Theory Comput.* **2012**, *8*, 618−628.
(93) Fabian, B.; Darvas, M.; Picaud, S.; Sega, M.; Jedlovszky, P. The Effect of Anaesthetics on the Properties of a Lipid Membrane in the Biologically Relevant Phase: A Computer Simulation Study. *Phys. Chem. Chem. Phys.* **2015**, *17*, 14750−14760.
(94) Fabian, B.; Sega, M.; Voloshin, V. P.; Medvedev, N. N.; Jedlovszky, P. Lateral Pressure Profile and Free Volume Properties in Phospholipid Membranes Containing Anesthetics. *J. Phys. Chem. B* **2017**, *121*, 2814−2824.
(95) Vemparala, S.; Saiz, L.; Eckenhoff, R. G.; Klein, M. L. Partitioning of Anesthetics into a Lipid Bilayer and Their Interaction with Membrane-Bound Peptide Bundles. *Biophys. J.* **2006**, *91*, 2815−2825.
(96) Chau, P. L.; Jedlovszky, P.; Hoang, P. N. M.; Picaud, S. Pressure Reversal of General Anaesthetics: A Possible Mechanism from Molecular Dynamics Simulations. *J. Mol. Liq.* **2009**, *147*, 128−134.
(97) Chau, P. L.; Tu, K. M.; Liang, K. K.; Todorov, I. T.; Roser, S. J.; Barker, R.; Matubayasi, N. The Effect of Pressure on Halothane Binding to Hydrated Dmpc Bilayers. *Mol. Phys.* **2012**, *110*, 1461−1467.
(98) Chau, P. L.; Hoang, P. N. M.; Picaud, S.; Jedlovszky, P. A Possible Mechanism for Pressure Reversal of General Anaesthetics from Molecular Simulations. *Chem. Phys. Lett.* **2007**, *438*, 294−297.
(99) Tu, K. C.; Tarek, M.; Klein, M. L.; Scharf, D. Effects of Anesthetics on the Structure of a Phospholipid Bilayer: Molecular Dynamics Investigation of Halothane in the Hydrated Liquid Crystal Phase of Dipalmitoylphosphatidylcholine. *Biophys. J.* **1998**, *75*, 2123−2134.
(100) Koubi, L.; Tarek, M.; Klein, M. L.; Scharf, D. Distribution of Halothane in a Dipalmitoyl Phosphatidylcholine Bilayer from Molecular Dynamics Calculations. *Biophys. J.* **2000**, *78*, 800−811.
(101) Tu, K. M.; Matubayasi, N.; Liang, K. K.; Todorov, I. T.; Chan, S. L.; Chau, P. L. A Possible Molecular Mechanism for the Pressure Reversal of General Anaesthetics: Aggregation of Halothane in POPC Bilayers at High Pressure. *Chem. Phys. Lett.* **2012**, *543*, 148−154.
(102) Koubi, L.; Saiz, L.; Tarek, M.; Scharf, D.; Klein, M. L. Influence of Anesthetic and Nonimmobilizer Molecules on the Physical Properties of a Polyunsaturated Lipid Bilayer. *J. Phys. Chem. B* **2003**, *107*, 14500−14508.
(103) Arcario, M. J.; Mayne, C. G.; Tajkhorshid, E. Atomistic Models of General Anesthetics for Use in in Silico Biological Studies. *J. Phys. Chem. B* **2014**, *118*, 12075−12086.
(104) Wieteska, J. R.; Welche, P. R. L.; Tu, K. M.; ElGamacy, M.; Csanyi, G.; Payne, M. C.; Chaue, P. L. Isoflurane Does Not Aggregate inside POPC Bilayers at High Pressure: Implications for Pressure Reversal of General Anaesthesia. *Chem. Phys. Lett.* **2015**, *638*, 116−121.
(105) Jerabek, H.; Pabst, G.; Rappolt, M.; Stockner, T. Membrane-Mediated Effect on Ion Channels Induced by the Anesthetic Drug Ketamine. *J. Am. Chem. Soc.* **2010**, *132*, 7990−7997.
(106) Hansen, A. H.; Sorensen, K. T.; Mathieu, R.; Serer, A.; Duelund, L.; Khandelia, H.; Hansen, P. L.; Simonsen, A. C. Propofol Modulates the Lipid Phase Transition and Localizes near the Headgroup of Membranes. *Chem. Phys. Lipids* **2013**, *175-176*, 84−91.
(107) Stimson, L. M.; Vattulainen, I.; Rog, T.; Karttunen, M. Exploring the Effect of Xenon on Biomembranes. *Cell. Mol. Biol. Lett.* **2005**, *10*, 563−569.
(108) Chen, J. L.; Chen, L.; Wang, Y.; Wang, X. G.; Zeng, S. W. Exploring the Effects on Lipid Bilayer Induced by Noble Gases Via Molecular Dynamics Simulations. *Sci. Rep.* **2015**, *5*, No. 17235.
(109) Yamamoto, E.; Akimoto, T.; Shimizu, H.; Hirano, Y.; Yasui, M.; Yasuoka, K. Diffusive Nature of Xenon Anesthetic Changes Properties of a Lipid Bilayer: Molecular Dynamics Simulations. *J. Phys. Chem. B* **2012**, *116*, 8989−8995.
(110) Koubi, L.; Tarek, M.; Bandyopadhyay, S.; Klein, M. L.; Scharf, D. Membrane Structural Perturbations Caused by Anesthetics and Nonimmobilizers: A Molecular Dynamics Investigation. *Biophys. J.* **2001**, *81*, 3339−3345.
(111) Koubi, L.; Tarek, M.; Bandyopadhyay, S.; Klein, M. L.; Scharf, D. Effects of the Nonimmobilizer Hexafluroethane on the Model Membrane Dimyristoylphosphatidylcholine. *Anesthesiology* **2002**, *97*, 848−855.
(112) Kandel, L.; Chortkoff, B. S.; Sonner, J.; Laster, M. J.; Eger, E. I., II Nonanesthetics Can Suppress Learning. *Anesth. Analg.* **1996**, *82*, 321−326.
(113) Baber, J.; Ellena, J. F.; Cafiso, D. S. Distribution of General-Anesthetics in Phospholipid-Bilayers Determined Using H-2 NMR and H-1-H-1 Noe Spectroscopy. *Biochemistry* **1995**, *34*, 6533−6539.
(114) North, C.; Cafiso, D. S. Contrasting Membrane Localization and Behavior of Halogenated Cyclobutanes That Follow or Violate the Meyer-Overton Hypothesis of General Anesthetic Potency. *Biophys. J.* **1997**, *72*, 1754−1761.
(115) Pohorille, A.; Wilson, M. A.; New, M. H.; Chipot, C. Concentrations of Anesthetics across the Water-Membrane Interface; the Meyer-Overton Hypothesis Revisited. *Toxicol. Lett.* **1998**, *100-101*, 421−430.
(116) Pohorille, A.; Wilson, M. A. Excess Chemical Potential of Small Solutes across Water-Membrane and Water-Hexane Interfaces. *J. Chem. Phys.* **1996**, *104*, 3760−3773.
(117) Strichartz, G. Molecular Mechanisms of Nerve Block by Local Anesthetics. *Anesthesiology* **1976**, *45*, 421−441.
(118) Pasenkiewicz-Gierula, M.; Rog, T.; Grochowski, J.; Serda, P.; Czarnecki, R.; Librowski, T.; Lochynski, S. Effects of a Carane Derivative Local Anesthetic on a Phospholipid Bilayer Studied by Molecular Dynamics Simulation. *Biophys. J.* **2003**, *85*, 1248−1258.
(119) Hata, T.; Sakamoto, T.; Matsuki, H.; Kaneshina, S. Partition Coefficients of Charged and Uncharged Local Anesthetics into Dipalmitoylphosphatidylcholine Bilayer Membrane: Estimation from Ph Dependence on the Depression of Phase Transition Temperatures. *Colloids Surf., B* **2001**, *22*, 77−84.
(120) Johnson, F. H.; Flagler, E. A. Hydrostatic Pressure Reversal of Narcosis in Tadpoles. *Science* **1950**, *112*, 91−92.
(121) Johnson, F. H.; Flagler, E. A. Activity of Narcotized Amphibian Larvae under Hydrostatic Pressure. *J. Cell. Comp. Physiol.* **1951**, *37*, 15−25.
(122) Sanders, R. D.; Franks, N. P.; Maze, M. Xenon: No Stranger to Anaesthesia. *Br. J. Anaesth.* **2003**, *91*, 709−717.
(123) Harris, P. D.; Barnes, R. The Uses of Helium and Xenon in Current Clinical Practice. *Anaesthesia* **2008**, *63*, 284−293.
(124) Brucken, A.; Coburn, M.; Rex, S.; Rossaint, R.; Fries, M. Current Developments in Xenon Research. *Anaesthesist* **2010**, *59*, 883.
(125) Cullen, S. C.; Gross, E. G. The Anesthetic Properties of Xenon in Animals and Human Beings, with Additional Observations on Krypton. *Science* **1951**, *113*, 580−582.
(126) Franks, N. P.; Dickinson, R.; de Sousa, S. L. M.; Hall, A. C.; Lieb, W. R. How Does Xenon Produce Anaesthesia? *Nature* **1998**, *396*, 324−324.
(127) de Sousa, S. L. M.; Dickinson, R.; Lieb, W. R.; Franks, N. P. Contrasting Synaptic Actions of the Inhalational General Anesthetics Isoflurane and Xenon. *Anesthesiology* **2000**, *92*, 1055−1066.
(128) Yamakura, T.; Harris, R. A. Effects of Gaseous Anesthetics Nitrous Oxide and Xenon on Ligand-Gated Ion Channels:

DOI: 10.1021/acs.chemrev.8b00366
Chem. Rev. XXXX, XXX, XXX−XXX

Comparison with Isoflurane and Ethanol. *Anesthesiology* **2000**, *93*, 1095−1101.
(129) Gruss, M.; Bushell, T. J.; Bright, D. P.; Lieb, W. R.; Mathie, A.; Franks, N. P. Two-Pore-Domain K^+ Channels Are a Novel Target for the Anesthetic Gases Xenon, Nitrous Oxide, and Cyclopropane. *Mol. Pharmacol.* **2004**, *65*, 443−452.
(130) Cantor, R. S. Breaking the Meyer-Overton Rule: Pedicted Effects of Varying Stiffness and Interfacial Activity on the Intrinsic Potency of Anesthetics. *Biophys. J.* **2001**, *80*, 2284−2297.
(131) Corringer, P. J.; Poitevin, F.; Prevost, M. S.; Sauguet, L.; Delarue, M.; Changeux, J. P. Structure and Pharmacology of Pentameric Receptor Channels: From Bacteria to Brain. *Structure* **2012**, *20*, 941−956.
(132) Miller, K. W. The Nature of Sites of General Anaesthetic Action. *Br. J. Anaesth.* **2002**, *89*, 17−31.
(133) Yamakura, T.; Bertaccini, E.; Trudell, J. R.; Harris, R. A. Anesthetics and Ion Channels: Molecular Models and Sites of Action. *Annu. Rev. Pharmacol. Toxicol.* **2001**, *41*, 23−51.
(134) Unwin, N. Refined Structure of the Nicotinic Acetylcholine Receptor at 4 Angstrom Resolution. *J. Mol. Biol.* **2005**, *346*, 967−989.
(135) Thompson, A. J.; Lester, H. A.; Lummis, S. C. R. The Structural Basis of Function in Cys-Loop Receptors. *Q. Rev. Biophys.* **2010**, *43*, 449−499.
(136) Hilf, R. J. C.; Dutzler, R. X-Ray Structure of a Prokaryotic Pentameric Ligand-Gated Ion Channel. *Nature* **2008**, *452*, 375−U312.
(137) Pan, J. J.; Chen, Q.; Willenbring, D.; Yoshida, K.; Tillman, T.; Kashlan, O. B.; Cohen, A.; Kong, X. P.; Xu, Y.; Tang, P. Structure of the Pentameric Ligand-Gated Ion Channel Elic Cocrystallized with Its Competitive Antagonist Acetylcholine. *Nat. Commun.* **2012**, *3*, No. 714.
(138) Bocquet, N.; Nury, H.; Baaden, M.; Le Poupon, C.; Changeux, J. P.; Delarue, M.; Corringer, P. J. X-Ray Structure of a Pentameric Ligand-Gated Ion Channel in an Apparently Open Conformation. *Nature* **2009**, *457*, 111−114.
(139) Hilf, R. J. C.; Dutzler, R. Structure of a Potentially Open State of a Proton-Activated Pentameric Ligand-Gated Ion Channel. *Nature* **2009**, *457*, 115−U122.
(140) Weng, Y.; Yang, L. Y.; Corringer, P. J.; Sonner, J. M. Anesthetic Sensitivity of the *Gloeobacter violaceus* Proton-Gated Ion Channel. *Anesth. Analg.* **2010**, *110*, 59−63.
(141) Cheng, M. H.; Coalson, R. D.; Cascio, M. Molecular Dynamics Simulations of Ethanol Binding to the Transmembrane Domain of the Glycine Receptor: Implications for the Channel Potentiation Mechanism. *Proteins: Struct., Funct., Genet.* **2008**, *71*, 972−981.
(142) Cheng, M. H. Y.; Cascio, M.; Coalson, R. D. Homology Modeling and Molecular Dynamics Simulations of the Alpha 1 Glycine Receptor Reveals Different States of the Channel. *Proteins: Struct., Funct., Genet.* **2007**, *68*, 581−593.
(143) Murail, S.; Wallner, B.; Trudell, J. R.; Bertaccini, E.; Lindahl, E. Microsecond Simulations Indicate That Ethanol Binds between Subunits and Could Stabilize an Open-State Model of a Glycine Receptor. *Biophys. J.* **2011**, *100*, 1642−1650.
(144) Haddadian, E. J.; Cheng, M. H. Y.; Coalson, R. D.; Xu, Y.; Tang, P. In Silico Models for the Human Alpha 4 Beta 2 Nicotinic Acetylcholine Receptor. *J. Phys. Chem. B* **2008**, *112*, 13981−13990.
(145) Liu, L. T.; Haddadian, E. J.; Willenbring, D.; Xu, Y.; Tang, P. Higher Susceptibility to Halothane Modulation in Open- Than in Closed-Channel Alpha 4 Beta 2 nAChR Revealed by Molecular Dynamics Simulations. *J. Phys. Chem. B* **2010**, *114*, 626−632.
(146) Liu, L. T.; Willenbring, D.; Xu, Y.; Tang, P. General Anesthetic Binding to Neuronal Alpha 4 Beta 2 Nicotinic Acetylcholine Receptor and Its Effects on Global Dynamics. *J. Phys. Chem. B* **2009**, *113*, 12581−12589.
(147) Yoluk, O.; Bromstrup, T.; Bertaccini, E. J.; Trudell, J. R.; Lindahl, E. Stabilization of the GluCl Ligand-Gated Ion Channel in the Presence and Absence of Ivermectin. *Biophys. J.* **2013**, *105*, 640−647.
(148) Carpenter, T. S.; Lau, E. Y.; Lightstone, F. C. A Role for Loop F in Modulating Gaba Binding Affinity in the Gaba(a) Receptor. *J. Mol. Biol.* **2012**, *422*, 310−323.
(149) Carpenter, T. S.; Lau, E. Y.; Lightstone, F. C. Identification of a Possible Secondary Picrotoxin-Binding Site on the Gaba(a) Receptor. *Chem. Res. Toxicol.* **2013**, *26*, 1444−1454.
(150) Henin, J.; Salari, R.; Murlidaran, S.; Brannigan, G. A Predicted Binding Site for Cholesterol on the Gaba(a) Receptor. *Biophys. J.* **2014**, *106*, 1938−1949.
(151) Woll, K. A.; Murlidaran, S.; Pinch, B. J.; Henin, J.; Wang, X. S.; Salari, R.; Covarrubias, M.; Dailey, W. P.; Brannigan, G.; Garcia, B. A.; et al. A Novel Bifunctional Alkylphenol Anesthetic Allows Characterization of Gamma-Aminobutyric Acid, Type A (Gaba(a)), Receptor Subunit Binding Selectivity in Synaptosomes. *J. Biol. Chem.* **2016**, *291*, 20473−20486.
(152) Chiara, D. C.; Dangott, L. J.; Eckenhoff, R. G.; Cohen, J. B. Identification of Nicotinic Acetylcholine Receptor Amino Acids Photolabeled by the Volatile Anesthetic Halothane. *Biochemistry* **2003**, *42*, 13457−13467.
(153) Nury, H.; Van Renterghem, C.; Weng, Y.; Tran, A.; Baaden, M.; Dufresne, V.; Changeux, J. P.; Sonner, J. M.; Delarue, M.; Corringer, P. J. X-Ray Structures of General Anaesthetics Bound to a Pentameric Ligand-Gated Ion Channel. *Nature* **2011**, *469*, 428−431.
(154) Fourati, Z.; Howard, R. J.; Heusser, S. A.; Hu, H. D.; Ruza, R. R.; Sauguet, L.; Lindahl, E.; Delarue, M. Structural Basis for a Bimodal Allosteric Mechanism of General Anesthetic Modulation in Pentameric Ligand-Gated Ion Channels. *Cell Rep.* **2018**, *23*, 993−1004.
(155) Sauguet, L.; Howard, R. J.; Malherbe, L.; Lee, U. S.; Corringer, P. J.; Harris, R. A.; Delarue, M. Structural Basis for Potentiation by Alcohols and Anaesthetics in a Ligand-Gated Ion Channel. *Nat. Commun.* **2013**, *4*, No. 1697.
(156) Laurent, B.; Murail, S.; Shahsavar, A.; Sauguet, L.; Delarue, M.; Baaden, M. Sites of Anesthetic Inhibitory Action on a Cationic Ligand-Gated Ion Channel. *Structure* **2016**, *24*, 595−605.
(157) Chen, Q.; Kinde, M. N.; Arjunan, P.; Wells, M. M.; Cohen, A. E.; Xu, Y.; Tang, P. Direct Pore Binding as a Mechanism for Isoflurane Inhibition of the Pentameric Ligand-Gated Ion Channel Elic. *Sci. Rep.* **2015**, *5*, No. 13833.
(158) Pan, J. J.; Chen, Q.; Willenbring, D.; Mowrey, D.; Kong, X. P.; Cohen, A.; Divito, C. B.; Xu, Y.; Tang, P. Structure of the Pentameric Ligand-Gated Ion Channel GLIC Bound with Anesthetic Ketamine. *Structure* **2012**, *20*, 1463−1469.
(159) Willenbring, D.; Liu, L. T.; Mowrey, D.; Xu, Y.; Tang, P. Isoflurane Alters the Structure and Dynamics of GLIC. *Biophys. J.* **2011**, *101*, 1905−1912.
(160) Arcario, M. J.; Mayne, C. G.; Tajkhorshid, E. A Membrane-Embedded Pathway Delivers General Anesthetics to Two Interacting Binding Sites in the Gloeobacter Violaceus Ion Channel. *J. Biol. Chem.* **2017**, *292*, 9480−9492.
(161) Chen, Q. A.; Cheng, M. H.; Xu, Y.; Tang, P. Anesthetic Binding in a Pentameric Ligand-Gated Ion Channel: GLIC. *Biophys. J.* **2010**, *99*, 1801−1809.
(162) Kash, T. L.; Jenkins, A.; Kelley, J. C.; Trudell, J. R.; Harrison, N. L. Coupling of Agonist Binding to Channel Gating in the Gaba(a) Receptor. *Nature* **2003**, *421*, 272−275.
(163) Xiu, X. N.; Hanek, A. P.; Wang, J. T.; Lester, H. A.; Dougherty, D. A. A Unified View of the Role of Electrostatic Interactions in Modulating the Gating of Cys Loop Receptors. *J. Biol. Chem.* **2005**, *280*, 41655−41666.
(164) Jha, A.; Cadugan, D. J.; Purohit, P.; Auerbach, A. Acetylcholine Receptor Gating at Extracellular Transmembrane Domain Interface: The Cys-Loop and M2-M3 Linker. *J. Gen. Physiol.* **2007**, *130*, 547−558.
(165) Cheng, M. H. Y.; Coalson, R. D.; Tang, P. Molecular Dynamics and Brownian Dynamics Investigation of Ion Permeation and Anesthetic Halothane Effects on a Proton-Gated Ion Channel. *J. Am. Chem. Soc.* **2010**, *132*, 16442−16449.

DOI: 10.1021/acs.chemrev.8b00366
Chem. Rev. XXXX, XXX, XXX−XXX

(166) Lee, W. Y.; Sine, S. M. Principal Pathway Coupling Agonist Binding to Channel Gating in Nicotinic Receptors. *Nature* **2005**, *438*, 243−247.
(167) Sala, F.; Mulet, J.; Sala, S.; Gerber, S.; Criado, M. Charged Amino Acids of the N-Terminal Domain Are Involved in Coupling Binding and Gating in Alpha 7 Nicotinic Receptors. *J. Biol. Chem.* **2005**, *280*, 6642−6647.
(168) Joseph, T. T.; Mincer, J. S. Common Internal Allosteric Network Links Anesthetic Binding Sites in a Pentameric Ligand-Gated Ion Channel. *PLoS One* **2016**, *11*, No. e0158795.
(169) Mowrey, D.; Cheng, M. H.; Liu, L. T.; Willenbring, D.; Lu, X. H.; Wymore, T.; Xu, Y.; Tang, P. Asymmetric Ligand Binding Facilitates Conformational Transitions in Pentameric Ligand-Gated Ion Channels. *J. Am. Chem. Soc.* **2013**, *135*, 2172−2180.
(170) Rayes, D.; De Rosa, M. J.; Sine, S. M.; Bouzat, C. Number and Locations of Agonist Binding Sites Required to Activate Homomeric Cys-Loop Receptors. *J. Neurosci.* **2009**, *29*, 6022−6032.
(171) Beato, M.; Groot-Kormelink, P. J.; Colquhoun, D.; Sivilotti, L. G. The Activation Mechanism of Alpha 1 Homomeric Glycine Receptors. *J. Neurosci.* **2004**, *24*, 895−906.
(172) Amin, J.; Weiss, D. S. Insights into the Activation Mechanism of P(1) Gaba Receptors Obtained by Coexpression of Wild Type and Activation-Impaired Subunits. *Proc. R. Soc. London, Ser. B* **1996**, *263*, 273−282.
(173) Hilf, R. J. C.; Bertozzi, C.; Zimmermann, I.; Reiter, A.; Trauner, D.; Dutzler, R. Structural Basis of Open Channel Block in a Prokaryotic Pentameric Ligand-Gated Ion Channel. *Nat. Struct. Mol. Biol.* **2010**, *17*, 1330−U1184.
(174) LeBard, D. N.; Henin, J.; Eckenhoff, R. G.; Klein, M. L.; Brannigan, G. General Anesthetics Predicted to Block the GLIC Pore with Micromolar Affinity. *PLoS Comput. Biol.* **2012**, *8*, No. e1002532.
(175) Nirthanan, S.; Garcia, G.; Chiara, D. C.; Husain, S. S.; Cohen, J. B. Identification of Binding Sites in the Nicotinic Acetylcholine Receptor for Tdbzl-Etomidate, a Photoreactive Positive Allosteric Effector. *J. Biol. Chem.* **2008**, *283*, 22051−22062.
(176) Ion, B. F.; Wells, M. M.; Chen, Q.; Xu, Y.; Tang, P. Ketamine Inhibition of the Pentameric Ligand-Gated Ion Channel GLIC. *Biophys. J.* **2017**, *113*, 605−612.
(177) Mowrey, D.; Chen, Q.; Liang, Y. H.; Liang, J.; Xu, Y.; Tang, P. Signal Transduction Pathways in the Pentameric Ligand-Gated Ion Channels. *PLoS One* **2013**, *8*, e64326.
(178) Li, X. Y.; Xie, F.; Zhang, J. C.; Su, J. G. Study, by Use of Coarse-Grained Models, of the Functionally Crucial Residues and Allosteric Pathway of Anesthetic Regulation of the Gloeobacter Violaceus Ligand-Gated Ion Channel. *Eur. Biophys. J.* **2014**, *43*, 623−630.
(179) Wood, J. N.; Boorman, J. Voltage-Gated Sodium Channel Blockers; Target Validation and Therapeutic Potential. *Curr. Top. Med. Chem.* **2005**, *5*, 529−537.
(180) Bagal, S. K.; Chapman, M. L.; Marron, B. E.; Prime, R.; Storer, R. I.; Swain, N. A. Recent Progress in Sodium Channel Modulators for Pain. *Bioorg. Med. Chem. Lett.* **2014**, *24*, 3690−3699.
(181) Brau, M. E.; Vogel, W.; Hempelmann, G. Fundamental Properties of Local Anesthetics: Half-Maximal Blocking Concentrations for Tonic Block of Na^+ and K^+ Channels in Peripheral Nerve. *Anesth. Analg.* **1998**, *87*, 885−889.
(182) Komai, H.; McDowell, T. S. Local Anesthetic Inhibition of Voltage-Activated Potassium Currents in Rat Dorsal Root Ganglion Neurons. *Anesthesiology* **2001**, *94*, 1089−1095.
(183) Doyle, D. A.; Morais Cabral, J.; Pfuetzner, R. A.; Kuo, A.; Gulbis, J. M.; Cohen, S. L.; Chait, B. T.; MacKinnon, R. The Structure of the Potassium Channel: Molecular Basis of K^+ Conduction and Selectivity. *Science* **1998**, *280*, 69−77.
(184) Smart, O. S.; Goodfellow, J. M.; Wallace, B. A. The Pore Dimensions of Gramicidin A. *Biophys. J.* **1993**, *65*, 2455−2460.
(185) Heginbotham, L.; Lu, Z.; Abramson, T.; MacKinnon, R. Mutations in the K^+ Channel Signature Sequence. *Biophys. J.* **1994**, *66*, 1061−1067.
(186) Parsegian, A. Energy of an Ion Crossing a Low Dielectric Membrane: Solutions to Four Relevant Electrostatic Problems. *Nature* **1969**, *221*, 844−846.
(187) Jiang, Y. X.; Lee, A.; Chen, J. Y.; Ruta, V.; Cadene, M.; Chait, B. T.; MacKinnon, R. X-Ray Structure of a Voltage-Dependent K^+ Channel. *Nature* **2003**, *423*, 33−41.
(188) Butterwick, J. A.; MacKinnon, R. Solution Structure and Phospholipid Interactions of the Isolated Voltage-Sensor Domain from Kvap. *J. Mol. Biol.* **2010**, *403*, 591−606.
(189) Long, S. B.; Campbell, E. B.; Mackinnon, R. Crystal Structure of a Mammalian Voltage-Dependent Shaker Family K^+ Channel. *Science* **2005**, *309*, 897−903.
(190) Chen, X. R.; Wang, Q. H.; Ni, F. Y.; Ma, J. P. Structure of the Full-Length Shaker Potassium Channel Kv1.2 by Normal-Mode-Based X-Ray Crystallographic Refinement. *Proc. Natl. Acad. Sci. U. S. A.* **2010**, *107*, 11352−11357.
(191) Long, S. B.; Campbell, E. B.; Mackinnon, R. Voltage Sensor of Kv1.2: Structural Basis of Electromechanical Coupling. *Science* **2005**, *309*, 903−908.
(192) Long, S. B.; Tao, X.; Campbell, E. B.; MacKinnon, R. Atomic Structure of a Voltage-Dependent K^+ Channel in a Lipid Membrane-Like Environment. *Nature* **2007**, *450*, 376−382.
(193) Payandeh, J.; Scheuer, T.; Zheng, N.; Catterall, W. A. The Crystal Structure of a Voltage-Gated Sodium Channel. *Nature* **2011**, *475*, 353−358.
(194) Payandeh, J.; Gamal El-Din, T. M.; Scheuer, T.; Zheng, N.; Catterall, W. A. Crystal Structure of a Voltage-Gated Sodium Channel in Two Potentially Inactivated States. *Nature* **2012**, *486*, 135−139.
(195) Lenaeus, M. J.; El-Din, T. M. G.; Ing, C.; Ramanadane, K.; Pomes, R.; Zheng, N.; Catterall, W. A. Structures of Closed and Open States of a Voltage-Gated Sodium Channel. *Proc. Natl. Acad. Sci. U. S. A.* **2017**, *114*, E3051−E3060.
(196) Sula, A.; Booker, J.; Ng, L. C. T.; Naylor, C. E.; DeCaen, P. G.; Wallace, B. A. The Complete Structure of an Activated Open Sodium Channel. *Nat. Commun.* **2017**, *8*, No. 14205.
(197) Zhang, X.; Ren, W.; DeCaen, P.; Yan, C.; Tao, X.; Tang, L.; Wang, J.; Hasegawa, K.; Kumasaka, T.; He, J.; et al. Crystal Structure of an Orthologue of the NaChBac Voltage-Gated Sodium Channel. *Nature* **2012**, *486*, 130−134.
(198) Bagnéris, C.; DeCaen, P. G.; Hall, B. A.; Naylor, C. E.; Clapham, D. E.; Kay, C. W. M.; Wallace, B. A. Role of the C-Terminal Domain in the Structure and Function of Tetrameric Sodium Channels. *Nat. Commun.* **2013**, *4*, No. 2465.
(199) McCusker, E. C.; Bagneris, C.; Naylor, C. E.; Cole, A. R.; D'Avanzo, N.; Nichols, C. G.; Wallace, B. A. Structure of a Bacterial Voltage-Gated Sodium Channel Pore Reveals Mechanisms of Opening and Closing. *Nat. Commun.* **2012**, *3*, No. 1102.
(200) Bagneris, C.; DeCaen, P. G.; Naylor, C. E.; Pryde, D. C.; Nobeli, I.; Clapham, D. E.; Wallace, B. A. Prokaryotic Navms Channel as a Structural and Functional Model for Eukaryotic Sodium Channel Antagonism. *Proc. Natl. Acad. Sci. U. S. A.* **2014**, *111*, 8428−8433.
(201) Naylor, C. E.; Bagneris, C.; DeCaen, P. G.; Sula, A.; Scaglione, A.; Clapham, D. E.; Wallace, B. A. Molecular Basis of Ion Permeability in a Voltage-Gated Sodium Channel. *EMBO J.* **2016**, *35*, 820−830.
(202) Shaya, D.; Findeisen, F.; Abderemane-Ali, F.; Arrigoni, C.; Wong, S.; Nurva, S. R.; Loussouarn, G.; Minor, D. L., Jr Structure of a Prokaryotic Sodium Channel Pore Reveals Essential Gating Elements and an Outer Ion Binding Site Common to Eukaryotic Channels. *J. Mol. Biol.* **2014**, *426*, 467−483.
(203) Shen, H. Z.; Zhou, Q.; Pan, X. J.; Li, Z. Q.; Wu, J. P.; Yan, N. Structure of a Eukaryotic Voltage-Gated Sodium Channel at near-Atomic Resolution. *Science* **2017**, *355*, No. eaal4326.
(204) OuYang, W.; Hemmings, H. C. Isoform-Selective Effects of Isoflurane on Voltage-Gated Na^+ Channels. *Anesthesiology* **2007**, *107*, 91−98.
(205) Shiraishi, M.; Harris, R. A. Effects of Alcohols and Anesthetics on Recombinant Voltage-Gated Na^+ Channels. *J. Pharmacol. Exp. Ther.* **2004**, *309*, 987−994.

DOI: 10.1021/acs.chemrev.8b00366
Chem. Rev. XXXX, XXX, XXX−XXX

(206) Clarkson, C. W.; Hondeghem, L. M. Mechanism for Bupivacaine Depression of Cardiac Conduction - Fast Block of Sodium-Channels During the Action-Potential with Slow Recovery from Block During Diastole. *Anesthesiology* **1985**, *62*, 396−405.
(207) Weidmann, S. The Effect of the Cardiac Membrane Potential on the Rapid Availability of the Sodium-Carrying System. *J. Physiol.* **1955**, *127*, 213−224.
(208) Hille, B. Local-Anesthetics - Hydrophilic and Hydrophobic Pathways for Drug-Receptor Reaction. *J. Gen. Physiol.* **1977**, *69*, 497−515.
(209) Strichartz, G. R. The Inhibition of Sodium Currents in Myelinated Nerve by Quaternary Derivatives of Lidocaine. *J. Gen. Physiol.* **1973**, *62*, 37−57.
(210) Khodorov, B.; Shishkova, L.; Peganov, E.; Revenko, S. Inhibition of Sodium Currents in Frog Ranvier Node Treated with Local-Anesthetics - Role of Slow Sodium Inactivation. *Biochim. Biophys. Acta, Biomembr.* **1976**, *433*, 409−435.
(211) Lee, S.; Goodchild, S. J.; Ahern, C. A. Local Anesthetic Inhibition of a Bacterial Sodium Channel. *J. Gen. Physiol.* **2012**, *139*, 507−516.
(212) Ouyang, W.; Jih, T. Y.; Zhang, T. T.; Correa, A. M.; Hemmings, H. C. Isoflurane Inhibits NaChBac, a Prokaryotic Voltage-Gated Sodium Channel. *J. Pharmacol. Exp. Ther.* **2007**, *322*, 1076−1083.
(213) Raju, S. G.; Barber, A. F.; LeBard, D. N.; Klein, M. L.; Carnevale, V. Exploring Volatile General Anesthetic Binding to a Closed Membrane-Bound Bacterial Voltage-Gated Sodium Channel Via Computation. *PLoS Comput. Biol.* **2013**, *9*, No. e1003090.
(214) Barber, A. F.; Carnevale, V.; Klein, M. L.; Eckenhoff, R. G.; Covarrubias, M. Modulation of a Voltage-Gated Na^+ Channel by Sevoflurane Involves Multiple Sites and Distinct Mechanisms. *Proc. Natl. Acad. Sci. U. S. A.* **2014**, *111*, 6726−6731.
(215) Kinde, M. N.; Bondarenko, V.; Granata, D.; Bu, W. M.; Grasty, K. C.; Loll, P. J.; Carnevale, V.; Klein, M. L.; Eckenhoff, R. G.; Tang, P.; et al. Fluorine-19 NMR and Computational Quantification of Isoflurane Binding to the Voltage-Gated Sodium Channel NaChBac. *Proc. Natl. Acad. Sci. U. S. A.* **2016**, *113*, 13762−13767.
(216) Kaczmarski, J. A.; Corry, B. Investigating the Size and Dynamics of Voltage-Gated Sodium Channel Fenestrations a Molecular Dynamics Study. *Channels* **2014**, *8*, 264−277.
(217) Martin, L. J.; Corry, B. Locating the Route of Entry and Binding Sites of Benzocaine and Phenytoin in a Bacterial Voltage Gated Sodium Channel. *PLoS Comput. Biol.* **2014**, *10*, No. e1003688.
(218) Ragsdale, D. S.; McPhee, J. C.; Scheuer, T.; Catterall, W. A. Molecular Determinants of State-Dependent Block of Na^+ Channels by Local-Anesthetics. *Science* **1994**, *265*, 1724−1728.
(219) Ahern, C. A.; Eastwood, A. L.; Dougherty, D. A.; Horn, R. Electrostatic Contributions of Aromatic Residues in the Local Anesthetic Receptor of Voltage-Gated Sodium Channels. *Circ. Res.* **2008**, *102*, 86−94.
(220) Smith, N. E.; Corry, B. Mutant Bacterial Sodium Channels as Models for Local Anesthetic Block of Eukaryotic Proteins. *Channels* **2016**, *10*, 225−237.
(221) Buyan, A.; Sun, D. L.; Corry, B. Protonation State of Inhibitors Determines Interaction Sites within Voltage-Gated Sodium Channels. *Proc. Natl. Acad. Sci. U. S. A.* **2018**, *115*, E3135−E3144.
(222) Patel, A. J.; Honore, E.; Lesage, F.; Fink, M.; Romey, G.; Lazdunski, M. Inhalational Anesthetics Activate Two-Pore-Domain Background K^+ Channels. *Nat. Neurosci.* **1999**, *2*, 422−426.
(223) Gibbons, S. J.; NunezHernandez, R.; Maze, G.; Harrison, N. L. Inhibition of a Fast Inwardly Rectifying Potassium Conductance by Barbiturates. *Anesth. Analg.* **1996**, *82*, 1242−1246.
(224) Vemparala, S.; Domene, C.; Klein, M. L. Interaction of Anesthetics with Open and Closed Conformations of a Potassium Channel Studied Via Molecular Dynamics and Normal Mode Analysis. *Biophys. J.* **2008**, *94*, 4260−4269.
(225) Domene, C.; Vemparala, S.; Klein, M. L.; Venien-Bryan, C.; Doyle, D. A. Role of Aromatic Localization in the Gating Process of a Potassium Channel. *Biophys. J.* **2006**, *90*, L01−L03.
(226) Tsao, D. H. H.; Casasfinet, J. R.; Maki, A. H.; Chase, J. W. Triplet-State Properties of Tryptophan Residues in Complexes of Mutated Escherichia-Coli Single-Stranded-DNA Binding-Proteins with Single-Stranded Polynucleotides. *Biophys. J.* **1989**, *55*, 927−936.
(227) Davies, L. A.; Zhong, Q. F.; Klein, M. L.; Scharf, D. Molecular Dynamics Simulation of Four-Alpha-Helix Bundles That Bind the Anesthetic Halothane. *FEBS Lett.* **2000**, *478*, 61−66.
(228) Tang, P.; Xu, Y. Large-Scale Molecular Dynamics Simulations of General Anesthetic Effects on the Ion Channel in the Fully Hydrated Membrane: The Implication of Molecular Mechanisms of General Anesthesia. *Proc. Natl. Acad. Sci. U. S. A.* **2002**, *99*, 16035−16040.
(229) Covarrubias, M.; Barber, A. F.; Carnevale, V.; Treptow, W.; Eckenhoff, R. G. Mechanistic Insights into the Modulation of Voltage-Gated Ion Channels by Inhalational Anesthetics. *Biophys. J.* **2015**, *109*, 2003−2011.
(230) Correa, A. M. Gating Kinetics of Shaker K^+ Channels Are Differentially Modified by General Anesthetics. *American Journal of Physiology-Cell Physiology* **1998**, *275*, C1009−C1021.
(231) Li, J. C.; Correa, A. M. Single-Channel Basis for Conductance Increase Induced by Isoflurane in Shaker H4ir K^+ Channels. *American Journal of Physiology-Cell Physiology* **2001**, *280*, C1130−C1139.
(232) Tinklenberg, J. A.; Segal, I. S.; Tianzhi, G.; Maze, M. Analysis of Anesthetic Action on the Potassium Channels of the Shaker Mutant of Drosophila. *Ann. N. Y. Acad. Sci.* **1991**, *625*, 532−539.
(233) Li, J. C.; Correa, A. M. Kinetic Modulation of Herg Potassium Channels by the Volatile Anesthetic Halothane. *Anesthesiology* **2002**, *97*, 921−930.
(234) Friederich, P.; Benzenberg, D.; Trellakis, S.; Urban, B. W. Interaction of Volatile Anesthetics with Human Kv Channels in Relation to Clinical Concentrations. *Anesthesiology* **2001**, *95*, 954−958.
(235) Covarrubias, M.; Rubin, E. Ethanol Selectively Blocks a Noninactivating K^+ Current Expressed in Xenopus-Oocytes. *Proc. Natl. Acad. Sci. U. S. A.* **1993**, *90*, 6957−6960.
(236) Covarrubias, M.; Vyas, T. B.; Escobar, L.; Wei, A. Alcohols Inhibit a Cloned Potassium Channel at a Discrete Saturable Site - Insights into the Molecular-Basis of General-Anesthesia. *J. Biol. Chem.* **1995**, *270*, 19408−19416.
(237) Harris, T.; Shahidullah, M.; Ellingson, J. S.; Covarrubias, M. General Anesthetic Action at an Internal Protein Site Involving the S4-S5 Cytoplasmic Loop of a Neuronal K^+ Channel. *J. Biol. Chem.* **2000**, *275*, 4928−4936.
(238) Barber, A. F.; Liang, Q. S.; Covarrubias, M. Novel Activation of Voltage-Gated K^+ Channels by Sevoflurane. *J. Biol. Chem.* **2012**, *287*, 40425−40432.
(239) Smith-Maxwell, C. J.; Ledwell, J. L.; Aldrich, R. W. Role of the S4 in Cooperativity of Voltage-Dependent Potassium Channel Activation. *J. Gen. Physiol.* **1998**, *111*, 399−420.
(240) Ledwell, J. L.; Aldrich, R. W. Mutations in the S4 Region Isolate the Final Voltage-Dependent Cooperative Step in Potassium Channel Activation. *J. Gen. Physiol.* **1999**, *113*, 389−414.
(241) Chen, R.; Gryn'ova, G.; Wu, Y. L.; Coote, M. L.; Chung, S. H. Mechanisms and Energetics of Potassium Channel Block by Local Anesthetics and Antifungal Agents. *Biochemistry* **2014**, *53*, 6786−6792.
(242) Ander, M.; Luzhkov, V. B.; Aqvist, J. Ligand Binding to the Voltage-Gated Kv1.5 Potassium Channel in the Open State - Docking and Computer Simulations of a Homology Model. *Biophys. J.* **2008**, *94*, 820−831.
(243) Decher, N.; Pirard, B.; Bundis, F.; Peukert, S.; Baringhaus, K. H.; Busch, A. E.; Steinmeyer, K.; Sanguinetti, M. C. Molecular Basis for Kv1.5 Channel Block - Conservation of Drug Binding Sites among Voltage-Gated K^+ Channels. *J. Biol. Chem.* **2004**, *279*, 394−400.
(244) Bradding, P.; Wulff, H. The K^+ Channels K(Ca)3.1 and K(V)1.3 as Novel Targets for Asthma Therapy. *Br. J. Pharmacol.* **2009**, *157*, 1330−1339.
(245) McNulty, M. M.; Edgerton, G. B.; Shah, R. D.; Hanck, D. A.; Fozzard, H. A.; Lipkind, G. M. Charge at the Lidocaine Binding Site

DOI: 10.1021/acs.chemrev.8b00366
Chem. Rev. XXXX, XXX, XXX−XXX

Residue Phe-1759 Affects Permeation in Human Cardiac Voltage-Gated Sodium Channels. *J. Physiol.* **2007**, *581*, 741−755.
(246) Bhattacharji, A.; Klett, N.; Go, R. C. V.; Covarrubias, M. Inhalational Anaesthetics and N-Alcohols Share a Site of Action in the Neuronal Shaw2 K-V Channel. *Br. J. Pharmacol.* **2010**, *159*, 1475−1485.
(247) Bhattacharji, A.; Kaplan, B.; Harris, T.; Qu, X. G.; Germann, M. W.; Covarrubias, M. The Concerted Contribution of the S4-S5 Linker and the S6 Segment to the Modulation of a K-V Channel by 1-Alkanols. *Mol. Pharmacol.* **2006**, *70*, 1542−1554.
(248) Lu, Z.; Klem, A. M.; Ramu, Y. Coupling between Voltage Sensors and Activation Gate in Voltage-Gated K^+ Channels. *J. Gen. Physiol.* **2002**, *120*, 663−676.
(249) Barber, A. F.; Liang, Q. S.; Amaral, C.; Treptow, W.; Covarrubias, M. Molecular Mapping of General Anesthetic Sites in a Voltage-Gated Ion Channel. *Biophys. J.* **2011**, *101*, 1613−1622.
(250) Liang, Q. S.; Anderson, W. D.; Jones, S. T.; Souza, C. S.; Hosoume, J. M.; Treptow, W.; Covarrubias, M. Positive Allosteric Modulation of Kv Channels by Sevoflurane: Insights into the Structural Basis of Inhaled Anesthetic Action. *PLoS One* **2015**, *10*, No. e0143363.
(251) Delemotte, L.; Tarek, M.; Klein, M. L.; Amaral, C.; Treptow, W. Intermediate States of the Kv1.2 Voltage Sensor from Atomistic Molecular Dynamics Simulations. *Proc. Natl. Acad. Sci. U. S. A.* **2011**, *108*, 6109−6114.
(252) Treptow, W.; Tarek, M. Environment of the Gating Charges in the Kv1.2 Shaker Potassium Channel. *Biophys. J.* **2006**, *90*, L64−L66.
(253) Stock, L.; Hosoume, J.; Treptow, W. Concentration-Dependent Binding of Small Ligands to Multiple Saturable Sites in Membrane Proteins. *Sci. Rep.* **2017**, *7*, No. 5734.
(254) Jorgensen, C.; Domene, C. Location and Character of Volatile General Anesthetics Binding Sites in the Transmembrane Domain of TRPV1. *Mol. Pharmaceutics* **2018**, *15*, 3920−3930.

Q

DOI: 10.1021/acs.chemrev.8b00366
Chem. Rev. XXXX, XXX, XXX−XXX

B.3 Exposure of the HIV-1 broadly neutralizing antibody 10E8 MPER epitope on the membrane surface by gp41 transmembrane domain scaffolds, *Biochim. Biophys. Acta.* 2018

B.3.1 Authorship and Permissions

<table>
<tr><td colspan="10">This declaration concerns the article entitled</td></tr>
<tr><td colspan="10">Exposure of the HIV-1 broadly neutralizing antibody 10E8 MPER epitope on the membrane surface by gp41 transmembrane domain scaffolds</td></tr>
<tr><td colspan="10">Publication status (tick one)</td></tr>
<tr><td>Draft manuscript</td><td></td><td>Submitted</td><td></td><td>In review</td><td></td><td>Accepted</td><td></td><td>Published</td><td>✓</td></tr>
<tr><td>Publication details</td><td colspan="9">*Biochim. Biophys. Acta*. 2018, 1860(6), 1259-1271
DOI: 10.1016/j.bbamem.2018.02.019

Received: 26 October 2017
Accepted: 20 February 2018
Published online: 23 February 2018</td></tr>
<tr><td>Candidates contribution to the paper (detailed and also given as a percentage)</td><td colspan="9">The candidate contributed to/considerably contributed/predominantly executed the…

Experimental work (50%): J. Torralba, E. Rujas and B. Apellaniz

Computational work (50%): V. Oakes and C. Domene

Formulation of ideas (Computational: 50%):
V. Oakes and C. Domene contributed equally.

Design of methodology (Computational: 50%):
V. Oakes and C. Domene contributed equally.

Experimental work (Computational: 100%):
V. Oakes: Performed simulations and analysis

Presentation of data in journal format (30%):
B. Apellaniz: Main author of manuscript and supporting information.
V. Oakes: Main author of text and figures relating to computational work and contributed equally to discussion.
All authors critically revised the manuscript.</td></tr>
<tr><td>Statement from Candidate</td><td colspan="9">This paper reports on original research I conducted during the period of my Higher Degree by Research candidature.</td></tr>
<tr><td>Signed</td><td colspan="5"></td><td>Date</td><td colspan="3"></td></tr>
</table>

B.3.2 Manuscript

BBA - Biomembranes 1860 (2018) 1259–1271

Contents lists available at ScienceDirect

BBA - Biomembranes

journal homepage: www.elsevier.com/locate/bbamem

Exposure of the HIV-1 broadly neutralizing antibody 10E8 MPER epitope on the membrane surface by gp41 transmembrane domain scaffolds

Victoria Oakes[a,c], Johana Torralba[b], Edurne Rujas[b], José L. Nieva[b], Carmen Domene[c,d,*], Beatriz Apellaniz[b,**]

[a] Department of Chemistry, Britannia House, 7 Trinity Street, King's College London, London SE1 1DB, UK
[b] Biofisika Institute (CSIC, UPV/EHU), Biochemistry and Molecular Biology Department, University of the Basque Country (UPV/EHU), PO Box 644, 48080 Bilbao, Spain
[c] Department of Chemistry, 1 South Building, Claverton Down Road, University of Bath, Bath BA2 7AY, UK
[d] Chemistry Research Laboratory, Mansfield Road, University of Oxford, Oxford OX1 3TA, UK

ARTICLE INFO

Keywords:
Molecular dynamics simulation
Transmembrane domain
Antigenicity
Vaccine development
HIV-1

ABSTRACT

The 10E8 antibody achieves near-pan neutralization of HIV-1 by targeting the remarkably conserved gp41 membrane-proximal external region (MPER) and the connected transmembrane domain (TMD) of the HIV-1 envelope glycoprotein (Env). Thus, recreating the structure that generates 10E8-like antibodies is a major goal of the rational design of anti-HIV vaccines. Unfortunately, high-resolution information of this segment in the native Env is lacking, limiting our understanding of the behavior of the crucial 10E8 epitope residues.

In this report, two sequences, namely, MPER-TMD1 (gp41 residues 671–700) and MPER-TMD2 (gp41 residues 671–709) were compared both experimentally and computationally, to assess the TMD as a potential membrane integral scaffold for the 10E8 epitope. These sequences were selected to represent a minimal (MPER-TMD1) or full-length (MPER-TMD2) TMD membrane anchor according to mutagenesis results reported by Yue et al. (2009) J. Virol. 83, 11,588. Immunochemical assays revealed that MPER-TMD1, but not MPER-TMD2, effectively exposed the MPER C-terminal stretch, harboring the 10E8 epitope on the surface of phospholipid bilayers containing a cholesterol concentration equivalent to that of the viral envelope. Molecular dynamics simulations, using the recently resolved TMD trimer structure combined with the MPER in a cholesterol-enriched model membrane confirmed these results and provided an atomistic mechanism of epitope exposure which revealed that TMD truncation at position A700 combined with N-terminal addition of lysine residues positively impacts epitope exposure. Overall, these results provide crucial insights into the design of effective MPER-TMD derived immunogens.

1. Introduction

The HIV-1 envelope glycoprotein (Env) is a class I viral fusion glycoprotein that initiates the infection cycle and the only protein on the viral particle accessible to the immune system. Since the publication in 2013 of the high-resolution cryo-EM [1] and x-ray [2] structures of the clade A BG505 strain SOSIP construct, a stabilized soluble prefusion Env trimer cleaved at position D664, several other native-like structures from the same [3] and other clades [4,5] have been reported and have provided detailed information on the architecture of the native gp41 ectodomain (for a comprehensive review of the available Env structures, see [6]). By comparison, less is known on the structure-function relationships regarding the MPER and TMD sequences after position D664. Besides its structural role in anchoring the Env complex to the viral membrane [7,8], the MPER-TMD region is required for cell-cell fusion, viral infectivity and immunosuppression [9–18]. Moreover, the highly conserved MPER sequence constitutes a vulnerability site on the Env complex targeted by broadly neutralizing antibodies (bnAbs)

Abbreviations: MPER, membrane-proximal external region; TMD, transmembrane domain; Env, HIV-1 envelope glycoprotein; MD, molecular dynamics; bNAb, broadly neutralizing antibody; CDR-H3, complementarity-determining region three of the heavy chain; HC, heavy chain; WT, wild-type; *p*BPA, *p*-benzoylphenylalanine; DMPC, 1,2-dimyristoyl-*sn*-glycero-3-phosphocholine; DHPC, 1,2-dihexanoyl-*sn*-glycero-3-phosphocholine; Chol, cholesterol; POPC, 1-palmitoyl-2-oleoyl-*sn*-glycero-3-phosphocholine; PA, L-α-phosphatidic acid; POPA, 1-palmitoyl-2-oleoyl-*sn*-glycero-3-phosphate; Rho-PE, 1,2-dioleoyl-*sn*-glycero-3-phosphoethanolamine-*N*-(lissamine rhodamine B sulfonyl); CD, circular dichroism; HFIP, 1,1,1,3,3,3-hexafluoro-2-propanol; N_P, number of atomic interaction pairs; MAb4E10, monoclonal antibody 4E10; HRP, horseradish peroxidase

* Correspondence to: C. Domene, Department of Chemistry, 1 South Building, Claverton Down Road, University of Bath, Bath BA2 7AY, UK.
** Correspondence to: B. Apellaniz, Departamento de Fisiología, Facultad de Farmacia, Universidad del País Vasco (UPV/EHU), Paseo de la Universidad, 7, 01006 Vitoria-Gasteiz, Spain.
E-mail addresses: C.Domene@bath.ac.uk (C. Domene), beatriz.apellaniz@ehu.eus (B. Apellaniz).

https://doi.org/10.1016/j.bbamem.2018.02.019
Received 26 October 2017; Received in revised form 30 January 2018; Accepted 20 February 2018
Available online 23 February 2018

[19–22]. Specifically, antibodies directed against the MPER C-terminal helix, such as 4E10 or 10E8, display near pan-neutralization activity in standard panels of HIV strains and isolates [23,24]. Since 10E8 is a more potent antibody that lacks polyreactivity, ongoing immunogen-design strategies target this antibody [19,22,25].

In this regard, previous studies suggested that the neutralization-competent structure of the MPER might also implicate part of the native TMD sequence [13,26–29]. Accordingly, 4E10 and 10E8 bnAbs bound to MPER expressed on the surface of the plasma membrane with significantly higher affinity when tethered to it via the TMD of HIV-1 gp41, rather than via the platelet-derived growth factor receptor TMD [26]. Supporting the involvement of the TMD in MPER antigenicity, we have recently reported NMR [28] and x-ray structural data [30] indicating that the C-terminal half of the MPER and the N-terminal half of the TMD (MPER-N-TMD) arrange into a continuous helix spanning residues 673 to 690. This observation was reinforced by the publication of a NMR structure of a HIV-1 clade D TMD trimer (isolate 92UG024.2, residues 677–716, HXB2 numbering) in DMPC:DHPC (1:2, mol:mol) bicelles [13]. Together, these results oppose the long-standing hypothesis that the helix bends at the MPER-TMD connection (residue K683) to allow TMD insertion into the membrane in an orientation perpendicular to the bilayer plane [31,32]. In accordance with the experimental evidence, we hypothesized that the unbent MPER-N-TMD helix might function as a scaffold to increase the affinity of anti-MPER antibodies at membrane surfaces [28] and found that indeed, the complete 10E8 epitope includes TMD residues beyond K683 [30].

In this work, we analyze the effect of elongating the continuous MPER-N-TMD α-helix towards the TMD C-terminus on the exposure of the 10E8 MPER epitope at membrane surfaces (Fig. 1). To this end, immunochemical assays and molecular dynamics (MD) simulations have been employed to analyze the potential of MPER-TMD derived sequences of different lengths to scaffold the 10E8 epitope when incorporated into liposomal vaccines with a cholesterol concentration that matches that of the viral envelope [33]. Moreover, the effect on epitope exposure of N- and/or C-terminal positive charge addition is analyzed. Our findings have the potential to aid the development of new vaccine formulations that effectively elicit the production of 10E8-like anti-MPER antibodies.

2. Materials and methods

2.1. Materials

Synthetic peptides derived from the gp41 MPER-TMD, *KKK*-^{671}NWFDITNWLWYIKLFIMIVGGLVGLRIVFA^{700}-*KKKK* (MPER-TMD1) and ^{671}NWFDITNWLWYIKLFIMIVGGLVGLRIVFAVLSVVN-RVR^{709} (MPER-TMD2) were produced by solid-phase synthesis using Fmoc chemistry as C-terminal carboxamides and purified by HPLC. 1-palmitoyl-2-oleoyl-*sn*-glycero-3-phophocholine (POPC), L-α-phosphatidic acid (Egg, Chicken) (PA), cholesterol (Chol), and 1,2-dioleoyl-*sn*-glycero-3-phosphoethanolamine-*N*-(lissamine rhodamine B sulfonyl) (Rho-PE) were purchased from Avanti Polar Lipids. Goat anti-Human IgG (Fab specific) was obtained from Sigma-Aldrich, rabbit anti-Human IgG-HRP and mouse anti-goat IgG-HRP from Santa Cruz Biotechnology. Monoclonal antibody 4E10 (MAb4E10) was kindly donated by D. Katinger (Polynum Inc., Vienna, Austria). 4E10 and 10E8 wild type Fabs, their non-functional mutant versions and their Trp100b$_{Hc}$*p*BPA substituted versions were produced as previously described [27,30].

2.2. Circular dichroism

Circular dichroism (CD) measurements were obtained from a thermally controlled Jasco J-810 circular dichroism spectropolarimeter calibrated routinely with (1*S*)-(+)-10-camphorsulfonic acid, ammonium salt. Samples consisted of lyophilized synthetic peptides dissolved at concentrations of 0.03 mM in 2 mM Hepes (pH, 7.4) buffer containing 25% (v/v) of the low-polarity organic solvent 1,1,1,3,3,3-hexafluoro-2-propanol (HFIP). Spectra were measured in a 1 mm path-length quartz cell initially equilibrated at 25 °C. Data were taken with a band-width of 1 nm at 100 nm/min speed, and the results of 20 scans were averaged.

2.3. Peptide reconstitution into liposomes

To ensure proper incorporation of the peptides into the vesicles, lipids and peptides (MPER-TMD1 and MPER-TMD2) were mixed in organic solvent prior to the production of the liposomes. Briefly, POPC, Chol and PA were dissolved in chloroform:methanol 1:2 (vol:vol) at 10:11:1 (mol:mol) ratio and were mixed with MPER-TMD1 or 2 (dissolved in % 100 ethanol) to achieve a peptide-to-lipid molar ratio of 1:50. The mixture was dried under a N_2 stream and traces of organic solvents were removed by 2 h vacuum pumping. Subsequently, the dried lipid films were subjected to 2 h of gentle hydration with H_2O using a N_2 gas bubbler to facilitate the subsequent dispersion of the dried lipid-peptide film in PBS aqueous buffer. Next, the multilamelar vesicles were bath sonicated (1 h, 55 °C) and subjected to 15 freeze and thaw cycles to obtain unilamelar vesicles. Chol concentration of liposome suspensions was determined by the cholesterol oxidase/peroxidase method (BioSystems, Barcelona, Spain), and found to be within the experimental error.

2.4. Liposome flotation assay

Following the method described by Yethon et al. [34], vesicle flotation experiments in sucrose gradients were performed to assess the association of 4E10 and 10E8 Fabs or their mutant counterparts to their epitopes presented by the MPER-TMD1 or MPER-TMD2 scaffolds in cholesterol-enriched membranes. In brief, 200 μL of a sample containing rhodamine-labeled liposomes (1.5 mM lipid concentration, 0.5 mol% Rho-PE) and peptide (30 μM peptide; 1:50 peptide-to-lipid molar ratio) was incubated with Fabs for 15 min at RT under constant stirring (800 rpm). 100 μL of the sample was adjusted to a sucrose concentration of 1.4 M in a final volume of 300 μL, and subsequently overlaid with 400 μL- and 300 μL-layers of 0.8 M and 0.5 M sucrose, respectively. The gradient was centrifuged at 436,000 × *g* for 3 h at 4 °C in a TLA 120.2 rotor (Beckman Coulter). After centrifugation, four 250 μL-fractions were collected. Material adhered to tubes was collected into a 5th fraction by washing with 250 μL of hot (100 °C) 1% (w/v) SDS. The presence of MPER-TMD truncated peptides and Fabs in the different fractions and in the original sample (input) was revealed by Western Blot analysis after Tris-Tricine SDS-PAGE separation. MAb4E10 (0.05 μg/mL) and rabbit anti-human-IgG-HRP, and goat anti-Human IgG (Fab specific) and mouse anti-goat IgG-HRP antibody pairs were used to reveal peptides and Fabs, respectively. The presence of liposomes in the different fractions was determined after measuring the fluorescence emission of the Rho-PE probe [12].

2.5. Photo-cross-linking assay

For the photo-cross-linking experiments, samples containing 1.5 μM Fab bearing the 10E8 or 4E10 W100b$_{Hc}$*p*BPA substitution and 30 μM of peptides MPER-TMD1 or MPER-TMD2 in solution (PBS) or reconstituted into membranes (1.5 mM lipid) were incubated for 15 min at RT and irradiated afterwards with UV light at 365 nm for 20 min at 4 °C, using a UVP B-100AP lamp. Finally, Fab heavy-chain-peptide adducts were separated by 15% Tris-Glicine SDS-PAGE and stained with Coomassie blue.

2.6. Molecular dynamics simulations

The atomic structures of the HIV-1 gp41 TMD trimer (PDB ID: 5JYN) [13] and the MPER-N-TMD helix (PDB ID: 5GHW) [30] were

[47].

3. Results

3.1. Design of the MPER-TMD1 and MPER-TMD2 peptide scaffolds

Fig. 1A describes the two sequences derived from the MPER-TMD region that were designed to upgrade our previous vaccines based on the MPER-N-TMD sequence (termed CpreTM in our recent work) [28]. To that end, these sequences included different sections of the native TMD sequence, due to the previously reported positive effect in 4E10 and 10E8 antibody binding to their epitopes [30,48]. The MPER-TMD1 sequence encompasses Env residues ^{671}**NWF**D**I**T**N**WL**W**Y**I**K**L**FIM-IVG*GLVGLRIVFA*^{700} (sequence numbering derived from the prototypic HXBc2 isolate) and embodies the unbent MPER-N-TMD helix (residues 673 to 690, underlined) [28,30] including the complete 10E8 epitope sequence (critical residues in bold) [24,30,49], which has been elongated to include part of the C-terminus of the TMD (in italics). The TMD portion in this sequence has been truncated at position A700 according to mutagenesis results reported by Yue et al. [9]. This mutant was found to represent a minimal TMD anchor, which allowed efficient transport of Env to the plasma membrane, and wild-type levels of cell-cell fusion [9]. Finally, three and four lysine residues were added to this sequence at the N- and C-termini, respectively, to match the hydrophobicity of our previously reported CpreTM sequence [28]. The MPER-TMD2 sequence (Env residues, ^{671}**NWF**N**I**T**N**WL**W**Y**I**K**L**FIMIVG*GLVGLRIVFAVL-SLVNRVR*^{709}) bears the 10E8 epitope (critical residues in bold), the MPER-N-TMD helix sequence (underlined) and the sequence assumed to span the full TMD (in italics) [50], which contains the minimal number of amino acids required for WT-like incorporation of Env and some degree of infectivity [9].

3.2. Experimental assessment of the antigenicity of MPER-TMD scaffolds

3.2.1. Secondary structure

Following synthesis, the secondary structures of MPER-TMD1 and MPER-TMD2 peptides were compared by circular dichroism in the low-polarity organic solvent HFIP that roughly mimics the membrane environment. As shown in Fig. 1B, the synthetic peptides adopted similar levels of α-helical conformation, as expected from previous structural studies [13,28], underpinning their further comparison as synthetic surrogates of the MPER-TM domain.

3.2.2. Incorporation into membranes and antigenicity

Next, we tested experimentally the capacity of the synthetic peptides to incorporate into cholesterol-enriched bilayers and expose the 10E8 MPER epitope at membrane surfaces. In those assays, MPER-TMD1 and MPER-TMD2 (Fig. 2A and B, respectively, 10 kDa panels) mostly co-floated with lipid vesicles (rhodamine emission spectra) upon physical separation of bound and unbound species by ultracentrifugation in a sucrose gradient. The absence of peptide in the SDS and 1st fractions (non-floated fractions) further confirmed that both peptides were effectively incorporated into vesicles containing 50 mol% cholesterol. The appropriate display (antigenicity) of the 10E8 bnAb epitope in the MPER-TMD peptides reconstituted into membranes was subsequently assayed (Fig. 2). To this end, the binding capacity of the reconstituted MPER-TMD peptides to a functional (neutralizing) wild type 10E8 Fab (Fig. 2, left panels) and to a non-functional (non-neutralizing) mutant Fab (Fig. 2, right panels) was compared. The 10E8 mutant Fab, termed 10E8 W100bD, was obtained by decreasing the hydrophobicity of the CDR-H3 loop after substitution of the critical tryptophan residue 100b of the CDR-H3 apex with Asp, a mutation that abrogates neutralization and binding to the epitopes in a membrane milieu [30]. Therefore, it comprises a valuable tool to discriminate functional and non-functional binding to the liposome-peptide formulations proposed as immunogens. The 10E8 wild type Fab, but not the W100bD mutant, effectively recognized the MPER-TMD1 peptide in the membrane, demonstrated by the 25 kDa bands corresponding to the Fab, co-floating with the liposomes bearing the peptide (Fig. 2A, left panel). This result reveals the capacity of MPER-TMD1 reconstituted into cholesterol-enriched vesicles to effectively expose the epitope of the 10E8 bnAb following a neutralization-competent pattern. In contrast, both wild type and mutant Fabs were recovered from the non-floated fractions when the epitope was presented by the MPER-TMD2 peptide in the surface of the liposomes (Fig. 2B) or when the epitope was absent (Fig. 2C). Overall, these results are consistent with the correct exposure of the epitope in the MPER-TMD1 scaffold when reconstituted into cholesterol-enriched liposomes and reveal its potential as an immunogen to elicit 10E8-like anti-MPER antibodies.

To determine whether the observed difference in antigenicity between the two MPER-TMD scaffolds was specific to the 10E8 antibody or could be reproduced with other anti-MPER antibodies, the same experiment was performed with Fab 4E10, whose epitope maps to the same region [24,51]. As shown in Fig. S1, wild type 4E10 Fab recognized and bound to MPER-TMD1 reconstituted into liposomes (Fig. S1A, left panel), but was recovered from the non-floating fractions either when the epitope was presented by the MPER-TMD2 scaffold (Fig. S1B, left panel) or in the absence of the epitope (Fig. S1C, left panel). Following the same strategy used with 10E8, a non-functional (non-neutralizing) 4E10 mutant Fab was also assayed to determine the relevance of the MPER-TMD1 scaffold as immunogen. This mutant, termed 4E10 Δloop, has an intact paratope while the tip of the CDR-H3 loop is ablated. Preservation of this loop is required for neutralization [27] but its deletion has a negligible effect on Fab binding to the epitope in solution, displaying near wild type affinity [49]. Similarly to 10E8 W100bD and in contrast to 10E8 or 4E10 wild type Fabs, 4E10 Δloop binding to MPER-TMD scaffolds reconstituted in a membrane was barely detected (Fig. S1, right panels). Together, these data suggest that the C-terminal MPER epitope targeted by these bnAbs is not properly exposed in the MPER-TMD2 scaffold.

Binding assays were next complemented with photo-cross-linking experiments. This approach allows scoring effective engagement of the epitope peptide with the antibody in an intact system [48] and serves to rule out the possibility that the antibodies bound to MPER-TMD2, but would dissociate during the ultracentrifugation protocol (Fig. 3). To carry out the experiment, the UV-sensitive unnatural amino acid *p*-benzoylphenylalanine (*p*BPA) [52,53], was genetically encoded at position Trp100b of the 10E8 Fab heavy chain (HC) CDR-H3 tip. Following incubation of the modified Fab with either MPER-TMD1 or MPER-TMD2 in solution or reconstituted into membranes, the samples were subjected to UV light, and the formation of covalent adducts analyzed by SDS-PAGE. As expected, an additional band corresponding to cross-linked peptide and Fab 10E8 HC was observed in MPER-TMD1 containing samples, both in solution and in liposomes, but not in samples containing MPER-TMD2 in liposomes, consistent with the flotation assay. However, a shift in the gel was also observed in MPER-TMD2 samples devoid of a lipid membrane, indicating that correct exposure of the epitope is reliant on its environment, with membrane insertion hindering recognition of the epitope by the anti-MPER antibody. The new band was absent in all cases before irradiation (UV^- lines) and in the absence of the epitope, demonstrating that UV-mediated cross-linking specifically causes the appearance of this band.

Flotation and photo-cross-linking experiments also revealed that MPER-TMD1 migrated on tricine-SDS-PAGE with an apparent molecular weight of 10 kDa (theoretical MW of 4.5 kDa for MPER-TMD1) revealing the potential of this peptide to form stable dimers even in the harsh conditions of the experiments (5 min at 100 °C and 1% SDS). On the contrary, MPER-TMD2 migrated as two bands, compatible with dimers and trimers, suggesting formation of stable higher-order oligomers in cholesterol-enriched membranes. This differential behavior might have implications in the effective exposure of the MPER epitope at the membrane surface.

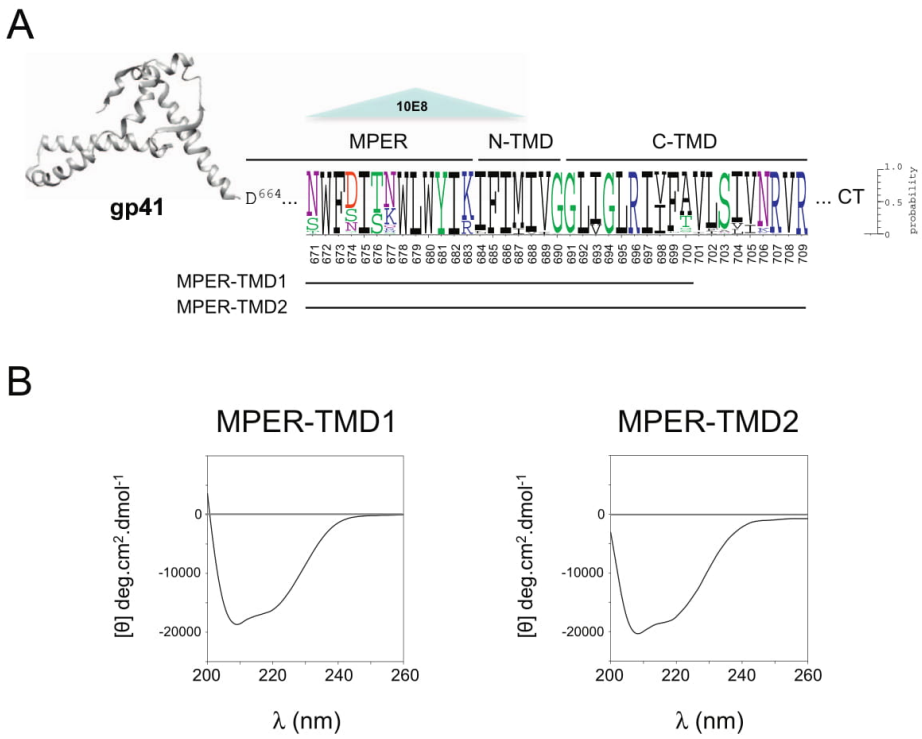

Fig. 1. Description and structure of the HIV-1 gp41 MPER-TMD sequences used in the present study. A) Weblogo representation of MPER-TMD sequence variability of all HIV-1/SIVcpz subtype genomes (filtered web, 5132 sequences) available at the LANL HIV Sequence Database (http://www.hiv.lanl.gov/content/sequence/NEWALIGN/align.html). Gp41 amino acids 671 to 709 are shown (HXBc2 prototypic isolate numbering) color-coded according to their chemical properties (polar - green, neutral - purple, basic - blue, acidic - red and hydrophobic - black) and lines below the logo span the sequences covered by the peptides used in this study. Lines above the logo depict the MPER, N-TMD and C-TMD domains of gp41, and the full epitope of 10E8 antibody is highlighted. The gp41 ectodomain (PDB ID: 5FUU) is shown as ribbons (dark grey). B) Secondary structure of MPER-TM domain derived synthetic peptides. Circular dichroism spectra of MPER-TMD1 and MPER-TMD2 peptides in the low polarity medium provided by 25% HFIP (left and right panels, respectively). (For interpretation of the references to color in this figure legend, the reader is referred to the web version of this article.)

superposed to create models of peptide trimers representing the MPER-TMD region with or without C-terminal truncations, and with or without N- and/or C-terminal lysine residues. Residues 671 to 689 were extracted from PDB 5GHW, with residues from 690 onwards obtained from PDB 5JYN, to ensure agreement between the peptide sequences used experimentally and computationally.

The N-termini of the peptides were modeled in a charged state whilst the C-termini were amidated. Default protonation states were used for ionizable residues. Water molecules were manually added to the region surrounding the protonated R696, in keeping with the presence of structured water molecules noted by Dev et al. [13]. Peptide assemblies MPER-TMD1 (no lysines, N-terminal lysines, C-terminal lysines, and N- and C-terminal lysines) and MPER-TMD2 (no lysines), were inserted into model membranes, containing POPC, POPA and cholesterol molecules in a 10:11:1 ratio, using the CHARMM-GUI Membrane Builder [35–37]. For this purpose, the replacement method was utilized. In this approach, pseudo atoms representing lipids are distributed around the protein, and replaced with molecules randomly selected from the associated lipid molecule library [35]. The system was solvated with approximately ~30,000 water molecules, with added NaCl to mimic to the 150 mM experimental concentration and achieve neutralization. NAMD2.9 was employed to perform MD simulations [38]. The CHARMM36 force field was used to describe the peptide and lipids [39], the TIP3P model for water [40], and standard parameters were used for ions [41]. The Particle Mesh Ewald method was used for the treatment of periodic electrostatic interactions, with an upper threshold of 1 Å for grid spacing [42]. Electrostatic and van der Waals forces were calculated every time step. A cut-off distance of 12 Å was used for van der Waals forces. A switching distance of 10 Å was chosen to smoothly truncate the non-bonded interactions. Only atoms in a Verlet pair list with a cut-off distance of 14 Å (reassigned every 20 steps) were considered [43]. The SETTLE algorithm was used to constrain all bonds involving hydrogen atoms to allow the use of a 2 fs time step throughout the simulation [44]. The Nose-Hoover-Langevin piston method was employed to control the pressure with a 200 fs period, 50 fs damping constant and a desired value of 1 atm [45,46]. The system was coupled to a Langevin thermostat to sustain a temperature of 298 K throughout. Systems were minimized for 1000 steps, and then subject to 4 ns of constrained dynamics to equilibrate. Four equilibration steps of 1 ns were performed, with restraints (force constant: 1 kcal/mol) imposed on different elements of the system to ensure gradual relaxation of the system; 1) protein atoms, lipid head groups, and water molecules within the trimer pore and in contact with R696 are restrained, in order to relax lipid tails and water molecules in the vicinity of the lipid headgroups; 2) protein atoms and water molecules within the trimer pore and in contact with R696 are restrained, so lipid molecules can adjust to the protein surface; 3) only protein atoms are restrained, to ensure internal water molecules, and those in contact with R696 residues, occupy the most energetically unfavourable positions; 4) protein backbone atoms are restrained, to allow optimisation of side-chain dynamics. Unconstrained dynamics was then performed for 200 ns. Analysis was performed using in-house TCL scripts for VMD

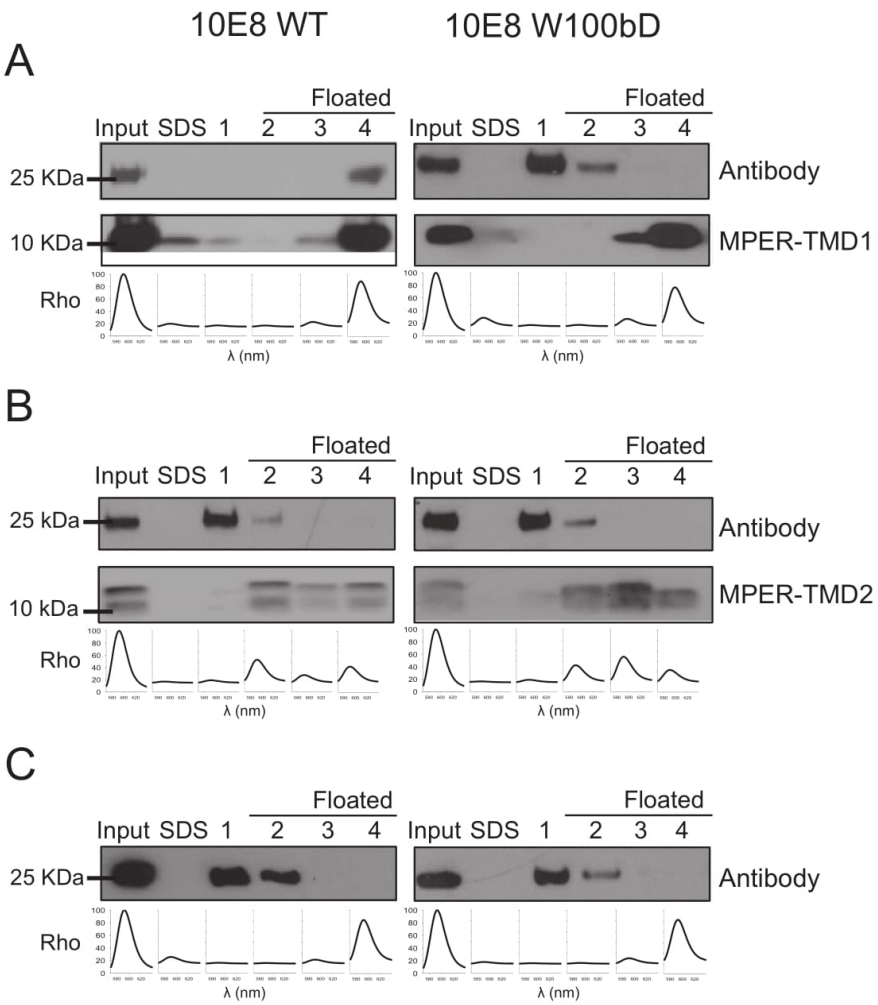

Fig. 2. Association of 10E8 Fab and its mutant version to MPER-TMD1 and MPER-TMD2 reconstituted into cholesterol-enriched vesicles proved by ultracentrifugation in a sucrose gradient. POPC:Chol:PA 10:11:1 (mol:mol) liposomes containing 0.5% of Rho-PE were reconstituted without peptide (A) or with 30 μM MPER-TMD1 (B) or MPER-TMD2 (C) at a 1:50 peptide-to-lipid molar ratio and were incubated for 15 min at RT and under constant stirring (800 rpm) with 0.07 mg/mL of 10E8 or 10E8 W100bD Fabs (from left to right). The samples were then subjected to ultracentrifugation in a sucrose gradient and harvested in 5 fractions. Peptides (10 kDa bands) and bound or unbound Fabs (25 kDa bands) were size-separated by tricine-PAGE-SDS and proved by Western blot. Effective flotation of the vesicles was monitored following the fluorescence emission of the rhodamine probe included in the liposomes as depicted by the spectra below each panel.

3.3. Molecular dynamics simulations of MPER-TMD derived peptide scaffolds

3.3.1. Construction of the models

To understand the molecular mechanism underlying the above experimental observations, molecular dynamics (MD) simulations of the MPER-TMD1 and MPER-TMD2 peptides inserted into HIV-1-like cholesterol-enriched membranes were performed. The starting models (Fig. 4A) were constructed by superposition of the MPER-N-TMD structure (PDB ID: 5GHW), residues 671–689, with residues 690–700 or 690–709 of the individual helices of the recently resolved TMD trimer (PDB ID: 5JYN), to form MPER-TMD1 and MPER-TMD2, respectively. As described earlier, synthetic peptides and lipids were mixed in organic phase to produce liposomal vaccines; peptides were not added to preformed liposomes from the aqueous phase. Moreover, the free energy change of transferring residues from 671 to 693 from interface to octanol is negative [54] and residues downstream K683 have a hydrophobicity profile compatible with that of a membrane-buried sequence [55]. Thus, rather than laying on the bilayer surface parallel to the plane of the membrane, the trimers were inserted into the membrane assuming in both cases a disposition parallel to the bilayer normal (Fig. 4A). MD simulations were performed for 200 ns (Fig. 4B), with the initial 100 ns period considered an equilibration period. Therefore, only the final 100 ns of the simulations is considered in the analysis presented hereafter.

3.3.2. Overall stability of the models

Firstly, the root-mean-square deviation (RMSD) of the Cα atoms from the initial structure was monitored over time to assess the stability of the epitope region in the MPER-TMD derived constructs (Fig. 5A).

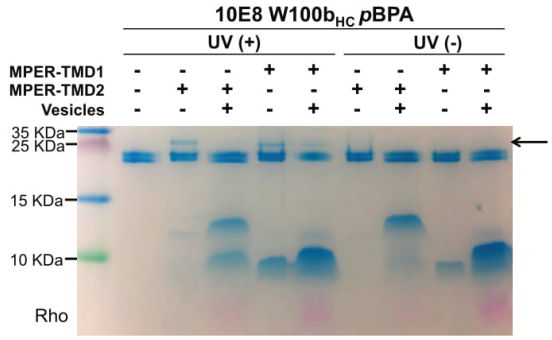

Fig. 3. Specific binding of 10E8 Fab to MPER-TMD1 and MPER-TMD2 reconstituted into cholesterol-enriched vesicles or in solution proved by photo-cross-linking. 0.07 mg/mL of 10E8 W100b$_{HC}$*p*BPA Fab was incubated alone, with the peptides in solution or with the peptides reconstituted into membranes, for 15 min at RT and under constant stirring (800 rpm), followed by irradiation with UV-light or no treatment. Peptides, heavy and light chains of the Fabs, and photo-cross-linked Fab-peptide adducts were detected by Coomassie-blue staining. Pink bands at the bottom of the gel revealed the presence of Rhodamine-labeled liposomes in the samples. The arrow points to the position of the photo-cross-linked product. (For interpretation of the references to color in this figure legend, the reader is referred to the web version of this article.)

The RMSD of MPER-TMD1 (4.4 ± 0.3 Å) is significantly higher than that of MPER-TMD2 (2.3 ± 0.2 Å), suggesting the assemblies adopt different configurations, with the latter resembling the initial construct most closely, based upon the NMR structure of the HIV-1 TMD and demonstrated by the calculated number of interaction pairs between adjacent helices (Fig. 5B) in each assembly. 300 to 450 atomic interaction pairs are present between adjacent helical pairs (CA > BC > AB) in MPER-TMD2, suggesting a near-symmetrical trimer assembly. An interaction number of this magnitude is only observed for the AC helix pair in MPER-TMD1, with the remaining number of pairwise interactions considerably reduced, to 237 and 118 between helices AB and BC, respectively. These observations suggest that the MPER-TMD1 trimer is unstable and might dissociate in a cholesterol-enriched bilayer, in agreement with earlier experimental results establishing the existence of MPER-TMD1 dimers (Fig. 2).

Moreover, inspection of the transmembrane helix tilt angle (τ) for residues 671–690, relative to the bilayer normal, showed noticeable differences between the trimers (Fig. 5C). At the beginning of the simulation (0 ns) helices A, B and C displayed tilt angles of 15.2°, 18.4° and 25.3°, respectively. In the last 100 ns of the simulation, helices A and B of the MPER-TMD2 trimer occupy a similar range, between 8 and 14° relative to the bilayer normal, whereas helix C fluctuates between 17 and 20°. Therefore, all of them display an increased verticality as compared to the initial model. In contrast, helices B and C of MPER-TMD1 display tilt angles of ca. 16° and 28°, equivalent to the initial model, whilst the tilt angle of helix A increases to ca. 24°. This result suggests that the assembly of the transmembrane trimer is noticeably perturbed.

3.3.3. Specific molecular interactions that define the observed conformations

To gain further insight at the molecular level into the interactions that contribute to the stabilization of the constructs in the simulations, we next analyzed the contacts between specific amino acids in each assembly and with the lipid bilayer. Specific interaction pairs are considered to be relevant if the number of atomic interaction pairs, N_P, is > 15. As the MPER-TMD1 structure is no longer symmetric, no residue pairs are identified with an average N_P of > 15 (Fig. 6A). Deconstruction of the MPER-TMD1 contact map into individual pairs of helices (Fig. 6B), identifies a prominent contact interface between monomers A and C, incorporating residue pairs W672-W680, I675-W680, W672-K683, L679-K683, L679-I686, L679-M687, I682-M687, I686-I693 and V689-I697 (N_P > 15), with L679-K683 and L679-M687 being the most prominent contacts (N_P > 25). This implies that monomers A and C shift relative to one another (region W672-V689 of A interacts with region W680-I697 of C) due to the increased tilt angle of helix A. On the other hand, region K683-I693 of monomer B interacts with region I686-R696 of A via residue pairs, K683-I686, M687-I686, I686-I693, M687-V689, G690-I693, I693-I693, and I693-R696 (N_P > 15), with I686-I693 and I693-R696 being the most prominent pairs identified. Finally, no residue pairs are identified (with N_P > 15) between monomer B and C. These results indicate that MPER-TMD1 contains two energetically favorable dimer interfaces, between the N-terminal regions of helices A and C and the C-terminal regions of A and B.

In contrast, in the MPER-TMD2 simulation, inter-helical interactions span the region between W678 and I697 with several residue pairs identified with N_P > 15 (Fig. 6C). Residue pairs W678-L679, I682-K683, F685-M687, F685-I686, I686-I686, L692-I693, I693-I693, and R696-I697 exceed this value, when averaged over the three helices. In this case, deconstruction of the MPER-TMD2 contact map into individual pairs of helices reveals that similar residues participate in pairwise interactions (Fig. 6D) consistent with the near-symmetrical conformation of the trimer. Overall, residues I686 and I693 corresponding to the *a* and *d* positions of the coiled-coil, are involved in 32% and 26% of the total number of interaction pairs, and thus, contribute to the stability of the trimer to the greatest extent.

Regarding interactions with lipids, residues K668 and W680 populate the head group region of the upper leaflet in helix A and residues K668 and K670 in helix C of the MPER-TMD1 simulation, whereas W672, F673 and W678 occupy this region in helix B (Fig. 7A). In the lower leaflet, C-terminal lysine residues inhabit the head group region in all helices, and also R696 in helix A, despite residing in the hydrophobic core. Critical residues that anchor the peptide to the hydrophobic membrane core, common to all helices, include Y681, L684, F685, I688, L692 and L695 (Fig. 7B). However, several differences between the helices are observed regarding acyl chain interactions, with W678 displaying an elevated number of interactions with the acyl chains in helices A and C, and W680 and M687 in helix B. Moreover, it's worth noting that C-terminal residues in helix C unfold to facilitate snorkeling of lysines 700 to 704 and to permit accommodation of the hydrophobic residues to the thickness of the bilayer (Fig. 1C). Similarly, helix A unfolds to accommodate the helix to the thickness of the hydrophobic core, in this case between residues G694 and V698. Helix B, which is less tilted, spans the membrane without unfolding. In the case of the MPER-TMD2 simulation, residues W680 and R709 in all three helices consistently populate the head group region of the upper and lower leaflets, respectively. Furthermore, besides the residues described to interact with the acyl chains in MPER-TMD1, interactions between residues M687, S691, I697, V698, F699, V701 and V702 and the hydrophobic core of the membrane were also recorded.

3.3.4. Accessibility of the 10E8 epitope residues

To assess accessibility of the epitope within the MPER-TMD scaffolds, the average number of atomic interactions of the main epitope residues, N671, W672, F673, T676, W680 and K683, with other protein residues was calculated (Table 1). These residues display approximately 100 interactions in MPER-TMD1 helix A, mainly resulting from W672 and K683. In helix B, the number of interactions is at a minimum, with K683 involved in an average of 8 interaction pairs and no interactions recorded for the other residues. Hence, the 10E8 epitope in helix B retains a large surface area to interact with other species. However, epitope residues in this helix are engaged in extensive lipid interactions (Fig. 7 and Table 2); W672 and F673 interact with the phospholipid head groups, and W680 and, to a lesser extent K683, interact with the hydrophobic core. In helix C, protein residues occlude the lower region of the epitope, with W680 and K683 involved in ca. 120 interaction

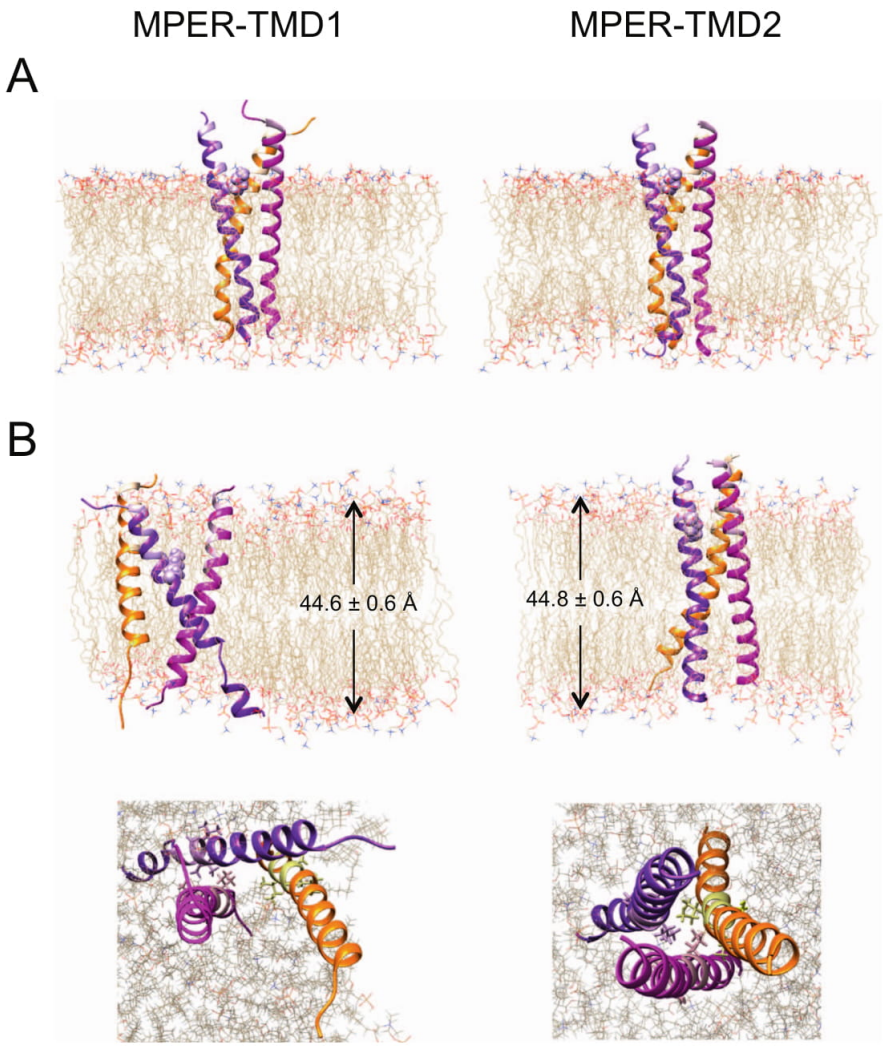

Fig. 4. Overview of the MPER-TM domain simulations. Snapshots of the MD simulations of MPER-TMD1 (left) and MPER-TMD2 (right) models (A) at time 0 ns (side view) and (B) at time 200 ns (side and top views). The structural models were constructed with UCSF Chimera using 5GHW and 5JNY structures deposited in the PDB. Helices A, B and C are colored in purple, pink and orange, respectively. Main 10E8 epitope residues (^{671}NWF–T—W–K^{683}) are colored lighter in each helix and K683 of one monomer is shown as spheres to mark the predicted starting point for the TMD. The arrows depict the average thickness of the bilayer, which was calculated as the distance between the projected mass distribution of the phosphorous atoms in the upper and lower leaflets, using the MEMPPLUGIN of VMD. (For interpretation of the references to color in this figure legend, the reader is referred to the web version of this article.)

pairs. In contrast, N-terminal epitope residues N671, W672 and F673 are not engaged in interactions with other residues or surrounding lipid molecules. Thus, the N-terminal part of helix C in MPER-TMD1 is exposed to the solvent and might effectively interact with the antibody.

Conversely, epitope residues in each of the three MPER-TMD2 helices display an average of 60–100 interactions in total, primarily constituted of residues K683 and W672 (Table 1). These interactions are the consequence of the near-symmetric trimer arrangement and the inward-facing orientation of these residues in the observed MPER-TMD2 conformation. Moreover, residue W680 displays interactions with the surrounding lipid molecules, both with the polar head groups or the acyl chains of the lipids (Fig. 7 and Table 2). As a result, the epitope can be considered inaccessible to incoming antibody molecules. These observations support the experimentally observed deficient antigenicity of MPER-TMD2.

3.3.5. Effect of the flanking lysines on the MPER-TMD1 model

Finally, to determine to what extent factors conditioning accessibility of 10E8 epitope on MPER-TMD1, i.e., loss of symmetry and interhelical interactions of the MPER-TMD1 trimer, depend on the truncation of the TMD at A700 and/or on the presence of lysine residues at both ends, three additional models were generated: 1) residues 671–700 without lysines (MPER-TMD1$_{no\text{-}lys}$); 2) residues 671–700 with three lysines at the N-terminus (MPER-TMD1$_{N}$) and 3) residues 671–700 with three lysines at the C-terminus (MPER-TMD1$_{C}$). MD simulations were performed for 200 ns, and the last 100 ns were considered for analysis (Figs. 8 and S2, and Tables S1–4).

MPER-TMD1$_{no\text{-}lys}$ resembles most closely the results obtained with the MPER-TMD2 construct devoid of lysines, with a RMSD of 2.6 ± 0.1 Å (Fig. S2A) and an increased verticality of the helices (tilt angles between 7 and 20°) (Fig. S2C). In contrast, RMSD values are

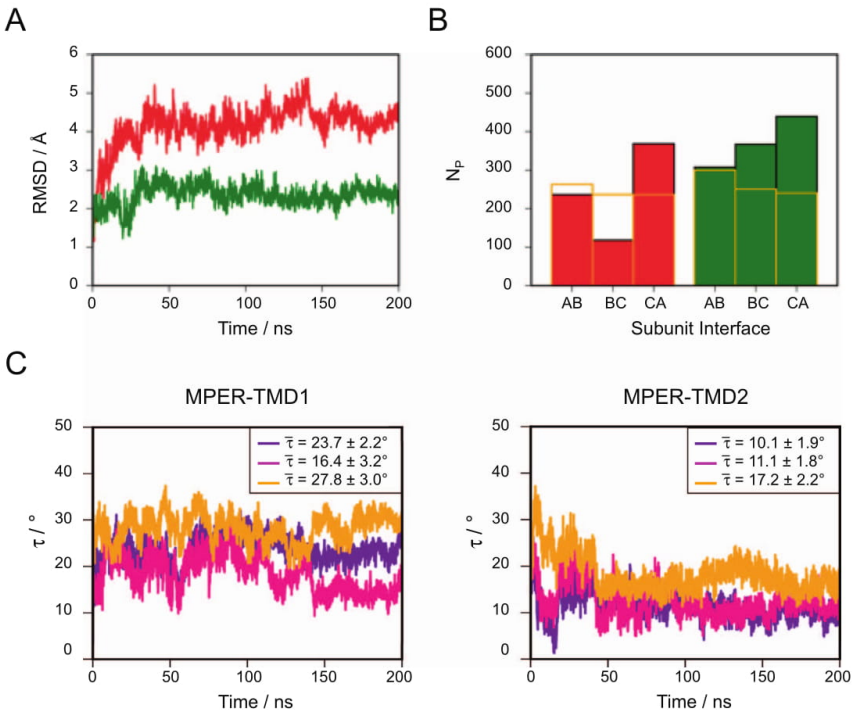

Fig. 5. Overall stability of the MPER-TM domain simulations. A) RMSD of the MPER-TM domain residues 671 to 690 in the MPER-TMD1 (red) and MPER-TMD2 (green) models over the course of the simulations. B) Average number of interaction pairs between subunit pairs in the MPER-TMD1 (red), MPER-TMD2 (green) and the initial situation (yellow outline) averaged from frames at 50 ps intervals. An interaction pair is counted if the distance between two atoms is < 4 Å. C) Tilt angle (τ) of individual helices (residues 671 to 690) with respect to the bilayer normal over the course of the simulations. Each helix is displayed in a different color (A–C helices, purple, pink and orange, respectively). The inset data represent the average tilt angle of each individual helix during the final 100 ns of the simulation. (For interpretation of the references to color in this figure legend, the reader is referred to the web version of this article.)

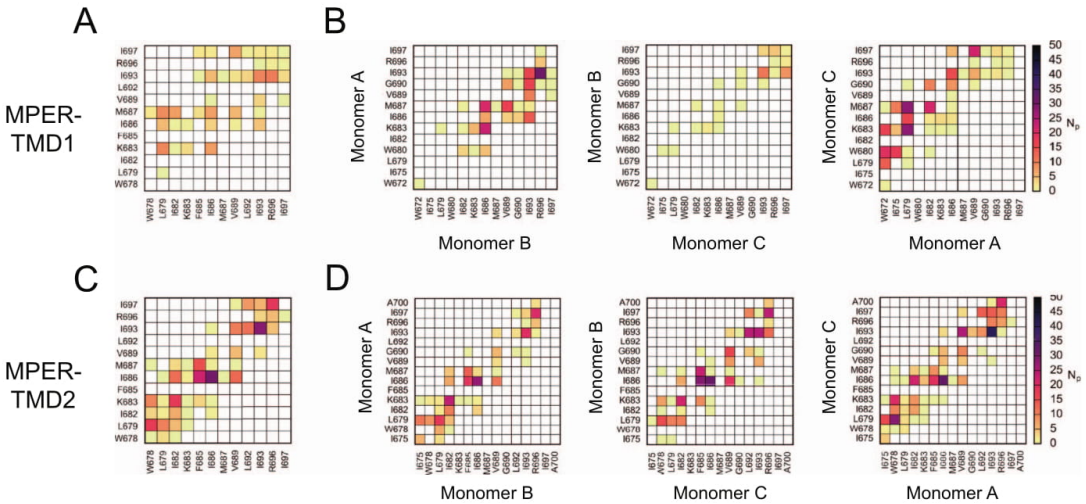

Fig. 6. Inter-helix interactions between protein residues in the MPER-TMD simulations. A) Number of interaction pairs between specific residues in the MPER-TMD1 simulation averaged over the three subunits and the trajectory. B) Deconstruction of the MPER-TMD1 residue contact map into individual helices. C) Number of interaction pairs between specific residues in the MPER-TMD2 simulation averaged over the three subunits and the trajectory. D) Deconstruction of the MPER-TMD2 residue contact map into individual helices.

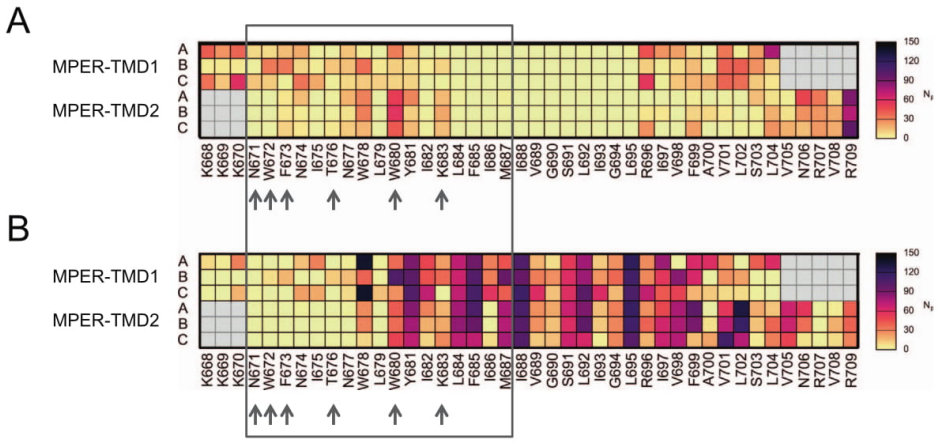

Fig. 7. Map of interactions between specific residues in the MPER-TMD simulations and the lipid membrane. Number of interaction pairs between residues in individual helices and (A) lipid head group atoms and (B) lipid tail atoms. The y-axis denotes the simulation and subunit. It is worth noting that not all residues defined on the x-axis are present in all peptides (grey areas), and specifically residues 700–704 are lysine residues in MPER-TMD1. The grey box and arrows highlight the 10E8 epitope region and the most important residues.

Table 1
Average number of interactions of 10E8 epitope residues.

Simulation	Helix	Average number of inter-helical interactions						
		N671	W672	F673	T676	W680	K683	Total
MPER-TMD1	A	0	61	0	4	8	33	106
	B	0	0	0	0	0	8	8
	C	1	0	0	11	64	57	131
MPER-TMD2	A	9	41	1	6	2	35	103
	B	6	42	0	7	3	39	97
	C	0	28	0	0	1	32	61

significantly higher for MPER-TMD1$_C$ (3.2 ± 0.3 Å) and especially, for MPER-TMD1$_N$ (4.7 ± 0.2 Å), the latter displaying a similar value to that of the MPER-TMD1 construct flanked by lysines. Similarly, two of the three helices of either N or C lysine-flanked assemblies display a significant increase in their tilt angles. However, unlike MPER-TMD2, inspection of the number of atomic interaction pairs between adjacent helical pairs in MPER-TMD1$_{no\text{-}lys}$ suggests a loss of symmetry in the latter, displaying an extensive contact interface between the CA helices (Fig. S2B), where residue pairs scoring $N_P > 15$ extend the full length of the MPER-TMD1 peptide (Fig. 8). This situation is replicated in MPER-TMD1$_N$, between helices A and B. The similarity of the evolved conformations provides evidence that truncation of the peptide at residue 700, destabilizes the symmetric trimer structure, preferring an assembly whereby two helices are closely associated, with the third attached by hydrophobic residues in the region between I682 and I693. Addition of lysine residues at the C-terminus in MPER-TMD1$_C$ and in the original MPER-TMD1 assembly flanked by lysines, promotes further destabilization of the observed 'dimer' interfaces, with the maximum number of inter-helical interactions capped at 350 (Fig. S2B), and with fewer residue pairs scoring $N_P > 15$ (Fig. 8). These results imply that truncation of the TMD causes a rearrangement of the TMD structure favoring trimer asymmetry and a dimer interface, which is partially inhibited by including lysines after A700.

When scoring interactions with lipids, a similar trend is exhibited for the three new simulations (Tables S1 and S2) and that of MPER-TMD1, regardless of the absence or presence of lysine tags, with W678 or W680 interacting with the phospholipid headgroups of the upper leaflet in at least one of the monomers in each assembly and, to a lesser extent, with K668 and K670 (MPER-TMD1$_N$, helix B) and W672 or F673 (MPER-TMD1$_C$, A and B helices, respectively). Furthermore, residues that strongly interact with the hydrophobic core of the membrane are conserved in all MPER-TMD1 simulations. Thus, due to the similar degree of insertion into the membrane of all the models, no interactions are recorded between MPER-TMD1$_{no\text{-}lys}$ or MPER-TMD1$_N$ C-terminal residues and the phospholipid headgroups in the lower leaflet, as opposed to constructs bearing lysines at the C-terminus, which display interactions through the lysine residues.

Finally, the average number of atomic interactions of the main epitope residues with adjacent helices (Table S3) and the surrounding lipids (Table S4) was calculated. In MPER-TMD1$_{no\text{-}lys}$ epitope residues in each of the three helices display an average of 60–110 interactions in total, primarily constituted of residues W672 and K683. Moreover, residue W680 displays extensive interactions with the surrounding lipid molecules. These results replicate those obtained for MPER-TMD2 and advocate that truncation to residue 700 alone is insufficient to expose the antibody epitope, despite destabilization of the symmetric trimer arrangement. In MPER-TMD1$_N$, the epitope in helix A can be considered

Table 2
Average number of lipid interactions of 10E8 epitope residues.

Simulation	Helix	Average number of lipid interactions							
		N671	W672	F673	T676	W680	K683	Total	Lipid + protein
MPER-TMD1	A	10	9	16	1	69	24	129	235
	B	2	41	50	25	117	48	283	291
	C	15	13	3	4	38	4	77	208
MPER-TMD2	A	0	0	7	2	95	33	137	240
	B	0	0	6	2	94	41	143	240
	C	0	1	11	6	92	44	154	215

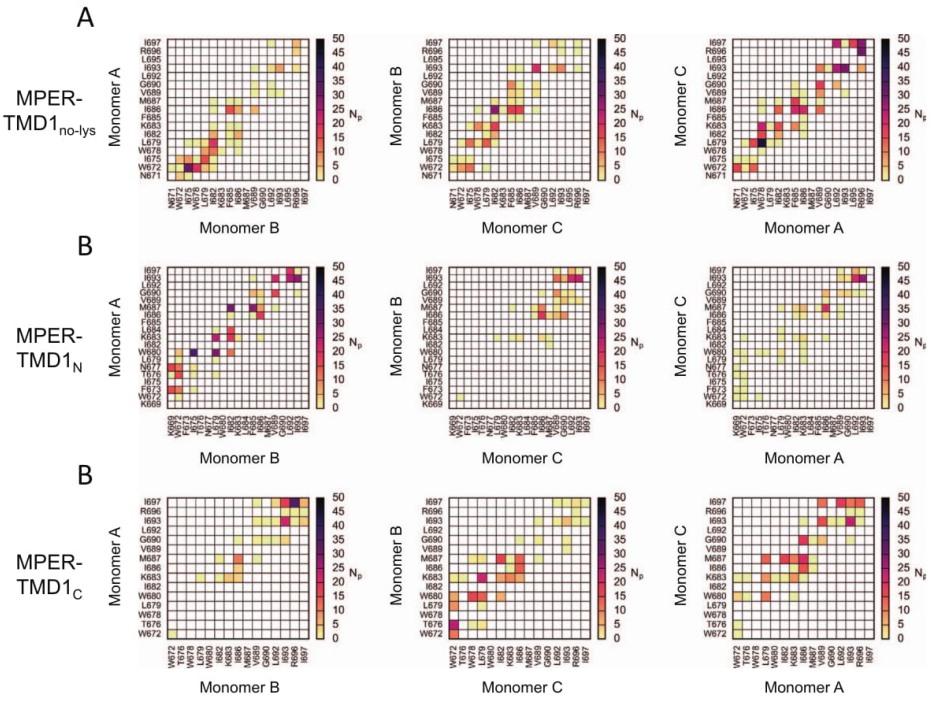

Fig. 8. Inter-helix interactions between protein residues in the MPER-TMD simulations. Number of interaction pairs between specific residues of individual helices in the A) MPER-TMD1$_{no\text{-}lys}$ simulation B) MPER-TMD1$_C$ simulation and C) MPER-TMD1$_N$ simulation.

unavailable, with nearly 200 atomic interactions in the region F673 to K683. The 50-recorded interactions for helix B primarily originate from W672. In helix C, only 10 protein interactions are observed from W680 and K683, which also dominate lipid interactions throughout. Similar to the MPER-TMD1 model flanked by lysines at both ends, these results reveal a single helix (C) where the N-terminal epitope residues (N671, W672 and F673) are exposed to solvent, engaging in minimal protein (1) and lipid (32) and might effectively interact with the antibody. Finally, in MPER-TMD$_C$, helix B displays the minimum number of protein (14) and lipid (42) interactions with such residues. These results suggest the addition of lysine residues to the N-terminus is an effective strategy for epitope exposure.

4. Discussion

In the present work, we have analyzed the effect of HIV-1 gp41 TM domain on the exposure of the MPER epitope at the surface of lipid bilayers. With this aim, we designed two MPER-TMD sequences based on previously reported mutagenesis studies of the TMD [9]: MPER-TMD1, in which the TMD was truncated at A700, and MPER-TMD2, which spans the full TMD up to R709 (Fig. 1). Given the critical role of the lipid membrane in various stages of the HIV virus cycle [56] and particularly, in the recognition of their epitopes by the antibodies 4E10 and 10E8 [30,48,57], it has been argued that not only Env structure but also its membrane environment should be preserved in the development of vaccines that aim to elicit anti-MPER antibodies targeting its C-terminal region (i.e., 4E10/10E8) [19,58]. Therefore, MPER-TMD1 and MPER-TMD2 were formulated in HIV-1 like cholesterol-enriched liposomal-vaccines [33] and immunochemical assays were performed to test the antigenicity of both candidates. The results revealed that MPER-TMD1, but not MPER-TMD2, was capable of specific and efficient antibody recognition by anti-MPER bnAbs (Figs. 2, 3 and S1). In addition, MPER-TMD1 was shown to migrate as dimers under denaturing conditions. Consistent with this behavior, reported mutagenesis studies of the TMD showed that truncation of residues 705 to 716 induced partial destabilization of the trimer [13]. Moreover, analyses of the NMR spectra of a gp41 construct terminating at residue 705 showed conformational flexibility in the CHR-MPER-TM region of gp41, pointing to the potential of this region to display conformations other than a stable trimer during the fusion process [59]. In contrast, our experimental data indicated that the longer MPER-TMD2 was reportedly more stable, demonstrated by the presence of dimers and trimers following denaturing treatment (Figs. 2, 3 and S1). This assorted dimer and trimer migration pattern was also reported for a similar peptide containing the full-length MPER (residues 661–708 plus four C-terminal lysines) incorporated into DMPC nanodiscs [29]. These results suggest that the TM domain is instrumental in the trimerization process, whereas the MPER domain does not play a significant role. However, opposing our results, high affinity recognition of bnAb 4E10 to that peptide was reported [29]. Besides N-terminal elongation and C-terminal addition of lysines, the physical and chemical properties of the selected lipids utilized in both studies were also dissimilar. The thickness of a DMPC bilayer is reported to be of around 35–37 Å [60,61], significantly thinner than that of cholesterol-enriched phospholipid bilayers [61] such as the viral envelope [33,62]. Cholesterol augments membrane physical properties such as rigidity and thickness, thereby affecting TMD helix accommodation within the lipid bilayer [63], and conceivably, modulating the MPER-scaffolding capacity, i.e., the antigenicity of the MPER-TMD constructs. This might account for the reported differences observed between the two studies and highlights the importance of the membrane composition in the design of liposomal vaccines targeting the 10E8 epitope.

The computational analysis of the candidate liposomal vaccines confirms the above experimental observations and reveals the

molecular mechanism underlying efficient epitope exposure in the MPER-TMD1 scaffold. Overall, two distinctive conformations of the MPER-TMD assemblies were observed. Whereas MPER-TMD2 closely resembles the three-fold assembly observed in the NMR structure of the HIV-1 TMD [13], the close association of the transmembrane helices is noticeably perturbed in all MPER-TMD1-based models resulting in an asymmetric assembly (Figs. 4–6, 8 and S2). Therefore, destabilization of the MPER-TMD1 trimer, can be attributed to truncation of the TMD following A700 to some extent. It should be emphasized that the residues involved in inter-helical interactions in the MPER-TMD2 trimer are all present in MPER-TMD1 assemblies; thus, it is primarily environmental interactions that influence the dynamics of the MPER-TMD derived scaffolds. Substantial interactions between V701 and L702 and the acyl tails, and between R709 and the phospholipid head groups, observed in MPER-TMD2 (Fig. 7) are lost upon truncation; thus, the observed reorientation of the helices to an asymmetric arrangement in MPER-TMD1-based assemblies can be attributed to the absence of lipid interactions with such residues. We speculate that, as previously demonstrated [9], R709 is particularly crucial for membrane anchoring, as truncation of the region following this residue results in a stable assembly, profoundly similar to the initial construct. In addition, the resulting conformation of MPER-TMD1 trimers bearing lysines accommodates for the positively charged lysine residues, which are predominantly excluded from the membrane hydrophobic core contributing to the perturbed conformation of the MPER-TMD1 trimer, the underlying α-helices and the bilayer. These effects were not detected in the MPER-TMD2 simulation, in which sequence composition, length and tilt angles are more compatible with the hydrophobic core dimensions of this bilayer. Moreover, MPER-TMD1 models devoid of lysines or with lysines at the N-terminus reveal a prominent new dimer interface indicating that TMD helices have the potential to adopt multiple conformations. It is tempting to speculate that in the context of the whole protein and due to the dynamic nature of Env [4,64,65] the TMD might suffer conformational changes, such as reorientations, variations in the tilt angles or dissociation events, which might perturb the viral envelope priming it for fusion with the cellular membrane, or alternatively, which might permit establishing interactions with TMD helices from adjacent trimers at crucial moments of the fusion cycle.

The specific molecular interactions of the residues within the epitope region might be used to rationalize the distinct antigenicity pattern of the MPER-TMD scaffolds (Tables 1, 2, and S1 and S2). Main epitope residues in MPER-TMD2 and in MPER-TMD1$_{no\text{-}lys}$ face the core of the trimer with crucial residues W672 and K683 engaged in inter-helix contacts and with W680 interacting with the lipid molecules. Although residue W680 is not essential for the binding of 4E10 and 10E8 to their epitopes in solution it is important for the viral-neutralization function of these antibodies [24,66–68]. Moreover, it was shown to modulate the immunogenicity of MPER-derived peptides by shifting the specificity of the immune response towards the N-terminus when W680 was embedded in the membrane [69]. Thus, in both models, the MPER epitope faces the interior of the trimer in a conformation that might hinder antibody recognition at membrane surfaces. These observations might have implications regarding the structure of the TMD in the context of the pre-fusion conformation of the native Env. Since the conformation of the MPER-TMD2 scaffold greatly resembles the original structure solved by NMR in bicelles [13], we hypothesize that such structure would not represent the neutralization competent structure recognized by 10E8. Consequently, the NMR structure is also likely to differ from the pre-fusion structure of the native Env which was recently solved by cryo-EM bound to two molecules of bnAb 10E8 [4]. In the case of the MPER-TMD1 construct flanked by lysines, epitope residues within each helix display a distinct interaction pattern. Epitope residues in helix B are not engaged in inter-helix interactions in helix B but are buried in the membrane, and thus, inaccessible to the antibodies. In contrast, epitope residues in helices A and C were not found to interact with lipids. However, similarly to MPER-TMD2, W672 and K683 in helix A are engaged in inter-helix interactions possibly precluding antibody recognition of the epitope. Finally, although C-terminal epitope residues W680 and K683 are interacting with residues in other helices, N-terminal epitope residues N671, W672 and F673 are fully exposed. A similar pattern is recorded for helix C in MPER-TMD1$_N$. Although both protein and lipid molecules will likely be perturbed to some extent by approach of the antibody, the data presented herein provide evidence that the epitope region undergoes conformational differences depending on the protein scaffold used to present the epitope, being considerably more likely that the antibody will recognize MPER-TMD1 or MPER-TMD1$_N$ than MPER-TMD2, MPER-TMD1$_{no\text{-}lys}$ or MPER-TMD1$_C$, where the epitope is either stably embedded in the trimer core or interacting with lipid molecules. We hypothesize that antibody recognition of the exposed epitope and subsequent binding to these peptides would require a two-step binding mechanism, in which the antibody would first approach the MPER and bind to the N-terminal residues. This interaction would conceivably alter the pre-existing inter-helix interactions at the C-terminal part of the epitope and the rest of the paratope could then be effectively accommodated.

Overall, these results suggest that inclusion of particular attributes that destabilize the trimer, i.e., truncation of the TMD, and expose the epitope, i.e., addition of N-terminal lysines, would likely aid the optimization of MPER-TMD derived peptides in the context of vaccine design. In the context of the virus, the intrinsic dynamics of Env [4] might transiently extract and expose the MPER leading to the engagement of B-cell receptors, but in the absence of these forces in the context of a minimal immunogen, MPER should be readily exposed to the immune system. In this regard, extensive mutagenesis studies, performed by Dev et al., examining the antigenic structure of the Env ectodomain [13] showed that even the most simple mutations in the TMD region (F685A, I686A, G690A, L692A, G694V, L695A, I697A) modulated the antigenic surface of Env and specifically, increased viral sensitivity to 10E8. Residues, F685, I686, L692 and I697 are involved in crucial inter-helical interactions in the MPER-TMD2 trimer only, thus it can be inferred that mutation of these residues might destabilize the canonical structure, and potentially lead to the exposure of expose the 10E8 epitope.

All in all, the immunochemical assays and in-depth MD analyses reported herein suggest that the structure-based design of effective liposomal vaccines based on the MPER-TMD might require a rational mutation strategy of the TMD along with a systematic analysis of the lipid bilayer, to achieve efficient exposure of the MPER epitope at the membrane surface. Overall, this study advances our understanding of the requirements that must be met by a liposome-based peptide-vaccine targeting this critical antigenic site on Env.

Note added in proof

Additional NMR data have been recently reported by Chiliveri et al. (J. Am. Chem. Soc. 2018, 140:34) compatible with the adoption by HIV-1 TMD (residues 677-716) of a monomeric helix structure in DMPC:DHPC (1:2, mol:mol) bicelles.

Transparency document

The http://dx.doi.org/10.1016/j.bbamem.2018.02.019 associated with this article can be found, in the online version.

Acknowledgments

Computational resources were awarded through RES in Magerit based in Spain at CeSViMa – Universidad Politécnica de Madrid. We thank RES for providing computational resources and technical support. We acknowledge the financial support of the Spanish Government (MINECO Grant BIO2015-64421-R) and the Basque Government (Grant IT838-13). BA was recipient of a post-graduate Grant (ESPDOC2015) from the University of the Basque Country (UPV/EHU), VO was

supported by a CASE studentship (BB/L015269/1) funded by BBSRC and Pfizer Neusentis and E.R. was recipient of a predoctoral fellowship (PRE_2014_2_264) from the Basque Government.

Author contributions

J.L.N, B.A., and CD conceived the research and designed the experiments; V.O. performed and analized the MD simulations. J.T. and B.A. performed and analyzed biophysical and immunochemical characterizations; E.R. produced the Fabs. V.O., C.D. and B.A. wrote the paper; all authors critically revised the manuscript and all authors approved it. The authors thank Dr. Sánchez-Eugenia for valuable discussions and technical advice.

Appendix A. Supplementary data

Supplementary data to this article can be found online at https://doi.org/10.1016/j.bbamem.2018.02.019.

References

[1] D. Lyumkis, J.P. Julien, N. de Val, A. Cupo, C.S. Potter, P.J. Klasse, D.R. Burton, R.W. Sanders, J.P. Moore, B. Carragher, I.A. Wilson, A.B. Ward, Cryo-EM structure of a fully glycosylated soluble cleaved HIV-1 envelope trimer, Science 342 (2013) 1484–1490, http://dx.doi.org/10.1126/science.1245627.
[2] J.P. Julien, A. Cupo, D. Sok, R.L. Stanfield, D. Lyumkis, M.C. Deller, P.J. Klasse, D.R. Burton, R.W. Sanders, J.P. Moore, A.B. Ward, I.A. Wilson, Crystal structure of a soluble cleaved HIV-1 envelope trimer, Science 342 (2013) 1477–1483, http://dx.doi.org/10.1126/science.1245625.
[3] M. Pancera, T. Zhou, A. Druz, I.S. Georgiev, C. Soto, J. Gorman, J. Huang, P. Acharya, G.Y. Chuang, G. Ofek, G.B. Stewart-Jones, J. Stuckey, R.T. Bailer, M.G. Joyce, M.K. Louder, N. Tumba, Y. Yang, B. Zhang, M.S. Cohen, B.F. Haynes, J.R. Mascola, L. Morris, J.B. Munro, S.C. Blanchard, W. Mothes, M. Connors, P.D. Kwong, Structure and immune recognition of trimeric pre-fusion HIV-1 Env, Nature 514 (2014) 455–461, http://dx.doi.org/10.1038/nature13808.
[4] J.H. Lee, G. Ozorowski, A.B. Ward, Cryo-EM structure of a native, fully glycosylated, cleaved HIV-1 envelope trimer, Science 351 (2016) 1043–1048, http://dx.doi.org/10.1126/science.aad2450.
[5] G. Ozorowski, J. Pallesen, N. de Val, D. Lyumkis, C.A. Cottrell, J.L. Torres, J. Copps, R.L. Stanfield, A. Cupo, P. Pugach, J.P. Moore, I.A. Wilson, A.B. Ward, Open and closed structures reveal allostery and pliability in the HIV-1 envelope spike, Nature 547 (2017) 360–363, http://dx.doi.org/10.1038/nature23010.
[6] A.B. Ward, I.A. Wilson, The HIV-1 envelope glycoprotein structure: nailing down a moving target, Immunol. Rev. 275 (2017) 21–32, http://dx.doi.org/10.1111/imr.12507.
[7] J.W. Dubay, S.J. Roberts, B.H. Hahn, E. Hunter, Truncation of the human immunodeficiency virus type 1 transmembrane glycoprotein cytoplasmic domain blocks virus infectivity, J. Virol. 66 (1992) 6616–6625.
[8] D. Gabuzda, U. Olshevsky, P. Bertani, W.A. Haseltine, J. Sodroski, Identification of membrane anchorage domains of the HIV-1 gp160 envelope glycoprotein precursor, J. Acquir. Immune Defic. Syndr. 4 (1991) 34–40, http://dx.doi.org/10.1097/00126334-199101000-00005.
[9] L. Yue, L. Shang, E. Hunter, Truncation of the membrane-spanning domain of human immunodeficiency virus type 1 envelope glycoprotein defines elements required for fusion, incorporation, and infectivity, J. Virol. 83 (2009) 11588–11598, http://dx.doi.org/10.1128/jvi.00914-09.
[10] L. Shang, L. Yue, E. Hunter, Role of the membrane-spanning domain of human immunodeficiency virus type 1 envelope glycoprotein in cell-cell fusion and virus infection, J. Virol. 82 (2008) 5417–5428, http://dx.doi.org/10.1128/JVI.02666-07.
[11] R.J. Owens, C. Burke, J.K. Rose, Mutations in the membrane-spanning domain of the human immunodeficiency virus envelope glycoprotein that affect fusion activity, J. Virol. 68 (1994) 570–574.
[12] B. Apellaniz, J.L. Nieva, Fusion-competent state induced by a C-terminal HIV-1 fusion peptide in cholesterol-rich membranes, Biochim. Biophys. Acta 1848 (2015) 1014–1022, http://dx.doi.org/10.1016/j.bbamem.2015.01.011.
[13] J. Dev, D. Park, Q. Fu, J. Chen, H.J. Ha, F. Ghantous, T. Herrmann, W. Chang, Z. Liu, G. Frey, M.S. Seaman, B. Chen, J.J. Chou, Structural basis for membrane anchoring of HIV-1 envelope spike, Science 353 (2016) 172–175, http://dx.doi.org/10.1126/science.aaf7066.
[14] K. Miyauchi, J. Komano, Y. Yokomaku, W. Sugiura, N. Yamamoto, Z. Matsuda, Role of the specific amino acid sequence of the membrane-spanning domain of human immunodeficiency virus type 1 in membrane fusion, J. Virol. 79 (2005) 4720–4729, http://dx.doi.org/10.1128/JVI.79.8.4720-4729.2005.
[15] A. Ashkenazi, O. Faingold, Y. Shai, HIV-1 fusion protein exerts complex immunosuppressive effects, Trends Biochem. Sci. 38 (2013) 345–349, http://dx.doi.org/10.1016/j.tibs.2013.04.003.
[16] E. Rotem, E.M. Reuven, Y.A. Klug, Y. Shai, The transmembrane domain of HIV-1 gp41 inhibits T-cell activation by targeting multiple T-cell receptor complex components through its GxxxG motif, Biochemistry 55 (2016) 1049–1057, http://dx.doi.org/10.1021/acs.biochem.5b01307.
[17] E.M. Reuven, M. Ali, E. Rotem, R. Schwarzter, A. Gramatica, A.H. Futerman, Y. Shai, The HIV-1 envelope transmembrane domain binds TLR2 through a distinct dimerization motif and inhibits TLR2-mediated responses, PLoS Pathog. 10 (2014) e1004248, , http://dx.doi.org/10.1371/journal.ppat.1004248.
[18] Y.A. Klug, E. Rotem, R. Schwarzer, Y. Shai, Mapping out the intricate relationship of the HIV envelope protein and the membrane environment, Biochim. Biophys. Acta 1859 (2017) 550–560, http://dx.doi.org/10.1016/j.bbamem.2016.10.012.
[19] B. Apellaniz, J.L. Nieva, The use of liposomes to shape epitope structure and modulate immunogenic responses of peptide vaccines against HIV MPER, Adv. Protein Chem. Struct. Biol. 99 (2015) 15–54, http://dx.doi.org/10.1016/bs.apcsb.2015.03.002.
[20] M. Montero, N.E. van Houten, X. Wang, J.K. Scott, The membrane-proximal external region of the human immunodeficiency virus type 1 envelope: dominant site of antibody neutralization and target for vaccine design, Microbiol. Mol. Biol. Rev. 72 (2008) 54–84, http://dx.doi.org/10.1128/MMBR.00020-07.
[21] L.E. McCoy, D.R. Burton, Identification and specificity of broadly neutralizing antibodies against HIV, Immunol. Rev. 275 (2017) 11–20, http://dx.doi.org/10.1111/imr.12484.
[22] N. Cerutti, J.L. Loredo-Varela, C. Caillat, W. Weissenhorn, Antigp41 membrane proximal external region antibodies and the art of using the membrane for neutralization, Curr. Opin. HIV AIDS 12 (2017) 250–256, http://dx.doi.org/10.1097/COH.0000000000000364.
[23] G. Stiegler, R. Kunert, M. Purtscher, S. Wolbank, R. Voglauer, F. Steindl, H. Katinger, A potent cross-clade neutralizing human monoclonal antibody against a novel epitope on gp41 of human immunodeficiency virus type 1, AIDS Res. Hum. Retrovir. 17 (2001) 1757–1765, http://dx.doi.org/10.1089/08892220152741450.
[24] J. Huang, G. Ofek, L. Laub, M.K. Louder, N.A. Doria-Rose, N.S. Longo, H. Imamichi, R.T. Bailer, B. Chakrabarti, S.K. Sharma, S.M. Alam, T. Wang, Y. Yang, B. Zhang, S.A. Migueles, R. Wyatt, B.F. Haynes, P.D. Kwong, J.R. Mascola, M. Connors, Broad and potent neutralization of HIV-1 by a gp41-specific human antibody, Nature 491 (2012) 406–412, http://dx.doi.org/10.1038/nature11544.
[25] A. Irimia, A.M. Serra, A. Sarkar, R. Jacak, O. Kalyuzhniy, D. Sok, K.L. Saye-Francisco, T. Schiffner, R. Tingle, M. Kubitz, Y. Adachi, R.L. Stanfield, M.C. Deller, D.R. Burton, W.R. Schief, I.A. Wilson, Lipid interactions and angle of approach to the HIV-1 viral membrane of broadly neutralizing antibody 10E8: insights for vaccine and therapeutic design, PLoS Pathog. 13 (2017) e1006212, , http://dx.doi.org/10.1371/journal.ppat.1006212.
[26] M. Montero, N. Gulzar, K.A. Klaric, J.E. Donald, C. Lepik, S. Wu, S. Tsai, J.P. Julien, A.J. Hessell, S. Wang, S. Lu, D.R. Burton, E.F. Pai, W.F. Degrado, J.K. Scott, Neutralizing epitopes in the membrane-proximal external region of HIV-1 gp41 are influenced by the transmembrane domain and the plasma membrane, J. Virol. 86 (2012) 2930–2941, http://dx.doi.org/10.1128/JVI.06349-11.
[27] B. Apellaniz, E. Rujas, P. Carravilla, J. Requejo-Isidro, N. Huarte, C. Domene, J.L. Nieva, Cholesterol-dependent membrane fusion induced by the gp41 membrane-proximal external region-transmembrane domain connection suggests a mechanism for broad HIV-1 neutralization, J. Virol. 88 (2014) 13367–13377, http://dx.doi.org/10.1128/JVI.02151-14.
[28] B. Apellaniz, E. Rujas, S. Serrano, K. Morante, K. Tsumoto, J.M. Caaveiro, M.A. Jimenez, J.L. Nieva, The atomic structure of the HIV-1 gp41 transmembrane domain and its connection to the immunogenic membrane-proximal external region, J. Biol. Chem. 290 (2015) 12999–13015, http://dx.doi.org/10.1074/jbc.M115.644351.
[29] T.M. Reichart, M.M. Baksh, J.K. Rhee, J.D. Fiedler, S.G. Sligar, M.G. Finn, M.B. Zwick, P.E. Dawson, Trimerization of the HIV transmembrane domain in lipid bilayers modulates broadly neutralizing antibody binding, Angew. Chem. Int. Ed. Eng. 55 (2016) 2688–2692, http://dx.doi.org/10.1002/anie.201508421.
[30] E. Rujas, J.M. Caaveiro, A. Partida-Hanon, N. Gulzar, K. Morante, B. Apellaniz, M. Garcia-Porras, M. Bruix, K. Tsumoto, J.K. Scott, M.A. Jimenez, J.L. Nieva, Structural basis for broad neutralization of HIV-1 through the molecular recognition of 10E8 helical epitope at the membrane interface, Sci. Rep. 6 (2016) 38177, http://dx.doi.org/10.1038/srep38177.
[31] Z.Y. Sun, K.J. Oh, M. Kim, J. Yu, V. Brusic, L. Song, Z. Qiao, J.H. Wang, G. Wagner, E.L. Reinherz, HIV-1 broadly neutralizing antibody extracts its epitope from a kinked gp41 ectodomain region on the viral membrane, Immunity 28 (2008) 52–63, http://dx.doi.org/10.1016/j.immuni.2007.11.018.
[32] N. Huarte, M. Lorizate, R. Maeso, R. Kunert, R. Arranz, J.M. Valpuesta, J.L. Nieva, The broadly neutralizing anti-human immunodeficiency virus type 1 4E10 monoclonal antibody is better adapted to membrane-bound epitope recognition and blocking than 2F5, J. Virol. 82 (2008) 8986–8996, http://dx.doi.org/10.1128/JVI.00846-08.
[33] B. Brugger, B. Glass, P. Haberkant, I. Leibrecht, F.T. Wieland, H.G. Krausslich, The HIV lipidome: a raft with an unusual composition, Proc. Natl. Acad. Sci. U. S. A. 103 (2006) 2641–2646, http://dx.doi.org/10.1073/pnas.0511136103.
[34] J.A. Yethon, R.F. Epand, B. Leber, R.M. Epand, D.W. Andrews, Interaction with a membrane surface triggers a reversible conformational change in Bax normally associated with induction of apoptosis, J. Biol. Chem. 278 (2003) 48935–48941, http://dx.doi.org/10.1074/jbc.M306289200.
[35] S. Jo, T. Kim, V.G. Iyer, W. Im, CHARMM-GUI: a web-based graphical user interface for CHARMM, J. Comput. Chem. 29 (2008) 1859–1865, http://dx.doi.org/10.1002/jcc.20945.
[36] S. Jo, J.B. Lim, J.B. Klauda, W. Im, CHARMM-GUI membrane builder for mixed bilayers and its application to yeast membranes, Biophys. J. 97 (2009) 50–58, http://dx.doi.org/10.1016/j.bpj.2009.04.013.
[37] E.L. Wu, X. Cheng, S. Jo, H. Rui, K.C. Song, E.M. Davila-Contreras, Y. Qi, J. Lee, V. Monje-Galvan, R.M. Venable, J.B. Klauda, W. Im, CHARMM-GUI membrane

builder toward realistic biological membrane simulations, J. Comput. Chem. 35 (2014) 1997–2004, http://dx.doi.org/10.1002/jcc.23702.
[38] J.C. Phillips, R. Braun, W. Wang, J. Gumbart, E. Tajkhorshid, E. Villa, C. Chipot, R.D. Skeel, L. Kale, K. Schulten, Scalable molecular dynamics with NAMD, J. Comput. Chem. 26 (2005) 1781–1802, http://dx.doi.org/10.1002/jcc.20289.
[39] J.B. Klauda, R.M. Venable, J.A. Freites, J.W. O'Connor, D.J. Tobias, C. Mondragon-Ramirez, I. Vorobyov, A.D. MacKerell Jr., R.W. Pastor, Update of the CHARMM all-atom additive force field for lipids: validation on six lipid types, J. Phys. Chem. B 114 (2010) 7830–7843, http://dx.doi.org/10.1021/jp101759q.
[40] W.L. Jorgensen, J. Chandrasekhar, J.D. Madura, R.W. Impey, M.L. Klein, Comparison of simple potential functions for simulating liquid water, J. Chem. Phys. 79 (1983) 926–935, http://dx.doi.org/10.1063/1.445869.
[41] D. Beglov, B. Roux, Finite representation of an infinite bulk system: solvent boundary potential for computer simulations, J. Chem. Phys. 100 (1994) 9050–9063, http://dx.doi.org/10.1063/1.466711.
[42] T. Darden, D. York, L. Pedersen, Particle mesh Ewald: an N·log(N) method for Ewald sums in large systems, J. Chem. Phys. 98 (1993) 10089–10092, http://dx.doi.org/10.1063/1.464397.
[43] L. Verlet, Computer "experiments" on classical fluids. I. Thermodynamical properties of Lennard-Jones molecules, Phys. Rev. 159 (1967) 98–103.
[44] S. Miyamoto, P.A. Kollman, SETTLE: an analytical version of the SHAKE and RATTLE algorithm for rigid water models, J. Comput. Chem. 13 (1992) 952–962, http://dx.doi.org/10.1002/jcc.540130805.
[45] S.E. Feller, Y. Zhang, R.W. Pastor, B.R. Brooks, Constant pressure molecular dynamics simulation: the Langevin piston method, J. Chem. Phys. 103 (1995) 4613–4621, http://dx.doi.org/10.1063/1.470648.
[46] G.J. Martyna, D.J. Tobias, M.L. Klein, Constant pressure molecular dynamics algorithms, J. Chem. Phys. 101 (1994) 4177–4189, http://dx.doi.org/10.1063/1.467468.
[47] W. Humphrey, A. Dalke, K. Schulten, VMD: visual molecular dynamics, J. Mol. Graph. 14 (1996) 33–38, http://dx.doi.org/10.1016/0263-7855(96)00018-5.
[48] E. Rujas, S. Insausti, M. Garcia-Porras, R. Sanchez-Eugenia, K. Tsumoto, J.L. Nieva, J.M. Caaveiro, Functional contacts between MPER and the anti-HIV-1 broadly neutralizing antibody 4E10 extend into the core of the membrane, J. Mol. Biol. 429 (2017) 1213–1226, http://dx.doi.org/10.1016/j.jmb.2017.03.008.
[49] E. Rujas, N. Gulzar, K. Morante, K. Tsumoto, J.K. Scott, J.L. Nieva, J.M. Caaveiro, Structural and thermodynamic basis of epitope binding by neutralizing and non-neutralizing forms of the anti-HIV-1 antibody 4E10, J. Virol. 89 (2015) 11975–11989, http://dx.doi.org/10.1128/JVI.01793-15.
[50] O.K. Haffar, D.J. Dowbenko, P.W. Berman, Topogenic analysis of the human immunodeficiency virus type 1 envelope glycoprotein, gp160, in microsomal membranes, J. Cell Biol. 107 (1988) 1677–1687, http://dx.doi.org/10.1083/jcb.107.5.1677.
[51] F.M. Brunel, M.B. Zwick, R.M. Cardoso, J.D. Nelson, I.A. Wilson, D.R. Burton, P.E. Dawson, Structure-function analysis of the epitope for 4E10, a broadly neutralizing human immunodeficiency virus type 1 antibody, J. Virol. 80 (2006) 1680–1687, http://dx.doi.org/10.1128/JVI.80.4.1680-1687.2006.
[52] R. Abe, J.M. Caaveiro, H. Kozuka-Hata, M. Oyama, K. Tsumoto, Mapping ultra-weak protein-protein interactions between heme transporters of *Staphylococcus aureus*, J. Biol. Chem. 287 (2012) 16477–16487, http://dx.doi.org/10.1074/jbc.M112.346700.
[53] T.S. Young, I. Ahmad, J.A. Yin, P.G. Schultz, An enhanced system for unnatural amino acid mutagenesis in *E. coli*, J. Mol. Biol. 395 (2010) 361–374, http://dx.doi.org/10.1016/j.jmb.2009.10.030.
[54] S.H. White, Translocons, thermodynamics, and the folding of membrane proteins, FEBS Lett. 555 (2003) 116–121.
[55] B. Apellaniz, S. Nir, J.L. Nieva, Distinct mechanisms of lipid bilayer perturbation induced by peptides derived from the membrane-proximal external region of HIV-1 gp41, Biochemistry 48 (2009) 5320–5331, http://dx.doi.org/10.1021/bi900504t.
[56] E.O. Freed, HIV-1 assembly, release and maturation, Nat. Rev. Microbiol. 13 (2015) 484–496, http://dx.doi.org/10.1038/nrmicro3490.
[57] E. Rujas, J.M. Caaveiro, S. Insausti, M. Garcia-Porras, K. Tsumoto, J.L. Nieva, Peripheral membrane interactions boost the engagement by an anti-HIV-1 broadly neutralizing antibody, J. Biol. Chem. 292 (2017) 5571–5583, http://dx.doi.org/10.1074/jbc.M117.775429.
[58] A. Irimia, A. Sarkar, R.L. Stanfield, I.A. Wilson, Crystallographic identification of lipid as an integral component of the epitope of HIV broadly neutralizing antibody 4E10, Immunity 44 (2016) 21–31, http://dx.doi.org/10.1016/j.immuni.2015.12.001.
[59] N.A. Lakomek, J.D. Kaufman, S.J. Stahl, J.M. Louis, A. Grishaev, P.T. Wingfield, A. Bax, Internal dynamics of the homotrimeric HIV-1 viral coat protein gp41 on multiple time scales, Angew. Chem. Int. Ed. Eng. 52 (2013) 3911–3915, http://dx.doi.org/10.1002/anie.201207266.
[60] N. Kucerka, M.P. Nieh, J. Katsaras, Fluid phase lipid areas and bilayer thicknesses of commonly used phosphatidylcholines as a function of temperature, Biochim. Biophys. Acta 1808 (2011) 2761–2771, http://dx.doi.org/10.1016/j.bbamem.2011.07.022.
[61] J. Pan, T.T. Mills, S. Tristram-Nagle, J.F. Nagle, Cholesterol perturbs lipid bilayers nonuniversally, Phys. Rev. Lett. 100 (2008) 198103, http://dx.doi.org/10.1103/PhysRevLett.100.198103.
[62] N. Huarte, P. Carravilla, A. Cruz, M. Lorizate, J.A. Nieto-Garai, H.G. Krausslich, J. Perez-Gil, J. Requejo-Isidro, J.L. Nieva, Functional organization of the HIV lipid envelope, Sci. Rep. 6 (2016) 34190, http://dx.doi.org/10.1038/srep34190.
[63] T.J. McIntosh, S.A. Simon, Bilayers as protein solvents: role of bilayer structure and elastic properties, J. Gen. Physiol. 130 (2007) 225–227, http://dx.doi.org/10.1085/jgp.200709841.
[64] J.B. Munro, J. Gorman, X. Ma, Z. Zhou, J. Arthos, D.R. Burton, W.C. Koff, J.R. Courter, A.B. Smith 3rd, P.D. Kwong, S.C. Blanchard, W. Mothes, Conformational dynamics of single HIV-1 envelope trimers on the surface of native virions, Science 346 (2014) 759–763, http://dx.doi.org/10.1126/science.1254426.
[65] J.B. Munro, W. Mothes, Structure and dynamics of the native HIV-1 Env trimer, J. Virol. 89 (2015) 5752–5755, http://dx.doi.org/10.1128/JVI.03187-14.
[66] M.B. Zwick, R. Jensen, S. Church, M. Wang, G. Stiegler, R. Kunert, H. Katinger, D.R. Burton, Anti-human immunodeficiency virus type 1 (HIV-1) antibodies 2F5 and 4E10 require surprisingly few crucial residues in the membrane-proximal external region of glycoprotein gp41 to neutralize HIV-1, J. Virol. 79 (2005) 1252–1261, http://dx.doi.org/10.1128/JVI.79.2.1252-1261.2005.
[67] T. Bradley, A. Trama, N. Tumba, E. Gray, X. Lu, N. Madani, F. Jahanbakhsh, A. Eaton, S.M. Xia, R. Parks, K.E. Lloyd, L.L. Sutherland, R.M. Scearce, C.M. Bowman, S. Barnett, S.S. Abdool-Karim, S.D. Boyd, B. Melillo, A.B. Smith, J. Sodroski 3rd, T.B. Kepler, S.M. Alam, F. Gao, M. Bonsignori, H.X. Liao, M.A. Moody, D. Montefiori, S. Santra, L. Morris, B.F. Haynes, Amino acid changes in the HIV-1 gp41 membrane proximal region control virus neutralization sensitivity, EBioMedicine 12 (2016) 196–207, http://dx.doi.org/10.1016/j.ebiom.2016.08.045.
[68] K.J. Nakamura, J.S. Gach, L. Jones, K. Semrau, J. Walter, F. Bibollet-Ruche, J.M. Decker, L. Heath, W.D. Decker, M. Sinkala, C. Kankasa, D. Thea, J. Mullins, L. Kuhn, M.B. Zwick, G.M. Aldrovandi, 4E10-resistant HIV-1 isolated from four subjects with rare membrane-proximal external region polymorphisms, PLoS One 5 (2010) e9786, , http://dx.doi.org/10.1371/journal.pone.0009786.
[69] M. Kim, L. Song, J. Moon, Z.Y. Sun, A. Bershteyn, M. Hanson, D. Cain, S. Goka, G. Kelsoe, G. Wagner, D. Irvine, E.L. Reinherz, Immunogenicity of membrane-bound HIV-1 gp41 membrane-proximal external region (MPER) segments is dominated by residue accessibility and modulated by stereochemistry, J. Biol. Chem. 288 (2013) 31888–31901, http://dx.doi.org/10.1074/jbc.M113.494609.

B.3.3 Supporting Information

Supplementary Material

Exposure of the HIV-1 broadly neutralizing antibody 10E8 MPER epitope on the membrane surface by gp41 transmembrane domain scaffolds

Victoria Oakes[a], *Johana Torralba*[b], *Edurne Rujas*[b], *José L. Nieva*[b], *Carmen Domene*[c,d,*], *and Beatriz Apellaniz*[b,**]

[a] Department of Chemistry, Britannia House, 7 Trinity Street, King's College London, London SE1 1DB, UK.
[b] Biofisika Institute (CSIC, UPV/EHU) and Biochemistry and Molecular Biology Department, University of the Basque Country (UPV/EHU), PO Box 644, 48080 Bilbao, Spain.
[c] Department of Chemistry, 1 South Building, Claverton Down Road, University of Bath, Bath BA2 7AY, UK.
[d] Chemistry Research Laboratory, Mansfield Road, University of Oxford, Oxford OX1 3TA, UK.

*Correspondence to: C. Domene, Department of Chemistry, 1 South Building, Claverton Down Road, University of Bath, Bath BA2 7AY, UK. E-mail: C.Domene@bath.ac.uk

**Correspondence to: B. Apellaniz, Departamento de Fisiología, Facultad de Farmacia, Universidad del País Vasco (UPV/EHU), Paseo de la Universidad, 7, 01006 Vitoria-Gasteiz, Spain. Telephone: 0034 94 5013438. E-mail: beatriz.apellaniz@ehu.eus

Figure S1: Association of 4E10 Fab and its mutant version to MPER-TMD1 and MPER-TMD2 reconstituted into cholesterol-enriched vesicles proved by ultracentrifugation in a sucrose gradient. POPC:Chol:PA 10:11:1 (mol:mol) liposomes containing 0.5 mol% of Rho-PE were reconstituted without peptide (A) or with 30 μM MPER-TMD1 (B) or MPER-TMD2 (C) at a 1:50 peptide-to-lipid molar ratio and were incubated for 15 min at RT and under constant stirring (800 rpm) with 0.07 mg/mL of 4E10 or 4E10 Δloop Fabs (from left to right). The samples were then subjected to ultracentrifugation in a sucrose gradient and harvested in 5 fractions. Peptides (10 kDa bands) and bound or unbound Fabs (25 kDa bands) were size-separated by tricine-PAGE-SDS and proved by Western blot. Effective flotation of the vesicles was monitored following the fluorescence emission of the rhodamine probe included in the liposomes as depicted by the spectra below each panel.

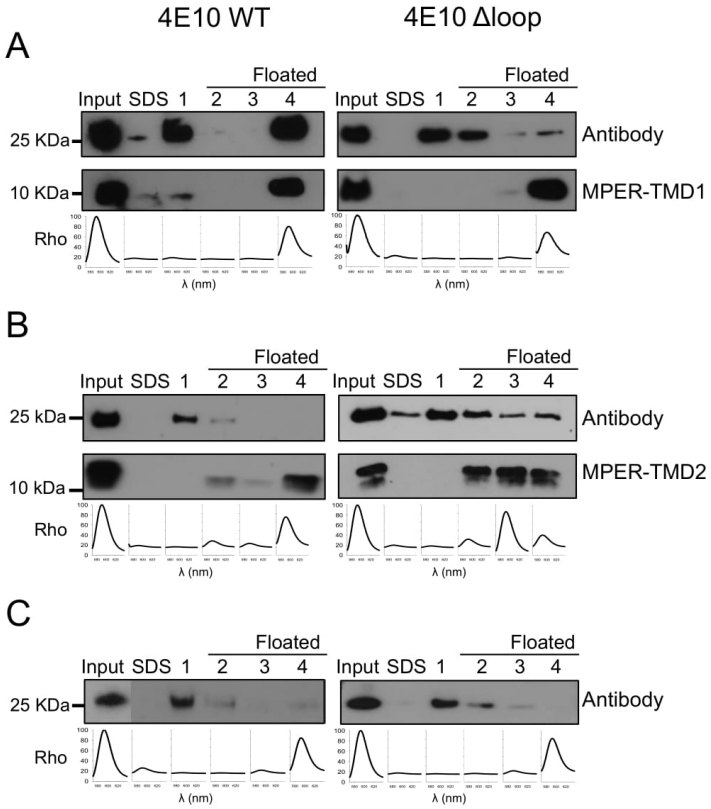

Figure S2. Overall stability of the MPER-TM domain in simulations. A) RMSD of the MPER-TM domain residues 671 to 690 in the MPER-TMD1$_{no\text{-}lys}$ (blue), MPER-TMD1$_C$ (green) and MPER-TMD1$_N$ (red) models over the course of the simulations. B) Average number of interaction pairs between subunit pairs in the MPER-TMD1$_{no\text{-}lys}$ (blue), MPER-TMD1$_N$ (red), MPER-TMD1$_C$ (green) and the initial model (yellow outline) averaged from frames at 50 ps intervals. An interaction pair is counted if the distance between two atoms is less than 4 Å. C) Tilt angle (τ) of individual helices (residues 671 to 690) with respect to the bilayer normal over the course of the simulations. Each helix of the trimers is displayed in a different color (A-C helices, purple, pink and orange, respectively). The inset data represent the average tilt angle of each individual helix in the final 100 ns of the simulation.

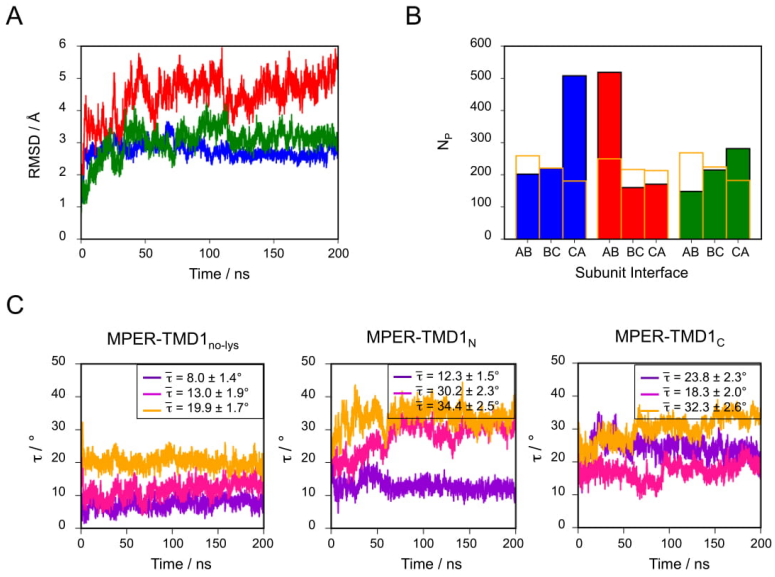

Table S1. Summary of the most prominent residues interacting with phospholipid headgroups.

Simulation	Helix	Headgroup Interactions (N_P>25)	
		Upper Leaflet	Lower Leaflet
MPER-TMD1$_{no\text{-}lys}$	A		
	B	W678 W680	
	C	W680	
MPER-TMD1$_N$	A	W678	R696 F699
	B	K668 K670 W680	A700
	C	W680	
MPER-TMD1$_C$	A	W672 W680	K702
	B	F673	K701 K702 K704
	C		R696 K701 K702

Table S2. Summary of the most prominent residues interacting with acyl chains.

Simulation	Helix	Acyl Tail Interactions (N_P>70)
MPER-TMD1$_{no-lys}$	A	W680 Y681 K683 L684 M687 I688 L695 I697 V698
	B	Y681 L684 F685 M687 I688 L692 L695 I697 V698 F699
	C	W678 Y681 L684 F685 I688 L692 L695 V698 F699
MPER-TMD1$_{N}$	A	Y681 I682 F685 I688 L695 V698
	B	W678 Y681 L684 M687 I688 L695 I697 V698
	C	W678 Y681 I682 L684 F685 I688 L695 I697 V698 F699
MPER-TMD1$_{C}$	A	W678 Y681 L684 F685 I688 L692 L695 V698 F699
	B	W678 Y681 I682 F685 I688 L692 L695 V698 F699
	C	W678 Y681 F685 I688 L692 L695 V698 F699

Table S3. Average number of inter-helical interactions of 10E8 epitope residues.

Simulation	Helix	Average Number of Inter-Helical Interactions						
		N671	W672	F673	T676	W680	K683	Total
MPER-TMD1$_{no-lys}$	A	22	62	0	0	0	1	**85**
	B	0	32	0	1	0	30	**62**
	C	3	48	0	1	1	54	**107**
MPER-TMD1$_{N}$	A	0	2	26	16	96	57	**197**
	B	0	44	0	0	0	7	**51**
	C	0	1	0	0	3	6	**10**
MPER-TMD1$_{C}$	A	0	4	0	28	0	29	**61**
	B	0	11	3	0	47	51	**112**
	C	0	55	0	0	15	28	**98**

Table S4. Average number of lipid interactions of 10E8 epitope residues.

Simulation	Helix	Average Number of Lipid Interactions							
		N671	W672	F673	T676	W680	K683	Total	Lipid + Protein
MPER-TMD1$_{no-lys}$	A	0	15	20	13	135	94	**277**	**362**
	B	0	0	8	3	99	43	**153**	**215**
	C	0	0	7	3	93	27	**130**	**237**
MPER-TMD1$_{N}$	A	1	0	0	0	33	20	**54**	**251**
	B	17	0	4	2	104	61	**188**	**239**
	C	6	17	9	1	71	46	**150**	**160**
MPER-TMD1$_{C}$	A	25	48	13	3	91	12	**192**	**254**
	B	5	1	36	1	66	8	**117**	**229**
	C	30	7	6	1	46	1	**91**	**189**